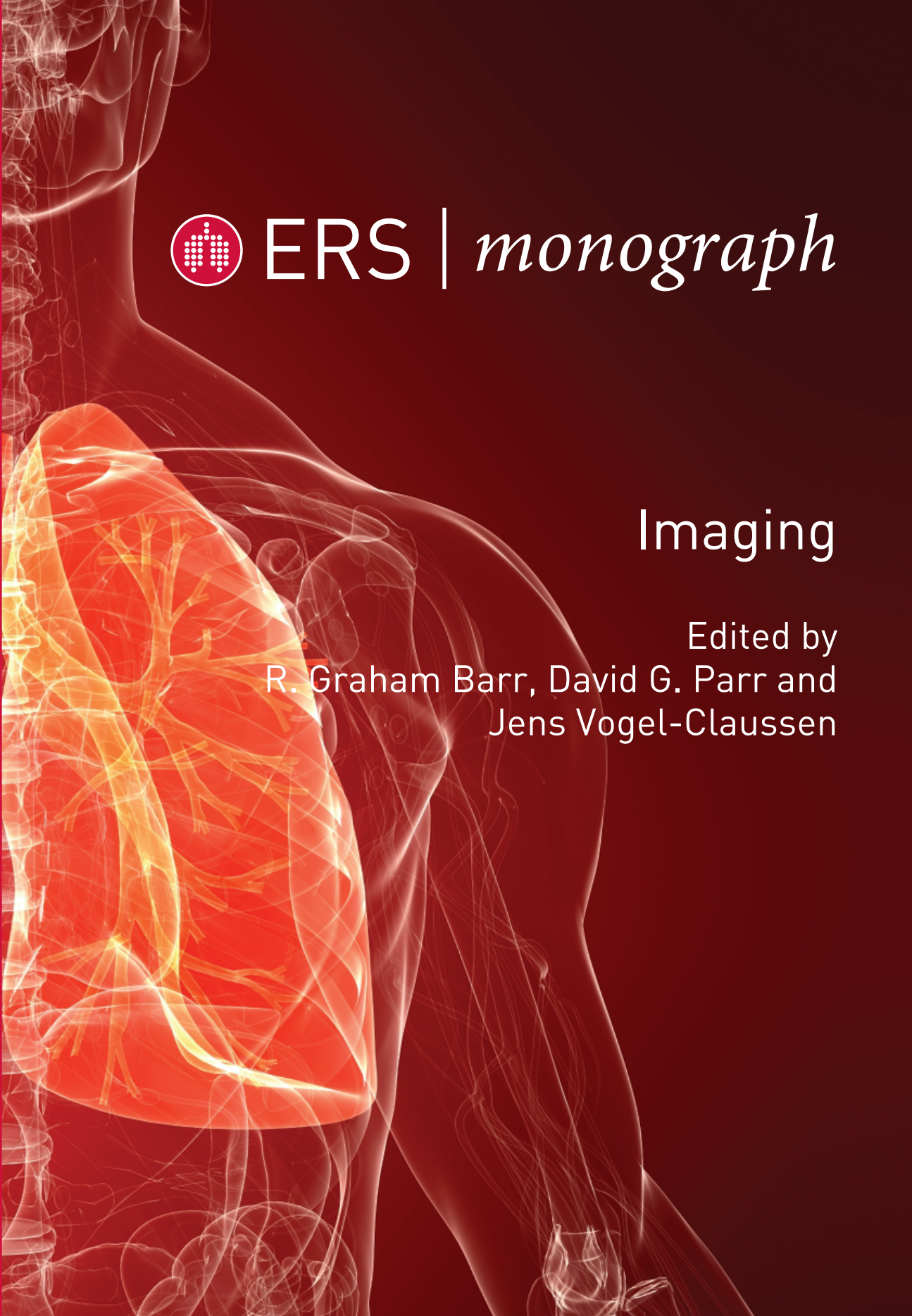

ERS | *monograph*

Imaging

Edited by
R. Graham Barr, David G. Parr and
Jens Vogel-Claussen

Imaging

Edited by
R. Graham Barr, David G. Parr
and Jens Vogel-Claussen

Editor in Chief
Robert Bals

This book is one in a series of *ERS Monographs*. Each individual issue provides a comprehensive overview of one specific clinical area of respiratory health, communicating information about the most advanced techniques and systems required for its investigation. It provides factual and useful scientific detail, drawing on specific case studies and looking into the diagnosis and management of individual patients. Previously published titles in this series are listed at the back of this *Monograph*.

ERS Monographs are available online at www.erspublications.com and print copies are available from www.ersbookshop.com

Continuing medical education (CME) credits are available through many issues of the *ERS Monograph*. Following evaluation, successful *Monographs* are accredited by the European Board for Accreditation in Pneumology (EBAP) for 5 CME credits. To earn CME credits, read the book of your choice (it is clearly indicated on the online table of contents whether CME credits are available) then complete the CME question form that is available at www.ers-education.org/e-learning/cme-tests.aspx

Editorial Board: Antonio Anzueto (San Antonio, TX, USA), Leif Bjermer (Lund, Sweden), John R. Hurst (London, UK) and Carlos Robalo Cordeiro (Coimbra, Portugal).

Managing Editor: Rachel White
European Respiratory Society, 442 Glossop Road, Sheffield, S10 2PX, UK
Tel: 44 114 2672860 | E-mail: Monograph@ersj.org.uk

Published by European Respiratory Society ©2015
December 2015
Print ISBN: 978-1-84984-065-1
Online ISBN: 978-1-84984-066-8
Print ISSN: 2312-508X
Online ISSN: 2312-5098
Printed by Latimer Trend and Company Ltd, Plymouth, UK

All material is copyright to European Respiratory Society. It may not be reproduced in any way including electronic means without the express permission of the company.

Statements in the volume reflect the views of the authors, and not necessarily those of the European Respiratory Society, editors or publishers.

COPE COMMITTEE ON PUBLICATION ETHICS

This journal is a member of and subscribes to the principles of the Committee on Publication Ethics.

FSC www.fsc.org MIX Paper from responsible sources FSC® C013436

THOMSON REUTERS BOOK CITATION INDEX INDEXED

ERS | monograph

Contents

Imaging

Number 70
December 2015

Preface v

Guest Editors vi

List of abbreviations viii

1. MRI methods for structural and functional assessment of the lungs: proton and multinuclear 1
Neil J. Stewart and Jim M. Wild

2. Radionuclide imaging 20
Frank M. Bengel

3. Chest radiography: performance, indications and interpretation 34
Dag Wormanns

4. Lung cancer: screening and staging 47
Theresa C. McLoud and Adam Bernheim

5. Pulmonary embolism 60
Sumit Karia and Nicholas Screaton

6. Chronic obstructive pulmonary disease 80
Robert A. Stockley and David G. Parr

7. Interstitial lung diseases 99
Cornelia Schaefer-Prokop and Helmut Prosch

8. The pleura 116
Cheng Xie and Fergus Gleeson

9. Pneumonia and acute respiratory distress syndrome 141
Caron S. Parsons and Emma J. Helm

10. Pulmonary hypertension 158
Cathelijne E.E. van der Bruggen, Onno A. Spruijt, Lilian J. Meijboom and Anton Vonk Noordegraaf

11. Asthma 171
Simonetta Baldi, Ruth Hartley, Chris Brightling and Sumit Gupta

12. Imaging cystic fibrosis lung disease with MRI 188
Mark O. Wielpütz and Hans-Ulrich Kauczor

13. The cardiopulmonary unit 207
Andrew J. Swift

14. Measurement of pulmonary structure and function 216
Miranda Kirby, Pierre Lane and Harvey O. Coxson

15. Regulatory perspective on the use of lung imaging in drug development 233
Laura Fregonese

16. Risks of thoracic CT 253
Jonathan G. Goldin and Katrina Beckett

17. Safety issues in MRI 263
Alex Frydrychowicz and Oliver Wieben

Preface

Robert Bals

"A picture is worth a thousand words"

Imaging of the lungs is a central step in the diagnosis of lung disease. While the classical chest image has its role in daily practice, in recent years multiple new techniques have been developed that often involve the use of computerised complex data analysis. Most respiratory physicians and other caregivers in respiratory medicine look at images of the lung on a daily basis. In comparison with other areas of medicine, imaging techniques are a major part of the diagnostic workup of patients with lung disease. For example, imaging techniques are critical for the diagnosis of pneumonia, essential for staging lung cancer and vital to the classification of interstitial lung disease. The use of imaging techniques in respiratory medicine also involves the close interaction of several disciplines, resulting in the constructive exchange of knowledge from different areas.

This *ERS Monograph* comprises chapters on specific techniques, such as MRI methods, chest radiography, and radionucleotide imaging, as well as individual disease areas. Additional sections focus on the use of imaging techniques in drug development and address safety and risk management when using imaging techniques.

The book also considers the speed at which developments have been made in medical technology. The application of computerised and highly specialised technologies implies the need for close communication between respiratory and imaging physicians. This multidisciplinary approach is reflected in the range of authors selected to write in this *Monograph*, providing readers with different views on the patient. The Guest Editors, R. Graham Barr, David G. Parr and Jens Vogel-Claussen, worked hard and very successfully in selecting the topics covered and integrating the different aspects of imaging into a comprehensive book on the current knowledge in the field.

I would like to thank the Guest Editors and all authors for their work on this excellent book. I hope readers find this book useful in their daily clinical practice.

Copyright ©ERS 2015. Print ISBN: 978-1-84984-065-1. Online ISBN: 978-1-84984-066-8. Print ISSN: 2312-508X. Online ISSN: 2312-5098.

Guest Editors

R. Graham Barr

R. Graham Barr is Associate Professor of Medicine, Associate Professor of Epidemiology, and Chief of the Division of General Medicine at Columbia University Medical Center (New York, NY, USA). He is a general internist and respiratory epidemiologist. He received his medical degree from McGill University (Montreal, QC, Canada), before undertaking residency training at Columbia Presbyterian Medical Center (New York, NY, USA). He went on to undertake a fellowship at Massachusetts General Hospital (Boston, MA, USA), a respiratory epidemiology fellowship at the Channing Laboratory (Brigham and Women's Hospital, Boston, MA, USA), and a doctorate in epidemiology from Harvard School of Public Health (Boston, MA, USA).

Graham Barr's research interests lie in emphysema and COPD, with a particular focus on pulmonary vascular damage and its role in cardiopulmonary function. He uses novel imaging approaches (CT and MRI) applied to population-based samples and is principal investigator of the Multi-Ethnic Study of Atherosclerosis (MESA) Lung Study, the MESA COPD Study, and the Columbia Clinical Center of SPIROMICS (Subpopulations and Intermediary Outcome Measures in COPD Study), in addition to running the spirometry reading centre for the Hispanic Community Health Study and the Long Life Family Study.

David G. Parr

David G. Parr is Clinical Director for the Cardio-Respiratory Division and Consultant Respiratory Physician at University Hospital Coventry (Coventry, UK). He trained at the University of Cambridge (Cambridge, UK), the London Hospital Medical College at the University of London (London, UK) and the University of Birmingham (Birmingham, UK). His clinical interests include COPD and α_1-antitrypsin deficiency, pulmonary vascular disease and interstitial lung disease, and his research interest is in quantitative imaging of chronic lung diseases.

Copyright ©ERS 2015. Print ISBN: 978-1-84984-065-1. Online ISBN: 978-1-84984-066-8. Print ISSN: 2312-508X. Online ISSN: 2312-5098.

Jens Vogel-Claussen

Jens Vogel-Claussen is Professor of Radiology, Vice-Chair of the Department of Diagnostic and Interventional Radiology and Section Chief of Cardiothoracic Imaging at the Hannover Medical School (Hanover, Germany). He undertook his doctoral thesis at Eberhard-Karls-Universität (Tübingen, Germany) before moving onto an internship at Broomfield Hospital (Chelmsford, UK) and a radiological residency at The John Hopkins University Hospital (Baltimore, MD, USA). Alongside his current position, he also holds a visiting faculty position at The Johns Hopkins University Hospital and is Principal Investigator within the German Center for Lung Research (DZL).

Jens Vogel-Claussen's research focuses on the translation of novel functional cardiopulmonary MRI techniques into the clinic for improved diagnosis and patient monitoring.

Jens Vogel-Claussen is a member of a number of committees. He is part of the expert panel for the American College of Radiology Appropriateness Criteria for Cardiac Imaging, and is part of the Young Investigator Awards Committee for the International Society for Magnetic Resonance in Medicine.

Jens Vogel-Claussen has had 71 peer-reviewed scientific articles published and has acted as a consulting editor for *Circulation: Cardiovascular Imaging*.

List of abbreviations

ADC	Apparent diffusion coefficient
COPD	Chronic obstructive pulmonary disease
CT	Computed tomography
CTEPH	Chronic thromboembolic pulmonary hypertension
EBUS	Endobronchial ultrasound
FDG	2-fluoro-2-deoxy-D-glucose
FDG-PET	2-fluoro-2-deoxy-D-glucose positron emission tomography
FEV1	Forced expiratory volume in 1 s
HRCT	High-resolution computed tomography
MIP	Maximum intensity projection
MRI	Magnetic resonance imaging
OCT	Optical coherence tomography
PET	Positron emission tomography
SPECT	Single photon emission computed tomography
UTE	Ultra-short echo time

Chapter 1

MRI methods for structural and functional assessment of the lungs: proton and multinuclear

Neil J. Stewart and Jim M. Wild

Despite the inherent challenges of MRI of the lungs, a number of quantitative techniques with high functional sensitivity have been established for regional assessment of multiple aspects of pulmonary structure and physiology. Conventional proton-based magnetic resonance methods provide noninvasive anatomical imaging and diagnostic measures of pulmonary perfusion, ventilation and gas-exchange functions. Multinuclear MRI of the lung, including hyperpolarised noble gas MRI with ^{3}He and ^{129}Xe, has matured into a sensitive functional tool for visualisation of pulmonary ventilation, quantification of gas diffusion and evaluation of alveolar microstructure. These minimally invasive, safe and nonionising radiation-based methods are well-suited to longitudinal assessment of disease progression and treatment response, and recent technological and methodological advances are facilitating the dissemination of previously unconventional techniques on a broader clinical scale. In this article, we review the established and developing procedures for proton and multinuclear MRI of the pulmonary system, with applicable clinical examples.

Conventional MRI involves nonionising radiofrequency radiation excitation and detection of protons (hydrogen nuclei, ^{1}H) within the lungs. Image contrast is provided by fundamental differences in the properties of tissues of interest, including proton density and magnetic resonance signal relaxation times. ^{1}H MRI of the lungs is inherently challenging due to the low proton density and complex magnetic environment posed by the tissue and air interfaces. Nevertheless, a variety of methods (both ^{1}H and multinuclear, the latter employing inhaled gases as contrast agents) have been developed to overcome these limitations and establish lung MRI as an important clinical tool for assessment of both lung structure and several aspects of regional pulmonary function, with high spatial and temporal resolutions.

In this chapter, an overview of ^{1}H and multinuclear MRI methodologies for the human lung is presented, from recognised clinical tools to recent technological advances. This work aims to provide respiratory physiologists, imaging scientists and clinicians with an introduction to the fundamental principles of magnetic resonance methods, and to highlight relevant clinical developments.

Academic Unit of Radiology, University of Sheffield, Sheffield, UK

Correspondence: Jim M. Wild, Academic Unit of Radiology, C Floor, Royal Hallamshire Hospital, Sheffield, S10 2JF, UK.
E-mail: j.m.wild@sheffield.ac.uk

Copyright ©ERS 2015. Print ISBN: 978-1-84984-065-1. Online ISBN: 978-1-84984-066-8. Print ISSN: 2312-508X. Online ISSN: 2312-5098.

^{1}H lung MRI methods

The abundance of air–tissue interfaces in the lungs creates a challenging magnetic environment; the large magnetic susceptibility difference between air and tissue gives rise to numerous local magnetic field inhomogeneities. As a result, the transverse relaxation time (T_2*) of ^{1}H in lung parenchyma and blood is extremely short [1], which makes magnetic resonance signal acquisition challenging from a hardware perspective. This, along with respiratory and cardiac motions, necessitates rapid image acquisition within a single breath-hold and/or accurate motion-triggering procedures.

Generally, a pulmonary MRI protocol comprises various pulse sequences, each targeted to examine specific aspects of the lung, including structure or tissue density, ventilation, gas exchange and perfusion. The clinical field strength of 1.5 T has historically been an appropriate choice for lung MRI [2]; the greater magnetic field inhomogeneity at 3 T leads to faster signal losses [3] and the additional signal-to-noise ratio (SNR) associated with higher field imaging of other areas (such as the brain) is less readily realisable in the lung. Furthermore, while low fields ($\leqslant$0.5 T) offer longer relaxation times, signal averaging is required to achieve sufficient SNR, lengthening the acquisition.

Spoiled gradient echo (SPGR), single-shot and segmented fast spin echo (FSE), and balanced steady-state free-precession (bSSFP) pulse sequences are the clinical workhorses for anatomical and structural ^{1}H MRI of the thorax (figure 1). The SPGR sequence comprises a low flip angle radiofrequency pulse to excite ^{1}H nuclei, followed by a frequency-encoding magnetic field gradient with a short echo time to overcome the rapid T_2* signal decay, and lastly, a spoiler gradient, which destroys any residual signal. 3D breath-hold SPGR acquisitions enable full lung coverage imaging, with image weighting from T_2* and a combination of proton density and the longitudinal (T_1) relaxation time. Although the lung parenchyma appears dark on SPGR images, they are suitable for anatomical referencing, lung volume measurements [4] and assessment of the mediastinum [5]. Furthermore, 3D SPGR is commonly combined with fat saturation methods or gadolinium contrast, which reduces the T_1 of the pulmonary blood vessels, enabling identification of enhancement in nodules, inflammation in bronchiectatic airways and delineation of mediastinal tumours [6]. Moreover, when combined with gadolinium contrast, these sequences allow visualisation of the pulmonary blood vessels with magnetic resonance angiography and lung perfusion MRI, as outlined below.

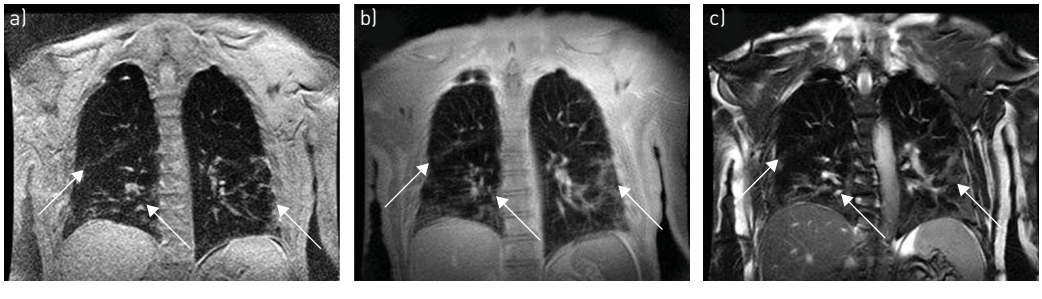

Figure 1. Anatomical and structural proton MRI of the lungs of a subject with idiopathic pulmonary fibrosis. a) Spoiled gradient echo, b) UTE and c) steady-state free precession images all highlight peripheral and basal fibrosis in both lungs, and an apparent scar in the mid right lung, as denoted by the arrows.

bSSFP sequences also require short echo time image encoding; however, the ^{1}H magnetisation is recycled rather than destroyed at the end of each encoding step, allowing higher flip angles compared with SPGR, leading to increased SNR at the expense of increased specific absorption rate (SAR) of patient heating by radiofrequency deposition. By virtue of the inherent mixed T_2 and T_1 relaxation time contrast, bSSFP images provide "bright blood" signal, with clear depiction of the pulmonary vessels and other fluids such as infiltrates and mucous in the lungs. The technique is particularly suited to assessment of central pulmonary emboli [7] and is a suitable diagnostic alternative to helical CT [8] in subjects at risk from ionising radiation exposure or contrast agents [9]. bSSFP imaging shows utility for appraisal of bronchiectasis, mucus plugging and atelectasis, with comparable diagnostic value to CT in cystic fibrosis (CF) patients [10], although currently inferior to CT in interstitial lung disease (ILD) [11]. For diseases characterised by significant tissue loss or reduced blood volume (*e.g.* COPD), morphological MRI with SPGR or bSSFP is inherently challenging and CT remains the first-line modality [9]. In addition to breath-hold structural imaging, bSSFP sequences are routinely applied for dynamic MRI of free-breathing subjects to evaluate respiratory cycle mechanics [12] and for quantitative lung volumetry [4], which has been validated against conventional spirometry tests [13].

Spin-echo sequences use trains of refocusing pulses to recover signal losses from magnetic field inhomogeneities (T_2^* decay), prior to image encoding. FSE images are weighted by the T_2 relaxation time ($>T_2^*$), and are well-suited to identification and evaluation of infiltrates, nodules and other fluids with long T_2 [14, 15]. Spin-echo acquisitions are lengthier and more SAR intensive than gradient-echo acquisitions, and acceleration techniques such as single-shot encoding (*e.g.* single-shot FSE (SSFSE)), half-Fourier encoding (*e.g.* half-Fourier single-shot turbo spin echo (HASTE)) or parallel imaging with multiple radiofrequency receiver coils, are commonly employed to reduce scan time. SSFSE MRI is sensitive to pulmonary oedema and bronchial wall thickening [16], and exhibits comparable efficacy to CT for detection of pneumonia and pulmonary nodules [15, 17]. In pathologies characterised by fibrotic tissue (*e.g.* CF), spin-echo sequences have been demonstrated as essentially comparable to CT and chest radiography [18]. High-field respiratory and cardiac-gated SSFSE MRI was reported to perform at least as well as CT for evaluation of ILD [19], and segmented FSE methods employing motion compensation (*e.g.* respiratory gating) show great potential for high-resolution imaging of multiple pathologies in the lungs [20]. Whilst FSE acquisitions are slower than bSSFP, dynamic SSFSE MRI can also be utilised to study respiratory mechanics. Using this approach, abnormal respiratory motion has been observed in emphysema subjects [21], and signal intensity changes between inspiratory and expiratory images correlate with pulmonary function testing [22].

Short tau inversion recovery (STIR) preparation sequences, employing an additional radiofrequency inversion pulse prior to standard radiofrequency excitation, can be combined with many of the aforementioned techniques to saturate the signal from fat, whilst simultaneously affording valuable T_1 and T_2 contrast benefits from the lung parenchyma. Consequently, STIR sequences provide delineation of fluid-filled regions, particularly lymph nodes [23], for which the method performs comparably to FDG-PET/CT [24]. In a recent study, a combination of STIR MRI and FDG-PET/CT was demonstrated to improve diagnostic capability for node staging in cancer patients [25]. Furthermore, turbo-inversion recovery magnitude has been shown to be sensitive to segmental inflammatory lung oedema corresponding to the severity of the regional allergic reaction determined by the percentage of eosinophils in bronchoalveolar lavage fluid 24 h after segmental allergen challenge in patients with asthma [26].

To overcome the low magnetic resonance signal from lung parenchyma and enhance the functionality of lung MRI, exogenous contrast agents are often introduced. Inhaled oxygen acts to decrease the parenchymal and pulmonary blood T_1, boosting the available magnetic resonance signal and improving the delineation of ventilated lung tissue. Oxygen-enhanced (OE)-MRI is typically implemented *via* one of two methods: 1) acquisition of inversion recovery prepared, T_1-weighted HASTE images at a number of different inversion times (T_I, the time between inversion and acquisition) [27, 28]; and 2) dynamic T_1 mapping with a Look–Locker sequence [29], wherein a series of fast, low flip angle gradient echo images are acquired in quick succession after a global inversion pulse [30] (figure 2). In both cases, acquisitions are performed alternately, with the subject breathing room air (21% oxygen) or pure (100%) oxygen. Data can be presented as O_2 signal enhancement maps or image intensities can be fitted on a pixel-wise basis to derive a lung T_1 map. The functional information afforded by OE-MRI comprises a combination of ventilation, gas-exchange and perfusion weighting. Assuming that signal enhancement maps predominantly reflect changes in pulmonary ventilation [31, 32] allows for regional depiction of ventilation defects and quantification of fractional ventilation (the fraction of gas turned over in one breathing cycle) from oxygen wash-in and wash-out [33]. In comparison with quantitative CT, magnetic resonance mapping of oxygen enhancement has been shown to be capable of evaluating pulmonary functional loss in COPD [34]. Owing to the exchange of oxygen across the air–blood barrier, OE-MRI can be used to assess gas-exchange limitation (*e.g.* in ILD) [35, 36]. OE-MRI transfer metrics have been

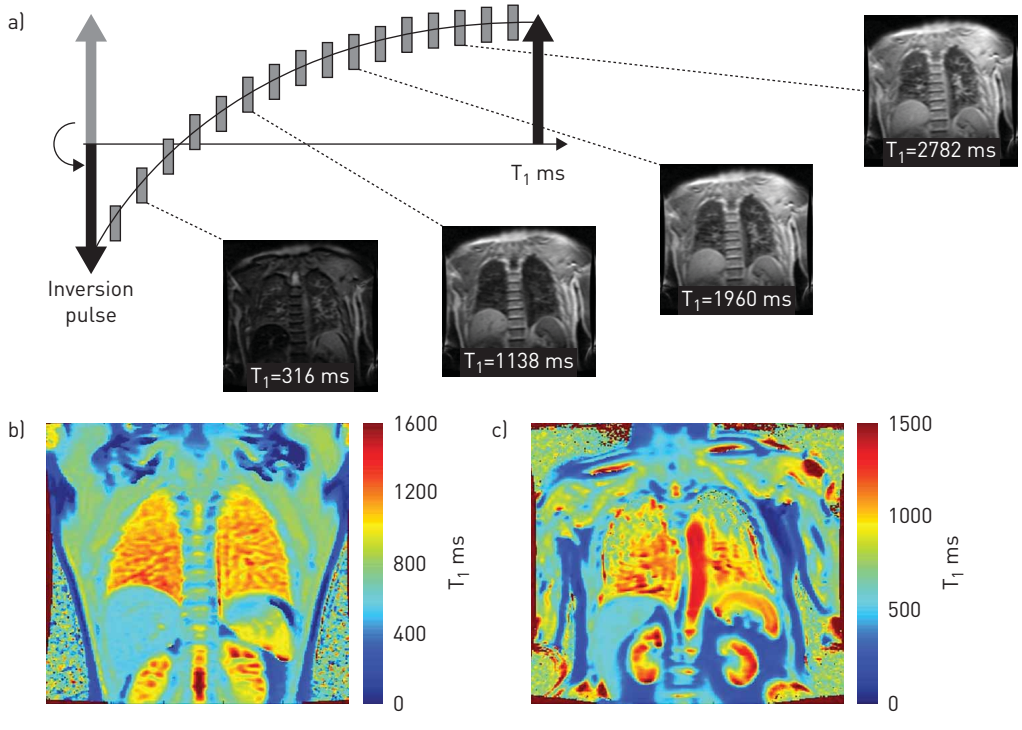

Figure 2. Oxygen-enhanced (OE) MRI of the lung parenchyma. a) Look–Locker inversion recovery acquisition strategy for obtaining a series of longitudinal relaxation time (T_1)-weighted gradient echo images at different inversion times. This acquisition scheme is repeated for the subject breathing normal air compared with pure (100%) oxygen. OE ^{1}H T_1 maps of the lungs of b) a healthy subject and c) a COPD subject. The healthy subject exhibits a generally uniform T_1 in the lungs, whilst abnormalities in emphysematous lung are depicted as regions of reduced T_1 (diminished oxygen uptake).

shown to provide comparable information to the transfer capacity of the lung for carbon monoxide (*T*LCO), but on a regional basis, in subjects with emphysema and ILD [37, 38]. Furthermore, areas of reduced T_1-enhancement on OE-MRI ("ventilation defects") have been observed to correspond with perfusion defects in CF patients [39].

Although functionally sensitive, inherently safe and noninvasive, OE-MRI is limited by long scan times, spatial resolution, volume coverage and its relatively small T_1 shortening/signal enhancement effect. Gadolinium chelates are routinely employed as magnetic resonance contrast agents to induce considerable T_1 shortening and signal enhancement in the pulmonary system and other organs [40, 41]. Dynamic contrast-enhanced MRI of the lung typically refers to the process of tracking the first passage of gadolinium through the pulmonary vascular circuit after intravenous contrast injection, providing unique information about pulmonary perfusion with excellent spatial and temporal resolution [42]. Moreover, with timing of the bolus, the arterial and venous enhancement of the pulmonary vessels can be separated to produce high-resolution magnetic resonance angiograms [43] (examples shown in figure 3). Typically, a rapid 3D gradient-echo sequence is employed in combination with acceleration techniques such as parallel imaging [44] and view sharing (*e.g.* time-resolved imaging of contrast kinetics (TRICKS) [45]). Dynamic contrast-enhanced perfusion imaging and magnetic resonance angiography offer increased sensitivity compared with non-contrast-enhanced techniques, which has been exploited for appraisal of pulmonary embolism [7, 43], where dynamic contrast-enhanced MRI and magnetic resonance angiography exhibit comparable or superior sensitivity to nuclear scintigraphy [46, 47]. Additionally, regional dynamic contrast-enhanced MRI perfusion abnormalities in emphysema patients have been observed to correlate with alveolar destruction on CT [48]. The technique is appropriate for assessment of post-operative lung

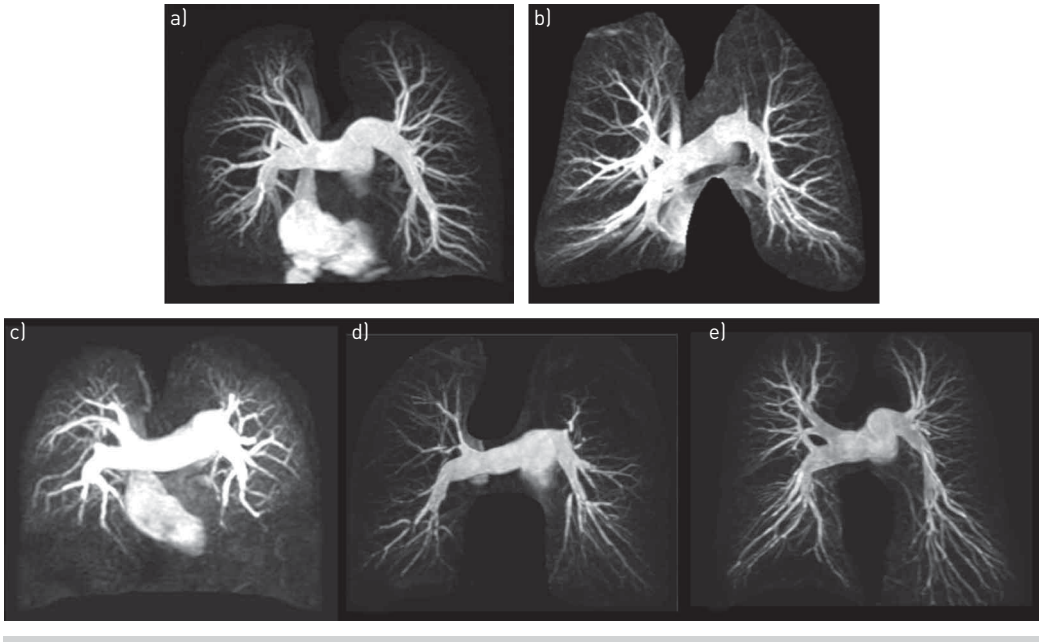

Figure 3. Contrast-enhanced magnetic resonance angiograms of the pulmonary arteries of patients with different subtypes of pulmonary hypertension (PH): a) idiopathic pulmonary arterial hypertension; b) PH with coexisting emphysema/COPD; c) PH in interstitial lung disease; d) thromboembolic PH; e) normal.

function and has been reported as a feasible nonionising radiation alternative to the current clinical standard of nuclear scintigraphy for evaluation of cancer resection surgery [49]. Dynamic contrast-enhanced MRI is also pertinent for studying perfusion impairment in vascular disease, such as pulmonary hypertension (PH), including pulmonary arterial hypertension (PAH) [50, 51], and magnetic resonance angiography screening for CTEPH [52] presents an equally sensitive technique to scintigraphy. In addition, magnetic resonance angiograms are used as replacements for catheter pulmonary angiography in the diagnosis of PAH in selected specialised centres. The dynamics of contrast uptake can be determined by placing regions of interest (ROIs) in different areas of the lung, in order to yield quantitative perfusion data from signal enhancement *versus* time curves (figure 4). Typically, one ROI is positioned at the pulmonary artery to derive the arterial input function, by which to normalise uptake dynamics. Quantitative parametric maps of perfusion can also be generated for regional quantification of pulmonary blood volume (PBV), blood flow (PBF) and mean transit time (MTT) of blood through the pulmonary circuit (MTT=PBV/PBF). A significant relationship has been observed between MTT and PBF values and mean pulmonary arterial pressure (mPAP) and pulmonary vascular resistance (PVR) from right heart catheter measurements, the clinical gold-standard metric in PAH [55]. Quantitative dynamic contrast-enhanced perfusion MRI offers diagnostic value in patients with PAH, where a decreased PBF, PBV and prolonged MTT have been measured in comparison to healthy subjects [50, 54]. Furthermore, in patients with COPD, dynamic contrast-enhanced MRI parameters appear to correlate with global pulmonary function including T_{LCO} [56], and in combined pulmonary fibrosis and emphysema, prolongation of MTT exhibits a correlation with mPAP and PVR [57].

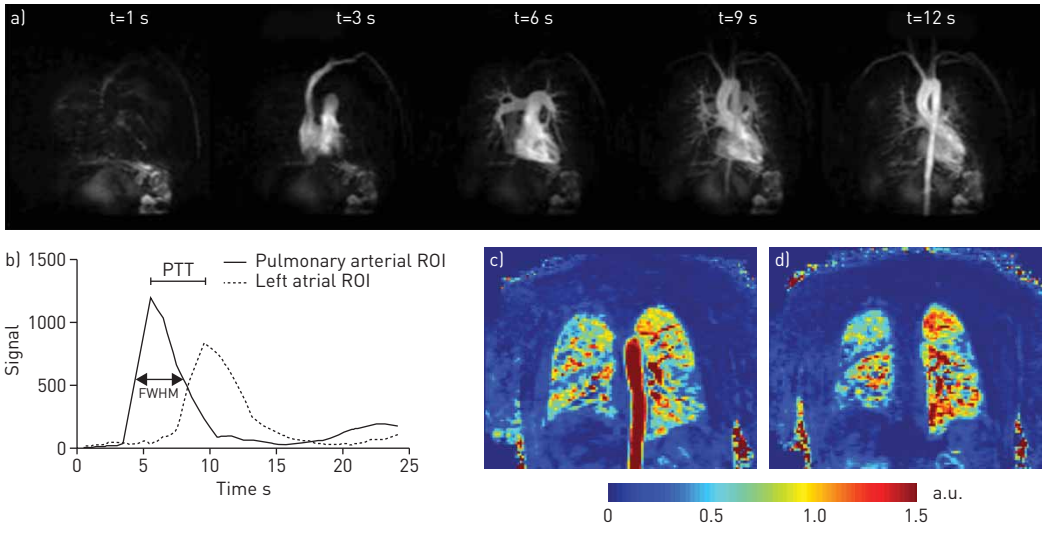

Figure 4. a) Time series of dynamic contrast-enhanced magnetic resonance images showing bolus passage through the pulmonary vasculature. Reproduced and modified from [53] with permission from the publisher. b) Contrast-enhanced magnetic resonance signal *versus* time curves for regions of interest (ROIs) placed at the position of the pulmonary artery and the left atrium. Note that the pulmonary transit time (PTT) equates to the mean pulmonary transit time of the contrast. FWHM: full width at half maximum. Reproduced and modified from [54] with permission from the publisher. c) Peak dynamic contrast-enhanced magnetic resonance signal (peak gadolinium concentration) map acquired from the lung of a subject with idiopathic pulmonary fibrosis (same subject as in figure 1). d) Another representative slice of the same patient as in c).

Table 1. Properties of ^{1}H, ^{3}He and ^{129}Xe relevant to lung MRI

Isotope	^{1}H	^{3}He	^{129}Xe
Isotopic abundance %	99.99	1.4×10^{-4}	26.44[#] 80–90[¶]
Gyromagnetic ratio MHz·T^{-1}	42.58	−32.44	−11.78
Self-diffusion coefficient cm^{2}·s^{-1}	2×10^{-5}	2.05	0.06
Cost £ per L	NA	~500	~20[#] ~150[¶]

NA: not applicable. [#]: natural-abundance Xe; [¶]: Xe enriched with the 129 isotope.

^{1}H MRI encompasses an array of methods for probing various aspects of pulmonary structure and function that are now routinely used in clinical practice in specialist centres, focusing specifically on high morbidity/high treatment cost diseases such as CF and PH, as a nonionising radiation alternative to CT. Development of the field continues with recent advances in UTE sequences for accelerated imaging with improved visualisation of the lung parenchyma and airway delineation [58]. The clinical potential of UTE in humans is promising, with comparable efficacy to CT for parenchymal assessment of patients with CF, lung cancer, ILD and emphysema [59]. In addition, Fourier decomposition MRI, where dynamic analysis of free breathing imaging can be used to generate maps of lung regions modulated by ventilation and cardiac pulsatility, thus providing surrogate maps of ventilation and perfusion from a single slice of the lung [60]. Like OE-MRI, Fourier decomposition MRI must be shown to be reproducible across centres and capable of providing volumetric lung coverage in order to be considered diagnostically beneficial in a clinical setting [61].

Multinuclear lung MRI methods

Alongside the development of ^{1}H lung MRI, MRI with the inhaled hyperpolarised noble gases ^{3}He and ^{129}Xe has become established as a versatile means of functional assessment of pulmonary ventilation, structure and gas exchange. ^{3}He and ^{129}Xe are intrinsically safe and unreactive, and possess similar nuclear spin properties to protons. Typical properties of these isotopes relevant to lung MRI are summarised in table 1, in comparison to ^{1}H. Due to their low density, signal enhancement is necessary to achieve sufficient SNR for *in vivo* magnetic resonance applications. Hyperpolarisation of these nuclei, affording a factor of 10^{5}–10^{6} increase in available magnetic resonance signal, is possible *via* collisional spin-exchange optical pumping [62] (or metastability-exchange optical pumping [63] of ^{3}He only). A number of high-throughput commercial systems are available for polarisation of ^{3}He and ^{129}Xe [64], and "home-built" ^{129}Xe systems with low-cost components can now attain comparable polarisation levels [65, 66].

Since the acquisition of the first images of pulmonary ventilation in human lungs with hyperpolarised ^{3}He in 1996 [67, 68] and ^{129}Xe in 1997 [69], inhaled noble gas MRI has rapidly evolved as a means to provide excellent depiction of pulmonary ventilation and quantification of pulmonary function that is not afforded by other methods [70, 71]. Ventilation MRI is typically performed under breath-hold after inhalation of $\leqslant$1 L of hyperpolarised gas, using fast gradient-echo or bSSFP sequences to acquire a stack of 2D slices or a 3D volume [72], providing high-resolution visualisation of the gas distribution in

the lungs, with image intensity proportional to gas density. In addition to breath-hold time constraints to avoid respiratory motion, rapid acquisition and low-excitation flip angles are imposed by the nonrenewable nature of the laser-induced hyperpolarisation.

The majority of clinically relevant lung imaging research with hyperpolarised gases to date has been performed with ^{3}He, exploiting its intrinsically higher gyromagnetic ratio compared with ^{129}Xe (table 1) and the fact that it was historically easier to polarise to levels prerequisite for *in vivo* MRI. ^{3}He ventilation MRI has been implemented in multicentre studies [73], is feasible at the clinical field strengths of 1.5 T [74] and 3 T [75], and has shown clinical utility in a number of pulmonary pathologies, particularly obstructive lung diseases in which ventilation heterogeneity presents as signal voids in the image. Ventilation defect distribution has been comprehensively studied in patients with asthma [76, 77], COPD [73, 78] and CF [79, 80]. Furthermore, the technique has exhibited sensitivity to ventilation abnormalities in pulmonary embolism [81] and chronic rejection of lung transplantation [82]. Dynamic ventilation MRI of inspiration has been facilitated by rapid spiral [83] and radial [84] image encoding schemes to track the passage of gas through the major airways and further evaluate flow restrictions in obstructive disease.

The availability of ^{3}He is becoming increasingly regulated because it is not naturally abundant and is solely generated as a by-product of tritium decay [85]. Xe is considerably cheaper and more readily available; it is naturally abundant in air (87 ppb), of which 26% comprises ^{129}Xe, and the ^{129}Xe fraction can be enriched to 80–90% by gas centrifuge techniques. Hyperpolarised ^{129}Xe is also a promising contrast agent for pulmonary ventilation imaging, with no loss in functional information compared with ^{3}He [86–88]. A side-by-side comparison of ^{3}He and ^{129}Xe ventilation images acquired from normal and abnormal lungs is presented in figure 5. Abnormalities in pulmonary ventilation in COPD have been observed on ^{3}He and ^{129}Xe MRI in a similar manner [86, 87], and preliminary evidence suggests that ^{129}Xe may be sensitive to small-scale defects [86, 90] by virtue of its low diffusion coefficient, which could be beneficial in early-stage disease detection. Fuelled by recent advancements in polarisation technology [64–66] and pulse sequences, high-quality ventilation imaging has been realised using natural-abundance Xe [89] and low dosages of enriched Xe [91], highlighting ^{129}Xe as a commercially scalable contrast agent for routine clinical studies.

The nonionising radiation nature of hyperpolarised gas MRI is suitable for longitudinal studies of disease progression or treatment response. For example, the increase in prevalence of ventilation defects in asthma patients after exercise and methacholine challenge [92], and the ventilation response to bronchodilator application in COPD and CF [93, 94], has been studied *via* multiple time-point ^{3}He ventilation imaging. Although Xe possesses anaesthetic properties [95], the low dosages used for lung MRI have been reported to be safe and tolerable over several breath-holds in humans [96, 97], which is promising for low-cost longitudinal screening of patients.

Hyperpolarised gas ventilation imaging can be combined with ^{1}H perfusion MRI in order to evaluate regional ventilation–perfusion matching [98]. The potential for pooled assessment of ventilation and perfusion abnormalities is important in pulmonary embolism [81, 99], and the alteration of ventilation–perfusion relationships has been studied with hyperpolarised ^{3}He and ^{1}H MRI in patients with pulmonary embolism and post-lung transplant [98]. Furthermore, techniques and hardware for same-breath acquisition of hyperpolarised gas ventilation images and ^{1}H anatomical images [100, 101] have been

recently developed that allow acquisition of complementary structural and functional magnetic resonance images that are inherently coregistered.

In addition to the visualisation of pulmonary ventilation, hyperpolarised gas MRI with ^{3}He and ^{129}Xe permits quantitative evaluation of alveolar microstructure. Diffusion-weighted MRI

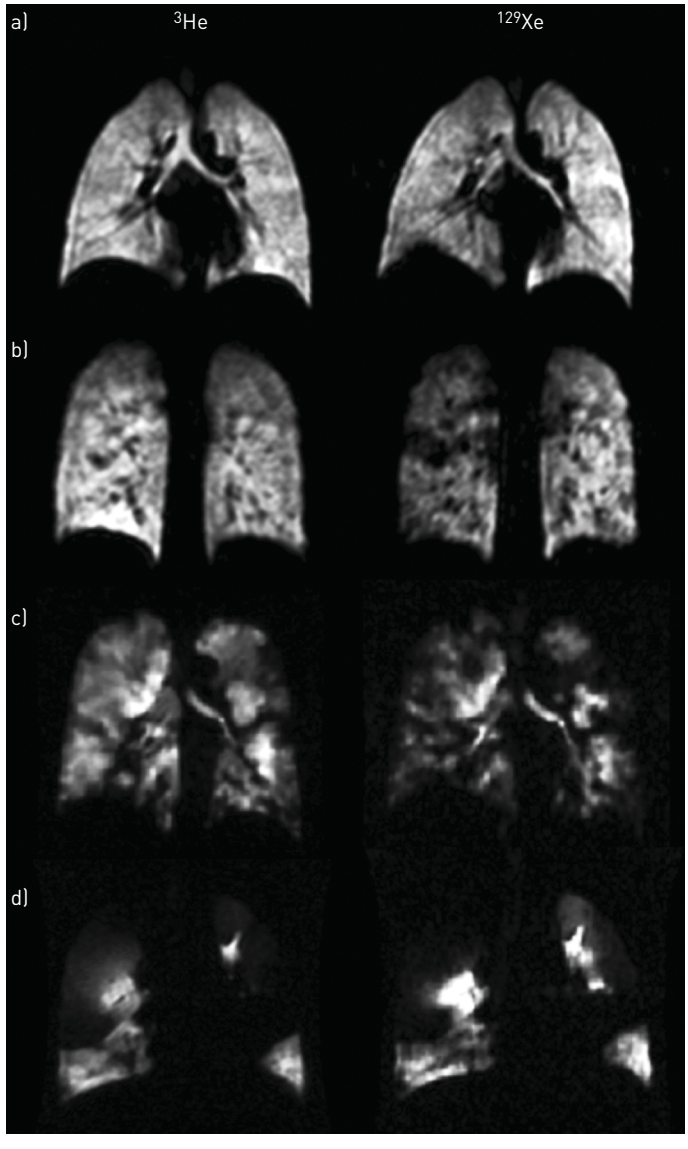

Figure 5. Comparison of ^{3}He and ^{129}Xe magnetic resonance ventilation images of the lungs of a) a healthy never-smoker, b) a healthy smoker (reproduced and modified from [89] with permission from the publisher), c) a patient with asthma and d) a patient with COPD. Progressively worse ventilation abnormalities can be seen from b) to d), with mild, patchy abnormalities in the smoker, more severe obstruction in the asthma subject, and large regions of completely unventilated lung in the COPD subject. All images were acquired with an optimised 3D steady-state pulse sequence [89]. The slice thickness and resolution for acquisitions a) and b) were identical. ^{3}He images for the asthma and COPD subjects were acquired with a lower slice thickness than ^{129}Xe images; however, for comparison, the ^{3}He images in c) and d) represent reconstructions that mimic the same slice thickness as the ^{129}Xe images.

enables measurement of the ADC of hyperpolarised gas in the lungs. The ^{3}He ADC is reduced when compared to its free diffusion coefficient due to the restricting alveolar walls; however, in the presence of tissue destruction (*e.g.* in emphysema), the ADC increases due to less restricted diffusion [102]. Various geometric [103, 104] and phenomenological [105, 106] models have been developed to relate observed ADC changes to quantitative physiological alterations in alveolar dimension or surface area/volume ratio. Comprehensive studies of ^{3}He diffusion-weighted MRI in emphysema patients [73, 107], asymptomatic smokers [108, 109] and asthma patients [110] have been performed to assess regional variations in diffusion restriction across the lungs, with good correlation to both spirometry [107, 111] and histology [112]. In addition, alterations in ^{3}He ADC have been mapped in the developing paediatric lung [113], and have been used as evidence of lung development post-pneumonectomy for adenocarcinoma [114] and alveolarisation in young adults [115].

Again, despite the predominant use of ^{3}He in patient studies, hyperpolarised ^{129}Xe ADC mapping is also effective for assessment of COPD [116], and direct comparisons between the two nuclei have highlighted agreement in the spatial distribution of ADC values and correlations in mean ADC values in healthy volunteers, COPD patients and ex-smokers [86, 117]. Moreover, mean ADC values were observed to correlate with T_{LCO} and mean Hounsfield units from CT [86, 117]. Figure 6 presents a comparison of ^{3}He and ^{129}Xe ADC maps acquired from healthy volunteers and COPD patients.

Although ventilation imaging and ADC mapping are undoubtedly the most established and widely applied hyperpolarised gas MRI techniques in a clinical setting, a number of additional techniques have been developed to further investigate specific aspects of lung function.

Multiple-breath ventilation imaging methods have been implemented to quantify lung ventilation through metrics of ventilation heterogeneity or fractional ventilation (gas turnover per respiratory cycle). Originally demonstrated using multiple sequential imaging acquisitions after a variable number of inhalations of hyperpolarised ^{3}He to study gas wash-in in small animals [118, 119], the technique has subsequently been modified to measure regional gas wash-out in humans to characterise ventilation heterogeneity [120, 121] by acquiring multiple images after sequential exhalation–inspiration cycles of ^{3}He. This technique provides analogous quantitative information to the nitrogen wash-out pulmonary function test, but on a regional rather than global scale, and preliminary evidence suggests its applicability to CF [122]. In comparison to fractional ventilation imaging with ^{1}H OE-MRI (*e.g.* [33]), multiple-breath hyperpolarised gas imaging is potentially advantageous as an absolutely quantitative regional measure of ventilation rather than a measure only proportional to lung ventilation.

Following a similar acquisition strategy of repeated ventilation images separated by a specific time gap, delayed ventilation of small airways can be investigated [78, 123], where apparently obstructed regions of the lung start to fill during the breath-hold period and present as ventilated regions in images acquired later. The technique has been used to assess collateral ventilation pathways in COPD [78]. Although delayed ventilation effects can also be highlighted indirectly by long-range magnetic resonance diffusion measurements [110], direct imaging methods may be preferred.

The dependence of the ^{3}He T_1 on alveolar oxygen tension (P_{O_2}) [124] can be exploited to infer alveolar P_{O_2} from T_1 changes over multiple magnetic resonance acquisitions during breath-hold [125, 126]. The alveolar P_{O_2} comprises information about ventilation, perfusion and gas exchange, and hyperpolarised gas P_{O_2} mapping MRI permits noninvasive regional

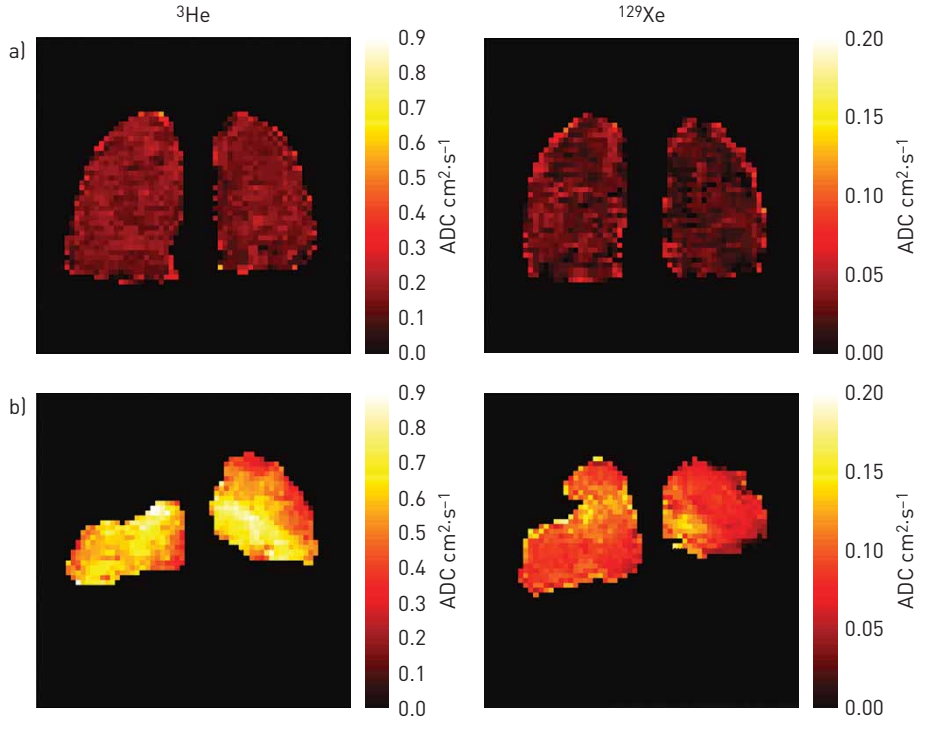

Figure 6. Example regional maps of the ADC of ^{3}He and ^{129}Xe in the lungs, derived from diffusion-weighted hyperpolarised gas MRI, using a 2D spoiled gradient echo sequence. a) One slice acquired from a healthy subject; the mean±SD global ADCs were 0.166±0.064 cm^2·s^{-1} and 0.032±0.018 cm^2·s^{-1} for ^{3}He and ^{129}Xe, respectively. b) One slice acquired from a patient with severe COPD, in which clear unventilated regions of the lung can be observed; mean ADCs were significantly increased to 0.594±0.131 cm^2·s^{-1} and 0.090±0.025 cm^2·s^{-1} for ^{3}He and ^{129}Xe, respectively.

quantification of oxygen uptake. Substantial delays between acquired magnetic resonance images are required to induce sufficient ^{3}He signal decay, necessitating long breath-holds, which can be partially overcome with 3D sequences [127] or variable flip angle strategies and conservative image encoding schemes [128, 129]. To date, preliminary studies in patients with COPD [123, 128] and post-lung transplant [129, 130] have shown that regional pathological abnormalities in P_{O_2} can be effectively detected. Nevertheless, application of this method to obstructive lung disease is limited by collateral ventilation [123].

Phase contrast velocimetry MRI offers a means to study gas flow in the lungs and major airways by sensitising the magnetic resonance acquisition to the ^{3}He gas velocity [131, 132]. The method has been validated *via* computational fluid dynamics modelling of the airways [133], and has important clinical implications for particle deposition and drug delivery in the respiratory system. Phase contrast velocimetry MRI was recently applied to examine flow oscillations in human lungs induced by cardiac motion [134] and shows potential for evaluation of pathological flow abnormalities in patients with obstructive lung disease.

Current developments of ^{129}Xe lung MRI techniques have been targeted towards detection of dissolved ^{129}Xe in the parenchyma and blood for noninvasive assessment of pulmonary gas exchange [135]. Xe is mildly soluble in somatic tissues and blood [136], and the ^{129}Xe isotope displays unique nuclear magnetic resonance (NMR) chemical shift signatures when dissolved

in lung tissues and plasma, and red blood cells (RBCs) [137, 138] (figure 7a). As such, this "dissolved-phase" ^{129}Xe can be detected separately from "gaseous-phase" ^{129}Xe in the alveoli.

Dynamic ^{129}Xe NMR spectroscopy (*e.g.* the chemical shift saturation recovery technique) permits studies of gas-exchange dynamics [141], which can be evaluated with mathematical models of diffusion [141, 142] to quantify global changes in lung microstructure [143], such as in COPD [140], and to detect alveolar septal thickening in ILD [139] (figure 7b), both of which correlated significantly with the T_{LCO} metric [139, 140].

Direct imaging of dissolved-phase ^{129}Xe in the lungs is challenging due to the very short T_2^* relaxation times and low concentration of dissolved Xe. One proposed method to separately image dissolved and gaseous ^{129}Xe is to exploit the large NMR chemical shift difference in their resonances to resolve the two compartments in a single image [144]. Although a promising surrogate of ventilation (gaseous ^{129}Xe) and perfusion (dissolved ^{129}Xe) in humans [144], this technique does not permit distinction of the tissue/plasma and RBC components. A number of rapid acquisition techniques with non-Cartesian image encoding schemes [145] have been introduced that exploit different echo times [146, 147] to distinguish these components and yield RBC images that delineate only ^{129}Xe that has traversed the air–blood barrier into the pulmonary capillaries. These methods have been employed to regionally visualise gas-exchange impairment in patients with COPD and asthma [140, 148] (figure 7c), and regions of low ^{129}Xe RBC signal have been reported to correlate visually with fibrosis on CT in IPF patients [149].

In contrast to direct imaging of dissolved-phase ^{129}Xe, an alternative technique has been proposed to indirectly probe gas-exchange function by studying the decay in ^{129}Xe gas signal following exchange-weighted radiofrequency pulses [150]. Entitled Xe polarisation transfer contrast [150, 151], this method has been applied to map the alveolar surface area/volume ratio in the human lungs [152], and regionally depict gas-exchange efficiency in the lungs of healthy volunteers and COPD subjects, in an attempt to quantify tissue loss due to emphysema [153, 154].

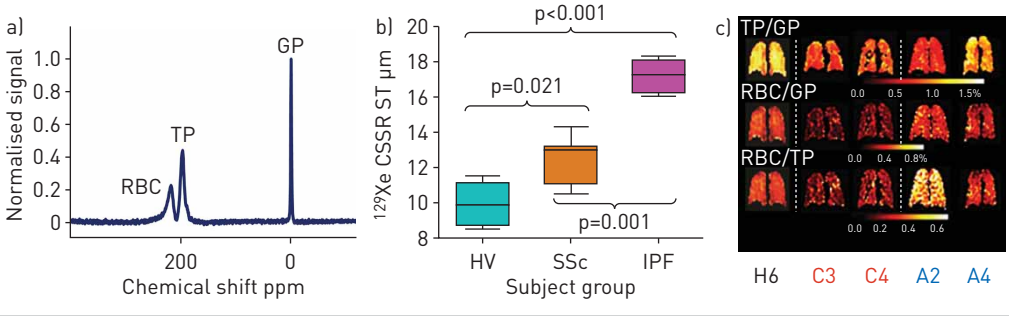

Figure 7. Magnetic resonance of pulmonary gas exchange with hyperpolarised ^{129}Xe. a) ^{129}Xe nuclear magnetic resonance (NMR) spectrum acquired from the human lungs, exhibiting distinct peaks from ^{129}Xe gas in the alveoli (GP), and ^{129}Xe dissolved in tissues and blood plasma (TP), and in red blood cells (RBC). b) Alveolar septal thickness (ST) values estimated from ^{129}Xe chemical shift saturation recovery (CSSR) in healthy volunteers (HV), scleroderma (SSc) patients and idiopathic pulmonary fibrosis (IPF) patients. ^{129}Xe CSSR is sufficiently sensitive to detect interstitial tissue thickening in both diseases. Data from [139]. c) Chemical shift imaging of ^{129}Xe in the lungs of a healthy subject (H6), two patients with COPD (C3 and C4) and two with asthma (A2 and A4), depicted in the form of maps of the ratio of signal intensities from each of the NMR peaks. In patients, the gas-exchange maps (RBC/GP and RBC/TP) were considerably more heterogeneous than in healthy subjects and the mean ratios were reduced in subjects with severe COPD. Reproduced and modified from [140] with permission from the publisher.

Exposure of hyperpolarised gas MRI to a broad clinical audience has historically been hindered by the commercial availability of specialised hardware and the relative expense of the isotopes when compared to other contrast agents. In recent years, fluorinated gas MRI, which exploits the nonzero nuclear spin of ^{19}F, has emerged as a prospective alternative means to visualise pulmonary ventilation. Fluorinated gases do not require hyperpolarisation; however, the innate magnetic resonance signal is typically low, necessitating continuous breathing of a fluorinated gas mixture prior to breath-hold imaging for adequate SNR (*e.g.* [155]). Although the SNR and resolution of ^{19}F lung MRI is presently inferior to that of hyperpolarised ^{3}He or ^{129}Xe, the possibility of human application has been demonstrated in healthy volunteers and patients with a variety of lung diseases using a perfluoropropane–oxygen mix and gradient-echo sequences [156], and subsequently, UTE sequences have been reported to offer enhanced SNR in healthy volunteers [157].

The advent of low-cost ^{129}Xe polarisers constructed from widely available components, in combination with reductions in gas cost afforded by naturally abundant Xe [89] and unpolarised ^{19}F [155], are paving the way for improved dissemination of multinuclear magnetic resonance methods in the clinic. In particular, hyperpolarised ^{129}Xe is emerging as a cost-effective contrast agent for high-quality MRI of pulmonary ventilation. In Sheffield, UK, we have recently taken the technique to clinical diagnostic referral with a regulatory licence for manufacture of hyperpolarised ^{3}He and ^{129}Xe gas for routine clinical lung imaging.

Conclusion

^{1}H lung MRI is now an established nonionising radiation alternative to CT for structural imaging of the lung and offers a range of techniques for quantitative investigation of diversified aspects of pulmonary function that have the potential to become clinically valuable. MRI with hyperpolarised noble gases provides exquisite depiction of lung ventilation and presents a quantitative functional tool for assessment of lung microstructure and gas exchange. Recent advances in magnetic resonance pulse sequence acquisition strategies, polarisation technology and image processing algorithms are promising for routine diagnostic lung imaging and clinical translation of these sensitive multinuclear lung MRI techniques.

References

1. Hatabu H, Alsop DC, Listerud J, *et al.* T2* and proton density measurement of normal human lung parenchyma using submillisecond echo time gradient echo magnetic resonance imaging. *Eur J Radiol* 1999; 29: 245–252.
2. Puderbach M, Hintze C, Ley S, *et al.* MR imaging of the chest: a practical approach at 1.5 T. *Eur J Radiol* 2007; 64: 345–355.
3. Bergin CJ, Glover GH, Pauly JM. Lung parenchyma: magnetic susceptibility in MR imaging. *Radiology* 1991; 180: 845–848.
4. Swift AJ, Woodhouse N, Fichele S, *et al.* Rapid lung volumetry using ultrafast dynamic magnetic resonance imaging during forced vital capacity maneuver: correlation with spirometry. *Invest Radiol* 2007; 42: 37–41.
5. Wielpütz M, Kauczor H-U. MRI of the lung: state of the art. *Diagn Interv Radiol* 2012; 18: 344–353.
6. Semelka RC, Balci NC, Wilber KP, *et al.* Breath-hold 3D gradient-echo MR imaging of the lung parenchyma: evaluation of reproducibility of image quality in normals and preliminary observations in patients with disease. *J Magn Reson Imaging* 2000; 11: 195–200.
7. Kluge A, Mueller C, Strunk J, *et al.* Experience in 207 combined MRI examinations for acute pulmonary embolism and deep vein thrombosis. *Am J Roentgenol* 2006; 186: 1686–1696.
8. Stein PD, Fowler SE, Goodman LR, *et al.* Multidetector computed tomography for acute pulmonary embolism. *N Engl J Med* 2006; 354: 2317–2327.

9. Biederer J, Mirsadraee S, Beer M, *et al.* MRI of the lung (3/3) – current applications and future perspectives. *Insights Imaging* 2012; 3: 373–386.
10. Failo R, Wielopolski PA, Tiddens HAWM, *et al.* Lung morphology assessment using MRI: a robust ultra-short TR/TE 2D steady state free precession sequence used in cystic fibrosis patients. *Magn Reson Med* 2009; 61: 299–306.
11. Rajaram S, Swift AJ, Capener D, *et al.* Lung morphology assessment with balanced steady-state free precession MR imaging compared with CT. *Radiology* 2012; 263: 569–577.
12. Fabel M, Wintersperger BJ, Dietrich O, *et al.* MRI of respiratory dynamics with 2D steady-state free-precession and 2D gradient echo sequences at 1.5 and 3 tesla: an observer preference study. *Eur Radiol* 2009; 19: 391–399.
13. Plathow C, Ley S, Fink C, *et al.* Evaluation of chest motion and volumetry during the breathing cycle by dynamic MRI in healthy subjects: comparison with pulmonary function tests. *Invest Radiol* 2004; 39: 202–209.
14. Biederer J, Busse I, Grimm J, *et al.* Sensitivity of MRI in detecting alveolar infiltrates: experimental studies. *RoFo* 2002; 174: 1033–1039.
15. Schroeder T, Ruehm SG, Debatin JF, *et al.* Detection of pulmonary nodules using a 2D HASTE MR sequence: comparison with MDCT. *Am J Roentgenol* 2005; 185: 979–984.
16. Hatabu H, Gaa J, Tadamura E, *et al.* MR imaging of pulmonary parenchyma with a half-Fourier single-shot turbo spin-echo (HASTE) sequence. *Eur J Radiol* 1999; 29: 152–159.
17. Eibel R, Herzog P, Dietrich O, *et al.* Pulmonary abnormalities in immunocompromised patients: comparative detection with parallel acquisition MR imaging and thin-section helical CT. *Radiology* 2006; 241: 880–891.
18. Puderbach M, Eichinger M, Haeselbarth J, *et al.* Assessment of morphological MRI for pulmonary changes in cystic fibrosis (CF) patients: comparison to thin-section CT and chest X-ray. *Invest Radiol* 2007; 42: 715–724.
19. Lutterbey G, Grohé C, Gieseke J, *et al.* Initial experience with lung-MRI at 3.0 T: comparison with CT and clinical data in the evaluation of interstitial lung disease activity. *Eur J Radiol* 2007; 61: 256–261.
20. Yi CA, Lee KS, Han J, *et al.* 3-T MRI for differentiating inflammation- and fibrosis-predominant lesions of usual and nonspecific interstitial pneumonia: comparison study with pathologic correlation. *Am J Roentgenol* 2008; 190: 878–885.
21. Suga K, Tsukuda T, Awaya H, *et al.* Impaired respiratory mechanics in pulmonary emphysema: evaluation with dynamic breathing MRI. *J Magn Reson Imaging* 1999; 10: 510–520.
22. Iwasawa T, Takahashi H, Ogura T, *et al.* Correlation of lung parenchymal MR signal intensity with pulmonary function tests and quantitative computed tomography (CT) evaluation: A pilot study. *J Magn Reson Imaging* 2007; 26: 1530–1536.
23. Ohno Y, Hatabu H, Takenaka D, *et al.* Metastases in mediastinal and hilar lymph nodes in patients with non–small cell lung cancer: quantitative and qualitative assessment with STIR turbo spin-echo MR imaging. *Radiology* 2004; 231: 872–879.
24. Ohno Y, Koyama H, Nogami M, *et al.* STIR turbo SE MR imaging *vs.* coregistered FDG-PET/CT: quantitative and qualitative assessment of N-stage in non-small-cell lung cancer patients. *J Magn Reson Imaging* 2007; 26: 1071–1080.
25. Morikawa M, Demura Y, Ishizaki T, *et al.* The effectiveness of ^{18}F-FDG PET/CT Combined with STIR MRI for diagnosing nodal involvement in the thorax. *J Nucl Med* 2009; 50: 81–87.
26. Vogel-Claussen J, Renne J, Hinrichs J, *et al.* Quantification of pulmonary inflammation after segmental allergen challenge using turbo-inversion recovery-magnitude magnetic resonance imaging. *Am J Respir Crit Care Med* 2014; 189: 650–657.
27. Edelman RR, Hatabu H, Tadamura E, *et al.* Noninvasive assessment of regional ventilation in the human lung using oxygen-enhanced magnetic resonance imaging. *Nat Med* 1996; 2: 1236–1239.
28. Hatabu H, Tadamura E, Chen Q, *et al.* Pulmonary ventilation: dynamic MRI with inhalation of molecular oxygen. *Eur J Radiol* 2001; 37: 172–178.
29. Look DC, Locker DR. Time saving in measurement of NMR and EPR relaxation times. *Rev Sci Instrum* 1970; 41: 250–251.
30. Jakob PM, Hillenbrand CM, Wang T, *et al.* Rapid quantitative lung ^{1}H T1 mapping. *J Magn Reson Imaging* 2001; 14: 795–799.
31. Ohno Y, Hatabu H, Takenaka D, *et al.* Oxygen-enhanced MR ventilation imaging of the lung. *Am J Roentgenol* 2001; 177: 185–194.
32. Chen Q, Jakob PM, Griswold MA, *et al.* Oxygen enhanced MR ventilation imaging of the lung. *Magma* 1998; 7: 153–161.
33. Sá RC, Cronin MV, Cortney Henderson A, *et al.* Vertical distribution of specific ventilation in normal supine humans measured by oxygen-enhanced proton MRI. *J Appl Physiol* 2010; 109: 1950–1959.
34. Ohno Y, Iwasawa T, Seo JB, *et al.* Oxygen-enhanced magnetic resonance imaging *versus* computed tomography. *Am J Respir Crit Care Med* 2008; 177: 1095–1102.
35. Hart K, Marshall H, Stewart NJ, *et al.* Quantitative lung T1 mapping and oxygen enhanced MRI in IPF. *Eur Respir J* 2014; 44: Suppl. 58, 1727.
36. Molinari F, Eichinger M, Risse F, *et al.* Navigator-triggered oxygen-enhanced MRI with simultaneous cardiac and respiratory synchronization for the assessment of interstitial lung disease. *J Magn Reson Imaging* 2007; 26: 1523–1529.

37. Müller CJ, Schwaiblmair M, Scheidler J, *et al.* Pulmonary diffusing capacity: assessment with oxygen-enhanced lung MR imaging – preliminary findings. *Radiology* 2002; 222: 499–506.
38. Ohno Y, Hatabu H, Takenaka D, *et al.* Dynamic oxygen-enhanced MRI reflects diffusing capacity of the lung. *Magn Reson Med* 2002; 47: 1139–1144.
39. Jakob PM, Wang T, Schultz G, *et al.* Assessment of human pulmonary function using oxygen-enhanced T1 imaging in patients with cystic fibrosis. *Magn Reson Med* 2004; 51: 1009–1016.
40. Caravan P, Ellison JJ, McMurry TJ, *et al.* Gadolinium(III) chelates as MRI contrast agents: structure, dynamics, and applications. *Chem Rev* 1999; 99: 2293–2352.
41. Kauczor H-U, Kreitner K-F. Contrast-enhanced MRI of the lung. *Eur J Radiol* 2000; 34: 196–207.
42. Hatabu H, Gaa J, Kim D, *et al.* Pulmonary perfusion: qualitative assessment with dynamic contrast-enhanced MRI using ultra-short TE and inversion recovery turbo FLASH. *Magn Reson Med* 1996; 36: 503–508.
43. Meaney JFM, Weg JG, Chenevert TL, *et al.* Diagnosis of pulmonary embolism with magnetic resonance angiography. *N Engl J Med* 1997; 336: 1422–1427.
44. Fink C, Risse F, Buhmann R, *et al.* Quantitative analysis of pulmonary perfusion using time-resolved parallel 3D MRI – initial results. *RoFo* 2004; 176: 170–174.
45. Korosec FR, Frayne R, Grist TM, *et al.* Time-resolved contrast-enhanced 3D MR angiography. *Magn Reson Med* 1996; 36: 345–351.
46. Ohno Y, Higashino T, Takenaka D, *et al.* MR angiography with sensitivity encoding (SENSE) for suspected pulmonary embolism: comparison with MDCT and ventilation–perfusion scintigraphy. *Am J Roentgenol* 2004; 183: 91–98.
47. Amundsen T, Torheim G, Kvistad KA, *et al.* Perfusion abnormalities in pulmonary embolism studied with perfusion MRI and ventilation-perfusion scintigraphy: an intra-modality and inter-modality agreement study. *J Magn Reson Imaging* 2002; 15: 386–394.
48. Jang YM, Oh Y-M, Seo JB, *et al.* Quantitatively assessed dynamic contrast-enhanced magnetic resonance imaging in patients with chronic obstructive pulmonary disease: correlation of perfusion parameters with pulmonary function test and quantitative computed tomography. *Invest Radiol* 2008; 43: 403–410.
49. Ohno Y, Hatabu H, Higashino T, *et al.* Dynamic perfusion MRI *versus* perfusion scintigraphy: prediction of postoperative lung function in patients with lung cancer. *Am J Roentgenol* 2004; 182: 73–78.
50. Ohno Y, Hatabu H, Murase K, *et al.* Quantitative assessment of regional pulmonary perfusion in the entire lung using three-dimensional ultrafast dynamic contrast-enhanced magnetic resonance imaging: Preliminary experience in 40 subjects. *J Magn Reson Imaging* 2004; 20: 353–365.
51. Fink C, Bock M, Puderbach M, *et al.* Partially parallel three-dimensional magnetic resonance imaging for the assessment of lung perfusion – initial results. *Invest Radiol* 2003; 38: 482–488.
52. Rajaram S, Swift AJ, Telfer A, *et al.* 3D contrast-enhanced lung perfusion MRI is an effective screening tool for chronic thromboembolic pulmonary hypertension: results from the ASPIRE Registry. *Thorax* 2013; 68: 677–678.
53. Swift AJ, Wild JM, Nagle SK, *et al.* Quantitative MR imaging of pulmonary hypertension: a practical approach to the current state of the art. *J Thorac Imaging* 2014; 29: 68–79.
54. Swift AJ, Telfer A, Rajaram S, *et al.* Dynamic contrast–enhanced magnetic resonance imaging in patients with pulmonary arterial hypertension. *Pulm Circ* 2014; 4: 61–70.
55. Ohno Y, Hatabu H, Murase K, *et al.* Primary pulmonary hypertension: 3D dynamic perfusion MRI for quantitative analysis of regional pulmonary perfusion. *Am J Roentgenol* 2007; 188: 48–56.
56. Hueper K, Parikh M, Prince MR, *et al.* Quantitative and semi-quantitative measures of regional pulmonary parenchymal perfusion by magnetic resonance imaging and their relationships to global lung perfusion and lung diffusing capacity – the MESA COPD study. *Invest Radiol* 2013; 48: 223–230.
57. Sergiacomi G, Bolacchi F, Cadioli M, *et al.* Combined pulmonary fibrosis and emphysema: 3D time-resolved MR angiographic evaluation of pulmonary arterial mean transit time and time to peak enhancement. *Radiology* 2010; 254: 601–608.
58. Johnson KM, Fain SB, Schiebler ML, *et al.* Optimized 3D ultrashort echo time pulmonary MRI. *Magn Reson Med* 2013; 70: 1241–1250.
59. Ohno Y, Koyama H, Yoshikawa T, *et al.* Pulmonary high-resolution ultrashort TE MR imaging: Comparison with thin-section standard- and low-dose computed tomography for the assessment of pulmonary parenchyma diseases. *J Magn Reson Imaging* 2015; 43: 512–532.
60. Bauman G, Puderbach M, Deimling M, *et al.* Non-contrast-enhanced perfusion and ventilation assessment of the human lung by means of Fourier decomposition in proton MRI. *Magn Reson Med* 2009; 62: 656–664.
61. Schönfeld C, Cebotari S, Voskrebenzev A, *et al.* Performance of perfusion-weighted Fourier decomposition MRI for detection of chronic pulmonary emboli. *J Magn Reson Imaging* 2015; 42: 72–79.
62. Walker TG, Happer W. Spin-exchange optical pumping of noble-gas nuclei. *Rev Mod Phys* 1997; 69: 629–642.
63. Colegrove F, Schearer L, Walters G. Polarization of He^3 gas by optical pumping. *Phys Rev* 1963; 132: 2561.
64. Hersman FW, Ruset IC, Ketel S, *et al.* Large production system for hyperpolarized ^{129}Xe for human lung imaging studies. *Acad Radiol* 2008; 15: 683–692.

65. Nikolaou P, Coffey AM, Walkup LL, *et al.* Near-unity nuclear polarization with an open-source ^{129}Xe hyperpolarizer for NMR and MRI. *Proc Natl Acad Sci USA* 2013; 110: 14150–14155.
66. Norquay G, Parnell SR, Xu X, *et al.* Optimized production of hyperpolarized ^{129}Xe at 2 bars for *in vivo* lung magnetic resonance imaging. *J Appl Phys* 2013; 113: 044908–044909.
67. Ebert M, Grossmann T, Heil W, *et al.* Nuclear magnetic resonance imaging with hyperpolarised helium-3. *Lancet* 1996; 347: 1297–1299.
68. MacFall JR, Charles HC, Black RD, *et al.* Human lung air spaces: potential for MR imaging with hyperpolarized He-3. *Radiology* 1996; 200: 553–558.
69. Mugler JP III, Driehuys B, Brookeman JR, *et al.* MR imaging and spectroscopy using hyperpolarized ^{129}Xe gas: preliminary human results. *Magn Reson Med* 1997; 37: 809–815.
70. Fain SB, Korosec FR, Holmes JH, *et al.* Functional lung imaging using hyperpolarized gas MRI. *J Magn Reson Imaging* 2007; 25: 910–923.
71. van Beek EJR, Wild JM, Kauczor H-U, *et al.* Functional MRI of the lung using hyperpolarized 3-helium gas. *J Magn Reson Imaging* 2004; 20: 540–554.
72. Wild JM, Woodhouse N, Paley MNJ, *et al.* Comparison between 2D and 3D gradient-echo sequences for MRI of human lung ventilation with hyperpolarized ^{3}He. *Magn Reson Med* 2004; 52: 673–678.
73. Van Beek EJR, Dahmen AM, Stavngaard T, *et al.* Hyperpolarised ^{3}He MRI versus HRCT in COPD and normal volunteers: PHIL trial. *Eur Respir J* 2009; 34: 1311–1321.
74. Deppe MH, Parra-Robles J, Ajraoui S, *et al.* Susceptibility effects in hyperpolarized He-3 lung MRI at 1.5 T and 3 T. *J Magn Reson Imaging* 2009; 30: 418–423.
75. Parraga G, Ouriadov A, Evans A, *et al.* Hyperpolarized ^{3}He ventilation defects and apparent diffusion coefficients in chronic obstructive pulmonary disease: preliminary results at 3.0 tesla. *Invest Radiol* 2007; 42: 384–391.
76. Altes TA, Powers PL, Knight-Scott J, *et al.* Hyperpolarized ^{3}He MR lung ventilation imaging in asthmatics: Preliminary findings. *J Magn Reson Imaging* 2001; 13: 378–384.
77. Tzeng Y-S, Lutchen K, Albert M. The difference in ventilation heterogeneity between asthmatic and healthy subjects quantified using hyperpolarized ^{3}He MRI. *J Appl Physiol* 2009; 106: 813–822.
78. Marshall H, Deppe MH, Parra-Robles J, *et al.* Direct visualisation of collateral ventilation in COPD with hyperpolarised gas MRI. *Thorax* 2012; 67: 613–617.
79. Bannier E, Cieslar K, Mosbah K, *et al.* Hyperpolarized ^{3}He MR for sensitive imaging of ventilation function and treatment efficiency in young cystic fibrosis patients with normal lung function. *Radiology* 2010; 255: 225–232.
80. Donnelly LF, MacFall JR, McAdams HP, *et al.* Cystic fibrosis: combined hyperpolarized ^{3}He-enhanced and conventional proton MR imaging in the lung – preliminary observations. *Radiology* 1999; 212: 885–889.
81. Altes TA, Mai VM, Munger TM, *et al.* Pulmonary embolism: comprehensive evaluation with MR Ventilation and perfusion scanning with hyperpolarized helium-3, arterial spin tagging, and contrast-enhanced MRA. *J Vasc Interv Radiol* 2005; 16: 999–1005.
82. Gast KK, Zaporozhan J, Ley S, *et al.* ^{3}He-MRI in follow-up of lung transplant recipients. *Eur Radiol* 2004; 14: 78–85.
83. Salerno M, Altes TA, Brookeman JR, *et al.* Dynamic spiral MRI of pulmonary gas flow using hyperpolarized ^{3}He: preliminary studies in healthy and diseased lungs. *Magn Reson Med* 2001; 46: 667–677.
84. Wild JM, Paley MNJ, Kasuboski L, *et al.* Dynamic radial projection MRI of inhaled hyperpolarized ^{3}He gas. *Magn Reson Med* 2003; 49: 991–997.
85. Shea DA, Morgan D. The Helium-3 Shortage: Supply, Demand, and Options for Congress. Washington, Congressional Research Service, 2010.
86. Kirby M, Svenningsen S, Owrangi A, *et al.* Hyperpolarized ^{3}He and ^{129}Xe MR imaging in healthy volunteers and patients with chronic obstructive pulmonary disease. *Radiology* 2012; 265: 600–610.
87. Svenningsen S, Kirby M, Starr D, *et al.* Hyperpolarized ^{3}He and ^{129}Xe MRI: differences in asthma before bronchodilation. *J Magn Reson Imaging* 2013; 38: 1521–1530.
88. Virgincar RS, Cleveland ZI, Sivaram Kaushik S, *et al.* Quantitative analysis of hyperpolarized ^{129}Xe ventilation imaging in healthy volunteers and subjects with chronic obstructive pulmonary disease. *NMR Biomed* 2013; 26: 424–435.
89. Stewart NJ, Norquay G, Griffiths PD, *et al.* Feasibility of human lung ventilation imaging using highly polarized naturally abundant xenon and optimized three-dimensional steady-state free precession. *Magn Reson Med* 2015; 74: 346–352.
90. Kirby M, Svenningsen S, Kanhere N, *et al.* Pulmonary ventilation visualized using hyperpolarized helium-3 and xenon-129 magnetic resonance imaging: differences in COPD and relationship to emphysema. *J Appl Physiol* 2013; 114: 707–715.
91. He M, Robertson SH, Kaushik SS, *et al.* Dose and pulse sequence considerations for hyperpolarized ^{129}Xe ventilation MRI. *Magn Reson Imaging* 2015; 33: 877–885.
92. Samee S, Altes T, Powers P, *et al.* Imaging the lungs in asthmatic patients by using hyperpolarized helium-3 magnetic resonance: assessment of response to methacholine and exercise challenge. *J Allergy Clin Immunol* 2003; 111: 1205–1211.

93. Kirby M, Mathew L, Heydarian M, *et al.* Chronic obstructive pulmonary disease: quantification of bronchodilator effects by using hyperpolarized He MR imaging. *Radiology* 2011; 261: 283–292.
94. Mentore K, Froh DK, de Lange EE, *et al.* Hyperpolarized HHe 3 MRI of the lung in cystic fibrosis: assessment at baseline and after bronchodilator and airway clearance treatment. *Acad Radiol* 2005; 12: 1423–1429.
95. Sanders RD, Franks NP, Maze M. Xenon: no stranger to anaesthesia. *Br J Anaesth* 2003; 91: 709–717.
96. Driehuys B, Martinez-Jimenez S, Cleveland ZI, *et al.* Chronic obstructive pulmonary disease: safety and tolerability of hyperpolarized ^{129}Xe MR imaging in healthy volunteers and patients. *Radiology* 2012; 262: 279–289.
97. Shukla Y, Wheatley A, Kirby M, *et al.* Hyperpolarized ^{129}Xe magnetic resonance imaging: tolerability in healthy volunteers and subjects with pulmonary disease. *Acad Radiol* 2012; 19: 941–951.
98. Lipson DA, Roberts DA, Hansen-Flaschen J, *et al.* Pulmonary ventilation and perfusion scanning using hyperpolarized helium-3 MRI and arterial spin tagging in healthy normal subjects and in pulmonary embolism and orthotopic lung transplant patients. *Magn Reson Med* 2002; 47: 1073–1076.
99. Hong C, Leawoods JC, Yablonskiy DA, *et al.* Feasibility of combining MR perfusion, angiography, and ^{3}He ventilation imaging for evaluation of lung function in a porcine model1. *Acad Radiol* 2005; 12: 202–209.
100. Rao M, Wild JM. RF instrumentation for same-breath triple nuclear lung MR imaging of ^{1}H and hyperpolarized ^{3}He and ^{129}Xe at 1.5 T. *Magn Reson Med* 2015 [In press DOI: 10.1002/mrm.25680].
101. Wild JM, Marshall H, Xu X, *et al.* Simultaneous imaging of lung structure and function with triple-nuclear hybrid MR imaging. *Radiology* 2013; 267: 251–255.
102. Saam BT, Yablonskiy DA, Kodibagkar VD, *et al.* MR imaging of diffusion of ^{3}He gas in healthy and diseased lungs. *Magn Reson Med* 2000; 44: 174–179.
103. Yablonskiy DA, Sukstanskii AL, Leawoods JC, *et al.* Quantitative *in vivo* assessment of lung microstructure at the alveolar level with hyperpolarized ^{3}He diffusion MRI. *Proc Natl Acad Sci USA* 2002; 99: 3111–3116.
104. Yablonskiy DA, Sukstanskii AL, Woods JC, *et al.* Quantification of lung microstructure with hyperpolarized ^{3}He diffusion MRI. *J Appl Physiol* 2009; 107: 1258–1265.
105. Parra-Robles J, Marshall H, Wild JM. Characterization of ^{3}He diffusion in lungs using a stretched exponential model. *Proc Intl Soc Mag Reson Med* 2013; 21: 0820.
106. Trampel R, Jensen JH, Lee RF, *et al.* Diffusional kurtosis imaging in the lung using hyperpolarized ^{3}He. *Magn Reson Med* 2006; 56: 733–737.
107. Salerno M, Lange EEd, Altes TA, *et al.* Emphysema: hyperpolarized helium 3 diffusion MR imaging of the lungs compared with spirometric indexes – initial experience. *Radiology* 2002; 222: 252–260.
108. Fain SB, Panth SR, Evans MD, *et al.* Early emphysematous changes in asymptomatic smokers: detection with ^{3}He MR imaging. *Radiology* 2006; 239: 875–883.
109. Swift AJ, Wild JM, Fichele S, *et al.* Emphysematous changes and normal variation in smokers and COPD patients using diffusion ^{3}He MRI. *Eur J Radiol* 2005; 54: 352–358.
110. Wang C, Altes TA, Mugler JP III, *et al.* Assessment of the lung microstructure in patients with asthma using hyperpolarized ^{3}He diffusion MRI at two time scales: comparison with healthy subjects and patients with COPD. *J Magn Reson Imaging* 2008; 28: 80–88.
111. Kirby M, Mathew L, Wheatley A, *et al.* Chronic obstructive pulmonary disease: longitudinal hyperpolarized ^{3}He MR imaging. *Radiology* 2010; 256: 280–289.
112. Woods JC, Choong CK, Yablonskiy DA, *et al.* Hyperpolarized ^{3}He diffusion MRI and histology in pulmonary emphysema. *Magn Reson Med* 2006; 56: 1293–1300.
113. Altes TA, Mata J, de Lange EE, *et al.* Assessment of lung development using hyperpolarized helium-3 diffusion MR imaging. *J Magn Reson Imaging* 2006; 24: 1277–1283.
114. Butler JP, Loring SH, Patz S, *et al.* Evidence for adult lung growth in humans. *N Engl J Med* 2012; 367: 244–247.
115. Narayanan M, Owers-Bradley J, Beardsmore CS, *et al.* Alveolarization continues during childhood and adolescence. *Am J Respir Crit Care Med* 2012; 185: 186–191.
116. Kaushik SS, Cleveland ZI, Cofer GP, *et al.* Diffusion-weighted hyperpolarized ^{129}Xe MRI in healthy volunteers and subjects with chronic obstructive pulmonary disease. *Magn Reson Med* 2011; 65: 1154–1165.
117. Kirby M, Ouriadov A, Svenningsen S, *et al.* Hyperpolarized ^{3}He and ^{129}Xe magnetic resonance imaging apparent diffusion coefficients: physiological relevance in older never- and ex-smokers. *Physiol Rep* 2014; 2: e12068.
118. Deninger AJ, Månsson S, Petersson JS, *et al.* Quantitative measurement of regional lung ventilation using ^{3}He MRI. *Magn Reson Med* 2002; 48: 223–232.
119. Emami K, Kadlecek SJ, Woodburn JM, *et al.* Improved technique for measurement of regional fractional ventilation by hyperpolarized ^{3}He MRI. *Magn Reson Med* 2010; 63: 137–150.
120. Deppe MH, Parra-Robles J, Ajraoui S, *et al.* Combined measurement of pulmonary inert gas washout and regional ventilation heterogeneity by MR of a single dose of hyperpolarized He-3. *Magn Reson Med* 2011; 65: 1076–1084.
121. Horn FC, Deppe MH, Marshall H, *et al.* Quantification of regional fractional ventilation in human subjects by measurement of hyperpolarized He-3 washout with 2D and 3D MRI. *J Appl Physiol* 2014; 116: 129–139.

122. Horn F, Horsley A, Smith L, *et al.* Visualising regional ventilation heterogeneity by linking multiple breath washout to ^{3}He MRI imaging. *Eur Respir J* 2014; 44: Suppl. 58, 546.
123. Marshall H, Parra-Robles J, Deppe MH, *et al.* ^{3}He p_{O_2} mapping is limited by delayed-ventilation and diffusion in chronic obstructive pulmonary disease. *Magn Reson Med* 2014; 71: 1172–1178.
124. Saam B, Happer W, Middleton H. Nuclear relaxation of ^{3}He in the presence of O_2. *Phys Rev A* 1995; 52: 862–865.
125. Deninger AJ, Eberle B, Bermuth J, *et al.* Assessment of a single-acquisition imaging sequence for oxygen-sensitive ^{3}He-MRI. *Magn Reson Med* 2002; 47: 105–114.
126. Deninger AJ, Eberle B, Ebert M, *et al.* Quantification of regional intrapulmonary oxygen partial pressure evolution during apnea by ^{3}He MRI. *J Magn Reson* 1999; 141: 207–216.
127. Wild JM, Fichele S, Woodhouse N, *et al.* 3D volume-localized p_{O_2} measurement in the human lung with ^{3}He MRI. *Magn Reson Med* 2005; 53: 1055–1064.
128. Hamedani H, Kadlecek SJ, Emami K, *et al.* A multislice single breath-hold scheme for imaging alveolar oxygen tension in humans. *Magn Reson Med* 2012; 67: 1332–1345.
129. Miller GW, Mugler JP, Altes TA, *et al.* A short-breath-hold technique for lung p_{O_2} mapping with ^{3}He MRI. *Magn Reson Med* 2010; 63: 127–136.
130. Gast K, Biedermann A, Herweling A, *et al.* Oxygen-sensitive ^{3}He-MRI in bronchiolitis obliterans after lung transplantation. *Eur Radiol* 2008; 18: 530–537.
131. de Rochefort L, Maître X, Fodil R, *et al.* Phase-contrast velocimetry with hyperpolarized ^{3}He for *in vitro* and *in vivo* characterization of airflow. *Magn Reson Med* 2006; 55: 1318–1325.
132. Collier GJ, Wild JM. *In vivo* measurement of gas flow in human airways with hyperpolarized gas MRI and compressed sensing. *Magn Reson Med* 2015; 73: 2255–2261.
133. de Rochefort L, Vial L, Fodil R, *et al. In vitro* validation of computational fluid dynamic simulation in human proximal airways with hyperpolarized ^{3}He magnetic resonance phase-contrast velocimetry. *J Appl Physiol* 2007; 102: 2012–2023.
134. Collier GJ, Marshall H, Rao M, *et al.* Observation of cardiogenic flow oscillations in healthy subjects with hyperpolarized ^{3}He MRI. *J Appl Physiol* 2015; 119: 1007–1014.
135. Mugler JP III, Altes TA. Hyperpolarized ^{129}Xe MRI of the human lung. *J Magn Reson Imaging* 2013; 37: 313–331.
136. Weathersby PK, Homer LD. Solubility of inert gases in biological fluids and tissue: a review. *Undersea Biomed Res* 1980; 7: 277–296.
137. Bifone A, Song YQ, Seydoux R, *et al.* NMR of laser-polarized xenon in human blood. *Proc Natl Acad Sci USA* 1996; 93: 12932–12936.
138. Ruppert K, Brookeman JR, Hagspiel KD, *et al.* NMR of hyperpolarized ^{129}Xe in the canine chest: spectral dynamics during a breath-hold. *NMR Biomed* 2000; 13: 220–228.
139. Stewart NJ, Leung G, Norquay G, *et al.* Experimental validation of the hyperpolarized ^{129}Xe chemical shift saturation recovery technique in healthy volunteers and subjects with interstitial lung disease. *Magn Reson Med* 2015; 74: 196–207.
140. Qing K, Mugler JP, Altes TA, *et al.* Assessment of lung function in asthma and COPD using hyperpolarized ^{129}Xe chemical shift saturation recovery spectroscopy and dissolved-phase MRI. *NMR Biomed* 2014; 27: 1490–1501.
141. Patz S, Muradyan I, Hrovat M, *et al.* Diffusion of hyperpolarized ^{129}Xe in the lung: a simplified model of ^{129}Xe septal uptake and experimental results. *N J Phys* 2011; 13: 015009.
142. Chang YV. MOXE: a model of gas exchange for hyperpolarized ^{129}Xe magnetic resonance of the lung. *Magn Reson Med* 2013; 69: 884–890.
143. Chang YV, Quirk JD, Ruset IC, *et al.* Quantification of human lung structure and physiology using hyperpolarized ^{129}Xe. *Magn Reson Med* 2014; 71: 339–344.
144. Mugler JP III, Altes TA, Ruset IC, *et al.* Simultaneous magnetic resonance imaging of ventilation distribution and gas uptake in the human lung using hyperpolarized xenon-129. *Proc Natl Acad Sci USA* 2010; 107: 21707–21712.
145. Cleveland ZI, Cofer GP, Metz G, *et al.* Hyperpolarized ^{129}Xe MR imaging of alveolar gas uptake in humans. *PLoS One* 2010; 5: e12192.
146. Driehuys B, Cofer GP, Pollaro J, *et al.* Imaging alveolar-capillary gas transfer using hyperpolarized ^{129}Xe MRI. *Proc Natl Acad Sci USA* 2006; 103: 18278–18283.
147. Reeder SB, Pineda AR, Wen Z, *et al.* Iterative decomposition of water and fat with echo asymmetry and least-squares estimation (IDEAL): application with fast spin-echo imaging. *Magn Reson Med* 2005; 54: 636–644.
148. Qing K, Ruppert K, Jiang Y, *et al.* Regional mapping of gas uptake by blood and tissue in the human lung using hyperpolarized xenon-129 MRI. *J Magn Reson Imaging* 2014; 39: 346–359.
149. Kaushik SS, Robertson SH, Freeman MS, *et al.* Single-breath clinical imaging of hyperpolarized ^{129}Xe in the airspaces, barrier, and red blood cells using an interleaved 3D radial 1-point Dixon acquisition. *Magn Reson Med* 2015 [In press DOI: 10.1002/mrm.25675].
150. Ruppert K, Brookeman JR, Hagspiel KD, *et al.* Probing lung physiology with xenon polarization transfer contrast (XTC). *Magn Reson Med* 2000; 44: 349–357.

151. Ruppert K, Mata JF, Wang HT, *et al.* XTC MRI: sensitivity improvement through parameter optimization. *Magn Reson Med* 2007; 57: 1099–1109.
152. Muradyan I, Butler JP, Dabaghyan M, *et al.* Single-breath xenon polarization transfer contrast (SB-XTC): Implementation and initial results in healthy humans. *J Magn Reson Imaging* 2013; 37: 457–470.
153. Dregely I, Mugler JP III, Ruset IC, *et al.* Hyperpolarized xenon-129 gas-exchange imaging of lung microstructure: first case studies in subjects with obstructive lung disease. *J Magn Reson Imaging* 2011; 33: 1052–1062.
154. Dregely I, Ruset IC, Mata JF, *et al.* Multiple-exchange-time xenon polarization transfer contrast (MXTC) MRI: initial results in animals and healthy volunteers. *Magn Reson Med* 2012; 67: 943–953.
155. Couch MJ, Ball IK, Li T, *et al.* Inert fluorinated gas MRI: a new pulmonary imaging modality. *NMR Biomed* 2014; 27: 1525–1534.
156. Halaweish AF, Moon RE, Foster WM, *et al.* Perfluoropropane gas as a magnetic resonance lung imaging contrast agent in humans. *Chest* 2013; 144: 1300–1310.
157. Couch MJ, Ball IK, Li T, *et al.* Pulmonary ultrashort echo time ^{19}F MR imaging with inhaled fluorinated gas mixtures in healthy volunteers: feasibility. *Radiology* 2013; 269: 903–909.

Conflict of interest: None declared.

Acknowledgements: The authors would like to thank Helen Marshall, Kerry Hart and Fung Chan at the University of Sheffield, Sheffield, UK.

Chapter 2

Radionuclide imaging

Frank M. Bengel

Radionuclide imaging techniques provide noninvasive information about global and regional lung function, physiology and biology. The ventilation/perfusion scan is an established test for detecting pulmonary embolism. Its clinical role has shifted from the acute setting towards the workup of CTEPH. Other routine clinical applications include quantification prior to lung surgery and assessment of right-left shunting. In lung cancer, PET with the glucose analogue ^{18}F deoxyglucose currently serves as a first line staging tool and may be used more extensively for monitoring of therapy in the future. Other imaging markers of molecular mechanisms are penetrating the clinical arena, *e.g.* in inflammatory conditions, and those are expected to lead to further molecular imaging applications in lung disease. Finally, the advent of hybrid imaging devices such as SPECT-CT, PET-CT and, more recently, PET/magnetic resonance, has led to the convergence of tomographic imaging techniques towards a multi-modality, multi-parametric environment for precise, integrated imaging of lung morphology, physiology and molecular function. This is expected to aid in the personalisation of pulmonary medicine.

Traditionally, imaging of the lung has been a major application of nuclear medicine techniques. The ventilation/perfusion (V'/Q') scan has been employed for detection of acute pulmonary embolism for decades [1]. With the advent of broadly and rapidly available multislice CT pulmonary angiography, however, the V'/Q' scan has lost relevance in the emergency setting [2, 3]. Nevertheless, the field has adapted to the changing demands of clinical pulmonary medicine. Methodological advances have led to the implementation of tomographic and hybrid imaging, and V'/Q' scans today are mostly employed in selected settings such as suspected CTEPH [4] or prior to reductive lung surgery [5]. Meanwhile, the advent of clinical molecular imaging established lung malignancies as an important application of radionuclide imaging, whereby FDG-PET is currently the standard for primary staging [6, 7]. Based on further methodological advances and novel radiopharmaceuticals, the transformation of the field of pulmonary nuclear medicine will continue. This chapter provides an overview of established and novel radiopharmaceuticals and nuclear imaging techniques in lung disease, along with a brief summary of their concurrent and predicted future clinical applications.

Radiopharmaceuticals for lung imaging

Currently available radiopharmaceuticals for imaging of the lung are summarised in table 1. The underlying principles are briefly outlined here.

Klinik für Nuklearmedizin, Medizinische Hochschule Hannover, Hannover, Germany

Correspondence: Frank M. Bengel, Klinik für Nuklearmedizin, Medizinische Hochschule Hannover, Carl-Neuberg-Str. 1, D-30625 Hannover, Germany. E-mail: bengel.frank@mh-hannover.de

Copyright ©ERS 2015. Print ISBN: 978-1-84984-065-1. Online ISBN: 978-1-84984-066-8. Print ISSN: 2312-508X. Online ISSN: 2312-5098.

Target: ventilation

Imaging of lung ventilation is achieved using either radioisotopes of inert gases such as ^{81m}Kr or ^{133}Xe or ^{99m}Tc-labelled compounds such as nebuliser-produced ^{99m}Tc aerosol or generator-produced ^{99m}Tc carbon microparticles (Technegas; Cyclomedia, Lucas Heights, Australia) [8, 9]. Gases have the advantage of a physiological biodistribution and kinetic studies, including a single-breath uptake phase, an equilibrium phase and a washout phase. But they also pose challenges for radiation safety due to their volatility, and they preclude tomographic imaging owing to their rapid kinetics. Technegas or aerosols allow for tomographic imaging because they are deposited in the bronchial tree according to their inhalation pattern. Depending on size of the particle and on airflow patterns (especially in obstruction), they may not reach bronchiolar or alveolar structures and cause hot spots due to clumping in more central bronchial regions. Additionally, residual ^{99m}Tc activity from the ventilation study may interfere with a subsequent perfusion study.

More recently, the generator product ^{68}Ga has been proposed for labelling of carbon particles and macro-aggregated albumin (MAA) in a manner similar to ^{99m}Tc, for use with more accurate PET technology [10].

Table 1. Radiopharmaceuticals for clinical lung imaging

Agent	Mechanism of accumulation	Imaging technique[#]	Typical activity[¶] MBq	Effective dose [¶] mSv·MBq^{-1}
^{81m}Kr	Gas (ventilation)	Planar	40–400	0.00003
^{133}Xe	Gas (ventilation)	Planar	200–500	0.0007
^{99m}Tc aerosol	Inhalation of aerosol	SPECT	20–40	0.0061
^{99m}Tc Technegas	Inhalation of carbon nanoparticle	SPECT	20–40	0.0046
^{68}Ga Galligas	Inhalation of carbon nanoparticle	PET	20–40	[+]
^{99m}Tc MAA	Capillary blockade (perfusion)	SPECT	40–150	0.011
^{68}Ga MAA	Capillary blockade (perfusion)	PET	25–60	[+]
^{18}F FDG	Glucose utilisation (tumour, inflammation)	PET	150–200	0.019
^{68}Ga DOTATOC/ DOTATATE	Somatostatin receptor (carcinoid, other NET)	PET	100–200	0.021[§]
^{67}Ga	Inflammation	SPECT	150–200	0.12
^{111}In WBCs	Inflammation	SPECT	10–20	0.59
^{123}I MIBG	Catecholamine analogue, alveolar cell integrity	SPECT	150–300	0.013

[#]: SPECT is often accompanied by planar scans; [¶]: according to practice guidelines of the Society of Nuclear Medicine and Molecular Imaging (SNMMI) [8] and the European Association of Nuclear Medicine (EANM) [9], except where indicated; [+]: activity according to [11], dose estimates not existing; [§]: according to [58]. MAA: macro-aggregated albumin; NET: neuroendocrine tumour; WBCs: white blood cells; MIBG: meta-iodobenzylguanidine.

Target: perfusion

Intravenously injected agents arrive in the pulmonary vascular bed as the first capillary bed. This enables the intravenous use of radiolabelled capillary blocking microspheres for studying lung perfusion. Typically, ^{99m}Tc-labelled MAA is used for this purpose [8, 9]. MAA is biodegradable and only a very small fraction of capillaries are blocked. Particle numbers of around 350 000 are common and show no effect on haemodynamics.

As for ventilation studies, it has recently been suggested that ^{68}Ga may be used as an alternative label for MAA in order to obtain PET images of perfusion [11]. The novel combination of ^{68}Ga Galligas and ^{68}Ga-MAA for PET, however, requires further validation beyond the current, albeit promising results from single centres.

Target: molecular mechanisms

While V'/Q' imaging has long been the mainstay of lung radionuclide imaging, the success of FDG-PET in lung cancer has triggered a trend towards broader use of more specific molecular imaging agents [12, 13]. While the glucose analogue FDG is primarily used to track elevated glycolysis in malignancies, it has also been discovered that FDG accumulates in inflammatory lesions [14]. This may not just complicate tumour imaging, it has also resulted in dedicated applications of PET for imaging inflammatory activity, *e.g.* sarcoidosis [15, 16]. Alternative tracers for imaging lung inflammation include ^{67}Ga or ^{111}In-labelled white blood cells.

Other clinically applicable molecular targets include the somatostatin receptor, which is overexpressed on carcinoid and other neuroendocrine tumours and readily identified using ^{111}In octreoscan for SPECT, or ^{68}Ga DOTATOC or DOTATATE for PET [17]. Injury of alveolar endothelial cells, which express the noradrenaline transporter, may be identified by reduced uptake of the catecholamine analogue ^{123}I meta-iodobenzylguanidine [18].

Lung radionuclide imaging techniques

Lung V'/Q' scans have typically been acquired using planar gamma camera images of the chest in multiple projections (figure 1). This enables robust identification of segmental abnormalities and the technique is supported by large-scale clinical studies [2, 3, 19–22]. However, tomographic techniques and additional advanced methods have been introduced more recently to improve the quality and information content of radionuclide lung images [23, 24].

Single photon emission computed tomography

Tomographic SPECT images are acquired by a rotating gamma camera. Following reconstruction, a three-dimensional volume is obtained which enables the depiction of tomographic images with increased spatial resolution and volumetric information. It has been suggested that SPECT increases both sensitivity and specificity of V'/Q' scans when compared to planar imaging [25, 26]. Hence, SPECT lung imaging is increasingly used as a standard technique [23].

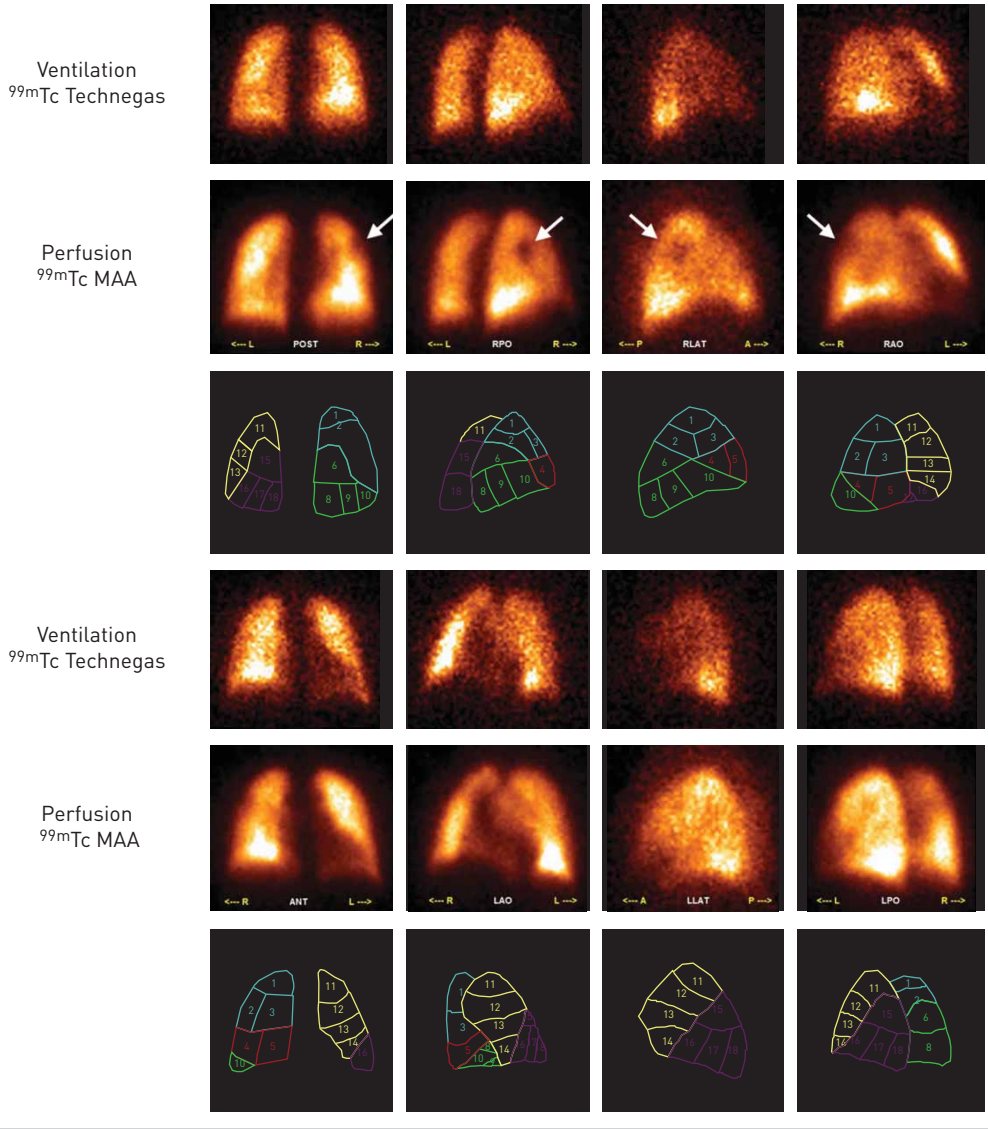

Figure 1. Case examples of planar ventilation/perfusion images in a patient with suspected pulmonary embolism. Ventilation/perfusion projections are displayed along with a standard colour-coded scheme showing the respective lung segments in each projection (Right upper lobe, blue: 1: apical; 2: posterior; 3: anterior. Right medial lobe, red: 4: lateral; 5: medial. Right lower lobe: 6: superior; 7: medial basal; 8: posterior basal; 9: lateral basal; 10: anterior basal. Left upper lobe, yellow: 11: apical posterior; 12: anterior; 13: superior lingual; 14: inferior lingual. Left lower lobe, purple: 15: superior; 16: anteromedial basal; 17: lateral basal; 18: posterior basal). Arrows indicate a clear perfusion defect in the lateral portion of the right upper lobe posterior segment (arrows), with normal ventilation. This mismatch is consistent with pulmonary embolism. POST: posterior; RPO: right posterior oblique; RLAT: right lateral; RAO: right anterior oblique; ANT: anterior; LAO: left anterior oblique; LLAT: left lateral; LPO: left posterior oblique; MAA: macro-aggregated albumin.

Hybrid imaging

The era of hybrid imaging has started with the introduction of integrated PET/CT systems, where tomographic PET images are fused with X-ray CT images obtained during the same

session. CT is used for attenuation correction of the nuclear dataset and refines the localisation of abnormalities in the radionuclide images [27]. Hybrid PET/CT has been a breakthrough for the use of FDG in oncology (figure 2). In lung cancer, it has been shown to improve diagnostic accuracy for nodal staging when compared with standalone PET or CT, or to the merging of separately obtained PET and CT scans [28].

Following the success of PET/CT, hybrid SPECT/CT systems were introduced. The added benefit of SPECT/CT has mostly been shown in the detection and localisation of small tumour lesions [29], but integration of CT-derived general morphology and segmental structure with radionuclide perfusion and ventilation signals may also improve the assessment of lung disease [30]. It should be noted that low-dose CTs without contrast suffice for the purpose of hybrid imaging (figure 3). Nevertheless, larger studies are necessary to identify the incremental diagnostic value of SPECT/CT over standalone SPECT in lung disease.

Finally, the latest generation of hybrid devices is the integrated PET/magnetic resonance system [31]. These systems hold great promise for a multi-parametric assessment of various diseases by integration of the molecular PET signal with simultaneously acquired tissue characteristics, function and morphology from MRI. Few applications in lung disease have been reported to date, but it is foreseeable that exciting new approaches will be introduced in the future [32].

Correction for respiratory motion

Advances in imaging technology are also focusing on the correction for respiratory motion. Acquisition of all types of nuclear images generally requires several minutes so that, unlike in radiology, breath hold imaging is not feasible. Images thus represent an average over the respiratory cycle and include motion-induced blurring and reduced resolution of target structures. The recent advent of list mode acquisition, where count detection is recorded

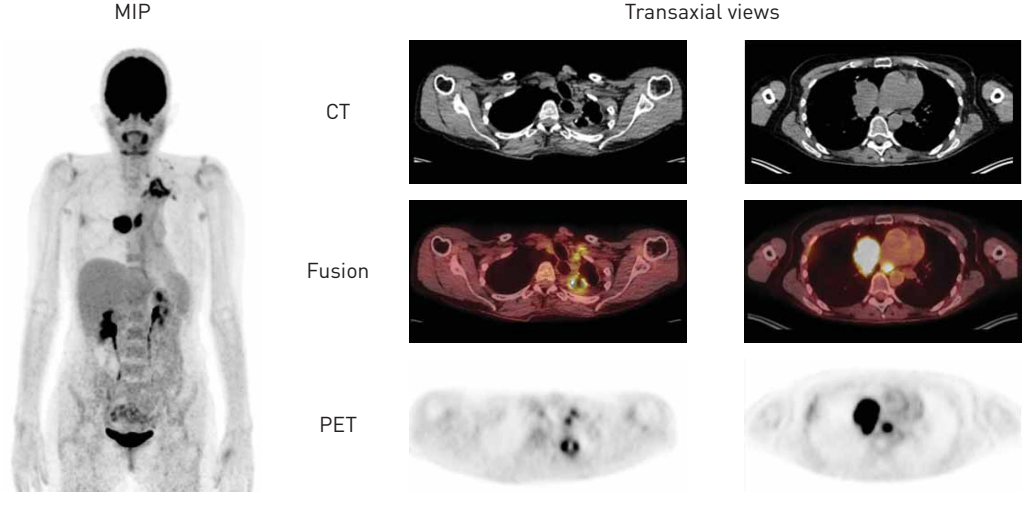

Figure 2. ^{18}F FDG-PET/CT in a patient with multiple non-small cell lung cancer (NSCLC) lesions. A large right hilar mass is confirmed as a tall-cell variant carcinoma, associated with an infra-carinal nodal metastasis. A left apical hypermetabolic region indicates recurrence of previously resected squamous cell carcinoma, along with multiple upper mediastinal and peri-clavicular nodal metastases.

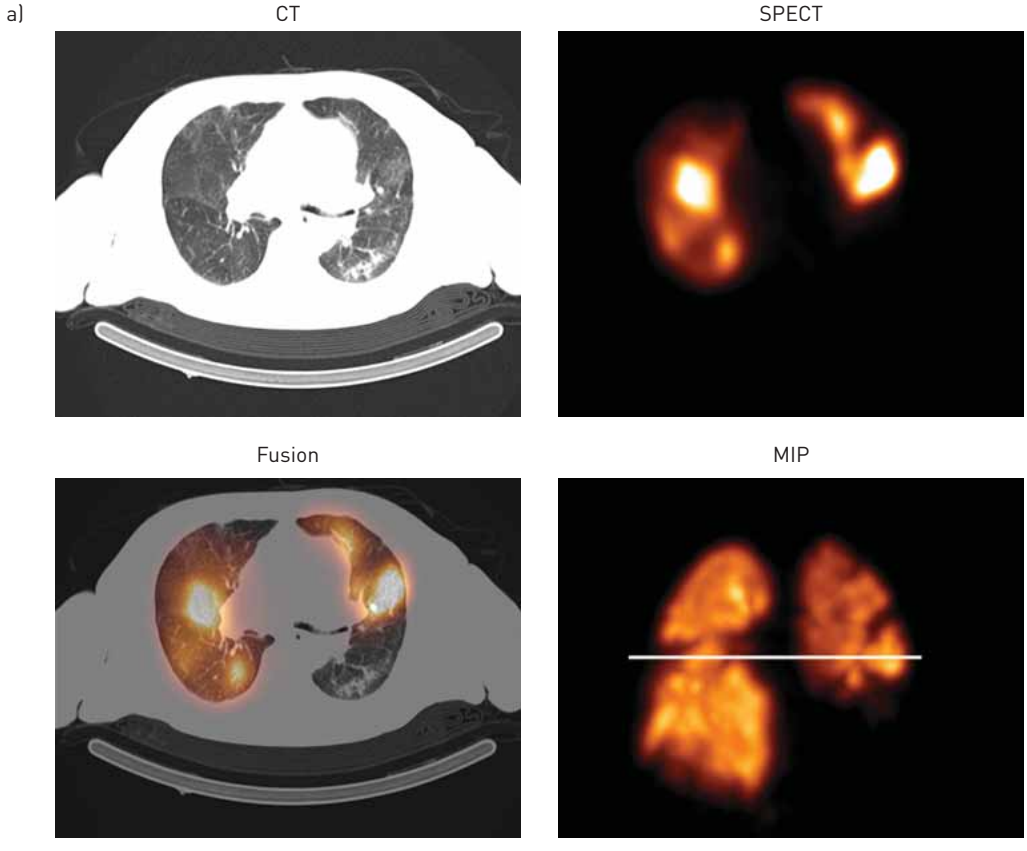

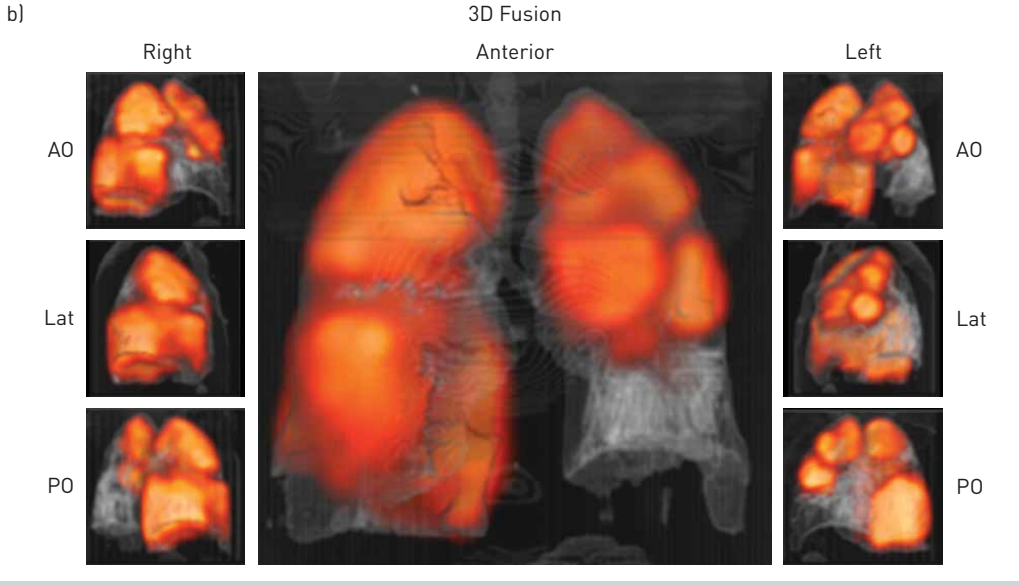

Figure 3. Hybrid lung perfusion SPECT/X-ray CT images in a patient with CTEPH. a) MIP and representative transaxial tomographic images show perfusion defects in left lower lobe and multiple additional bilateral segmental and subsegmental regions. CT shows structural abnormalities in only a fraction of hypoperfused regions. b) 3D SPECT/CT fusion images in multiple projections provide illustrative overview of multiple perfusion defects. AO: anterior oblique; Lat: lateral; PO: posterior oblique.

continuously, along with the establishment of techniques to track and record the respiratory cycle led to the introduction of respiratory gated, or motion frozen tomographic images. Such techniques were first introduced for PET/CT where they result in increased contrast and higher detection frequency for small intrapulmonary lesions [33]. More recently, respiratory motion correction has also been introduced for SPECT, where it may improve the visualisation of perfusion defects [34], and for PET V'/Q' scans [35].

Quantification

Traditionally, quantification has been a strength of nuclear imaging techniques. Since the introduction of digital imaging, planar V'/Q' scans have been used to assess split ventilation and perfusion between left and right lung, and to determine the relative contribution of upper, mid and lower portions of the lungs. This is achieved using region of interest technique in anterior and posterior projections, along with geometric means. Left to right shunt volumes are assessed similarly by determining radioactivity in brain and kidney (or whole body) relative to lungs. Such quantitative measures are clinically useful in planning surgery or assessing the effects of therapeutic interventions [36, 37]. The advent of SPECT/CT may provide even higher accuracy because it enables CT-based definition of lobar and segmental regions [38], which can be transferred to the volumetric perfusion and ventilation SPECT datasets for an anatomically accurate quantitative assessment (figure 4).

Clinical applications

A brief summary of the clinical applications of lung radionuclide imaging is given in the following. More detail will be provided in the respective disease-focused chapters of the *Monograph*.

Acute pulmonary embolism

Before the introduction of multislice CT for noninvasive pulmonary angiography, the V'/Q' scan was the primary diagnostic test in suspected pulmonary embolism. Clinical application was mostly defined by the criteria established from the Prospective Investigation of Pulmonary Embolism Diagnosis (PIOPED) study [3], in which an entirely negative scan safely rules out pulmonary embolism and a clearly positive scan with V'/Q' mismatch in multiple segments rules in pulmonary embolism. The broad spectrum of other, less clear patterns, called the intermediate probability scans, resulted in diagnostic uncertainty and often exposed the technique to criticism. As a consequence, PIOPED criteria were discussed controversially, modified, and frequently not employed at centres which used advanced techniques not reflected in the original study (which used planar perfusion scans and single projection ^{133}Xe ventilation studies) [21, 39–43]. Several centres pursued the goal to be more accurate in studies falling into the intermediate category, *e.g.* by using Technegas and/or tomographic techniques for increased specificity and increased sensitivity in smaller embolic lesions. Large-scale clinical trials such as PIOPED, however, were not completed owing to heterogeneity of technology availability and clinical practice.

Since the PIOPED II study established CT angiography as an accurate technique [2], increasing availability of CT in emergency departments and the fast completion of a scan have moved V'/Q' scans into the background. Today, the V'/Q' scan is considered a second line test in acute pulmonary embolism by actual guidelines [44], which should be employed

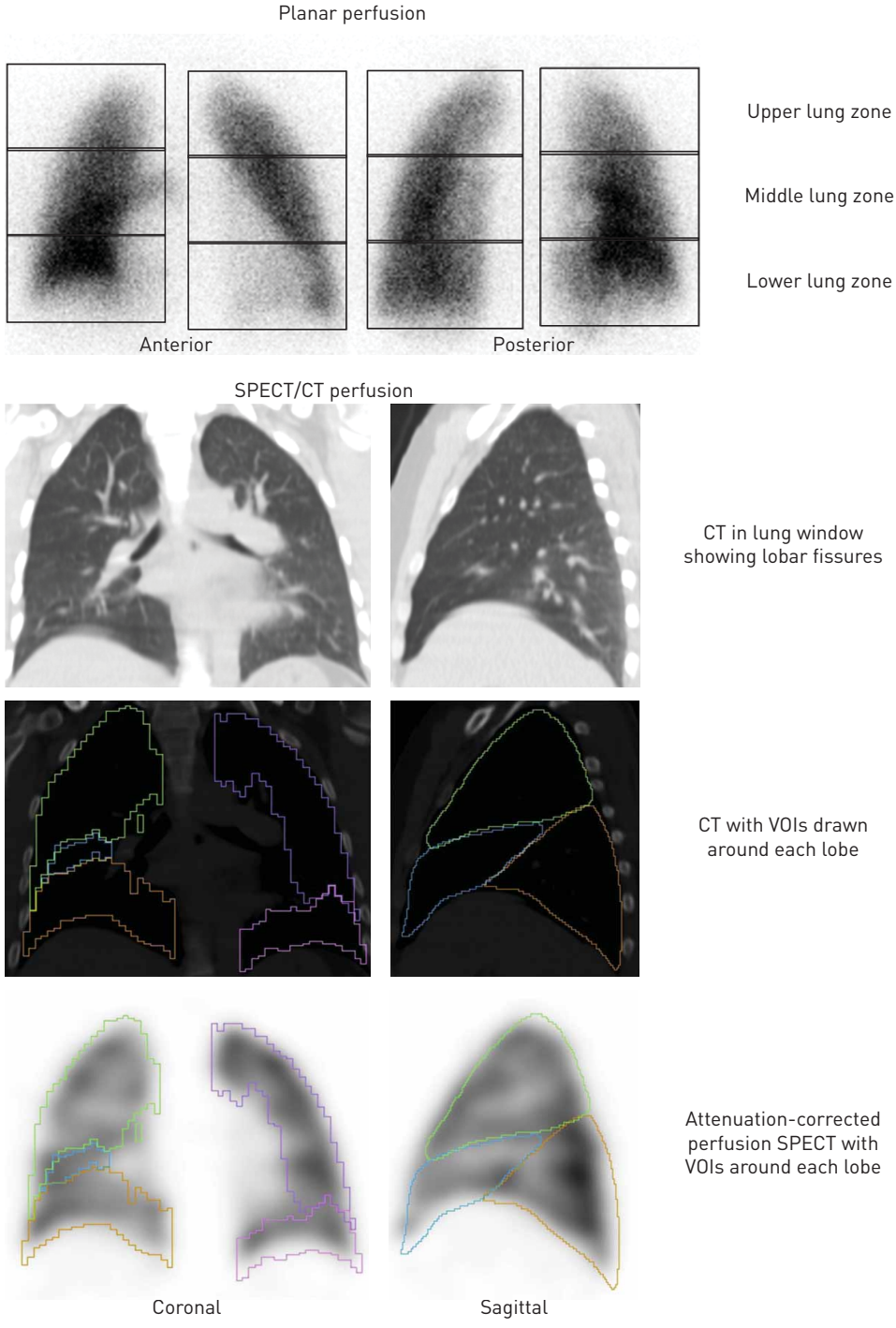

Figure 4. Quantitative assessment of regional lung perfusion. Planar images (top) are analysed using box-shaped regions of interest for both lungs and respective upper, middle and lower fields. Geometric means are determined from anterior and posterior projections. Tomographic SPECT/X-ray CT (SPECT/CT; bottom) provides the advantage that lobar borders can be determined three dimensionally based on CT structural information, then transferred to SPECT for accurate quantification of perfusion per lobe. Reproduced and modified from [38] with permission from the publisher. VOI: volume of interest.

preferentially in subjects with contraindications to CT contrast agent and in pregnant women [45]. Recent reports of clinical practice, however, show that V'/Q' scans are still performed by a considerable fraction of large-scale clinical centres and that advanced techniques such as SPECT and SPECT/CT are now employed in a majority of sites where V'/Q' scans are still part of clinical routine [23]. This suggests the presence of sufficient critical mass to conduct multi-center efforts for evaluation of the diagnostic and prognostic value of advanced tomographic V'/Q' studies in acute pulmonary embolism.

Chronic thromboembolic pulmonary hypertension

In CTEPH, where timing and acute availability of the diagnostic test is less critical, the situation differs from acute pulmonary embolism. Here, clinical guidelines still recommend V'/Q' scans as a first line test to rule in or rule out pulmonary embolism as the underlying cause of pulmonary hypertension, a progressive disease with a poor prognosis [44]. Identifying chronic thromboembolism as a cause of pulmonary hypertension has major clinical implications because surgery could provide cure of the condition. Some studies suggest that V'/Q' scans have a higher accuracy in CTEPH than CT-based methods, mostly because of higher sensitivity [46]. This may be attributed to a major difference between both techniques, where V'/Q' scans identify abnormalities on the peripheral tissue (alveolar/capillary) level, while CT focuses on the macroscopic pulmonary vasculature. Smaller peripheral chronic emboli which cause hypertension may thus be identified more readily by V'/Q' scans. Although large-scale comparative clinical data are still missing, it also is to be assumed that information about the compromise of tissue function is more closely linked to outcome than information about morphological features of the major supplying arteries. This may be in analogy to chronic coronary artery disease, where tissue ischaemia has been identified as a prognostic marker that is superior to coronary artery stenosis for guidance of therapy [47].

Quantitative V'/Q' imaging

In patients prior to lung-reductive surgery because of COPD or tumours, quantification of perfusion and ventilation in right *versus* left lung and in lung segments relative to each other may be beneficial in the planning of the procedure, in order to avoid post-surgical compromise by resection of best-perfused or ventilated regions. Furthermore, the technique provides information about outcome [48] and it may be used to determine the effect of therapy after the intervention [5, 36].

Right-to-left shunts

Due to the capillary-blocking nature of MAA, after intravenous injection, accumulation in organs supplied by the systemic circulation can only occur in the presence of a right-to-left shunt. MAA then typically accumulates in those organs which receive the majority of cardiac output, such as brain and kidney (figure 5). Radioactivity in thyroid and stomach, which may be present due to free pertechnetate especially at later times after injection when MAA degradation has started to occur, should not be mistaken for a shunt. By calculation of a relative ratio of brain/renal to lung uptake, a shunt volume index can be calculated. Typically, any value above 10% is considered abnormal [49]. This elegant and robust technique can be employed in any situation where right/left shunt is suspected, independent of cardiac, pulmonary or vascular location of the shunt, and independent of a paediatric/congenital or adult/acquired disease.

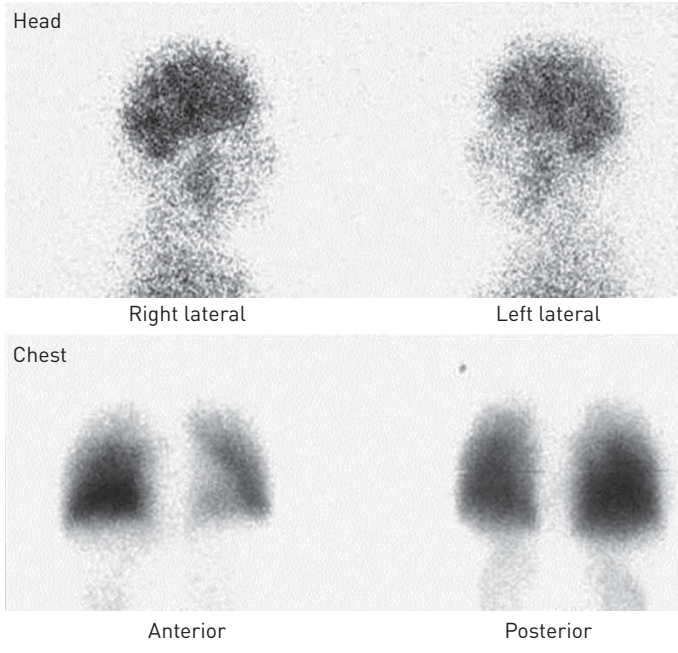

Figure 5. Scintigraphic assessment of right to left shunt volume with Tc-99 m macro-aggregated albumin (MAA). Planar lateral images of the head/neck region (top) show accumulation of the capillary blocking radiotracer MAA in brain after intravenous injection. Planar images of chest/upper abdomen (middle) show homogeneous distribution in both lungs, but additional accumulation in both kidneys again confirms shunting to left circulation. Quantification by region of interest technique is used to calculate geometric means and determines shunt volume as counts in brain relative to lungs. For the lung, geometric mean counts were 255244 and 268446 for anterior and posterior, respectively, and the average was 306665. For the brain, geometric mean counts were 15333 and 14876 for left lateral and right lateral, respectively, and the average was 15103. Shunt index = 27.47% (normal <5%).

Lung tumours

Glycolysis is enhanced in multiple malignant tumours, providing the foundation for metabolic imaging with ^{18}F FDG-PET. While the advent of FDG-PET/CT and, more recently, PET/magnetic resonance, has revolutionised the clinical practice of nuclear medicine in general, the diagnostic usefulness of this molecular imaging technique is specifically well documented in lung cancer. Given the extensive body of available literature on this topic, the interested reader is referred to dedicated review articles [6, 12]. In brief, randomised trials provide evidence that FDG-PET is useful for identifying malignancy in solitary pulmonary nodules, and for staging of small cell and non-small cell lung cancer. Alternative tracers, such as somatostatin-receptor ligands for carcinoid and other neuroendocrine tumours, are increasingly available [17]. The clinical value of PET is emphasised and put into the perspective of stepwise diagnostic workup approaches.

Importantly, PET also holds great potential to serve as a guide towards adequate individual therapy in lung cancer. Given the increasing versatility of drug and radiation therapy in lung cancer, and the trend towards personalisation of therapy, PET has gradually evolved from a purely diagnostic tool to a multifunctional imaging modality that can be utilised for treatment selection, adaptation, early response monitoring and follow-up [12]. Evidence for the usefulness in therapy guidance is increasing and the field is evolving towards a future perspective as a key modality in the clinical management of lung cancer [7, 50].

Inflammatory diseases

The inflammatory component of various lung diseases, such as autoimmune disorders, pulmonary fibrosis or sarcoidosis, is increasingly emphasised as a factor determining outcome and as a target of therapy [51–53]. Additionally, chronic infectious diseases pose an increasing problem for early detection and adequate treatment. Targeted imaging of lung inflammation has therefore seen a revival. In the past, techniques such as ^{67}Ga scans or ^{111}In-labelled white blood cell scans were employed for fever of unknown origin, sarcoidosis, other granulomatous or toxic conditions [54]. Today, FDG-PET has replaced those tests in many situations owing to its lower radiation exposure, higher resolution and faster scan protocol (figure 6). While the evidence for FDG as an inflammation marker is increasing, its limited specificity, stemming from the fact that multiple cell types exhibit increased glucose uptake in disease conditions, is also recognised. This is a stimulus for the development and implementation of other, more specific molecular markers for targeted imaging of inflammation and infection [55, 56].

Future perspective

As the field of medicine is moving towards a personalised treatment of disease based on individual biologic and functional characteristics, diagnostic tests which provide robust, quantitative information about structure and function will be of increasing importance. Additionally, increasing molecular specificity will be sought after. Radionuclide techniques

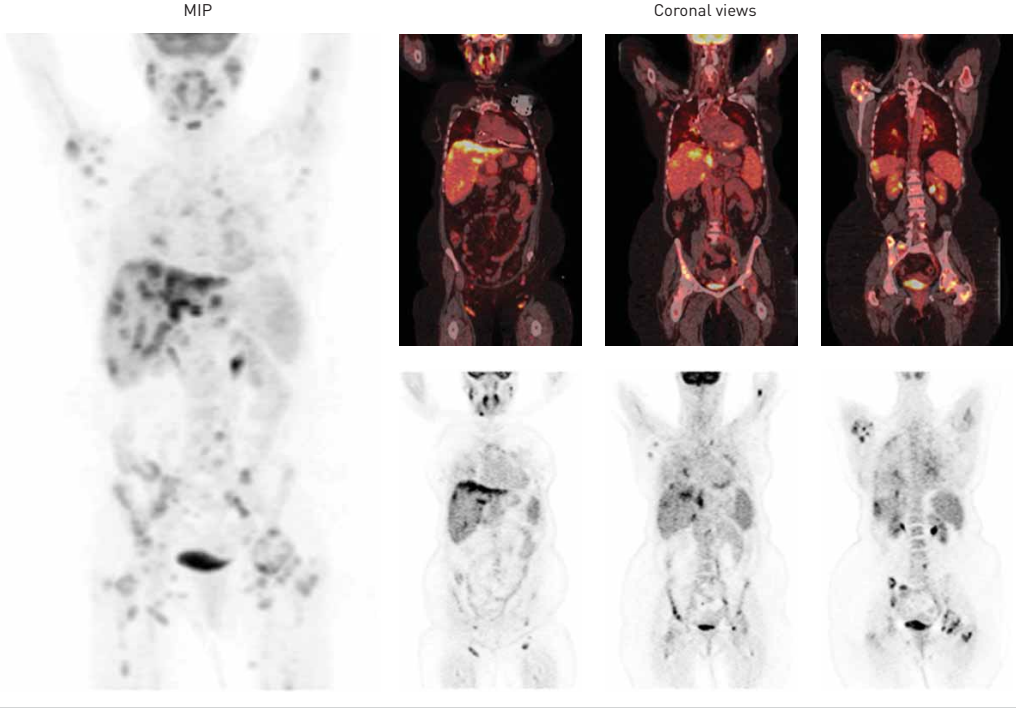

Figure 6. ^{18}F FDG-PET/CT in a patient with sarcoidosis. Multiple metabolically active lesions are depicted in lymph nodes, bone, lungs, cardiac region and liver, suggestive of extensive multi-organ involvement of this noncaseating granulomatous disease. Reproduced and modified from [59] with permission from the publisher.

are well positioned to play an important role in this regard. A broader spectrum of molecular-targeted tracers such as chemokine receptor ligands, integrin ligands, matrix-metalloproteinase ligands, endothelin receptor ligands, tracers targeting angiotensin-converting enzyme or angiotensin receptors *etc.* are undergoing preclinical and clinical validation [57]. Many of those agents are explored outside of pulmonary medicine but it is likely that they will enter the field of lung imaging, too. Together with the current generation of hybrid imaging devices, such integrated molecular/anatomic information is expected to contribute to advances on the path towards personalised diagnosis and therapy.

Conclusion

In summary, pulmonary nuclear medicine has long been defined by the clinical application and limitations of planar V'/Q' imaging in acute pulmonary embolism. While the importance of this specific application has declined significantly, the field has seen exciting new developments in other directions. Hybrid SPECT/CT and PET/CT imaging have emerged as the new clinical standard. Corrective algorithms for respiratory motion have been developed and quantitative assessment techniques have been refined. Based on the unique success of FDG-PET, which is now a first line technique in lung cancer staging, other tracers for molecular imaging are penetrating the clinical arena. These new developments will broaden the versatility, accuracy and specificity of pulmonary radionuclide imaging, and they provide a foundation for the future establishment of multiple novel applications.

References

1. Wellman HN. Pulmonary thromboembolism: current status report on the role of nuclear medicine. *Semin Nucl Med* 1986; 16: 236–274.
2. Stein PD, Fowler SE, Goodman LR, *et al.* Multidetector computed tomography for acute pulmonary embolism. *N Engl J Med* 2006; 354: 2317–2327.
3. Investigators P. Value of the ventilation/perfusion scan in acute pulmonary embolism. Results of the prospective investigation of pulmonary embolism diagnosis (PIOPED). *JAMA* 1990; 263: 2753–2759.
4. Konstantinides SV. 2014 ESC Guidelines on the diagnosis and management of acute pulmonary embolism. *Eur Heart J* 2014; 35: 3145–3146.
5. Win T, Tasker AD, Groves AM, *et al.* Ventilation-perfusion scintigraphy to predict postoperative pulmonary function in lung cancer patients undergoing pneumonectomy. *AJR Am J Roentgenol* 2006; 187: 1260–1265.
6. Zhao L, He ZY, Zhong XN, *et al.* (18)FDG-PET/CT for detection of mediastinal nodal metastasis in non-small cell lung cancer: a meta-analysis. *Surg Oncol* 2012; 21: 230–236.
7. Skoura E, Datseris IE, Platis I, *et al.* Role of positron emission tomography in the early prediction of response to chemotherapy in patients with non-small-cell lung cancer. *Clin Lung Cancer* 2012; 13: 181–187.
8. Parker JA, Coleman RE, Grady E, *et al.* SNM practice guideline for lung scintigraphy 4.0. *J Nucl Med Technol* 2012; 40: 57–65.
9. Bajc M, Neilly JB, Miniati M, *et al.* EANM guidelines for ventilation/perfusion scintigraphy : Part 1. Pulmonary imaging with ventilation/perfusion single photon emission tomography. *Eur J Nucl Med Mol Imaging* 2009; 36: 1356–1370.
10. Kotzerke J, Andreeff M, Wunderlich G. PET aerosol lung scintigraphy using Galligas. *Eur J Nucl Med Mol Imaging* 2010; 37: 175–177.
11. Hofman MS, Beauregard JM, Barber TW, *et al.* 68Ga PET/CT ventilation-perfusion imaging for pulmonary embolism: a pilot study with comparison to conventional scintigraphy. *J Nucl Med* 2011; 52: 1513–1519.
12. Grootjans W, de Geus-Oei LF, Troost EG, *et al.* PET in the management of locally advanced and metastatic NSCLC. *Nat Rev Clin Oncol* 2015; 12: 395–407.
13. Francis R, Segard T, Morandeau L. Novel molecular imaging in lung and pleural diseases. *Respirology* 2011; 16: 1173–1188.

14. Hashefi M, Curiel R. Future and upcoming non-neoplastic applications of PET/CT imaging. *Ann N Y Acad Sci* 2011; 1228: 167–174.
15. Sobic-Saranovic D, Artiko V, Obradovic V. FDG PET imaging in sarcoidosis. *Semin Nucl Med* 2013; 43: 404–411.
16. Glaudemans AW, de Vries EF, Galli F, *et al.* The use of (18)F-FDG-PET/CT for diagnosis and treatment monitoring of inflammatory and infectious diseases. *Clin Dev Immunol* 2013; 2013: 623036.
17. Lococo F, Cesario A, Paci M, *et al.* PET/CT assessment of neuroendocrine tumors of the lung with special emphasis on bronchial carcinoids. *Tumour Biol* 2014; 35: 8369–8377.
18. Suga K, Okada M, Kunihiro M, *et al.* Impaired lung 123I-MIBG uptake on SPECT in pulmonary emphysema. *J Nucl Med* 2011; 52: 1378–1384.
19. Gottschalk A, Stein PD, Sostman HD, *et al.* Very low probability interpretation of V/Q lung scans in combination with low probability objective clinical assessment reliably excludes pulmonary embolism: data from PIOPED II. *J Nucl Med* 2007; 48: 1411–1415.
20. Dalen JE. New PIOPED recommendations for the diagnosis of pulmonary embolism. *Am J Med* 2006; 119: 1001–1002.
21. Freitas JE, Sarosi MG, Nagle CC, *et al.* Modified PIOPED criteria used in clinical practice. *J Nucl Med* 1995; 36: 1573–1578.
22. Webber MM, Gomes AS, Roe D, *et al.* Comparison of Biello, McNeil, and PIOPED criteria for the diagnosis of pulmonary emboli on lung scans. *AJR Am J Roentgenol* 1990; 154: 975–981.
23. Le Roux PY, Pelletier-Galarneau M, de Laroche R, *et al.* Pulmonary scintigraphy for the diagnosis of acute pulmonary embolism: a survey of current practices in Australia, Canada and France. *J Nucl Med* 2015; 56: 1212–1217.
24. Kan Y, Yuan L, Meeks JK, *et al.* The accuracy of V/Q SPECT in the diagnosis of pulmonary embolism: a meta-analysis. *Acta Radiol* 2015; 56: 565–572.
25. Roach PJ, Bailey DL, Schembri GP, *et al.* Transition from planar to SPECT V/Q scintigraphy: rationale, practicalities, and challenges. *Semin Nucl Med* 2010; 40: 397–407.
26. Bailey DL, Roach PJ. Why SPECT for V/Q lung scanning? *Semin Nucl Med* 2010; 40: 395–396.
27. Beyer T, Townsend DW, Brun T, *et al.* A combined PET/CT scanner for clinical oncology. *J Nucl Med* 2000; 41: 1369–1379.
28. Lardinois D, Weder W, Hany TF, *et al.* Staging of non-small-cell lung cancer with integrated positron-emission tomography and computed tomography. *N Engl J Med* 2003; 348: 2500–2507.
29. Buck AK, Nekolla S, Ziegler S, *et al.* SPECT/CT. *J Nucl Med* 2008; 49: 1305–1319.
30. Lu Y, Lorenzoni A, Fox JJ, *et al.* Non-contrast perfusion SPECT/CT: a new test for the expedited, high accuracy diagnosis of acute pulmonary embolism. *Chest* 2014; 145: 1079–1088.
31. Wehrl HF, Sauter AW, Divine MR, *et al.* Combined PET/MR: a technology becomes mature. *J Nucl Med* 2015; 56: 165–168.
32. Dutta J, Huang C, Li Q, *et al.* Pulmonary imaging using respiratory motion compensated simultaneous PET/MR. *Med Phys* 2015; 42: 4227.
33. Chi A, Nguyen NP. 4D PET/CT as a Strategy to Reduce Respiratory Motion Artifacts in FDG-PET/CT. *Front Oncol* 2014; 4: 205.
34. Darwesh RM, Shin E, Morgan PS, *et al.* Improved visualization of perfusion defects by respiratory-gated SPECT: a phantom simulation study. *Nucl Med Commun* 2014; 35: 189–196.
35. Callahan J, Hofman MS, Siva S, *et al.* High-resolution imaging of pulmonary ventilation and perfusion with 68Ga-VQ respiratory gated (4-D) PET/CT. *Eur J Nucl Med Mol Imaging* 2014; 41: 343–349.
36. Hauck RW, Romer W, Schulz C, *et al.* Ventilation perfusion scintigraphy and lung function testing to assess metal stent efficacy. *J Nucl Med* 1997; 38: 1584–1589.
37. Lu G, Shih WJ, Chou C, *et al.* Tc-99 m MAA total-body imaging to detect intrapulmonary right-to-left shunts and to evaluate the therapeutic effect in pulmonary arteriovenous shunts. *Clin Nucl Med* 1996; 21: 197–202.
38. Toney LK, Wanner M, Miyaoka RS, *et al.* Improved prediction of lobar perfusion contribution using technetium-99m-labeled macroaggregate of albumin single photon emission computed tomography/computed tomography with attenuation correction. *J Thorac Cardiovasc Surg* 2014; 148: 2345–2352.
39. Christiansen F, Nilsson T, Mare K, *et al.* Adding a visual linear scale probability to the PIOPED probability of pulmonary embolism. *Acta Radiol* 1997; 38: 458–463.
40. Anderson GB. Noninvasive testing in the diagnosis of pulmonary embolism. PIOPED revisited. *Chest* 1996; 109: 5–6.
41. Jacobson AF. Pulmonary embolism diagnosis: PIOPED and beyond. *Eur J Nucl Med* 1994; 21: 371–374.
42. Gottschalk A, Sostman HD, Coleman RE, *et al.* Ventilation-perfusion scintigraphy in the PIOPED study. Part II. Evaluation of the scintigraphic criteria and interpretations. *J Nucl Med* 1993; 34: 1119–1126.
43. Gottschalk A, Juni JE, Sostman HD, *et al.* Ventilation-perfusion scintigraphy in the PIOPED study. Part I. Data collection and tabulation. *J Nucl Med* 1993; 34: 1109–1118.
44. Konstantinides SV, Torbicki A, Agnelli G, *et al.* 2014 ESC guidelines on the diagnosis and management of acute pulmonary embolism. *Eur Heart J* 2014; 35: 3033–3069, 3069a–3069k.
45. Leung AN, Bull TM, Jaeschke R, *et al.* American Thoracic Society documents: an official American Thoracic Society/Society of Thoracic Radiology Clinical Practice Guideline–Evaluation of Suspected Pulmonary Embolism in Pregnancy. *Radiology* 2012; 262: 635–646.

46. Tunariu N, Gibbs SJ, Win Z, *et al.* Ventilation-perfusion scintigraphy is more sensitive than multidetector CTPA in detecting chronic thromboembolic pulmonary disease as a treatable cause of pulmonary hypertension. *J Nucl Med* 2007; 48: 680–684.
47. Phillips LM, Hachamovitch R, Berman DS, *et al.* Lessons learned from MPI and physiologic testing in randomized trials of stable ischemic heart disease: COURAGE, BARI 2D, FAME, and ISCHEMIA. *J Nucl Cardiol* 2013; 20: 969–975.
48. Jamadar DA, Kazerooni EA, Martinez FJ, *et al.* Semi-quantitative ventilation/perfusion scintigraphy and single-photon emission tomography for evaluation of lung volume reduction surgery candidates: description and prediction of clinical outcome. *Eur J Nucl Med* 1999; 26: 734–742.
49. Ito K, Kurihara K, Ishibashi A, *et al.* Cut-off value for normal versus abnormal right-to-left shunt percentages using (99 m)Tc-macroaggregated albumin. *Nucl Med Commun* 2011; 32: 936–940.
50. Sauter AW, Schwenzer N, Divine MR, *et al.* Image-derived biomarkers and multimodal imaging strategies for lung cancer management. *Eur J Nucl Med Mol Imaging* 2015; 42: 634–643.
51. Adams H, Keijsers RG, Korenromp IH, *et al.* FDG PET for gauging of sarcoid disease activity. *Semin Respir Crit Care Med* 2014; 35: 352–361.
52. Chen DL, Atkinson JJ, Ferkol TW. FDG PET imaging in cystic fibrosis. *Semin Nucl Med* 2013; 43: 412–419.
53. El-Chemaly S, Malide D, Yao J, *et al.* Glucose transporter-1 distribution in fibrotic lung disease: association with 18F-2-fluoro-2-deoxyglucose-PET scan uptake, inflammation, and neovascularization. *Chest* 2013; 143: 1685–1691.
54. Schuster DM, Alazraki N. Gallium and other agents in diseases of the lung. *Semin Nucl Med* 2002; 32: 193–211.
55. Ning X, Seo W, Lee S, *et al.* PET imaging of bacterial infections with fluorine-18-labeled maltohexaose. *Angew Chem Int Ed Engl* 2014; 53: 14096–14101.
56. Roivainen A, Jalkanen S, Nanni C. Gallium-labelled peptides for imaging of inflammation. *Eur J Nucl Med Mol Imaging* 2012; 39: Suppl 1, S68–S77.
57. Wollenweber T, Bengel FM. Cardiac molecular imaging. *Semin Nucl Med* 2014; 44: 386–397.
58. Sandstrom M, Velikyan I, Garske-Roman U, *et al.* Comparative biodistribution and radiation dosimetry of 68Ga-DOTATOC and 68Ga-DOTATATE in patients with neuroendocrine tumors. *J Nucl Med* 2013; 54: 1755–1759.
59. Schatka I, Bengel FM. Advanced imaging of cardiac sarcoidosis. *J Nucl Med* 2014; 55: 99–106.

Disclosures: F.M. Bengel reports grants and personal fees from GE Healthcare, grants from Siemens AG, and grants and personal fees from Mallinckrodt Pharma, outside this work.

Chapter 3

Chest radiography: performance, indications and interpretation

Dag Wormanns

This chapter provides information on basic technical aspects concerning acquisition of chest radiography. Different patient positions for chest radiography and their specifics are discussed, especially the limitations of portable chest radiography. Indications for chest radiography of intensive care unit patients are presented, and some specific aspects regarding interpretation of these chest radiographs are reviewed. The Fleischer Society proposed a glossary of terms for chest imaging. Some of the definitions that are especially important to reporting chest radiography are explained and illustrated.

For almost all thoracic diseases, chest radiography constitutes the first step in diagnostic investigations employing imaging. The following descriptions of the technical aspects of radiographs relate to digital radiography (direct detection of the x-ray radiation by a digital sensor) and computed radiography (x-rays draw the radiographic image on a photosensitive phosphor imaging plate which is housed in a cassette; after exposure the imaging plate is read and digitised by a computed radiography reader). These techniques are now available in most European radiological facilities. This chapter does not deal with older, conventional radiography using film-foil systems.

Erect projection

Plain chest radiography is performed with the patient standing, provided the patient's general condition allows this. The standing patient is imaged in the posterior–anterior projection with their chest resting against the detector, resulting in a focus–detector distance of 1.5–2 m. Table 1 summarises the imaging parameters. The posterior–anterior projection results in the least pronounced geometric magnification of the heart and mediastinum, and enables the most accurate assessment of heart size. To avoid superimposition of the lung fields, the scapulae must be rotated in the lateral direction. To achieve this, the patient should rest their hands on their hips and rotate their elbows in the ventral direction as far as possible. Alternatively, the patient may grasp the handles at both sides of the detector or, if no handles are mounted, wrap both arms around the detector. In both of these positions the scapulae are rotated in the ventral direction.

Evangelische Lungenklinik Berlin, Berlin, Germany

Correspondence: Dag Wormanns, Evangelische Lungenklinik Berlin, Lindenberger Weg 27, D-13125 Berlin, Germany.
E-mail: dag.wormanns@elk-berlin.de

Copyright ©ERS 2015. Print ISBN: 978-1-84984-065-1. Online ISBN: 978-1-84984-066-8. Print ISSN: 2312-508X. Online ISSN: 2312-5098.

Table 1. Imaging parameters for erect projection and portable chest radiography

	Erect projection	Portable chest radiography
Imaging technique	Bulky wall unit	Mobile x-ray machine
Tube voltage kV	110–150	70–110
Nominal focal spot value	⩽1.3	⩽1.3
Focus–detector distance cm	150–200	90–120
Automatic exposure	Lateral measurement field	None
Exposure time ms	<20	<20
Anti-scatter grid	r 12 (8), none	Required in case of obesity; not needed with digital radiography
Radiation dose	⩽5 µGy, SC 400	⩽5 µGy, SC 400, recommended current-time product 1–5 mAs

Data from [1].

If the patient's general condition does not permit image acquisition with the patient standing, a seated acquisition should be performed. For seated acquisition the patient leans their back against the detector meaning that the beam will be in the anterior–posterior projection. The diaphragm is thus higher than in a standing patient, the inspiration depth is less and the basal portions of the lung are accordingly less inflated.

A lateral projection is also performed in the standing position, with the arms raised. In this case, the patient's left side normally rests against the detector because the heart is more sharply and accurately rendered in this position due to its proximity to the detector. Generally, the lung nearest the detector can be imaged more sharply than the lung which is further away. If the clinical issue requires maximum image quality and critical details are very difficult to visualise, a right-sided projection to represent right-sided pathology is useful in some cases.

Chest radiographs should be exposed following deep inspiration because full inflation of the lungs allows for the best detection of pulmonary pathology. The previously common practice of exposing radiographs in expiration to exclude pneumothorax is now obsolete for the following reasons [2, 3]. 1) An expiration film allows no assessment of cardiopulmonary status, because the lungs are inadequately inflated and the lung vasculature appears more pronounced. Other relevant findings can be masked, for example small pneumonic infiltrates or incipient left heart failure. 2) There is no comparability with previous or subsequent radiographs. 3) Modern equipment can detect sufficiently large pneumothoraxes when acquisition is carried out during inspiration.

For radiographic diagnosis of chest diseases, high-kilovoltage radiography performed at approximately 125 kV is used. This practice increases the transradiancy of calcareous structures, especially bones, making them relatively transparent and reducing the otherwise obstructive overlay of the lung fields by the ribs. At the same time, the bony structures allow only a limited assessment. For issues related to the thoracic skeleton, low-kilovoltage radiography at a tube voltage of 60–75 kV is preferred (figure 1).

Portable chest radiography

Portable chest radiography is commonly employed to diagnose bedridden or otherwise immobile patients, especially in intensive care units (ICUs), trauma bays, emergency rooms and nursing homes. In this case, the mobile detector is placed under the thorax of the patient lying on their back, and the tube of the mobile x-ray unit is positioned above the patient. The focus–detector distance should be 90–120 cm. Bedridden patients should be imaged in an erect or semi-erect position, whenever possible. Table 1 shows the essential imaging parameters. Portable chest radiography provides a lower image quality than imaging a standing patient; the reasons for this are as follows [4]. 1) The smaller focus–detector distance increases geometric distortion so that the mediastinal width and heart's dimensions appear larger. 2) The heart is further away from the detector, and geometrically more enlarged if the patient lies with their back on the detector. 3) The lung volumes are diminished and the diaphragm is standing higher. 4) Lung perfusion in supine portable radiographs exhibits no gravity-induced caudo–cranial gradient; basal–apical redistribution of lung perfusion cannot be diagnosed. 5) Because a lower tube voltage is used in portable chest radiography the bony overlays are more distinct. 6) Mobile devices have a lower generator power that results in a longer exposure time and greater likelihood of motion blur due to breathing and heart pulsations.

The patient's position (supine, semi-erect, and erect) should be noted on the image. Furthermore, information on respiration parameters is helpful in interpreting images of mechanically ventilated patients. For obese patients an anti-scatter grid can improve image quality, but at the expense of a slightly higher radiation exposure. If the x-ray tube is not placed above the centre of the detector equipped with an anti-scatter grid a typical but uncommon artefact results. Comparing the radiotransparency of the axillae on both sides helps distinguish this artefact from a pathological opacity of a hemithorax. Unequal

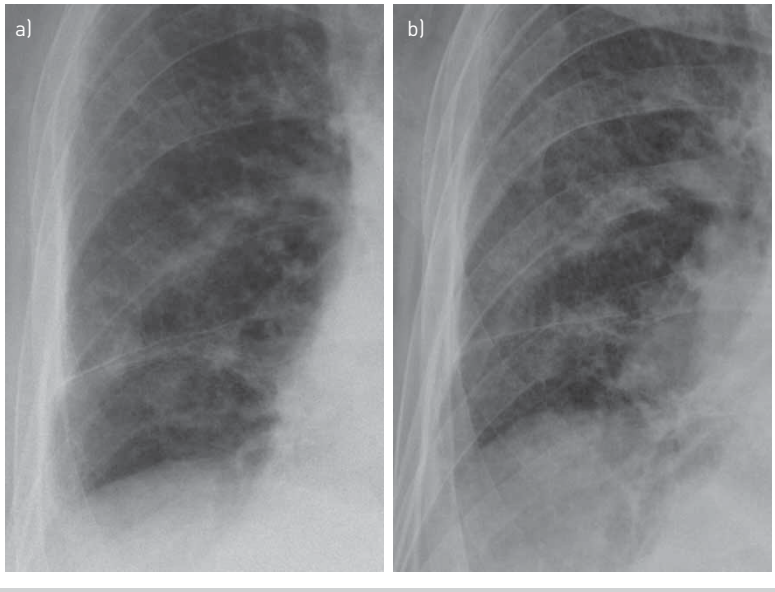

Figure 1. a) High-kilovoltage (125 kV tube voltage) *versus* b) low-kilovoltage (75 kV tube voltage) chest radiography of nonspecific interstitial pneumonia. The low-kilovoltage image shows marked overlay of the ribs compromising visibility of lung parenchyma. Magnified views of the chest radiographs are shown.

radiotransparency here suggests a grid artefact (figure 2). Other common reasons such as rotation and overlying materials should be excluded.

Indications for chest radiography in intensive care

The need for routine, daily chest radiography of every patient in ICUs was a subject of discussion for many years. However, a current meta-analysis has revealed no advantages of daily radiographic examinations compared with simply event-driven chest radiography [5]. Routine daily chest radiography examinations in ICUs should therefore be relegated to the past [5–9]. In its appropriateness criteria, the American College of Radiology lists the indications shown in table 2.

Special aspects of ICU patients

Atelectasis is the most common cause of pulmonary opacity on chest radiography performed in ICUs. Two-thirds of all atelectases affect the left lower lobe, followed by the right lower lobe and right upper lobe [10]. There are several causes of atelectasis: bronchus obstruction due to mucus or blood; passive or relaxation atelectasis as a result of pleural effusion or cardiomegaly; and relaxation due to a pneumothorax, a tube malposition or the constant supine position of the patient. Radiologically, atelectasis manifests itself as an increase in opacity, which can lead to de-silhouetting a neighbouring diaphragm or heart contour. Large atelectases may show signs of volume reduction, like mediastinal distortion, relocation of interlobar fissures (usually the right minor fissure is the only interlobar fissure visible on a portable chest radiograph) and a bundling of pulmonary structures. An

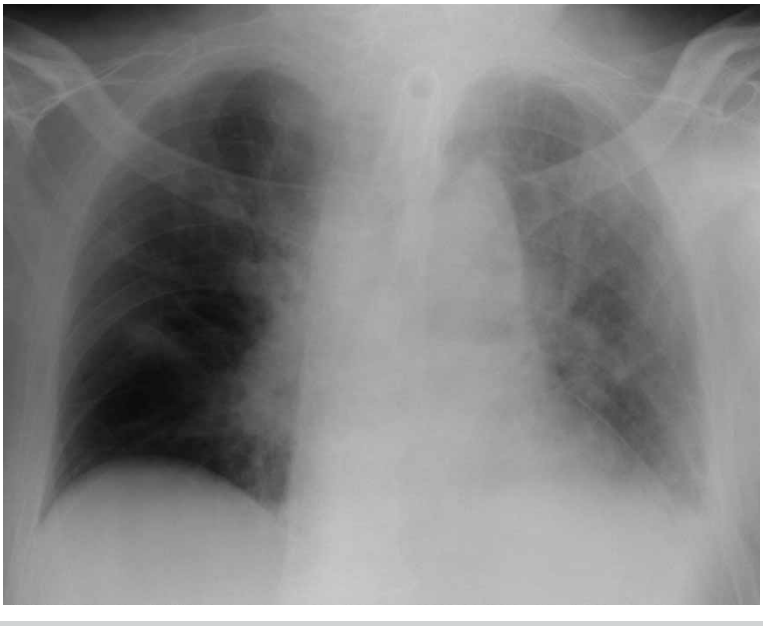

Figure 2. Portable chest radiography with a grid artefact. Note the homogeneous opacity of the left hemithorax and the different transparency of both axillae. Other reasons for asymmetric opacity include rotation, pleural effusion, *etc.*

Table 2. Indications for chest radiography in intensive care unit (ICU) patients

Indication	Level of recommendation	Comments
Admission to ICU	7	
Stable patient, no change in clinical status	3	
Patient exhibiting clinical deterioration	9	
Following insertion of catheter or drainage	9	
Following removal of chest tube	5	Data are largely based on studies of patients following cardiothoracic surgery. Therefore, this may not be generalisable to all indications for chest tube removal.

Level of recommendation: 1–3 usually not appropriate; 4–6 may be appropriate; 7–9 usually appropriate. Reproduced and modified from [9] with permission from the publisher.

increase in volume of an atelectasis which has existed for some time suggests a superinfection in the case of corresponding clinical findings [4].

The difficult radiological differential diagnosis of pneumonia in ICU patients is shown in table 3.

Pleural effusion is a common finding on chest radiographs in ICU patients. Cross-sectional imaging modalities such as ultrasound and CT are more sensitive in the detection of pleural effusions than chest radiography. On erect chest radiography the lateral projection depicts pleural effusions of more than 50 mL, whereas effusions of more than 100 mL are visible in the frontal projection. In contrast, pleural effusions of several hundred millilitres can remain invisible in the supine position on a portable chest radiograph as the dorsal collection of pleural fluid results in a diffuse opacity increase of the affected hemithorax, which may be hard to detect.

Many ventilation regimes use a positive end-expiratory pressure (PEEP). This opens previously existent atelectases, including microatelectases, and reduces pulmonary oedema due to the changed pressure conditions in the lung parenchyma. The result is an apparent improvement in the chest radiograph. Previously existent, pathological, pulmonary opacities such as oedema and atelectases become less visible. However, ventilation using PEEP does not directly improve the underlying pathological processes.

Definition of terms

The Fleischner Society glossary of terms [11] contains a full vocabulary for describing the radiological findings of chest disease. Most of the terms are related to CT as the most informative imaging method for almost all lung diseases. The following paragraphs will define terms used to describe findings and imaging patterns on chest radiography. Only a selection of the whole set of terms are presented here; CT-specific vocabulary as well as definitions of anatomy or individual lung diseases were omitted.

Table 3. Differential diagnoses of nosocomial pneumonia in intensive care unit patients with pulmonary opacity on the radiograph

Differential diagnosis	Notes
Atelectasis	Often recognisable pulmonary volume loss due to shifts in other anatomical structures.
Pleural effusion	Diffuse opacity increasing in the basal direction; possibly recognisable as a lateral pleural opacity.
Pulmonary oedema	Usually symmetrical; possibly including cardiomegaly as an indication of cardiac genesis, or clinical indications of another cause (*e.g.* renal failure or sepsis).
Pulmonary infarction	After occurrence of pulmonary embolism; often pleural, triangular opacity, also multiple opacities.
Acute respiratory distress syndrome	Bilateral opacity; no clinical findings indicating bacterial infection, notable respiratory insufficiency.
Alveolar haemorrhage	Due to therapy (drug toxicity) or in the context of a known underlying disease.
Drug toxicity	To be taken into consideration in the event of antibiotic-refractory bilateral opacity. No pathognomonic radiological findings; indications are sometimes provided by a chronological coincidence of radiological findings with administration or discontinuation of certain drugs.
Post-operative changes	After thoracic surgery: intrapulmonary haematomas, lymphatic drainage disorder, pulmonary venous drainage disorder.

Air bronchogram

A pattern of air-filled bronchi surrounded by compacted lung parenchyma. This sign implies a patency of the proximal airways and a loss in the air content of the surrounding alveolar spaces due to atelectasis or consolidation. In rare cases, this sign results from a displacement of air *via* an expansive process of the interstitium, for example, in the event of lymphoma [11].

Apical cap

An apical cap is a cap-like compression of the tip of the lung, occurring particularly in old age. Apical caps are caused by apical, intrapulmonary, pleural fibrosis with resultant shrinkage and consecutive widening of extrapleural fatty tissue [12]. Another cause that has also been discussed is chronic ischaemia with resultant formation of hyaline, visceral, pleural thickening [13, 14]. A similar apical opacity also included under the term apical cap is found in the case of aortic rupture, as well as other apical, pleural or extrapleural fluid collections [11].

Atelectasis

Reduced ventilation of lung tissue, usually caused by resorption of air in the lung parenchyma due to bronchial obstruction, compression or relaxation. The radiological correlate is a volumetric reduction of the affected lung area with simultaneous opacity up to consolidation. The volume reduction can displace the mediastinum, pulmonary fissures, bronchial and vascular structures, and raise the diaphragm.

Bronchiectasis

Bronchiectasis is irreversible bronchial dilation, which is usually due to a chronic infection, proximal obstruction of the bronchus, or a congenital anomaly [15]. On the radiograph, bronchus dilatation is directly recognisable if the calibre is larger than that of accompanying, normal-calibre pulmonary artery or if the bronchial lumen is lacking in taper toward the periphery. According to morphology, a distinction is made between cylindrical, varicose and cystic (sacciform) bronchiectases, each representing different severities of the disease [16–18].

Bulla

Bulla are defined as an air space measuring at least 1 cm and enclosed by a thin wall (maximum 1 mm), they are often several centimetres in size and are usually accompanied by emphysema of the surrounding lung. Paucity of peripheral pulmonary vessels, with or without bullous change, is often the only radiographic sign of pulmonary emphysema.

Bullous emphysema

Lung destruction characterised by large bullae in the context of lung emphysema.

Cavity

A cavity is a central, air-filled space in a consolidation, mass or nodule. It is usually caused by bronchial drainage of central necrotic material and results in demarcation of a strongly radiotransparent, central area in the radiograph or CT scan. In the case of cavities within an inflammatory consolidation, the latter can regress and leave a persistent, thin-walled cavity.

Consolidation

Consolidation is a pathological process, including exudate in the case of pneumonia, which completely displaces air from the alveolar spaces. The radiograph shows homogeneously increased density of the lung parenchyma, so that the affected lung parenchyma appears to have a soft-tissue density (figure 3). Open bronchi may be visible within the consolidation (air bronchogram). The consolidation differs from a mass or nodule due to a lack of a rounded contour. The antonym of ground-glass opacity.

Ground-glass opacity

The radiograph shows an opacity of only slightly reduced radiotransparency, in which the vascular structures are no longer clearly distinguishable (figure 4). Ambiguous in terms of differential diagnosis, the underlying pathological process leads to a partial replacement of air in the alveolar spaces by fluid or tissue; a thickening of the interstitium by fluid or tissue; or a partial alveolar collapse or increased capillary blood volume. Thus, the process ultimately always leads to partial displacement of air [8, 19]. The antonym of consolidation.

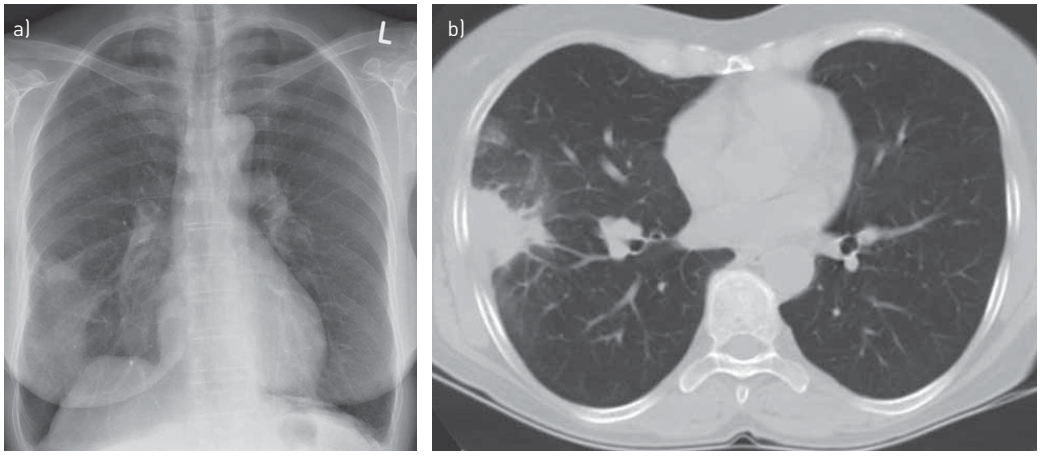

Figure 3. Consolidation in the right lower lobe: a) chest radiography and b) the corresponding CT.

Infiltrate

Infiltrate describes increased opacity of a lung area, caused by an alveolar or interstitial disease of the lung parenchyma. The term describes neither a specific morphology nor a specific aetiology of pathological changes, and is therefore controversial due to its ambiguity and lack of substance [20]. Therefore, it should no longer be used for describing findings, but should be replaced by a more precise description of the opacity [11]; see the terms consolidation and ground-glass opacity.

Interlobular septal thickening

Thickened interlobular septa are usually caused by hydrostatic pulmonary oedema or lymphangitic spread of carcinoma. On a frontal chest radiograph, they are recognisable, above all, as horizontal, short, linear basal opacities emanating from lateral pleura and known as septal lines (Kerley B-lines).

Linear atelectasis

The term linear atelectasis describes, in projection radiography, a nearly horizontal, linear opacity (ranging from a few millimetres to over 1 cm in length) in two projections, mostly in the basal parts of the lung. This feature corresponds to subsegmental atelectasis.

Mass

Mass is used to describe a pulmonary or pleural opacity with a size of at least 3 cm; smaller lesions are referred as nodules. This term is usually used to describe lesions of soft-tissue density. Distinct from the term consolidation, use of the term mass implies a presumably tumorous genesis. Mass is commonly used in radiology to describe all tumour-like lesions including extrapulmonary ones, regardless of their location and size.

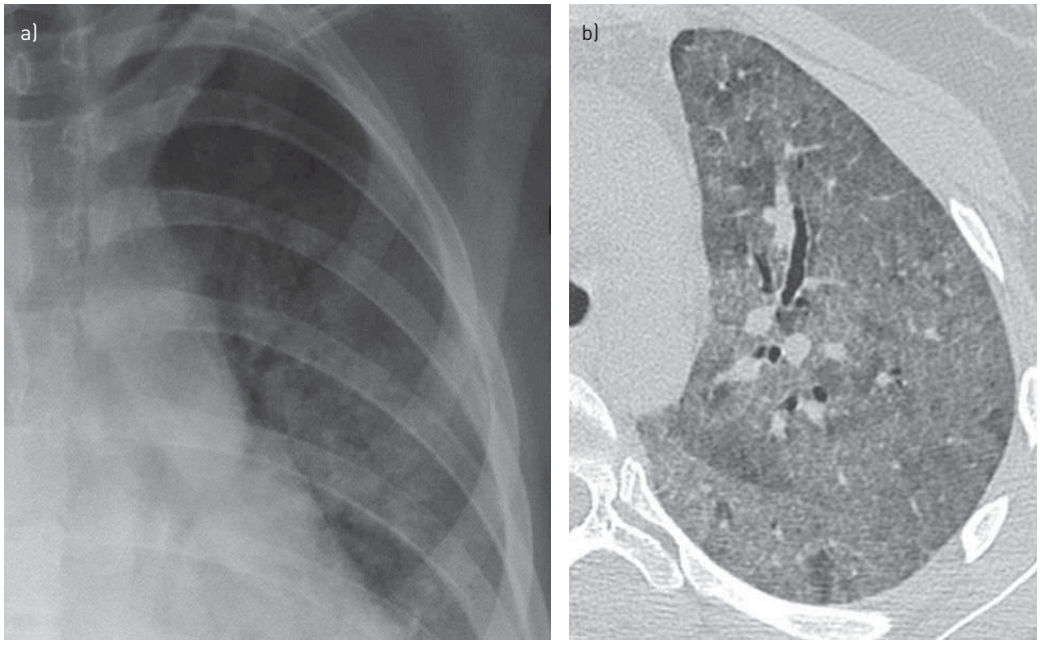

Figure 4. Ground-glass opacity in the left lung: a) magnified view of a chest radiograph and b) magnified view of the corresponding HRCT.

Miliary pattern

The radiograph shows numerous, diffuse and uniformly distributed, small, rounded opacities. The pattern typifies a haematogenous distribution in the lung parenchyma, as in the case of diffuse pulmonary metastasis or miliary tuberculosis.

Nodular pattern

A radiological pattern with numerous, small, rounded opacities (figure 5). The distribution is not necessarily uniform; a preference for apical or basal location is often evident.

Nodule

The radiograph shows an approximately round opacity with a maximum diameter of 3 cm and sharp or blurred definition. Acinar nodules usually occur multiply, have fuzzy boundaries, a size of 5–8 mm and a density predominantly equivalent to that of ground-glass opacity. Acinar nodules are presumed to represent acini filled with exudate or transudate. The term pseudonodule is used to describe a structure which simulates a nodule in the radiograph, such as a rib fracture, skin lesion, mammilla or summation effects [21].

Oligaemia

A regional or, less frequently, generalised reduction in pulmonary blood volume. It appears as a decrease in the number and diameter of visible vessels, as well as decreased lung density.

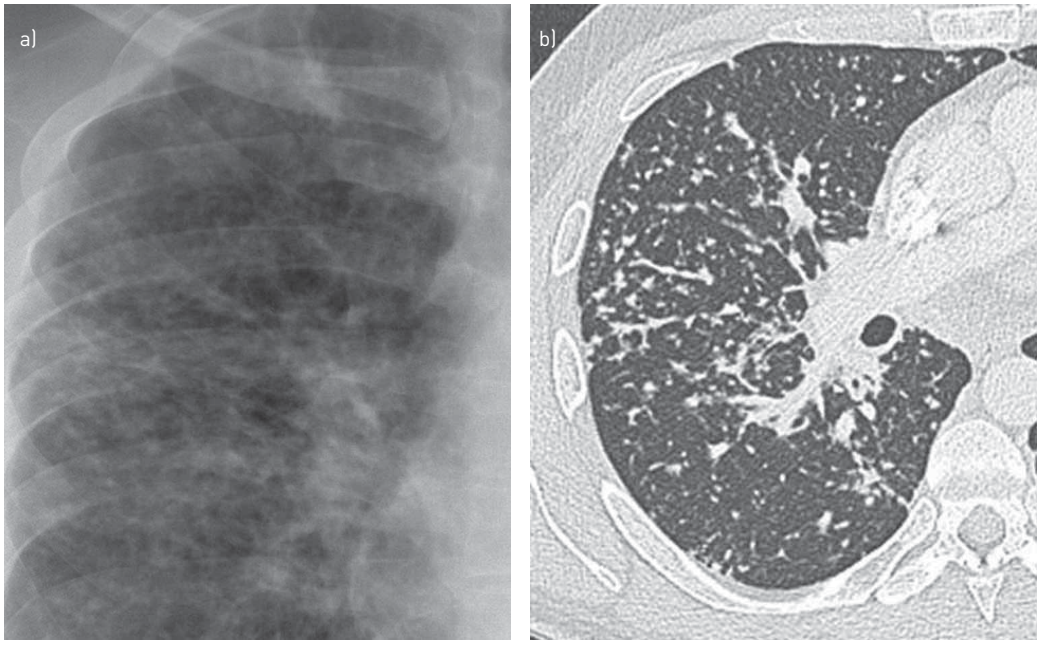

Figure 5. Nodular pattern: a) magnified view of a chest radiograph and b) magnified view of the corresponding HRCT.

Opacity

On the radiograph, opacity refers to any decrease in radiotransparency of the lung parenchyma compared with the normal state, regardless of the extent. The terms consolidation and ground-glass opacity describe the compaction more specifically and therefore should be used preferably.

Parenchymal band

A parenchymal band is visible as a linear opacity on the radiograph. The pleura may be thickened or retracted at the site of contact. In pathological terms, pleuroparenchymal fibrosis is involved here, the pathogenesis of which is attributable to the pleura. Parenchymal bands are therefore encountered most often in conjunction with asbestos-associated pleural thickening, but also occur post-inflammation and are not a typical sign of lung fibrosis [11, 22, 23].

Progressive massive fibrosis

Pathologically, progressive massive fibrosis refers to slow-growing conglomerates of dust particles and collagen deposits, which mostly occur in the event of heavy exposure to inorganic dusts (especially in the case of coal-workers pneumoconiosis) [24].

Radiology reveals bilateral masses with a predominantly perihilar localisation, especially in the upper lobes, usually with simultaneous presence of a nodular pattern and, possibly, emphysematous destruction of the lung parenchyma in the vicinity of the masses. Similar findings occur also in sarcoidosis and talcosis [25, 26].

Reticular pattern

A radiological pattern that appears as countless, small, linear opacities aligned in different directions, which are collectively visible as a mesh (figure 6). The term reticular pattern is not synonymous with a honeycomb pattern [11].

Reticulonodular pattern

A radiological pattern that arises from combination of a reticular pattern with a nodular pattern; the radiograph shows a meshed pattern of small, linear opacities with numerous, superimposed small nodules.

Right paratracheal stripe

The posterior–anterior radiograph shows a smoothly demarcated stripe of soft-tissue density extending from the medial end of the right clavicle vertically to the right tracheobronchial angle, next to the right margin of the trachea; the stripe includes the right tracheal wall, paratracheal connective tissue and pleura [27]. It is normally no wider than 4 mm. It is visible in 94% of normal individuals, and can be widened or rendered indefinable by increased mediastinal fat. The most common pathological cause for its widening, irregularity or indistinguishability is a paratracheal lymphadenopathy [11].

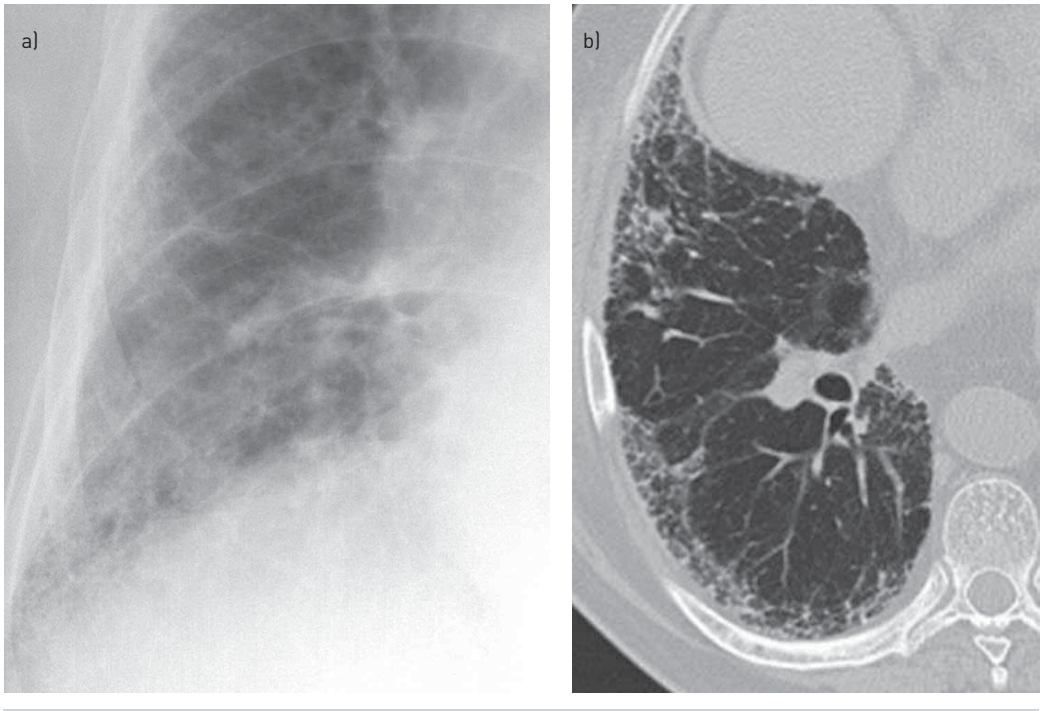

Figure 6. Reticular pattern: a) magnified view of a chest radiograph and b) magnified view of the corresponding HRCT.

Rounded atelectasis

A pleural, approximately half-spherical or triangular consolidation with smooth edges as well as tails, which resemble a comet's and are aligned toward the hilum. This feature is caused by a visceral pleural thickening that leads to folding of lung tissue and consecutive atelectasis.

Conclusion

In this chapter technical considerations of chest radiography and specifics of portable chest radiography in the ICU, especially its indications and interpretation, have been discussed. Adherence to the glossary of terms presented will contribute to better understandability of radiological reports.

References

1. Bundesärztekammer. Leitlinie der Bundesärztekammer zur Qualitätssicherung in der Röntgendiagnostik [Guideline of the German Medical Association for Quality Assurance in Diagnostic Radiology]. www.bundesaerztekammer.de/fileadmin/user_upload/downloads/LeitRoentgen2008Korr2.pdf Date last updated: March 12, 2008. Date last accessed: June 20, 2015.
2. Bradley M, Williams C, Walshaw MJ. The value of routine expiratory chest films in the diagnosis of pneumothorax. *Arch Emerg Med* 1991; 8: 115–116.
3. Seow A, Kazerooni EA, Pernicano PG, *et al.* Comparison of upright inspiratory and expiratory chest radiographs for detecting pneumothoraces. *AJR Am J Roentgenol* 1996; 166: 313–316.
4. Eisenhuber E, Schaefer-Prokop CM, Prosch H, *et al.* Bedside chest radiography. *Respir Care* 2012; 57: 427–443.
5. Oba Y, Zaza T. Abandoning daily routine chest radiography in the intensive care unit: meta-analysis. *Radiology* 2010; 255: 386–395.
6. Graat ME, Choi G, Wolthuis EK, *et al.* The clinical value of daily routine chest radiographs in a mixed medical-surgical intensive care unit is low. *Crit Care* 2006; 10: R11.
7. Hendrikse KA, Gratama JWC, ten Hove W, *et al.* Low value of routine chest radiographs in a mixed medical-surgical ICU. *Chest* 2007; 132: 823–828.
8. Remy-Jardin M, Giraud F, Remy J, *et al.* Importance of ground-glass attenuation in chronic diffuse infiltrative lung disease: pathologic-CT correlation. *Radiology* 1993; 189: 693–698.
9. Suh RD, Genshaft SJ, Kirsch J, *et al.* ACR Appropriateness Criteria: Intensive Care Unit Patients. https://acsearch.acr.org/docs/69452/Narrative/ Date last updated: February 26, 2015. Date last accessed: June 19, 2015.
10. Shevland JE, Hirleman MT, Hoang KA, *et al.* Lobar collapse in the surgical intensive care unit. *Br J Radiol* 1983; 56: 531–534.
11. Hansell DM, Bankier AA, MacMahon H, *et al.* Fleischner Society: glossary of terms for thoracic imaging. *Radiology* 2008; 246: 697–722.
12. Im JG, Webb WR, Han MC, *et al.* Apical opacity associated with pulmonary tuberculosis: high-resolution CT findings. *Radiology* 1991; 178: 727–731.
13. Dail DH. Pulmonary apical cap. *Am J Surg Pathol* 2001; 25: 1344.
14. Yousem SA. Pulmonary apical cap: a distinctive but poorly recognized lesion in pulmonary surgical pathology. *Am J Surg Pathol* 2001; 25: 679–683.
15. Kang EY, Miller RR, Müller NL. Bronchiectasis: comparison of preoperative thin-section CT and pathologic findings in resected specimens. *Radiology* 1995; 195: 649–654.
16. Grenier P, Maurice F, Musset D, *et al.* Bronchiectasis: assessment by thin-section CT. *Radiology* 1986; 161: 95–99.
17. Kim JS, Müller NL, Park CS, *et al.* Cylindrical bronchiectasis: diagnostic findings on thin-section CT. *AJR Am J Roentgenol* 1997; 168: 751–754.
18. Naidich DP, McCauley DI, Khouri NF, *et al.* Computed tomography of bronchiectasis. *J Comput Assist Tomogr* 1982; 6: 437–444.
19. Remy-Jardin M, Remy J, Giraud F, *et al.* Computed tomography assessment of ground-glass opacity: semiology and significance. *J Thorac Imaging* 1993; 8: 249–264.
20. Patterson HS, Sponaugle DN. Is infiltrate a useful term in the interpretation of chest radiographs? Physician survey results. *Radiology* 2005; 235: 5–8.

21. Erasmus JJ, Connolly JE, McAdams HP, *et al.* Solitary pulmonary nodules: Part I. Morphologic evaluation for differentiation of benign and malignant lesions. *Radiographics* 2000; 20: 43–58.
22. Akira M, Yamamoto S, Inoue Y, *et al.* High-resolution CT of asbestosis and idiopathic pulmonary fibrosis. *AJR Am J Roentgenol* 2003; 181: 163–169.
23. Akira M, Yamamoto S, Yokoyama K, *et al.* Asbestosis: high-resolution CT-pathologic correlation. *Radiology* 1990; 176: 389–394.
24. Wagner JC, Wusteman FS, Edwards JH, *et al.* The composition of massive lesions in coal miners. *Thorax* 1975; 30: 382–388.
25. Chong S, Lee KS, Chung MJ, *et al.* Pneumoconiosis: comparison of imaging and pathologic findings. *Radiographics* 2006; 26: 59–77.
26. Ward S, Heyneman LE, Reittner P, *et al.* Talcosis associated with IV abuse of oral medications: CT findings. *AJR Am J Roentgenol* 2000; 174: 789–793.
27. Savoca CJ, Austin JH, Goldberg HI. The right paratracheal stripe. *Radiology* 1977; 122: 295–301.

Disclosures: None declared.

Chapter 4

Lung cancer: screening and staging

Theresa C. McLoud[1] and Adam Bernheim[2]

Lung cancer screening has become a reality in the USA. Results of the National Lung Screening Trial showed a 20% mortality benefit in a defined population for annual screening with CT. However, the benefits of CT screening in high-risk individuals was accompanied by a very high false-positive rate, which in most cases resulted in multiple short-term additional follow-up CT examinations. In the USA, screening and insurance reimbursement are required by federal law for eligible current and former smokers with both private and public insurance. The American College of Radiology has developed a reporting system (Lung-RADS) that associates findings with guideline-based management decisions. The most recently revised seventh edition of the lung cancer TNM staging system correlates with patient prognosis and is now utilised for small cell lung cancer, nonsmall cell lung cancer and bronchopulmonary carcinoid tumours. The assignment of correct tumour (T), nodal (N) and metastasis (M) classifications is crucial not only to allow for clear physician communication across specialties, but also to direct appropriate therapy in this patient population.

Lung cancer remains the leading cause of death from malignancy, with approximately 1.6 million deaths occurring worldwide in 2012 [1]. Approximately 70% of cases have incurable disease at presentation, which is either metastatic or locally advanced [1]. The overall 5-year survival still remains low at 17% [1]. Lung cancer that is detected early in its course demonstrates much better survival data. Survival in nonsmall cell lung cancer stage I is >70%, and small peripheral <1 cm lung cancers have survival rates >80% [2]. Diagnosis of lung cancer early in preclinical stages has a higher cure rate and therefore high-risk asymptomatic individuals are likely to benefit from screening.

Lung cancer screening

The introduction of helical and subsequently multidetector CT in the 1990s led to a number of feasibility studies in which CT was used as a screening tool for the detection of early asymptomatic lung cancer. Observational single-arm trials were conducted for several years in many countries including the USA, Japan and Europe [3–8]. These studies

[1]Dept of Radiology, Massachusetts General Hospital and Harvard Medical School, Boston, MA, USA. [2]Emory University Hospital, Atlanta, GA, USA.

Correspondence: Theresa C. McLoud, Dept of Radiology, Massachusetts General Hospital, 55 Fruit Street, Boston, MA 02114, USA. E-mail: tmcloud@partners.org

Copyright ©ERS 2015. Print ISBN: 978-1-84984-065-1. Online ISBN: 978-1-84984-066-8. Print ISSN: 2312-508X. Online ISSN: 2312-5098.

established the sensitivity of low-dose CT for early lung cancer detection. They also tested algorithms for diagnostic work-up and demonstrated a reduction in the incidence of advanced nonsmall cell lung cancer with screening. A high percentage (84–93%) of stage I lung cancers were noted [3–5]. With regard to diagnostic algorithms, these studies provided evidence that peripheral nodules larger than 8–10 mm in size required further investigation because of a high likelihood of lung cancer. Smaller nodules (<8 mm diameter) could be managed with CT follow-up to determine interval growth, indicating the likelihood of malignancy.

Subsequently, several prospective randomised control trials were undertaken both in the USA and Europe. These included the National Lung Screening Trial (NLST) in the USA [9] and the NELSON (Dutch-Belgian randomised lung cancer screening trial) and other trials in Europe [10–14]. The results of the NLST were published in 2011 [15]. The study enrolled 53 454 individuals. It was a randomised national study, and the population group included individuals between the ages of 55 and 74 years with a history of ⩾30 pack-years of current or prior smoking. The enrollees underwent three annual screens. The study group received low-dose CT and the control group underwent standard chest radiography. CT was conducted with low-dose (1.5 mSv) helical and multidetector CT. The study was designed to determine lung cancer specific mortality and had a 90% power to detect a 20% reduction in lung cancer in the screened group. A positive screen consisted of the detection of a nodule or nodules >4 mm in diameter or other abnormalities suspicious of lung cancer. Follow-up was recommended based on nodule size, with larger nodules requiring diagnostic work-up. Results reported in 2011 indicated a 20% reduction in lung cancer mortality in the CT arm as well as an overall mortality reduction from all causes of 6.7%. More lung cancers were detected with CT than with standard radiography and a true stage shift was observed in the CT arm, with more lung cancers identified in earlier stages. There were few major complications from diagnostic work-ups conducted in cases suspicious for lung cancer, with a very low rate of complications in lesions that eventually were proven to be benign.

However, there are a number of disadvantages of screening reported by this study. The first was a high false positivity rate. 39% of subjects in the CT arm had a positive scan over the course of the 3-year screening period and 95% of the positive screens were false positives with no evidence of confirmed lung cancer. The second disadvantage of CT screening was the exposure to radiation. However, the technique delivered a mean whole body effective dose of 1.4 mSv in the NLST, which represents about one fifth of the dose of a diagnostic chest CT scan [15]. In an extensive review of the benefits and harms of CT screening for lung cancer, Bach *et al.* [16] concluded that the benefits of CT screening of high-risk individuals outweigh the small risk of cancer deaths from radiation exposure. Their data included a review of 591 citations, eight randomised trials and 13 cohort studies of low-dose CT screening.

There are methods to improve the positive predictive value and decrease the large number of false positives encountered with CT screening for lung cancer. The NLST interpretation algorithm was dichotomous. The NELSON trial in Europe has a two-step process that has been able to decrease the number of false positives based on nodule size [10]. Nodules smaller than 4–6 mm are considered negative and continue with annual incidence screens; those >1 cm are considered positive and undergo a definitive work-up. There is an indeterminate group consisting of nodules between 6 and 10 mm in diameter. If a nodule in this range is found in the prevalence screen, individuals undergo a 3-month follow-up. The study is considered positive if there is >25% growth, at which point these patients

undergo definitive work-up. The negative group has annual screening CT. This approach has improved the positive predictive value to 36% in the prevalence scan and 42% in the incidence scan.

Many American medical professional societies have recommended lung cancer screening for individuals meeting the criteria of the NLST with slight modifications. These include the American College of Chest Physicians, the American Cancer Society, the American Association of Thoracic Surgery and the National Comprehensive Cancer Network [16, 17]. More recently, the US Preventive Services Task Force has developed a recommendation (grade B for CT lung cancer screening of high-risk patients) that recommends screening according to the NLST criteria [18]. This recommendation requires private insurers in the USA to provide coverage of lung cancer screening in patients that meet these criteria.

Table 1. Designation of tumour (T) classification

Tumour characteristic	Tumour classification
Size (long-axis dimension) cm	
⩽2	T1a
>2 and ⩽3	T1b
>3 and ⩽5	T2a
>5 and ⩽7	T2b
>7	T3
Pleural and/or pericardial invasion	
Visceral pleura	T2a (if size ⩽5 cm) or T2b (if >5 and ⩽7 cm)
Pericardial pleura	T3
Mediastinal pleura	T3
Parietal pericardium	T3
Central airway invasion	
Endobronchial tumour >2 cm from carina	T2a (if size ⩽5 cm) or T2b (if >5 and ⩽7 cm)
Endobronchial tumour <2 cm from carina, but not involving carina	T3
Endobronchial tumour extends to carina	T4
Lung atelectasis	
Tumour causes atelectasis of less than entire lung	T2a (if size ⩽5 cm) or T2b (if >5 and ⩽7 cm)
Tumour causes atelectasis of entire lung	T3
Satellite nodule(s)	
Within the same lobe	T3
Within a different lobe in the same lung	T4
Soft tissue invasion	
Chest wall, including superior sulcus	T3
Diaphragm	T3
Mediastinum	T4
Heart or great vessels	T4
Oesophagus	T4
Trachea	T4
Bone invasion	
Rib	T3
Vertebral body	T4
Nerve invasion	
Phrenic nerve	T3
Recurrent laryngeal nerve	T4

In 2015, the Centers for Medicare and Medicaid Services (CMS), a US federal agency, approved lung cancer screening with eligibility criteria of ages 55–77 years, >30 pack-years of smoking in a current smoker or one who had quit within 15 years. This decision provides coverage for all eligible individuals aged >65 years. The CMS decision included several screening requirements, including: 1) a written order from the physician for the initial and subsequent screens; 2) an office visit with the referring physician for shared decision making, during which the risk of false positives and false negatives would be discussed; and 3) encouragement to stop smoking through use of smoking cessation services. CMS also set requirements for radiologists' eligibility to interpret CT scans for lung screening and also required an accredited imaging centre that met specifications for CT equipment. Finally, CMS requires collection and submission of data to a national registry for each screen performed [19].

Subsequent to this decision, the American College of Radiology developed a reporting system called Lung-RADS (Lung Imaging Reporting and Data System). It is similar to BI-RADS (Breast Imaging Reporting and Data System), which is widely used for reporting mammography. It provides numerical categories that associate findings with guideline-based management decisions. Lung-RADS includes four categories. Categories 1 and 2 are considered a negative screen. Findings include a classification of nodules by density (solid or sub-solid) and by size. There are management guidelines for each of the four categories, as well a statement of the probability of malignancy in each category and the estimated population prevalence [20].

Despite the results of the NLST, it is not certain that its results can be broadly generalised in other screening settings, particularly in community-based screening [21]. Also, surgical mortality in the NLST subjects undergoing thoracic surgery was 1% compared with the national average in the USA of 3–5% [21]. In addition, overdiagnosis, *i.e.* the detection of tumours that will not become lethal cancers, has been estimated to be as high as 20% of

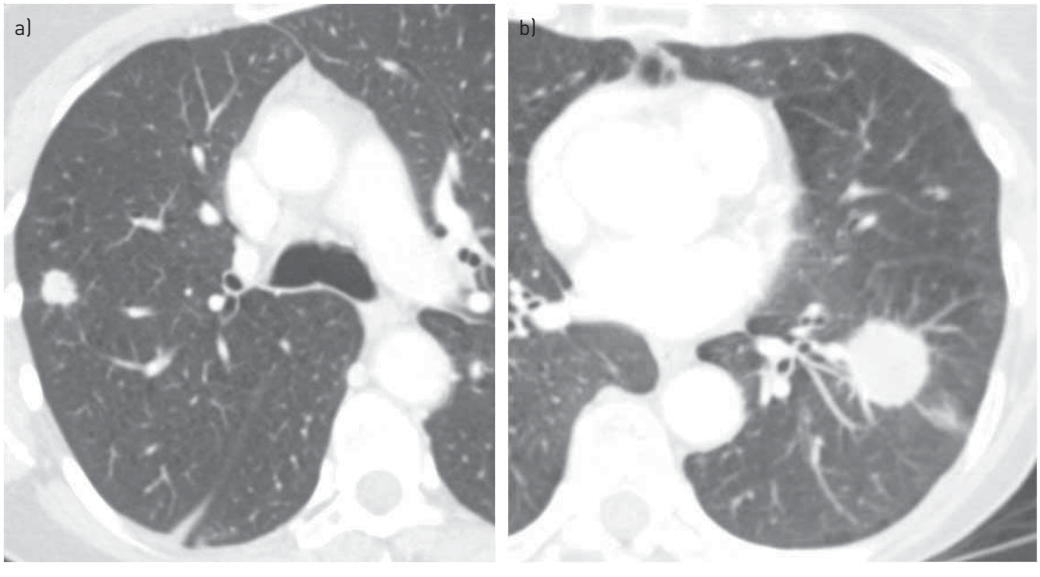

Figure 1. Axial CT imaging in two different patients with T1 lung cancer demonstrates a) a T1a tumour that is ⩽2 cm and b) a T1b tumour measuring >2 but ⩽3 cm.

cancers found in the NLST. None of the European trials so far has indicated an acceptable mortality benefit from lung cancer screening. However, these trials are small and they may not have had the power to detect such a benefit. The results of the NELSON trial hopefully will be published next year. The European randomised lung cancer CT screening project (EUCT) will pool the data and results from European trials to determine optimal screening populations and optimal screening intervals. It will also examine possible refinements of inclusion criteria to include exposures linked to lung cancer (*e.g.* asbestos or radon), family history of lung cancer and more elderly populations. Recommendations for screening will probably follow, once this project is completed.

Finally, the issue of cost-effectiveness must be addressed. A recent publication from the NLST estimates that the incremental cost-effectiveness ratio for screening with low-dose CT *versus* no screening was USD 81 000 per quality-adjusted life-year (QALY) gained. This is below the recently recommended USD 100 000 per QALY gain threshold for healthcare in the USA [22]. The same recommendation may well not apply to the European situation.

Implementation of a lung cancer screening programme requires a major institutional and departmental effort. The stakeholders include hospital leadership, referral providers and a multidisciplinary chain consisting of radiologists, thoracic surgeons, pulmonologists, medical oncologists, radiation oncologists and a patient navigator, as well as support staff such as a research coordinator. Components of a successful programme include tools for outreach in education, including websites with a programme description and information for referring clinicians as well as patients. Protocols should be developed according to the NLST and American College of Radiology standards for image acquisition, and image

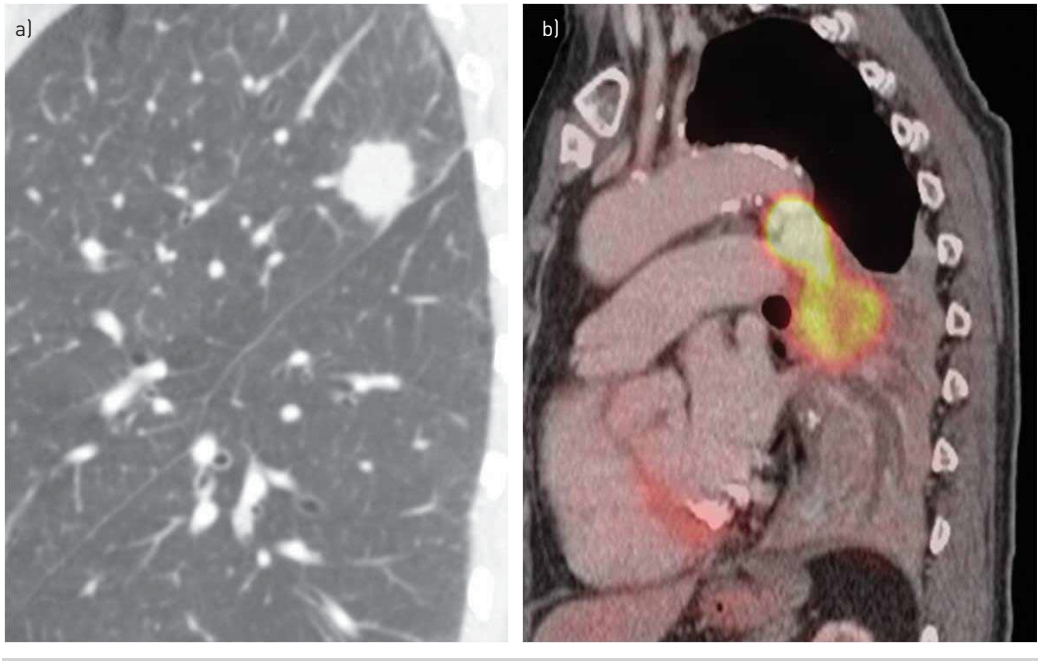

Figure 2. Lung cancer in patients with T2 disease. a) Sagittal CT image of a 2.7-cm pulmonary nodule with evidence of visceral pleural invasion, which is classified as T2a status. b) Sagittal fused PET/CT image of a 6.3-cm FDG-avid left hilar mass causing left lower lobar atelectasis in this patient with T2b squamous cell carcinoma.

review should be performed by radiologists experienced in CT nodule detection and management. Computer-aided detection and software for volumetric measurements of nodules are extremely helpful. Management and reporting of findings should follow an

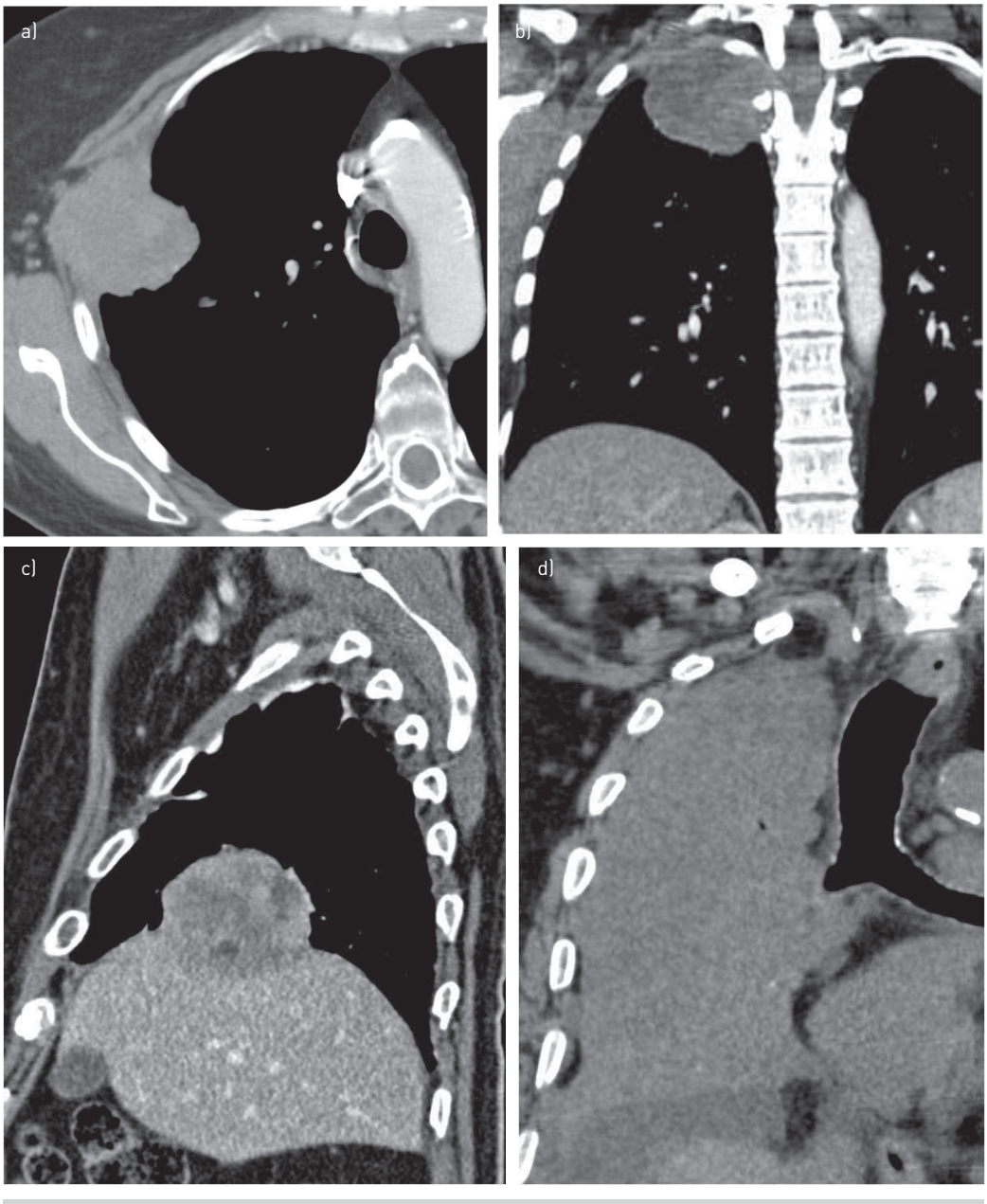

Figure 3. Lung cancer in four different patients with T3 disease. a) A tumour with definite chest wall invasion seen on axial CT imaging. b) A 6.2-cm superior sulcus tumour identified on coronal CT imaging. c) A 6.8-cm tumour with diaphragmatic invasion demonstrated on sagittal CT imaging. d) A 5.8-cm right hilar mass with an endobronchial component in the right mainstem bronchus >2 cm from the carina (but not involving the carina) and with atelectasis of the entire right lung, seen on coronal CT imaging.

algorithm such as the Lung-RADS recommendations. Communication of results in a timely fashion to both physicians and patients is required.

In conclusion, lung cancer screening is already occurring in the USA and probably will occur in Europe in the near future. Based on the American experience, implementation of European lung cancer screening programmes will require a cumulative effort on the part of physicians, specialty societies and patient advocacy organisations armed with convincing data from European trials. Lobbying of national governments and their healthcare ministries will be crucial. It presents a unique challenge and opportunity to reduce mortality from this lethal disease.

Lung cancer staging

Appropriate staging of lung cancer is critical not only for its prognostic value, but also as a mechanism for guiding appropriate therapy. Those patients with early-stage lung cancer

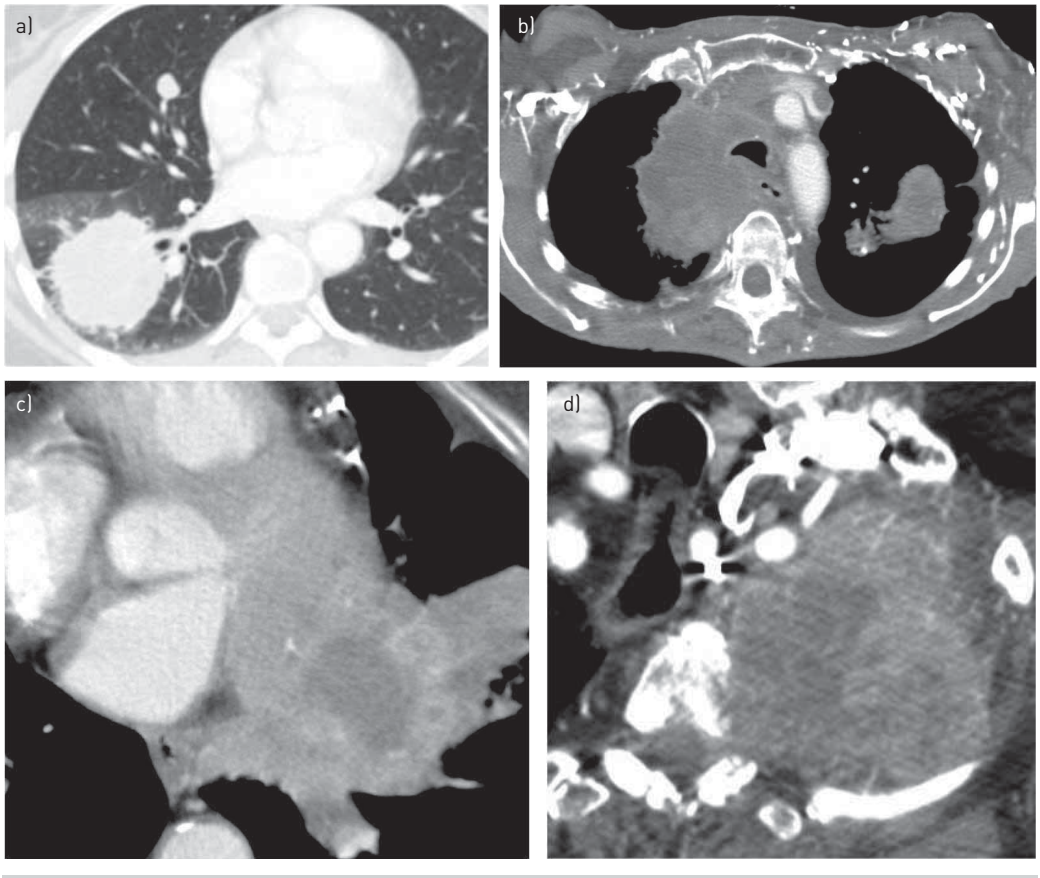

Figure 4. Lung cancer in a set of four different patients with T4 disease. a) A 6.3-cm right lower lobe large cell carcinoma with a 7-mm satellite nodule in the right middle lobe seen on axial CT imaging. b) A right upper lobe tumour with direct mediastinal invasion, including invasion of the superior vena cava and trachea, seen on axial CT imaging. c) A 9.5-cm squamous cell carcinoma with encasement of the left ventricle, left pulmonary veins and coronary arteries, depicted on axial CT imaging. d) A 9.5-cm left upper lobe adenocarcinoma with invasion of the T3 vertebra, identified on axial CT imaging.

may be candidates for curative surgical resection, whereas the assignment of an advanced stage of disease can preclude unnecessary surgery and serve as a basis for determination of an appropriate radiation and/or chemotherapy regimen. The TNM (tumour, nodes, metastasis) staging system, adopted in 2009 by the International Union Against Cancer and the American Joint Committee on Cancer, is based upon proposals submitted by the International Association for the Study of Lung Cancer. This is a revised version of a previous staging system and is now in its seventh edition. It is currently the accepted standard for lung cancer staging and is based on epidemiological prognostic data obtained between 1990 and 2000 by the Cancer Research and Biostatistics office from 100 869 lung cancer patients from 45 institutions across 20 countries [23, 24]. The system now applies to small cell lung cancer, nonsmall cell lung cancer and bronchopulmonary carcinoid tumours.

TNM classification

T classification

Tumour classification is defined by the location and size of the primary malignancy, as well as by invasion of adjacent structures and presence and location of satellite nodules (table 1). Tumour size, as measured in its long-axis dimension, correlates inversely with prognosis. A designation of T1 is assigned for a tumour ⩽3 cm that is completely surrounded by lung, is at least as peripheral as a lobar bronchus, and does not show invasion, nodal disease or metastasis. There is a subdivision to differentiate between T1a tumours (which are ⩽2 cm) and T1b tumours (which are >2 and ⩽3 cm) (figure 1), based upon a statistically significant difference between the 5-year survival rates of 77% and 71%, respectively [25]. A similar subdivision exists for patients with T2 disease, as T2a tumours (>3 and ⩽5 cm) and T2b tumours (>5 and ⩽7 cm) feature 5-year survival rates of 58% and 49%, respectively, in the absence of invasion, nodal disease or metastases [25]. Tumours >7 cm are classified as T3 and have a 5-year survival rate of 35% [25].

Tumour size is not the only relevant factor in determination of T status. Tumours ⩽5 cm that invade the visceral pleura (figure 2a), are located within a mainstem bronchus but >2 cm from the carina, or cause atelectasis of less than an entire lung are considered T2a. Tumours with these characteristics that are >5 and ⩽7 cm are designated T2b (figure 2b).

T3 status is assigned if a tumour is located within a mainstem bronchus but <2 cm from the carina (but does not involve the carina), causes atelectasis of an entire lung, or has a satellite nodule within the same lobe. T3 is also the appropriate tumour status designation for any malignancy that invades the pericardial pleura, mediastinal pleura, parietal pericardium, chest wall or diaphragm (figure 3). Osseous invasion into a rib or phrenic nerve invasion likewise warrant T3 status.

A tumour with a T4 designation has the worst prognosis and is assigned for any endobronchial lesion that involves the carina. Moreover, a satellite nodule within a different lobe but in the same lung is considered T4 status; invasion of the mediastinum, heart, great vessels, oesophagus and trachea qualifies as T4 disease; and osseous invasion of a vertebral body or recurrent laryngeal nerve invasion similarly confers T4 status (figure 4).

Table 2. Designation of nodal (N) classification

Extent of lymphadenopathy	Lymph node classification
No lymphadenopathy	N0
Ipsilateral peripheral or hilar lymphadenopathy	N1
Ipsilateral mediastinal lymphadenopathy (includes subcarinal involvement)	N2
Contralateral mediastinal, contralateral hilar, or supraclavicular lymphadenopathy	N3

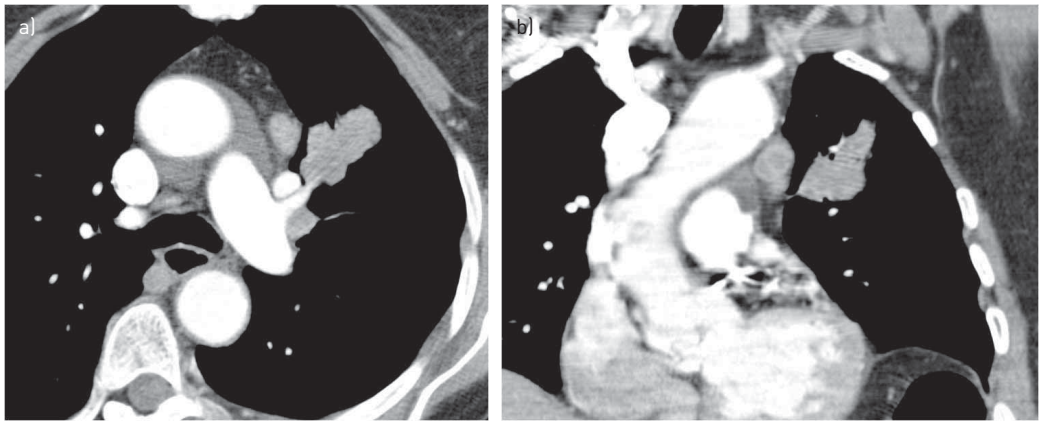

Figure 5. Axial CT imaging in a) axial and b) coronal planes demonstrates a primary lung cancer in the left upper lobe with ipsilateral mediastinal lymphadenopathy in this patient with N2 disease.

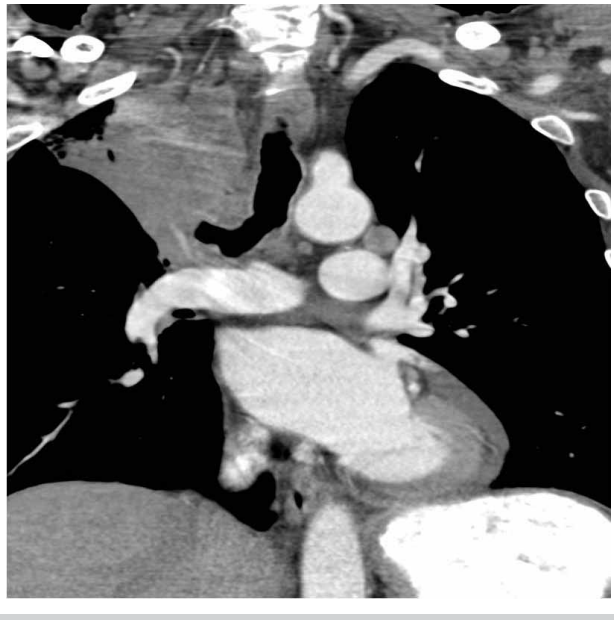

Figure 6. Coronal CT imaging in a patient with a right upper lobe mass and contralateral mediastinal lymphadenopathy, defining N3 status.

Table 3. Designation of metastasis (M) classification

Extent of metastatic disease	Metastasis classification
No metastatic disease	M0
Spread of disease to the contralateral lung, pleural space or pericardial space	M1a
Distant metastatic disease	M1b

The T classification is best assessed with CT, although MRI may be helpful in selected cases where soft tissue invasion is uncertain on CT, such as for evaluation of potential invasion of a neural foramen, brachial plexus or superior sulcus. PET with FDG has a limited role in designation of T status, although it is helpful in selected cases, such as differentiating a central FDG-avid tumour from distal non-FDG-avid atelectasis [26].

N classification

Nodal status is determined by extent of lymph node involvement (table 2) and correlates with prognosis. The 5-year survival rates for lung cancer in patients with any T classification and no metastases (M0) are 42% for N0 disease, 29% for N1 disease, 16% for N2 disease and 7% for N3 disease [23].

For purposes of lung cancer staging, lymphadenopathy is divided into seven specific zones: the supraclavicular, upper, aortopulmonary, subcarinal, lower, hilar/intralobar and peripheral zones [27]. This simplified and unified nodal staging system is new, replacing the previously utilised Mountain–Dresler system [28]. The absence of disease spread to lymph nodes defines N0 disease. Ipsilateral peripheral or hilar lymph node involvement confers N1 status, whereas ipsilateral mediastinal (including upper, lower and aortopulmonary) or subcarinal lymph node involvement defines N2 disease (figure 5). Any disease spread to contralateral mediastinal, contralateral hilar, or supraclavicular and/or scalene lymph node stations on either side is designated as N3 status (figure 6).

PET/CT is a helpful modality for determination of N status, and the combined use of PET and CT is more accurate than PET or CT imaging alone.

M classification

Metastatic spread of disease is classified as either M0, M1a or M1b (table 3). Patients with no metastases have M0 status. Lung cancer that has spread to involve the contralateral lung, pleural space (including pleural nodularity or malignant pleural effusion) or pericardial space (including pericardial nodularity or malignant pericardial effusion) warrants an M1a designation, whereas M1b status is reserved for those patients with distant metastatic spread of disease (figure 7). The differentiation between M1a disease and M1b disease is manifested in a statistically significant difference in 5-year survival rates, which are 2% and 1%, respectively [23].

Staging system

Once the tumour, nodal and metastasis classifications have been established, overall lung cancer staging can be determined (table 4). Although there is a level of variability between

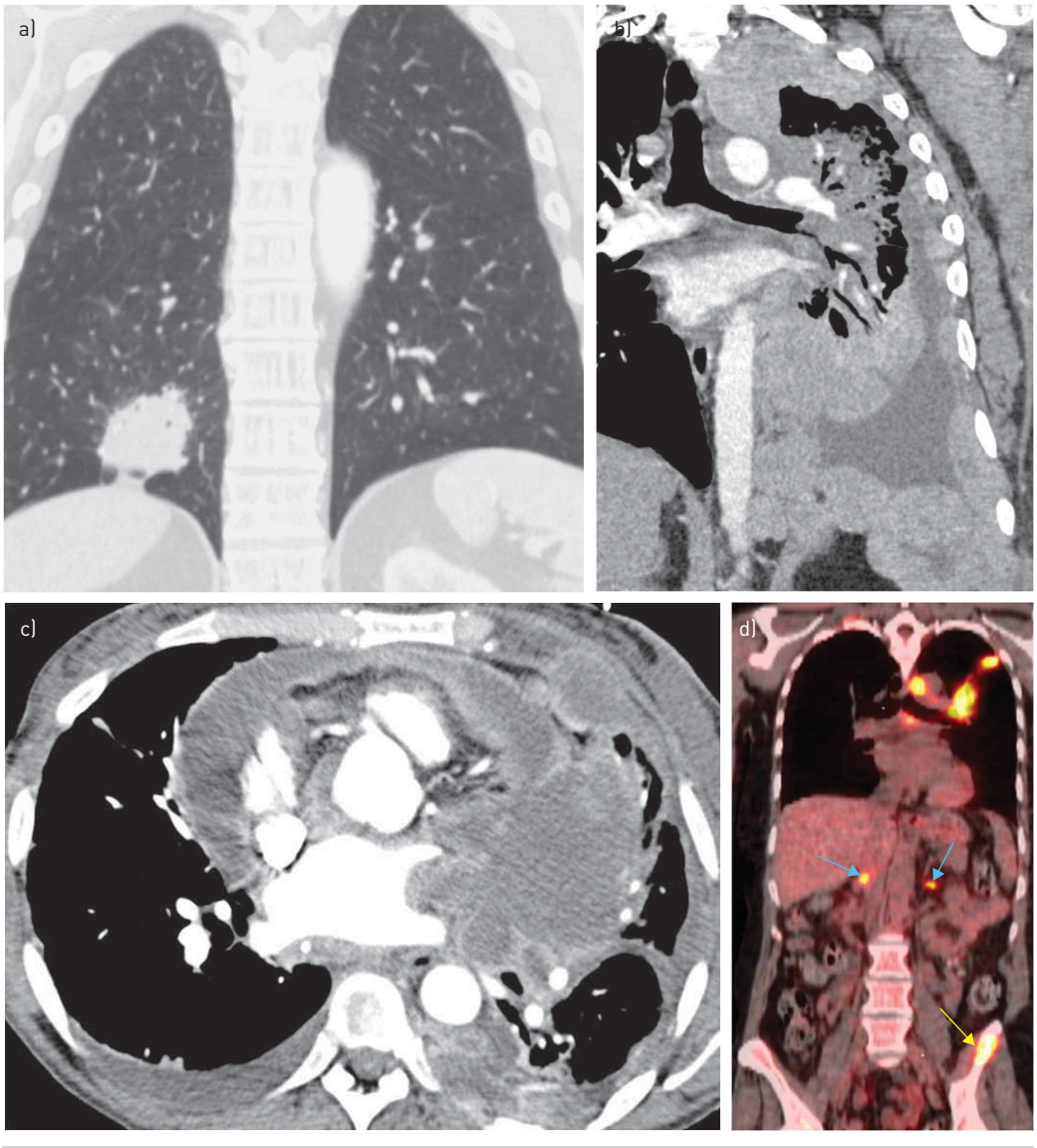

Figure 7. Lung cancer in a set of four different patients with metastatic disease. a) A 5.2-cm right lower lobe adenocarcinoma with a metastatic 5-mm nodule in the left lower lobe, as seen on coronal CT imaging in this patient with M1a disease. b) A 7.4-cm left hilar adenocarcinoma with circumferential left pleural metastases, as demonstrated on CT imaging in this patient with M1a disease. c) A 10.8-cm left hilar adenocarcinoma with both malignant pericardial and pleural disease, as identified on axial CT imaging in this patient with M1a disease. d) An FDG-avid 3.3-cm left upper lobe adenocarcinoma with distant metastatic spread to both adrenal glands (blue arrows) and the left iliac bone (yellow arrow), as seen on coronal fused PET/CT imaging in this patient with M1b disease.

institutions and particular surgeons depending on each individual case, as a general rule nonsmall cell lung cancer patients with disease no greater than stage IIIA are considered to be amenable to surgical therapy, whereas those patients with stage IIIB or stage IV disease are typically not surgical candidates. This staging system is now employed for small cell lung cancer as well, replacing a previous classification system that divided patients into those with limited or with extensive disease. Moreover, bronchopulmonary carcinoid

Table 4. Lung cancer stage groupings

	N0	N1	N2	N3
T1a	IA	IIA	IIIA	IIIB
T1b	IA	IIA	IIIA	IIIB
T2a	IB	IIA	IIIA	IIIB
T2b	IIA	IIB	IIIA	IIIB
T3	IIB	IIIA	IIIA	IIIB
T4	IIIA	IIIA	IIIB	IIIB
M1a	IV	IV	IV	IV
M1b	IV	IV	IV	IV

tumours have shown an inverse correlation between TNM stage and 5-year survival and are now also staged according to this system [29].

Conclusion

Appropriate assignment of disease stage in lung cancer patients is based on determination of tumour classification, nodal status and absence or presence of metastasis, according to the most recently updated seventh edition of the TNM system. Imaging is at the core of assessing disease stage in lung cancer patients, although surgical, bronchoscopic (EBUS) or other invasive confirmation of nodal or metastatic disease is necessary to pathologically confirm staging, as appropriate. Staging carries both prognostic and therapeutic implications. The staging system is widely accepted, allowing synergy between radiology and pulmonology, medical oncology, surgical oncology, radiation oncology and pathology departments to deliver optimal care in this patient population.

References

1. American Cancer Society. Cancer Facts and Figures 2015. www.cancer.org/acs/groups/content/@editorial/documents/document/acspc-044552.pdf
2. National Cancer Institute. Non-Small Cell Lung Cancer Treatment – for health professionals (PDQ). www.cancer.gov/types/lung/hp/non-small-cell-lung-treatment-pdq Date last udpated: September 3, 2015.
3. Kaneko M, Eguchi K, Ohmatsu H, *et al.* Peripheral lung cancer: screening and detection with low-dose spiral CT *vs* radiography. *Radiology* 1996; 201: 798–802.
4. Sone S, Takashima S, Li F, *et al.* Mass screening for lung cancer with mobile spiral computed tomography scanner. *Lancet* 1998; 351: 1242–1245.
5. Henschke CI, McCauley DI, Yankelevitz DF, *et al.* Early Lung Cancer Action Project: overall design and findings from baseline screening. *Lancet* 1999; 354: 99–105.
6. Swensen SJ, Jett JR, Hartman TE, *et al.* CT screening for lung cancer: five-year prospective experience. *Radiology* 2005; 235: 259–265.
7. Nawa T, Nakagawa T, Kusano S, *et al.* Lung cancer screening using low-dose spiral CT: results of baseline and 1-year follow-up studies. *Chest* 2002; 122: 15–20.
8. Diederich S, Wormanns D, Semik M, *et al.* Screening for early lung cancer with low-dose spiral CT: prevalence in 817 asymptomatic smokers. *Radiology* 2002; 222: 773–781.
9. National Lung Screening Trial Research Team. The National Lung Screening Trial: overview and study design. *Radiology* 2011; 258: 243–253.
10. van Iersel CA, de Koning HJ, Draisma G, *et al.* Risk-based selection from the general population in a screening trial: selection criteria, recruitment and power for the Dutch-Belgian randomised lung cancer multi-slice CT screening trial (NELSON). *Int J Cancer* 2007; 120: 868–874.
11. Pedersen JH, Ashraf H, Dirksen A, *et al.* The Danish randomized lung cancer CT screening trial – overall design and results of the prevalence round. *J Thorac Oncol* 2009; 4: 608–614.

12. Lopes Pegna A, Picozzi G, Mascalchi M, *et al.* Design, recruitment and baseline results of the ITALUNG trial for lung cancer screening with low-dose CT. *Lung Cancer* 2009; 64: 34–40.
13. Infante M, Cavuto S, Lutman FR, *et al.* A randomized study of lung cancer screening with spiral computed tomography: three-year results from the DANTE trial. *Am J Respir Crit Care Med* 2009; 180: 445–453.
14. Becker N, Delorme S, Kauczor HU. LUSI: the German component of the European trial on the efficacy of multislice-CT for the early detection of lung cancer. *Onkologie* 2008; 31: Suppl. 1, PO320.
15. National Lung Screening Trial Research Team. Reduced lung-cancer mortality with low-dose computed tomographic screening. *N Engl J Med* 2011; 365: 395–409.
16. Bach PB, Mirkin JN, Oliver TK, *et al.* Benefits and harms of CT screening for lung cancer: a systematic review. *JAMA* 2012; 307: 2418–2429.
17. Wood DE, Eapen GA, Ettinger DS, *et al.* Lung cancer screening. *J Natl Compr Canc Netw* 2012; 10: 240–265.
18. Moyer VA, US Preventive Services Task Force. Screening for lung cancer: US Preventive Services Task Force recommendation statement. *Ann Intern Med* 2014; 160: 330–338.
19. Centers for Medicare and Medicaid Services. Decision Memo for Screening for Lung Cancer with Low Dose Computed Tomography (LDCT) (CAG-00439N). www.cms.gov/medicare-coverage-database/details/nca-decision-memo.aspx?NCAId=274 Date last updated: February 5, 2015.
20. American College of Radiology. Lung-RADS Version 1.0 Assessment Categories. Release date: April 28, 2014. www.acr.org/~/media/ACR/Documents/PDF/QualitySafety/Resources/LungRADS/AssessmentCategories.pdf
21. Tanoue LT, Tanner NT, Gould MK, *et al.* Lung cancer screening. *Am J Respir Crit Care Med* 2015; 191: 19–33.
22. Black WC, Gareen IF, Soneji SS, *et al.* Cost-effectiveness of CT screening in the National Lung Screening Trial. *N Engl J Med* 2014; 371: 1793–1802.
23. Goldstraw P, Crowley J, Chansky K, *et al.* The IASLC Lung Cancer Staging Project: proposals for the revision of the TNM stage groupings in the forthcoming (seventh) edition of the TNM Classification of malignant tumours. *J Thorac Oncol* 2007; 2: 706–714.
24. Sculier JP, Chansky K, Crowley JJ, *et al.* The impact of additional prognostic factors on survival and their relationship with the anatomical extent of disease expressed by the 6th Edition of the TNM Classification of Malignant Tumors and the proposals for the 7th Edition. *J Thorac Oncol* 2008; 3: 457–466.
25. Rami-Porta R, Ball D, Crowley J, *et al.* The IASLC Lung Cancer Staging Project: proposals for the revision of the T descriptors in the forthcoming (seventh) edition of the TNM classification for lung cancer. *J Thorac Oncol* 2007; 2: 593–602.
26. Kligerman S, Digumarthy S. Staging of non-small cell lung cancer using integrated PET/CT. *AJR Am J Roentgenol* 2009; 193: 1203–1211.
27. Kligerman S. The clinical staging of lung cancer through imaging: a radiologist's guide to the revised staging system and rationale for the changes. *Radiol Clin North Am* 2014; 52: 69–83.
28. Rusch VW, Asamura H, Watanabe H, *et al.* The IASLC Lung Cancer Staging Project: a proposal for a new international lymph node map in the forthcoming seventh edition of the TNM classification for lung cancer. *J Thorac Oncol* 2009; 4: 568–577.
29. Travis WD, Brambilla E, Rami-Porta R, *et al.* Visceral pleural invasion: pathologic criteria and use of elastic stains: proposal for the 7th edition of the TNM classification for lung cancer. *J Thorac Oncol* 2008; 3: 1384–1390.

Disclosures: None declared.

Chapter 5

Pulmonary embolism

Sumit Karia and Nicholas Screaton

Pulmonary embolism is a common condition that has significant associated morbidity and mortality. Anticoagulation is an effective treatment, but is not without significant complications. Pulmonary embolism often presents nonspecifically and imaging is central to establishing a diagnosis. CT pulmonary angiography is now the standard imaging test, benefiting from availability, rapid acquisition, high accuracy in identifying pulmonary embolism and complementary roles in patient risk stratification. In patients not found to have pulmonary embolism CT pulmonary angiography may offer an alternative diagnosis.

A rapid increase in CT pulmonary angiography numbers have been mirrored by a falling diagnostic yield and have led to concerns of overuse both from a resource and radiation exposure perspective. To avoid unnecessary imaging adherence to guidelines, appropriate use of clinical scoring systems and D-dimer tests are essential. Technological developments, *e.g.* dual-energy CT pulmonary angiography pulmonary blood volume imaging, can improve CT pulmonary angiography sensitivity and risk stratification.

Perfusion scintigraphy is widely used in pregnancy, benefiting from a high negative predictive value and significant reduction in maternal radiation dose compared with CT pulmonary angiography. Magnetic resonance pulmonary angiography offers benefits of no radiation exposure and additional functional information, but limited availability and variable diagnostic quality has limited its use.

Pulmonary embolism is a relatively common condition with an incidence of 60–70 per 100 000. It is the third most common acute cardiovascular presentation following myocardial infarction and stroke [1]. Untreated acute pulmonary embolism is fatal in up to 30% of patients. Mortality is reduced to 2–10% with timely diagnosis and treatment with anticoagulation [2]. Patients typically present with nonspecific symptoms such as dyspnoea and chest pain, so the clinical differential diagnosis is wide. Timely diagnosis and institution of therapy is the key to improving outcome, but the risk of haemorrhagic complications from unnecessary anticoagulation is high. Rapidly securing an accurate diagnosis is, therefore, essential and imaging plays a fundamental role in this regard.

CT pulmonary angiography was first introduced in the 1990s following the advent of spiral CT [3]. While initially its sensitivity at subsegmental level was questioned, the rapid

Dept of Radiology, Papworth Hospital, Cambridge, UK.

Correspondence: Nicholas Screaton, Dept of Radiology, Papworth Hospital, Papworth Everard, Cambridge, CB23 3RE, UK.
E-mail: Nicholas.screaton@papworth.nhs.uk

Copyright ©ERS 2015. Print ISBN: 978-1-84984-065-1. Online ISBN: 978-1-84984-066-8. Print ISSN: 2312-508X. Online ISSN: 2312-5098.

evolution of CT technology, particularly the proliferation of detector rows, improved rotation time and optimisation of contrast medium administration, has led to CT pulmonary angiography now being the reference standard for pulmonary embolism diagnosis. It also plays an important role in prognostic risk stratification, and can differentiate acute from chronic thromboembolic disease.

Although CT pulmonary angiography is the most commonly used diagnostic investigation in the pathway of a patient with suspected pulmonary embolism, ventilation/perfusion (V'/Q') scintigraphy is still used in most institutions due to its high negative predictive value. In addition, V'/Q' scintigraphy has an important role in certain patient groups with suspected pulmonary embolism. The use of novel CT and MRI techniques will also be briefly discussed.

Diagnostic pathway in suspected pulmonary embolism

CT pulmonary angiography has become the reference standard imaging technique for suspected pulmonary embolism, but V'/Q' scintigraphy remains a widely used technique, especially in patients with renal failure or allergy to iodinated contrast medium. V'/Q' scintigraphy is widely accepted as the first choice modality in investigation of the pregnant patient with suspected pulmonary embolism, which is further discussed later in this chapter.

There has been an explosion in the volume of imaging performed in recent years largely driven by the availability and rapid acquisition of multidetector CT. This has resulted in a 14-fold increase in the number of referrals for CT pulmonary angiography [4], associated with a reduction in the diagnostic yield [5]. These figures raise concern that the seeming overuse of CT pulmonary angiography may result in its use as a screening modality rather than a diagnostic test [6]. To try and address the potential overuse of CT pulmonary angiography and imaging overall, both national (*e.g.* the British Thoracic Society [7] and National Institute for Health and Care Excellence [8], in the UK) and international [9–11] guidelines have been established. These aid clinicians in the appropriate selection of patients who require imaging.

Patient selection prior to imaging

Clinical presentation

The clinical presentation of pulmonary embolism is nonspecific and has a wide range of clinical manifestations, ranging from asymptomatic to shock and death. Chest pain is a frequent symptom and usually due to pleural irritation by distal pulmonary infarction. In large pulmonary embolism, chest pain may have characteristics typical of angina, which may reflect right ventricular ischaemia. Breathlessness is another common symptom that may be acute and severe in central pulmonary embolism and mild and transient in peripheral pulmonary embolism. It is important to consider pulmonary embolism as a cause of worsening breathlessness in patients with known cardiac or respiratory disease, such as underlying COPD [9]. First line investigations including blood gas analysis often reveal hypoxaemia, but up to 40% of patients with pulmonary embolism will have normal arterial oxygen saturation [12]. Electrocardiographic findings classically reflect right heart strain (right axis deviation, right bundle branch block or S1Q3T3 pattern), but more commonly the ECG demonstrates sinus tachycardia, which is seen in 40% of patients [9]. The chest radiograph is frequently abnormal with a multitude of nonspecific findings such as atelectasis, consolidation or pleural effusion. An alternative diagnosis such as pneumothorax

can rarely be identified, but an unremarkable chest radiograph can be useful in helping to triage patients for further investigation with V'/Q' scintigraphy as the diagnostic yield of the two techniques in combination is raised compared with V'/Q' scintigraphy alone [13].

Clinical scoring systems

As briefly outlined above, guidelines exist that utilise clinical scoring systems to aid clinicians in the appropriate selection of patients who require investigation (namely imaging) in suspected pulmonary embolism. The most commonly used clinical prediction tool is the Wells score [14], which is based up on a 7-point clinical score that either separates patients into low, moderate and high-risk groups or dichotomises clinical risk into pulmonary embolism likely or pulmonary embolism unlikely (table 1).

While most parameters in the Wells score are objective, there is significant subjectivity weighting towards the clinicians overall impression of the likelihood of pulmonary embolism. The Wells score is well validated. When clinical score is low and the D-dimer test is negative, the likelihood of pulmonary embolism during follow-up was only 0.2% [15]. Objective scoring systems such as the Geneva score are also widely used and show no significant differences in overall accuracy compared with the Wells score [16].

D-dimer

Plasma D-dimer is a degradation product of cross-linked fibrin, a marker of thrombus formation. The specificity and sensitivity of D-dimer (at 500 $\mu g \cdot L^{-1}$) for venous thromboembolism are 55% and 95%, respectively [17]. Elevated D-dimer can also be seen in renal failure, sepsis, malignancy and pregnancy, and accordingly the positive predictive value of elevated D-dimer is low. The strength of D-dimer testing lies in its high negative predictive value in the context of low clinical likelihood; in this group an incidence of missed pulmonary embolism was 0.5% over 3 months [15]. However, in patients with a high probability clinical score and negative D-dimer test, this does not avoid the need for further investigation to rule out pulmonary embolism due to the high prevalence of pulmonary embolism in this patient group. Therefore, D-dimer is not routinely performed in patients with high clinical probability.

Table 1. The seven-point Wells scoring system

Variable	Score
Clinical signs and symptoms of deep vein thrombosis	3
Pulmonary embolism is the most likely diagnosis, or is equally likely	3
Heart rate >100 beats per min	1.5
Immobilisation for at least 3 days, or surgery in the previous 4 weeks	1.5
Previous, objectively diagnosed pulmonary embolism or deep vein thrombosis	1.5
Haemoptysis	1
Malignancy (with ongoing treatment, treated within the past 6 months or palliative)	1

For the three-level score: score <2, low probability; score 2–6, moderate probability; score >6, high probability. For the two-level score: score <4, pulmonary embolism unlikely; score ⩾4, pulmonary embolism likely. Data from [11].

Since D-dimer levels increase with age, it has been suggested that in older patients raising the D-dimer cut-off threshold at which imaging investigation for pulmonary embolism is indicated may improve the specificity of the test. RIGHINI *et al.* [18] suggest using a D-dimer cut-off threshold determined by age×10 $\mu g \cdot L^{-1}$ in patients over 50 years of age to improve specificity without a significant increase in false negative results.

The use of scoring systems is important to ensure preservation of the effectiveness of CT pulmonary angiography along with avoidance of excessive radiation, use of contrast medium and overdiagnosis. Diagnostic algorithms for patient investigation have been produced (figure 1), and through their utilisation a 20–30% reduction in the number of CT pulmonary angiography examinations undertaken can be achieved [19].

Choice of imaging test

V′/Q′ *SPECT*

Traditional planar *V′/Q′* scintigraphy was the most commonly undertaken imaging test for the diagnosis of pulmonary embolism before the era of multidetector CT. The technique is based upon the use of injected ^{99m}Tc-labelled macroaggregated albumin particles, which lodge in the pulmonary capillaries allowing assessment of lung perfusion. Assessment of ventilation is typically performed with inhaled or aerosol forms of ^{133}Xe or ^{99m}Tc. A pulmonary embolism typically results in reduced perfusion to a segment of lung with preserved ventilation in this region; a mismatched defect. The ventilation component can potentially (in patients with a normal chest radiograph) be omitted without affecting the diagnostic accuracy. Studies have shown that perfusion scintigraphy combined with chest radiography can offer sensitivity and specificity values comparable to CT pulmonary angiography [20]. Further benefits of scintigraphy include use in patients with renal failure or known allergy to iodinated contrast medium and in those with poor intravenous access that may preclude satisfactory *i.v.* access for CT pulmonary angiography. Limitations of this technique involve the time taken to acquire images (20–30 min) and limited out of hours availability. Planar *V′/Q′* scintigraphy has previously been limited by the number of nondiagnostic studies [21], as discussed earlier this has partially been addressed by the use of chest radiography and perfusion scintigraphy in combination; however, development of SPECT *V′/Q′* has attempted to further improve the diagnostic yield.

SPECT *V′/Q′* has a higher sensitivity (97% *versus* 76%) and specificity (91% *versus* 85%) than planar *V′/Q′* scintigraphy [22, 23], along with fewer indeterminate results [24, 25]. SPECT *V′/Q′* has a similar accuracy to CT pulmonary angiography in the detection of pulmonary embolism [22]. Both planar and SPECT *V′/Q′* involve lower radiation doses than CT pulmonary angiography and should be considered the first line investigation in patients with a normal chest radiograph, particularly young and pregnant patients, the latter will be discussed in more detail later in the chapter.

CT pulmonary angiography

CT pulmonary angiography carries a negative predictive value in the range of 94%–100% for assessment of patients with suspected pulmonary embolism [26]. A negative CT pulmonary angiography is associated with a low risk of venous thromboembolism (1.7%) at 3 months [27], and typically avoids the need for anticoagulation, unless required for another reason such as atrial fibrillation. The PIOPED (Prospective Investigation of Pulmonary Embolism Diagnosis) II study showed that patients with negative CT pulmonary angiography but high clinical probability scores had a 40% rate of pulmonary embolism. The study recommended

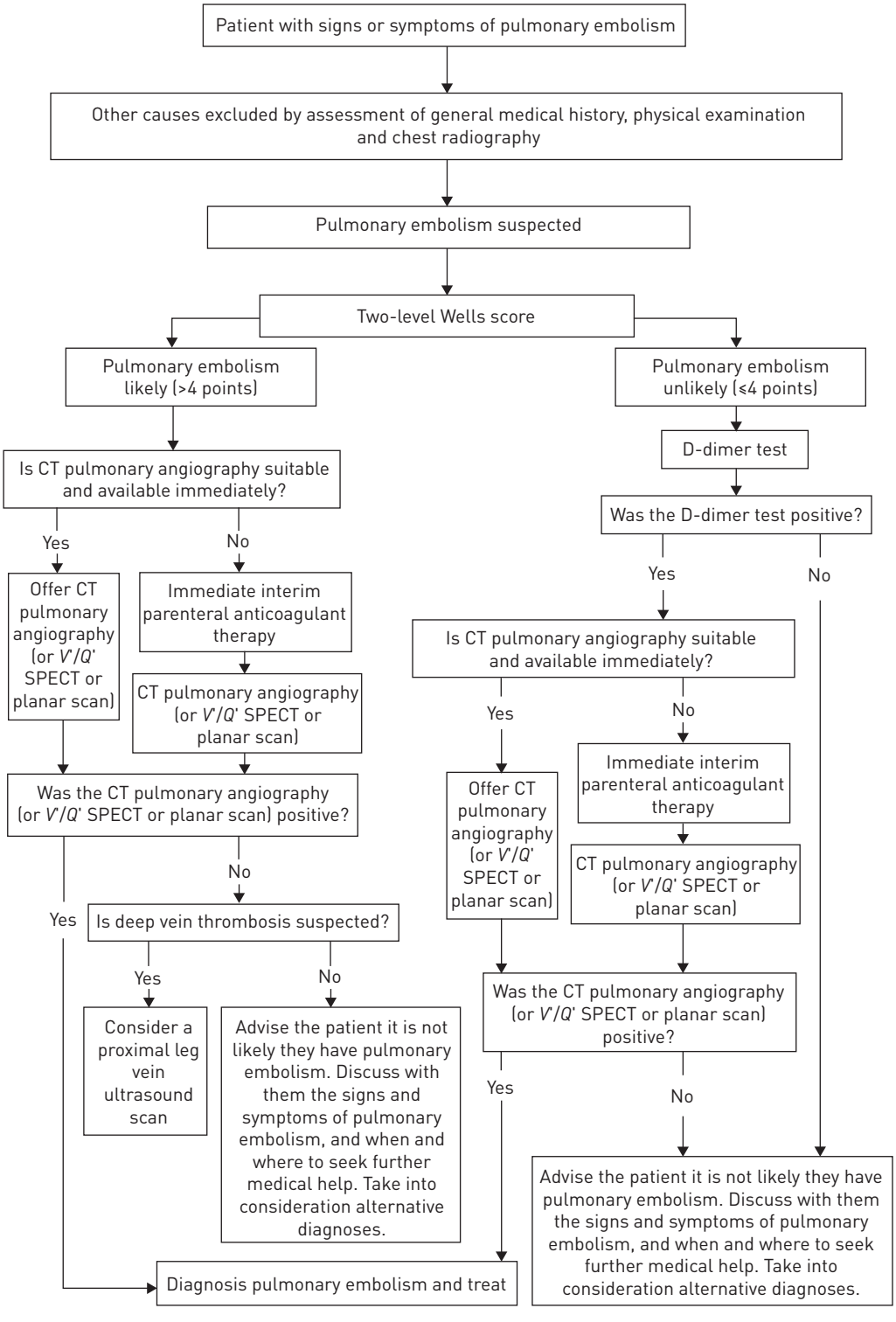

Figure 1. Pathway for the assessment of a patient with suspected pulmonary embolism. *V'/Q'*: ventilation/perfusion. Reproduced from [8] with permission from the publisher. This material was accurate at the time of going to press.

further imaging in such situations, commonly with *V′/Q′* scintigraphy [28]. CT technology has significantly advanced since 2006 and CT pulmonary angiography is widely accepted as the reference standard for the diagnosis of pulmonary embolism in the majority of patients.

Considerations for the pregnant patient with suspected pulmonary embolism

Figure 1 outlines the imaging algorithm in a general patient population, but the pregnant patient represents a specific challenge for which dedicated algorithms have been developed.

Pregnancy is associated with a fivefold increased risk for pulmonary embolism, with the risk being highest in the early post-partum period. Imaging the pregnant patient with suspected pulmonary embolism is a controversial subject with concerns focused on the radiation exposure to both mother and fetus. The lack of evidence-based clinical scoring systems coupled with pregnancy related D-dimer elevation result in reported rates of pulmonary embolism in pregnant patients undergoing CT pulmonary angiography of 3.7% [29]. The fetal dose is low with both CT pulmonary angiography and *V′/Q′*, in the range of 0.1–0.8 mGy for *V′/Q′* scintigraphy compared with 0.01–0.66 mGy with CT pulmonary angiography. The maternal dose, in particular the effective dose to the radiosensitive glandular breast tissue is considerably higher, at 10–70 mGy per breast for CT pulmonary angiography compared with 0.22–0.28 mGy for *V′/Q′* scintigraphy. Many advocate half dose perfusion scintigraphy (planar or SPECT) for patients with normal chest radiography and no history of asthma or chronic lung disease, in this case diagnostic results can be

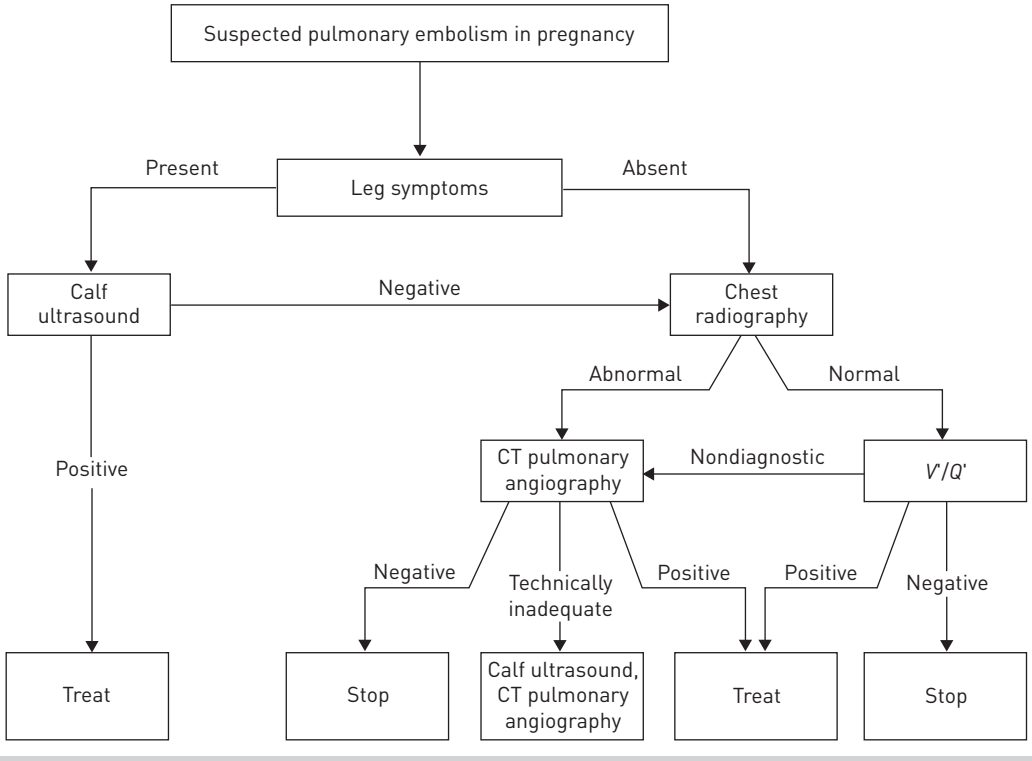

Figure 2. Diagnostic algorithm for suspected pulmonary embolism in pregnancy. *V′/Q′*: ventilation/perfusion. Reproduced and modified from [31] with permission from the publisher.

achieved in 97% of patients [30]. Several guidelines exist for the assessment of such patients, the guidelines from the American Thoracic Society and Society of Thoracic Radiology are the mostly commonly used (figure 2) [31].

Optimising CT pulmonary angiography protocol

Indeterminate CT pulmonary angiography examinations remain problematic, occurring in ~7% of all studies undertaken. Commonly cited reasons for indeterminate examinations include respiratory motion artefacts followed by poor contrast enhancement [32]. With CT pulmonary angiography being performed with increasing frequency, careful attention to technique optimisation is essential in order to reduce both the indeterminate rate and population radiation exposure.

Dose optimisation

CT contributes 70% of medical radiation and CT pulmonary angiography represents a significant proportion of the examinations performed. Systematic attention to dose reduction is essential. Modifications to CT pulmonary angiography protocols permit dramatic reductions in radiation dose while maintaining diagnostic image quality. Dose reduction techniques generic to all CT examinations include modulation of tube current and voltage, helical pitch and iterative reconstruction.

In the context of contrast-enhanced imaging lowering tube voltage is particularly effective in reducing radiation dose as there is better matching of the average photon energy range to the k-edge of iodine (figure 3). Care should be taken in larger patients as the reduced tube voltage can result in unacceptable image noise.

High pitch protocols have become widely available with the advent of dual-source scanners. These allow for short acquisition times, which limit respiratory and cardiac motion artefacts and permit reduction in the volume of contrast medium used. In comparison with standard pitch CT pulmonary angiography studies (pitch 0.9) use of an ultra-high pitch mode (pitch 2.8) demonstrated improved visualisation of cardiac structures and less lung parenchymal motion with overall lower mean effective dose [33]. High pitch scanning is therefore useful in patients who are not able to hold their breath. These high pitch techniques have had limitations in obese patients; however, the use of dual source technology and higher power generators in newer scanners has largely remedied this issue.

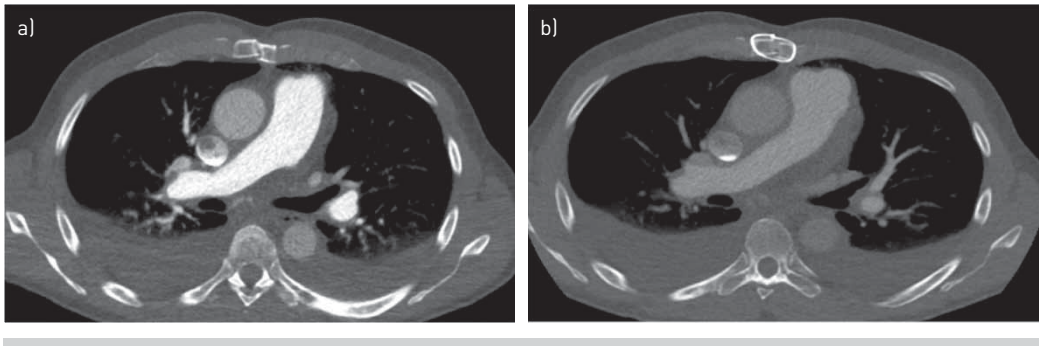

Figure 3. Axial contrast-enhanced dual-energy CT in a 50-year-old man who had previously undergone pulmonary endarterectomy surgery. Improved contrast resolution is seen at a) 90 kV *versus* b) 150 kV.

Intravenous contrast medium administration

CT pulmonary angiography protocol evolution over recent years has reduced contrast medium burden. This has been partly driven by the opportunity provided by shorter acquisition times, but also by perceived risk of nephrotoxicity and the expense of contrast medium. However, McDonald *et al.* [34], in a recent large meta-analysis (25 950 patients) indicated that the risk of nephrotoxicity associated with *i.v.* contrast medium may have been overstated. In this study there was no significant difference in rates of acute kidney injury, dialysis or death between patients who received contrast medium compared with those who did not. In addition, groups previously considered at high risk for contrast medium induced nephropathy, such as pre-existing diabetes mellitus, congestive heart failure or renal failure, do not have an increased risk of acute kidney injury, dialysis or death following contrast medium administration [35].

For optimal detection of pulmonary embolism, opacification of blood to >211 HU using an iodinated contrast agent is required in order to confidently identify a low attenuation thrombus as a filling defect within the opacified vascular lumen [36]. Suboptimal images may result either from an artefact resulting from concentrated contrast medium (figure 4a) or from suboptimal vascular opacification due to a range of causes.

Timing of peak attenuation and image acquisition is vital for diagnostic CT pulmonary angiography. Broadly, two techniques can be used to optimise contrast timing. In the first technique, known as the test bolus technique, a pre-bolus of 10–20 mL of contrast agent is injected and a time attenuation curve generated at the level of the main pulmonary artery using serial single-slice imaging. The second technique, bolus tracking, involves serial assessment of the main contrast bolus and the CT pulmonary angiography acquisition is triggered when threshold attenuation is reached. The test bolus technique, although more time consuming, appears to improve mean contrast opacification of the main pulmonary artery when compared with the bolus tracking method [37].

The haemodynamic effects of changes in intrathoracic pressure during breathing and breath-hold may result in transient interruption to the contrast medium column within the pulmonary vasculature. Deep inspiration can have a twofold effect on the contrast bolus:

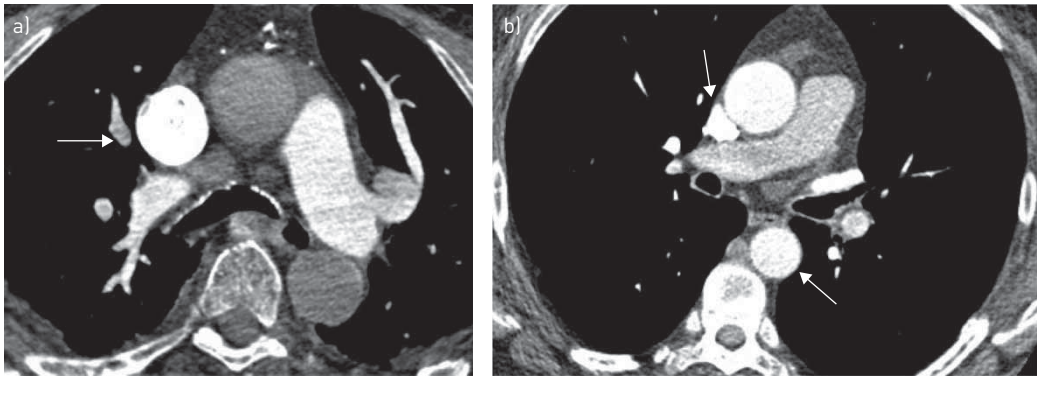

Figure 4. Contrast-enhanced CT pulmonary angiography in two different patients. a) An example of dense contrast medium in the superior vena cava causing some attenuation of the adjacent right upper lobe pulmonary artery segmental branch (arrow). b) The typical features that arise due to a Valsalva manoeuvre. There is limited contrast medium within the pulmonary vasculature and dense contrast opacification of the superior vena cava and aorta (arrows).

inadvertent Valsalva manoeuvre can inhibit thoracic venous inflow while there can be an additional increase in unopacified blood returning from the inferior vena cava (figure 4b). Shallow inspiration is advised, for patients who cannot comply with this shallow free breathing or an expiratory breath-hold are preferred [38]. In order to achieve satisfactory enhancement, as outlined earlier, an injection rate of 5 $mL \cdot s^{-1}$ is preferred.

CT optimisation in pregnancy

While, as indicated earlier, perfusion scintigraphy may be preferred to exclude pulmonary embolism in pregnancy this technique may not be available in all institutions, particularly out of hours. CT pulmonary angiography has previously suffered from a higher rate of nondiagnostic examinations in pregnant women than in non-pregnant women [39]. This is thought to be due to reduced pulmonary artery enhancement due to a combination of hyperdynamic circulation and breathing issues that increase the risk of Valsalva manoeuvre and mixing of non-opacified blood from the inferior vena cava. Techniques to overcome these problems include use of bolus triggering with short delays, high injection flow rates or increased volume of contrast medium and avoidance of deep inspiration [40]. Methods of dose reduction for CT pulmonary angiography include reduced z-axis coverage (from the aortic arch to the dome of diaphragm), low peak kV imaging, use of bismuth breast shields and oral barium shielding the fetus [30, 38].

The appearance of thromboembolic disease on CT pulmonary angiography images and its mimics

CT pulmonary angiography provides an opportunity to evaluate the pulmonary vasculature, lungs and heart even in non-ECG-gated studies. It is essential that each of these components is routinely systematically evaluated. CT pulmonary angiography is able to rule in and out the diagnosis of pulmonary embolism with a high level of accuracy. Importantly, CT pulmonary angiography also offers an alternative diagnosis in up to 43% of patients. However, despite this most patients undergo no change in therapeutic management, reaffirming that the principle use of CT pulmonary angiography is to exclude pulmonary embolism [41].

Acute pulmonary emboli

The findings of acute pulmonary embolism are well documented and are summarised in table 2 and figure 5. Direct signs of acute pulmonary embolism are characterised by well-defined filling defects within the contrast column either within or occluding the vascular lumen.

Table 2. Features of acute pulmonary embolism

Vascular abnormalities	Parenchymal abnormalities
Intraluminal filling defect that maybe complete or incomplete	Pulmonary infarct, which is typically subpleural and wedge shaped
Acute angles with vessel wall	Atelectasis
Enlargement of the occluded vessel	Mosaic attenuation
Right ventricular "free-floating" thrombus	

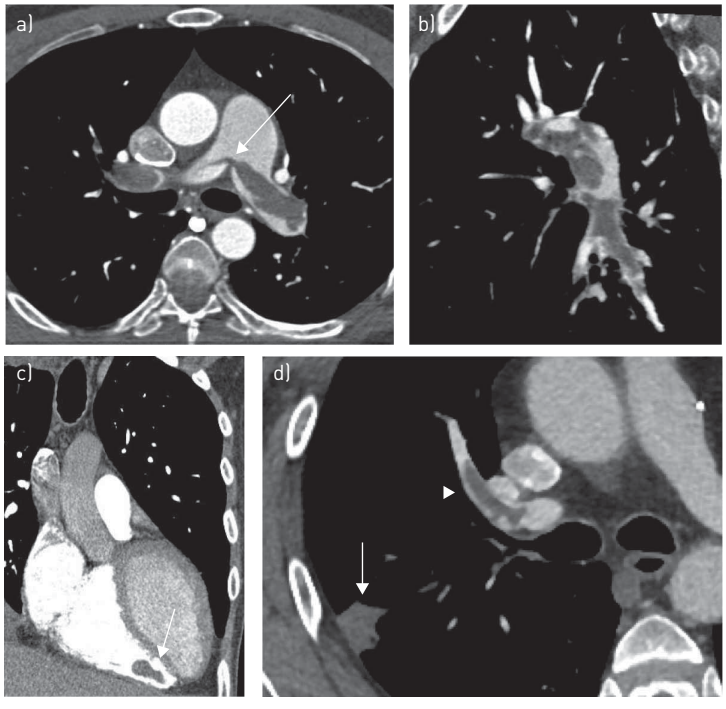

Figure 5. Acute pulmonary emboli in the a) axial and b) sagittal planes. Note the central location of the thrombus forming acute angles with the vessel walls. A thrombus extending across the pulmonary trunk, a so-called "saddle embolus" is indicated by an arrow in a. c) The presence or absence of an intracardiac thrombus should always be actively sought. d) The typical appearances of a peripheral wedge-shaped pulmonary infarct (arrow) in a patient with acute pulmonary emboli (arrowhead).

Chronic thromboembolic disease

The majority of cases of acute pulmonary embolism resolve without sequalae. In a minority the emboli undergo organisation, recanalisation and retraction resulting in chronic pulmonary thromboembolic disease. CTEPH may develop due to proximal occlusion or stenosis of the pulmonary arteries, but with sustained pulmonary hypertension a secondary small vessel vasculopathy can develop in non-obstructed vascular beds, which may further contribute to pulmonary hypertension. In order to maintain pulmonary blood flow there is commonly shunting of blood from the systemic to pulmonary circulation *via* bronchial and non-bronchial collateral vessels [42]. Dilated bronchial arteries seen on imaging can help distinguish CTEPH from other causes such idiopathic pulmonary hypertension [43]. Importantly, bronchial artery hypertrophy is a significant predictor for survival following pulmonary thromboendarterectomy [44].

Features of CTEPH at CT pulmonary angiography (figure 6) include an abrupt decrease in vessel diameter, vascular occlusion with small run-off vessels, mural thrombi that may cause vessel narrowing, intimal irregularity, bands and webs. Typically, in contrast to the central filling defects with acute angles to the vessel wall of acute emboli, the organised material in chronic disease runs in an eccentric fashion along the vessel wall forming obtuse angles. A band is defined as a ribbon-like structure anchored to the vessel wall at two ends with a free unattached mid portion, often orientated in the direction of blood flow along the long axis of the vessel. Webs are bands that have

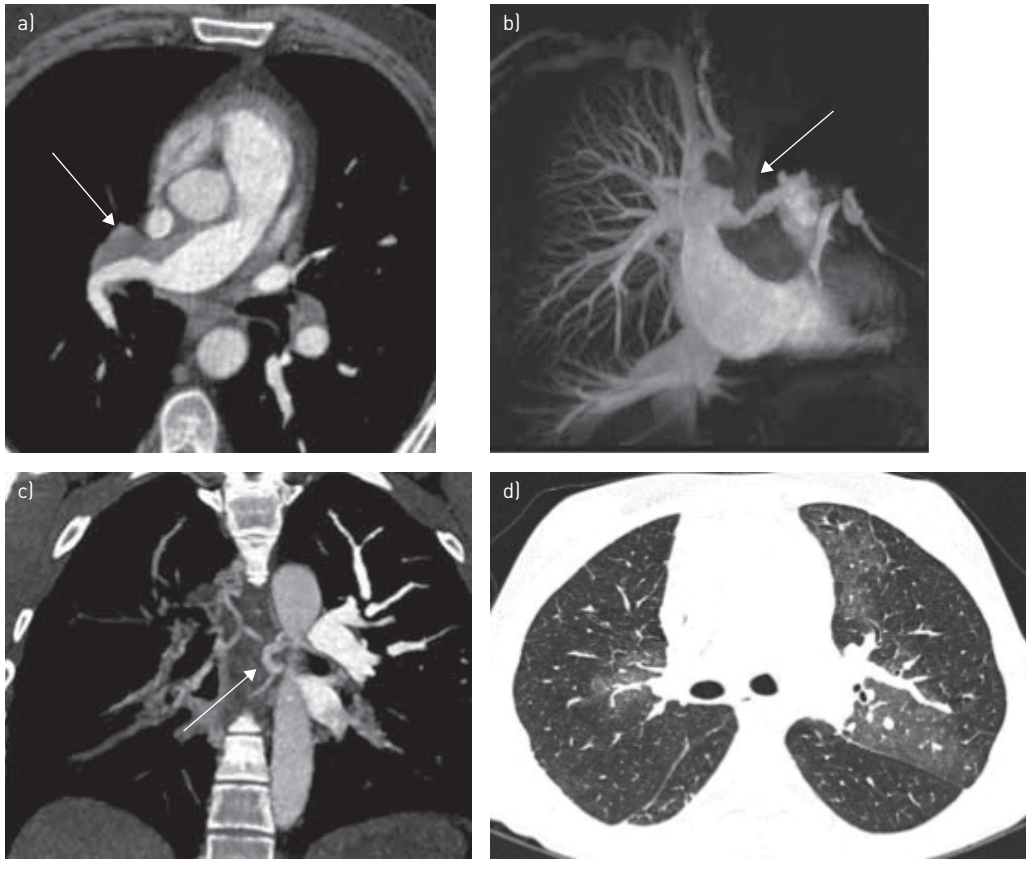

Figure 6. Features of CTEPH. a) An eccentric thrombus in the right main pulmonary artery forming obtuse angles with the vessel wall (arrow). b) Contrast enhanced coronal MRI shows an eccentric thrombus in the left main pulmonary artery (arrow) with almost no ipsilateral pulmonary arterial enhancement. c) Bronchial artery hypertrophy seen in a MIP image (arrow). d) Marked mosaic attenuation, which reflects regional reductions in lung parenchymal perfusion.

branches and form networks of varying complexity [45]. Post-stenotic dilatation or aneurysm formation may occur [42]. Mosaic attenuation caused by non-uniform lung perfusion is a useful sign.

In cases of chronic thromboembolic disease it is vital to look for evidence of complicating pulmonary hypertension. Similarly, in patients with acute pulmonary embolism it is important to identify signs suggestive of prior chronic disease.

Following acute pulmonary embolism routine echocardiography screening is not supported by current evidence, mainly due to the low incidence of chronic thromboembolic disease resulting in a low screening yield [46]. Instead clinical follow-up is suggested with echocardiography remaining the initial investigation to assess for evidence of pulmonary hypertension. V'/Q' scintigraphy has excellent sensitivity and specificity in the diagnosis of CTEPH, 96–97% and 90–95%, respectively. V'/Q' scintigraphy does not however establish the magnitude or distribution of disease, information which is vital for assessment of potential pulmonary thromboendarterectomy surgery [7].

Nonthrombotic pulmonary embolism

The term nonthrombotic pulmonary embolism describes embolisation to the pulmonary arteries of fragments of tissue, microorganisms, foreign material, chemical agents or gas, and excludes bland thrombus (both embolic and *in situ* formation). Depending on the nature of the embolised material, together with mechanical obstruction, there may also be a severe secondary local and systemic inflammatory response. Although a rare entity, it is important to recognise nonthrombotic pulmonary embolism to ensure appropriate and timely management [47].

Pulmonary artery sarcoma is a rare intravascular malignancy that is frequently misdiagnosed as chronic thromboembolic pulmonary embolic disease or even acute pulmonary emboli. On CT, a pulmonary artery sarcoma is typically characterised by a large filling defect stenosing or occluding the left or right main pulmonary artery and often extending into the pulmonary trunk. Expansion of the involved vessel(s) and extraluminal tumour extension is common [48]. ^{18}F-FDG-PET has some use in both diagnosis and monitoring response to therapy [49]; however, there have been reports of poor or heterogeneous FDG uptake in histologically proven pulmonary artery sarcoma [50].

Developments and controversies in pulmonary embolism imaging

Subsegmental pulmonary embolism overdiagnosis

Recently attention has focused on the potential overdiagnosis of pulmonary embolism at CT pulmonary angiography. Overdiagnosis represents the concept that for some pulmonary emboli the risk of treatment may outweigh its benefits. The high spatial resolution of CT allows identification of filling defects in subsegmental arteries as small as 2–3 mm in diameter. The clinical significance of isolated subsegmental emboli is controversial. Some authorities suggest that small emboli are a common occurrence and part of normal existence with a normal function of the lung being to remove them [51]. Others suggest all emboli should be managed equally [52].

Understanding the outcome in patients with such emboli, both treated and untreated, is vital to unlock this controversy but such evidence is difficult to come by. In a cohort of 93 patients with isolated subsegmental pulmonary embolism, Donato *et al.* [53] showed that there was no recurrence pulmonary embolism or death in the patients who did not receive anticoagulation. In the same study, in the cohort of patients treated with anticoagulation the risk of haemorrhage (5.7%) was greater than the risk of recurrent venous thromboembolism (0.7%). Population studies also support this evidence showing an increase in incidence of diagnosed pulmonary embolism with proliferation of CT pulmonary angiography use and minimal change in mortality [54]. This concept has placed more value on the correct use of clinical scoring tools with the aim being to reduce the number of CT pulmonary angiography examinations undertaken.

The recommendations of the Fleischner Society [17] reinforce the fact that the clinical relevance of small peripheral pulmonary embolism and the need to treat remain subjects of debate. Recent work by Stein *et al.* [55] indicates that it appears safe not to treat patients with subsegmental emboli if the patient's risk factor for pulmonary embolism was transient and

resolves, if there is good pulmonary–respiratory reserve, no evidence of deep vein thrombosis on serial ultrasound and no history of central venous catheterisation or atrial fibrillation.

Acute pulmonary embolism: prognostic risk assessment using CT pulmonary angiography

In the setting of acute pulmonary embolism it is vital to identify patients at high risk of mortality as this will influence both the potential for reperfusion therapy with *i.v.* thrombolytic agents and the requirement for closer monitoring. Increasingly, low risk patients are anticoagulated on an ambulatory pathway from hospital or entirely in the community.

The patient cohort at highest risk of mortality (>15%) are those with clinical markers of shock or hypotension (defined as a systolic blood pressure <90 mmHg or a pressure drop ⩾40 mmHg for >15 min). In this population current guidelines recommend emergency treatment with thrombolysis or embolectomy unless contraindicated [56]. In patients who do not meet the immediate criteria for reperfusion the presence of right ventricular dysfunction identifies patients in an intermediate risk group in which close monitoring is needed to detect future haemodynamic compromise.

Patient triage has traditionally been carried out using clinical parameters (haemodynamic instability or hypotension) and biochemical markers (troponin and natriuretic peptide elevation) [57]. A strength of CT pulmonary angiography is its ability to comprehensively assess the pulmonary vasculature, heart and lungs in a single examination. In haemodynamically stable patients with pulmonary embolism, the diagnostic CT pulmonary angiography can readily identify morphological changes in right ventricular dilatation reflecting right ventricular dysfunction, which correlates well with an increased 30-day mortality [58]. Right ventricle/left ventricle (RV/LV) ratio is the most commonly used marker of right ventricular dysfunction, being influenced by right ventricular dilatation resulting from increased pulmonary vascular resistance and decreased left ventricle size due to reduced pre-load (figure 7) [38].

On standard axial imaging an RV/LV ratio (measured from inner wall to inner wall at their widest points at the level of the atrioventricular valves) greater than 1 is a strong predictor of short term (<3 month) mortality [59]. While some authors have advocated the use of four-chamber multiplanar reconstructions [60], Stein *et al.* [61] showed no significant difference between assessments of right ventricular enlargement using this method compared with simple axial measurements. Routine use of subjective evaluation of right ventricular dilatation on axial images is also supported by the study of Kumamaru *et al.* [62]. They showed that subjective assessment of the RV/LV ratio has similar performance to objective axial and reformatted four-chamber images with good interobserver agreement (κ=0.83) [62].

Volumetric ventricular analysis for assessment of right ventricular dilatation has been assessed on non-ECG-gated CT pulmonary angiography. There was better correlation of RV/LV automated volume changes than RV/LV diameter ratio changes with regard to adverse outcome (admission to intensive care and 30 day mortality) and pulmonary arterial obstruction index [63]. Further work has supported these findings; however, the authors comment that the requirement for dedicated software tools compounded with the increased time required for analysis is disadvantageous in the emergency setting [64]. Leftward bowing of the interventricular septum is another useful but nonspecific sign of increased right heart pressure.

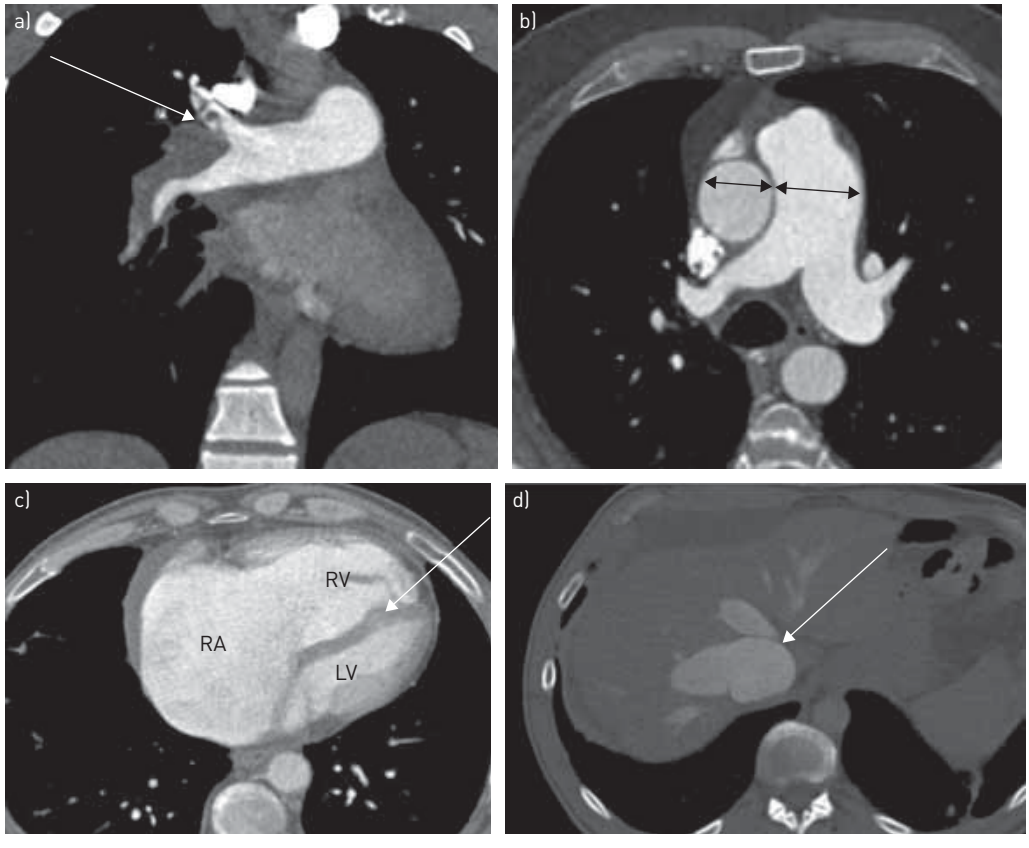

Figure 7. a) A sub-acute thrombus in the right upper lobe (arrow) with chronic laminated right main pulmonary artery thrombus. b) Dilatation of the main pulmonary artery in comparison to the aorta. c) Enlargement of the right atrium (RA) with relative enlargement of the right ventricle (RV) compared with the left ventricle (LV). Note the leftward deviation of the interventricular septum (arrow). d) Illustrates reflux of contrast medium into the inferior vena cava and hepatic veins (arrow).

Measurement of the main pulmonary artery diameter or ratio of the diameter of the main pulmonary artery to the aorta is widely described as a useful sign to identify pulmonary hypertension, but has not been shown to be an indicator of mortality or severity of acute pulmonary embolism [65]. Reflux of *i.v.* contrast medium into the inferior vena cava/hepatic veins may reflect tricuspid insufficiency, a surrogate marker of right ventricular dysfunction. A study that graded the degree of reflux into the inferior vena cava/hepatic veins using a visual scale demonstrated that substantial grades of reflux could predict early mortality in patients with acute pulmonary embolism [63]. As expected evaluation of the diameter of the superior venous cava and azygous vein also reflect changes in right heart pressure and confer prognostic information [65].

There are several scoring systems that allow a semi-quantitative measurement of the location and degree of pulmonary arterial thrombus (so-called clot burden). Developed in the era of CT, scoring systems by Qanadli *et al.* [66] and Mastora *et al.* [67] are used to quantify the burden of acute pulmonary embolism. van der Meer *et al.* [59] showed an 11.2-fold increase in pulmonary embolism related mortality for patients with an obstruction index of more than 40%. However, other studies have shown no significant association between obstructive index and mortality in patients with acute pulmonary

embolism [68]. These discrepant results are in part due to the wide variety in individual patients' pre-existing comorbidities that may affect baseline cardiorespiratory function. For example, in patients with severe pre-existing lung disease even small thrombi may precipitate worsening right ventricular dysfunction and confer increased mortality risk.

Novel CT techniques

Computer-assisted detection

Computer-assisted detection systems for assessment of pulmonary embolism have been developed over recent years in an attempt to improve detection of pulmonary embolism, particularly of peripheral emboli. Studies have shown computer-assisted detection systems can identify 77.4% of pulmonary embolisms that were originally missed at first reading [69]. Computer-assisted detection systems can improve the sensitivity of pulmonary embolism detection for inexperienced readers [70], with no significant change in reading time [71]. However, false positive detection marks are a problem and often relate to image quality [72] and reconstruction technique [73].

Dual-energy CT

Conventional single-energy CT depicts anatomical structures based upon differences in x-ray attenuation, which is largely influenced by their atomic number. Dual-energy CT allows structures with similar density but different elemental composition to be differentiated according to differences in electron density. Dual-energy CT can be performed using dual-source scanners or a single source scanner with rapid energy switching or specialised detector material. The fundamental benefit of dual-energy CT pulmonary angiography is quantification of the amount of iodine within tissues. Dual-energy pulmonary blood volume (PBV) maps are generated that represent the relative iodine concentration in the lung parenchyma at the acquisition time point, which is a surrogate marker of perfusion [74].

PBV images have the potential to complement native CT pulmonary angiography interpretation, increasing sensitivity for detection of small emboli by identification of peripheral subsegmental perfusion defects [75]. However, perfusion defects on PBV maps may also result from lung parenchymal disease so careful attention must be paid to avoid a false positive result (figure 8).

The extent of perfusion defects identified on dual-energy CT can be quantified. Apfaltrer *et al.* [76] have suggested a potential role for dual-energy CT in risk stratification, with correlation between the volume of perfusion defect and adverse clinical outcome (intensive care admission or death).

Magnetic resonance imaging

The increased use of CT with associated radiation exposure and iodinated contrast medium has led to research into the development of MRI for the diagnosis of pulmonary embolism. Initially the long image acquisition times were unsuitable in acute imaging, but recent developments have led to shorter acquisition times for standard contrast-enhanced magnetic resonance angiography. Additional perfusion and functional imaging complement standard angiographic data. Findings on magnetic resonance correlate with those on CT, namely vascular and parenchymal signs. In addition, cardiac morphological and functional assessment provides quantitative assessment of ventricular function that can be utilised for longitudinal follow-up of such patients.

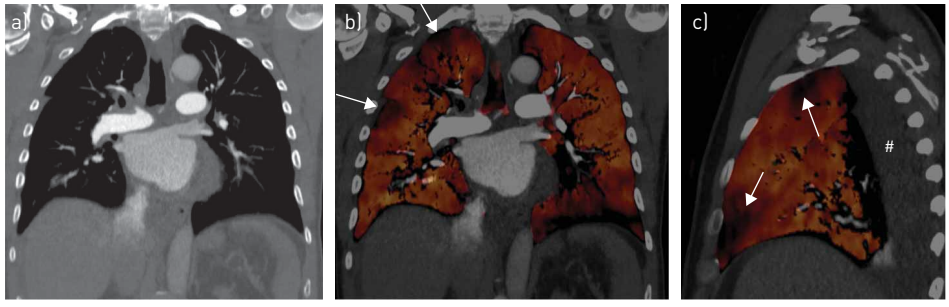

Figure 8. Images from the same 50-year-old man who had previously undergone pulmonary endarterectomy surgery shown in figure 3. a) Coronal multiplanar reformatted image with corresponding dual-energy CT pulmonary blood volume maps in the b) coronal and c) sagittal planes showing peripheral wedge-shaped defects in the right lung which correspond to untreated distal CTEPH. Care must be taken to assess for false positive perfusion defects such as those caused by pleural effusion (# in c).

A prospective study comparing current MRI techniques with CT pulmonary angiography demonstrated higher sensitivity for proximal (97.7–100%) than for segmental (68.0–91.7%) and subsegmental (21.4–33.3%) pulmonary embolism. Overall, 30% of results were inconclusive on MRI. The authors concluded that MRI cannot currently be used as a stand-alone test to exclude pulmonary embolism, but offers a helpful adjunct if positive [77]. The PIOPED III study demonstrated that combining magnetic resonance angiography and venography improves sensitivity compared with magnetic resonance angiography alone in patients with technically adequate images. The caveat is that with the two phases of imaging technically adequate images are more difficult to obtain [78]. The use of gadolinium-based contrast agents limits the use of contrast-enhanced magnetic resonance angiography in patients with renal failure (owing to the risk of nephrogenic systemic fibrosis) and also in pregnant patients where the risks are uncertain [79]. This has led to further interest in unenhanced MRI in the diagnosis of pulmonary embolism. One study compared the sensitivity and specificity of perfusion, unenhanced 2D steady state free precession and contrast-enhanced 3D angiographic MRI sequences in addition to CT pulmonary angiography [80]. They demonstrated that contrast-enhanced angiographic sequences showed higher sensitivity (82.9–89.7%) and specificity (98.5–100%). The sensitivity and specificity of unenhanced sequences alone were 68.7–76.4% and 96.1–99.1%, respectively. It is worth noting that although the overall sensitivity was lower with the unenhanced sequences the sensitivity remained high for the detection of proximal pulmonary embolism (92.7–100%) [80].

In recent years there has been some interest in using molecular MRI techniques in the visualisation of thrombus. In a phase II trial a fibrin-specific contrast agent was administered to patients with confirmed thrombi (non-pulmonary embolism). Enhanced imaging showed high signal amplification around the thrombi, typically at the clot surface, with significantly enhanced contrast in comparison to the surrounding blood pool and soft tissue [81].

Summary

The assessment of a patient with suspected pulmonary embolism is a complex pathway, but initially requires clinical scoring and D-dimer measurement in the majority of patients. This ensures low risk patients are not exposed to unnecessary investigation. CT pulmonary angiography is the most common first line investigation but requires careful attention to

technique to ensure the test remains diagnostic while reducing radiation exposure. Dual-energy CT is a technical advancement that appears to further improve the detection of peripheral emboli; however, recent questions have been raised as to the ideal treatment of such patients. Other newer imaging modalities hope to provide functional information, which could further help in risk stratification of patients into groups that require close monitoring or reperfusion therapy.

References

1. Goldhaber SZ. Pulmonary embolism. *Lancet* 2004; 363: 1295–1305.
2. Nikolaou K, Thieme S, Sommer W, *et al.* Diagnosing pulmonary embolism: new computed tomography applications. *J Thorac Imaging* 2010; 25: 151–160.
3. Remy-Jardin M, Remy J, Deschildre F, *et al.* Diagnosis of pulmonary embolism with spiral CT: comparison with pulmonary angiography and scintigraphy. *Radiology* 1996; 200: 699–706.
4. Wiener RS, Schwartz LM, Woloshin S. When a test is too good: how CT pulmonary angiograms find pulmonary emboli that do not need to be found. *BMJ* 2013; 347: f3368.
5. David S, Beddy P, Babar J, *et al.* Evolution of CT pulmonary angiography: referral patterns and diagnostic yield in 2009 compared with 2006. *Acta Radiol* 2012; 53: 39–43.
6. Costantino MM, Randall G, Gosselin M, *et al.* CT angiography in the evaluation of acute pulmonary embolus. *AJR Am J Roentgenol* 2008; 191: 471–474.
7. British Thoracic Society Standards of Care Committee Pulmonary Embolism Guideline Development Group. British Thoracic Society guidelines for the management of suspected acute pulmonary embolism. *Thorax* 2003; 58: 470–483.
8. National Institute for Health and Care Excellence (NICE). NICE pathway for venous thromboembolism. Manchester, NICE, 2015. http://pathways.nice.org.uk/pathways/venous-thromboembolism
9. Konstantinides SV. 2014 ESC Guidelines on the diagnosis and management of acute pulmonary embolism. *Eur Heart J* 2014; 35: 3145–3146.
10. Jaff MR, McMurtry MS, Archer SL, *et al.* Management of massive and submassive pulmonary embolism, iliofemoral deep vein thrombosis, and chronic thromboembolic pulmonary hypertension: a scientific statement from the American Heart Association. *Circulation* 2011; 123: 1788–1830.
11. Kearon C, Akl EA, Comerota AJ, *et al.* Antithrombotic therapy for VTE disease: antithrombotic therapy and prevention of thrombosis, 9th ed: American College of Chest Physicians evidence-based clinical practice guidelines. *Chest* 2012; 141: Suppl., e419S–e494S.
12. Rodger MA, Carrier M, Jones GN, *et al.* Diagnostic value of arterial blood gas measurement in suspected pulmonary embolism. *Am J Respir Crit Care Med* 2000; 162: 2105–2108.
13. Daftary A, Gregory M, Daftary A, *et al.* Chest radiograph as a triage tool in the imaging-based diagnosis of pulmonary embolism. *AJR Am J Roentgenol* 2005; 185: 132–134.
14. Wells PS, Ginsberg JS, Anderson DR, *et al.* Use of a clinical model for safe management of patients with suspected pulmonary embolism. *Ann Intern Med* 1998; 129: 997–1005.
15. Wells PS, Anderson DR, Rodger M, *et al.* Excluding pulmonary embolism at the bedside without diagnostic imaging: management of patients with suspected pulmonary embolism presenting to the emergency department by using a simple clinical model and d-dimer. *Ann Intern Med* 2001; 135: 98–107.
16. Ceriani E, Combescure C, Le Gal G, *et al.* Clinical prediction rules for pulmonary embolism: a systematic review and meta-analysis. *J Thromb Haemost* 2010; 8: 957–970.
17. Remy-Jardin M, Pistolesi M, Goodman LR, *et al.* Management of suspected acute pulmonary embolism in the era of CT angiography: a statement from the Fleischner Society. *Radiology* 2007; 245: 315–329.
18. Righini M, Van Es J, Den Exter PL, *et al.* Age-adjusted D-dimer cutoff levels to rule out pulmonary embolism: the ADJUST-PE study. *JAMA* 2014; 311: 1117–1124.
19. Huisman MV, Klok FA. How I diagnose acute pulmonary embolism. *Blood* 2013; 121: 4443–4448.
20. Sostman HD, Miniati M, Gottschalk A, *et al.* Sensitivity and specificity of perfusion scintigraphy combined with chest radiography for acute pulmonary embolism in PIOPED II. *J Nucl Med* 2008; 49: 1741–1748.
21. Sostman HD, Stein PD, Gottschalk A, *et al.* Acute pulmonary embolism: sensitivity and specificity of ventilation-perfusion scintigraphy in PIOPED II study. *Radiology* 2008; 246: 941–946.
22. Reinartz P, Wildberger JE, Schaefer W, *et al.* Tomographic imaging in the diagnosis of pulmonary embolism: a comparison between V/Q lung scintigraphy in SPECT technique and multislice spiral CT. *J Nucl Med* 2004; 45: 1501–1508.
23. Stein PD, Freeman LM, Sostman HD, *et al.* SPECT in acute pulmonary embolism. *J Nucl Med* 2009; 50: 1999–2007.

24. Quirce R, Ibáñez-Bravo S, Jiménez-Bonilla J, *et al.* Contribution of V/Q SPECT to planar scintigraphy in the diagnosis of pulmonary embolism. *Rev Esp Med Nucl Imagen Mol* 2014; 33: 153–158.
25. Laurence IJ, Redman SL, Corrigan AJ, *et al.* V/Q SPECT imaging of acute pulmonary embolus – a practical perspective. *Clin Radiol* 2012; 67: 941–948.
26. Swensen SJ, Sheedy PF 2nd, Ryu JH, *et al.* Outcomes after withholding anticoagulation from patients with suspected acute pulmonary embolism and negative computed tomographic findings: a cohort study. *Mayo Clin Proc* 2002; 77: 130–138.
27. Donato AA, Scheirer JJ, Atwell MS, *et al.* Clinical outcomes in patients with suspected acute pulmonary embolism and negative helical computed tomographic results in whom anticoagulation was withheld. *Arch Intern Med* 2003; 163: 2033–2038.
28. Stein PD, Woodard PK, Weg JG, *et al.* Diagnostic pathways in acute pulmonary embolism: recommendations of the PIOPED II investigators. *Am J Med* 2006; 119: 1048–1055.
29. Shahir K, Goodman LR, Tali A, *et al.* Pulmonary embolism in pregnancy: CT pulmonary angiography *versus* perfusion scanning. *AJR Am J Roentgenol* 2010; 195: W214–W220.
30. Pahade JK, Litmanovich D, Pedrosa I, *et al.* Quality initiatives: imaging pregnant patients with suspected pulmonary embolism: what the radiologist needs to know. *Radiographics* 2009; 29: 639–654.
31. Leung AN, Bull TM, Jaeschke R, *et al.* American Thoracic Society documents: an official American Thoracic Society/Society of Thoracic Radiology Clinical Practice Guideline – evaluation of suspected pulmonary embolism in pregnancy. *Radiology* 2012; 262: 635–646.
32. Jones SE, Wittram C. The indeterminate CT pulmonary angiogram: imaging characteristics and patient clinical outcome. *Radiology* 2005; 237: 329–337.
33. Hou DJ, Tso DK, Davison C, *et al.* Clinical utility of ultra high pitch dual source thoracic CT imaging of acute pulmonary embolism in the emergency department: are we one step closer towards a non-gated triple rule out? *Eur J Radiol* 2013; 82: 1793–1798.
34. McDonald JS, McDonald RJ, Comin J, *et al.* Frequency of acute kidney injury following intravenous contrast medium administration: a systematic review and meta-analysis. *Radiology* 2013; 267: 119–128.
35. McDonald RJ, McDonald JS, Carter RE, *et al.* Intravenous contrast material exposure is not an independent risk factor for dialysis or mortality. *Radiology* 2014; 273: 714–725.
36. Wittram C. How I do it: CT pulmonary angiography. *AJR Am J Roentgenol* 2007; 188: 1255–1261.
37. Rodrigues JC, Mathias H, Negus IS, *et al.* Intravenous contrast medium administration at 128 multidetector row CT pulmonary angiography: bolus tracking *versus* test bolus and the implications for diagnostic quality and effective dose. *Clin Radiol* 2012; 67: 1053–1060.
38. Devaraj A, Sayer C, Sheard S, *et al.* Diagnosing acute pulmonary embolism with computed tomography: imaging update. *J Thorac Imaging* 2015; 30: 176–192.
39. U-King-Im JM, Freeman SJ, Boylan T, *et al.* Quality of CT pulmonary angiography for suspected pulmonary embolus in pregnancy. *Eur Radiol* 2008; 18: 2709–2715.
40. Schaefer-Prokop C, Prokop M. CTPA for the diagnosis of acute pulmonary embolism during pregnancy. *Eur Radiol* 2008; 18: 2705–2708.
41. van Es J, Douma RA, Schreuder SM, *et al.* Clinical impact of findings supporting an alternative diagnosis on CT pulmonary angiography in patients with suspected pulmonary embolism. *Chest* 2013; 144: 1893–1899.
42. Castañer E, Gallardo X, Ballesteros E, *et al.* CT diagnosis of chronic pulmonary thromboembolism. *Radiographics* 2009; 29: 31–50.
43. Remy-Jardin M, Duhamel A, Deken V, *et al.* Systemic collateral supply in patients with chronic thromboembolic and primary pulmonary hypertension: assessment with multi-detector row helical CT angiography. *Radiology* 2005; 235: 274–281.
44. Kauczor HU, Schwickert HC, Mayer E, *et al.* Spiral CT of bronchial arteries in chronic thromboembolism. *J Comput Assist Tomogr* 1994; 18: 855–861.
45. Wittram C, Kalra MK, Maher MM, *et al.* Acute and chronic pulmonary emboli: angiography-CT correlation. *AJR Am J Roentgenol* 2006; 186: Suppl. 2, S421–S429.
46. Klok FA, van Kralingen KW, van Dijk AP, *et al.* Prospective cardiopulmonary screening program to detect chronic thromboembolic pulmonary hypertension in patients after acute pulmonary embolism. *Haematologica* 2010; 95: 970–975.
47. Han D, Lee KS, Franquet T, *et al.* Thrombotic and nonthrombotic pulmonary arterial embolism: spectrum of imaging findings. *Radiographics* 2003; 23: 1521–1539.
48. Yi CA, Lee KS, Choe YH, *et al.* Computed tomography in pulmonary artery sarcoma: distinguishing features from pulmonary embolic disease. *J Comput Assist Tomogr* 2004; 28: 34–39.
49. Ote EL, Oriuchi N, Miyashita G, *et al.* Pulmonary artery intimal sarcoma: the role of ^{18}F-fluorodeoxyglucose positron emission tomography in monitoring response to treatment. *Jpn J Radiol* 2011; 29: 279–282.
50. Lee DH, Jung TE, Lee JH, *et al.* Pulmonary artery intimal sarcoma: poor 18F-fluorodeoxyglucose uptake in positron emission computed tomography. *J Cardiothorac Surg* 2013; 8: 40.

51. Gurney JW. No fooling around: direct visualization of pulmonary embolism. *Radiology* 1993; 188: 618–619.
52. Condliffe R, Elliot CA, Hughes RJ, *et al.* Management dilemmas in acute pulmonary embolism. *Thorax* 2014; 69: 174–180.
53. Donato AA, Khoche S, Santora J, *et al.* Clinical outcomes in patients with isolated subsegmental pulmonary emboli diagnosed by multidetector CT pulmonary angiography. *Thromb Res* 2010; 126: e266–e270.
54. Wiener RS, Schwartz LM, Woloshin S. Time trends in pulmonary embolism in the United States: evidence of overdiagnosis. *Arch Intern Med* 2011; 171: 831–837.
55. Stein PD, Goodman LR, Hull RD, *et al.* Diagnosis and management of isolated subsegmental pulmonary embolism: review and assessment of the options. *Clin Appl Thromb Hemost* 2012; 18: 20–26.
56. Torbicki A, Perrier A, Konstantinides S, *et al.* Guidelines on the diagnosis and management of acute pulmonary embolism: the Task Force for the Diagnosis and Management of Acute Pulmonary Embolism of the European Society of Cardiology (ESC). *Eur Heart J* 2008; 29: 2276–2315.
57. Kucher N, Goldhaber SZ. Cardiac biomarkers for risk stratification of patients with acute pulmonary embolism. *Circulation* 2003; 108: 2191–2194.
58. Becattini C, Agnelli G, Germini F, *et al.* Computed tomography to assess risk of death in acute pulmonary embolism: a meta-analysis. *Eur Respir J* 2014; 43: 1678–1690.
59. van der Meer RW, Pattynama PM, van Strijen MJ, *et al.* Right ventricular dysfunction and pulmonary obstruction index at helical CT: prediction of clinical outcome during 3-month follow-up in patients with acute pulmonary embolism. *Radiology* 2005; 235: 798–803.
60. Schoepf UJ, Kucher N, Kipfmueller F, *et al.* Right ventricular enlargement on chest computed tomography: a predictor of early death in acute pulmonary embolism. *Circulation* 2004; 110: 3276–3280.
61. Stein PD, Matta F, Yaekoub AY, *et al.* Reconstructed 4-chamber views compared with axial imaging for assessment of right ventricular enlargement on CT pulmonary angiograms. *J Thromb Thrombolysis* 2009; 28: 342–347.
62. Kumamaru KK, Hunsaker AR, Bedayat A, *et al.* Subjective assessment of right ventricle enlargement from computed tomography pulmonary angiography images. *Int J Cardiovasc Imaging* 2012; 28: 965–973.
63. Aviram G, Rogowski O, Gotler Y, *et al.* Real-time risk stratification of patients with acute pulmonary embolism by grading the reflux of contrast into the inferior vena cava on computerized tomographic pulmonary angiography. *J Thromb Haemost* 2008; 6: 1488–1493.
64. Henzler T, Krissak R, Reichert M, *et al.* Volumetric analysis of pulmonary CTA for the assessment of right ventricular dysfunction in patients with acute pulmonary embolism. *Acad Radiol* 2010; 17: 309–315.
65. Ghaye B, Ghuysen A, Bruyere PJ, *et al.* Can CT pulmonary angiography allow assessment of severity and prognosis in patients presenting with pulmonary embolism? What the radiologist needs to know. *Radiographics* 2006; 26: 23–39.
66. Qanadli SD, El Hajjam M, Vieillard-Baron A, *et al.* New CT index to quantify arterial obstruction in pulmonary embolism: comparison with angiographic index and echocardiography. *AJR Am J Roentgenol* 2001; 176: 1415–1420.
67. Mastora I, Remy-Jardin M, Masson P, *et al.* Severity of acute pulmonary embolism: evaluation of a new spiral CT angiographic score in correlation with echocardiographic data. *Eur Radiol* 2003; 13: 29–35.
68. Ghaye B, Ghuysen A, Willems V, *et al.* Severe pulmonary embolism: pulmonary artery clot load scores and cardiovascular parameters as predictors of mortality. *Radiology* 2006; 239: 884–891.
69. Kligerman SJ, Lahiji K, Galvin JR, *et al.* Missed pulmonary emboli on CT angiography: assessment with pulmonary embolism-computer-aided detection. *AJR Am J Roentgenol* 2014; 202: 65–73.
70. Blackmon KN, Florin C, Bogoni L, *et al.* Computer-aided detection of pulmonary embolism at CT pulmonary angiography: can it improve performance of inexperienced readers? *Eur Radiol* 2011; 21: 1214–1223.
71. Wittenberg R, Berger FH, Peters JF, *et al.* Acute pulmonary embolism: effect of a computer-assisted detection prototype on diagnosis – an observer study. *Radiology* 2012; 262: 305–313.
72. Wittenberg R, Peters JF, Sonnemans JJ, *et al.* Impact of image quality on the performance of computer-aided detection of pulmonary embolism. *AJR Am J Roentgenol* 2011; 196: 95–101.
73. Lahiji K, Kligerman S, Jeudy J, *et al.* Improved accuracy of pulmonary embolism computer-aided detection using iterative reconstruction compared with filtered back projection. *AJR Am J Roentgenol* 2014; 203: 763–771.
74. Hagspiel KD, Flors L, Housseini AM, *et al.* Pulmonary blood volume imaging with dual-energy computed tomography: spectrum of findings. *Clin Radiol* 2012; 67: 69–77.
75. Pontana F, Faivre JB, Remy-Jardin M, *et al.* Lung perfusion with dual-energy multidetector-row CT (MDCT): feasibility for the evaluation of acute pulmonary embolism in 117 consecutive patients. *Acad Radiol* 2008; 15: 1494–1504.
76. Apfaltrer P, Bachmann V, Meyer M, *et al.* Prognostic value of perfusion defect volume at dual energy CTA in patients with pulmonary embolism: correlation with CTA obstruction scores, CT parameters of right ventricular dysfunction and adverse clinical outcome. *Eur J Radiol* 2012; 81: 3592–3597.
77. Revel MP, Sanchez O, Couchon S, *et al.* Diagnostic accuracy of magnetic resonance imaging for an acute pulmonary embolism: results of the 'IRM-EP' study. *J Thromb Haemost* 2012; 10: 743–750.
78. Stein PD, Gottschalk A, Sostman HD, *et al.* Methods of prospective investigation of pulmonary embolism diagnosis III (PIOPED III). *Semin Nucl Med* 2008; 38: 462–470.

79. Hochhegger B, Ley-Zaporozhan J, Marchiori E, *et al.* Magnetic resonance imaging findings in acute pulmonary embolism. *Br J Radiol* 2011; 84: 282–287.
80. Revel MP, Sanchez O, Lefort C, *et al.* Diagnostic accuracy of unenhanced, contrast-enhanced perfusion and angiographic MRI sequences for pulmonary embolism diagnosis: results of independent sequence readings. *Eur Radiol* 2013; 23: 2374–2382.
81. Spuentrup E, Botnar RM, Wiethoff AJ, *et al.* MR imaging of thrombi using EP-2104R, a fibrin-specific contrast agent: initial results in patients. *Eur Radiol* 2008; 18: 1995–2005.

Disclosures: None declared.

Chapter 6

Chronic obstructive pulmonary disease

Robert A. Stockley[1] and David G. Parr[2]

Routine radiological investigation has long been part of the regular assessment of patients with a diagnosis of COPD. However, practical interpretation and use (especially of newer radiological techniques) can often provide confusion and identify unexpected pathology. Recent advances in understanding the radiological as well as clinical phenotypes of COPD patients and the frequency of incidental findings will lead to more focused patient management and appropriate subsequent investigations.

COPD is one of the leading causes of morbidity and mortality in the world but is a preventable and treatable disease. It is defined in physiological terms by the presence of persistent airflow limitation that is usually progressive. This is associated with an enhanced chronic inflammatory response in the airways and the lung to inhaled noxious particles or gases, the commonest sources being the smoking of tobacco and pollution arising from the use of biomass fuels. The diagnosis of COPD is based on the demonstration of airflow obstruction using spirometry in the context of a history of breathlessness, cough or sputum production, and a history of exposure to risk factors for the disease.

While use of the umbrella term, COPD, may have facilitated the delivery of clinical care, it belies the complexity of the disease and effectively lumps together quite distinct pathophysiological conditions. The causes of the pathognomonic persistent airflow obstruction include emphysema, asthma, chronic bronchitis, bronchiectasis, bronchiolitis and bullous disease, and the great heterogeneity seen clinically (which has been addressed in a recent statement by the Fleischner Society [1]) has led to the provocative proposal that COPD would be better viewed as a collection of orphan diseases [2]. In addition, there has been increasing recognition of the extrapulmonary comorbidities of COPD, which include atheromatous cardiovascular disease, osteoporosis, myopathy, dementia and malignancy (particularly bronchogenic carcinoma).

[1]University Hospitals Birmingham NHS Foundation Trust, Birmingham, UK. [2]University Hospitals Coventry and Warwickshire NHS Trust, Coventry, UK.

Correspondence: Robert A. Stockley, University Hospitals Birmingham NHS Foundation Trust, Lung Function Dept, Mindelsohn Way, Edgbaston, Birmingham, B15 2GW, UK. E-mail: r.a.stockley@bham.ac.uk

Copyright ©ERS 2015. Print ISBN: 978-1-84984-065-1. Online ISBN: 978-1-84984-066-8. Print ISSN: 2312-508X. Online ISSN: 2312-5098.

Chronic bronchitis

Chronic bronchitis is defined in historical terms as a cough productive of sputum on most days for at least 3 months in two or more successive years, other causes having been excluded. Consequently, imaging is not required for diagnosis. Nevertheless, the histopathological changes in the airways walls (mucous gland hypertrophy and hyperplasia, goblet cell hyperplasia, squamous metaplasia and chronic inflammation), with the associated mucus plugging of smaller airways, may lead to detectable changes on imaging. In the majority of patients, plain chest radiography is normal but bronchial wall thickening with ring shadows and "tramline" opacities may indicate bronchiectasis (figure 1), and "increased lung markings" (sometimes referred to irreverently as the "dirty lung") have been ascribed to the morphological changes that are seen with microscopy in chronic bronchitis. There has been some contention over the significance, if any, of these changes and, since the diagnosis is one based on historical details, the argument seems academic. Furthermore, the appearance of airway wall thickening and air trapping on HRCT in smokers and ex-smokers is not limited to those with abnormal spirometry, since they are also seen in some individuals with normal lung function. Consequently, the clinical role of imaging in the assessment of patients with chronic productive cough is that of excluding causes other than chronic bronchitis.

Emphysema

In contrast to chronic bronchitis, emphysema is defined in pathological terms, namely "a condition of the lung characterised by abnormal, permanent enlargement of airspaces distal to the terminal bronchiole, accompanied by the destruction of their walls, and without obvious fibrosis. . . . the orderly appearance of the acinus and its components is disturbed and may be lost" [3]. Clearly, it is not practical for the diagnosis of emphysema in routine clinical practice to be made using histopathological examination of *ex vivo* tissue,

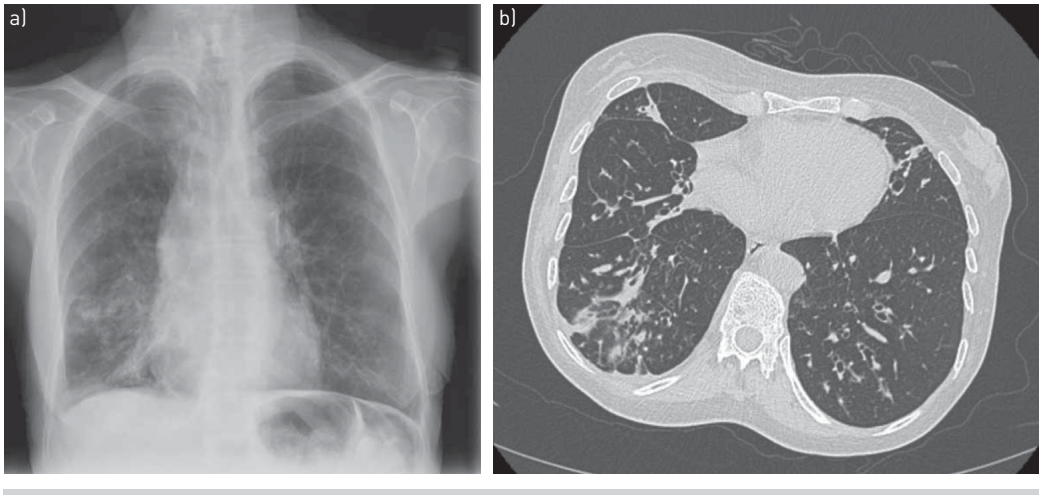

Figure 1. a) Plain chest radiography shows basal "tramline" linear opacities in the left lower zone and patchy linear opacities in the right lower zone. b) HRCT imaging provides confirmation that the changes evident on the plain film are due to predominantly basal tubular bronchiectasis with mucus plugging and areas of fibrotic atelectasis.

and so reliance has historically been on examination findings, the pattern of clinical and physiological impairment, supported by plain chest radiography. The presence of thoracic hyperexpansion, hyperresonant percussion note and reduced breath sounds are encapsulated in the outmoded, but still informative, descriptive term of the "pink puffer", indicative of an emphysematous clinical phenotype. Coexistence of impaired gas transfer and airflow obstruction, particularly when associated with static hyperinflation, is consistent with the presence of emphysema in patients with COPD, although this pathophysiological pattern is not specific for COPD with emphysema and may also be influenced by the distribution of emphysema (as discussed later).

The plain chest radiograph may show changes that reflect hyperinflation, bullae, vascular changes and increased markings (figure 2).

Hyperinflation is indicated by a number of features. One of these features is a low diaphragm. The border of the right hemidiaphragm in the midclavicular line is considered low if it is visible at or below the anterior end of the sixth rib but, in isolation, this feature may occur in other obstructive lung diseases, such as asthma. A second feature of hyperinflation is a flattened hemidiaphragm. The best predictor of emphysema on a posteroanterior chest radiograph is diaphragmatic flattening [4], which may be objectively assessed by measuring the perpendicular height of the diaphragmatic silhouette above a line drawn between the cardiophrenic and the costophrenic angles. This morphological change is also reflected in an obtuse costophrenic angle, which may be evident on either a posteroanterior or lateral chest radiograph. A third feature is increased retrosternal airspace. An increased distance between the anterior border of the ascending aorta and the posterior surface of the sternum at a point 3 cm below the manubriosternal joint is indicative of hyperinflation. However, there is lack of agreement on what this distance should be (figures range from 2.5 to 4.5 cm) and a lateral radiograph is required. Finally, a vertical,

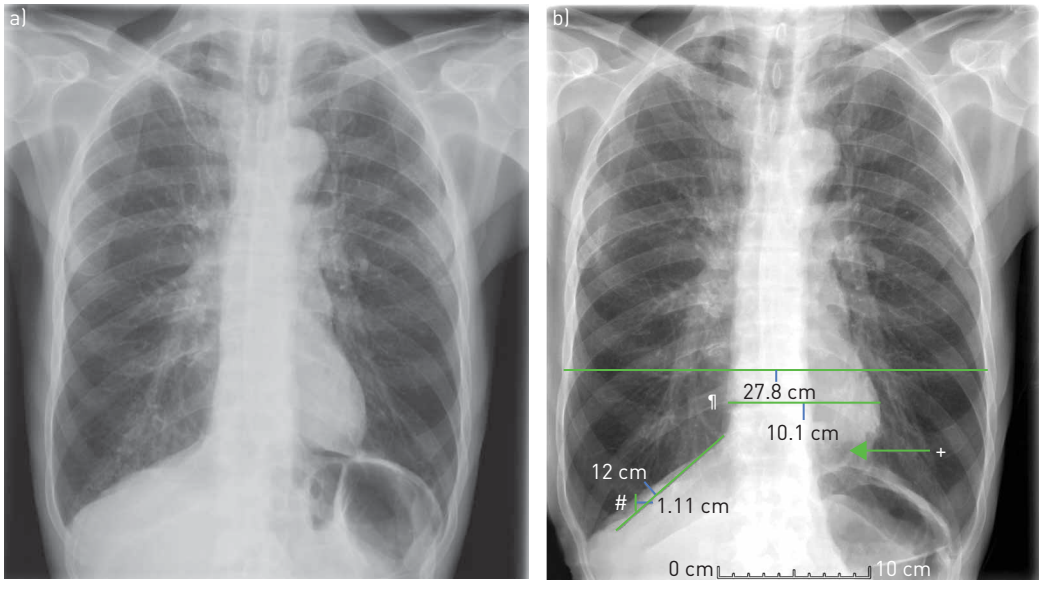

Figure 2. Emphysema. a) Plain chest radiograph, and b) annotated radiograph to illustrate the characteristic features of emphysema: low, flattened diaphragm (#) and a vertical, narrow cardiac silhouette (¶), with lung visible beneath the apex (+).

narrow cardiac silhouette with lung visible beneath the apex is also a feature of hyperinflation (figure 2b).

A number of vascular changes have been associated with the presence of emphysema, including increased transradiancy of the lung fields, reduced number and size of pulmonary vessels, and distortion of the normal vascular pattern. The predictive value of arterial deficiency has been shown to be similar to that described for hyperinflation but, in practice, the interpretation of vascularity is prone to subjectivity. In summary, while the chest radiograph is an insensitive tool for the diagnosis of mild and moderate emphysema, when the changes described are evident, they are highly specific for emphysema (between 95% and 100%) [5].

The advent of CT has enabled even very mild emphysema to be detected and, in addition, provides valuable information on pathological subtype, distribution and severity of emphysema, as well as the diagnosis of comorbid conditions.

Centrilobular emphysema is seen most commonly in patients with usual COPD and appears initially as ill-defined areas of low density without walls, giving a moth-eaten appearance (figure 3a). It is usually most evident in the upper lobes [6] but, as the severity increases, the distribution becomes more extensive, involving the lower parts of the lung, and the low-attenuation areas increase in size. Consequent margination of the interlobular septa may give the appearance of thin-walled cysts to such a degree that this can occasionally lead to the erroneous diagnosis of other conditions, such as lymphangioleiomyomatosis (and *vice versa*), or be confused with bronchiectatic airways.

Panlobular emphysema is most commonly, but not exclusively, associated with α_1-antitrypsin deficiency, and leads to a diffuse loss of attenuation across the lung lobule that may be difficult to detect, particularly in early disease (figure 3b).

In the early stages of disease, the pattern of destruction in the lung lobule differs significantly between these two forms of emphysema, thereby making a confident diagnosis possible. In addition, panlobular emphysema is typically found in the basal as opposed to the apical lung region. The two subtypes of emphysema frequently coexist but, as the severity of disease worsens, the distinguishing morphological features are less distinct and classification is then largely dependent on inference, based on the apicobasal pattern of distribution.

Paraseptal emphysema appears on CT as well-defined areas of low density that have distinct thin walls and which are located adjacent to the pleural surfaces (figure 3c). When

Figure 3. CT appearances of emphysema. a) Centrilobular emphysema in a patient with usual COPD. b) Panlobular emphysema in a patient with α_1-antitrypsin deficiency. c) Paraseptal emphysema.

extensive, a "saw-tooth" appearance may be produced but, unlike established centrilobular and panlobular emphysema, the presence of paraseptal emphysema does not seem to be associated with significant functional impairment.

Bullae and bullous emphysema are emphysematous spaces that have a diameter >1 cm when measured in the distended state. Bullae enlarge at a variable rate and may vary in size from 1 cm to larger than the whole hemithorax, when the extension of a giant bulla may lead to it crossing the anterior or posterior junctional areas. Idiopathic giant bullae may expand at the expense of the remaining lung, giving rise to the expression "vanishing lung syndrome". The appearance on both a plain chest radiograph and CT is that of an avascular transradiant area with a surrounding boundary wall, which is usually of hairline thickness. CT is more sensitive than plain radiography but differentiation between large bullae and a pneumothorax may still be problematic; sections of the bulla wall may appear thicker when abutting the pleura or adjacent collapsed lung and the presence of air on both sides of the bulla wall (the "double-wall" sign) may allow easier differentiation. However, ventilation scintigraphy may be the final arbiter by the demonstration of slow exchange of air between bulla and connecting bronchus. The differential diagnosis of bullous disease also includes sarcoidosis and Langerhans histiocytosis, and, in the presence of infection or haemorrhage, the development of an air-fluid level may mimic a lung abscess (figure 4). An infected bulla will probably have a thinner wall with a sharper inner margin than an abscess, and will be associated with less adjacent pneumonitis. Differentiation may also be possible based on clinical presentation but disappearance following resolution may occur in both infected/haemorrhagic bullae and abscesses.

The association of idiopathic pulmonary fibrosis (IPF) with emphysema has been proposed as a new clinical syndrome in smokers, termed combined pulmonary fibrosis and emphysema (CPFE) [7]. In addition to the presence of paraseptal and centrilobular emphysema in the upper lungs on CT, changes in the lower lung regions include honeycombing, reticular opacities and traction bronchiectasis (figure 5) [8, 9]. Emphysema and fibrosis may occur concurrently in the same area of the lung in some patients. CPFE is increasingly considered to be a distinct syndrome rather than a sub-phenotype of IPF or

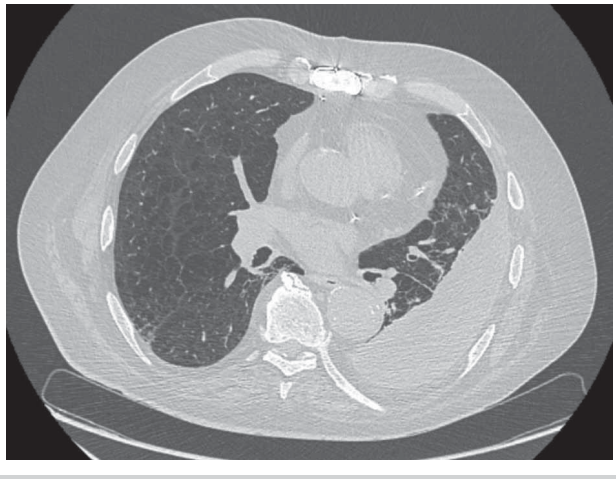

Figure 4. CT appearance of multiple air-fluid levels within emphysematous bullae in a patient with α_1-antitrypsin deficiency (PiZ phenotype).

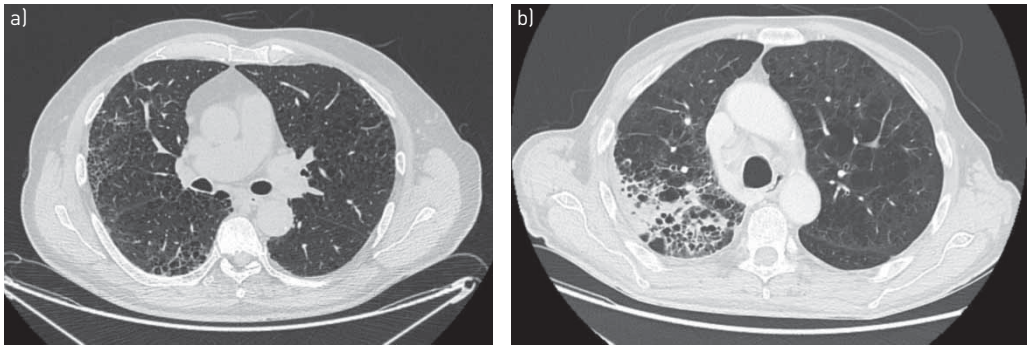

Figure 5. a) Combined pulmonary fibrosis and emphysema (CPFE) in a patient with preserved spirometry, with a total lung capacity of 87% predicted and transfer factor of the lung for carbon monoxide of 55% predicted (transfer coefficient of the lung for carbon monoxide of 67% predicted). b) HRCT appearance of consolidation in a patient with centrilobular emphysema who presented with pneumonia. This appearance may occasionally be misinterpreted as honeycombing if the pre-existence of emphysema is not appreciated.

COPD, or the coincidental coexistence of two conditions with common causative risk factors. The prognosis is particularly poor and determined by the severity of restriction (forced vital capacity) and the presence of pulmonary hypertension (PH), which tends to be severe (see later in this chapter) [10]. Pulmonary function tests typically indicate greatly reduced gas transfer in the presence of preserved lung volumes, and minimal or absent airflow obstruction [11], and this pattern of impairment should, therefore, prompt further investigation with HRCT imaging.

Differential diagnosis

Breathlessness, cough and sputum production with episodic worsening of symptoms are not specific for COPD and may arise from other conditions that are incorrectly ascribed to COPD, or may coexist with COPD. A detailed clinical history, appropriate examination and lung function testing will frequently be diagnostic but there are occasions when imaging is required for confirmatory diagnosis.

Tracheobronchomalacia (also labelled as "flat trachea syndrome") presents with the symptoms of COPD and is characterised by excessive collapse of the central airways on expiration. The cause is ascribed to weakness of the airway walls from cartilage softening, often with exaggerated anterior movement of the posterior membrane. The consequent flattening of the trachea on expiration leads to exercise intolerance from breathlessness and may also prevent effective clearance of sputum that may be associated with recurrent lower respiratory tract infections [12]. Characteristic changes to the tracheal lumen can be visualised by bronchoscopy but this invasive investigation has largely been superseded by the use of biphasic CT, which shows a normal tracheal aperture on inspiration but flattening or obliteration of the lumen on expiration (figure 6). Fixed narrowing of the central airways may also be misdiagnosed as irreversible airflow obstruction arising from COPD. A combination of imaging modalities can greatly improve understanding of symptom causation and treatment options in these atypical presentations (figure 7). Tracheobronchomalacia may also be seen on dynamic CT imaging in combination with tracheobronchial wall thickening and/or calcification in patients with relapsing polychondritis. Auricular chondritis is the most

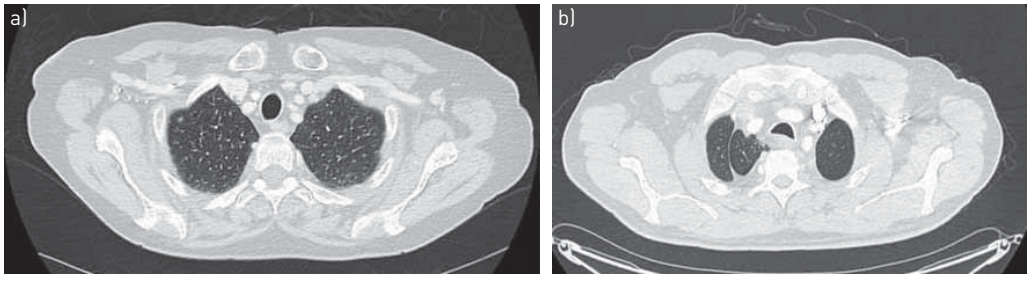

Figure 6. Tracheobronchomalacia. a) Inspiratory CT showing normal axial appearance of trachea. b) Expiratory CT demonstrating flattening of trachea and abnormal anterior bowing of the posterior membrane.

common initial presentation but this, and other disease features, may go unnoticed unless specifically sought during clinical assessment.

Pulmonary hypertension

Elevation of pulmonary vascular resistance arises in COPD secondary to hypoxia-induced vasoconstriction and the destruction of the pulmonary vasculature that occurs in emphysema. This may lead to PH, right ventricular hypertrophy and right ventricular failure, which contribute to morbidity and mortality. COPD is by far the most common cause of PH on account of its high prevalence [13, 14] but, generally, the PH is not severe; the mean pulmonary artery pressure (PAP) is between 20 and 25 mmHg and right ventricular function is therefore usually not altered. The rate of PH progression in COPD is normally slow, with an increase in mean PAP of <1 mmHg per year, but PH may worsen during exercise, sleep and exacerbations, and may also occur in overlap syndromes (*e.g.* coexisting obstructive sleep apnoea and combined COPD/interstitial lung disease). Furthermore, a small proportion of COPD patients (1–3%) may present with "disproportionate" PH, defined by symptoms of breathlessness and exercise limitation that are worse than predicted by the severity of airflow obstruction, and with a resting PAP >35–40 mmHg. The presence of PH is a strong predictor of mortality in COPD, with an inverse correlation between mean PAP and pulmonary vascular resistance values and survival [15, 16]. COPD patients with mean PAP values >25 mmHg experience a 5-year survival rate of only 36%, with pulmonary haemodynamics being a far stronger predictor of survival than the FEV_1 or gas transfer indices. The combination of pulmonary fibrosis and emphysema in CPFE is particularly associated with the development of PH, with prevalence estimates of PH in CPFE approaching 30–50% [9, 17]. When PH is present, the pattern of physiological impairment is that of markedly impaired transfer factor of the lung for carbon monoxide, with normal or mildly subnormal lung volumes and an absence of demonstrable airflow obstruction, and prognosis is particularly poor.

The identification of PH in patients with COPD is evidently important but, in the absence of symptoms that are distinct from uncomplicated COPD, it may be difficult to differentiate the development of PH from the clinical picture of COPD. Consequently, it is easy to miss the diagnosis unless the appropriate investigations are performed in patients with profound hypoxaemia at rest or on minimal exercise, when there is markedly reduced carbon monoxide diffusing capacity, or if the rate of clinical deterioration is not matched by the decline in pulmonary function. The plain chest radiograph may show cardiomegaly, central arterial dilatation (of the main pulmonary artery and hilar arteries) and upper zone vessel

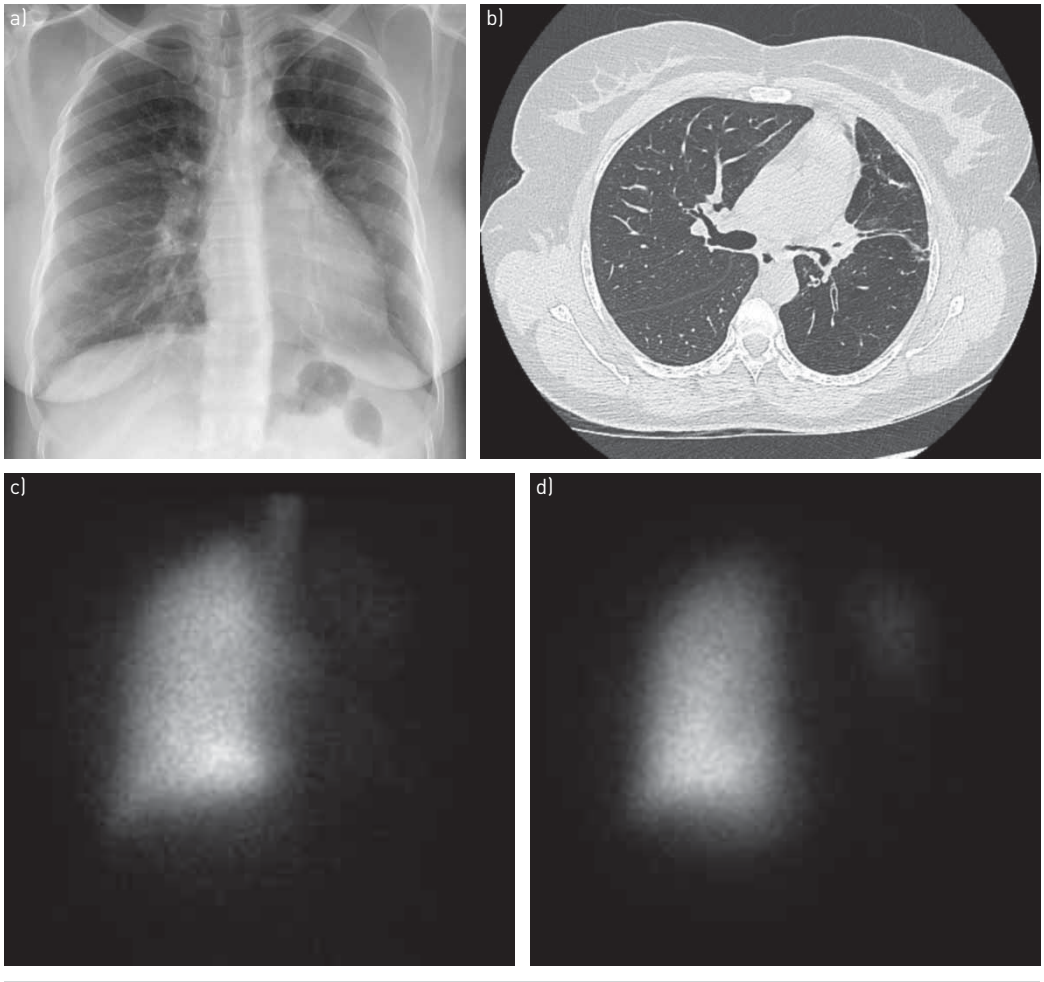

Figure 7. Misdiagnosis of COPD in a patient who presented with breathlessness and wheeze, associated with reduced peak flow measurements that did not improve with bronchodilator therapy. There was a history of tuberculosis. a) Plain chest radiograph shows retrocardiac linear opacities with a "tramline" appearance and reduced definition of the left hemidiaphragmatic silhouette. Full lung function testing revealed a pattern of impairment comparable to that seen following pneumonectomy. b) HRCT imaging demonstrates a severe narrowing of the left main stem bronchus, reduced density of the left lung and some bronchiectatic airways. c) Ventilation and d) perfusion scintigraphy showing loss of ventilation and perfusion of the left lung, which was reflected in a pattern of impairment of lung function testing comparable to that seen following pneumonectomy. Bronchoscopy confirmed stenotic narrowing of the left main stem bronchus that was presumed to be secondary to previous mycobacterial infection.

enlargement, in addition to the usual features of COPD (figure 8). The dimensions of the right descending pulmonary artery are often used as a guide, and the upper limit of normal for the transverse diameter at the mid-point of the vessel of 17 mm is cited as indicative of dilatation [18]. However, the plain chest radiograph is insensitive and may appear normal in patients with severe PH. Measurements of the main pulmonary artery diameter on CT do correlate well with mean PAP and a number of different approaches have been advocated [19–21]. An alternative practical and simple rule that can be used is that pulmonary arterial hypertension is likely when the diameter of the main pulmonary artery exceeds that of the adjacent ascending aorta (provided it is recognised that, with a negative predictive value of 44%, the absence of this feature does not exclude PH) (figure 9) [22].

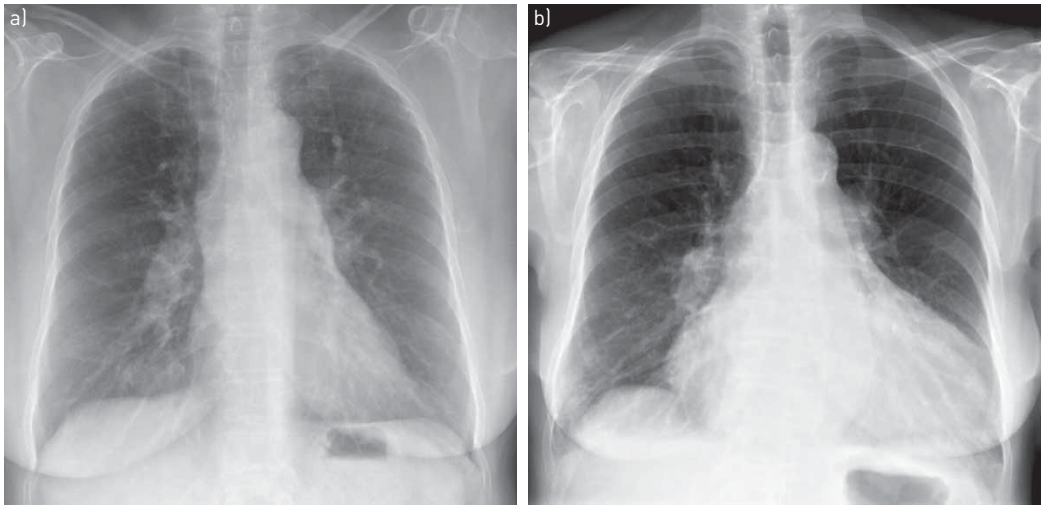

Figure 8. Plain chest radiographic appearance in COPD with pulmonary hypertension (PH). a) Prominent central pulmonary artery and increased transverse diameter of the right pulmonary artery in a patient with severe COPD and PH. b) Cardiomegaly and central arterial dilatation in a patient with COPD and PH.

Echocardiography is the initial modality for noninvasive diagnosis of PH in COPD, with a positive predictive value of 32% and negative predictive value of 93% [23, 24]. Cardiac MRI is now assuming a significant role in the clinical assessment of COPD patients, particularly given the technical difficulties in obtaining a sufficiently good window for ultrasound to assess the right ventricle in the presence of emphysema. A recent nested case–control study suggests that reduced right ventricle dimensions are present in patients with COPD and that these correlate with objective measures of emphysema on CT [25]. However, the gold standard for the diagnosis of PH remains right heart catheterisation, which should be considered in patients with COPD under the following circumstances: when there is clinical worsening and progressive exercise limitation that is disproportionate to ventilatory impairment; when there are progressive gas exchange abnormalities that are disproportionate

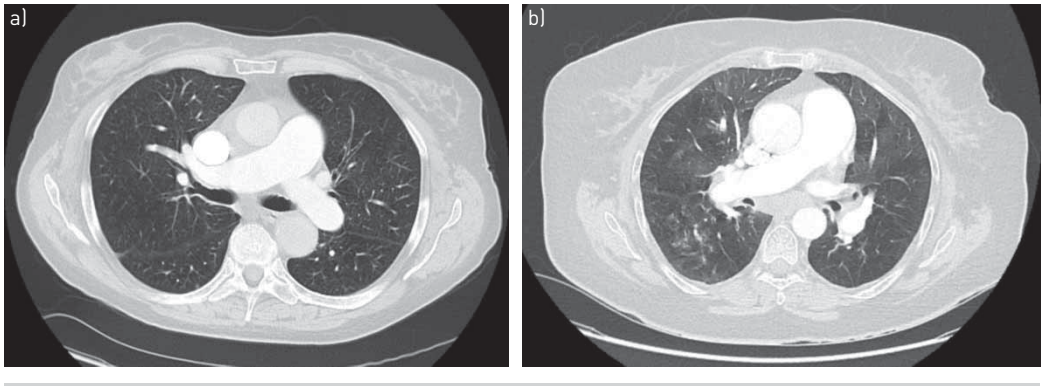

Figure 9. CT appearance of pulmonary hypertension in COPD. a) Increased diameter of the main pulmonary artery relative to that of the adjacent ascending aorta. b) CT pulmonary angiography showing an increased diameter of the main pulmonary artery relative to that of the adjacent ascending aorta with a subtle mosaic attenuation pattern in the parenchyma. The patient had presented repeatedly with worsening breathlessness that was attributed to infective exacerbations of COPD and was eventually shown to have CTEPH.

to ventilatory impairment; and as part of evaluation for lung transplantation. The findings of a recent study indicate that COPD patients with mean PAP >40 mmHg demonstrated cardiovascular rather than ventilatory limitation to exercise, in contrast to patients without PH and those with moderate PH (mean PAP 31 mmHg) who were limited by ventilatory impairment [26]. Consequently, there is a clinical need to assess the severity of PH in COPD patients accurately (which cannot be achieved by imaging alone) in order to identify phenotypic subgroups for a tailored approach to therapy.

Lung volume reduction surgery

Emphysematous destruction increases the compliance of the lung through a reduction in the number and integrity of elastic fibres, which in health are responsible for retractive forces in the inflated lung. These inward forces are normally counterbalanced by the outward forces of the chest wall, which, in the presence of emphysema, lead to lung hyperinflation. In addition, the altered parenchymal compliance reduces elastic recoil, with the result that the small airways have a predilection for collapse. Air trapping ensues on even mild exertion, leading to dynamic hyperinflation.

Hyperinflation increases the work of breathing and symptoms of breathlessness, particularly on exercise. There is evidence to suggest that hyperinflation may also impair cardiac performance [27]. Removal of emphysematous regions of the lung may reduce hyperinflation, with the potential to enhance lung function and quality of life [28]. Lung volume reduction (LVR) through surgical resection has been extensively studied and, if applied to carefully selected cases, is effective. However, it is now rarely performed, due to a high incidence of complications, and less invasive methods are now favoured. These methods include installation of endobronchial valves [29, 30] or lung sealant [31, 32] into affected lobes, thermal vapour ablation of selected lobes [33, 34] or "coiling" of the worst affected lung regions [35, 36].

Whichever technique is utilised to achieve LVR, patient selection is critical. In patients with physiological criteria of hyperinflation, the greatest advantage from surgical LVR is observed in patients with upper lobe dominant emphysema assessed using CT [37]. In contrast, LVR surgery in patients with α_1-antitrypsin deficiency, where the pattern of emphysema distribution is predominantly basal, is now believed to be of short-lived benefit [38]. The degree of emphysema heterogeneity is also associated with LVR surgery outcomes, and a combination of CT imaging and scintigraphy may be used to differentiate and target regions of the lung with the most pronounced morphological and functional features of emphysema [39]. In this study of 250 patients, those with marked heterogeneity experienced an improvement in FEV_1 of 61%, compared with an improvement of 35% in patients with homogeneous distribution [39]. Similar findings were observed in a further study that looked at bilateral LVR surgery and showed improvements in FEV_1 of 68% for upper lobe dominant disease, 47% for lower dominant disease and 37% for homogeneous disease [40]. The outcome has also been shown to be better when the more severe emphysema is peripherally distributed [41].

Interventional bronchoscopy now offers minimally invasive techniques, such as endobronchial valves, coils or sealant, as an alternative to LVR surgery. Endobronchial valves reduce lobar volume by allowing air to escape from a pulmonary lobe while preventing air from entering. The presence of collateral ventilation prevents effective lobar collapse and is therefore a potential obstacle to the effectiveness of the technique. Endobronchial coiling offers an

alternative to valves with the advantage that it is independent of collateral ventilation but, unlike endobronchial valves, is effectively irreversible. As with LVR surgery, CT is used for patient selection, not only to identify emphysema heterogeneity but also to assess the integrity of interlobar fissures, as a surrogate for interlobar collaterals. Fissure "completeness" on CT is associated with the magnitude of therapeutic lobar volume reduction and improvement in FEV1 following valve placement. It has been possible with CT imaging to identify the influence of valve position on the effectiveness of lobar isolation and consequent lobar collapse, and to identify the associated volume changes in the adjacent less emphysematous lung [29]. Scintigraphy may also be used to provide an assessment of perfusion [42] that may supplement the morphological selection criteria provided by CT. The proportion of patients that respond to treatment with endobronchial valves is 52% in highly selected patients compared with 39% for the remainder [42].

CT is fundamental to the preoperative screening and assessment of patients for LVR surgery. Visual inspection of imaging for the assessment of emphysema severity, distribution and heterogeneity and fissure completeness is, however, subject to observer variability and is time consuming. Consequently, the radiologist is increasingly being replaced by semi-automated software, as discussed in another chapter of this *Monograph* [43].

The recent more widespread use of CT scanning has emphasised the presence of emphysema in a significant proportion of patients with COPD (up to 60%), as well as those who do not have COPD diagnosed by conventional spirometric criteria, where it can vary from 10–45% depending on the stringency of the diagnosis [44]. This is of more than theoretical interest, as the emphysema phenotype demonstrates a more rapid subsequent deterioration in physiology [45] and increased mortality [46], even in patients with normal spirometry [47]. In the absence of disease-modifying therapy for this phenotype, its recognition (particularly early in disease) enables a more focused preventative approach and encourages effective smoking cessation, especially in α_1-antitrypsin deficiency, where it is recognised that emphysematous change may precede spirometric abnormality by some 15 years [48].

Bronchiectasis

Bronchiectasis is a permanent dilatation of the airways and is classified pathologically into three main types: tubular, varicose and saccular/cystic [49]. The condition is usually associated with a chronic cough productive of large daily amounts of sputum that is often purulent in nature. Multiple defects of the innate and secondary immune systems have been identified [50], although in a significant proportion there is no recognised cause or association. In the past, the diagnosis was confirmed by bronchography to outline the airways. CT scanning is now the radiological investigation of choice for the diagnosis of bronchiectasis and is far more sensitive than the "tramline" changes sometimes seen on routine chest radiography. The changes relate to dilated and nontapering airways, especially when visible near the margins of the lung. The classical "signet ring" appearance of the airway indicates that its dimension exceeds that of the accompanying vessel (figure 10a) and reflects minimal change seen typically in tubular bronchiectasis. Varicose change (figure 10b) is also found in patients with COPD but cystic change (figure 10c) is uncommon. Munro *et al.* [51] demonstrated that patients with a primary diagnosis of COPD had a high prevalence of bronchiectasis on CT scans if they also had regular production of purulent sputum. This reflects a high sputum content of neutrophils in response to a high colonising bacterial load [52].

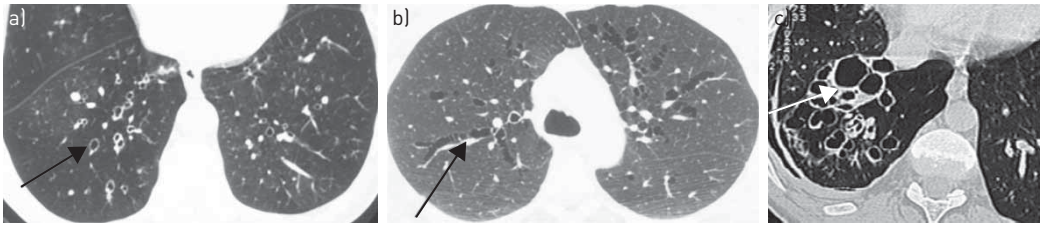

Figure 10. CT scans with arrows indicating a) the classical signet ring sign in tubular bronchiectasis, b) varicose bronchiectasis, and c) cystic bronchiectasis.

Studies have shown that bronchiectatic change is identifiable on ~30% of CT scans from patients with symptoms of COPD who present with an exacerbation [44]. Subsequent large cohort studies have shown the prevalence of bronchiectasis in COPD to be as low as 4% [53], although this may reflect patient acquisition strategy and clinical phenotype. Recent evidence has shown that, when bronchiectasis is present, COPD patients have an increased exacerbation frequency [54] and mortality [55], although the reasons for the latter remain unexplained [56]. Whether the presence of previously unrecognised bronchiectasis has implications for patient management remains unknown. However, it seems sensible to ensure that exacerbations are characterised and purulent episodes treated with antibiotics as in COPD in general. Whether those with recurrent exacerbations or permanently purulent secretions should be treated with longer or continual courses of higher dose oral or inhaled antibiotics, as in patients with a primary diagnosis of bronchiectasis [57], remains unknown at present.

Routine CT scanning

The use of contemporary cross-sectional imaging, such as CT, in the characterisation of COPD, is beneficial in the majority of clinical situations. Consequently, CT scanning is becoming increasingly used in the assessment of patients with COPD. However, the unintended consequence may be that unsuspected abnormalities, such as pulmonary embolism or pulmonary nodules, are identified and these findings can create dilemmas in clinical management. This is particularly pertinent in a population with risk factors associated with an increased risk of developing bronchogenic carcinoma [58] and CT is widely used in lung cancer screening, especially for subjects who fulfil the National Lung Screening Trial criteria (aged 55–74 years with ⩾30 pack-year smoking history), as discussed in another chapter of this *Monograph* [59]. Additional investigations may therefore be considered necessary to identify whether therapeutic intervention is required, or to establish whether the abnormality that has been identified is merely incidental. The clinical and financial implications of this increased activity may be significant. Benign peripheral nodules are often seen on HRCT scans in COPD, occurring in up to 30% of all patients [60, 61]. This has resulted in the development of guidelines on how to assess this often incidental finding [62]. The nodules may be transient and inflammatory in nature [61], or long standing. Features such as small size (<8 mm) smooth outline and calcification are all factors suggesting a non-malignant aetiology: larger and infiltrating lesions suggest a malignant aetiology. These features are used to determine whether, or especially the frequency with which, to follow up the lesions. Current guidelines vary from an initial 3-month follow-up to annual review for 2 years or more. Nodule progression or baseline characteristics may define the frequency and/or further diagnostic intervention [62].

Notwithstanding this potential disadvantage of expensive and excessive investigations, it has been suggested that pulmonary embolism should be routinely sought in all contrast-enhanced CT of the chest, until the level of risk associated with small "incidental" emboli is understood, irrespective of the indication for the investigation [63, 64].

Exacerbations

Exacerbations are defined as an acute worsening of symptoms that exceeds usual variability. This can include a decrease in wellbeing, increased cough, wheeze, development of chest pain and a change in the three cardinal symptoms of dyspnoea, sputum production and sputum purulence [65]. Although these symptoms are classically associated with an infective or bronchospastic deterioration (hence routine therapy of antibiotics, steroids and bronchodilators), they are relatively nonspecific.

COPD patients are susceptible to pneumonia, pneumothorax, thromboembolic disease and complications of associated cardiovascular disease, including infarction and heart failure. Clinical assessment is helpful in differentiating these causes of exacerbation but radiological assessment is essential. Routine chest radiography and CT scanning can identify pneumonic consolidation and pneumothoraces, although large bullous disease can sometimes mimic the latter, especially when pleural adhesions are present. In this instance, inhalation of radiolabelled gases will slowly outline bullae but not pneumothoraces.

The cause of COPD exacerbations may be unidentifiable in up to 30% of events. There may, therefore, be concern that worsening symptoms reflect additional thromboembolic complications. The diagnosis of thromboembolic disease can present both a clinical and radiological problem. Pleuritic chest pain is not uncommon in COPD, representing infection, mucus plugging and cough-induced rib fractures (related to osteoporosis). Ventilation/perfusion (V'/Q') scanning is almost impossible to interpret as COPD patients have both matched and unmatched defects arising from poor ventilation with a secondary reduction in perfusion and areas of emphysema. For this reason, CT pulmonary angiography has now become the investigation of choice, providing evidence of blocked (rather than attenuated) pulmonary vasculature. In addition, evidence of mucus plugging can be detected as part of the CT scan itself.

It is understood that the incidence of pulmonary embolism is increased in patients with COPD and figures from *post mortem* studies suggest that the prevalence of pulmonary embolism may exceed one-half of COPD-related deaths. Since the clinical presentation of pulmonary embolism is frequently nonspecific, identification of the cause of symptomatic deterioration can be problematic. This can be difficult in the presence of chronic respiratory disease, which may mask or confound abnormalities identified on investigations. This is particularly the case for patients with COPD, who will usually have abnormal V'/Q' isotope imaging, which classically shows patchy and unmatched ventilation and perfusion patterns but may show matched defects that cannot be distinguished from pulmonary infarction secondary to pulmonary embolism (figure 11). Consequently, a higher proportion of V'/Q' scintigraphy is nondiagnostic in patients with COPD with suspected pulmonary embolism, compared with patients without COPD [66]. CT allows visualisation of embolus-related filling defects within the pulmonary arterial tree down to subsegmental level and has eclipsed the use of isotope scanning in diagnostic pathways. Therefore, it should now be possible to exclude pulmonary embolism as the cause of increased symptoms in the chronic respiratory patient with reasonable confidence (figure 12).

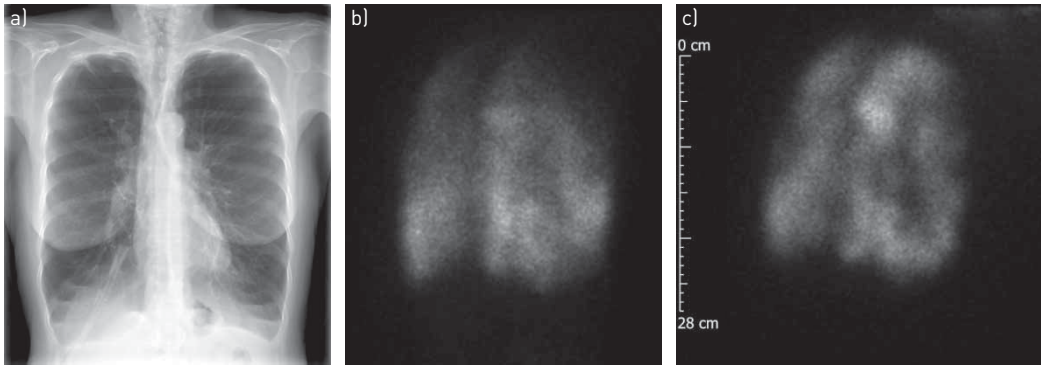

Figure 11. Diagnosis of pulmonary embolism in COPD exacerbations. a) Plain chest radiograph of a patient with severe COPD who presented with symptoms of worsening breathlessness, which was suspected to be secondary to acute pulmonary embolism. There are features that strongly suggest the presence of severe emphysema. b) Ventilation scintigraphy was nondiagnostic because the multiple matched defects evident do not allow the distinction between emphysema and pulmonary infarction that may be secondary to pulmonary embolism. c) Perfusion scintigraphy.

Notwithstanding the advantage provided by CT, the likelihood of pulmonary embolism presenting as an acute exacerbation of COPD remains disputed. In a prospective study of COPD patients who had been referred with "severe" exacerbations to the lung department of a teaching hospital, subjects underwent lower-limb venous ultrasonography and CT pulmonary angiography [67]. The prevalence of pulmonary embolism was reported to be 25%. This figure contrasts starkly with the 3% prevalence of pulmonary embolism identified in a later study [68]. In this later study, evidence of pulmonary embolism was sought in all patients (whether or not clinically suspected) following a standardised algorithm based on D-dimer testing, lower-limb venous ultrasonography and CT. Pulmonary embolism was ruled out by a D-dimer value <500 $\mu g \cdot L^{-1}$ in only 28 (23%) patients.

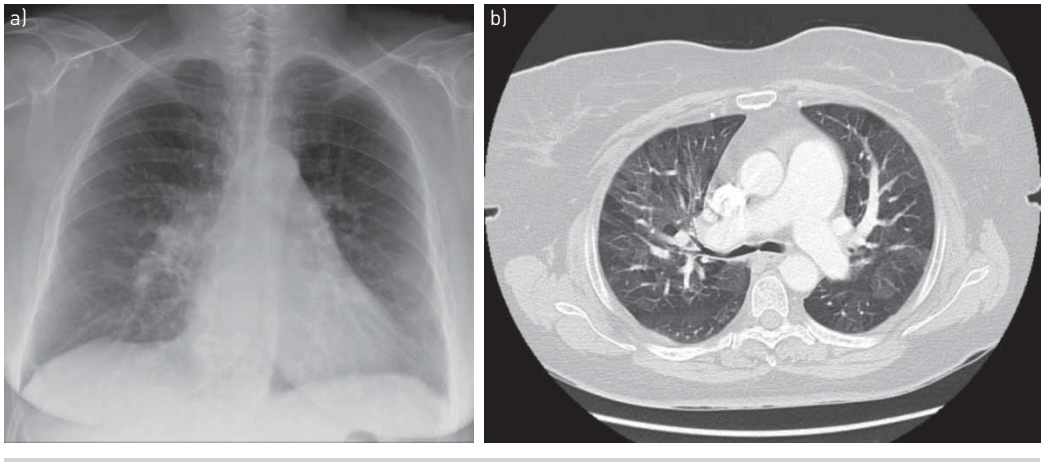

Figure 12. CTEPH in a patient with COPD who had presented repeatedly with worsening symptoms of cough, wheeze and breathlessness that were ascribed to infective exacerbations of COPD. a) Plain chest radiograph. b) CT pulmonary angiography with mosaic perfusion and increased diameter of the main pulmonary artery relative to the ascending aorta.

The discrepancy in prevalence between these two studies probably reflects differences in patient selection. In the former study, subjects were selected to exclude patients with symptoms of increased sputum volume or sputum purulence (in addition to excluding those with a clear explanatory diagnosis, such as pneumonia), whereas the latter study did not exclude subjects with symptoms of an infective exacerbation (although subjects with an obvious alternative cause, such as lobar pneumonia, pneumothorax or pulmonary oedema, were excluded). More recently, a systematic review with an effective sample size of 550 patients concluded that one in four COPD patients who require hospitalisation for an acute exacerbation may have pulmonary embolism with an overall prevalence of 19.9%. Whatever the precise prevalence, it is clear that a diagnosis of pulmonary embolism must be considered as a cause for unexplained deterioration indicative of exacerbations. The performance of a systematic diagnostic work-up to estimate the clinical probability of pulmonary embolism (including previous history, evidence of deep vein thrombosis, haemoptysis, immobility, malignancy, *etc.*) and the use of D-dimer testing to avoid unnecessary imaging are not precluded by the presence of COPD [66]. Given the high proportion of nondiagnostic V'/Q' scintigraphy scans in patients with COPD, CT pulmonary angiography imaging is the investigation of choice.

Comorbidities

It is well recognised that diseases in other systems are associated with COPD more frequently than by chance alone even when co-risk factors are accounted for [69]. This raises the possibility that common inflammatory processes play a significant role in the pathophysiology of COPD as well as cardiovascular disease, osteoporosis [70] and lung cancer [71]. The importance and management of these comorbidities require that they should be sought and treated appropriately, especially as cardiovascular diseases alone are a major cause of mortality in COPD.

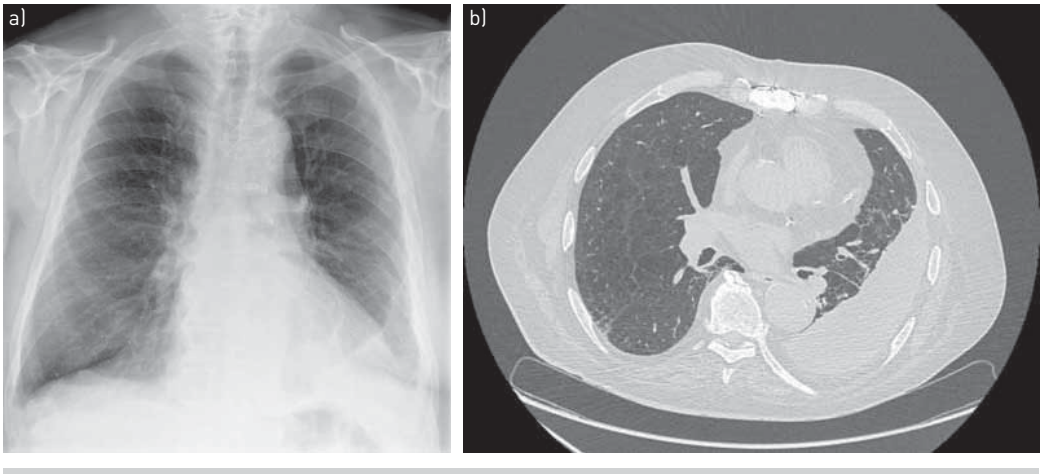

Figure 13. a) Plain chest radiograph and b) CT appearance of a patient with COPD who illustrates the complexity of clinical management due to extensive comorbidities. The severity of airflow obstruction (FEV_1 was 64% predicted) was a poor reflection of the severe impairment arising from coexisting emphysema, ischaemic heart disease (with extensive arterial calcification), pneumonia with empyema, multiple myeloma and chronic spinal cysts, with paraplegia and long-term wheelchair use.

Radiological evidence of the presence of comorbidities may be detected inadvertently as part of the specific assessment of COPD patients (cardiovascular diseases and malignancy) or specifically sought because of the high prevalence (osteoporosis). CT scanning is becoming regularly used in the assessment of COPD especially in secondary care. This detects not only the presence of emphysema and bronchiectasis, both of which have an impact on prognosis [45, 55], but also the presence of malignancy, which can occur in ~7% of COPD patients [58]. Interestingly, the lung tumours are almost twice as likely to be centrally distributed in patients with emphysema than in controls [72] and hence are less likely to be amenable to surgical intervention.

Recent studies have highlighted the relationship of aortic and coronary artery calcification seen on CT scan, with cardiovascular risk [73]. Although it could be argued that all COPD patients should be assessed for cardiovascular risk (in view of the high prevalence), the presence of such calcification (figure 13) should clearly trigger further assessment of potential risk factors and their treatment.

COPD patients also have a high prevalence of osteoporosis, which is present, overall, in about 35% of patients [74]. The presence of vertebral fractures can be seen radiologically in 35–59% of COPD patients, depending on the severity of airflow obstruction [75]. This has led to the development of a five-point approach to an evaluation and treatment plan for fracture prevention in COPD [76]. This includes the use of dual-energy X-ray absorptiometry scans and spinal radiography, together with the fracture risk assessment tool (FRAX; World Health Organization Collaborating Centre for Metabolic Bone Diseases, University of Sheffield, Sheffield, UK; http://shef.ac.uk/FRAX/tool.aspx), to select patients for fracture prevention therapy.

References

1. Lynch DA, Austin JH, Hogg JC, *et al.* CT-definable subtypes of chronic obstructive pulmonary disease: a statement of the Fleischner Society. *Radiology* 2015; 277: 192–205.
2. Rennard SI, Vestbo J. The many "small COPDs": COPD should be an orphan disease. *Chest* 2008; 134: 623–627.
3. The definition of emphysema. Report of a National Heart, Lung, and Blood Institute, Division of Lung Diseases workshop. *Am Rev Respir Dis* 1985; 132: 182–185.
4. Nicklaus TM, Stowell DW, Christiansen WR, *et al.* The accuracy of the roentgenologic diagnosis of chronic pulmonary emphysema. *Am Rev Respir Dis* 1966; 93: 889–899.
5. Sanders C. The radiographic diagnosis of emphysema. *Radiol Clin North Am* 1991; 29: 1019–1030.
6. Foster WL Jr, Pratt PC, Roggli VL, *et al.* Centrilobular emphysema: CT-pathologic correlation. *Radiology* 1986; 159: 27–32.
7. Cottin V, Cordier JF. The syndrome of combined pulmonary fibrosis and emphysema. *Chest* 2009; 136: 1–2.
8. Wiggins J, Strickland B, Turner-Warwick M. Combined cryptogenic fibrosing alveolitis and emphysema: the value of high resolution computed tomography in assessment. *Respir Med* 1990; 84: 365–369.
9. Cottin V, Nunes H, Brillet PY, *et al.* Combined pulmonary fibrosis and emphysema: a distinct underrecognised entity. *Eur Respir J* 2005; 26: 586–593.
10. Mejia M, Carrillo G, Rojas-Serrano J, *et al.* Idiopathic pulmonary fibrosis and emphysema: decreased survival associated with severe pulmonary arterial hypertension. *Chest* 2009; 136: 10–15.
11. Heathcote KL, Cockcroft DW, Fladeland DA, *et al.* Normal expiratory flow rate and lung volumes in patients with combined emphysema and interstitial lung disease: a case series and literature review. *Can Respir J* 2011; 18: e73–e76.
12. Leong P, Bardin PG, Lau KK. What's in a name? Expiratory tracheal narrowing in adults explained. *Clin Radiol* 2013; 68: 1268–1275.
13. Chaouat A, Bugnet AS, Kadaoui N, *et al.* Severe pulmonary hypertension and chronic obstructive pulmonary disease. *Am J Respir Crit Care Med* 2005; 172: 189–194.
14. Andersen KH, Iversen M, Kjaergaard J, *et al.* Prevalence, predictors, and survival in pulmonary hypertension related to end-stage chronic obstructive pulmonary disease. *J Heart Lung Transplant* 2012; 31: 373–380.

15. Oswald-Mammosser M, Weitzenblum E, Quoix E, *et al.* Prognostic factors in COPD patients receiving long-term oxygen therapy. Importance of pulmonary artery pressure. *Chest* 1995; 107: 1193–1198.
16. Wells JM, Washko GR, Han MK, *et al.* Pulmonary arterial enlargement and acute exacerbations of COPD. *N Engl J Med* 2012; 367: 913–921.
17. Cottin V, Le Pavec J, Prévot G, *et al.* Pulmonary hypertension in patients with combined pulmonary fibrosis and emphysema syndrome. *Eur Respir J* 2010; 35: 105–111.
18. Chang CH. The normal roentgenographic measurement of the right descending pulmonary artery in 1,085 cases. *Am J Roentgenol Radium Ther Nucl Med* 1962; 87: 929–935.
19. Kuriyama K, Gamsu G, Stern RG, *et al.* CT-determined pulmonary artery diameters in predicting pulmonary hypertension. *Invest Radiol* 1984; 19: 16–22.
20. Haimovici JB, Trotman-Dickenson B, Halpern EF, *et al.* Relationship between pulmonary artery diameter at computed tomography and pulmonary artery pressures at right-sided heart catheterization. *Acad Radiol* 1997; 4: 327–334.
21. Tan RT, Kuzo R, Goodman LR, *et al.* Utility of CT scan evaluation for predicting pulmonary hypertension in patients with parenchymal lung disease. *Chest* 1998; 113: 1250–1256.
22. Ng CS, Wells AU, Padley SP. A CT sign of chronic pulmonary arterial hypertension: the ratio of main pulmonary artery to aortic diameter. *J Thorac Imaging* 1999; 14: 270–278.
23. Arcasoy SM, Christie JD, Ferrari VA, *et al.* Echocardiographic assessment of pulmonary hypertension in patients with advanced lung disease. *Am J Respir Crit Care Med* 2003; 167: 735–740.
24. Fisher MR, Criner GJ, Fishman AP, *et al.* Estimating pulmonary artery pressures by echocardiography in patients with emphysema. *Eur Respir J* 2007; 30: 914–921.
25. Kawut SM, Poor HD, Parikh MA, *et al.* Cor pulmonale parvus in chronic obstructive pulmonary disease and emphysema: the MESA COPD study. *J Am Coll Cardiol* 2014; 64: 2000–2009.
26. Boerrigter BG, Bogaard HJ, Trip P, *et al.* Ventilatory and cardiocirculatory exercise profiles in COPD: the role of pulmonary hypertension. *Chest* 2012; 142: 1166–1174.
27. Watz H, Waschki B, Meyer T, *et al.* Decreasing cardiac chamber sizes and associated heart dysfunction in COPD: role of hyperinflation. *Chest* 2010; 138: 32–38.
28. Brantigan OC, Mueller E. Surgical treatment of pulmonary emphysema. *Am Surg* 1957; 23: 789–804.
29. Sciurba FC, Ernst A, Herth FJ, *et al.* A randomized study of endobronchial valves for advanced emphysema. *N Engl J Med* 2010; 363: 1233–1244.
30. Venuta F, Anile M, Diso D, *et al.* Long-term follow-up after bronchoscopic lung volume reduction in patients with emphysema. *Eur Respir J* 2012; 39: 1084–1089.
31. Refaely Y, Dransfield M, Kramer MR, *et al.* Biologic lung volume reduction therapy for advanced homogeneous emphysema. *Eur Respir J* 2010; 36: 20–27.
32. Magnussen H, Kramer MR, Kirsten AM, *et al.* Effect of fissure integrity on lung volume reduction using a polymer sealant in advanced emphysema. *Thorax* 2012; 67: 302–308.
33. Snell G, Herth FJ, Hopkins P, *et al.* Bronchoscopic thermal vapour ablation therapy in the management of heterogeneous emphysema. *Eur Respir J* 2012; 39: 1326–1333.
34. Gompelmann D, Eberhardt R, Herth FJ, *et al.* Technology update: bronchoscopic thermal vapor ablation for managing severe emphysema. *Med Devices* 2014; 7: 335–341.
35. Slebos DJ, Klooster K, Ernst A, *et al.* Bronchoscopic lung volume reduction coil treatment of patients with severe heterogeneous emphysema. *Chest* 2012; 142: 574–582.
36. Shah PL, Zoumot Z, Singh S, *et al.* Endobronchial coils for the treatment of severe emphysema with hyperinflation (RESET): a randomised controlled trial. *Lancet Respir Med* 2013; 1: 233–240.
37. Fishman A, Martinez F, Naunheim K, *et al.* A randomized trial comparing lung-volume-reduction surgery with medical therapy for severe emphysema. *N Engl J Med* 2003; 348: 2059–2073.
38. Tutic M, Bloch KE, Lardinois D, *et al.* Long-term results after lung volume reduction surgery in patients with α_1-antitrypsin deficiency. *J Thorac Cardiovasc Surg* 2004; 128: 408–413.
39. Weder W, Tutic M, Lardinois D, *et al.* Persistent benefit from lung volume reduction surgery in patients with homogeneous emphysema. *Ann Thorac Surg* 2009; 87: 229–236.
40. McKenna RJ Jr, Brenner M, Fischel RJ, *et al.* Should lung volume reduction for emphysema be unilateral or bilateral? *J Thorac Cardiovasc Surg* 1996; 112: 1331–1338.
41. Nakano Y, Coxson HO, Bosan S, *et al.* Core to rind distribution of severe emphysema predicts outcome of lung volume reduction surgery. *Am J Respir Crit Care Med* 2001; 164: 2195–2199.
42. Argula RG, Strange C, Ramakrishnan V, *et al.* Baseline regional perfusion impacts exercise response to endobronchial valve therapy in advanced pulmonary emphysema. *Chest* 2013; 144: 1578–1586.
43. Kirby M, Lane P, Coxson HO. Measurement of pulmonary structure and function. *In*: Barr RG, Parr DG, Vogel-Claussen J, eds. Imaging (ERS Monograph). Sheffield, European Respiratory Society, 2015; pp. 216–232.
44. O'Brien C, Guest PJ, Hill SL, *et al.* Physiological and radiological characterisation of patients diagnosed with chronic obstructive pulmonary disease in primary care. *Thorax* 2000; 55: 635–642.

45. Nishimura M, Makita H, Nagai K, *et al.* Annual change in pulmonary function and clinical phenotype in chronic obstructive pulmonary disease. *Am J Respir Crit Care Med* 2012; 185: 44–52.
46. Haruna A, Muro S, Nakano Y, *et al.* CT scan findings of emphysema predict mortality in COPD. *Chest* 2010; 138: 635–640.
47. Oelsner EC, Hoffman EA, Folsom AR, *et al.* Association between emphysema-like lung on cardiac computed tomography and mortality in persons without airflow obstruction: a cohort study. *Ann Intern Med* 2014; 161: 863–873.
48. Holme J, Stockley JA, Stockley RA. Age related development of respiratory abnormalities in non-index α_1-antitrypsin deficient studies. *Respir Med* 2013; 107: 387–393.
49. Whitwell F. A study of the pathology and pathogenesis of bronchiectasis. *Thorax* 1952; 7: 213–239.
50. McShane PJ, Naureckas ET, Tino G, *et al.* Non-cystic fibrosis bronchiectasis. *Am J Respir Crit Care Med* 2013; 188: 647–656.
51. Munro NC, Cooke JC, Currie DC, *et al.* Comparison of thin section computed tomography with bronchography for identifying bronchiectatic segments in patients with chronic sputum production. *Thorax* 1990; 45: 135–139.
52. Hill AT, Campbell EJ, Hill SL, *et al.* Association between airway bacterial load and markers of airway inflammation in patients with stable chronic bronchitis. *Am J Med* 2000; 109: 288–295.
53. Agusti A, Calverley PM, Celli B, *et al.* Characterisation of COPD heterogeneity in the ECLIPSE cohort. *Respir Res* 2010; 11: 122.
54. Patel IS, Vlahos I, Wilkinson TM, *et al.* Bronchiectasis, exacerbation indices, and inflammation in chronic obstructive pulmonary disease. *Am J Respir Crit Care Med* 2004; 170: 400–407.
55. Martínez-García MA, de la Rosa Carrillo D, Soler-Cataluña JJ, *et al.* Prognostic value of bronchiectasis in patients with moderate-to-severe chronic obstructive pulmonary disease. *Am J Respir Crit Care Med* 2013; 187: 823–831.
56. Stockley RA. Bronchiectasis with chronic obstructive pulmonary disease: association or a further phenotype? *Am J Respir Crit Care Med* 2013; 187: 786–788.
57. Pasteur MC, Bilton D, Hill AT. British Thoracic Society guideline for non-CF bronchiectasis. *Thorax* 2010; 65: Suppl. 1, i1–i58.
58. Wilson DO, Weissfeld JL, Balkan A, *et al.* Association of radiographic emphysema and airflow obstruction with lung cancer. *Am J Respir Crit Care Med* 2008; 178: 738–744.
59. McLoud TC, Bernheim A. Lung cancer: screening and staging. *In*: Barr RG, Parr DG, Vogel-Claussen J, eds. Imaging (ERS Monograph). Sheffield, European Respiratory Society, 2015; pp. 47–59.
60. Henschke CI, Yankelevitz DF, Naidich DP, *et al.* CT screening for lung cancer: suspiciousness of nodules according to size on baseline scans. *Radiology* 2004; 231: 164–168.
61. Subramanian DR, Edgar R, Ward H, *et al.* Prevalence and radiological outcomes of lung nodules in α_1-antitrypsin deficiency. *Respir Med* 2013; 107: 863–869.
62. Callister ME, Baldwin DR, Akram AR, *et al.* British Thoracic Society guidelines for the investigation and management of pulmonary nodules. *Thorax* 2015; 70: Suppl. 2, ii1–ii54.
63. Ritchie G, McGurk S, McCreath C, *et al.* Prospective evaluation of unsuspected pulmonary embolism on contrast enhanced multidetector CT (MDCT) scanning. *Thorax* 2007; 62: 536–540.
64. Karia S, Screaton N. Pulmonary embolism. *In*: Barr RG, Parr DG, Vogel-Claussen J, eds. Imaging (ERS Monograph). Sheffield, European Respiratory Society, 2015; pp. 60–79.
65. Anthonisen NR, Manfreda J, Warren CP, *et al.* Antibiotic therapy in exacerbations of chronic obstructive pulmonary disease. *Ann Intern Med* 1987; 106: 196–204.
66. Hartmann IJ, Hagen PJ, Melissant CF, *et al.* Diagnosing acute pulmonary embolism: effect of chronic obstructive pulmonary disease on the performance of D-dimer testing, ventilation/perfusion scintigraphy, spiral computed tomographic angiography, and conventional angiography. *Am J Respir Crit Care Med* 2000; 162: 2232–2237.
67. Tillie-Leblond I, Mastora I, Radenne F, *et al.* Risk of pulmonary embolism after a negative spiral CT angiogram in patients with pulmonary disease: 1-year clinical follow-up study. *Radiology* 2002; 223: 461–467.
68. Rutschmann OT, Cornuz J, Poletti PA, *et al.* Should pulmonary embolism be suspected in exacerbation of chronic obstructive pulmonary disease? *Thorax* 2007; 62: 121–125.
69. Gershon AS, Mecredy GC, Guan J, *et al.* Quantifying comorbidity in individuals with COPD: a population study. *Eur Respir J* 2015; 45: 51–59.
70. Sevenoaks MJ, Stockley RA. Chronic obstructive pulmonary disease, inflammation and co-morbidity – a common inflammatory phenotype? *Respir Res* 2006; 7: 70.
71. King PT. Inflammation in chronic obstructive pulmonary disease and its role in cardiovascular disease and lung cancer. *Clin Transl Med* 2015; 4: 68.
72. Lim J, Shin KM, Lee K, *et al.* Relationship between emphysema severity and the location of lung cancer in patients with chronic obstructive lung disease. *AJR Am J Roentgenol* 2015; 205: 540–545.
73. Dransfield MT, Huang F, Nath H, *et al.* CT emphysema predicts thoracic aortic calcification in smokers with and without COPD. *COPD* 2010; 7: 404–410.
74. Graat-Verboom L, Wouters EF, Smeenk FW, *et al.* Current status of research on osteoporosis in COPD: a systematic review. *Eur Respir J* 2009; 34: 209–218.

75. Nuti R, Siviero P, Maggi S, *et al.* Vertebral fractures in patients with chronic obstructive pulmonary disease: the EOLO Study. *Osteoporos Int* 2009; 20: 989–998.
76. Romme EA, Geusens P, Lems WF, *et al.* Fracture prevention in COPD patients; a clinical 5-step approach. *Respir Res* 2015; 16: 32.

Disclosures: R.A. Stockley has received: personal fees for advisory board membership from AstraZeneca, MedImmune, Almirall, Boehringer Ingelheim, CSL Behring, Kamada, Baxter, Chiesi, Polyphor and Grifols; payment for lectures from AstraZeneca, Nycomed, Takeda, Boehringer Ingelheim, CSL Behring and Grifols; and fees for travel to meetings from Boehringer Ingelheim, CSL Behring and Grifols. He has also received unrestricted research funding from Grifols, the West Midlands Chest Fund (Birmingham, UK), the National Institute for Health Research (London, UK) and the Alpha-1 Foundation (Coral Gables, FL, USA). D.G. Parr has received personal fees from CSL Behring and Grifols, and conference sponsorship from AstraZeneca, Boehringer Ingelheim and Grifols.

Chapter 7

Interstitial lung diseases

Cornelia Schaefer-Prokop[1,2] and Helmut Prosch[3]

Until recently, CT has been regarded as the most important and valuable radiological modality for detecting, analysing and diagnosing diffuse interstitial lung disease, based on the unsurpassed morphological detail provided by HRCT.

Volumetric HRCT offers a number of advantages over discontinuous axial thin-section CT slices, of which the most important are improved detection of subtle disease, better and more accurate comparability, and superior quantitative measures. A number of processing options, such as maximum and minimum intensity projections, ease analysis of HRCT patterns. The most recent developments in detector and reconstruction technology have made up for the disadvantages of continuous *versus* discontinuous data acquisition of the past, allowing for substantial dose savings. In addition to technical aspects, this chapter outlines the principles of HRCT interpretation using a four-pattern approach, and lists key findings to differentiate the most frequent interstitial lung diseases.

The term interstitial lung disease (ILD) refers to a heterogeneous group of diffuse lung diseases characterised by a varying mixture of inflammation and fibrosis. These diseases differ greatly in aetiology, clinical course, radiological presentation and histopathology.

The differential diagnosis of ILD requires a multidisciplinary approach that involves biochemical analysis, bronchoalveolar lavage and radiological examinations in addition to physical examination, pulmonary function tests and an extensive history that includes smoking status. Surgical lung biopsies are required in cases with discrepant clinical and radiological features, and if the histological diagnosis alters the prognosis and/or therapy [1].

Thin-section CT has a central role in the diagnostic workup of ILD; it represents the cornerstone of detection, characterisation and diagnosis of diffuse ILDs because it provides unsurpassed morphological detail. Recent publications have underlined its growing role in quantifying parenchymal changes and predicting prognosis and disease outcome [2, 3].

In this chapter, we focus on several technical details and principles of pattern analysis. Since it is beyond the scope of this chapter to describe in detail the HRCT findings of the various ILDs, we will instead focus on key findings for differential diagnosis, describe some pitfalls

[1]Dept of Radiology, Meander Medical Centre, Amersfoort, The Netherlands. [2]Dept of Radiology, Radboud University, Nijmegen, The Netherlands. [3]Dept of Biomedical Imaging and Image-guided Therapy, Medical University of Vienna, Vienna, Austria.

Correspondence: Cornelia Schaefer-Prokop, Meander Medical Center, Maatweg 3, 3813 TZ Amersfoort, The Netherlands. E-mail: cornelia.schaeferprokop@gmail.com

Copyright ©ERS 2015. Print ISBN: 978-1-84984-065-1. Online ISBN: 978-1-84984-066-8. Print ISSN: 2312-508X. Online ISSN: 2312-5098.

and outline the most recent developments in disease quantification. For pattern analysis of the various ILDs, there are a plethora of other publications and books available [4, 5].

Technical aspects

Traditionally, CT and HRCT have been differentiated by the use of a section thickness of <1.5 mm and an edge-enhancing, high-resolution reconstruction kernel in HRCT. Since the advent of thin-section CT, which enables coverage of the whole chest within one breath hold, essentially each chest CT is a HRCT.

Several developments have contributed to the fact that, over the last several years, discontinuous HRCT acquisition has been increasingly replaced by volumetric data acquisition. 1) Modern CT scanners allow for the acquisition of volumetric HRCT with high image quality at acceptable dose levels. 2) Modern scanners are faster, allowing for a single continuous scan in deep breath-hold rather than the acquisition of discontinuous slices with multiple scans, which require repetitive breath-hold manoeuvres. 3) Volumetric 2D and 3D display techniques, such as multiplanar reconstructions (MPRs), maximum and minimum intensity projections (MIPs and MinIPs), as well as advanced volumetric quantification techniques, are possible only with continuous volumetric data acquisition. 4) Volumetric scans allow for an easier and also more precise comparison of disease development over time. 5) Volumetric scans more reliably capture subtle and focal disease, which are potentially missed when data are discontinuously acquired.

New acquisition and reconstruction techniques, among which are 3D-dose modulation [6] and iterative reconstruction (IR) [7, 8], allow for substantial dose reduction, further supported by the intrinsic high contrast between normally aerated and pathological lung parenchyma. Although first-generation IRs produced images of lower noise, they were criticised for modifying the visual appearance of images (being either smoothed or pixelated), especially with the increased weighting of IR [7, 9]. The more recent generation of so-called model-based IRs, active in the raw data space, however, aims to reduce noise and maintain image sharpness, thus having less impact on the visual image impression [10]. *In vivo* studies have described an improved detection of ground-glass opacities, pulmonary nodules and emphysema even with first-generation IRs [9, 11]. Similarly, an excellent intermethod agreement when comparing IR and filtered backprojection images for the detection of emphysema, ground-glass opacities, bronchiectasis, honeycombing and nodules has been reported [12]. To our knowledge, no study has yet been published that evaluates the impact on the diagnostic evaluation of diffuse ILD; nevertheless, modern IR may well provide a substantial (around 50%) dose reduction of volumetric HRCT for ILD, which represents an important step forward in terms of radiation protection.

Scans are routinely obtained at full inspiration with the lungs fully expanded; this optimises the contrast between low-attenuation aerated airspace and high-attenuation lung structures and various abnormalities. The guidelines of the British Thoracic Society (BTS) recommend the routine use of expiratory scans at a patient's initial HRCT evaluation [13]. The rationale behind this is the potential value of air trapping for the differential diagnosis, which can be more readily appreciated on an expiratory scan, even in the absence of inspiratory scan abnormalities, and the fact that the functional cause of respiratory disability is not always known, especially during the initial diagnostic phase. Because of dose considerations, expiratory scans can be obtained at predetermined levels or as discontinuous clusters.

Alternatively, the expiratory scan can also be obtained with volumetric data acquisition at low-dose conditions [14]. BANKIER *et al.* [15] carried out a systematic comparison of expiratory CT scans obtained with 120 kV, 80 mAs, and simulated 60 mAs, 40 mAs and 20 mAs scans and found that, although diagnostic confidence decreased and interreader variability increased with a decreasing dose, diagnostic accuracy for the detection of air trapping was not affected.

Scans after full expiration are obtained to display lobular areas of air trapping. Air trapping refers to lobular, sharply demarcated areas of hypertransparency caused by air trapped at expiration by a check-valve mechanism of the small airways. The discovery of air trapping as an indirect sign of small airway disease is an important diagnostic finding in all diseases with an obstructive or combined obstructive/restrictive lung function impairment. Diseases in which air trapping is found highlight the importance of expiratory CT scans in the diagnostic workup of hypersensitivity pneumonitis, collagen vascular diseases, such as Sjögren's syndrome and rheumatoid arthritis, and also sarcoidosis and diseases with predominant airway pathology, such as asthma and cystic fibrosis. Sharply demarcated areas of air trapping need to be differentiated from ill-defined areas of varying parenchymal density at expiration. The latter is seen frequently and has been interpreted as "inhomogeneous emptying" of the lung at expiration.

Expiratory CT scans are also used to interpret a mosaic pattern seen at inspiration. A mosaic pattern is defined as areas of varying density, sharply demarcated by interlobular septa. An increased contrast between hypo- and hyperattenuated areas at expiration demarcates air trapping as the pathology and bronchiolitis as the underlying disease. There are fewer vascular structures visible in the "black" areas of hypoattenuation due to the Euler–Liljestrand reflex, which causes vascular constriction in areas of lower ventilation. Importantly, there should be no signs of pulmonary hypertension, as pulmonary hypertension may also lead to hypoattenuation due to hypoperfusion. A decreased contrast between hypo- and hyperattenuated areas at expiration, however, demarcates ground-glass opacity as the pathology and an acute alveolar/interstitial process as the underlying disease. There is no difference in vascular calibre in the areas of different attenuation. Pronounced differences in vascular diameter between the areas of attenuation indicate true mosaic perfusion. Additional signs of pulmonary hypertension, such as dilated central pulmonary arteries and a pathological arterio–bronchial ratio, may be present, suggesting a recurrent pulmonary embolism.

Although discrimination of the different underlying diseases is also possible by analysing the vascular diameters only, many radiologists consider the information about the increased contrast differences caused by air trapping the most valuable.

Data processing and image display

HRCT produces an isotropic data set, which enables contiguous visualisation of the lung parenchyma in 3D and creates 2D MPR in any arbitrary plane. Primarily, planar (coronal and sagittal) reconstructions are routinely performed and considered a standard part of any HRCT data set (figure 1) [14, 16, 17].

Coronal reformations facilitate the display of disease distribution, for example, the craniocaudal gradient that represents a key finding in idiopathic pulmonary fibrosis (IPF), or upper lobe predominance in sarcoidosis or Langerhan's cell histiocytosis (LCH). The advantages of sagittal MPR include the sharp delineation of interlobar fissures, and thus, an

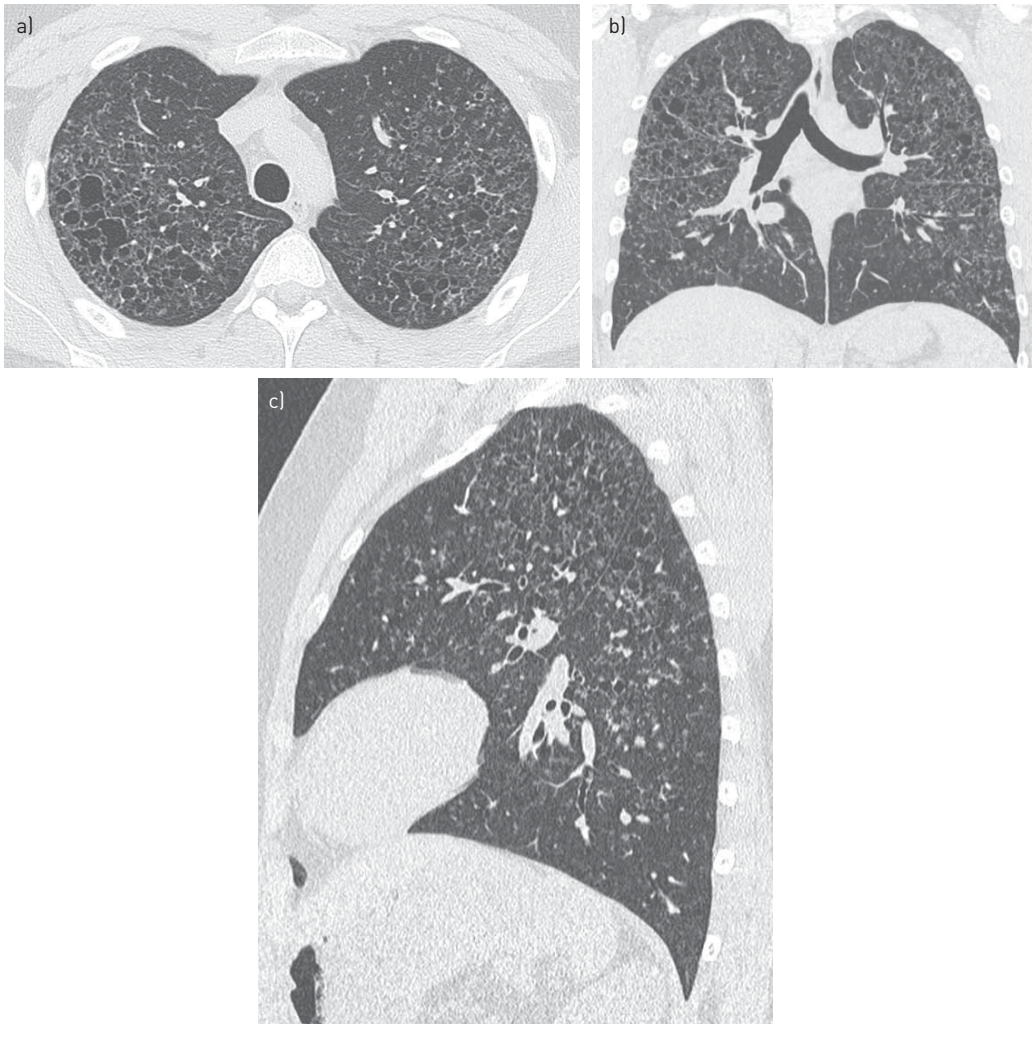

Figure 1. Isotropic resolution in all three dimensions allows for a) axial, b) coronal and c) sagittal reconstructions with highly detailed resolution. While pattern analysis is performed on axial slices, the multiplanar reconstructions nicely demonstrate the craniocaudal distribution of disease in this patient with Langerhan's cell histiocytosis.

improved anatomic localisation of lesions close to the lobar border or lesions with a transfissural extent [18]. Sagittal images also ease the evaluation of subtle disease in the dorsobasal recesses of the lower lobes. Although there is a high level of concordance between reading coronal and axial slices, with regard to the identification of parenchymal disease, there is general agreement that coronal and sagittal MPRs have a complementary role, but are not regarded as the scan plane used for primary diagnostic evaluation [14].

Maximum and minimum intensity projections

MIP is a 3D display technique, which presents the voxel of maximum intensity along the path of X-rays. To retain spatial information, MIPs are usually reconstructed with a

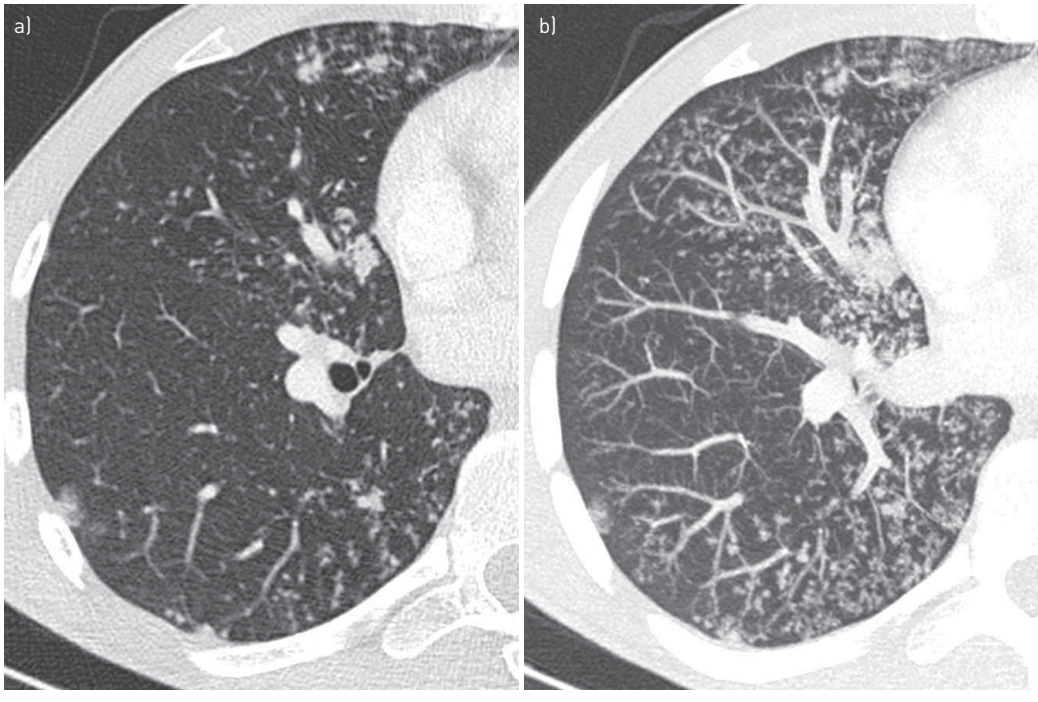

Figure 2. a) A 1-mm axial slice and b) a 10-mm maximum intensity projection (MIP) demonstrating the better visualisation of the distribution of a nodular pattern in MIP in a patient with the tree-in-bud sign due to endobronchial spreading of tuberculosis.

thickness between 5 and 10 mm, depending on the indication (figure 2). Since they largely facilitate the differentiation between tubular (vascular structures) and nodular densities, the major advantage of MIPs lies in demonstrating the distribution of nodules [16, 19]. The analysis of nodule distribution in relation to the secondary pulmonary lobule (for example, perilymphatic, centrilobular or random) is one of the key elements for the differential diagnosis of ILD with a nodular pattern.

Finally, MIP sections of variable thickness allow an assessment of the size and location of pulmonary vessels. Recognising enlarged pulmonary veins is useful in differentiating the diagnosis of pulmonary oedema from other causes of diffuse ground-glass attenuation. In the case of a mosaic attenuation pattern, MIP contributes to the differentiation of ground-glass attenuation (normal vascular diameter) and mosaic perfusion (altered vascular diameter) [16].

MinIPs are less commonly used, but have been shown to facilitate the assessment of lung disease associated with decreased attenuation. MinIPs are created by projecting the voxel with the lowest attenuation value for every view throughout the volume onto a 2D image (figure 3) [14]. MinIP enhances the visualisation of air trapping as a result of small airway disease, yielding increased observer confidence and inter-reader agreement. MinIPs increase visualisation of the bronchi below the subsegmental level [16], facilitating the differentiation of bronchiectasis from honeycombing. The presence of honeycombing represents a key finding for the diagnosis of usual interstitial pneumonia (UIP)/IPF [20], but differentiation from tubular bronchiectasis or subpleural emphysema can be difficult, and a relatively large inter-reader disagreement, even between experienced radiologists, has been described [21].

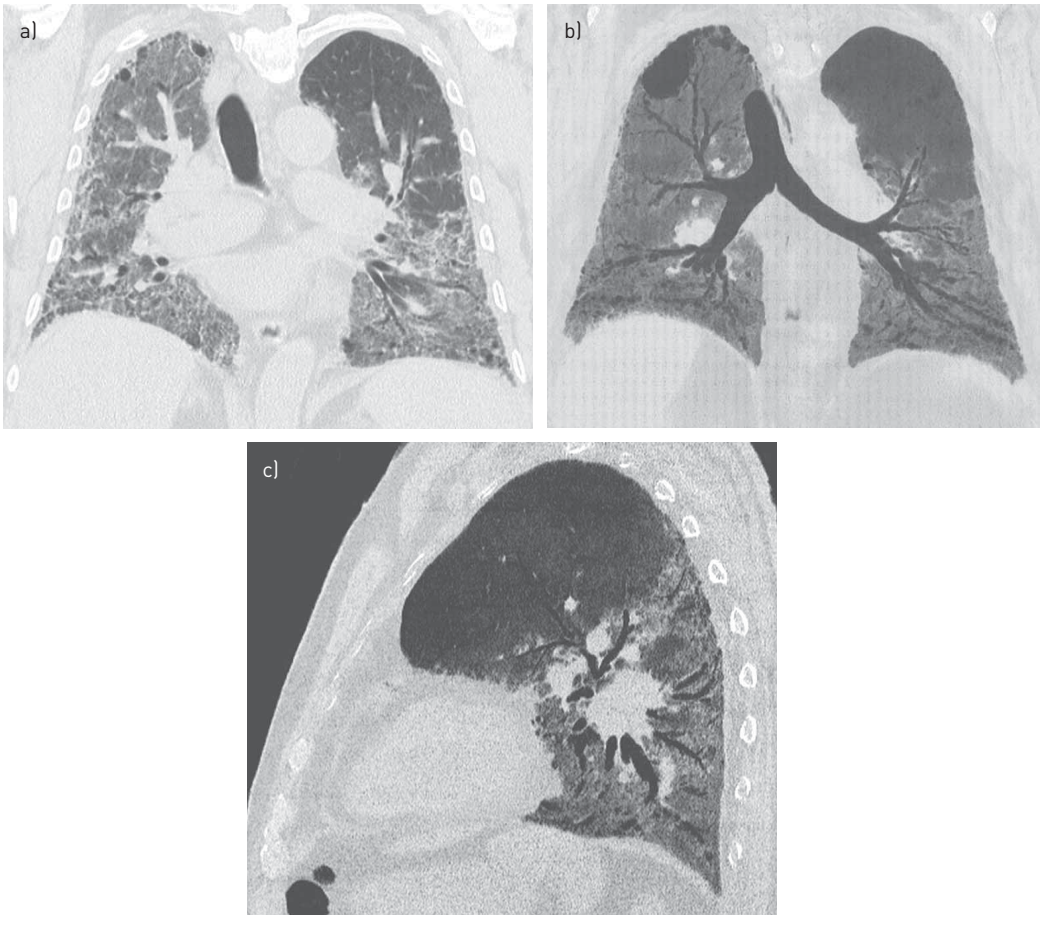

Figure 3. a) A 1-mm coronal multiplanar reconstruction (MPR), and b and c) a 10-mm minimum intensity projection demonstrating the better visualisation of bronchiectasis; increased peribronchial parenchymal density increases the visualisation of ectatic peripheral bronchi.

Quantitative CT as an imaging biomarker

CT is increasingly being used to stage and quantify the extent of ILD in both clinical practice and in treatment trials [3]. The continuous data acquisition of CT with high isotropic resolution provides unique options for computer-supported quantification of diffuse lung disease. There has been a history in quantifying emphysema and airway disease in COPD patients with the ultimate goal of identifying different phenotypes in the COPD spectrum [22]. Recently, these computer-based analysis efforts have been expanded to ILD [3].

Quantification of the extent of ILD, both at a single time point and longitudinally, poses a challenge for several reasons: 1) mostly, diffuse ILD consists of a mix of various patterns that show a considerable overlap, making it difficult to clearly distinguish one from the other; 2) the characterisation of the pattern is influenced by inspiration depth, motion artefacts and other overlying diseases, such as infection; and 3) the extent of architectural distortions in all three spatial dimensions and within the lobular anatomy is difficult to assess.

Multiple studies have shown that the type and extent of parenchymal changes, including accompanying airway pathology, correlate with lung function, disease progression, response to therapy and, last but not least, disease prognosis [2, 23, 24]. However, the extent of correlation is quite variable for the different diseases and highly dependent on the type of pathology and thus, the appreciated HRCT pattern. Nevertheless, the analysis of HRCT findings has been extended from a pure diagnostic tool to an important contributor of information that can help to determine therapy and prognosis, and thus, patient management.

By analysing aetiology, HRCT patterns, histopathological data and outcome, Wells and Hirani [13] proposed five categories, ranging from self-limited inflammation to stable fibrosis, disease with risk of progression, inexorably progressive fibrosis or explosive acute diffuse lung disease. The advantage of such a classification is that, once an individual has been confidently classified into one of these groups clinico-radiologically, longitudinal disease behaviour can be predicted and invasive diagnostic procedures are unnecessary. Prognosis is the primary aim of this classification and treatment might be tailored to stable fibrosis as opposed to potentially progressive fibrosis [25].

Goh *et al.* [24] proposed combining a relatively simple visual quantification of HRCT changes with pulmonary function. First, the disease extent on CT was differentiated into minimal (<20% involved in lung area) or severe (>20% involved in lung area). For the subgroup of patients in which the disease extent was not readily classifiable on HRCT (so-called indeterminate), the distinction between limited and extensive was based on forced vital capacity threshold values below or beyond 70% predicted. Using this relatively simple two-step approach, the authors were able to discriminate two groups of patients with significantly different outcomes, and thus, prognosis.

A similar approach that combines the extent of disease on HRCT with pulmonary function tests has been successfully applied to patients with sarcoidosis and connective tissue diseases. For example, the severity of traction bronchiectasis, the extent of honeycombing and the diffusing capacity of the lungs for carbon monoxide (*D*LCO) were found to be strongly associated with mortality in connective tissue disease-related fibrotic lung disease [23]. Similarly, fibrosis exceeding 20% in extent, the diameter ratio between the aorta and the main pulmonary artery, and a composite score of pulmonary function tests established a significantly more effective prediction for mortality in sarcoidosis patients than any of the factors individually [2].

There has been an increasing interest in the use of automatic CT quantification as an imaging biomarker to document disease response to treatment, disease progression and, eventually, prognosis. Such a biomarker should be measurable, but also reproducible and linked to relevant clinical outcome parameters [26]. To meet the first two demands, rigorous standardisation of imaging protocols over several sites and time points is needed. The underlying technique of automatic, texture-analysis-based CT quantification is beyond the scope of this chapter. There have been a number of studies evaluating the use of a computer-derived quantitative lung fibrosis score to assess baseline disease extent and changes over time in patients with IPF [27] and in scleroderma patients treated with cyclophosphamide [28]. While this algorithm focuses solely on fibrotic changes, a different approach is used by the so-called CALIPER (computer-aided lung informatics for pathology evaluation and rating) software, which associates a certain group of neighbouring voxels to one of five basic patterns (normal, emphysema, ground-glass, honeycombing and reticular) to arrive at the complete lung volume [29]. A recently published position paper by the Hansell *et al.* [3] on behalf of the Fleischner Society acknowledged that CT has the potential not only to select the most

appropriate patients to be included in treatment trials, but also to represent a study end-point in conjunction with other markers. This recent development has been fuelled by the increasing precision with which image processing software can quantify diffuse lung diseases.

Image analysis

A possible and widely accepted approach for the analysis of HRCT in the context of ILD is based on the four patterns of radiomorphological findings [4, 5]. This technique yields a structured and also standardised HRCT analysis, and also provides, together with the clinical history (for example, acute *versus* chronic), immunological findings and associated imaging findings (for example, lymphadenopathy, pleural effusion), the basis for a differential diagnosis.

The four patterns are: 1) nodular opacities; 2) septal/reticular changes with or without parenchymal distortion; 3) diseases with increased density, including ground-glass opacity and consolidations; and 4) diseases with decreased density, mosaic pattern and cysts.

While this "four-pattern approach" reflects purely the radiological findings, it should be extended to include clinical information about disease development (acute, subacute or chronic), and immunological, laboratory and histopathological findings, if available. Both the American Thoracic Society (ATS)/European Respiratory Society (ERS) statements from 2002 to 2011 stress the fact that a key feature of the diagnostic approach is the dynamic and integrated interaction between clinician, radiologist and histopathologist before a final diagnosis is made [20, 30].

Alternative approaches for the analysis of fibrotic diseases have been described. Churg and Müller [31] proposed three classes reflecting prognosis rather than providing a specific diagnosis (ground-glass with no, mild and coarse reticulation, reflecting the cellular and increased extent of fibrosis with architectural distortion). Leslie [32] reported six patterns based on radiological/histopathological correlations ranging from acute lung injury to chronic inflammation (ground-glass and consolidations), fibrosis (reticulation), granulomatous changes (nodules), cystic diseases and very subtle diseases.

Nodular pattern

Pulmonary nodules are categorised according to size, attenuation, margination and localisation. A general categorisation of size results in micronodules (<3 mm), nodules (3–30 mm) and masses (>30 mm). Depending on the attenuation, nodules represent solid or ground-glass opacities. Solid nodules may be sharply or poorly marginated, whereas ground-glass nodules are often poorly marginated. A surrounding area with increased ground-glass density is called a "halo". The halo sign may be caused by acute inflammation or haemorrhage. Based on localisation with regard to the anatomy of the secondary lobule, three main distribution categories of nodules are differentiated: perilymphatic, random and centrilobular (figure 4). MIPs are most helpful in analysing the distribution of nodules.

Perilymphatic distribution

These occur along the bronchovascular bundles, the interlobar fissures, the interlobular septa and the subpleural regions. Central, perihilar nodules along the bronchovascular bundle, individually or clustered, are most typical of sarcoidosis. The nodules usually

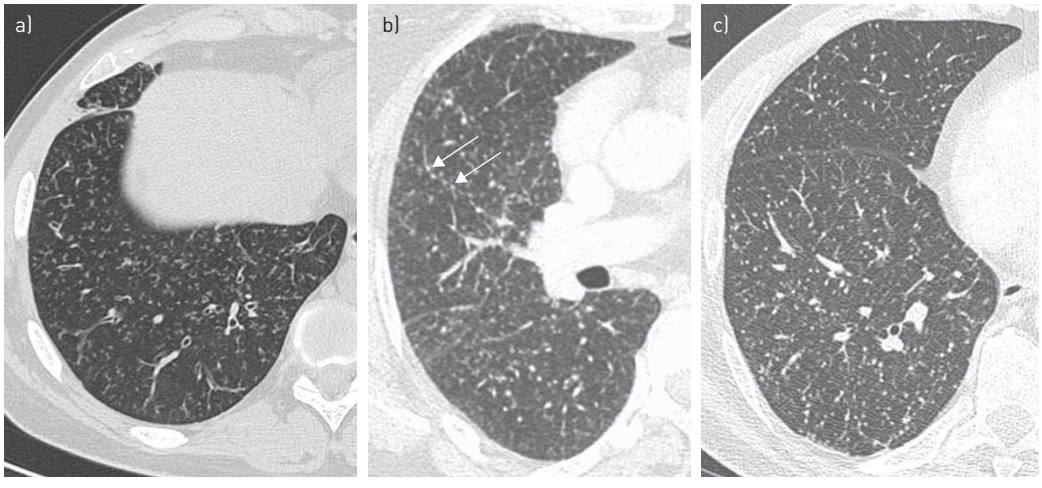

Figure 4. Examples of a) centrilobular, b) perilymphatic (nodules along the septa (arrows), pleural and bronchovascular structures)) and c) random nodular distribution. a) Bronchiolitis, b) sarcoidosis and c) miliary tuberculosis.

measure <5 mm, are well-defined and regularly marginated. They have a predominance for the perihilar regions and the upper lobes, which is particularly well depicted on coronal reformations. A confluence of granulomas may result in larger, irregularly marginated nodules (galaxy sign), ground-glass opacities or consolidations [33].

There might be an overlap between irregularly thickened interlobular septa caused by lymphangitis carcinomatosa and perilobular sarcoidosis, with nodules predominantly along the interlobular septa. While lymphangitis carcinomatosa is frequently associated with pleural effusion and strong thickening of the central bronchovascular interstitium, it is never characterised by lung distortion. Sarcoidosis, however, can lead to heavy distortion and there is usually no pleural effusion.

Random distribution

Typical for a random distribution is uniformity throughout the lung without a preference for certain anatomical structures. The involvement tends to be bilateral and symmetrical. A nodular pattern with a random distribution in relation to leading structures of the secondary lobule, is indicative of a disease process with haematogenous spread, as seen in metastatic disease, miliary tuberculosis or fungal infections.

Centrilobular distribution

Centrilobular nodules are limited to the centrilobular regions and are never in contact with fissures or the pleura. They originate either from the respiratory bronchioles or terminal bronchioli, or from the peripheral pulmonary artery branches. The nodules are a distance of at least several millimetres from the interlobular septa and fissures, and 5–10 mm from the pleural surface, resulting in the characteristic subpleural sparing. They present as ill-defined, centrilobular ground-glass opacities in hypersensitivity pneumonitis or respiratory bronchiolitis. Nodules that are a bit larger, mostly ill-defined or consisting of solid components with a ground-glass halo are caused by (infectious) bronchiolitis or small foci of bronchopneumonia.

Tree-in-bud sign

The "tree-in-bud sign" represents small branching opacities with nodular endings, which also show a centrilobular distribution; these opacities represent small airway disease with wall-thickened and/or secretion-filled small airways.

Septal/reticular pattern with or without signs of parenchymal distortion

Thickening of the lung interstitium caused by fluid, fibrous tissue, or cellular infiltration usually results in an increase in reticular or linear opacities on HRCT. Interlobular septal thickening is differentiated from intralobular septal thickening, although they are primarily seen together.

For differential diagnosis, what is most important is whether increased reticular margins are associated with signs of parenchymal distortion (for example, traction bronchiectasis) that suggest the diagnosis of fibrosis, or whether there are no signs of distortion as seen, for example, in crazy paving.

Any diseases that cause alveolar filling and subsequent filling of intra- and interlobular lymphatics will cause a pattern of crazy paving, which is the combination of ground-glass and reticular densities. Such conditions are seen in oedema, bleeding and pneumonic infiltrations, but also in alveolar proteinosis, storage diseases or lymphoproliferative disorders.

When caused by fibrosis, intralobular interstitial thickening results in traction bronchiectasis and bronchiolectasis, as well as displacement and thickening of interlobular septae and fissures. The most recent 2013 ATS and ERS classification distinguishes UIP, the specific histopathological pattern seen in IPF, from six non-IPF subtypes: acute interstitial pneumonia (AIP); respiratory bronchiolitis ILD (RB-ILD); desquamative interstitial pneumonia (DIP); organising pneumonia (OP); lymphoid interstitial pneumonia (LIP); and nonspecific interstitial pneumonia (NSIP) [34].

Usual interstitial pneumonia in idiopathic pulmonary fibrosis

UIP in IPF carries a particularly poor prognosis: its 5-year survival rate is ~15–30%. Because of prognostic and, recently, also therapeutic differences, UIP/IPF is separated from the remaining ILDs. The definition of IPF is a specific form of chronic, progressive fibrosing interstitial pneumonia of unknown cause, which occurs primarily in older adults, is limited to the lungs and is associated with the histopathological and/or radiological pattern of UIP. It must be stressed that the radiological pattern of UIP is nonspecific for IPF. As is also true of other forms of interstitial pneumonia, including ILDs associated with environmental exposure, medication or systemic diseases may lead to a UIP pattern; thus, these diseases must be excluded before diagnosing IPF. UIP is characterised by the presence of reticular opacities associated with traction bronchiectasis. Honeycombing is critical for making a definite diagnosis following the criteria outlined by Raghu *et al.* [20]. For the HRCT-based diagnosis of UIP, ground-glass opacity may be present, but is less extensive than reticulation. The distribution of parenchymal changes is predominantly basal and subpleural in UIP (figure 5). Coexistent pleural abnormalities (for example, pleural plaques, calcifications, pleural effusion) suggest an alternative aetiology of the UIP pattern. Also, findings such as micronodules, air trapping, cysts, extensive ground-glass opacities, consolidation or a peribronchovascular-predominant distribution are findings inconsistent with UIP and suggest an alternative diagnosis. A heterogeneous process with fibrosis of varying severity and appearance, alternating with normal lung and nonsegmental distribution, is suggestive of UIP (even when honeycombing is not present) as opposed to NSIP [35].

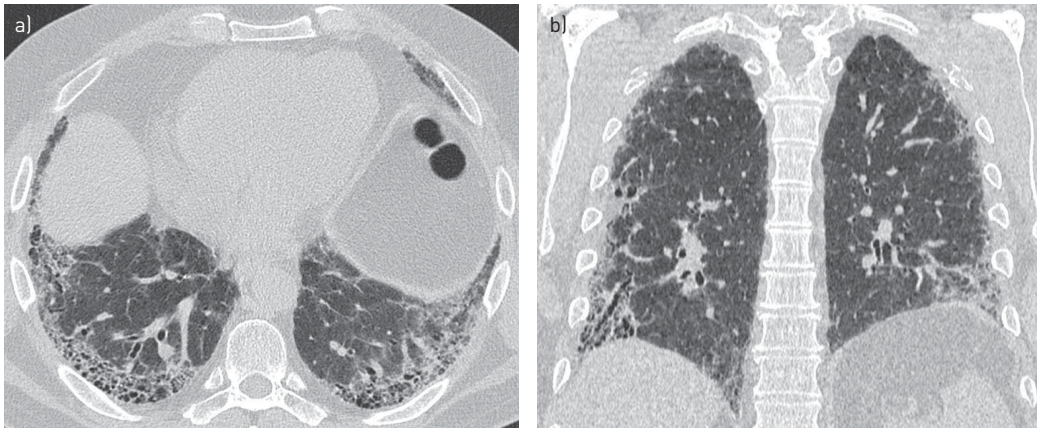

Figure 5. a) Definite usual interstitial pneumonia with honeycombing in a subpleural and mostly basal distribution. There is traction bronchiectasis and very few ground-glass opacities. b) The basal predominance of the changes is best appreciated on coronal (as shown here) or sagittal reformations.

A UIP pattern on HRCT is a highly accurate sign of the presence of UIP on surgical lung biopsy. In the absence of honeycombing, but with imaging features otherwise meeting the criteria for UIP, the HRCT findings are regarded as representing a possible UIP [20]. Definite and possible UIP share similar clinical characteristics and outcomes (except for differences in *D*LCO); lung biopsy to confirm microscopic honeycombing in patients with possible UIP may not be necessary [36]. Interobserver agreement was only moderate among experienced radiologists when using the current ATS/ERS classification of definite/possible or inconclusive UIP [37]. Subclassifying possible UIP as "probable" or "indeterminate" based on HRCT findings revealed the actual histological diagnosis of UIP in 80 *versus* 50% cases, indicating that many of the cases with features consistent with UIP, although not definite, indeed represent UIP [38].

UIP is not specific for IPF. UIP is also seen in a number of other ILDs, such as asbestosis (pleural plaques and calcifications), sarcoidosis (upper lobe disease, heavy parenchymal distortion, associated nodular disease in perilymphatic distribution) or hypersensitivity pneumonitis (bronchovascularly centred fibrosis, air trapping, relative sparing of the posterior costophrenic recesses). UIP can also be seen in the context of drug-induced lung disease and collagen vascular diseases (especially in rheumatoid arthritis).

Nonspecific interstitial pneumonia

NSIP forms the second group of lung fibroses, having quite a variable clinical, radiological and histological presentation. It may be idiopathic, but is more commonly associated with collagen vascular diseases, hypersensitivity pneumonitis, drug-induced lung disease or slowly healing diffuse alveolar damage. The question has been raised whether so-called idiopathic NSIP represents an ill-defined or early stage of a connective tissue disease (undifferentiated connective tissue disease) [39].

The typical HRCT features are ground-glass opacities, irregular linear (reticular) opacities and traction bronchiectasis. It has a peripheral and basal predominance, with typically (but not always present) relative sparing of the immediate subpleural space in the dorsal regions of the lower lobes. A more acute inflammatory (cellular) type of NSIP that presents with

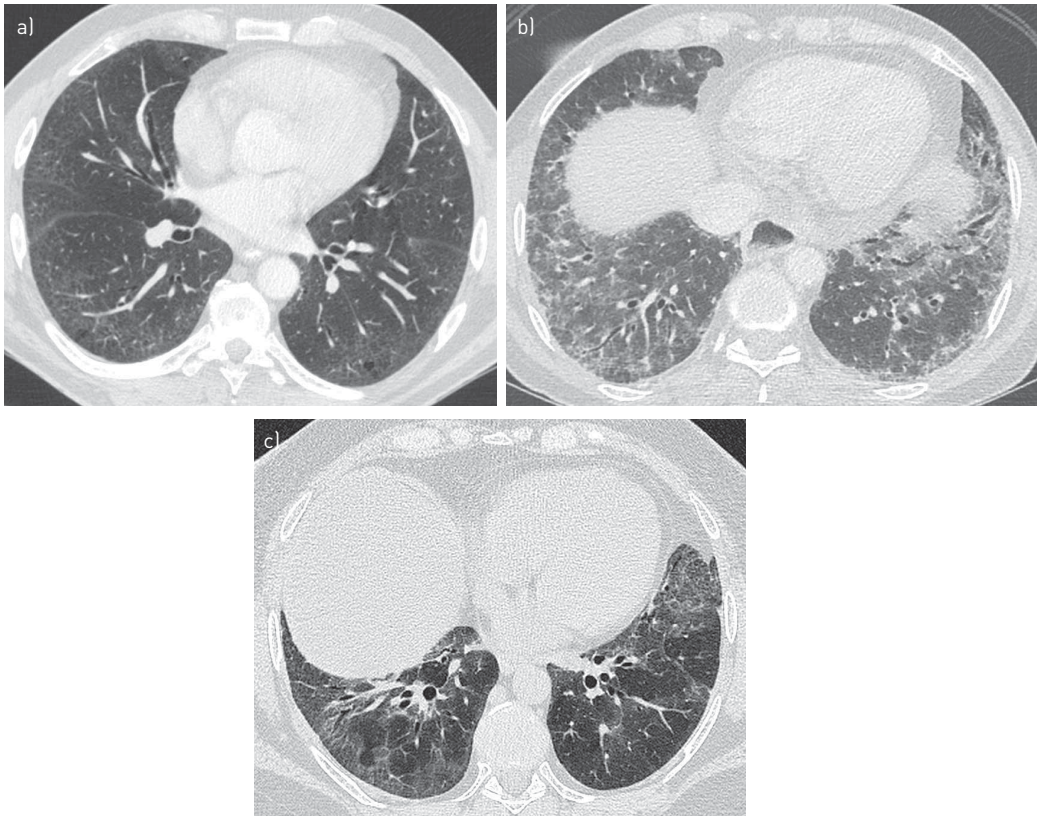

Figure 6. The "many faces" of nonspecific interstitial pneumonia: a) subpleural bands of reticulation and ground-glass opacity (systemic sclerosis); b) diffuse fine reticulation and traction bronchiectasis (systemic sclerosis); and c) patchy areas of ground-glass opacity and traction bronchiectasis.

predominant ground-glass opacities is differentiated from the more fibrotic type that presents with reticulation and traction bronchiectasis. In contrast to UIP, NSIP can also demonstrate a very patchy distribution throughout the whole lung. NSIP is typically characterised by a more uniform pattern, indicating the same stage of evolution of disease, as compared to UIP which presents with multitemporal and morphological heterogeneity (figure 6).

Increased density

As the lung parenchyma consists mainly of air-filled alveolar spaces, there is only little attenuation of X-rays; therefore, the lung parenchyma appears almost black on chest radiographs and CT. If air is partially displaced from the lung parenchyma, attenuation increases, creating a hazy opacity of the lung with preservation of bronchial and vascular margins called ground-glass. If air is completely or almost completely displaced from the airspaces, the attenuation of X-rays is even higher, leading to a homogeneous increase in attenuation that obscures the margins of vessels and airway walls, defined as "consolidation".

A number of pathological changes may lead to increased lung density. Basically, any process that displaces air from the lung will lead to an increase in lung density. This displacement of air can be caused either by a filling of airspaces with fluid or cells or interstitial thickening, as in lung fibrosis, or a combination of both.

In ILDs, a diffuse increase in lung density can be observed in a number of diseases, including NSIP, hypersensitivity pneumonitis, DIP or OP. However, based on CT findings of increased lung density alone, it cannot be determined whether the underlying cause is an interstitial or alveolar process. To narrow the differential diagnosis, additional CT findings, such as bronchiectasis or air trapping, and the distribution of the findings are necessary (figure 7). In most cases, clinical and laboratory data are also needed, and occasionally even histology, to narrow the differential diagnosis.

AIP, acute exacerbation of IPF and acute respiratory distress syndrome

AIP (acute exacerbation of IPF and acute respiratory distress syndrome) manifests histopathologically as diffuse alveolar damage. Consequently, there is clinical, pathological and radiological overlap between these entities that present with new-onset, widely distributed areas of ground-glass opacity and consolidations on CT. CT findings correlate with the pathological phases of diffuse alveolar damage: the presence of traction bronchiectasis in ground-glass opacities and consolidations correlates with the late proliferative and fibrotic phase, while the absence of widened bronchi correlates with the exudative and early proliferative phases. The extent of opacification can be used as a prognostic indicator [40].

Organising pneumonia

OP is a common reaction pattern secondary to lung injury caused by pulmonary infection, connective tissue diseases, inflammatory bowel disease, inhalation injury, hypersensitivity pneumonitis, drug toxicity, malignancy, radiation therapy or aspiration, but can also be idiopathic. OP can present with a wide variety of HRCT findings with increased density, ranging from a more nodular pattern to geographically demarcated ground-glass opacity or focal consolidations [41]. Suggestive for OP (as opposed to infectious pneumonia) are sharply demarcated consolidations in a peripheral subpleural distribution or following the

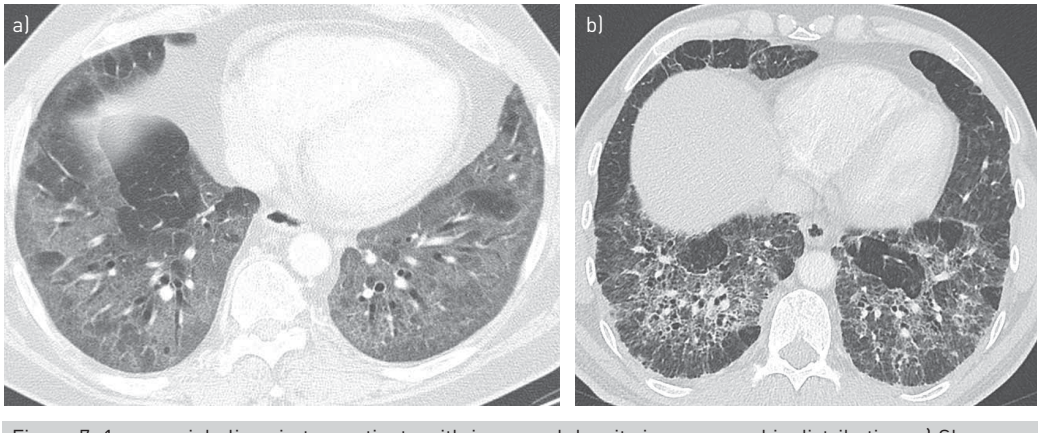

Figure 7. 1-mm axial slices in two patients with increased density in a geographic distribution. a) Shows no sign of distortion (desquamative interstitial pneumonia). b) Shows bronchiectasis and reticulation as signs of fibrosis. In addition, there are areas of air trapping (chronic hypersensitivity pneumonitis).

bronchovascular bundles. Mostly, areas with increased density show dilated, air-filled bronchi without signs of underlying distortion. A patchy distribution is described as the "atoll sign", demonstrating islands with a peripheral, rim-like consolidation around central areas of ground-glass opacification (reversed halo). Densities along the border of the secondary lobules produce arcade-like or polygonal structures and are described as a perilobular pattern.

Decreased density/cysts

The term cyst by itself is nonspecific and refers to a well-circumscribed round or irregular lesion with a visible wall. The wall is usually thin (<2–3 mm), but can have uniform or variable thickness. Cysts can be very small and diffuse, but also large and confluent, resulting in bizarre, polygonal shapes. The presence of a definable wall demonstrated on CT differentiates cysts from emphysema.

Cysts are the leading pattern of specific lung diseases, such as LCH or lymphangioleiomyomatosis (LAM) (figure 8). Other, more rare diseases with cysts are LIP or Birt–Hogg–Dubé syndrome.

An incidental lung cyst, ranging from 5 to 22 mm and located in all lobes, without other HRCT abnormalities and without a history of lung disease or signs of architectural distortion, has been reported as a normal finding in older patients [42].

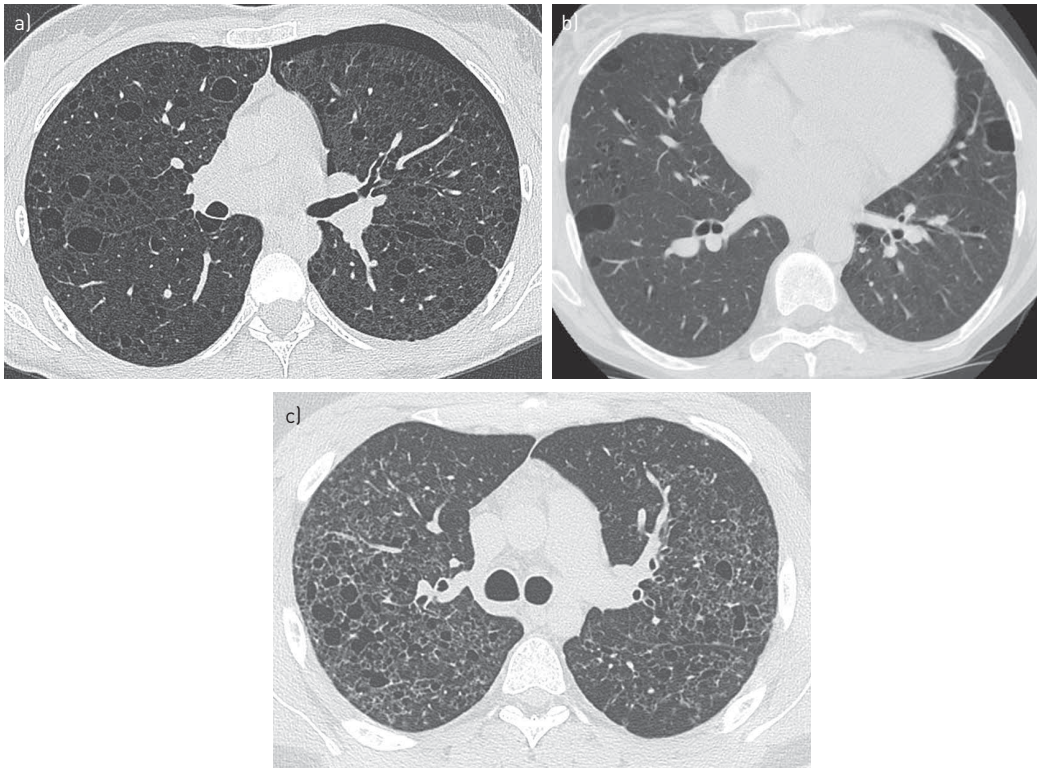

Figure 8. Patterns of cystic parenchymal disease density: a) lymphangiomyomatosis with uniform cysts and a pneumothorax on the left side; b) subpleural cysts in lymphocytic interstitial pneumonia; c) bizarrely shaped cysts predominantly located in the upper lobes in Langerhan's cell histiocytosis.

In the early phases, LCH has a typical nodular pattern with multiple, <10-mm centrilobular nodules with irregular margins. Later, these nodules increase in size and have a tendency to cavitate and develop into cystic lesions. The cysts are often confluent, have bizarre or irregular shapes and are usually thin walled. LCH is predominantly located in the upper lobes, with sparing of the costophrenic sinus, which is better depicted on coronal reformations than on cross-sectional images.

Lymphoid interstitial pneumonia

LIP is uncommon and usually considered as part of a spectrum of pulmonary lymphoproliferative disorders, ranging from benign to malignant lymphomas. Mostly, LIP is associated with Sjögren's syndrome, HIV infection or other immunological disorders. On HRCT, typical findings are sharply demarcated cysts in a subpleural distribution, with intraluminal septae associated with diffuse ground-glass opacities of the lung parenchyma. Poorly defined centrilobular nodules, thickening of the bronchovascular bundles, patchy ground-glass opacities and focal consolidations also belong to this spectrum. In cases with consolidations, a lymphoma must be excluded.

Lymphangioleiomyomatosis

LAM usually occurs in young women and is frequently associated with recurrent pneumothorax and pleural effusion. The cysts are distributed bilaterally and diffusely throughout the lung, involving both the upper and lower lobes, with additional involvement of the lung bases. These cysts are thin walled (ranging from barely visible to 4 mm in thickness), round and measure 0.2–5 cm.

Sometimes, it may prove difficult to distinguish LAM and LCH from emphysema. A helpful finding is that the cystic spaces in LAM and LCH do not have any central nodular opacities, whereas the cystic spaces seen with centrilobular emphysema contain a small central nodular opacity that represents the centrilobular artery.

Overlap patterns

A number of ILDs are associated with such a characteristic pattern on HRCT that differential diagnosis is strongly promoted by image findings, for example, LCH, LAM, end-stage lung disease of UIP and certain stages of sarcoidosis. Other diseases show a combination of findings that considerably overlap with a number of possible diagnoses, which is often the case in advanced disease with considerable parenchymal destruction. For example, there can be considerable overlap between sarcoidosis stage IV, UIP/IPF or chronic hypersensitivity pneumonitis. A study that evaluated the spectrum of CT diagnoses in patients with biopsy-proven UIP/IPF included NSIP in 53%, chronic hypersensitivity pneumonitis in 12% and sarcoidosis in 9% [43].

Similarly, it is also possible that one disease or disease spectrum may present with varying HRCT patterns. Smoking-related lung disease is one example of such overlapping ILDs. RB-ILD, DIP, LCH and the combination of emphysema and fibrosis described as combined pulmonary fibrosis and emphysema belong to the spectrum of smoking-induced lung changes. RB-ILD consists of centrilobular acinar ground-glass nodules that may be confluent to areas of ground-glass opacities and a mild reticular pattern, mainly in the lower lung zones in the minority of patients. DIP shares HRCT features similar to those encountered in RB-ILD, although the distribution is diffuse in DIP and more bronchiolocentric in RB-ILD.

The typical HRCT feature of DIP is diffuse ground-glass opacity, sometimes in a geographic distribution, and reticulation is uncommon. Care should be taken to differentiate the spectrum of smoking-related diseases from combined pulmonary fibrosis and emphysema, the latter describing the combination of emphysema and obvious areas of fibrosis (mostly UIP) at the lung base that influences pulmonary function tests and has an overall dismal prognosis, with a high risk for pulmonary hypertension.

Summary

Continuous volumetric HRCT offers a number of advantages over discontinuous axial thin-section CT slices, of which the most important are an improved detection of subtle disease, better and more accurate comparability and superior quantitative measures. A number of processing options, such as MIP and MinIP, facilitate the analysis of HRCT patterns. The most recent developments in detector and reconstruction technology have compensated for the disadvantage of continuous *versus* discontinuous data acquisition of the past, allowing for substantial dose reductions. HRCT represents a central cornerstone within the multidisciplinary workup of ILD. A systematic, four-pattern approach to CT findings helps to define an appropriate (differential) diagnosis. Prognostic and more recent therapeutic options emphasise the importance of reliably differentiating between UIP/IPF and non-UIP diseases.

References

1. Deconinck B, Verschakelen J, Coolen J, *et al.* Diagnostic workup for diffuse parenchymal lung disease: schematic flowchart, literature review, and pitfalls. *Lung* 2013; 191: 19–25.
2. Walsh SL, Wells AU, Sverzellati N, *et al.* An integrated clinicoradiological staging system for pulmonary sarcoidosis: a case-cohort study. *Lancet Respir Med* 2014; 2: 123–130.
3. Hansell DM, Goldin JG, King TE Jr, *et al.* CT staging and monitoring of fibrotic interstitial lung diseases in clinical practice and treatment trials: a position paper from the Fleischner Society. *Lancet Respir Med* 2015; 3: 483–496.
4. Webb RW, Nestor LM, Naidich DP. High-Resolution CT of the Lung. Philadelphia, Lippincott Williams & Wilkins, 2014.
5. Verschakelen JA, De Wever W. Computed Tomography of the Lung: A Pattern Approach. Berlin, Springer, 2007.
6. Kubo T, Ohno Y, Kauczor HU, *et al.* Radiation dose reduction in chest CT: review of available options. *Eur J Radiol* 2014; 83: 1953–1961.
7. Prakash P, Kalra MK, Ackman JB, *et al.* Diffuse lung disease: CT of the chest with adaptive statistical iterative reconstruction technique. *Radiology* 2010; 256: 261–269.
8. Baumueller S, Winklehner A, Karlo C, *et al.* Low-dose CT of the lung: potential value of iterative reconstructions. *Eur Radiol* 2012; 22: 2597–2606.
9. Pontana F, Duhamel A, Pagniez J, *et al.* Chest computed tomography using iterative reconstruction *vs* filtered back projection (Part 2): image quality of low-dose CT examinations in 80 patients. *Eur Radiol* 2011; 21: 636–643.
10. Katsura M, Matsuda I, Akahane M, *et al.* Model-based iterative reconstruction technique for radiation dose reduction in chest CT: comparison with the adaptive statistical iterative reconstruction technique. *Eur Radiol* 2012; 22: 1613–1623.
11. Christe A, Charimo-Torrente J, Roychoudhury K, *et al.* Accuracy of low-dose computed tomography (CT) for detecting and characterizing the most common CT-patterns of pulmonary disease. *Eur J Radiol* 2013; 82: 142–150.
12. Ohno Y, Takenaka D, Kanda T, *et al.* Adaptive iterative dose reduction using 3D processing for reduced- and low-dose pulmonary CT: comparison with standard-dose CT for image noise reduction and radiological findings. *AJR Am J Roentgenol* 2012; 199: 477–485.
13. Wells AU, Hirani N. Interstitial lung disease guideline. *Thorax* 2008; 63: Suppl. 5, 1–58.
14. Prosch H, Schaefer-Prokop CM, Eisenhuber E, *et al.* CT protocols in interstitial lung diseases: a survey among members of the European Society of Thoracic Imaging and a review of the literature. *Eur Radiol* 2013; 23: 1553–1563.
15. Bankier AA, Schaefer-Prokop C, De Maertelaer V, *et al.* Air trapping: comparison of standard-dose and simulated low-dose thin-section CT techniques. *Radiology* 2007; 242: 898–906.

16. Beigelman-Aubry C, Hill C, Guibal A, *et al.* Multi-detector row CT and postprocessing techniques in the assessment of diffuse lung disease. *Radiographics* 2005; 25: 1639–1652.
17. Walsh SL, Nair A, Hansell DM. Post-processing applications in thoracic computed tomography. *Clin Radiol* 2013; 68: 433–448.
18. Eibel R, Türk TR, Kulinna C, *et al.* Mehrschicht-spiral-CT der lunge: multiplanare rekonstruktionen und maximum-intensitäts-projektionen in der detektion von lungenrundherden. [Multidetector-row CT of the lungs: multiplanar reconstructions and maximum intensity projections for the detection of pulmonary nodules.] *Rofo Fortschr Geb Rontgenstr Neuen Bildgeb Verfahr* 2001; 173: 815–821.
19. Remy-Jardin M, Remy J, Artaud D, *et al.* Diffuse infiltrative lung disease: clinical value of sliding-thin-slab maximum intensity projection CT scans in the detection of mild micronodular patterns. *Radiology* 1996; 200: 333–339.
20. Raghu G, Collard HR, Egan JJ, *et al.* An official ATS/ERS/JRS/ALAT statement: idiopathic pulmonary fibrosis: evidence-based guidelines for diagnosis and management. *Am J Respir Crit Care Med* 2011; 183: 788–824.
21. Watadani T, Sakai F, Johkoh T, *et al.* Interobserver variability in the CT assessment of honeycombing in the lungs. *Radiology* 2013; 266: 936–944.
22. Lynch DA, Austin JH, Hogg JC, *et al.* CT-definable subtypes of chronic obstructive pulmonary disease: a statement of the Fleischner Society. *Radiology* 2015; 277: 192–205.
23. Walsh SL, Sverzellati N, Devaraj A, *et al.* Connective tissue disease related fibrotic lung disease: high resolution computed tomographic and pulmonary function indices as prognostic determinants. *Thorax* 2014; 69: 216–222.
24. Goh NS, Desai SR, Veeraraghavan S, *et al.* Interstitial lung disease in systemic sclerosis: a simple staging system. *Am J Respir Crit Care Med* 2008; 177: 1248–1254.
25. Albert RK, Spiro SG, Jett JR. Clinical Respiratory Medicine: Expert Consult. 3rd Edn. Philadelphia, Mosby/Elsevier, 2008.
26. Goldin JG. Computed tomography as a biomarker in clinical trials imaging. *J Thorac Imaging* 2013; 28: 291–297.
27. Kim HJ, Brown MS, Chong D, *et al.* Comparison of the quantitative CT imaging biomarkers of idiopathic pulmonary fibrosis at baseline and early change with an interval of 7 months. *Acad Radiol* 2015; 22: 70–80.
28. Kim HJ, Brown MS, Elashoff R, *et al.* Quantitative texture-based assessment of one-year changes in fibrotic reticular patterns on HRCT in scleroderma lung disease treated with oral cyclophosphamide. *Eur Radiol* 2011; 21: 2455–2465.
29. Bartholmai BJ, Raghunath S, Karwoski RA, *et al.* Quantitative computed tomography imaging of interstitial lung diseases. *J Thorac Imaging* 2013; 28: 298–307.
30. American Thoracic Society/European Respiratory Society International Multidisciplinary Consensus Classification of the Idiopathic Interstitial Pneumonias. *Am J Respir Crit Care Med* 2002; 165: 277–304.
31. Churg A, Müller NL. Cellular *vs* fibrosing interstitial pneumonias and prognosis: a practical classification of the idiopathic interstitial pneumonias and pathologically/radiologically similar conditions. *Chest* 2006; 130: 1566–1570.
32. Leslie KO. My approach to interstitial lung disease using clinical, radiological and histopathological patterns. *J Clin Pathol* 2009; 62: 387–401.
33. Criado E, Sánchez M, Ramírez J, *et al.* Pulmonary sarcoidosis: typical and atypical manifestations at high-resolution CT with pathologic correlation. *Radiographics* 2010; 30: 1567–1586.
34. Walsh SL, Hansell DM. Diffuse interstitial lung disease: overlaps and uncertainties. *Eur Radiol* 2010; 20: 1859–1867.
35. Gruden JF, Panse PM, Leslie KO, *et al.* UIP diagnosed at surgical lung biopsy, 2000–2009: HRCT patterns and proposed classification system. *AJR Am J Roentgenol* 2013; 200: 458–467.
36. Lee JW, Shehu E, Gjonbrataj J, *et al.* Clinical findings and outcomes in patients with possible usual interstitial pneumonia. *Respir Med* 2015; 109: 510–516.
37. Walsh SL, Calandriello L, Sverzellati N, *et al.* Interobserver agreement for the ATS/ERS/JRS/ALAT criteria for a UIP pattern on CT. *Thorax* 2015 [in press; DOI: 10.1136/thoraxjnl-2015-207252.
38. Chung JH, Chawla A, Peljto AL, *et al.* CT scan findings of probable usual interstitial pneumonitis have a high predictive value for histologic usual interstitial pneumonitis. *Chest* 2015; 147: 450–459.
39. Kinder BW, Collard HR, Koth L, *et al.* Idiopathic nonspecific interstitial pneumonia: lung manifestation of undifferentiated connective tissue disease? *Am J Respir Crit Care Med* 2007; 176: 691–697.
40. Fujimoto K, Taniguchi H, Johkoh T, *et al.* Acute exacerbation of idiopathic pulmonary fibrosis: high-resolution CT scores predict mortality. *Eur Radiol* 2012; 22: 83–92.
41. Roberton BJ, Hansell DM. Organizing pneumonia: a kaleidoscope of concepts and morphologies. *Eur Radiol* 2011; 21: 2244–2254.
42. Copley SJ, Wells AU, Hawtin KE, *et al.* Lung morphology in the elderly: comparative CT study of subjects over 75 years old *versus* those under 55 years old. *Eur Radiol* 2009; 251: 566–573.
43. Sverzellati N, Wells AU, Tomassetti S, *et al.* Biopsy-proved idiopathic pulmonary fibrosis: spectrum of nondiagnostic thin-section CT diagnoses. *Radiology* 2010; 254: 957–964.

Disclosures: None declared.

Chapter 8

The pleura

Cheng Xie and Fergus Gleeson

A chest radiograph is the most common means of identifying pleural disease; however, physician-performed ultrasound is now frequently performed prior to other investigations. As experience with this technique improves, ultrasound will be used more commonly to identify pleural and diaphragmatic thickening and nodularity, and for the diagnosis of pneumothorax and, potentially, cardiac failure. Ultrasound can guide intervention and can also be used to assess treatment success post-pleurodesis. Multislice CT (MSCT) remains a common investigation for the detection of mediastinal and extrapleural disease, and provides an excellent overview of the volume of pleural disease. MSCT remains the technique of choice in differentiating benign from malignant disease, but new developments in MRI and PET/CT suggest they may also have a role. Both MRI and PET/CT may also play a role in helping differentiate different malignancies or subtypes of malignancies, and may be used as biomarkers for prognosis and disease response.

Imaging modalities including chest radiograph, ultrasound, multislice CT (MSCT), MRI and PET combined with CT (PET/CT) play an essential part in the diagnostic examination and management of pleural disease. In this chapter, we address the important roles of these imaging tools in the management of pleural diseases.

Imaging modalities

Patients with pleural disease may present with a variety of symptoms, and most commonly have a chest radiograph as their initial imaging. An erect posteroanterior (PA) radiograph is the preferred method. It has more diagnostic sensitivity than an anteroposterior radiograph for detecting air or fluid. The advent of physician-performed ultrasound, and easy access to CT, has made lateral and decubitus views redundant.

Pleural disease identified on chest radiograph is most commonly further investigated with ultrasound. A trained operator using a variable/high-frequency (7.5–12 MHz) linear or curvilinear array transducer probe can readily examine the pleura, scanning between the intercostal spaces. This technique can be used to investigate pleural fluid, air or solid tissue, both benign and malignant. It is most commonly used in the assessment of effusions, and can be used to guide aspiration, biopsy or drain insertion at the same sitting.

MSCT is commonly performed in patients with effusions, and in cases of pleural thickening without fluid. It enables visualisation of both benign and malignant pleural

Dept of Radiology, Churchill Hospital, Oxford University Hospitals NHS Trust, Oxford, UK.

Correspondence: Fergus Gleeson, Dept of Radiology, Churchill Hospital, Old Road, Headington, Oxford, UK.
E-mail: fergus.gleeson@ouh.nhs.uk

Copyright ©ERS 2015. Print ISBN: 978-1-84984-065-1. Online ISBN: 978-1-84984-066-8. Print ISSN: 2312-508X. Online ISSN: 2312-5098.

disease. It can be performed without intravenous contrast if benign pleural thickening is being investigated, but for the majority of cases, *i.v.* contrast enables better visualisation and characterisation of pleural disease, particularly in the presence of an effusion. Scanning should be performed in the portal venous phase; if an effusion of unknown aetiology is being investigated, a dual-bolus technique to enable the exclusion of pulmonary emboli and the simultaneous assessment of the pleura should be performed [1, 2]. Additionally, MSCT offers the advantage of multiplanar reconstruction, which enables the assessment of the diseased pleura in three-dimensional planes.

In highly selected cases, MRI may be of value. MRI avoids the use of ionising radiation and nonionic contrast media. It also has greater soft tissue contrast resolution than CT; this may occasionally be of value when assessing local invasion along the chest wall, mediastinum and diaphragm [3–5]. To achieve optimal MRI quality, dedicated body coils and specific sequences should be tailored for the individual patient. T1-weighted images can help differentiate pleural abnormalities from extrapleural fat. However, contrast differences between tumour deposits and surrounding muscle can be minimal and difficult to visualise. In these situations, T2/proton density-weighted images and the use of gadolinium-based contrast will offer better differentiation [3, 6]. Dynamic contrast-enhanced and diffusion-weighted imaging appear to be promising in the evaluation of pleural malignancy [7–9].

PET/CT is increasingly used in selected patients and in assessing new therapies in pleural malignancy. The differentially increased uptake of ^{18}FDG in malignant tissue in comparison to benign disease has been reported to be of value in their differentiation [10–16]. The semi-quantitative measurement of the metabolic activity of malignant lesions and subsequent changes during and after treatment are also promising predictors of disease progression and treatment monitoring [17–19].

Anatomy of the pleura

Identification of the normal pleura may become important in the identification of disease, such as the identification of a visceral pleural edge as confirmation of the presence of a pneumothorax, or the absence of the horizontal fissure on a PA chest radiograph in middle lobe collapse. Other than the fissures, the normal pleura is not visible on MSCT, unless there is a pneumothorax; what is commonly interpreted as the pleura along the chest wall is in fact predominantly the innermost intercostal muscle (figure 1). Identification of incomplete fissures (figure 2) is important in patients being considered for lung volume reduction treatments, as their partial absence is associated with collateral ventilation, which reduces treatment success; in surgical patients it requires surgical completion of the fissure.

Pleural diseases

Pneumothorax

A chest radiograph remains the first investigation in the majority of patients with suspected pneumothorax, although an increasing number of patients in critical care now have their pneumothorax diagnosed on ultrasound. On chest radiograph, air in the pleural space pushes the visceral layer away from the chest wall and it can be seen as a thin curved line.

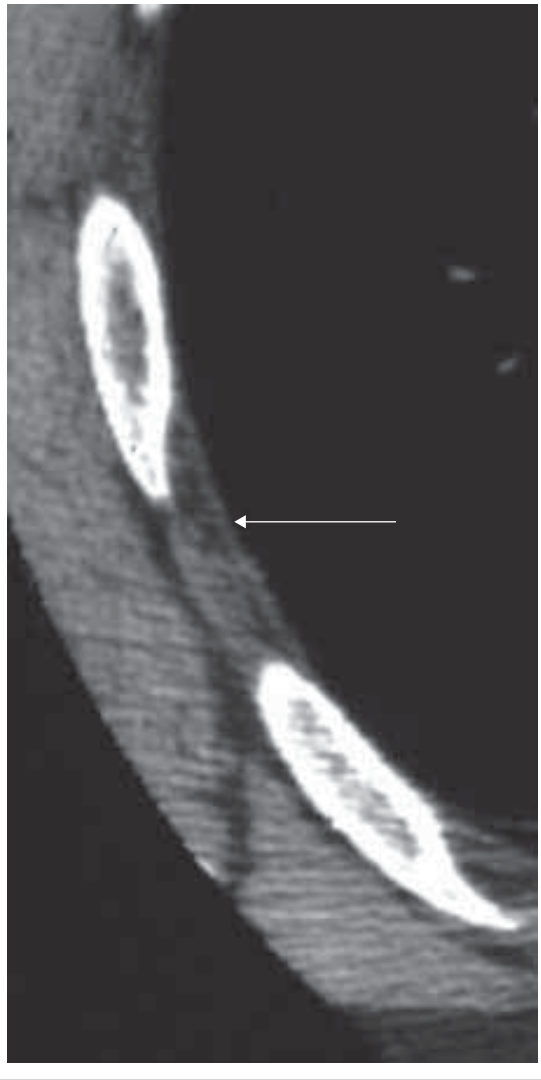

Figure 1. Cross-sectional CT image of the pleural stripe, which is mostly composed of the innermost intercostal muscle (arrow) in-between two ribs.

Lateral to this linear visceral layer, there is an increase in radiolucency and no visible pulmonary vasculature. Depending on its size, and the patient's body habitus, a small pneumothorax can be difficult to detect. If detection is critical and there is clinical doubt, a CT should be performed. The expiratory film has been shown to be less effective as a strategy for the detection of small pneumothorax and is no longer performed [20]. In critically ill patients, a chest radiograph may be taken in the supine position. On these films, it is important to inspect for hyperlucency at the upper quadrant of the abdomen delineating a sharp hemidiaphragm, as well as gas collected in the lateral costophrenic sulcus represented by the deep sulcus sign (figure 3) [21]. In suspected cases of tension pneumothorax, decompression is indicated before any imaging investigation.

In the interpretation of the chest radiograph for a pneumothorax, it is important to separate artefacts that may falsely represent a linear visceral layer. Common pitfalls include

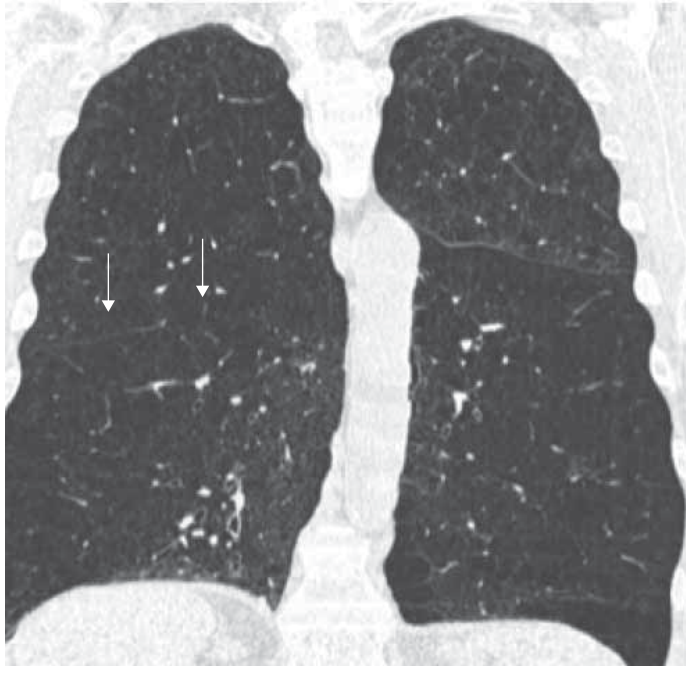

Figure 2. Coronal CT reconstruction demonstrating an incomplete oblique fissure on the right (arrows).

the companion shadows located at the apex and along the medial edge of the scapula, skin folds, lines and tubes, and overlying clothing and bed sheets.

MSCT is highly sensitive in detecting small pneumothoraces. It can be used to assess the size of the pneumothorax and identify a cause, such as a subpleural bulla (figure 4). According to the British Thoracic Society (BTS) guidelines, a large pneumothorax consists of >2 cm rim of air; <2 cm is classified as a small pneumothorax [22]. The American College of Chest Physicians (CHEST) guidelines use the apex-to-cupola distance of >3 cm as large and <3 cm as small pneumothorax [23]. In addition, MSCT is routinely used following trauma; in patients when chest drain placement is required it can provide imaging guidance if the pneumothorax is loculated or there are other complicating factors making accurate drain placement critical [17].

Pleural effusion

On the erect chest radiograph, fluid accumulates at the costophrenic recesses, producing a blunted costophrenic angle; as the fluid volume increases, the degree of basal opacification increases, although large effusions may depress or invert the hemidiaphragm resulting in a greater volume of fluid being present than suspected on the chest radiograph. Pleural effusions with a volume of >200 mL are usually detectable on erect PA chest radiograph. Pleural fluid may be loculated and not produce the characteristic curved meniscus sign, as is seen with subpulmonary effusions, making them harder to detect. On chest radiograph, pleural effusion should be suspected if there is an apparent raised hemidiaphragm with the apex of the hemidiaphragm deviated laterally, increase in opacification below the

Figure 3. Supine chest radiograph demonstrating a right-sided deep sulcus sign (arrow).

diaphragm such that the pulmonary vessels behind the diaphragm are not seen on the chest radiograph, and on the left, the gastric air bubble is more than 1 cm below the hemidiaphragm [24–26]. In the supine or semi-erect positions, the radiological signs of pleural effusion include: the apical cap, which is a curved radio-opacification at the lung

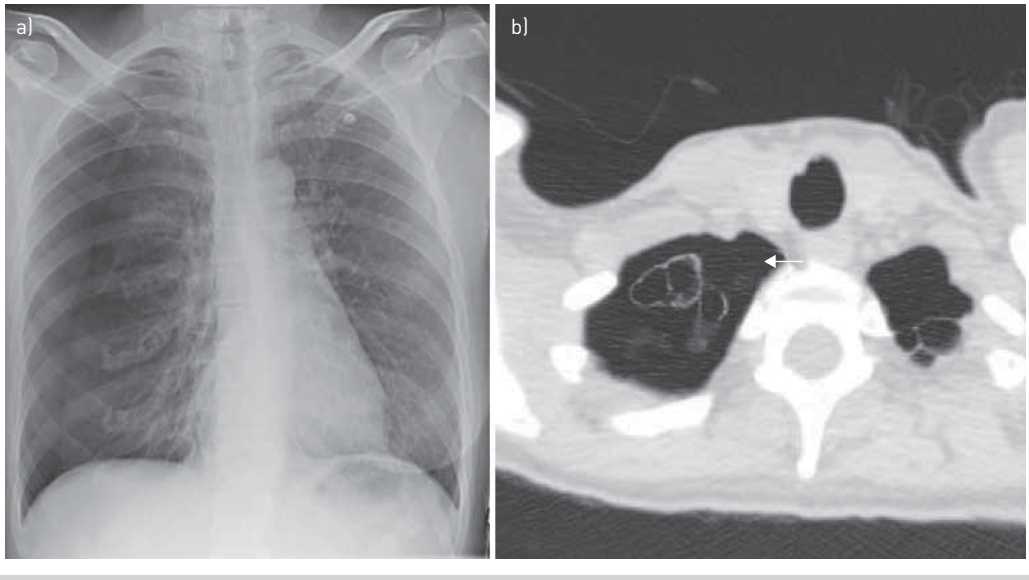

Figure 4. a) Chest radiograph demonstrating a right-sided pneumothorax. b) CT demonstrating right-sided apical pulmonary blebs (arrow), not visible on the chest radiograph. They are also seen at the left apex.

apex (the most dependent area when the patient is lying flat); a veil-like opacification of the affected side; blunted costophrenic angles; and a poorly defined hemidiaphragm [27–29].

On the chest radiograph, the major and minor fissures should also be inspected for signs of pleural effusion. A curvilinear opacification that is distinct at the medial aspect and ill-defined superolaterally at the location of the major fissure suggests pleural effusion in the fissure [30, 31]. Fluid that has accumulated into the lateral aspect of the minor fissure will slightly increase the separation between the opposing lobes resulting in a double concave opacification called the thorn sign [32].

The advent of physician-performed ultrasound has resulted in its increased use to detect or confirm the presence of small effusions on PA and supine chest radiographs performed in critically ill patients. Alongside detection, ultrasound may provide useful information on the nature of the effusion and the presence of important characteristics such as septations and pleural nodularity (figure 5). Differences in fluid echogenicity can help differentiate between transudative and exudative effusions, with transudates typically being anechoic, and exudates being of variable echogenicity depending on their aetiology [33–35].

Ultrasound can also be used to decide on the treatment of effusions and whether treatment has been effective. The identification of septations in parapneumonic effusions and empyema may influence both the decision to place a drain and the site of its placement; the presence of gross visceral pleural thickening in entrapped lung may influence the use of pleurodesis or indwelling pleural catheter placement in malignant effusions [36, 37]. In animal models, ultrasound has been used to evaluate the efficacy of pleurodesis [38].

MSCT is used in specific clinical scenarios to image patients with pleural effusions, and will be discussed in detail in the appropriate sections to follow.

Figure 5. Appearance on ultrasound of pleural effusion due to empyema with septations.

Pleural infections

The classical development of a parapneumonic effusion and empyema occurs in three stages: exudative, fibrinopurulent and organisational [39]. During the exudative phase, the inflammatory response increases the membrane permeability of the visceral pleural layer [40]. This results in pleural effusion. Further unchecked progression of pleural effusion leads to the fibrinopurulent stage; the parapneumonic effusion becomes complicated, with an increase in viscosity, purulence, a positive microbial culture, and elevated lactate dehydrogenase and fibrin content [41]. If untreated or unsuccessfully treated, the final stage is the organisational phase; fibroblasts deposit fibroblastic tissue and the pleura progresses to a thick, inelastic "peel" that impairs chest movement [42, 43].

Imaging can be useful at different stages of the disease. A chest radiograph is often a good starting point for patients with suspected pneumonia. The presence of an effusion with pneumonia, specifically the presence of a loculated effusion, may indicate a parapneumonic effusion or empyema, and specific features of the effusion should raise concerns that the patient has developed a complicated parapneumonic effusion or empyema. Loculation is either due to pleural adhesions being present secondary to prior pleural infection or trauma, including prior thoracic surgery, or to the development of a fibrinopurulent effusion, or the effusion presenting at the organisational stage (figure 6). Failure of the lung to re-expand (trapped lung sign) or a persistent hydropneumothorax suggests established fibroblastic changes to the pleura, or in the appropriate clinical context malignancy rather than infection.

At the fibrinopurulent stage, the increase in fibrin leads to septations and these can be detected by ultrasound (figure 5). Patients with a pleural effusion and septations identified on ultrasound have been shown to have a higher morbidity and mortality compared to those without septations [44]. Ultrasound guidance is now recommended for all pleural fluid sampling and drain placement, as it has been shown to reduce complications [17, 45–47].

Contrast-enhanced MSCT demonstrates pleural thickening and enhancement, with the parietal and visceral pleura separated at an oblique angle, the split pleura sign (figure 7) [48, 49]. Other MSCT signs used to identify complicated parapneumonic collections and empyema include: enhancement of the parietal pleural layer, present in >90% cases and shown to have high sensitivity and specificity [50, 51]; presence of multiple bubbles in the effusion; and extrapleural signs such as an increase in the thickness and attenuation of the adjacent extrapleural fat [50, 52, 53]. MSCT allows assessment of the underlying lung for associated or causal disease, such as adjacent pneumonia or airway infection, or an associated bronchogenic carcinoma or endobronchial cause, such as an inhaled foreign body. MSCT helps in the differentiation of empyema and abscess, as the split pleura sign is absent in empyema, and the abscess usually makes an acute angle with the adjacent pleural surface (figure 8). Another distinguishing feature is that the spherical, thick-walled abscess replaces the lung parenchyma; in contrast, a loculated empyema has a thinner wall and typically displaces the surrounding area of lung [54, 55].

MSCT also plays a role in the assessment of atypical and chronic empyema, and those associated with a complication following development, such as a bronchopleural fistula (BPF) (figure 9). On MSCT, acute tuberculous empyema may be diagnosed by the presence of miliary nodularity, upper lobe airway nodularity or pulmonary cavitation. Chronic

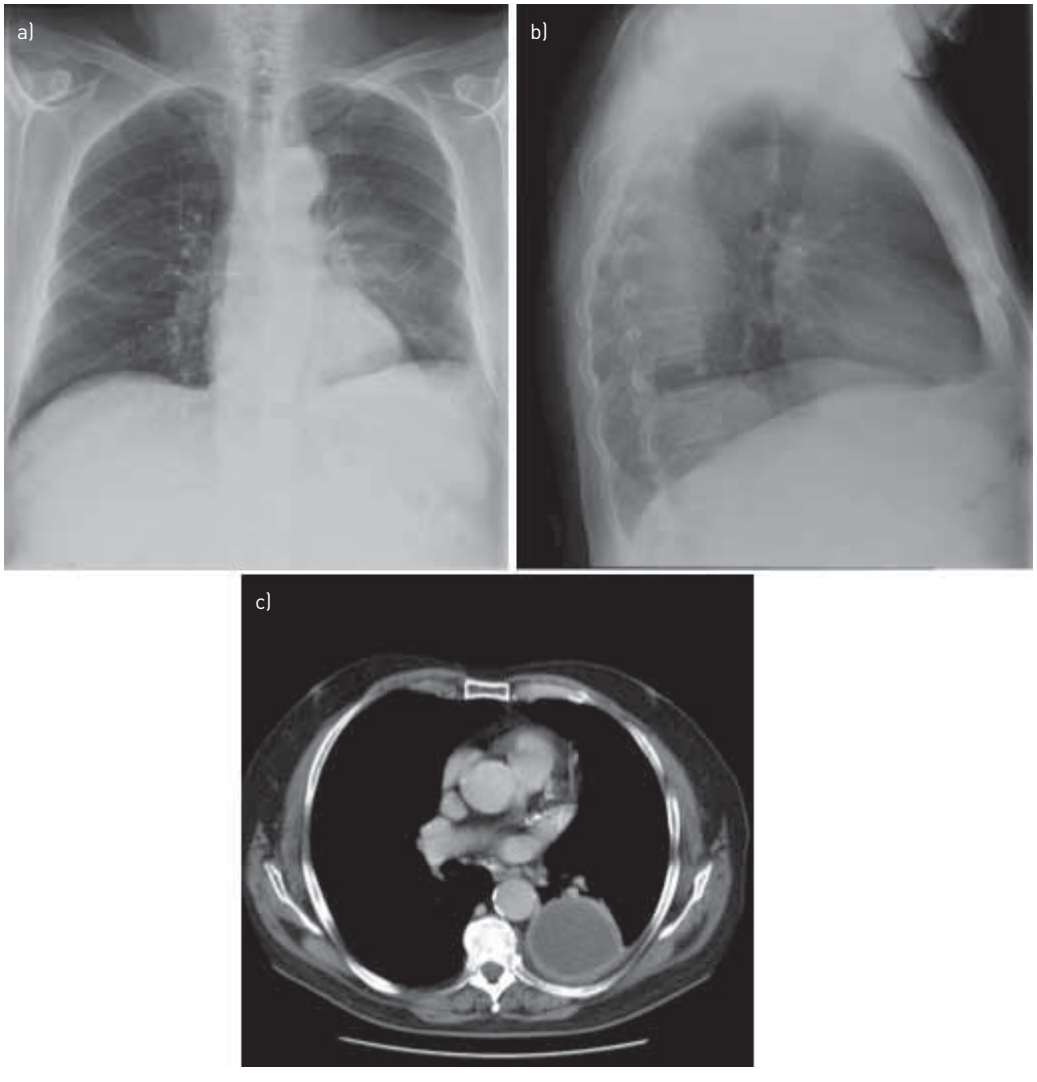

Figure 6. Left-sided loculated empyema. a) Frontal chest radiograph demonstrating areas of increased opacification behind and adjacent to the left heart border. b) Lateral view demonstrating effusion posteriorly with loculation. c) Axial CT with contrast demonstrating a rim enhancing loculated empyema.

tuberculous empyema can manifest as a thick rind of pleura that consists of a loculated pleural collection with a significant amount of calcification in the pleural layers. The surrounding ribs may show periosteal reaction [56, 57]. BPF or empyema necessitans (pleural infection extension into the chest wall) are readily diagnosed on MSCT [58, 59], with image reconstructions either as three-dimensional images or using specific algorithms such as minimal intensity projection, which are particularly useful for diagnosing BPF. Chronic pleural infection can also cause severe pleural fibrosis (fibrothorax). MSCT findings include extensive pleural thickening and calcification due to significant fibrosis of the pleura, with a reduction in size of the hemithorax [59].

MRI plays a very limited role in the assessment of pleural effusion and empyema. On T1-weighted images, effusion and empyema have a low signal. On T2-weighted images,

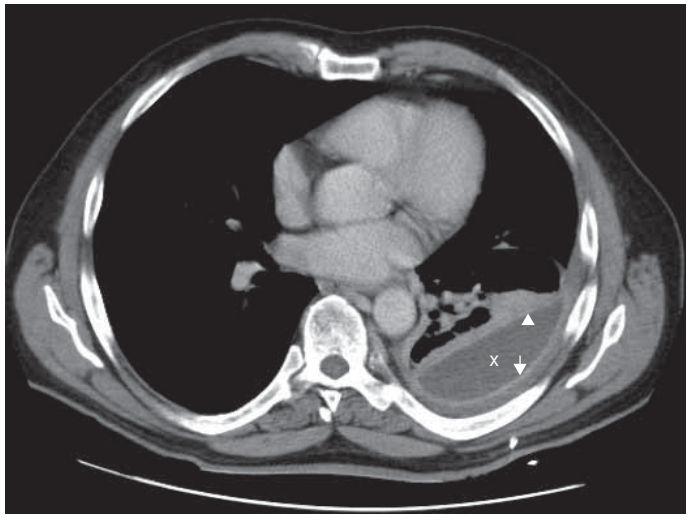

Figure 7. Cross-sectional, contrast-enhanced CT image of the thorax demonstrating the split pleura sign. A left-sided empyema (cross) is encased between the thickened parietal (arrow) and visceral (arrowhead) pleural layers.

they have a high signal. In addition, the extrapleural fat enhancement as seen on MSCT also has high signal intensity on fat-suppressed, T2-weighted images. MRI can also show loculations and septations (figure 10), and generally, magnetic resonance appearances show good correlation with CT [60, 61]. Studies on advanced MRI sequences (triple echo, diffusion-weighted imaging sequences) have demonstrated the capacity to differentiate between transudate and exudate with high sensitivity and specificity [61–63].

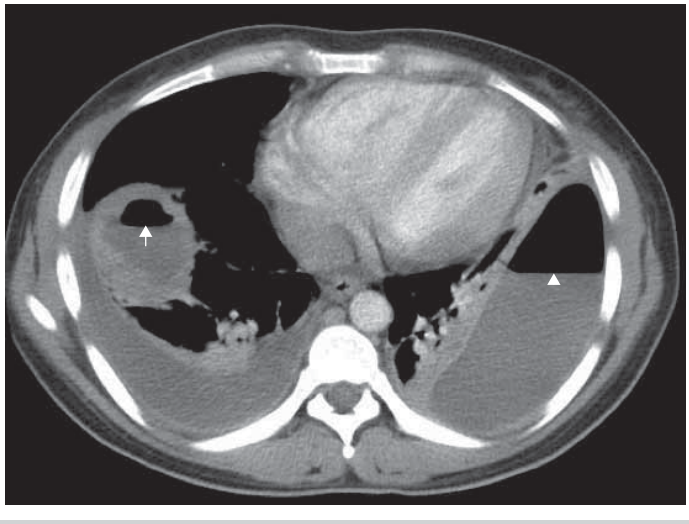

Figure 8. Contrast-enhanced axial CT thorax showing a right lower lobe abscess with an air–fluid level (arrow). There is a left empyema also with an air–fluid level (arrowhead). Notice the thick-walled abscess, and the passive/compressive left lower lobe atelectasis. The abscess makes an acute angle with the visceral pleura, and the left empyema also appears to make an acute angle with the chest wall. Care needs to be taken when interpreting this sign.

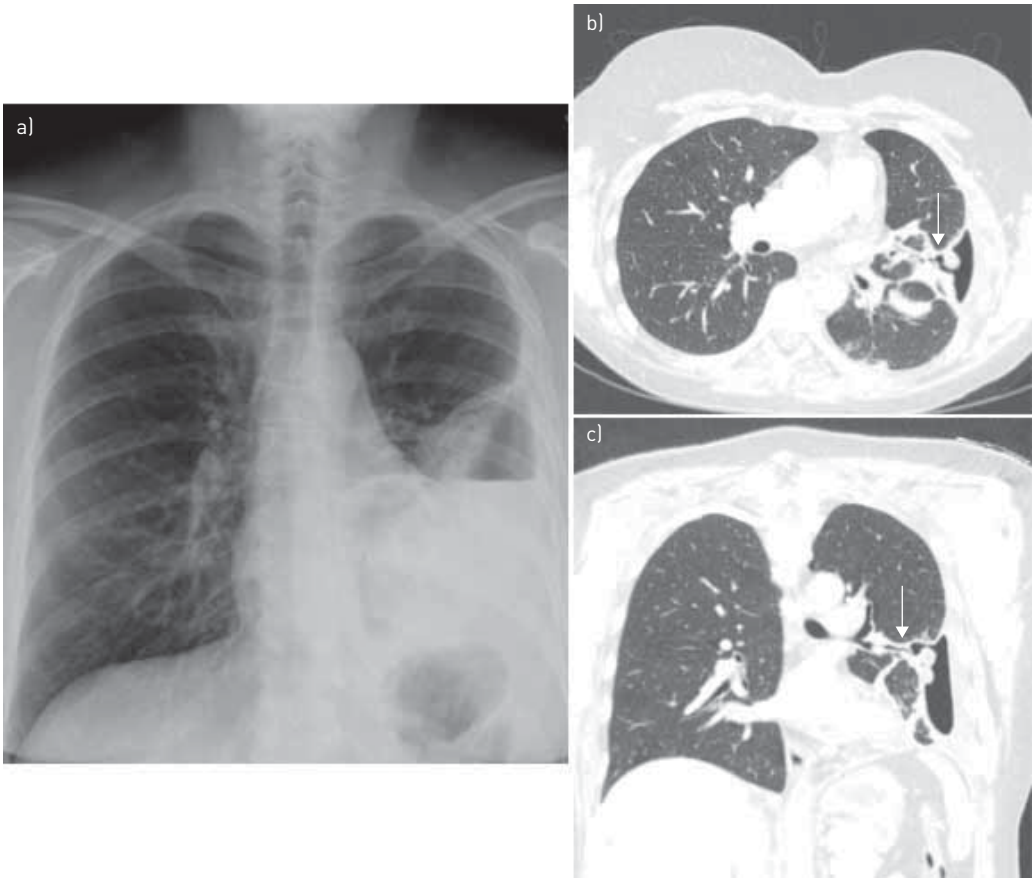

Figure 9. a) Chest radiograph showing an air–fluid level in the left thoracic cavity due to a pyopneumothorax, secondary to a bronchopleural fistula that is best seen on b) and c) the CT scans (arrows).

Pleural thickening

Depending on the clinical context, pleural thickening can be of unknown aetiology and may be identified incidentally on chest radiograph. The associated clinical symptoms may be nonspecific, such as dyspnoea and chest pain, and clinical history is critical to guide investigation into its aetiology. The most common aetiology is in part determined by the epidemiology of the disease in the patient population referred, with prior infection being the cause more commonly reported in some parts of the world and asbestos exposure in others. In the UK and Europe, the most common cause requiring investigation is asbestos-related pleural disease. Nonasbestos aetiologies can be a consequence of infection (tuberculous empyema), previous chest injury (surgery, haemothorax), rheumatoid arthritis, fibrosing pleuritis, post-radiotherapy, drugs and rarer causes, such as Erdheim–Chester disease.

For asbestos-related pleural disease, pleural plaques are the most common manifestation with diffuse visceral pleural thickening less commonly seen. Asbestos-related pleural plaques are the radiographic "calling card" of prior asbestos exposure. Their presence is confirmation of a patient's prior exposure to asbestos. Asbestos exposure resulting in pleural plaque formation characteristically has a long latent period of >20 years [64, 65].

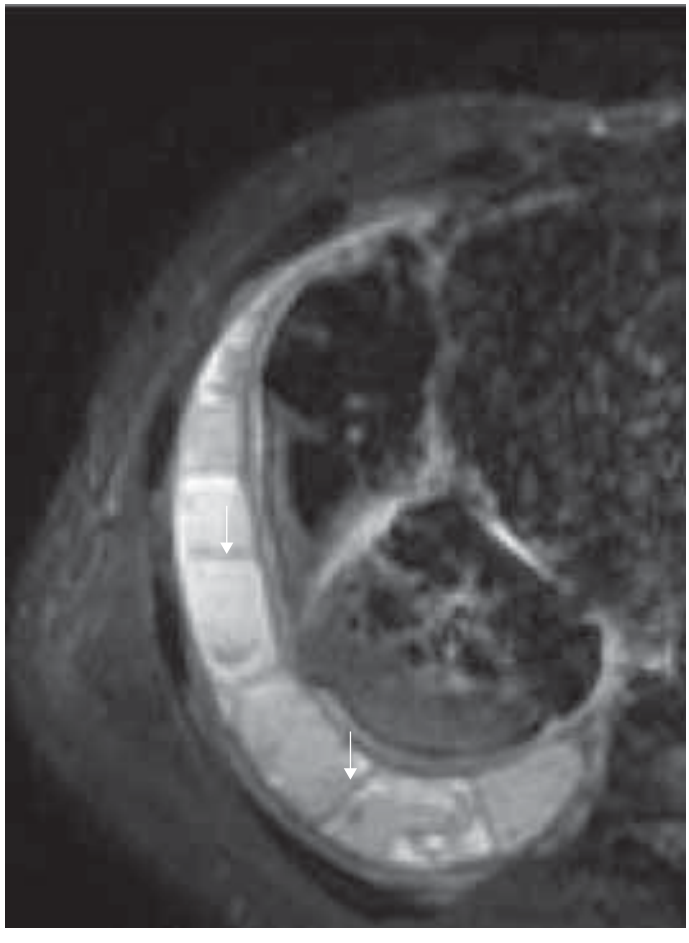

Figure 10. Cross-sectional, T2-weighted MRI of the lungs demonstrating high-signal pleural effusion in the right lung. The septations (arrows) are easily identified on T2 sequences due to their contrast with the high-signal pleural fluid.

Pleural plaques tend to occur in specific places, although as their number increases they become more widespread and may increase in size. They are characteristically seen along the anterior and paravertebral pleural surfaces and on the diaphragmatic pleura. They may be difficult to identify on chest radiograph until they are calcified, and can be mistaken for a possible pulmonary nodule, prompting investigation by CT. Pleural plaques appear on CT as well-defined areas of pleural thickening, with a "rolled edge", that is thicker at the edges than centrally, although smooth-edged plaques are frequently seen on CT. They are distinct from underlying rib and extrapleural fat, separated by a thin layer of fatty tissue. Over time, they can progress in size, shape, thickness and calcification; they may be associated with interstitial parenchymal lines ("hairy plaques") [64–67].

Lynch *et al.* [68] classified pleural plaques according to their CT appearance: 1) minimal pleural plaques, less than 1 mm thick, 1–3 cm long and few in number; 2) moderate pleural plaques, 1–3 mm thick, 2–5 cm long and multiple; 3) severe pleural plaques, thicker than 3 mm, clearly indenting the adjacent lung, up to 8 cm in craniocaudal dimension and extensive in width.

In contradistinction to asbestos-related pleural plaques, diffuse pleural thickening is a disease of the visceral pleura, and may consequently be associated with parenchymal bands (figure 11) and rounded atelectasis (figure 12).

Asbestos-related pleural effusion usually occurs prior to the development of diffuse visceral pleural thickening, and is commonly asymptomatic. The mechanism of injury causing effusion and thickening is from asbestos fibres reaching the pleural cavity and triggering pleuritis, effusion and fibrosis [64, 65]. Fibrosis is initially and mainly in the visceral pleural layer, which progressively becomes attached to the parietal pleural layer. Clinical symptoms are dependent on the severity of diffuse visceral pleural thickening. Unlike diffuse visceral pleural thickening, pleural plaques predominantly affect the parietal pleura [66, 67]. A chest radiograph is usually the first imaging investigation. The diagnosis may be suspected due to increased pleural shadowing, most commonly laterally and basally, possibly with a small pleural effusion, although this is often only identified on a subsequent CT. The pleural thickening may be unilateral or bilateral. The revised 2003 International Labour Office Classification states that diffuse visceral pleural thickening is present only when it is accompanied by and in continuity with an obliterated costophrenic angle [69]. It is the "splinting" of the diaphragm secondary to its involvement along with the adjacent pulmonary disease that may be responsible for the clinical symptoms and abnormal lung function. MSCT is almost invariably performed to confirm or refute the diagnosis of diffuse visceral pleural thickening. It has been shown to have higher sensitivity and be more specific than the plain film in the differentiation of diffuse visceral pleural thickening from extrapleural fat [70, 71]. There are radiographic definitions of diffuse pleural thickening, namely a continuous sheet of pleural thickening >5 cm wide, >8 cm in craniocaudal extent and >3 mm thick. However, it is important to note that this was not a definition for diffuse visceral pleural thickening, an area of frequent confusion in medicolegal cases [68, 72].

In most cases, diffuse visceral pleural thickening is associated with other pulmonary changes: rounded atelectasis, parenchymal bands and areas of focal pulmonary fibrosis. Involvement of the visceral pleura can be confirmed when there is distortion of the adjacent lung with parenchymal bands. In contrast, plaques mostly involve the parietal pleural surface and are not associated with parenchymal bands. Rounded atelectasis (also

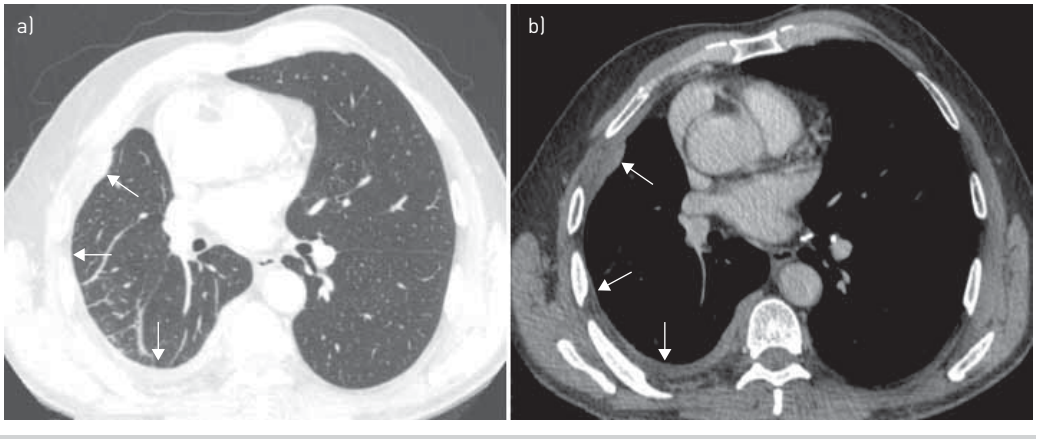

Figure 11. Axial CT chest images of a) the lung window and b) the soft tissue window demonstrating diffuse pleural thickening of the right lung, causing reduced right lung volume and with characteristic parenchymal bands. Note its smooth appearance and that it does not involve the mediastinal pleura.

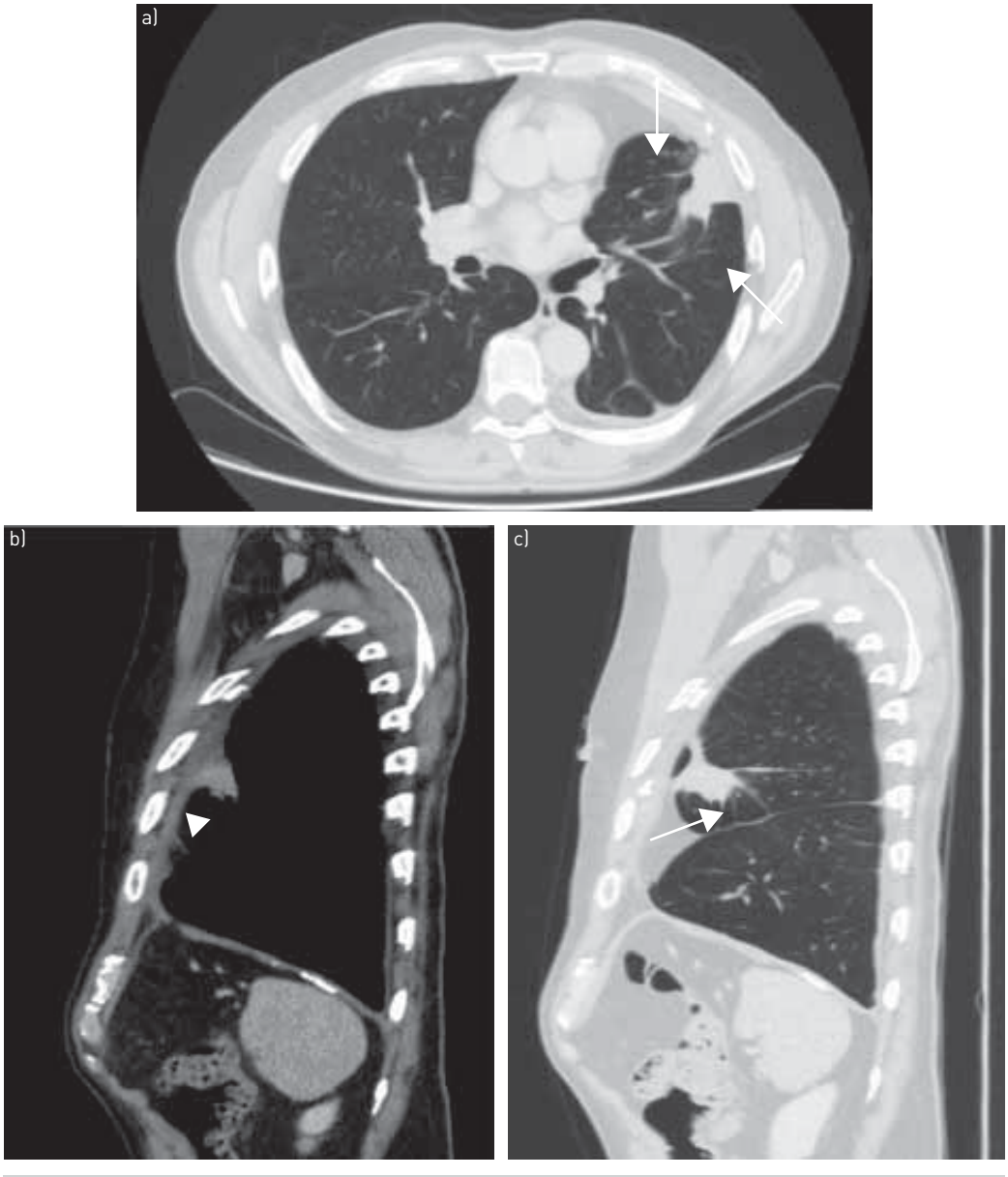

Figure 12. Axial CT on a) the lung window, b) sagittal reconstruction images on the lung window and c) the mediastinal window, showing a 3-cm mass, that is associated with adjacent pleural thickening (arrowhead) and has vessels "swirling" into it (arrows), the so-called "comet tails". This is characteristic of rounded atelectasis. It is important to assess all features and use reconstructions, as on first view on the axial images it may appear to be a potential malignant mass.

known as Blesovsky syndrome or folded lung) is the infolding of the fibrotic visceral pleura accompanied by collapse of the affected area [71]. The rounded atelectasis causes distortion of nearby bronchi and vessels producing a curvilinear opacification, the "comet tail" sign (figure 12) [73]. Parenchymal bands are usually related to moderate pleural fibrosis, in which 2–5-cm linear opacities can be seen between the lung and the pleura [71, 74].

Areas of focal pleural thickening are described as "crow's feet", which are small pleuroparenchymal fibrous bands [75].

Malignant pleural thickening

Metastatic pleural disease

Bronchogenic carcinoma, breast cancer, lymphoma, and gastrointestinal and genitourinary malignancies are the main causes of metastatic disease to the pleura [76]. Contrast-enhanced MSCT is the imaging investigation of choice. The signs of malignant pleural thickening on CT are: parietal pleural thickening >1 cm; nodularity; involvement of the mediastinal pleura; and circumferential thickening (figure 13) [77]. Other findings to consider are rib crowding, a raised hemidiaphragm and an associated pleural effusion. Sampling an associated effusion may provide a positive cytological diagnosis, and should be performed using ultrasound guidance [78]. Ultrasound may also provide diagnostic information in patients with suspected malignant effusion; Qureshi *et al.* [79] demonstrated that involvement of the diaphragm and pleural nodularity provided similar sensitivity and specificity to CT in the diagnosis of malignancy (figure 14).

MRI and PET/CT are not routinely used in the diagnosis or assessment of pleural malignancy. MRI can be useful in the assessment of malignant invasion along the chest wall and diaphragm. Malignant pleural thickening is well depicted on T1-weighted, fat-saturated post-contrast sequences, where it is seen to enhance avidly. On T2-weighted images, malignant pleural thickening will have high signal intensity relative to the surrounding muscle, and be of higher signal than muscle on short tau inversion recovery sequences. The appearances on magnetic resonance correlates well with CT [80]. PET/CT

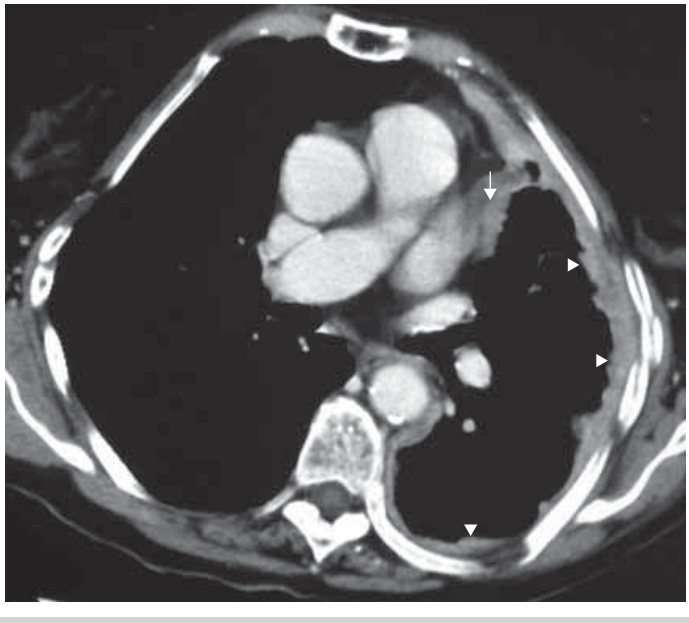

Figure 13. Axial CT chest image showing irregular nodular pleural thickening on the left lung (arrowheads), which extends into the mediastinal pleural surface (arrow).

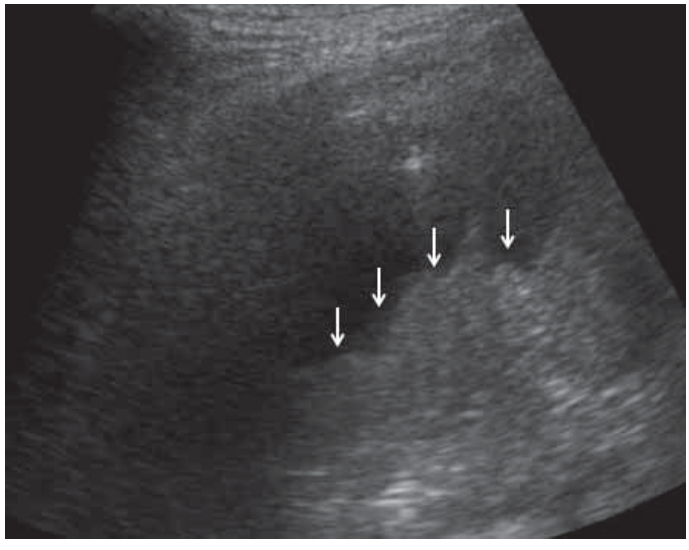

Figure 14. Appearance on ultrasound of irregular markedly thickened pleura (arrows), which is characteristic of malignant pleural thickening and an effusion.

has also been reported to be useful in differentiating benign from malignant disease. These modalities will be discussed in detail in the subsequent section.

Malignant pleural mesothelioma

The majority of patients with malignant pleural mesothelioma (MPM) present with a pleural effusion that is commonly associated with volume loss and pleural nodularity, visible on chest radiograph. Most commonly, MSCT is performed, although the advent of physician-performed ultrasound often enables an ultrasound scan to be performed on the patient's first visit to the clinic or hospital, and has been shown to be of value in detecting pleural nodules and thickening [3, 60, 79, 81]. MSCT can be used to assess nodal and pulmonary involvement, rib invasion and bone metastases if present, and distant metastatic disease. Unfortunately, MSCT is poor at detecting subtle chest wall invasion [82–84]. MRI, with its high soft tissue contrast resolution, may be of value in selected cases for a more precise assessment of local invasion along the chest wall, mediastinum and diaphragm, and further differentiation between T3 and T4 disease [3–5, 9, 85]. On T1-weighted images, tumour deposits can be difficult to detect because they are usually isointense or mildly hyperintense compared to the surrounding muscle. Higher signal difference between tumour and muscle on T2-weighted and proton density-weighted images provide better assessment of local invasion. Gadolinium-based contrast will also produce enhancement of the affected sites [3, 6]. In addition, perfusion MRI using gadolinium can be used to demonstrate tumour vascularity, which has been shown in assessing response to anti-angiogenic agents [86]. More recently, diffusion-weighted imaging has been used to differentiate benign from malignant disease (figure 15) [87, 88]. Diffusion-weighted imaging uses the different movement of water molecules in tissues for their characterisation; malignant tissue tends to be more structured and compact than benign tissue. Differences in signal using diffusion-weighted imaging result in hyperintense speckles, which has been described as "pointillism" after the dot technique used by Neo-Impressionist painters. It has been shown to have ~92% sensitivity and ~86%

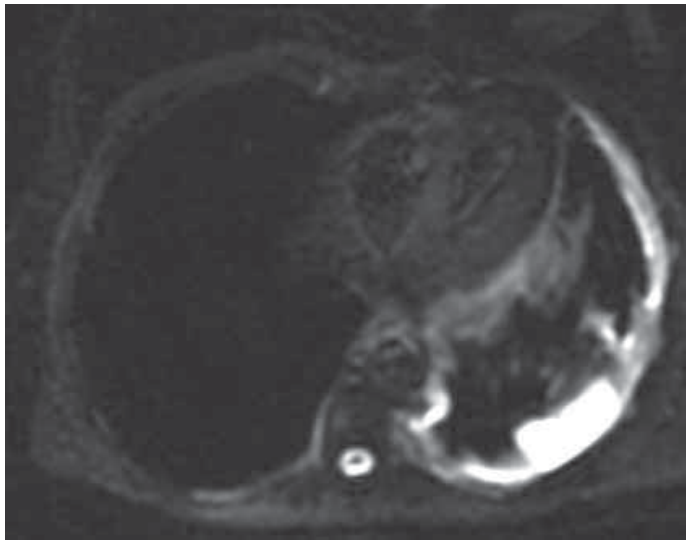

Figure 15. Axial diffusion-weighted magnetic resonance chest image showing high-signal malignant pleural thickening. The appearance is consistent with either malignant pleural mesothelioma or metastatic pleural disease.

specificity in detecting MPM [7, 8, 85]. As with MSCT, its ability to identify malignant nodal involvement is limited [89]. PET/CT appears to be of greater value in detecting nodal involvement in MPM and has additional value in detecting distant metastases (figure 16), assessing disease response and as a prognostic biomarker [17].

As with MRI, PET/CT has been reported to be of value in differentiating benign and malignant disease (figures 17 and 18) with sensitivities of 92–97% and specificities of 75–100% [10–16]. A recent meta-analysis of 16 studies indicated 95% sensitivity and 82% specificity for PET/CT in differentiating between malignant and benign pleural lesions [90]. These figures have to be tempered with the consideration that they include patients in whom there is no difficulty in making the diagnosis on CT; also, its true value in distinguishing benign from malignant disease in patients in whom the diagnosis is uncertain on CT is unknown. PET/CT has been shown to be better than CT alone in staging MPM [17, 91–93], and to impact on treatment decisions (figure 16) [92–94]. Unfortunately, PET/CT may be a source of false-negative results in patients with less aggressive tumours, such as epithelioid MPM, and a source of false-positive results in patients with infectious or inflammatory pleuritis (figure 19) [13, 90, 95–97].

Alongside its diagnostic capabilities, perhaps more important roles for FDG PET/CT are its use as a biomarker and its early assessment of response to therapy. High FDG uptake in MPM is significantly associated with a poor survival [16, 98].

PET/CT imaging of MPM appears to enable a more accurate evaluation of tumour volume and burden. This has been particularly useful in providing prognostic measures to help monitor treatment response [17–19]. Treatment response in MPM is assessed using the modified Response Evaluation Criteria in Solid Tumour (RECIST) [99]. Measurement of disease response is difficult even using the modified RECIST because of alteration of the chest wall morphology secondary to the tumour; there is considerable ongoing work using computer software to help measure tumour volumes before and during therapy more

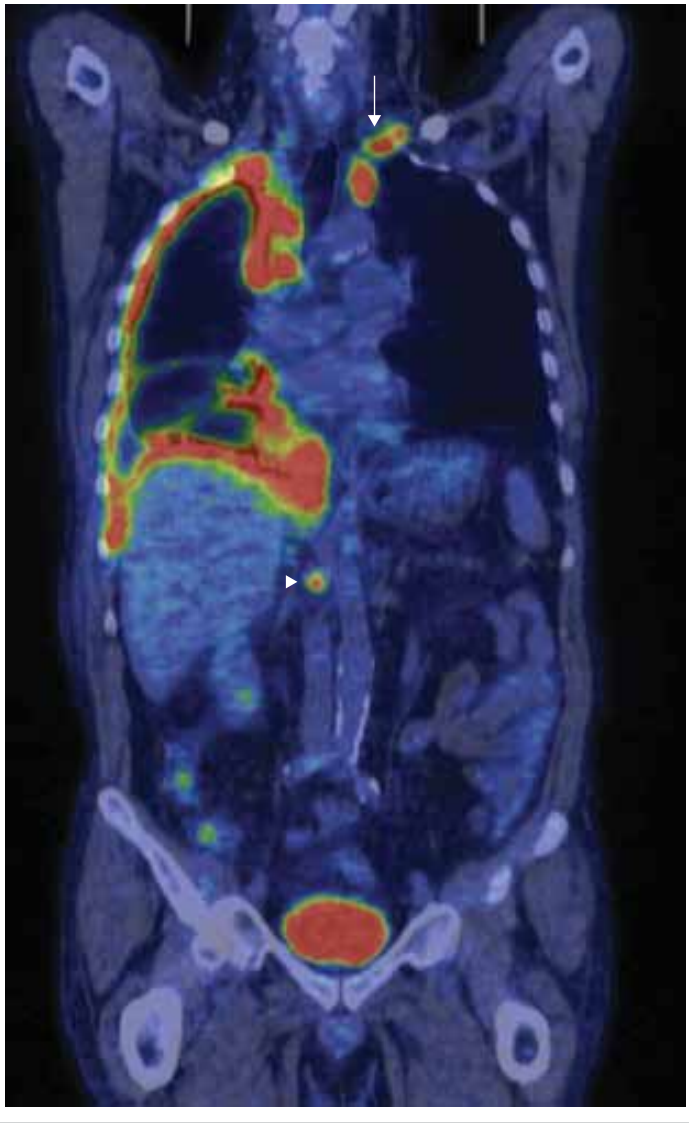

Figure 16. Coronal reconstruction of a PET/CT image in a patient with mesothelioma, showing diffuse pleural and diaphragmatic thickening with elevated FDG uptake on the right. There is left superior mediastinal nodal metastatic disease (arrow), and an FDG-avid metastatic coeliac node (arrowhead).

reliably [100–102]. Studies on several PET measurements of metabolic tumour response, such as the standardised uptake value (SUV_{max}), metabolic tumour volume (MTV) and total glycolytic volume (TGV), have been shown to be of prognostic value in predicting disease progression and survival [103–110]. More recent studies have provided further evidence that MTV, TGV and change in SUV_{max} before and after treatment are strong predictors of disease-free progression and overall survival [111, 112]. In addition, malignant tumours with high SUV and glycolytic volume compared to those with lower metabolic measurements are associated with significantly shorter survival (median survival 9.7 months compared with 21 months; p=0.02) [113]. These PET measurements have also contributed to planning the target volume for radiotherapy and monitoring treatment response. This is particularly useful for identifying areas for radiotherapy in incompletely

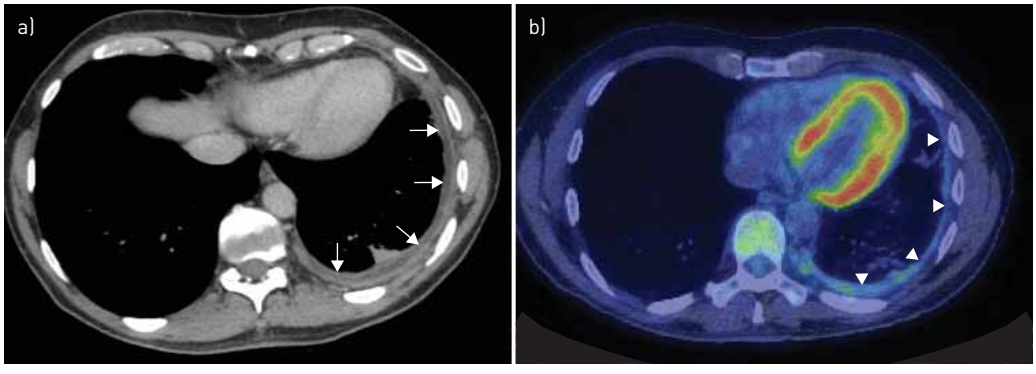

Figure 17. Axial CT image of the chest. a) Diffuse pleural thickening (arrows) of the left lung is consistent with previous asbestos exposure. b) Overlying PET image demonstrates minimal FDG uptake (arrowheads), which excludes malignant disease.

resected disease, in which PET/CT can differentiate tumour from post-operative changes, thereby enabling more targeted radiotherapy [81]. Researchers have also demonstrated that PET/CT detects a metabolic tumour response prior to morphological changes on CT. These findings are associated with improved patient survival and more accurate predictors of survival than CT alone [14, 103, 107, 114–116].

Uncommon and rare pleural tumours

Pleural fibroma or solitary fibrous tumour originates from the visceral pleura. It is usually found incidentally on chest radiograph as a well-defined round pleural mass. Occasionally, it can be pedunculated and change position with respiration. Further assessment with CT will show a homogeneous soft tissue mass, but larger lesions may have a heterogeneous appearance corresponding to calcifications (figure 20) [117]. It has a characteristic appearance post-intravenous contrast on CT, and may be of considerable size at

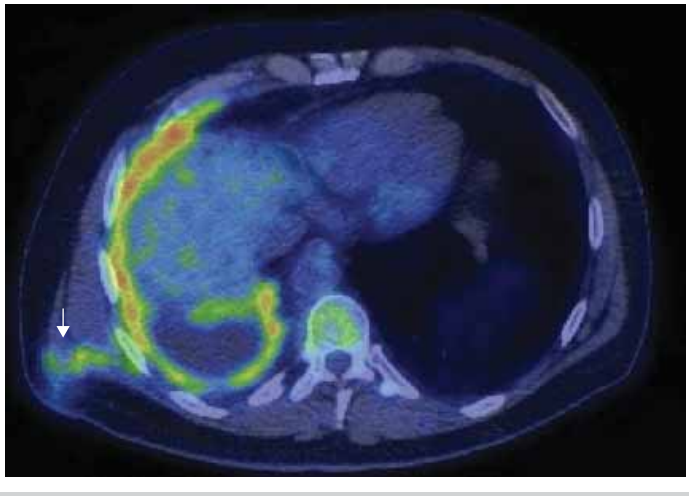

Figure 18. Axial coregistered PET/CT image of the thorax demonstrating increased FDG uptake in the thickened pleura on the right due to mesothelioma, with tumour extension along the drain/thoracoscope site (arrow).

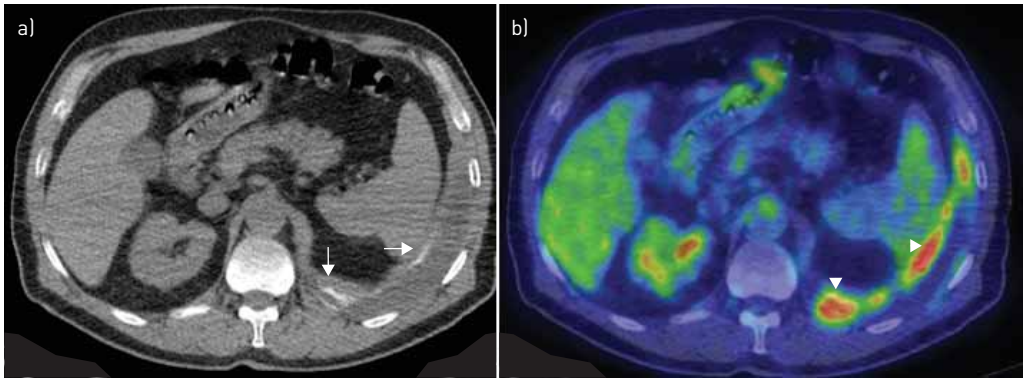

Figure 19. Axial CT of the upper abdomen. a) Left-sided pleural effusion with high attenuation material within it, due to a prior talc pleurodesis (arrows). b) Coregistered PET/CT image indicated elevated FDG uptake due to inflammation from the talc (arrowheads).

presentation as it is for the most part asymptomatic. As they enlarge they tend to develop an extensive collateral circulation from adjacent intercostal and diaphragmatic arteries. These are important to recognise, as they may potentially be embolised prior to resection to reduce surgical blood loss. It is important that the diagnosis is made without biopsy, as larger pleural fibromas may undergo central necrosis and sarcomatous change, and have been reported to develop pleural metastases following percutaneous biopsy. Additionally, it is important that surgical resection is complete, because they may recur if not, and repeat surgery is more complex and less often successful [118–121].

Pleural lipomas are a rare benign pleural tumour, most often discovered incidentally on CT, where they are seen as a homogeneous fatty mass (Hounsfield Unit <−50) with occasional soft tissue stranding [122, 123]. MRI can further confirm their character if needed; they show high signal intensity on T1-weighted images (figure 21) and moderate intensity on T2-weighted images.

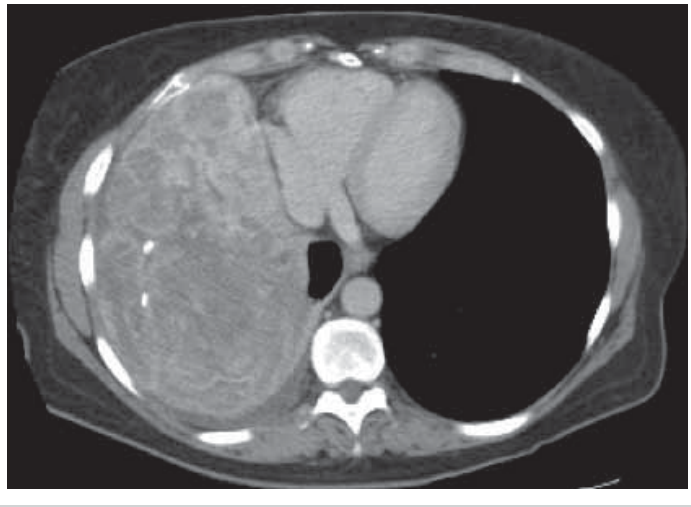

Figure 20. Axial CT chest image showing a heterogeneously enhancing pleural fibroma with areas of calcification, as typically occurs in larger tumours. It occupies a large volume of the right hemithorax; it indents rather than invades the right atrium.

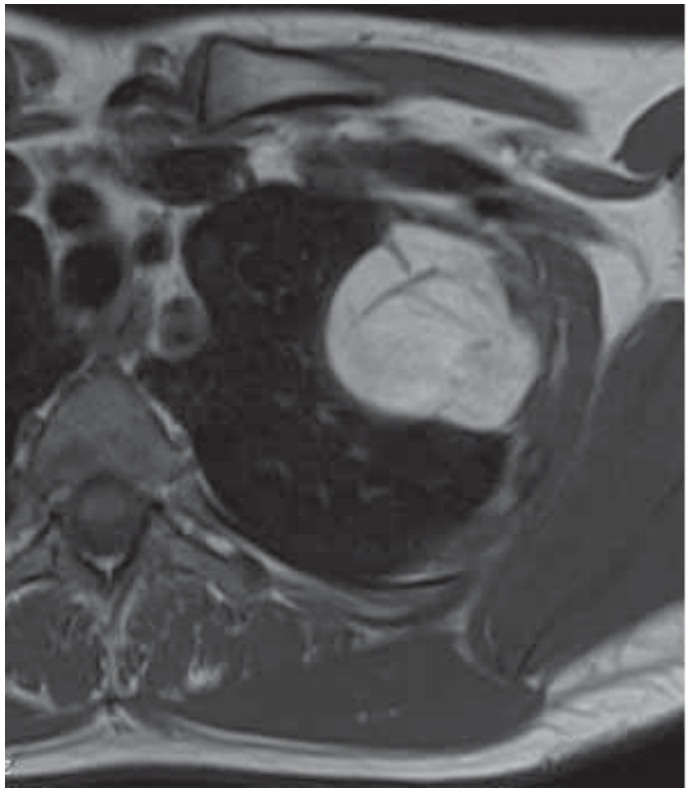

Figure 21. Cross-sectional, T1-weighted MRI image of the chest showing a homogeneous high-signal mass arising from the pleura. The appearance is consistent with a uniform fatty mass indicating a pleural lipoma.

Primary pleural liposarcomas are rare malignant pleural tumours. Patients can present with chest pain or soft tissue swelling due to their extension into the intercostal muscle. CT examination demonstrates a heterogeneous mass with components of fat, fibrous septae and nodular soft tissue [123]. Further assessment with MRI shows low signal intensity on T1-weighting and high intensity on T2-weighting as a result of myxoid degeneration. There is moderate signal intensity on fat suppression sequences.

Conclusion

In the investigation of pleural diseases, a chest radiograph is performed as the initial investigation; however, ultrasound is increasingly used for the detection of pleural nodules and fluid prior to other investigations. MSCT remains the modality of choice for the assessment of benign and malignant pleural conditions. In selected cases, MRI and PET/CT can provide additional findings for disease differentiation, prognosis and response to therapy.

References

1. Hooper C, Laurence I, Harvey J, *et al.* The role of CT pulmonary angiography in the investigation of unilateral pleural effusions. *Respiration* 2014; 87: 26–31.
2. Raj V, Kirke R, Bankart MJ, *et al.* Multidetector CT imaging of pleura: comparison of two contrast infusion protocols. *Br J Radiol* 2011; 84: 796–799.

3. Nickell LT Jr, Lichtenberger JP 3rd, Khorashadi L, *et al.* Multimodality imaging for characterization, classification, and staging of malignant pleural mesothelioma. *Radiographics* 2014; 34: 1692–1706.
4. Patz EF Jr, Shaffer K, Piwnica-Worms DR, *et al.* Malignant pleural mesothelioma: value of CT and MR imaging in predicting resectability. *AJR Am J Roentgenol* 1992; 159: 961–966.
5. Heelan RT, Rusch VW, Begg CB, *et al.* Staging of malignant pleural mesothelioma: comparison of CT and MR imaging. *AJR Am J Roentgenol* 1999; 172: 1039–1047.
6. Truong MT, Viswanathan C, Godoy MB, *et al.* Malignant pleural mesothelioma: role of CT, MRI, and PET/CT in staging evaluation and treatment considerations. *Semin Roentgenol* 2013; 48: 323–334.
7. Coolen J, De Keyzer F, Nafteux P, *et al.* Malignant pleural disease: diagnosis by using diffusion-weighted and dynamic contrast-enhanced MR imaging: initial experience. *Radiology* 2012; 263: 884–892.
8. Gill RR, Umeoka S, Mamata H, *et al.* Diffusion-weighted MRI of malignant pleural mesothelioma: preliminary assessment of apparent diffusion coefficient in histologic subtypes. *AJR Am J Roentgenol* 2010; 195: W125–W130.
9. Coolen J, Verschakelen J, De Wever W. MRI of pleural diseases. *Curr Opin Pulm Med* 2015; 21: 399–406.
10. Bénard F, Sterman D, Smith RJ, *et al.* Metabolic imaging of malignant pleural mesothelioma with fluorodeoxyglucose positron emission tomography. *Chest* 1998; 114: 713–722.
11. Gerbaudo VH, Sugarbaker DJ, Britz-Cunningham S, *et al.* Assessment of malignant pleural mesothelioma with (18)F-FDG dual-head gamma-camera coincidence imaging: comparison with histopathology. *J Nucl Med* 2002; 43: 1144–1149.
12. Kramer H, Pieterman RM, Slebos DJ, *et al.* PET for the evaluation of pleural thickening observed on CT. *J Nucl Med* 2004; 45: 995–998.
13. Duysinx B, Nguyen D, Louis R, *et al.* Evaluation of pleural disease with 18-fluorodeoxyglucose positron emission tomography imaging. *Chest* 2004; 125: 489–493.
14. Carretta A, Landoni C, Melloni G, *et al.* 18-FDG positron emission tomography in the evaluation of malignant pleural diseases: a pilot study. *Eur J Cardiothorac Surg* 2000; 17: 377–383.
15. Bury T, Paulus P, Dowlati A, *et al.* Evaluation of pleural diseases with FDG-PET imaging: preliminary report. *Thorax* 1997; 52: 187–189.
16. Yildirim H, Metintas M, Entok E, *et al.* Clinical value of fluorodeoxyglucose-positron emission tomography/computed tomography in differentiation of malignant mesothelioma from asbestos-related benign pleural disease: an observational pilot study. *J Thorac Oncol* 2009; 4: 1480–1484.
17. van Zandwijk N, Clarke C, Henderson D, *et al.* Guidelines for the diagnosis and treatment of malignant pleural mesothelioma. *J Thorac Dis* 2013; 5: E254–E307.
18. Tsutani Y, Takuwa T, Miyata Y, *et al.* Prognostic significance of metabolic response by positron emission tomography after neoadjuvant chemotherapy for resectable malignant pleural mesothelioma. *Ann Oncol* 2013; 24: 1005–1010.
19. Fuccio C, Spinapolice EG, Ferretti A, *et al.* ^{18}F-FDG-PET/CT in malignant mesothelioma. *Biomed Pharmacother* 2013; 67: 539–542.
20. Schramel FM, Golding RP, Haakman CD, *et al.* Expiratory chest radiographs do not improve visibility of small apical pneumothoraces by enhanced contrast. *Eur Respir J* 1996; 9: 406–409.
21. Gordon R. The deep sulcus sign. *Radiology* 1980; 136: 25–27.
22. Henry M, Arnold T, Harvey J. BTS guidelines for the management of spontaneous pneumothorax. *Thorax* 2003; 58: Suppl. 2, 39–52.
23. Baumann MH, Strange C, Heffner JE, *et al.* Management of spontaneous pneumothorax: an American College of Chest Physicians Delphi consensus statement. *Chest* 2001; 119: 590–602.
24. Vix VA. Roentgenographic recognition of pleural effusion. *JAMA* 1974; 229: 695–698.
25. Schwarz MI, Marmorstein BL. A new radiologic sign of subpulmonic effusion. *Chest* 1975; 67: 176–178.
26. Petersen JA. Recognition of infrapulmonary pleural effusion. *Radiology* 1960; 74: 34–41.
27. Ruskin JA, Gurney JW, Thorsen MK, *et al.* Detection of pleural effusions on supine chest radiographs. *AJR Am J Roentgenol* 1987; 148: 681–683.
28. Möller A. Pleural effusion. Use of the semi-supine position for radiographic detection. *Radiology* 1984; 150: 245–249.
29. Hessen I. Roentgen examination of pleural fluid; a study of the localization of free effusions, the potentialities of diagnosing minimal quantities of fluid and its existence under physiological conditions. *Acta Radiol Suppl* 1951; 86: 1–80.
30. Weiss W, Boucot KR, Gefter WI. Localized interlobar effusion in congestive heart failure. *Ann Intern Med* 1953; 38: 1177–1186.
31. Feder BH, Wilk SP. Localized interlobar effusion in heart failure; phantom lung tumor. *Dis Chest* 1956; 30: 289–297.
32. Oestreich AE, Haley C. Pleural effusion: the thorn sign. Not a rare finding. *Chest* 1981; 79: 365–366.

33. Chen HJ, Tu CY, Ling SJ, *et al.* Sonographic appearances in transudative pleural effusions: not always an anechoic pattern. *Ultrasound Med Biol* 2008; 34: 362–369.
34. Yang PC, Luh KT, Chang DB, *et al.* Value of sonography in determining the nature of pleural effusion: analysis of 320 cases. *AJR Am J Roentgenol* 1992; 159: 29–33.
35. Lomas DJ, Padley SG, Flower CD. The sonographic appearances of pleural fluid. *Br J Radiol* 1993; 66: 619–624.
36. Brutsche MH, Tassi GF, Györik S, *et al.* Treatment of sonographically stratified multiloculated thoracic empyema by medical thoracoscopy. *Chest* 2005; 128: 3303–3309.
37. Salamonsen MR, Lo AK, Ng AC, *et al.* Novel use of pleural ultrasound can identify malignant entrapped lung prior to effusion drainage. *Chest* 2014; 146: 1286–1293.
38. Zhu Z, Donnelly E, Dikensoy O, *et al.* Efficacy of ultrasound in the diagnosis of pleurodesis in rabbits. *Chest* 2005; 128: 934–939.
39. Andrews NC, Parker EF, Shaw RR, *et al.* Management of non-tuberculous empyema: a statement of the subcommittee on surgery from American Thoracic Society. *Am Rev Respir Dis* 1962; 85: 935–936.
40. Grove CS, Lee YC. Vascular endothelial growth factor: the key mediator in pleural effusion formation. *Curr Opin Pulm Med* 2002; 8: 294–301.
41. Chung CL, Chen CH, Sheu JR, *et al.* Proinflammatory cytokines, transforming growth factor-beta1, and fibrinolytic enzymes in loculated and free-flowing pleural exudates. *Chest* 2005; 128: 690–697.
42. Alemán C, Alegre J, Monasterio J, *et al.* Association between inflammatory mediators and the fibrinolysis system in infectious pleural effusions. *Clin Sci (Lond)* 2003; 105: 601–607.
43. Sasse SA, Jadus MR, Kukes GD. Pleural fluid transforming growth factor-beta1 correlates with pleural fibrosis in experimental empyema. *Am J Respir Crit Care Med* 2003; 168: 700–705.
44. Chen CH, Chen W, Chen HJ, *et al.* Transthoracic ultrasonography in predicting the outcome of small-bore catheter drainage in empyemas or complicated parapneumonic effusions. *Ultrasound Med Biol* 2009; 35: 1468–1474.
45. Davies HE, Davies RJ, Davies CW. Management of pleural infection in adults: British Thoracic Society Pleural Disease Guideline 2010. *Thorax* 2010; 65: Suppl. 2, 41–53.
46. Maskell NA, Gleeson FV, Davies RJ. Standard pleural biopsy *versus* CT-guided cutting-needle biopsy for diagnosis of malignant disease in pleural effusions: a randomised controlled trial. *Lancet* 2003; 361: 1326–1330.
47. Adams RF, Gray W, Davies RJ, *et al.* Percutaneous image-guided cutting needle biopsy of the pleura in the diagnosis of malignant mesothelioma. *Chest* 2001; 120: 1798–1802.
48. Kraus GJ. The split pleura sign. *Radiology* 2007; 243: 297–298.
49. Stark DD, Federle MP, Goodman PC, *et al.* Differentiating lung abscess and empyema: radiography and computed tomography. *AJR Am J Roentgenol* 1983; 141: 163–167.
50. Waite RJ, Carbonneau RJ, Balikian JP, *et al.* Parietal pleural changes in empyema: appearances at CT. *Radiology* 1990; 175: 145–150.
51. Aquino SL, Webb WR, Gushiken BJ. Pleural exudates and transudates: diagnosis with contrast-enhanced CT. *Radiology* 1994; 192: 803–808.
52. Takasugi JE, Godwin JD, Teefey SA. The extrapleural fat in empyema: CT appearance. *Br J Radiol* 1991; 64: 580–583.
53. Kearney SE, Davies CW, Tattersall DJ, *et al.* The characteristics and significance of thoracic lymphadenopathy in parapneumonic effusion and empyema. *Br J Radiol* 2000; 73: 583–587.
54. McLoud TC. CT and MR in pleural disease. *Clin Chest Med* 1998; 19: 261–276.
55. Hanna JW, Reed JC, Choplin RH. Pleural infections: a clinical-radiologic review. *J Thorac Imaging* 1991; 6: 68–79.
56. Sahn SA, Iseman MD. Tuberculous empyema. *Semin Respir Infect* 1999; 14: 82–87.
57. Hulnick DH, Naidich DP, McCauley DI. Pleural tuberculosis evaluated by computed tomography. *Radiology* 1983; 149: 759–765.
58. Bhatt GM, Austin HM. CT demonstration of empyema necessitatis. *J Comput Assist Tomogr* 1985; 9: 1108–1109.
59. Glicklich M, Mendelson DS, Gendal ES, *et al.* Tuberculous empyema necessitatis. Computed tomography findings. *Clin Imaging* 1990; 14: 23–25.
60. Qureshi NR, Gleeson FV. Imaging of pleural disease. *Clin Chest Med* 2006; 27: 193–213.
61. Davis SD, Henschke CI, Yankelevitz DF, *et al.* MR imaging of pleural effusions. *J Comput Assist Tomogr* 1990; 14: 192–198.
62. Baysal T, Bulut T, Gökirmak M, *et al.* Diffusion-weighted MR imaging of pleural fluid: differentiation of transudative *vs* exudative pleural effusions. *Eur Radiol* 2004; 14: 890–896.
63. Inan N, Arslan A, Akansel G, *et al.* Diffusion-weighted MRI in the characterization of pleural effusions. *Diagn Interv Radiol* 2009; 15: 13–18.
64. Nishimura SL, Broaddus VC. Asbestos-induced pleural disease. *Clin Chest Med* 1998; 19: 311–329.

65. Hillerdal G. The pathogenesis of pleural plaques and pulmonary asbestosis: possibilities and impossibilities. *Eur J Respir Dis* 1980; 61: 129–138.
66. Yates DH, Browne K, Stidolph PN, *et al.* Asbestos-related bilateral diffuse pleural thickening: natural history of radiographic and lung function abnormalities. *Am J Respir Crit Care Med* 1996; 153: 301–306.
67. Rudd RM. New developments in asbestos-related pleural disease. *Thorax* 1996; 51: 210–216.
68. Lynch DA, Gamsu G, Aberle DR. Conventional and high resolution computed tomography in the diagnosis of asbestos-related diseases. *Radiographics* 1989; 9: 523–551.
69. International Labour Organization. ILO International Classification of Radiographs of Pneumoconioses. Geneva, International Labour Organization, 2003.
70. Selikoff IJ. The occurrence of pleural calcification among asbestos insulation workers. *Ann N Y Acad Sci* 1965; 132: 351–367.
71. American Thoracic Society. Diagnosis and initial management of nonmalignant diseases related to asbestos. *Am J Respir Crit Care Med* 2004; 170: 691–715.
72. Remy-Jardin M, Sobaszek A, Duhamel A, *et al.* Asbestos-related pleuropulmonary diseases: evaluation with low-dose four-detector row spiral CT. *Radiology* 2004; 233: 182–190.
73. Partap VA. The comet tail sign. *Radiology* 1999; 213: 553–554.
74. Gevenois PA, de Maertelaer V, Madani A, *et al.* Asbestosis, pleural plaques and diffuse pleural thickening: three distinct benign responses to asbestos exposure. *Eur Respir J* 1998; 11: 1021–1027.
75. Smith KA, Sykes LJ, McGavin CR. Diffuse pleural fibrosis: an unreliable indicator of heavy asbestos exposure? *Scand J Work Environ Health* 2003; 29: 60–63.
76. Neragi-Miandoab S. Malignant pleural effusion, current and evolving approaches for its diagnosis and management. *Lung Cancer* 2006; 54: 1–9.
77. Leung AN, Müller NL, Miller RR. CT in differential diagnosis of diffuse pleural disease. *AJR Am J Roentgenol* 1990; 154: 487–492.
78. Cheng S, Mohammed TL. Metastatic disease to the lungs and pleura: an overview. *Semin Roentgenol* 2013; 48: 335–343.
79. Qureshi NR, Rahman NM, Gleeson FV. Thoracic ultrasound in the diagnosis of malignant pleural effusion. *Thorax* 2009; 64: 139–143.
80. Plathow C, Klopp M, Thieke C, *et al.* Therapy response in malignant pleural mesothelioma: role of MRI using RECIST, modified RECIST and volumetric approaches in comparison with CT. *Eur Radiol* 2008; 18: 1635–1643.
81. Armato SG 3rd, Labby ZE, Coolen J, *et al.* Imaging in pleural mesothelioma: a review of the 11th International Conference of the International Mesothelioma Interest Group. *Lung Cancer* 2013; 82: 190–196.
82. Kruse M, Sherry SJ, Paidpally V, *et al.* FDG PET/CT in the management of primary pleural tumors and pleural metastases. *AJR Am J Roentgenol* 2013; 201: W215–W226.
83. Corson N, Sensakovic WF, Straus C, *et al.* Characterization of mesothelioma and tissues present in contrast-enhanced thoracic CT scans. *Med Phys* 2011; 38: 942–947.
84. Gopar-Nieto R, Aguilar-Madrid G, Sotelo-Martínez L, *et al.* Malignant pleural mesothelioma: accuracy of CT against immunohistochemical test among the Mexican population. *Arch Med Res* 2015; 46: 107–111.
85. Coolen J, De Keyzer F, Nafteux P, *et al.* Malignant pleural mesothelioma: visual assessment by using pleural pointillism at diffusion-weighted MR imaging. *Radiology* 2015; 274: 576–584.
86. Hylton N. Dynamic contrast-enhanced magnetic resonance imaging as an imaging biomarker. *J Clin Oncol* 2006; 24: 3293–3298.
87. Koh DM, Blackledge M, Padhani AR, *et al.* Whole-body diffusion-weighted MRI: tips, tricks, and pitfalls. *AJR Am J Roentgenol* 2012; 199: 252–262.
88. Koh DM, Collins DJ. Diffusion-weighted MRI in the body: applications and challenges in oncology. *AJR Am J Roentgenol* 2007; 188: 1622–1635.
89. Knuuttila A, Halme M, Kivisaari L, *et al.* The clinical importance of magnetic resonance imaging *versus* computed tomography in malignant pleural mesothelioma. *Lung Cancer* 1998; 22: 215–225.
90. Treglia G, Sadeghi R, Annunziata S, *et al.* Diagnostic accuracy of 18F-FDG-PET and PET/CT in the differential diagnosis between malignant and benign pleural lesions: a systematic review and meta-analysis. *Acad Radiol* 2014; 21: 11–20.
91. Mavi A, Basu S, Cermik TF, *et al.* Potential of dual time point FDG-PET imaging in differentiating malignant from benign pleural disease. *Mol Imaging Biol* 2009; 11: 369–378.
92. Erasmus JJ, Truong MT, Smythe WR, *et al.* Integrated computed tomography-positron emission tomography in patients with potentially resectable malignant pleural mesothelioma: staging implications. *J Thorac Cardiovasc Surg* 2005; 129: 1364–1370.
93. Ambrosini V, Rubello D, Nanni C, *et al.* Additional value of hybrid PET/CT fusion imaging *vs*. conventional CT scan alone in the staging and management of patients with malignant pleural mesothelioma. *Nucl Med Rev Cent East Eur* 2005; 8: 111–115.

94. Wilcox BE, Subramaniam RM, Peller PJ, *et al.* Utility of integrated computed tomography-positron emission tomography for selection of operable malignant pleural mesothelioma. *Clin Lung Cancer* 2009; 10: 244–248.
95. Treglia G, Sadeghi R, Annunziata S, *et al.* Diagnostic performance of fluorine-18-fluorodeoxyglucose positron emission tomography in the assessment of pleural abnormalities in cancer patients: a systematic review and a meta-analysis. *Lung Cancer* 2014; 83: 1–7.
96. Spitilli MG, Treglia G, Calcagni ML, *et al.* Malignant pleural mesothelioma: utility of 18 F-FDG PET. *Ann Ital Chir* 2007; 78: 393–396.
97. Roca E, Laroumagne S, Vandemoortele T, *et al.* 18F-fluoro-2-deoxy-d-glucose positron emission tomography/computed tomography fused imaging in malignant mesothelioma patients: looking from outside is not enough. *Lung Cancer* 2013; 79: 187–190.
98. Yamamuro M, Gerbaudo VH, Gill RR, *et al.* Morphologic and functional imaging of malignant pleural mesothelioma. *Eur J Radiol* 2007; 64: 356–366.
99. Byrne MJ, Nowak AK. Modified RECIST criteria for assessment of response in malignant pleural mesothelioma. *Ann Oncol* 2004; 15: 257–260.
100. Liu F, Zhao B, Krug LM, *et al.* Assessment of therapy responses and prediction of survival in malignant pleural mesothelioma through computer-aided volumetric measurement on computed tomography scans. *J Thorac Oncol* 2010; 5: 879–884.
101. Labby ZE, Straus C, Caligiuri P, *et al.* Variability of tumor area measurements for response assessment in malignant pleural mesothelioma. *Med Phys* 2013; 40: 081916.
102. Armato SG 3rd, Nowak AK, Francis RJ, *et al.* Observer variability in mesothelioma tumor thickness measurements: defining minimally measurable lesions. *J Thorac Oncol* 2014; 9: 1187–1194.
103. Francis RJ, Byrne MJ, van der Schaaf AA, *et al.* Early prediction of response to chemotherapy and survival in malignant pleural mesothelioma using a novel semiautomated 3-dimensional volume-based analysis of serial 18F-FDG PET scans. *J Nucl Med* 2007; 48: 1449–1458.
104. Flores RM, Akhurst T, Gonen M, *et al.* Positron emission tomography defines metastatic disease but not locoregional disease in patients with malignant pleural mesothelioma. *J Thorac Cardiovasc Surg* 2003; 126: 11–16.
105. Krüger S, Pauls S, Mottaghy FM, *et al.* Integrated FDG PET-CT imaging improves staging in malignant pleural mesothelioma. *Nuklearmedizin* 2007; 46: 239–243.
106. Gerbaudo VH, Mamede M, Trotman-Dickenson B, *et al.* FDG PET/CT patterns of treatment failure of malignant pleural mesothelioma: relationship to histologic type, treatment algorithm, and survival. *Eur J Nucl Med Mol Imaging* 2011; 38: 810–821.
107. Veit-Haibach P, Schaefer NG, Steinert HC, *et al.* Combined FDG-PET/CT in response evaluation of malignant pleural mesothelioma. *Lung Cancer* 2010; 67: 311–317.
108. Lee HY, Hyun SH, Lee KS, *et al.* Volume-based parameter of 18)F-FDG PET/CT in malignant pleural mesothelioma: prediction of therapeutic response and prognostic implications. *Ann Surg Oncol* 2010; 17: 2787–2794.
109. Nowak AK, Francis RJ, Phillips MJ, *et al.* A novel prognostic model for malignant mesothelioma incorporating quantitative FDG-PET imaging with clinical parameters. *Clin Cancer Res* 2010; 16: 2409–2417.
110. Abakay A, Komek H, Abakay O, *et al.* Relationship between 18 FDG PET-CT findings and the survival of 177 patients with malignant pleural mesothelioma. *Eur Rev Med Pharmacol Sci* 2013; 17: 1233–1241.
111. Klabatsa A, Chicklore S, Barrington SF, *et al.* The association of 18F-FDG PET/CT parameters with survival in malignant pleural mesothelioma. *Eur J Nucl Med Mol Imaging* 2014; 41: 276–282.
112. Lopci E, Zucali PA, Ceresoli GL, *et al.* Quantitative analyses at baseline and interim PET evaluation for response assessment and outcome definition in patients with malignant pleural mesothelioma. *Eur J Nucl Med Mol Imaging* 2015; 42: 667–675.
113. Sharif S, Zahid I, Routledge T, *et al.* Does positron emission tomography offer prognostic information in malignant pleural mesothelioma? *Interact Cardiovasc Thorac Surg* 2011; 12: 806–811.
114. Feigen M, Lee ST, Lawford C, *et al.* Establishing locoregional control of malignant pleural mesothelioma using high-dose radiotherapy and (18) F-FDG PET/CT scan correlation. *J Med Imaging Radiat Oncol* 2011; 55: 320–332.
115. Pehlivan B, Topkan E, Onal C, *et al.* Comparison of CT and integrated PET-CT based radiation therapy planning in patients with malignant pleural mesothelioma. *Radiat Oncol* 2009; 4: 35.
116. Ceresoli GL, Chiti A, Zucali PA, *et al.* Early response evaluation in malignant pleural mesothelioma by positron emission tomography with [18F]fluorodeoxyglucose. *J Clin Oncol* 2006; 24: 4587–4593.
117. Chong S, Kim TS, Cho EY, *et al.* Benign localized fibrous tumour of the pleura: CT features with histopathological correlations. *Clin Radiol* 2006; 61: 875–882.
118. de Perrot M, Fischer S, Bründler MA, *et al.* Solitary fibrous tumors of the pleura. *Ann Thorac Surg* 2002; 74: 285–293.

119. Magdeleinat P, Alifano M, Petino A, *et al.* Solitary fibrous tumors of the pleura: clinical characteristics, surgical treatment and outcome. *Eur J Cardiothorac Surg* 2002; 21: 1087–1093.
120. Sung SH, Chang JW, Kim J, *et al.* Solitary fibrous tumors of the pleura: surgical outcome and clinical course. *Ann Thorac Surg* 2005; 79: 303–307.
121. Boddaert G, Guiraudet P, Grand B, *et al.* Solitary fibrous tumors of the pleura: a poorly defined malignancy profile. *Ann Thorac Surg* 2015; 99: 1025–1031.
122. Gaerte SC, Meyer CA, Winer-Muram HT, *et al.* Fat-containing lesions of the chest. *Radiographics* 2002; 22: Spec No, S61–S78.
123. Munk PL, Lee MJ, Janzen DL, *et al.* Lipoma and liposarcoma: evaluation using CT and MR imaging. *AJR Am J Roentgenol* 1997; 169: 589–594.

Disclosures: None declared.

Pneumonia and acute respiratory distress syndrome

Caron S. Parsons[1] and Emma J. Helm[2]

Radiology has an essential role in the diagnosis, characterisation, management and follow-up of both pneumonia and acute respiratory distress syndrome (ARDS). When imaging is used in conjunction with clinical and laboratory findings, the differential list can be significantly reduced. In the majority of cases, chest radiography provides more than adequate information to manage the patient with pneumonia or ARDS appropriately; however, CT is useful when there is a discrepancy between clinical findings and radiographic findings or when the patient fails to respond to empirical therapies. CT also has a particular role trying to optimise ventilation strategies in the patient with ARDS.

In the European Union, approximately 3 370 000 cases of community-acquired pneumonia (CAP) are expected annually and about 1 million are hospitalised [1]. In 2011, the direct cost of pneumonia and acute lower respiratory tract infections in Europe was €2.5 billion [2]. Imaging plays a crucial role in the detection, management and follow-up of patients with pneumonia [3]. The chest radiograph provides adequate information for the majority of patients with pneumonia; however, an increasing number of patients now undergo CT, particularly in the presence of a normal or equivocal chest radiograph.

Acute respiratory distress syndrome (ARDS) represents a spectrum of lung disease characterised by the sudden onset of inflammatory pulmonary oedema secondary to a wide range of local or systemic insults. ARDS is responsible for approximately 5% of hospitalised, mechanically ventilated patients [4].

In this chapter, we summarise the main imaging findings of pneumonia and ARDS. We focus on the features that may help to distinguish the wide range of aetiological organisms that cause pneumonia and discuss the best imaging approach for ARDS and pneumonia.

Pneumonia

Pneumonia is defined as infection of the lower respiratory tract and lung parenchyma, resulting in a clinical presentation of fever, cough, dyspnoea and malaise. It is a significant

[1]Warwick Medical School, University of Warwick, Coventry, UK. [2]University Hospitals Coventry and Warwickshire, Coventry, UK.

Correspondence: Emma J. Helm, University Hospital Coventry and Warwickshire, Clifford Bridge Road, Coventry, CV2 2DX, UK. E-mail: emma.helm@uhcw.nhs.uk

Copyright ©ERS 2015. Print ISBN: 978-1-84984-065-1. Online ISBN: 978-1-84984-066-8. Print ISSN: 2312-508X. Online ISSN: 2312-5098.

cause of morbidity and mortality. In 2010, lower respiratory tract infections were ranked as the fourth most common cause of death across the globe, and the ninth in Western Europe [5]. CAP refers to pneumonia acquired outside of hospitals or healthcare facilities [6]. Nosocomial pneumonia (NP) is defined as infection that occurs 48 h after hospital admission or within 48 h of discharge from hospital [7]. Ventilator-associated pneumonia (VAP) is defined as pulmonary infection not present at the time of commencement of mechanical ventilation [8].

Choice of imaging modality

Imaging plays an important role in the diagnosis, characterisation, management and follow-up of pneumonia. Diagnostic yield is improved with the addition of clinical and microbiological features [3].

Radiography

Radiography remains the initial imaging modality of choice for the assessment of the patient with suspected pneumonia due to its wide availability, reasonable sensitivity, low cost and low radiation dose. A chest radiograph is recommended by both the American Thoracic Society (ATS) and British Thoracic Society (BTS) in the initial evaluation of hospital-acquired pneumonia [9, 10]. In addition, the BTS recommends a chest radiograph for patients in the community, where the diagnosis is in doubt, where progress following treatment is unsatisfactory or where there is suspicion of an underlying pathology, such as lung cancer [11].

The diagnosis of pneumonia is based on several clinical criteria, but it is essential to demonstrate the presence of a pulmonary infiltrate on imaging [12, 13]. Some caution must be exercised in patients with suspected pneumonia as several studies have demonstrated only moderate interobserver agreement in the diagnosis of CAP [14], with only fair agreement in intensive care unit (ICU) patients [15]. In NP, the radiographic appearance of a pulmonary infiltrate may be delayed in neutropenia, uraemia, diabetes and alcoholism [16, 17]. Further roles of chest radiography include detecting complications and monitoring disease at follow-up.

Adverse features and complications on the chest radiograph

Radiographic abnormalities, such as cavitation, pleural effusion, hilar or mediastinal lymphadenopathy, volume loss and failure of infiltrates to resolve, are all features that merit consideration of the possibility of atypical organisms, tuberculosis (TB), empyema, abscess, underlying tumour or lymphoma. Table 1 describes the relative frequency of different radiographic findings according to some of the more common bacterial pathogens.

Follow-up with a chest radiograph

Radiological recovery from pneumonia lags behind clinical recovery and slow resolution is more marked in cases of *Legionella* pneumonia, which can take up to 6 months to clear completely. Streptococcal pneumonia typically takes 3–5 months to resolve completely [18]. Other factors that may contribute to slow resolution include increased age and multilobar involvement. Guidelines for CAP recommend a follow-up chest radiograph at 6 weeks for patients with persisting signs or symptoms, patients >50 years of age and for smokers [11]. Other authors suggest waiting 12–14 weeks before investigating nonresolving pneumonia [19].

Table 1. Typical and additional features of bacterial pneumonia

Organism	Typical pattern on chest radiograph	Cavitation	Pleural effusion	Abscess/ empyema	Lymphadenopathy	Special features
Streptococcus	Focal or lobar consolidation	– If present consider *Pseudomonas*	++	–	–	Air bronchograms
Mycoplasma	Bronchopneumonia	–	+	–	++ (children) – (adults)	Extrapulmonary involvement: arthralgia, myalgia
Legionella	Single focus or multifocal consolidation	–	+	–	+	Slow radiological resolution
Klebsiella	Focal or lobar consolidation	+	+++	+	–	Expanded lobe and bulging fissures
Pseudomonas	Bronchopneumonia	++	+	–	–	
Staphylococcus	Bronchopneumonia	+	++	++	–	

The approximate frequency of findings is as follows. –: rare; +: <25%; ++: 25–50%; +++: >50%.

Computed tomography

CT provides excellent delineation of the distribution of pulmonary findings, and is the most sensitive modality for depicting parenchymal infection [20]. In a retrospective review of emergency department patients who had an eventual diagnosis of pneumonia, CT demonstrated pneumonia in 27% of patients with a normal or nondiagnostic chest radiograph [21]. More patients are undergoing chest CT when there is a high index of suspicion of pneumonia in the setting of normal or equivocal radiographic findings [22–26]. CT often provides significant additional findings; in a study of emergency department immunocompetent patients who underwent both a chest radiograph and CT for investigation of CAP, 16% had additional or alternative findings, including pulmonary embolism and lung cancer. An additional 8% were diagnosed with pulmonary TB [27].

Although certain features, such as centrilobular nodules are more common in *Mycoplasma*, viral and fungal pneumonias, CT has little to add to the differential diagnosis of the various bacterial types of pneumonia [28]. Despite this, CT does have a role in the differentiation of infectious from noninfectious causes of acute parenchymal abnormality, such as asymmetric cardiac pulmonary oedema, pulmonary embolism, cryptogenic organising pneumonia and pulmonary haemorrhage [3].

In the setting of NP, VAP or opportunistic infection, CT has a role in guiding the clinician as to which lobes to sample if bronchoscopy is being used to obtain microbiological samples.

Magnetic resonance imaging

There has been growing interest in the use of MRI as an alternative imaging method of lung parenchyma [29–32]. Although MRI is more time-consuming and costly than CT, there is still considerable interest in its use due to its lack of ionising radiation [24], particularly in the paediatric and young adult populations [33].

Imaging quality is limited by the low signal intensity of the normal aerated lung with its low proton density and susceptibility artefact from multiple air–tissue interfaces [34]. Breathing and cardiac motion are significant limiting factors. However, pathological tissue has an increased proton density due to exudative accumulation of water and cells, which reduces the amount of air in the alveoli and airways, thereby decreasing the susceptibility artefact [35]. Image quality has been improved by using T2-weighted turbo spin echo sequences [36]. In a study of 16 patients with pneumonia, MRI was able to demonstrate the same quantity and morphology of abnormalities as CT in 75% of patients. MRI demonstrated features such as cavitation, air crescents, reticular infiltrates, ground-glass opacity and consolidation. In addition, it depicted necrotising pneumonia with the reversed halo sign before CT in 25% of patients [35]. The equivalence of MRI to CT has been demonstrated in pulmonary TB [37].

Ultrasound

If consolidation abuts the pleural surface, it is possible to visualise it with an ultrasound. In the acute phase of consolidation the lung appears solid and has an echo pattern similar to that of the liver. Other features include branching linear anechoic structures representing fluid-filled bronchi or echogenic locules of air, which represent air bronchograms. It is possible to detect lung abscesses with ultrasound, including those not visible on chest radiograph (figure 1) [38].

Radiographic patterns

There are five typical radiographic patterns of abnormality that are recognised as being associated with specific organisms, to the extent that they may be of diagnostic benefit [39]. These patterns should only be used as a guide since appearances can be modified by pre-existing lung disease and immunocompromise.

Bronchopneumonia

CAP, NP and VAP can all cause a bronchopneumonia pattern. *Staphylococcus aureus* and *Pseudomonas aeruginosa* are the two most common organisms that cause lobular or bronchopneumonia. Organisms attack terminal and respiratory bronchioles, following which

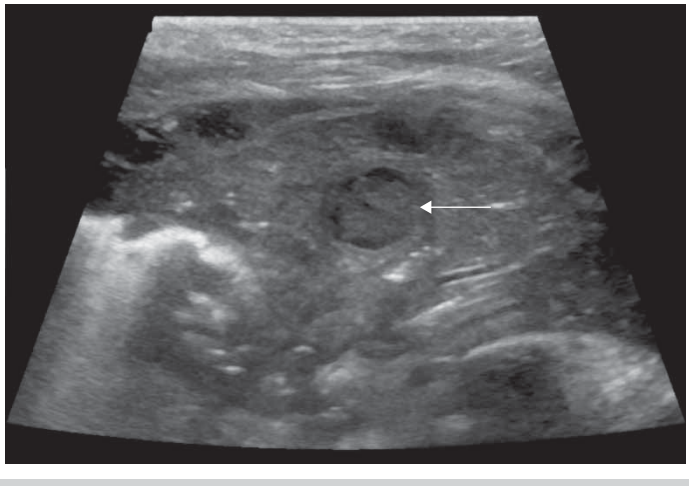

Figure 1. Thoracic ultrasound of a child with empyema depicting a small abscess in the lung parenchyma.

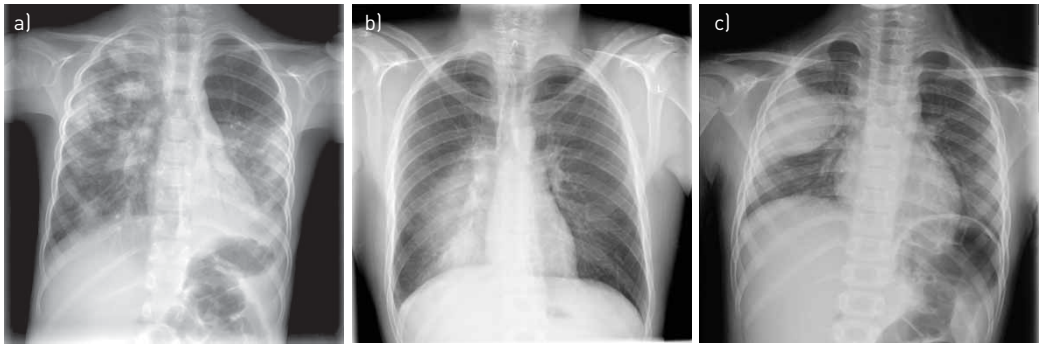

Figure 2. a) Chest radiograph demonstrating bronchopneumonia with patchy bilateral infiltrates as well as an area of more dense consolidation (with air bronchograms) behind the heart on the left. b) Chest radiograph demonstrating lobar pneumonia in the right lower lobe. c) Chest radiograph of a child demonstrating a classic round pneumonia appearance.

inflammation involves adjacent lung parenchyma resulting in the typical multifocal, heterogeneous opacities sited along the course of airways (figure 2a) [17]. The inflammatory response often leads to necrotising bronchiolitis and tissue necrosis; thus, abscess formation is common [40]. With time the patchy opacities can become more confluent resulting in dense consolidation. Since the infection originates in the airways, air bronchograms are seen infrequently.

Lobar pneumonia

This pattern of disease is most commonly associated with Streptococcal pneumonia, the most common cause of CAP in adults. Other organisms that commonly cause lobar pneumonia include the gram-negative bacilli, *Mycoplasma pneumoniae* and *Legionella pneumophila* [3, 41]. Infection develops in peripheral airspaces and spreads through the terminal airways, pores of Kohn and canals of Lambert to the adjacent lung; this produces a homogeneous opacity involving partial or complete segments of lung. Spread of infection is contained by the pleura [39]. Airways are not usually involved and therefore lung volumes are not reduced. Air bronchograms may be present. Consolidation is often basal and usually solitary, but can affect any lobe (figure 2b) [42].

Interstitial pneumonia

This pattern of disease is most frequently described in viral and *Pneumocystis carinii* pneumonia (PCP). Histopathologically, oedema and lymphocytic infiltration widen the alveolar septa and later the interlobular septa. This is followed by capillary leakage leading to haemorrhagic interstitial and/or alveolar oedema [43]. Interstitial changes cause a wide range of appearances on chest radiograph, including reticular, reticulonodular, nodular, alveolar and ground-glass densities. A mixed pattern of these findings can be seen; disease is often bilateral and diffusely distributed [3]. Hyperinflation is commonly seen due to the associated bronchiolitis and airway obstruction [44].

Round pneumonia

This appearance was first described in 1954 and is most commonly seen in children [45, 46]. It is not seen frequently in adults, and is often misinterpreted as possible lung cancer. To avoid an unnecessary lung biopsy, this entity should always be considered in patients with a solitary pulmonary opacity on chest radiograph (figure 2c); it can occur in patients of any age and without a preceding history of cough or fever [47].

Aspiration pneumonia

Predisposing factors include reduced levels of consciousness, neuromuscular conditions and alcoholism [48]. Aspiration should be considered in the outpatient setting if appropriate risk factors are present, because it has been suggested that aspiration is a factor in 5–15% of CAP [49]. Aspiration does not always lead to infection and imaging features are dependent on the nature of the aspirated material. Acute aspiration of gastric acid with a pH <2.5 will rapidly disseminate throughout the airways and lung parenchyma. Severity of the subsequent chemical pneumonitis is directly related to the volume of aspirated material.

Bilateral, symmetrical, diffuse opacities in the dependent portions of the lungs are typical findings [50], which usually start to improve within the first week [51]. Aspiration of partially digested food, where gastric acid has been neutralised, will generate a less severe reaction with small heterogeneous opacities that often clear within 24–48 h [48]. If symptoms do not improve, bacterial infection should be considered [52], particularly in alcoholic patients and those with poor oral hygiene [53].

CT patterns

In lobar, interstitial pneumonia and bronchopneumonia, CT patterns generally follow those seen in radiography but there are additional features depicted only on CT, such as subtle ground-glass opacities and tree-in-bud nodularity.

Airspace consolidation

CT demonstrates dense consolidation with air bronchograms. It also depicts the number of affected segments and can show small areas of subsegmental consolidation, which may not be visible on chest radiograph [21].

Ground-glass opacities

Ground-glass opacity is defined as increased density of the lung parenchyma without obscuration of the pulmonary vasculature [54]. It occurs as a result of a wide variety of interstitial and alveolar processes, and is often a nonspecific finding [55, 56]. In the context of pneumonia, ground-glass opacity is most often seen at the margins of the consolidated lung due to partial filling of the alveoli. Less commonly, groung-glass opacity is the solitary or predominant finding and, in the correct clinical context, should raise the suspicion of opportunistic infections such as PCP [57] and cytomegalovirus pneumonia [58, 59].

Centrilobular nodules

These are nodules centrally located within the secondary pulmonary lobule, and can be well or poorly defined. They are typically sited 5–10 mm from the pleural surface and usually do not touch the pleura itself (figure 3a). As the secondary pulmonary lobules are of similar size, centrilobular nodules tend to be evenly distributed [60]. This pattern is seen in the endobronchial spread of TB and other causes of bronchopneumonia. If there is no clinical indication of infection, other differentials such as hypersensitivity pneumonitis and respiratory bronchiolitis should be considered [61].

Tree-in-bud

This sign describes a pattern of branching Y-shaped and V-shaped opacities, which resemble a budding tree [62]. It is characteristically seen in infectious small airways disease and reflects inflammation of small peripheral bronchioles in combination with secretions in the airway lumen and peribronchiolar inflammation [63, 64]. A tree-in-bud pattern almost

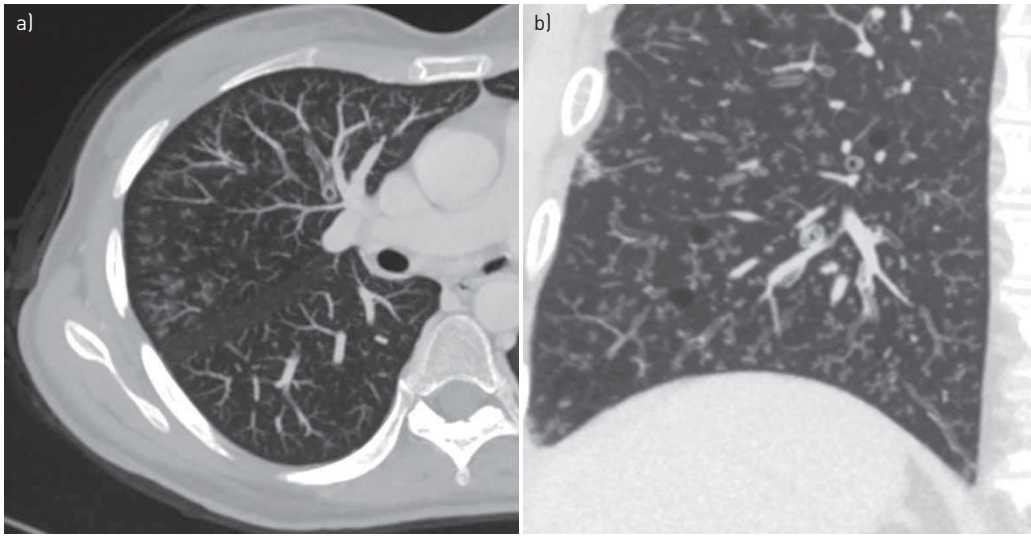

Figure 3. a) Axial CT scan showing ill-defined, ground-glass centrilobular nodules in the right upper lobe. b) Coronal CT showing tree-in-bud pattern affecting the right lower lobe.

always indicates endobronchial spread of infection, in particular TB and *Mycobacterium avium intracellulare* (figure 3b). This feature is seen relatively frequently in the setting of CAP [65], the most frequent aetiological organisms being viral and *M. pneumoniae* [17].

Causative agent

Bacterial pneumonia

Pulmonary TB

TB is the most common infectious cause of death worldwide, responsible for 1.2 million deaths in 2010 [5]. There are two main radiological patterns of disease, which reflect the two main pathophysiological processes: primary TB and post-primary TB.

Primary TB. Many immunocompetent patients with primary TB will have no radiological findings of note [66], and therefore a high index of suspicion is required in making the diagnosis [67]. Primary TB manifests as four main entities: parenchymal disease, lymphadenopathy, pleural effusion and miliary nodules. Any combination of the four can be present [68]. In adults the most common manifestation is consolidation, most frequently in the middle and lower lobes [68]. Multilobar consolidation can occur [69] and can be seen without lymphadenopathy in up to 81% of adults [70]. Radiographic resolution of parenchymal lesions occurs in approximately two thirds of cases [68]. The remainder will form an area of scarring (Ghon focus) which, when associated with mediastinal or hilar lymphadenopathy, is known as a Ranke complex [71].

Lymphadenopathy is the hallmark radiological presentation in children, with the right paratracheal and hilar sites being the most commonly affected [72]. Bilateral lymphadenopathy occurs in about a third of cases and CT is significantly more sensitive at demonstrating lymphadenopathy. The involved nodes are typically large, enhance peripherally and demonstrate central low density due to caseous necrosis (figure 4a) [70, 73].

Miliary TB is a rarer presentation of primary TB, and is more common in older people and the immunocompromised. Randomly distributed nodules (1–4 mm) are seen predominantly in the upper zones (figure 4b). Associated septal thickening can also be seen. [76].

Post-primary TB. This form of TB develops after reactivation of previously dormant primary infection. The most common radiological appearance is of poorly defined consolidation involving the apical and posterior segments of the upper lobes and the superior segments of the lower lobes [77]. Cavitation due to liquefaction of caseous necrosis and early connection with the tracheobronchial tree [69–71] is seen in 45% of chest radiographs (figure 4c).

Acute bronchogenic spread occurs in 20% of post-primary TB cases and occurs following breakdown of lobar infection or a ruptured lymph node into a bronchus. CT demonstrates centrilobular nodules and tree-in-bud opacities, and accurately depicts the extent of the disease [74].

Differentiation between active and inactive TB. TB leaves its mark on imaging long after resolution of clinical disease and it can be difficult to differentiate between active

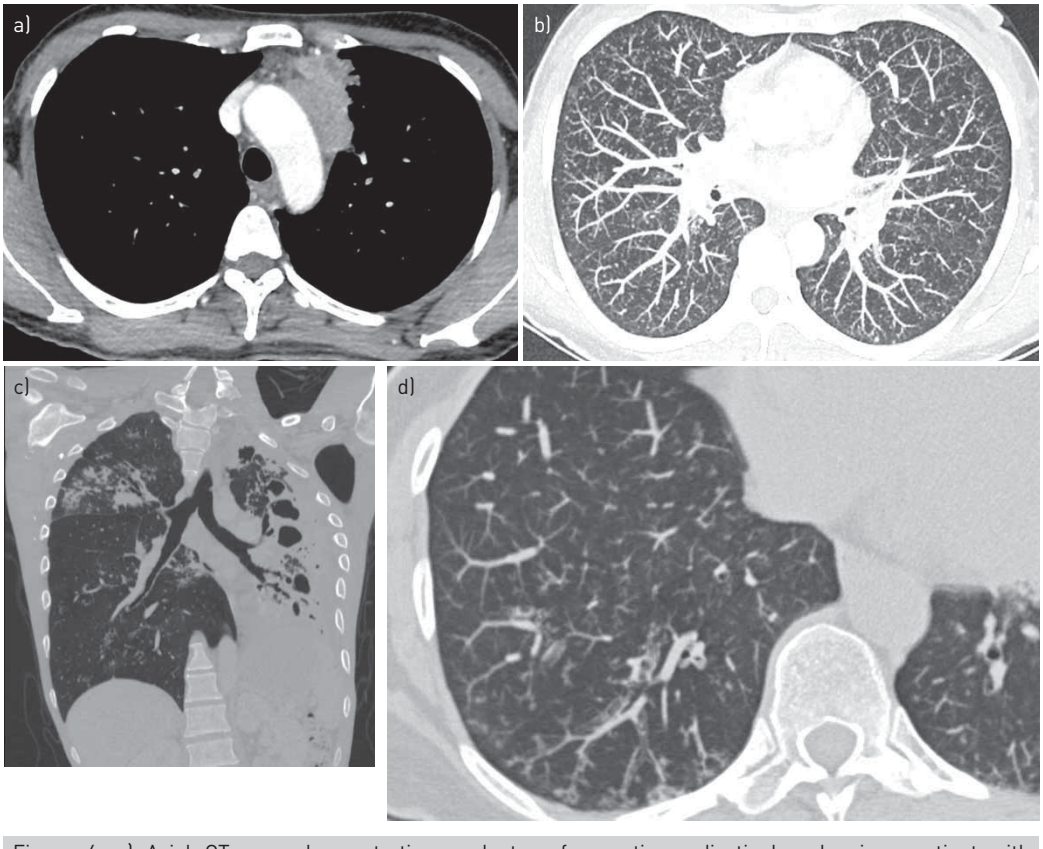

Figure 4. a) Axial CT scan demonstrating a cluster of necrotic mediastinal nodes in a patient with tuberculosis (TB). b) Axial CT with MIP depicting miliary nodules in a patient with active TB. c) Coronal CT demonstrating extensive cavitating TB in the left upper and lower lobes. d) Axial CT demonstrating tree-in-bud opacities in the periphery of the right lower lobe of a patient with *Mycobacterium abscessus*.

and inactive disease on the basis of chest radiograph alone. Accuracy of diagnosis from an initial radiograph is only 34% for primary TB and 59% for post-primary TB [66]. The finding of tree-in-bud opacification on CT is suggestive of recently disseminated disease; it has 91% sensitivity for the diagnosis of primary TB, 80% sensitivity for identifying active disease and 89% sensitivity for the diagnosis of inactive disease [75]. It is essential to bear in mind the ATS guidelines, which recommend that any abnormality seen in the context of TB (parenchymal, nodal or pleural with or without calcification) should be considered indeterminate; inactivity can only be assumed on the basis of 6 months' stability [76].

Nontuberculous mycobacteria

Nontuberulous mycobacteria are increasingly recognised as an important cause of chronic pulmonary infection in both immunocompetent [77] and immunocompromised [78] patients. NTM disease is increasing in prevalence and is most commonly caused by *M. avium intracellulare* and *Mycobacterium kansasii* [79].

Clinical and radiological findings can be classified into classic and nonclassic infection. Classic infection typically affects older Caucasian men with underlying lung disease, such as COPD and pulmonary fibrosis [80], with linear and nodular parenchymal opacities in the apical and posterior segments of the upper lobes being difficult to distinguish from post-primary TB. Small single or multiple cavities in the upper lobes are also commonly seen [81].

Nonclassic infection usually affects older women without a preceding history of lung disease [77, 82]. Characteristic imaging findings are cylindrical bronchiectasis, tree-in-bud opacities and centrilobular nodules (up to 3 mm) (figure 4d). Disease is typically located in the upper lobes, middle lobe or lingula. Airspace opacity, cavitation and lymphadenopathy are infrequent in this group [82].

Viral pneumonia

Viral pneumonia in adults can be classified into atypical pneumonia in the immunocompetent host and viral pneumonia in the immunocompromised host [83]. The role of imaging in viral pneumonia includes detection of disease and its extent, assessing response to treatment and guidance of interventional diagnostic procedures [84].

Radiographic findings

Chest radiographs may be normal or may demonstrate unilateral consolidation, bilateral patchy infiltrates, nodules, bronchial wall thickening or small pleural effusions. Lobar consolidation is rare [84].

CT findings

CT findings will be dependent on the underlying pathological processes, which include diffuse alveolar damage, intra-alveolar haemorrhage and interstitial inflammatory cell infiltration [85].

Influenza

Influenza viruses cause seasonal upper respiratory tract infections, endemic infections and unpredictable pandemics, such as the so-called Spanish flu of 1918 [86]. The influenza type A virus can cause pneumonia in older patients and the immunocompromised [87]. CT demonstrates diffuse or patchy areas of ground-glass opacities mixed in with consolidation. Centrilobular nodules typically represent alveolar haemorrhage [43].

Pneumonia in the immunocompromised host

Immunocompromised patients are vulnerable to a wide range of organisms. Over the last 30 years there has been a steady rise in the number of patients affected by HIV/AIDS, high-dose chemotherapy regimens, organ and bone marrow transplantation and immunosuppressant therapy [24, 88]. Many of the organisms causing CAP in the immunocompetent also cause pneumonia in the immunosuppressed [3].

Pneumocystis *pneumonia*

PCP is caused by *Pneumocystis jirovecii*, a yeast-like fungus. It is most common in patients with a CD4 count <100 cells·mm^{-3} [89]. Normal chest radiographs are seen in up to 39% of patients at presentation [90]. Abnormal chest radiographs demonstrate diffuse bilateral interstitial infiltrates, followed by the development of alveolar consolidation. Hilar lymphadenopathy and effusion are rare [91]. CT is a reliable method of distinguishing between pneumocystis pneumonia and other differentials [92]. The most common CT finding is ground-glass opacity in a mosaic or geographic pattern, where normal secondary pulmonary lobules are interspersed with diseased lobules (figure 5). This pattern may be in a perihilar, diffuse or upper lobe distribution. Other CT findings include miliary nodules, focal masses, reticular interstitial disease and cystic lesions [93]. Multiple thin-walled cysts are often seen, which may cause pneumothorax [94].

Allergic bronchopulmonary aspergillosis

This uncommon disorder usually occurs in asthmatics but can also be seen in those with cystic fibrosis, Kartagener's syndrome or following lung transplant [95]. Radiographic findings in the acute phase include consolidation, tubular areas of increased opacity in a bronchial distribution, and atelectasis usually involving the upper lobes. CT findings consist of mucoid impaction and bronchiectasis involving predominantly the segmental and subsegmental bronchi of the upper lobes [96].

Candidiasis

Candida species are increasingly recognised as a source of pneumonia in the immunocompromised [97, 98]. Radiographic appearances include unilateral and bilateral lobar or segmental airspace disease [99], and occasionally cavitation [100]. Airway spread of fungi results in bronchopneumonia or multiple pulmonary nodules; haematogenous spread results in miliary nodules [101]. The most common CT finding is of multiple bilateral nodules often associated with areas of airspace consolidation. In a series of 17 patients, five demonstrated a halo of ground-glass opacities around the nodules; the CT halo sign is also seen in other fungal diseases, such as invasive aspergillosis and actinomycosis [102].

Acute respiratory distress syndrome

Definition

ARDS is a type of acute diffuse lung injury characterised by acute respiratory failure and hypoxaemia, which may occur following a number of insults. It is a common cause of admission to the ICU and has a mortality of approximately 50% [103].

The definition of ARDS was recently revised by a large working group [104]. The group specified the following "Berlin" criteria for a diagnosis of ARDS: onset within 1 week of a

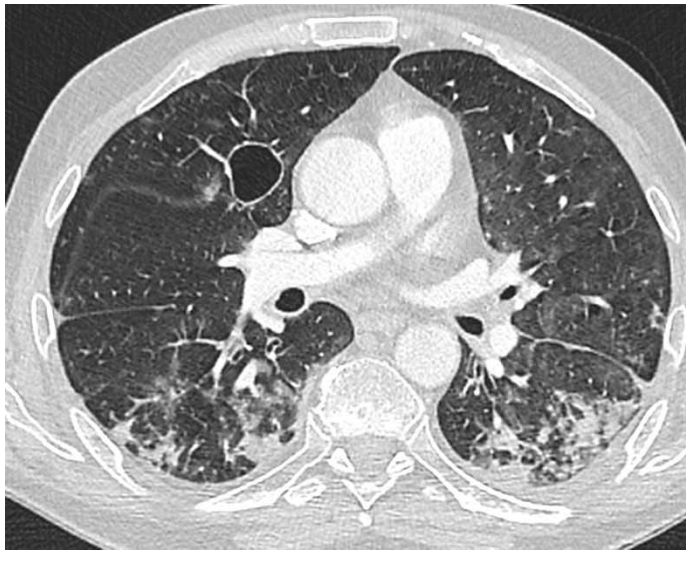

Figure 5. Axial CT scan of a patient with *Pneumocystis carinii* pneumonia demonstrating patchy bilateral infiltrates, ground-glass opacity and a cyst in the right upper lobe.

known clinical insult or new/worsening respiratory symptoms; bilateral opacities on chest imaging not fully explained by effusions; lobar/lung collapse or nodules; and respiratory failure not fully explained by cardiac failure or fluid overload. These criteria replace the previous American-European Consensus Conference (AECC) criteria [105].

Pathology

Pathologically, ARDS is characterised by diffuse alveolar damage *i.e.* alveolar haemorrhage, hyaline membranes, inflammatory cell infiltrates and protein-rich oedema fluid [106]. If the patient survives the acute illness, there is frequently fibrin deposition and collagen formation leading to pulmonary fibrosis.

Aetiology

A number of insults are recognised as risk factors for ARDS including: pneumonia; sepsis; aspiration; major trauma; inhalational injury; pancreatitis; burns; multiple transfusions; drug overdose; and drowning [104]. Historically, ARDS was classified into two categories according to whether the insult was pulmonary or extrapulmonary, but because multiple risk factors often coexist in a single patient with a large amount of overlap seen in the two categories, less emphasis has been placed on this subclassification in recent times.

Role of imaging in ARDS

Imaging is important in the diagnosis and monitoring of ARDS. The key role of imaging in the diagnosis of ARDS is enshrined in the Berlin criteria mentioned earlier [104]. The use of the term "chest imaging" in the Berlin criteria is a deliberate refinement of the previous AECC definition [105], which referred to opacities on chest radiograph, and recognises that an increasing number of patients will undergo CT during their acute presentation. Imaging

is also important in distinguishing ARDS from other conditions, which may affect the lungs of critically ill patients including VAP, and for detecting other complications of ventilation, such as barotrauma and air-leak phenomena.

Plain radiography

Chest radiography remains the most widely used imaging modality in the evaluation of patients with ARDS and suspected ARDS. While no chest radiograph pattern can be considered diagnostic of ARDS, the findings of bilateral, ill-defined pulmonary infiltrates on chest radiograph are typical (figure 6a). It should be noted that chest radiograph findings typically lag behind clinical findings and that a normal chest radiograph in the first 24 h after presentation does not preclude the diagnosis [107]. Findings are usually symmetrical, although if pneumonia or aspiration is the cause of ARDS, this may not be the case.

The main differential diagnosis for ARDS on chest radiograph is cardiogenic pulmonary oedema. Features pointing towards this as an alternative diagnosis include perihilar distribution of infiltrates, upper lobe blood diversion, pleural effusions and cardiomegaly. The distinction is not always possible as cardiogenic oedema and ARDS may coexist. When a chest radiograph is performed to diagnose acute respiratory illness, the Berlin group specify that: "possible radiographic interpretations are: consistent, inconsistent, and equivocal for the diagnosis of ARDS" [105]. They provide a series of 12 radiographs, which show four example films for each of these interpretations. Factors that may hamper interpretation of the chest radiograph, leading to an equivocal film, include patient obesity, expiratory films and overlying structures, such as cooling blankets. The authors point out that in the case of an equivocal chest radiograph, clinical context and temporal evolution may help to determine whether ARDS is the most likely explanation of the chest radiograph findings.

Computed tomography

Although CT is more expensive and time-consuming than chest radiography, it frequently provides additional information, suggesting alternative diagnoses or identifying complications.

The typical appearance of ARDS on CT is of opacification with an anteroposterior and craniocaudal density gradient (figure 6b). Typically, the most posteroinferior lung shows consolidation, the middle third shows ground-glass opacities and the most anterosuperior lung is either normal or less dense than normal due to hyperinflation [108]. The changes are gravity dependent and reverse direction if the patient is changed from supine to prone position [109]. Changes are normally fairly symmetrical so that asymmetric consolidation should raise the possibility of superadded infection [110]. Other complications readily diagnosed by CT include pulmonary embolus, lung abscess, empyema, pneumothorax and pneumomediastinum.

There has been considerable interest in the use of CT to guide ventilator settings and ventilation strategies. Ventilation in ARDS aims to achieve maximum recruitment of nonaerated alveoli while avoiding unnecessary pressures that may cause barotrauma. Quantitative CT has been used to measure the effect of different types of ventilation. In quantitative CT, the lung is classified into four categories according to the degree of aeration, for example: non-aerated (100 to −100 HU); poorly inflated (−100 to −500 HU); normal lung (−500 to −900 HU); and hyperinflated lung (−900 to −1000 HU) [108]. Computer algorithms can then be used to estimate the percentage of imaged lung that lies

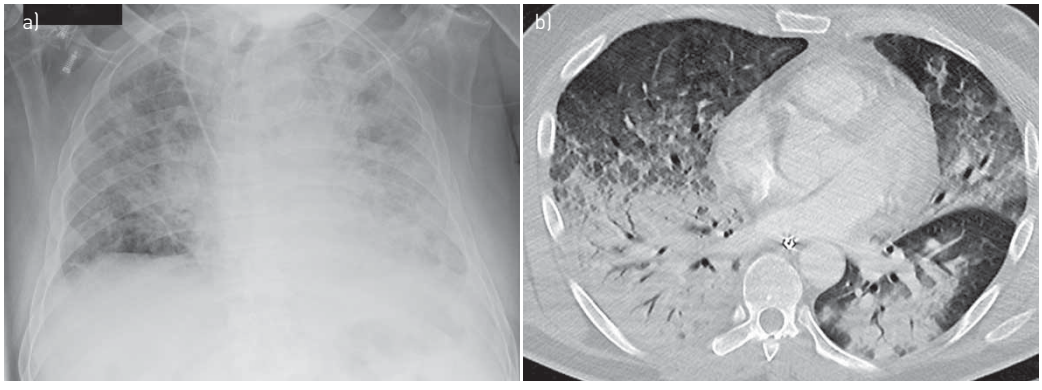

Figure 6. a) Chest radiograph of a patient with acute respiratory distress syndrome (ARDS) following a total knee replacement. b) Axial CT scan of a trauma patient with ARDS, demonstrating the gravitational distribution of consolidation, ground-glass opacity and normally aerated lung.

in each of the categories. By performing scans before and after adjusting ventilator settings, it is possible to assess the overall and regional effect of the change and assess whether more alveolar units have been recruited. While this is not yet routinely used in clinical practice [111], it is a powerful research tool that has been used to assess the effect of prone positioning [109], high-frequency oscillatory ventilation [112], different levels of positive end-expiratory pressure [113], and negative pressure ventilation [114].

Positron emission tomography

Recently, FDG-PET has been used to evaluate the lungs of patients with ARDS. Interestingly, areas of lung that appear normal on CT frequently show increased isotope uptake on FDG-PET, suggesting that there is active inflammation preceding the development of visible CT abnormality [115].

Conclusion

The diagnostic approach to pneumonia should consider the patient's demographic background to classify pneumonia as a community-acquired, nosocomial or immunocompromised subtype. Although there is considerable overlap of chest radiograph and CT features between the various types of pneumonia, correlation of imaging features with clinical and microbiological findings can limit the differential diagnosis of aetiological agents. A chest radiograph is often adequate in the radiological evaluation of the patient with pneumonia, but CT can guide the search for less common infections such as PCP, fungal disease or nontuberculous mycobacteria; it can also help with the identification of complications, and can identify a significant underlying or coexisting pathology, such as lung cancer or pulmonary embolus.

Chest imaging, both with chest radiograph and CT is critical to the diagnosis of ARDS as enshrined in the recent Berlin guidelines [104]. Quantitative CT has led to insights into optimising ventilation strategy in patients with this condition.

References

1. Gibson GJ, Loddenkemper R, Lundbäck B, *et al.* Respiratory health and disease in Europe: the new European Lung White Book. *Eur Respir J* 2013; 42: 559–563.

2. The economic burden of lung disease. *In*: Gibson GJ, Loddenkemper R, Sibille Y, *et al.* eds. The European Lung White Book: Respiratory Health and Disease in Europe. 2nd Edn. Sheffield, European Respiratory Society, 2013; pp. 16–27.
3. Franquet T. Imaging of pneumonia: trends and algorithms. *Eur Respir J* 2001; 18: 196–208.
4. Esteban A, Ferguson ND, Meade MO, *et al.* Evolution of mechanical ventilation in response to clinical research. *Am J Respir Crit Care Med* 2008; 177: 170–177.
5. Lozano R, Naghavi M, Foreman K, *et al.* Global and regional mortality from 235 causes of death for 20 age groups in 1990 and 2010: a systematic analysis for the Global Burden of Disease Study 2010. *Lancet* 2012; 380: 2095–2128.
6. Remington LT, Sligl WI. Community-acquired pneumonia. *Curr Opin Pulm Med* 2014; 20: 215–224.
7. Höffken G, Niederman MS. Nosocomial pneumonia: the importance of a de-escalating strategy for antibiotic treatment of pneumonia in the ICU. *Chest* 2002; 122: 2183–2196.
8. Chastre J, Fagon JY. Ventilator-associated pneumonia. *Am J Respir Crit Care Med* 2002; 165: 867–903.
9. Masterton RG, Galloway A, French G, *et al.* Guidelines for the management of hospital-acquired pneumonia in the UK: report of the working party on hospital-acquired pneumonia of the British Society for Antimicrobial Chemotherapy. *J Antimicrob Chemother* 2008; 62: 5–34.
10. American Thoracic Society, Infectious Diseases Society of America. Guidelines for the management, of adults with hospital-acquired, ventilator-associated, and healthcare-associated pneumonia. *Am J Respir Crit Care Med* 2005; 171: 388–416.
11. Lim WS, Baudouin SV, George RC, *et al.* BTS guidelines for the management of community acquired pneumonia in adults: update 2009. *Thorax* 2009; 64: Suppl. 3, 1–55.
12. Torres A, Aznar R, Gatell JM, *et al.* Incidence, risk, and prognosis factors of nosocomial pneumonia in mechanically ventilated patients. *Am Rev Respir Dis* 1990; 142: 523–528.
13. Bartlett JG, Mundy LM. Community-acquired pneumonia. *N Engl J Med* 1995; 333: 1618–1624.
14. Hopstaken RM, Witbraad T, van Engelshoven JM, *et al.* Inter-observer variation in the interpretation of chest radiographs for pneumonia in community-acquired lower respiratory tract infections. *Clin Radiol* 2004; 59: 743–752.
15. Loeb MB, Carusone SB, Marrie TJ, *et al.* Interobserver reliability of radiologists' interpretations of mobile chest radiographs for nursing home-acquired pneumonia. *J Am Med Dir Assoc* 2006; 7: 416–419.
16. Zornoza J, Goldman AM, Wallace S, *et al.* Radiologic features of gram-negative pneumonias in the neutropenic patient. *AJR Am J Roentgenol* 1976; 127: 989–996.
17. Herold CJ, Sailer JG. Community-acquired and nosocomial pneumonia. *Eur Radiol* 2004; 14: Suppl. 3, 2–20.
18. Kyprianou A, Hall CS, Shah R, *et al.* The challenge of nonresolving pneumonia. Knowing the norms of radiographic resolution is key. *Postgrad Med* 2003; 113: 79–82.
19. El Solh AA, Aquilina AT, Gunen H, *et al.* Radiographic resolution of community-acquired bacterial pneumonia in the elderly. *J Am Geriatr Soc* 2004; 52: 224–229.
20. Romano L, Pinto A, Merola S, *et al.* Intensive-care unit lung infections: the role of imaging with special emphasis on multi-detector row computed tomography. *Eur J Radiol* 2008; 65: 333–339.
21. Hayden GE, Wrenn KW. Chest radiograph *vs.* computed tomography scan in the evaluation for pneumonia. *J Emerg Med* 2009; 36: 266–270.
22. Gruden JF, Huang L, Turner J, *et al.* High-resolution CT in the evaluation of clinically suspected *Pneumocystis carinii* pneumonia in AIDS patients with normal, equivocal, or nonspecific radiographic findings. *AJR Am J Roentgenol* 1997; 169: 967–975.
23. Logan PM, Primack SL, Miller RR, *et al.* Invasive aspergillosis of the airways: radiographic, CT, and pathologic findings. *Radiology* 1994; 193: 383–388.
24. Heussel C, Kauczor HU, Ullmann AJ. Pneumonia in neutropenic patients. *Eur Radiol* 2004; 14: 256–271.
25. Tanaka N, Matsumoto T, Kuramitsu T, *et al.* High resolution CT findings in community-acquired pneumonia. *J Comput Assist Tomogr* 1996; 20: 600–608.
26. Yeh JJ, Chen SC, Chen CR, *et al.* A high-resolution computed tomography-based scoring system to differentiate the most infectious active pulmonary tuberculosis from community-acquired pneumonia in elderly and non-elderly patients. *Eur Radiol* 2014; 24: 2372–2384.
27. Banker PD, Jain VR, Haramati LB. Impact of chest CT on the clinical management of immunocompetent emergency department patients with chest radiographic findings of pneumonia. *Emerg Radiol* 2007; 14: 383–388.
28. Reittner P, Ward S, Heyneman L, *et al.* Pneumonia: high-resolution CT findings in 114 patients. *Eur Radiol* 2003; 13: 515–521.
29. Moore EH, Webb WR, Muller N, *et al.* MRI of pulmonary airspace disease: experimental model and preliminary clinical results. *AJR Am J Roentgenol* 1986; 146: 1123–1128.
30. Primack SL, Mayo JR, Hartman TE, *et al.* MRI of infiltrative lung disease: comparison with pathologic findings. *J Comput Assist Tomogr* 1994; 18: 233–238.
31. Herold CJ, Kuhlman JE, Zerhouni EA. Pulmonary atelectasis: signal patterns with MR imaging. *Radiology* 1991; 178: 715–720.

32. Webb WR. The role of magnetic resonance imaging in the assessment of patients with lung cancer: a comparison with computed tomography. *J Thorac Imaging* 1989; 4: 65–75.
33. Montella S, Maglione M, Bruzzese D, *et al.* Magnetic resonance imaging is an accurate and reliable method to evaluate non-cystic fibrosis paediatric lung disease. *Respirology* 2012; 17: 87–91.
34. Cutillo AG, Ganesan K, Ailion DC, *et al.* Alveolar air-tissue interface and nuclear magnetic resonance behavior of lung. *J Appl Physiol* 1991; 70: 2145–2154.
35. Leutner CC, Gieseke J, Lutterbey G, *et al.* MR imaging of pneumonia in immunocompromised patients: comparison with helical CT. *AJR Am J Roentgenol* 2000; 175: 391–397.
36. Haddad JL, Rofsky NM, Ambrosino MM, *et al.* T2-weighted MR imaging of the chest: comparison of electrocardiograph-triggered conventional and turbo spin-echo and nontriggered turbo spin-echo sequences. *J Magn Reson Imaging* 1995; 5: 325–329.
37. Busi Rizzi E, Schininà V, Cristofaro M, *et al.* Detection of pulmonary tuberculosis: comparing MR imaging with HRCT. *BMC Infect Dis* 2011; 11: 243.
38. Wrightson JM, Fysh ET. Image interpretation: related thoracic structures. *In*: Tobin CL, Lee YG, Gleeson F, Rahman N, Feller-Kopman D, eds. Pleural Ultrasound for Clinicians: a Text and E-book. Boca Raton, CRC Press, 2014; pp. 71–90.
39. Tarver RD, Teague SD, Heitkamp DE, *et al.* Radiology of community-acquired pneumonia. *Radiol Clin North Am* 2005; 43: 497–512, viii.
40. Gharib AM, Stern EJ. Radiology of pneumonia. *Med Clin North Am* 2001; 85: 1461–1491.
41. Lévy M, Dromer F, Brion N, *et al.* Community-acquired pneumonia: importance of initial noninvasive bacteriologic and radiographic investigations. *Chest* 1988; 93: 43–48.
42. Reynolds JH, McDonald G, Alton H, *et al.* Pneumonia in the immunocompetent patient. *Br J Radiol* 2014; 83: 998–1009.
43. Kim EA, Lee KS, Primack SL, *et al.* Viral pneumonias in adults: radiologic and pathologic findings. *Radiographics* 2002; 22: Suppl. 1, 137–149.
44. Sharma S, Maycher B, Eschun G. Radiological imaging in pneumonia: recent innovations. *Curr Opin Pulm Med* 2007; 13: 159–169.
45. Ackerman LV, Elliott GV, Alanis M. Localized organizing pneumonia; its resemblance to carcinoma; a review of its clinical, roentgenographic and pathologic features. *Am J Roentgenol Radium Ther Nucl Med* 1954; 71: 988–996.
46. Kim YW, Donnelly LF. Round pneumonia: imaging findings in a large series of children. *Pediatr Radiol* 2007; 37: 1235–1240.
47. Wagner AL, Szabunio M, Hazlett KS, *et al.* Radiologic manifestations of round pneumonia in adults. *AJR Am J Roentgenol* 1998; 170: 723–726.
48. Marom EM, McAdams HP, Erasmus JJ, *et al.* The many faces of pulmonary aspiration. *AJR Am J Roentgenol* 1999; 172: 121–128.
49. Marik PE. Aspiration pneumonitis and aspiration pneumonia. *N Engl J Med* 2001; 344: 665–671.
50. Franquet T, Giménez A, Rosón N, *et al.* Aspiration diseases: findings, pitfalls, and differential diagnosis. *Radiographics* 2000; 20: 673–685.
51. Washington L, Palacio D. Imaging of bacterial pulmonary infection in the immunocompetent patient. *Semin Roentgenol* 2007; 42: 122–145.
52. Landay MJ, Christensen EE, Bynum LJ. Pulmonary manifestations of acute aspiration of gastric contents. *AJR Am J Roentgenol* 1978; 131: 587–592.
53. Bartlett JG, Finegold SM. Anaerobic infections of the lung and pleural space. *Am Rev Respir Dis* 1974; 110: 56–77.
54. Miller WT Jr, Shah RM. Isolated diffuse ground-glass opacity in thoracic CT: causes and clinical presentations. *AJR Am J Roentgenol* 2005; 184: 613–622.
55. Engeler CE, Tashjian JH, Trenkner SW, *et al.* Ground-glass opacity of the lung parenchyma: a guide to analysis with high-resolution CT. *AJR Am J Roentgenol* 1993; 160: 249–251.
56. Leung AN, Miller RR, Müller NL. Parenchymal opacification in chronic infiltrative lung diseases: CT-pathologic correlation. *Radiology* 1993; 188: 209–214.
57. Kuhlman JE, Kavuru M, Fishman EK, *et al. Pneumocystis carinii* pneumonia: spectrum of parenchymal CT findings. *Radiology* 1990; 175: 711–714.
58. Moon JH, Kim EA, Lee KS, *et al.* Cytomegalovirus pneumonia: high-resolution CT findings in ten non-AIDS immunocompromised patients. *Korean J Radiol* 2000; 1: 73–78.
59. Waxman AB, Goldie SJ, Brett-Smith H, *et al.* Cytomegalovirus as a primary pulmonary pathogen in AIDS. *Chest* 1997; 111: 128–134.
60. Webb WR, Higgins CB. Thoracic Imaging. Pulmonary and Cardiovascular Radiology. 2nd Edn. Philadelphia, Wolters Kluwer, 2010.
61. Boitsios G, Bankier AA, Eisenberg RL. Diffuse pulmonary nodules. *AJR Am J Roentgenol* 2010; 194: W354–W366.

62. Abbott GF, Rosado-de-Christenson ML, Rossi SE, *et al.* Imaging of small airways disease. *J Thorac Imaging* 2009; 24: 285–298.
63. Eisenhuber E. The tree-in-bud sign. *Radiology* 2002; 222: 771–772.
64. Aquino SL, Gamsu G, Webb WR, *et al.* Tree-in-bud pattern: frequency and significance on thin section CT. *J Comput Assist Tomogr* 1996; 20: 594–599.
65. Shiley KT, Van Deerlin VM, Miller WT Jr. Chest CT features of community-acquired respiratory viral infections in adult inpatients with lower respiratory tract infections. *J Thorac Imaging* 2010; 25: 68–75.
66. Jeong YJ, Lee KS. Pulmonary tuberculosis: up-to-date imaging and management. *AJR Am J Roentgenol* 2008; 191: 834–844.
67. Skoura E, Zumla A, Bomanji J. Imaging in tuberculosis. *Int J Infect Dis* 2015; 32: 87–93.
68. Burrill J, Williams CJ, Bain G, *et al.* Tuberculosis: a radiologic review. *Radiographics* 2007; 27: 1255–1273.
69. Lee KS, Song KS, Lim TH, *et al.* Adult-onset pulmonary tuberculosis: findings on chest radiographs and CT scans. *AJR Am J Roentgenol* 1993; 160: 753–758.
70. Leung AN. Pulmonary tuberculosis: the essentials. *Radiology* 1999; 210: 307–322.
71. Van Dyck P, Vanhoenacker FM, Van den Brande P, *et al.* Imaging of pulmonary tuberculosis. *Eur Radiol* 2003; 13: 1771–1785.
72. Leung AN, Müller NL, Pineda PR, *et al.* Primary tuberculosis in childhood: radiographic manifestations. *Radiology* 1992; 182: 87–91.
73. Pombo F, Rodríguez E, Mato J, *et al.* Patterns of contrast enhancement of tuberculous lymph nodes demonstrated by computed tomography. *Clin Radiol* 1992; 46: 13–17.
74. Lee KS, Im JG. CT in adults with tuberculosis of the chest: characteristic findings and role in management. *AJR Am J Roentgenol* 1995; 164: 1361–1367.
75. Lee KS, Hwang JW, Chung MP, *et al.* Utility of CT in the evaluation of pulmonary tuberculosis in patients without AIDS. *Chest* 1996; 110: 977–984.
76. Diagnostic standards and classification of tuberculosis in adults and children. *Am J Respir Crit Care Med* 2000; 161: 1376–1395.
77. Jeong YJ, Lee KS, Koh WJ, *et al.* Nontuberculous mycobacterial pulmonary infection in immunocompetent patients: comparison of thin-section CT and histopathologic findings 1. *Radiology* 2004; 231: 880–886.
78. Horsburgh CR Jr. *Mycobacterium avium* complex infection in the acquired immunodeficiency syndrome. *N Engl J Med* 1991; 324: 1332–1338.
79. O'Brien RJ, Geiter LJ, Snider DE Jr. The epidemiology of nontuberculous mycobacterial diseases in the United States. Results from a national survey. *Am Rev Respir Dis* 1987; 135: 1007–1014.
80. Miller WT Jr. Spectrum of pulmonary nontuberculous mycobacterial infection. *Radiology* 1994; 191: 343–350.
81. Wittram C, Weisbrod GL. *Mycobacterium avium* complex lung disease in immunocompetent patients: radiography-CT correlation. *Br J Radiol* 2002; 75: 340–344.
82. Moore EH. Atypical mycobacterial infection in the lung: CT appearance. *Radiology* 1993; 187: 777–782.
83. Sullivan CJ, Jordan MC. Diagnosis of viral pneumonia. *Semin Respir Infect* 1988; 3: 148–161.
84. Franquet T. Imaging of pulmonary viral pneumonia. *Radiology* 2011; 260: 18–39.
85. Yeldandi AV, Colby TV. Pathologic features of lung biopsy specimens from influenza pneumonia cases. *Hum Pathol* 1994; 25: 47–53.
86. Reid AH, Taubenberger JK, Fanning TG. The 1918 Spanish influenza: integrating history and biology. *Microbes Infect* 2001; 3: 81–87.
87. Tillett HE, Smith JW, Clifford RE. Excess morbidity and mortality associated with influenza in England and Wales. *Lancet* 1980; 1: 793–795.
88. Escuissato DL, Gasparetto EL, Marchiori E, *et al.* Pulmonary infections after bone marrow transplantation: high-resolution CT findings in 111 patients. *AJR Am J Roentgenol* 2005; 185: 608–615.
89. Brown MJ, Miller RR, Müller NL. Acute lung disease in the immunocompromised host: CT and pathologic examination findings. *Radiology* 1994; 190: 247–254.
90. Kuhlman JE. Pneumocystic infections: the radiologist's perspective. *Radiology* 1996; 198: 623–635.
91. Shah RM, Kaji AV, Ostrum BJ, *et al.* Interpretation of chest radiographs in AIDS patients: usefulness of CD4 lymphocyte counts. *Radiographics* 1997; 17: 47–58.
92. Hidalgo A, Falcó V, Mauleón S, *et al.* Accuracy of high-resolution CT in distinguishing between *Pneumocystis carinii* pneumonia and non-*Pneumocystis carinii* pneumonia in AIDS patients. *Eur Radiol* 2003; 13: 1179–1184.
93. Boiselle PM, Crans CA Jr, Kaplan MA. The changing face of *Pneumocystis carinii* pneumonia in AIDS patients. *AJR Am J Roentgenol* 1999; 172: 1301–1309.
94. Feurestein IM, Archer A, Pluda JM, *et al.* Thin-walled cavities, cysts, and pneumothorax in *Pneumocystis carinii* pneumonia: further observations with histopathologic correlation. *Radiology* 1990; 174: 697–702.
95. Chong S, Lee KS, Yi CA, *et al.* Pulmonary fungal infection: imaging findings in immunocompetent and immunocompromised patients. *Eur J Radiol* 2006; 59: 371–383.

96. Franquet T, Müller NL, Giménez A, *et al.* Spectrum of pulmonary aspergillosis: histologic, clinical, and radiologic findings. *Radiographics* 2001; 21: 825–837.
97. Franquet T, Müller NL, Lee KS, *et al.* Pulmonary candidiasis after hematopoietic stem cell transplantation: thin-section CT findings. *Radiology* 2005; 236: 332–337.
98. Leung AN, Gosselin MV, Napper CH, *et al.* Pulmonary infections after bone marrow transplantation: clinical and radiographic findings. *Radiology* 1999; 210: 699–710.
99. Buff SJ, McLelland R, Gallis HA, *et al. Candida albicans* pneumonia: radiographic appearance. *AJR Am J Roentgenol* 1982; 138: 645–648.
100. Kassner EG, Kauffman SL, Yoon JJ, *et al.* Pulmonary candidiasis in infants: clinical, radiologic, and pathologic features. *AJR Am J Roentgenol* 1981; 137: 707–716.
101. Verfaillie C, Weisdorf D, Haake R, *et al.* Candida infections in bone marrow transplant recipients. *Bone Marrow Transplant* 1991; 8: 177–184.
102. Gaeta M, Blandino A, Scribano E, *et al.* Computed tomography halo sign in pulmonary nodules: frequency and diagnostic value. *J Thorac Imaging* 1999; 14: 109–113.
103. Villar J, Blanco J, Añón JM, *et al.* The ALIEN study: incidence and outcome of acute respiratory distress syndrome in the era of lung protective ventilation. *Intensive Care Med* 2011; 37: 1932–1941.
104. ARDS Definition Task Force, Ranieri VM, Rubenfeld GD, *et al.* Acute respiratory distress syndrome. *JAMA* 2012; 307: 2526–2533.
105. Ferguson ND, Fan E, Camporota L, *et al.* The Berlin definition of ARDS: an expanded rationale, justification, and supplementary material. *Intensive Care Med* 2012; 38: 1573–1582.
106. Katzenstein AL, Bloor CM, Leibow AA. Diffuse alveolar damage–the role of oxygen, shock, and related factors. A review. *Am J Pathol* 1976; 85: 209–228.
107. Desai SR. Acute respiratory distress syndrome: imaging of the injured lung. *Clin Radiol* 2002; 57: 8–17.
108. Gattinoni L, Caironi P, Pelosi P, *et al.* What has computed tomography taught us about the acute respiratory distress syndrome? *Am J Respir Crit Care Med* 2001; 164: 1701–1711.
109. Gattinoni L, Pelosi P, Vitale G, *et al.* Body position changes redistribute lung computed-tomographic density in patients with acute respiratory failure. *Anesthesiology* 1991; 74: 15–23.
110. Sheard S, Rao P, Devaraj A. Imaging of acute respiratory distress syndrome. *Respir Care* 2012; 57: 607–612.
111. Gattinoni L, Cressoni M. Quantitative CT in ARDS: towards a clinical tool? *Intensive Care Med* 2010; 36: 1803–1804.
112. Luecke T, Herrmann P, Kraincuk P, *et al.* Computed tomography scan assessment of lung volume and recruitment during high-frequency oscillatory ventilation. *Crit Care Med* 2005; 33: Suppl. 3, 155–162.
113. Pelosi P, Rocco PR, de Abreu MG. Use of computed tomography scanning to guide lung recruitment and adjust positive-end expiratory pressure. *Curr Opin Crit Care* 2011; 17: 268–274.
114. Helm E, Talakoub O, Grasso F, *et al.* Use of dynamic CT in acute respiratory distress syndrome (ARDS) with comparison of positive and negative pressure ventilation. *Eur Radiol* 2009; 19: 50–57.
115. Bellani G, Caironi P. Lung imaging during acute respiratory distress syndrome: CT- and PET-scanning. *Trends Anaesth Crit Care* 2011; 1: 203–209.

Disclosures: None declared.

Chapter 10

Pulmonary hypertension

Cathelijne E.E. van der Bruggen[1], Onno A. Spruijt[1], Lilian J. Meijboom[2] and Anton Vonk Noordegraaf[1]

Pulmonary hypertension (PH) is a haemodynamic condition that leads to a progressive increase in pulmonary vascular resistance and mean pulmonary artery pressure. Irrespective of its aetiology, the main cause of death in PH patients is right ventricular (RV) failure. Noninvasive imaging techniques play an essential role in diagnosing PH and monitoring disease progression. This chapter provides an overview of the most important noninvasive imaging tools for assessing pulmonary pressures, RV function and monitoring.

Pulmonary hypertension (PH) is a haemodynamic condition defined as a mean pulmonary arterial pressure (mPAP) ⩾25 mmHg measured invasively with right heart catheterisation (RHC); it is a rapidly progressive and fatal disease, even in the modern treatment era [1]. Although primarily a lung disease, the prognosis of PH patients is closely related to right ventricular (RV) function [2–6]. Initially, RV function adapts to the increased afterload with several compensatory mechanisms; however, ultimately these are not sufficient to prevent progression to RV dysfunction and failure.

Despite the fact that all five PH entities as described in the updated clinical classification agreed in Nice in 2013 (table 1) are characterised by an increased pulmonary vascular resistance (PVR) and mPAP, the underlying mechanisms, prognosis and treatment strategies vary significantly [1]. A critical distinction is between pre- and post-capillary PH, as post-capillary PH patients do not respond to pulmonary arterial hypertension (PAH)-specific treatments. Therefore, arriving at the right diagnosis by means of a complete evaluation of both haemodynamics and RV function, is of the utmost importance.

In addition to RHC measurements, several noninvasive imaging techniques are available to the clinician and these are essential to make the correct diagnosis. Furthermore, given the increased knowledge of disease progression and the importance of timely referral for lung transplantation, noninvasive imaging techniques are indispensable in disease monitoring. In this chapter, we provide an overview of the imaging techniques involved in the diagnostic process as summarised in figure 1. We also discuss how to monitor PH patients over time.

[1]Dept of Pulmonary Medicine, Institute for Cardiovascular Research, VU University Medical Center, Amsterdam, The Netherlands. [2]Dept of Radiology, VU University Medical Center, Amsterdam, The Netherlands.

Correspondence: Anton Vonk Noordegraaf, Dept of Pulmonary Medicine, VU University Medical Center, De Boelelaan 1117, ZH 4F004, 1007 MB Amsterdam, PO Box 7057, The Netherlands. E-mail: a.vonk@vumc.nl

Copyright ©ERS 2015. Print ISBN: 978-1-84984-065-1. Online ISBN: 978-1-84984-066-8. Print ISSN: 2312-508X. Online ISSN: 2312-5098.

Table 1. Clinical classification of pulmonary hypertension

Group 1. Pulmonary arterial hypertension (PAH)
- 1.1 Idiopathic PAH
- 1.2 Heritable PAH
- 1.3 Drug- and toxin-induced
- 1.4 Associated PAH (connective tissue disease, HIV infection, portal hypertension, congenital heart disease, schistosomiasis and chronic haemolytic anaemia)

1'. Pulmonary veno-occlusive disease or pulmonary capillary haemangiomatosis
1". Persistent pulmonary hypertension of the newborn (PPHN)
Group 2. Pulmonary hypertension due to left heart disease
- 2.1 Systolic dysfunction
- 2.2 Diastolic dysfunction
- 2.3 Valvular heart disease
- 2.4 Congenital/acquired left heart inflow/outflow tract obstruction and congenital cardiomyopathies

Group 3. Pulmonary hypertension due to chronic lung diseases or hypoxia
- 3.1 Chronic obstructive pulmonary disease
- 3.2 Interstitial lung disease
- 3.3 Other pulmonary diseases with a mixed restrictive and obstructive pattern
- 3.4 Sleep-disordered breathing
- 3.5 Alveolar hypoventilation disorders
- 3.6 Chronic exposure to high altitude
- 3.7 Developmental abnormalities

Group 4. Chronic thromboembolic pulmonary hypertension (CTEPH)
Group 5. Pulmonary hypertension due to unclear or multifactorial mechanisms
- 5.1 Haematological disorders
- 5.2 Systemic disorders
- 5.3 Metabolic disorders
- 5.4 Others

Reproduced and modified from [1] with permission from the publisher.

The diagnostic process

Because of the nonspecific and subtle onset of symptoms at presentation (exercise-induced dyspnoea, syncope, unexplained fatigue), most PH patients are diagnosed when the disease is already at an advanced stage [7–9]. Early detection and therefore early initiation of treatment can improve clinical outcome. Often, noninvasive imaging techniques, such as CT and cardiac echocardiography, are performed during the diagnostic work-up of patients presenting with shortness of breath. Both techniques provide the opportunity to assess highly sensitive and specific parameters that either point towards PH or rule it out.

Computed tomography

CT performed routinely in patients presenting with shortness of breath may provide important clues about the presence of PH. The most extensively studied parameter that predicts PH on CT pulmonary angiography is a diameter ratio >1 for the pulmonary artery (PA) to ascending aorta (AA), measured at the level of the bifurcation of the pulmonary trunk [10–13]. In 2014, a meta-analysis showed a relatively high sensitivity of 74% and a specificity of 81% for this diagnostic test [14]. In 2014, Spruijt *et al.* [15] showed an increased predictive value and sensitivity of CT pulmonary angiography when ventricular measurements were added to the PA:AA ratio. Other important parameters are PA *versus* bronchus diameter and

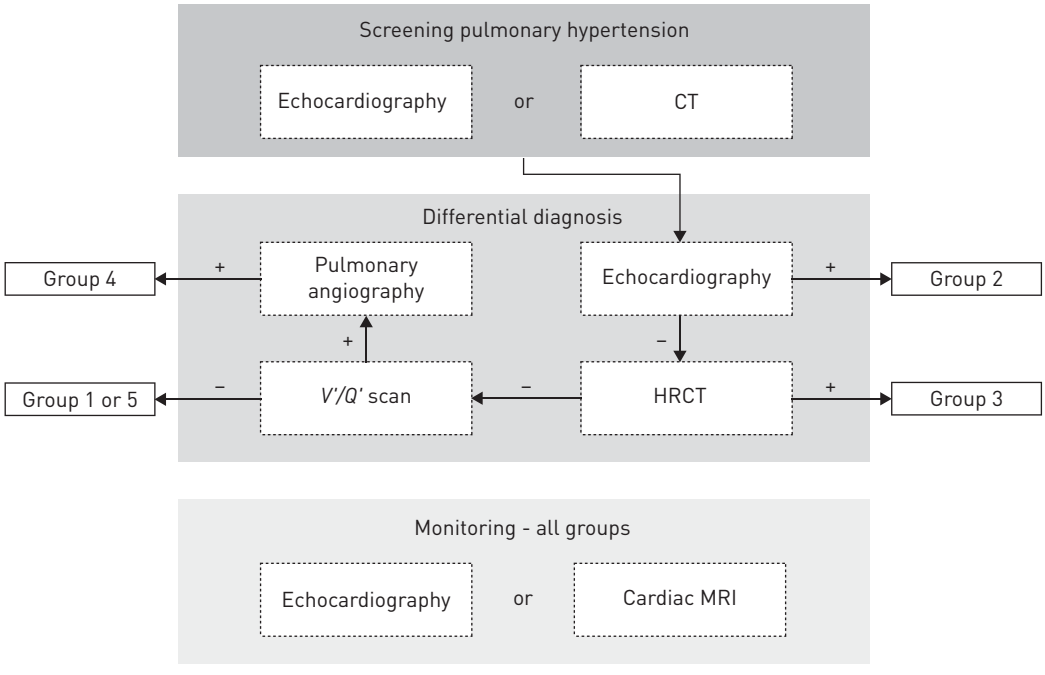

Figure 1. Screening, diagnosing and monitoring pulmonary hypertension. *V'/Q'*: ventilation/perfusion.

RV hypertrophy. Hence, isolated CT pulmonary angiography measurements are not enough to rule out or confirm PAH. Echocardiography is recommended as the next diagnostic step.

Echocardiography

Echocardiography is a noninvasive, inexpensive and widely available technique and therefore attractive as a screening tool to estimate pulmonary pressure and assess RV function. Yock and Popp [16] were the first to find a strong correlation between echo-Doppler (ED)-derived estimated pulmonary pressures and RHC-derived RV pressures, using the simplified Bernouilli equation to calculate the pressure gradient between the RV and right atrium (RA). More recent studies showed a tendency to both under- and overestimate using this method, particularly at higher pressures [17–19]. Thus, despite the initial impressive associations, ED-derived pressures cannot be used as a substitute for invasive pressure measurements during RHC. Nevertheless, this method remains a reliable and adequate screening tool for PH. An apical four-chamber view showing RV hypertrophy, dilatation or RA dilation may further indicate a diagnosis of PH.

Making the correct diagnosis

When PH is the likely diagnosis, based on the results of an echocardiography or CT scan, or confirmed by means of RHC, multiple underlying causes should be considered. Noninvasive imaging modalities play an important role in arriving at the correct diagnosis. In the following section, we discuss the added value of imaging techniques in the diagnostic process according to the current ERS diagnostic guidelines, summarised in figure 1.

Excluding the most common causes of PH: PH due to left heart disease and hypoxia/lung disease

PH due to left heart disease (PH-LHD) (classified as group 2 PH) is the most common cause of PH. It is defined as a mPAP ⩾25 mmHg at rest, accompanied by a pulmonary arterial wedge pressure >15 mmHg [20]. The presence of PH in combination with heart failure (HF) with preserved or reduced ejection fraction (EF), results in more severe symptoms and reduced exercise tolerance, and is associated with high morbidity and mortality in comparison to HF patients without PH [21–23]. Diagnosing PH-LHD correctly is crucial in the diagnostic process, given the potential detrimental effects of drugs used to treat pre-capillary disease in patients suffering from PH-LHD [24].

Echocardiography plays a crucial role in diagnosing PH-LHD, especially by allowing a distinction to be made between diastolic and systolic HF or by showing a combination of both conditions [25, 26]. Although diagnosing systolic HF is a straightforward process, diagnosing diastolic HF remains a challenge. Left atrial dilatation may be one of the most sensitive echocardiographic parameters to diagnose diastolic HF [27, 28]. HRCT plays a minor role in the diagnosis of PH-LHD, although mosaic perfusion patterns and ground-glass opacities might be indicative of the disease.

The prevalence of PH due to hypoxia/lung diseases varies from 5 to 36% in COPD to around 12% in idiopathic pulmonary fibrosis patients, and an estimated 40% in patients with combined pulmonary fibrosis and emphysema [29–33]. Although dyspnoea and reduced exercise tolerance in this patient group is usually not primarily due to circulatory limitations, PH is a strong predictor of mortality and therefore important to acknowledge [34].

Estimating pulmonary pressures may be challenging in group 3 PH patients. Several factors, such as hyperinflation of the lungs and alterations in heart position, may influence the accuracy of assessing the velocity of the tricuspid regurgitation jet. In previous studies, pulmonary pressures could be estimated in 44–87% of patients, depending on disease severity [35–38]. Moreover, since sensitivity and specificity are lower compared to other PH groups and the positive predictive value is poor (87%), reliance on echocardiography can lead to overestimation of PH prevalence [37, 39, 40]. Using RV characteristics, PH can be reliably excluded by the absence of RV abnormalities (RV hypertrophy, dilation or systolic dysfunction) [39].

Notably, since COPD and other lung diseases have a high prevalence, the presence of PH may be coincidental. Noninvasive imaging in combination with pulmonary function and exercise testing may play an important role in differentiating between group 1 and group 3 patients. HRCT plays a crucial role in the assessment of underlying lung disease as a possible cause of PH (group 3).

Chronic thromboembolic pulmonary hypertension

If PH-LHD and PH due to hypoxia/lung disease are excluded as the underlying cause of PH, the next diagnostic step is to study the probability of CTEPH.

The first description of CTEPH dates back to the 1920s, when Barnes and Yater [41] recognised nonresolving thromboemboli as a possible cause of RV failure. Nearly a century

later, even though knowledge has increased dramatically, the pathogenesis of CTEPH is still not fully understood. The main contributors of disease development and progression are persistent vascular obstruction, small-vessel arteriopathy and vasoconstriction [42]. Even though it is suggested that 1–4% of patients with acute pulmonary emboli (APE) develop CTEPH, a large subgroup of CTEPH patients (25–63%) does not have a previous history of APE or deep venous thrombi, making it challenging to assess true incidence and prevalence [43–45].

For 60–80% of patients, a potentially curative treatment is available: pulmonary endarterectomy (PEA). This surgical procedure involves the eradication of obstructive tissue from the pulmonary arteries during circulatory arrest. Although the procedure is invasive and carries considerable mortality, the long-term outcomes of PEA with regard to functional status, quality of life and haemodynamics are very positive [46–48]. Therefore, it is of the utmost importance to diagnose CTEPH early and, further, to recognise patients eligible for PEA.

Diagnosis is based on two criteria: 1) PH ascertained by RHC; 2) at least one larger defect as shown by radionuclide ventilation/perfusion (V'/Q') scanning after at least 3 months of adequate anticoagulation therapy [20, 49, 50]. In recent years, CT angiography has largely replaced V'/Q' scanning. Even though earlier studies suggested a superior sensitivity of V'/Q' scanning, novel studies have shown comparable or non-inferior accuracy of CT angiography in diagnosing CTEPH [51–53]. A recent study by Rajaram *et al.* [54] showed similar sensitivity (94%) using 3D contrast-enhanced lung perfusion MRI, with the advantage of being able to better assess regional perfusion abnormalities without using potentially harmful ionising radiation.

If V'/Q' is suggestive for CTEPH, further diagnostic steps are required to assess if patients are suitable for PEA. CT and pulmonary angiography play an important role in this process. Whereas CT angiography might be superior when assessing central lesions, pulmonary angiography performs better in imaging more peripheral lesions. Vascular abnormalities that can be observed with CTEPH consist of completely obstructed vessels due to organised thrombi (sudden loss of contrast-filled vessels) and partly obstructed vessels (narrowed vasculature, arterial webs and bands) [55]. A typical example of CTEPH imaging is shown in figure 2.

Parenchymal signs visible on CT angiography may include a mosaic perfusion pattern, bronchial anomalies and focal ground-glass opacities. Moreover, bronchial circulation can increase thirty-fold in CTEPH patients, leading to bronchial hypervascularisation, which manifests as dilatation and tortuosity at CT angiography [56–58]. Recent developments of dual-energy CT suggest improved detection of peripheral thromboembolic disease in the future [59, 60]. The use of MRI in diagnosing CTEPH is emerging, particularly because of the large benefits to be derived from combined perfusion measurements and magnetic resonance angiography, and how these may be used to assess RV function [54, 61].

The less common causes of PH: PAH or PH with unclear or multifactorial mechanisms

PAH is primarily a disease of the pulmonary vasculature, which is characterised by progressive vascular remodelling and narrowing of the pre-capillary pulmonary arteries. It may be idiopathic (IPAH) in nature or associated with an underlying condition, such as congenital heart disease (CHD), connective tissue disease or HIV/AIDS, or a genetic mutation (mostly mutations of bone morphogenetic protein receptor, type II (*BMPR2*)).

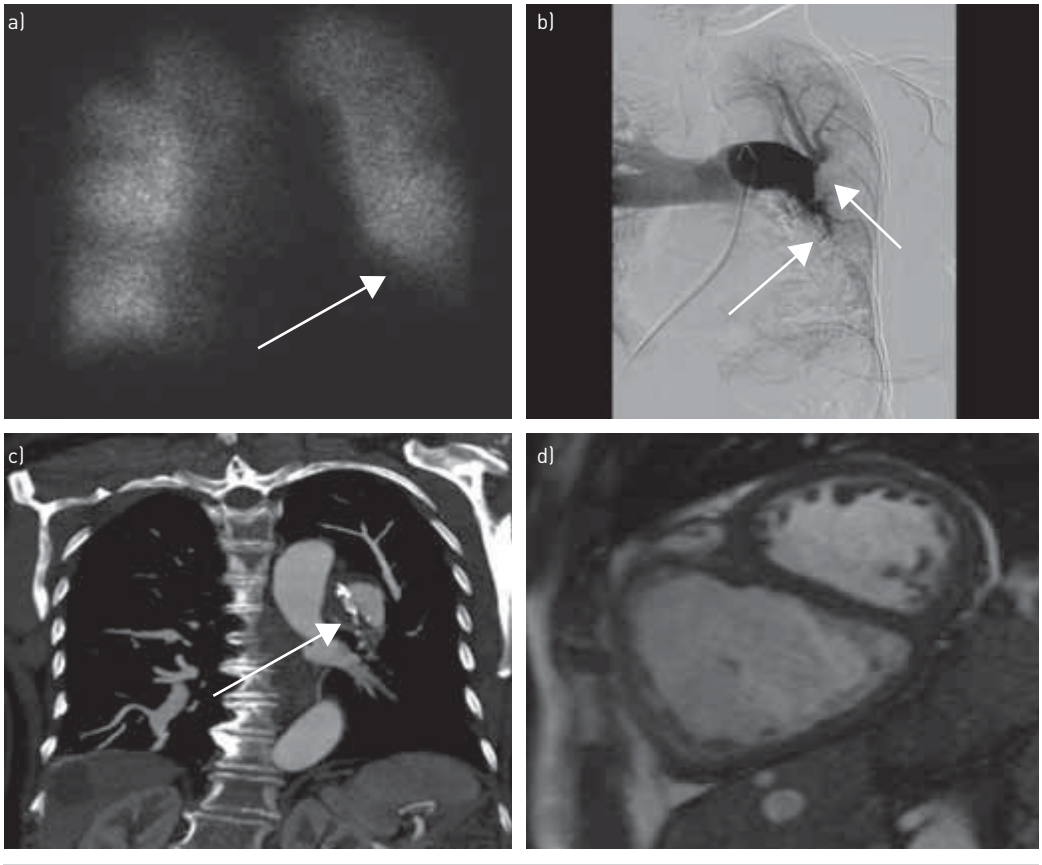

Figure 2. Images from a 59-year-old CTEPH patient. a) Ventilation/perfusion scan; the arrow indicates a perfusion defect. b) Pulmonary angiography; the arrows indicate perfusion defects. c) CT angiography; the arrow indicates the location and organisation of calcified intraluminal thrombi. d) Cardiac MRI showing the typical features of a pressure-overloaded right ventricle (RV): RV hypertrophy, dilatation and intraventricular septal flattening (D-shaped left ventricle).

Despite the different origins, the different groups share a similar clinical presentation and pathological changes of the lung microvasculature [20]. As PAH is a rare disease, population-based estimates of incidence and prevalence are not available. However, large registries from France, the UK and the USA report an incidence of 2–8 cases per million population per year [9, 62–66]. Diagnosis is primarily based on the absence of other causes of pre-capillary disease, mostly PH due to lung disease and CTEPH.

Besides clinical history, and physical examination and laboratory analysis, noninvasive imaging techniques may give important clues to differentiate patients within group 1 PAH.

PAH is a common complication in patients born with a congenital heart defect, as a response to chronic volume overload of pulmonary circulation as caused by a left-to-right shunt. A cardiac MRI and transthoracic or transoesophageal echocardiography are important diagnostic tools to diagnose systemic to pulmonary shunts, Eisenmenger's syndrome or small heart defects. Furthermore, a recent study found that PA calcifications, mural thrombi and centrilobular ground-glass opacities, as identified at CT, strongly indicate PAH-CHD [67].

An abdominal ultrasound may be very helpful where there is clinical suspicion of portal hypertension. To improve diagnostic accuracy, a colour Doppler ultrasound may be added.

Pulmonary veno-occlusive disease is a very rare cause of PH and is often misdiagnosed as IPAH. A definite diagnosis can only be made *via* a surgical biopsy, but as this is contraindicated in PH patients, a noninvasive diagnostic approach is needed. Hallmarks at HRCT typically are bilateral thickening of the interlobular septae, ground-glass opacities and interstitial oedema [68–70].

Group 5, PH with unclear and/or multifactorial mechanisms, is a very heterogeneous group with different pathogeneses and aetiologies, varying from systemic disorders to haematological diseases. Diagnosis is primarily based on physical examination and laboratory testing.

Disease severity and monitoring

Currently available therapies target the pulmonary vasculature, predominantly by vasodilation. Despite a wide range of therapeutic options, only partial reductions in PVR are achieved. These are not sufficient to achieve normal PVR values in the majority of patients, and therefore cannot prevent progression to right HF in PAH patients [2]. Furthermore, there is a very heterogeneous response to an increased afterload, independent of the amount of pressure itself, as shown in figure 3. As RV function is closely related to prognosis, when monitoring PH patients it is important to measure: systolic RVEF; tricuspid annular systolic excursion (TAPSE); RV fractional area change (RVFAC); diastolic function (RV end-diastolic volume); and isovolumic relaxation. The use of CT as a monitoring tool is limited due to the relatively high radiation use and a lack of clinically applicable parameters that are reflective of changes in pressure or function. Meanwhile, a broad range of cardiac MRI and echocardiography parameters have been shown to be reproducible, prognostic and sensitive to treatment [3, 4, 6, 71, 72].

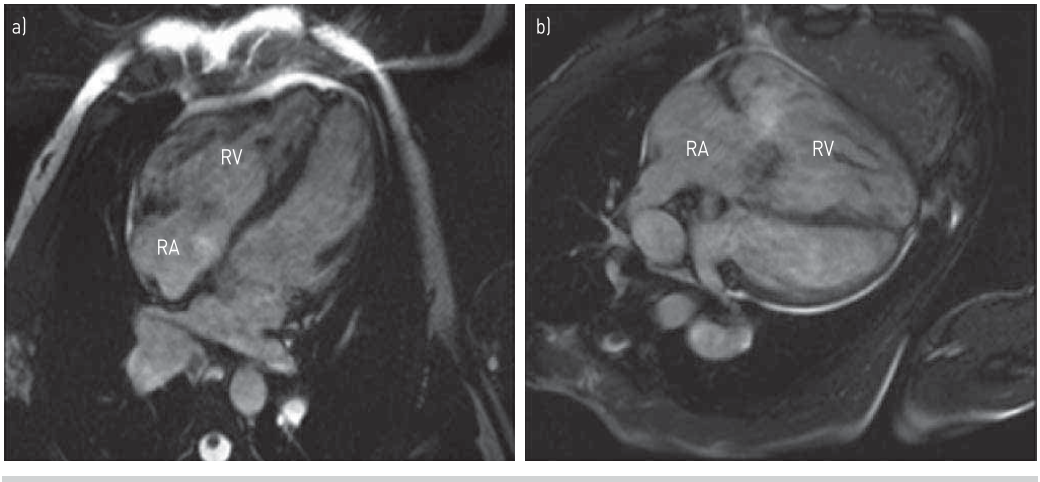

Figure 3. Cardiac adaptation is independent of pressure overload. Four-chamber cardiac MRI obtained for two patients with a different cardiac response to a similar pressure overload. a) The adapted right ventricle (RV) of patient A shows a hypertrophied RV accompanied by a small right atrium (RA). b) The failing RV of patient B shows RV dilatation together with a dilated RA, despite an even lower pressure overload (mean pulmonary artery pressure of 45 mmHg (patient B) compared to 55 mmHg (patient A)).

Echocardiography

Echocardiography is widely used to monitor PAH; it is highly cost-effective, widely available and safe. Despite the difficulties associated with assessing the complex anatomy of the highly trabeculated RV, 2D imaging, transthoracic echocardiography and Doppler imaging can provide important information on chamber size, and left ventricular (LV) and RV function [26, 73]. A major drawback of using echocardiography in the follow-up of PH patients is the lack of longitudinal studies assessing echocardiographic parameters over time.

The guidelines of the American Society of Echocardiography provide a comprehensive summary of echocardiographic parameters of the right heart [26]. The two most important parameters of RV systolic function are TAPSE and RVFAC. TAPSE is a measure used to assess longitudinal shortening. In contrast to the LV, which contracts almost uniformly in both transverse and longitudinal planes, the RV contracts predominantly along the longitudinal plane [74]. Baseline measurements of TAPSE have proved to be of great prognostic importance [3]. In end-stage disease, longitudinal shortening reaches a lower limit; thereafter RV function deteriorates due to a loss of circumferential shortening [75]. The second parameter, RVFAC, combines longitudinal and transverse RV shortening. Although this parameter best reflects MRI-derived RVEF [76, 77], assessing RVFAC might be challenging in severely dilated RVs.

Recent advances in echocardiography have led to the emergence of promising new 2D techniques. RV strain is a measurement of myocardial deformation. The myocardium deforms *via* longitudinal and circumferential shortening as a result of sarcomere shortening. RV strain can be used to assess global and regional RV function. A worsening RV systolic strain is associated with increased pulmonary pressure and decreased functional class [78, 79]. Furthermore, studies have shown that RV systolic strain is a predictor of morbidity and mortality and can improve after PH therapy [80]. However, no normative values are available as yet, so more research and experience is needed before being applied in clinical practice.

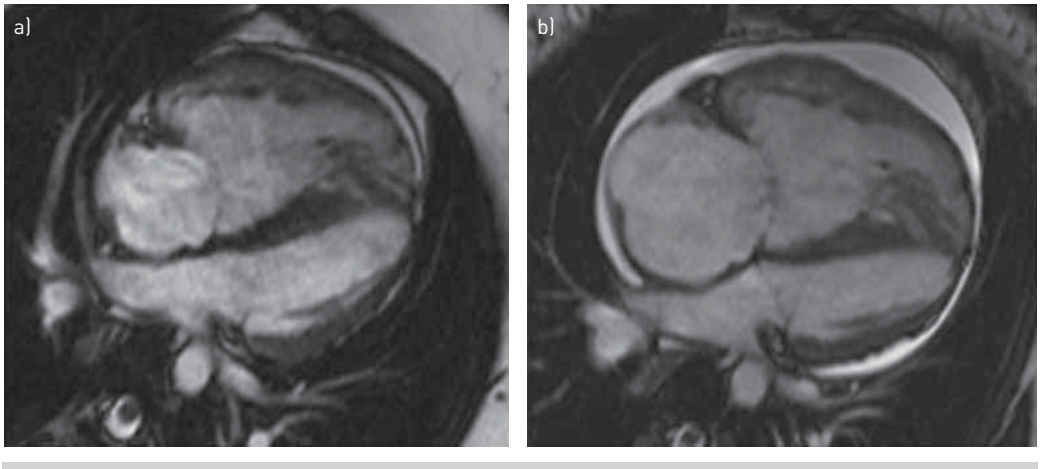

Figure 4. Pulmonary hypertension over time. Scans of an idiopathic pulmonary arterial hypertension patient at a) baseline and b) after 3 years of follow-up. a) A compensated right heart is shown, consisting of a hypertrophied right ventricle (RV), relatively small right atrium (RA) and no pericardial effusion. b) A failing dilated RV is shown, together with a dilated RA and pericardial effusion.

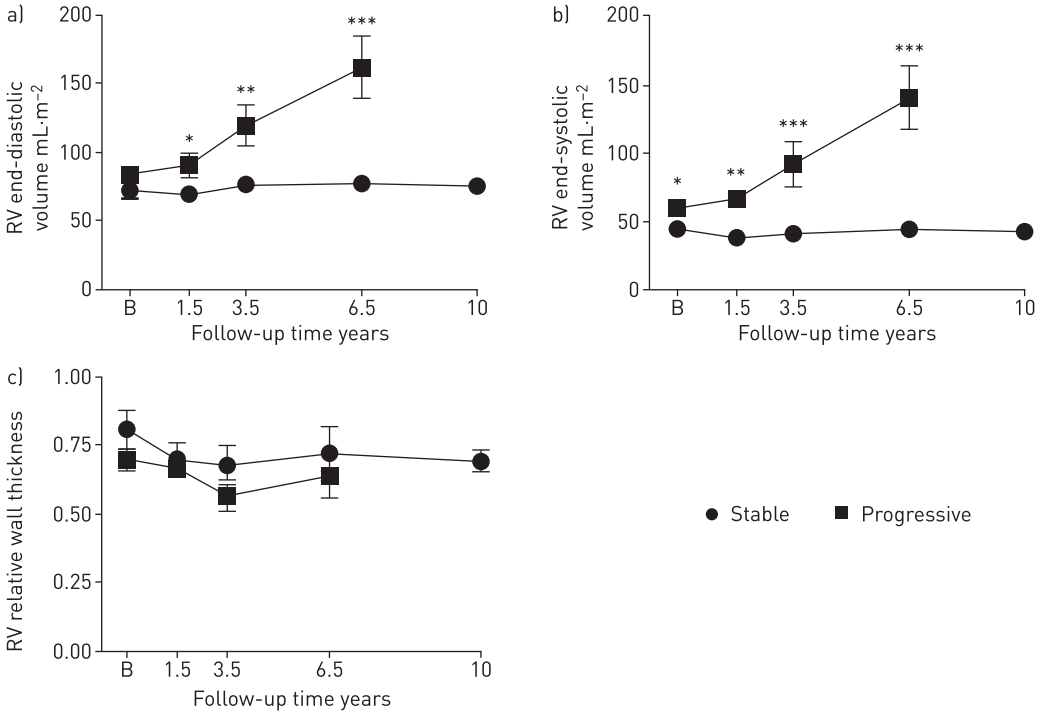

Figure 5. The importance of right ventricular (RV) function. a) RV end-diastolic and b) RV end-systolic volume increased progressively in patients whose disease was progressing, but remained unchanged in stable patients (interaction p-value for both <0.01). c) RV relative wall thickness was comparable in both groups at follow-up. Data are shown as mean±SEM. B: baseline. *: p<0.05 between groups; **: p<0.01 between groups; ***: p<0.001 between groups. Reproduced and modified from [81] with permission from the publisher.

Cardiac MRI

A cardiac MRI provides accurate, high-resolution, 3D quantitative information about ventricular volumes, mass, flows, structure and function without the need for ionising radiation and toxic contrast agents. Furthermore, cardiac MRI is the gold standard for assessing cardiac volumes. Despite being a more expensive and more time-consuming analysis, with only limited availability, cardiac MRI is regarded as the ideal monitoring tool for patients with PAH. Figure 4 shows the cardiac MRI scans of a PH patient over time.

Stroke volume, RV volumes, RVEF and LV end-diastolic volume are strongly predictive of survival both at baseline and during follow-up [2, 6]. Interestingly, a dilating RV and atrophying LV may be observed before clinical symptoms manifest, providing the opportunity to intervene at an early stage of RV failure, as shown in figure 5 [81]. One of the key measurements of systolic RV function is RVEF, calculated by dividing stroke volume by end-diastolic volume. Underscoring the importance of this measure, Van de Veerdonk *et al.* [2] showed that changes in RVEF, not PVR, predict outcome.

More detailed information about the RV myocardium can be obtained with cardiac MRI tagging to assess myocardial deformation, with delayed contrast-enhanced imaging with gadolinium, or by myocardial T1 mapping to assess regional fibrosis [82–84]. In some studies, delayed contrast enhancement was seen at the interventricular insertion points,

suggesting focal fibrosis [15, 85, 86]. No studies have been published so far that study the significance and usefulness of these measurements in the follow-up of PH patients.

Besides cardiac developments in MRI, recent studies have focused on the role of MRI in estimating pulmonary pressures. A reliable, noninvasive measure for pulmonary haemodynamics is an interesting and popular research topic, because it could make invasive procedures such as RHC unnecessary. Promising results in the studies by REITER and co-workers [87, 88] and KREITNER *et al.* [89] indicate that the use of MRI-derived velocity parameters enable an accurate, noninvasive assessment of pulmonary haemodynamics. However, further research involving multiple subgroups of PH patients is needed before this can be applied to clinical practice.

Conclusion

Noninvasive imaging techniques have a clear and vital role in both diagnosing and following up PH patients. The initial tools to identify PH are echocardiography and CT; however, RHC is still required for a definitive diagnosis. Subsequently, various noninvasive imaging techniques can be performed, depending on clinical suspicion and previous medical history. The most common forms of PH, groups 2 and 3, can be excluded using echocardiography and HRCT, respectively. A V'/Q' scan followed by CT angiography or pulmonary angiography provides additional information about the presence of chronic pulmonary emboli, as observed in CTEPH. When monitoring patients, cardiac MRI is the most informative and accurate tool, followed by echocardiography. Future imaging techniques will focus on gaining more insight into the RV myocardium, but it is still questionable whether these techniques will eventually be applied to clinical practice.

References

1. Simonneau G, Gatzoulis MA, Adatia I, *et al.* Updated clinical classification of pulmonary hypertension. *J Am Coll Cardiol* 2013; 62: Suppl. 25, D34–D41.
2. Van de Veerdonk MC, Kind T, Marcus JT, *et al.* Progressive right ventricular dysfunction in patients with pulmonary arterial hypertension responding to therapy. *J Am Coll Cardiol* 2011; 58: 2511–2519.
3. Forfia PR, Fisher MR, Mathai SC, *et al.* Tricuspid annular displacement predicts survival in pulmonary hypertension. *Am J Respir Crit Care Med* 2006; 174: 1034–1041.
4. Ghio S, Pazzano AS, Klersy C, *et al.* Clinical and prognostic relevance of echocardiographic evaluation of right ventricular geometry in patients with idiopathic pulmonary arterial hypertension. *Am J Cardiol* 2011; 107: 628–632.
5. Benza RL, Miller DP, Gomberg-Maitland M, *et al.* Predicting survival in pulmonary arterial hypertension: insights from the Registry to Evaluate Early and Long-Term Pulmonary Arterial Hypertension Disease Management (REVEAL). *Circulation* 2010; 122: 164–172.
6. Van Wolferen SA, Marcus JT, Boonstra A, *et al.* Prognostic value of right ventricular mass, volume, and function in idiopathic pulmonary arterial hypertension. *Eur Heart J* 2007; 28: 1250–1257.
7. Badesch DB, Raskob GE, Elliott CG, *et al.* Pulmonary arterial hypertension: baseline characteristics from the REVEAL Registry. *Chest* 2010; 137: 376–387.
8. Strange G, Gabbay E, Kermeen F, *et al.* Time from symptoms to definitive diagnosis of idiopathic pulmonary arterial hypertension: the delay study. *Pulm Circ* 2013; 3: 89–94.
9. Ling Y, Johnson MK, Kiely DG, *et al.* Changing demographics, epidemiology, and survival of incident pulmonary arterial hypertension: results from the pulmonary hypertension registry of the United Kingdom and Ireland. *Am J Respir Crit Care Med* 2012; 186: 790–796.
10. Ng CS, Wells AU, Padley SP. A CT sign of chronic pulmonary arterial hypertension: the ratio of main pulmonary artery to aortic diameter. *J Thorac Imaging* 1999; 14: 270–278.
11. Tan RT, Kuzo R, Goodman LR, *et al.* Utility of CT scan evaluation for predicting pulmonary hypertension in patients with parenchymal lung disease. Medical College of Wisconsin Lung Transplant Group. *Chest* 1998; 113: 1250–1256.

12. Sanal S, Aronow WS, Ravipati G, *et al.* Prediction of moderate or severe pulmonary hypertension by main pulmonary artery diameter and main pulmonary artery diameter/ascending aorta diameter in pulmonary embolism. *Cardiol Rev* 2006; 14: 213–214.
13. Gan CT, Lankhaar JW, Westerhof N, *et al.* Noninvasively assessed pulmonary artery stiffness predicts mortality in pulmonary arterial hypertension. *Chest* 2007; 132: 1906–1912.
14. Shen Y, Wan C, Tian P, *et al.* CT-base pulmonary artery measurement in the detection of pulmonary hypertension: a meta-analysis and systematic review. *Medicine (Baltimore)* 2014; 93: e256.
15. Spruijt OA, Bogaard HJ, Heijmans MW, *et al.* Predicting pulmonary hypertension with standard computed tomography pulmonary angiography. *Int J Cardiovasc Imaging* 2015; 31: 871–879.
16. Yock PG, Popp RL. Noninvasive estimation of right ventricular systolic pressure by Doppler ultrasound in patients with tricuspid regurgitation. *Circulation* 1984; 70: 657–662.
17. Hinderliter AL, Willis PW 4th, Barst RJ, *et al.* Effects of long-term infusion of prostacyclin (epoprostenol) on echocardiographic measures of right ventricular structure and function in primary pulmonary hypertension. Primary Pulmonary Hypertension Study Group. *Circulation* 1997; 95: 1479–1486.
18. Fisher MR, Forfia PR, Chamera E, *et al.* Accuracy of Doppler echocardiography in the hemodynamic assessment of pulmonary hypertension. *Am J Respir Crit Care Med* 2009; 179: 615–621.
19. Greiner S, Jud A, Aurich M, *et al.* Reliability of noninvasive assessment of systolic pulmonary artery pressure by Doppler echocardiography compared to right heart catheterization: analysis in a large patient population. *J Am Heart Assoc* 2014; 3: e001103.
20. Galiè N, Hoeper MM, Humbert M, *et al.* Guidelines for the diagnosis and treatment of pulmonary hypertension: the Task Force for the Diagnosis and Treatment of Pulmonary Hypertension of the European Society of Cardiology (ESC) and the European Respiratory Society (ERS), endorsed by the International Society of Heart and Lung Transplantation (ISHLT). *Eur Heart J* 2009; 30: 2493–2537.
21. Guazzi M, Borlaug BA. Pulmonary hypertension due to left heart disease. *Circulation* 2012; 126: 975–990.
22. Fang JC, DeMarco T, Givertz MM, *et al.* World Health Organization Pulmonary Hypertension group 2: pulmonary hypertension due to left heart disease in the adult – a summary statement from the Pulmonary Hypertension Council of the International Society for Heart and Lung Transplantation. *J Heart Lung Transplant* 2012; 31: 913–933.
23. Ghio S, Gavazzi A, Campana C, *et al.* Independent and additive prognostic value of right ventricular systolic function and pulmonary artery pressure in patients with chronic heart failure. *J Am Coll Cardiol* 2001; 37: 183–188.
24. Lundgren J, Rådegran G. Pathophysiology and potential treatments of pulmonary hypertension due to systolic left heart failure. *Acta Physiol (Oxf)* 2014; 211: 314–333.
25. Lang RM, Badano LP, Mor-Avi V, *et al.* Recommendations for cardiac chamber quantification by echocardiography in adults: an update from the American Society of Echocardiography and the European Association of Cardiovascular Imaging. *J Am Soc Echocardiogr* 2015; 28: 1–39.
26. Rudski LG, Lai WW, Afilalo J, *et al.* Guidelines for the echocardiographic assessment of the right heart in adults: a report from the American Society of Echocardiography endorsed by the European Association of Echocardiography, a registered branch of the European Society of Cardiology, and the Canadian Society of Echocardiography. *J Am Soc Echocardiogr* 2010; 23: 685–713.
27. Kurt M, Wang J, Torre-Amione G, *et al.* Left atrial function in diastolic heart failure. *Circ Cardiovasc Imaging* 2009; 2: 10–15.
28. Motoki H, Borowski AG, Shrestha K, *et al.* Impact of left ventricular diastolic function on left atrial mechanics in systolic heart failure. *Am J Cardiol* 2013; 112: 821–826.
29. Andersen KH, Iversen M, Kjaergaard J, *et al.* Prevalence, predictors, and survival in pulmonary hypertension related to end-stage chronic obstructive pulmonary disease. *J Heart Lung Transplant* 2012; 31: 373–380.
30. Hamada K, Nagai S, Tanaka S, *et al.* Significance of pulmonary arterial pressure and diffusion capacity of the lung as prognosticator in patients with idiopathic pulmonary fibrosis. *Chest* 2007; 131: 650–656.
31. Kimura M, Taniguchi H, Kondoh Y, *et al.* Pulmonary hypertension as a prognostic indicator at the initial evaluation in idiopathic pulmonary fibrosis. *Respiration* 2013; 85: 456–463.
32. Cottin V, Le Pavec J, Prévot G, *et al.* Pulmonary hypertension in patients with combined pulmonary fibrosis and emphysema syndrome. *Eur Respir J* 2010; 35: 105–111.
33. Chaouat A, Bugnet AS, Kadaoui N, *et al.* Severe pulmonary hypertension and chronic obstructive pulmonary disease. *Am J Respir Crit Care Med* 2005; 172: 189–194.
34. Oswald-Mammosser M, Weitzenblum E, Quoix E, *et al.* Prognostic factors in COPD patients receiving long-term oxygen therapy. Importance of pulmonary artery pressure. *Chest* 1995; 107: 1193–1198.
35. Torbicki A, Skwarski K, Hawrylkiewicz I, *et al.* Attempts at measuring pulmonary arterial pressure by means of Doppler echocardiography in patients with chronic lung disease. *Eur Respir J* 1989; 2: 856–860.
36. Homma A, Anzueto A, Peters JI, *et al.* Pulmonary artery systolic pressures estimated by echocardiogram *vs* cardiac catheterization in patients awaiting lung transplantation. *J Heart Lung Transplant* 2001; 20: 833–839.

37. Tramarin R, Torbicki A, Marchandise B, *et al.* Doppler echocardiographic evaluation of pulmonary artery pressure in chronic obstructive pulmonary disease. A European multicentre study. Working Group on Noninvasive Evaluation of Pulmonary Artery Pressure. European Office of the World Health Organization, Copenhagen. *Eur Heart J* 1991; 12: 103–111.
38. Bach DS, Curtis JL, Christensen PJ, *et al.* Preoperative echocardiographic evaluation of patients referred for lung volume reduction surgery. *Chest* 1998; 114: 972–980.
39. Arcasoy SM, Christie JD, Ferrari VA, *et al.* Echocardiographic assessment of pulmonary hypertension in patients with advanced lung disease. *Am J Respir Crit Care Med* 2003; 167: 735–740.
40. Laaban JP, Diebold B, Zelinski R, *et al.* Noninvasive estimation of systolic pulmonary artery pressure using Doppler echocardiography in patients with chronic obstructive pulmonary disease. *Chest* 1989; 96: 1258–1262.
41. Barnes AR, Yater WM. Failure of right ventricle due to ancient thrombus. *M Clin North America* 1929; 12: 1610.
42. Piazza G, Goldhaber SZ. Chronic thromboembolic pulmonary hypertension. *N Engl J Med* 2011; 364: 351–360.
43. Becattini C, Agnelli G, Pesavento R, *et al.* Incidence of chronic thromboembolic pulmonary hypertension after a first episode of pulmonary embolism. *Chest* 2006; 130: 172–175.
44. Pengo V, Lensing AW, Prins MH, *et al.* Incidence of chronic thromboembolic pulmonary hypertension after pulmonary embolism. *N Engl J Med* 2004; 350: 2257–2264.
45. Riedel M, Stanek V, Widimsky J, *et al.* Longterm follow-up of patients with pulmonary thromboembolism. Late prognosis and evolution of hemodynamic and respiratory data. *Chest* 1982; 81: 151–158.
46. Jenkins D. Pulmonary endarterectomy: the potentially curative treatment for patients with chronic thromboembolic pulmonary hypertension. *Eur Respir Rev* 2015; 24: 263–271.
47. Ishida K, Masuda M, Tanabe N, *et al.* Long-term outcome after pulmonary endarterectomy for chronic thromboembolic pulmonary hypertension. *J Thorac Cardiovasc Surg* 2012; 144: 321–326.
48. Mayer E, Klepetko W. Techniques and outcomes of pulmonary endarterectomy for chronic thromboembolic pulmonary hypertension. *Proc Am Thorac Soc* 2006; 3: 589–593.
49. Wilkens H, Lang I, Behr J, *et al.* Chronic thromboembolic pulmonary hypertension (CTEPH): updated Recommendations of the Cologne Consensus Conference 2011. *Int J Cardiol* 2011; 154: Suppl. 1, S54–S60.
50. Condliffe R, Kiely DG, Gibbs JS, *et al.* Prognostic and aetiological factors in chronic thromboembolic pulmonary hypertension. *Eur Respir J* 2009; 33: 332–338.
51. He J, Fang W, Lv B, *et al.* Diagnosis of chronic thromboembolic pulmonary hypertension: comparison of ventilation/perfusion scanning and multidetector computed tomography pulmonary angiography with pulmonary angiography. *Nucl Med Commun* 2012; 33: 459–463.
52. Sugiura T, Tanabe N, Matsuura Y, *et al.* Role of 320-slice CT imaging in the diagnostic workup of patients with chronic thromboembolic pulmonary hypertension. *Chest* 2013; 143: 1070–1077.
53. Tanabe N, Sugiura T, Tatsumi K. Recent progress in the diagnosis and management of chronic thromboembolic pulmonary hypertension. *Respir Investig* 2013; 51: 134–146.
54. Rajaram S, Swift AJ, Telfer A, *et al.* 3D contrast-enhanced lung perfusion MRI is an effective screening tool for chronic thromboembolic pulmonary hypertension: results from the ASPIRE Registry. *Thorax* 2013; 68: 677–678.
55. Ley S, Ley-Zaporozhan J, Pitton MB, *et al.* Diagnostic performance of state-of-the-art imaging techniques for morphological assessment of vascular abnormalities in patients with chronic thromboembolic pulmonary hypertension (CTEPH). *Eur Radiol* 2012; 22: 607–616.
56. Endrys J, Hayat N, Cherian G. Comparison of bronchopulmonary collaterals and collateral blood flow in patients with chronic thromboembolic and primary pulmonary hypertension. *Heart* 1997; 78: 171–176.
57. Ley S, Kreitner KF, Morgenstern I, *et al.* Bronchopulmonary shunts in patients with chronic thromboembolic pulmonary hypertension: evaluation with helical CT and MR imaging. *AJR Am J Roentgenol* 2002; 179: 1209–1215.
58. Shimizu H, Tanabe N, Terada J, *et al.* Dilatation of bronchial arteries correlates with extent of central disease in patients with chronic thromboembolic pulmonary hypertension. *Circ J* 2008; 72: 1136–1141.
59. Ameli-Renani S, Rahman F, Nair A, *et al.* Dual-energy CT for imaging of pulmonary hypertension: challenges and opportunities. *Radiographics* 2014; 34: 1769–1790.
60. Dournes G, Verdier D, Montaudon M, *et al.* Dual-energy CT perfusion and angiography in chronic thromboembolic pulmonary hypertension: diagnostic accuracy and concordance with radionuclide scintigraphy. *Eur Radiol* 2014; 24: 42–51.
61. Henzler T, Schmid-Bindert G, Schoenberg SO, *et al.* Diffusion and perfusion MRI of the lung and mediastinum. *Eur J Radiol* 2010; 76: 329–336.
62. Peacock AJ, Murphy NF, McMurray JJ, *et al.* An epidemiological study of pulmonary arterial hypertension. *Eur Respir J* 2007; 30: 104–109.
63. Humbert M, Sitbon O, Chaouat A, *et al.* Pulmonary arterial hypertension in France: results from a national registry. *Am J Respir Crit Care Med* 2006; 173: 1023–1030.
64. Tueller C, Stricker H, Soccal P, *et al.* Epidemiology of pulmonary hypertension: new data from the Swiss registry. *Swiss Med Wkly* 2008; 138: 379–384.

65. Hurdman J, Condliffe R, Elliot CA, *et al.* ASPIRE registry: assessing the Spectrum of Pulmonary hypertension Identified at a REferral centre. *Eur Respir J* 2012; 39: 945–955.
66. Frost AE, Badesch DB, Barst RJ, *et al.* The changing picture of patients with pulmonary arterial hypertension in the United States: how REVEAL differs from historic and non-US Contemporary Registries. *Chest* 2011; 139: 128–137.
67. Rajaram S, Swift AJ, Condliffe R, *et al.* CT features of pulmonary arterial hypertension and its major subtypes: a systematic CT evaluation of 292 patients from the ASPIRE Registry. *Thorax* 2015; 70: 382–387.
68. Montani D, Achouh L, Dorfmüller P, *et al.* Pulmonary veno-occlusive disease: clinical, functional, radiologic, and hemodynamic characteristics and outcome of 24 cases confirmed by histology. *Medicine (Baltimore)* 2008; 87: 220–233.
69. Montani D, Price LC, Dorfmüller P, *et al.* Pulmonary veno-occlusive disease. *Eur Respir J* 2009; 33: 189–200.
70. Resten A, Maitre S, Humbert M, *et al.* Pulmonary hypertension: CT of the chest in pulmonary venoocclusive disease. *AJR Am J Roentgenol* 2004; 183: 65–70.
71. Yeo TC, Dujardin KS, Tei C, *et al.* Value of a Doppler-derived index combining systolic and diastolic time intervals in predicting outcome in primary pulmonary hypertension. *Am J Cardiol* 1998; 81: 1157–1161.
72. Raymond RJ, Hinderliter AL, Willis PW, *et al.* Echocardiographic predictors of adverse outcomes in primary pulmonary hypertension. *J Am Coll Cardiol* 2002; 39: 1214–1219.
73. McLaughlin VV, Archer SL, Badesch DB, *et al.* ACCF/AHA 2009 Expert Consensus Document on Pulmonary Hypertension. A report of the American College of Cardiology Foundation Task Force on Expert Consensus Documents and the American Heart Association developed in collaboration with the American College of Chest Physicians; American Thoracic Society, Inc.; and the Pulmonary Hypertension Association. *J Am Coll Cardiol* 2009; 53: 1573–1619.
74. Rushmer RF, Crystal DK, Wagner C. The functional anatomy of ventricular contraction. *Circ Res* 1953; 1: 162–170.
75. Mauritz GJ, Kind T, Marcus JT, *et al.* Progressive changes in right ventricular geometric shortening and long-term survival in pulmonary arterial hypertension. *Chest* 2012; 141: 935–943.
76. Shiran H, Zamanian RT, McConnell MV, *et al.* Relationship between echocardiographic and magnetic resonance derived measures of right ventricular size and function in patients with pulmonary hypertension. *J Am Soc Echocardiogr* 2014; 27: 405–412.
77. Kind T, Mauritz G-J, Marcus JT, *et al.* Right ventricular ejection fraction is better reflected by transverse rather than longitudinal wall motion in pulmonary hypertension. *J Cardiovasc Magn Reson* 2010; 12: 35.
78. Haeck ML, Scherptong RW, Marsan NA, *et al.* Prognostic value of right ventricular longitudinal peak systolic strain in patients with pulmonary hypertension. *Circ Cardiovasc Imaging* 2012; 5: 628–636.
79. Li Y, Xie M, Wang X, *et al.* Right ventricular regional and global systolic function is diminished in patients with pulmonary arterial hypertension: a 2-dimensional ultrasound speckle tracking echocardiography study. *Int J Cardiovasc Imaging* 2013; 29: 545–551.
80. Hardegree EL, Sachdev A, Villarraga HR, *et al.* Role of serial quantitative assessment of right ventricular function by strain in pulmonary arterial hypertension. *Am J Cardiol* 2013; 111: 143–148.
81. Van de Veerdonk MC, Marcus JT, Westerhof N, *et al.* Signs of right ventricular deterioration in clinically stable patients with pulmonary arterial hypertension. *Chest* 2015; 147: 1063–1071.
82. García-Álvarez A, García-Lunar I, Pereda D, *et al.* Association of myocardial T1-mapping CMR with hemodynamics and RV performance in pulmonary hypertension. *JACC Cardiovasc Imaging* 2015; 8: 76–82.
83. Shehata ML, Harouni AA, Skrok J, *et al.* Regional and global biventricular function in pulmonary arterial hypertension: a cardiac MR imaging study. *Radiology* 2013; 266: 114–122.
84. Mewton N, Liu CY, Croisille P, *et al.* Assessment of myocardial fibrosis with cardiovascular magnetic resonance. *J Am Coll Cardiol* 2011; 57: 891–903.
85. Blyth KG, Groenning BA, Martin TN, *et al.* Contrast enhanced-cardiovascular magnetic resonance imaging in patients with pulmonary hypertension. *Eur Heart J* 2005; 26: 1993–1999.
86. McCann GP, Gan CT, Beek AM, *et al.* Extent of MRI delayed enhancement of myocardial mass is related to right ventricular dysfunction in pulmonary artery hypertension. *AJR Am J Roentgenol* 2007; 188: 349–355.
87. Reiter G, Reiter U, Kovacs G, *et al.* Magnetic resonance-derived 3-dimensional blood flow patterns in the main pulmonary artery as a marker of pulmonary hypertension and a measure of elevated mean pulmonary arterial pressure. *Circ Cardiovasc Imaging* 2008; 1: 23–30.
88. Reiter G, Reiter U, Kovacs G, *et al.* Blood flow vortices along the main pulmonary artery measured with MR imaging for diagnosis of pulmonary hypertension. *Radiology* 2015; 275: 71–79.
89. Kreitner K-F, Wirth GM, Krummenauer F, *et al.* Noninvasive assessment of pulmonary hemodynamics in patients with chronic thromboembolic pulmonary hypertension by high temporal resolution phase-contrast MRI: correlation with simultaneous invasive pressure recordings. *Circ Cardiovasc Imaging* 2013; 6: 722–729.

Disclosures: None declared.

Chapter 11

Asthma

Simonetta Baldi[1,3], Ruth Hartley[1,3], Chris Brightling[1] and Sumit Gupta[1,2]

Asthma imaging is undergoing an exciting transformation. From simply being a tool to assess for asthma mimics and conditions associated with asthma, imaging in asthma is now being used to provide quantitative assessment of morphology, function and pathogenic processes at the molecular level, opening up a variety of research and clinical prospects. Imaging in asthma can be used to obtain detailed structural and functional information, which can help in understanding pathophysiology, identify at-risk patients, monitor disease progression and assess response to therapy. Current and emerging imaging techniques in asthma are discussed in this chapter.

The gamut of new technologies that has emerged in recent years allows noninvasive, comprehensive anatomical and detailed functional assessment of the lungs. This has contributed significantly to the development of asthma imaging. Parameters such as FEV_1, symptom scores or frequency of exacerbations can only provide a global assessment of dysfunction in asthma and therefore are unable to capture the heterogeneity of asthma. Imaging-derived structural and physiological data allow us to study pathophysiological phenomena in asthma. Imaging is set to play an instrumental part in better assessing heterogeneity in asthma and detect response to therapy much earlier than traditionally employed methods. Key imaging modalities in asthma and their application are discussed in this chapter.

Computed tomography

CT is the workhorse of pulmonary imaging. However, in the clinical evaluation of asthma, CT plays a limited role, helping to identify asthma mimics and asthma-associated conditions. Current guidelines recommend the use of CT for the evaluation of refractory asthma [1–3]. Advances in CT and post-processing techniques have facilitated multiplanar reconstructions, three-dimensional surface and volume rendering of the airway tree and lung parenchyma, detailed quantitative analysis and virtual bronchoscopy [4–6]. Current CT provides sub-millimetre spatial resolution. Dual-energy thoracic CT, in addition to tremendously improving temporal resolution, has made lung ventilation and perfusion imaging possible. Quantitative CT analysis, with robust standardisation, can play an important role in linking lung structure alterations with abnormalities in lung function.

[1]Dept of Infection, Inflammation and Immunity, Institute for Lung Health, University of Leicester, Leicester, UK. [2]Radiology Dept, Glenfield Hospital, University Hospitals of Leicester NHS Trust, Leicester, UK. [3]Both authors contributed equally.

Correspondence: Sumit Gupta, Dept of Infection, Inflammation and Immunity, Institute for Lung Health, University of Leicester, Leicester LE3 9QP, UK. E-mail: drsumitgupta@yahoo.com

Copyright ©ERS 2015. Print ISBN: 978-1-84984-065-1. Online ISBN: 978-1-84984-066-8. Print ISSN: 2312-508X. Online ISSN: 2312-5098.

Proximal airways

Qualitative and quantitative assessment of proximal airways is possible in asthma, with qualitative assessment demonstrating several structural changes. Bronchiectasis [7–17] and bronchial wall thickening [7–11, 13–17] are prevalent in asthma. Bronchiectasis is associated with longer disease duration [7, 10, 11, 17] and poorer lung function [7, 17]. Association of CT-determined bronchiectasis with disease severity has been observed by some researchers [17, 18] but not others [12, 14]. In contrast, both asthma severity and longer disease duration have been shown to be associated with bronchial wall thickening [7, 9, 10, 13, 14, 16]. Other abnormal radiological findings seen on CT of asthma patients were mucus plugging, centrilobular opacities, mosaic lung attenuation and atelectasis [8, 16, 19].

Initial quantitative analysis techniques involved manual or digital delineation of the inner and outer airway wall boundaries on CT image to calculated lumen and airway wall dimensions [20, 21]. Currently used quantitative CT analyses have been made possible with advances in CT technology and post-processing techniques. Volumetric CT scans with near isotropic voxels are used for three-dimensional analysis of the airway tree, enabling reconstruction of images in a plane orthogonal to the long axis of the airway, thereby minimising quantification errors due to oblique orientation [22]. Aysola *et al.* [23] have shown a correlation between epithelial or lamina reticularis thickness on biopsy specimens of asthma subjects and CT indices of airway remodelling. Similar associations between pathological and CT indices of remodelling have been demonstrated by others [24].

Gupta *et al.* [25] showed in a cross-sectional study that the right upper lobe apical segmental bronchus (RB1) per cent wall area was associated with the preceding burden of neutrophilic inflammation assessed by temporal analysis of induced sputum. The same group of researchers found that despite similar degrees of airway eosinophilic inflammation, non-asthmatic eosinophilic bronchitis subjects lacked airway wall thickening and lumen narrowing compared to severe asthma subjects [26]. CT-assessed airway remodelling has also been shown to be associated with other markers of airway inflammation in sputum, such as elastase [27], transforming growth factor-β [28] and the ratio of matrix metalloproteinase-9 to tissue inhibitor of metalloproteinase-1 [27, 29, 30]. In contrast, other studies failed to show an association between airway remodelling and airway inflammation [31–33].

Airway morphometry has been used to delineate differences between asthma patients and healthy controls. Asthma patients have been shown to have increased airway wall dimensions that may [23, 32, 33] or may not be associated with disease severity [21, 26, 34, 35]. Airway wall thickening in asthma has been shown to correlate with airway hyperresponsiveness [23, 25, 33, 36] and airflow limitation [23, 25, 32, 37]. Air trapping on expiratory CT [37, 38] has also been shown to correlate to airway wall thickening assessed on inspiratory CT. Contradictory results in other studies comparing airway morphometry between asthma and healthy subjects show no difference in airway wall dimensions [25, 39]. However, these studies show that asthma patients have smaller airway lumen dimensions (figure 1) [25, 39, 40], despite patients being on bronchodilator treatment and bronchodilator administration prior to the CT scan. These observed differences in remodelling pattern may be secondary to the lack of quantitative CT standardisation, variable patient population, differences in morphometry technique or disease heterogeneity. Quantitative CT indices were used to identify three asthma clusters by Gupta *et al.* [39] (figure 2). This suggests that disease heterogeneity is an important feature of asthma and perhaps the discrepancy in previous airway morphometry studies is secondary to the selection of a variable asthma population. Further assessment of a subset of severe asthma patients from this cohort showed that, when grouped into quantitative CT-derived clusters, a

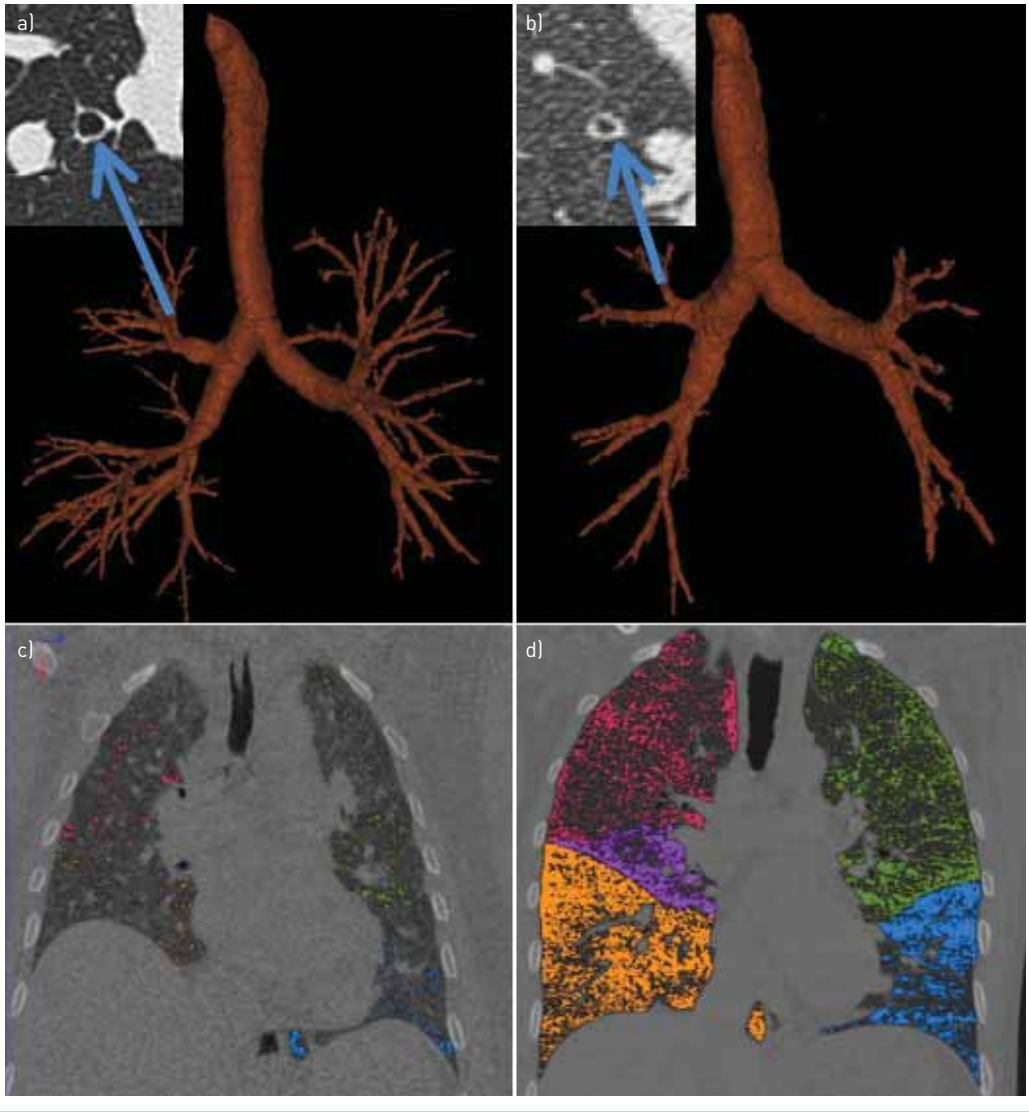

Figure 1. Three-dimensional reconstruction of an airway tree from a) a healthy subject and b) a severe asthmatic subject using automated software illustrating that in healthy subjects sub-segmental airways can be reconstructed to more generations than in asthma. This is due to increased airway narrowing and closure in asthma. The insets illustrate the cross-section of the right upper lobe apical segmental bronchus in a) healthy and b) severe asthma showing that the lumen is narrowed in asthma. Coronal section of expiratory CT from c) a healthy subject and d) a severe asthma subject showing increased low attenuation areas (colour coded according to lung lobes) in severe asthma compared with a healthy subject. Reproduced and modified from [39] with permission from the publisher.

differential temporal pattern of airway remodelling is seen [41]. These findings highlight the important role imaging could play in identifying new asthma phenotypes.

CT attenuation of the bronchial wall was found by Lederlin *et al.* [42] to be greater in patients with asthma compared to healthy subjects. Moreover, bronchial wall attenuation, compared to other quantitative CT indices, showed better correlation with physiological parameters of airflow limitation and mast cell infiltration.

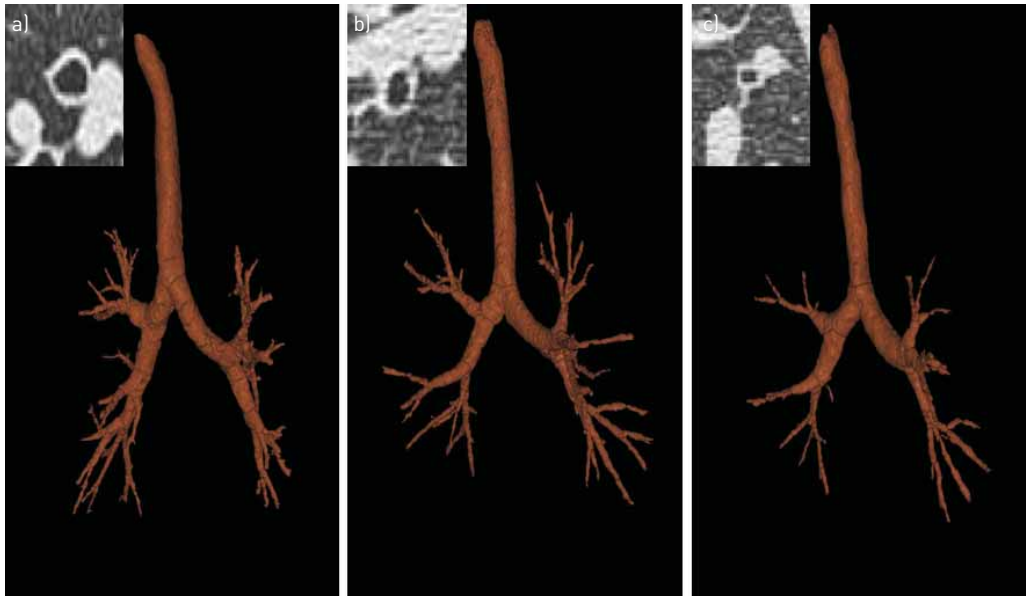

Figure 2. Pictures of the segmented airway tree and the right upper lobe apical segmental bronchus CT cross-section (insets) of asthma patients from three different quantitative CT-derived clusters. a) Cluster one: severe air trapping and bronchial lumen dilatation. b) Cluster two: moderate air trapping only. c) Cluster three: severe air trapping and bronchial luminal narrowing. Reproduced and modified from [39] with permission from the publisher.

Distal airways

Small airways in asthma have been shown to be the site of increased airflow resistance, despite normal spirometry and normal plethesmographic airway resistance [43, 44]. Indirect assessment of small airway remodelling is possible with thoracic CT. Although the causes of small airway dysfunction in asthma are poorly understood, it is accepted that it leads to reduced lung ventilation [45]. Reduced ventilation in turn leads to reduced perfusion of these areas of the lungs. The resulting regional decreased attenuation in the lungs [45] is called air trapping and can be quantified using CT lung densitometry. Emphysema quantification using lung densitometry is a well-established technique [46, 47]. Similarly, various quantitative CT indices of air trapping can be assessed: low attenuation areas with a threshold of −850 HU [38] or −900 HU [48] in expiration; differences between expiratory and inspiratory lung attenuation [49]; the ratio of the mean lung density between expiration and inspiration [37]; and the lowest 10th percentile lung attenuation frequency distribution [50]. It is pertinent to standardise CT lung densitometry, particularly for assessment of the change in longitudinal or interventional studies.

Quantitative CT has been used by several researchers to assess air trapping as an indirect measure of small airway remodelling (figure 1) [38, 39, 51, 52]. Quantitative CT-assessed air trapping has been shown to correlate with impaired lung function tests in asthma subjects [38, 40, 53]. Quantitative CT-assessed air trapping is linked to asthma severity [53, 54], and was found to be significantly higher in a population of uncontrolled asthmatics during an exacerbation as compared to controlled asthmatics and healthy controls [55]. In a study by Busacker *et al.* [38], the presence of quantitative CT-assessed air trapping in asthmatics was associated with an increased risk of having asthma-related hospital and intensive therapy unit admissions and longer disease duration. The association between quantitative

CT-assessed air trapping and airway hyperresponsiveness [50, 54] suggests that small airways may play an important role in determining this hallmark feature of asthma.

The ability of quantitative CT-assessed air trapping to assess response to treatment has also been investigated. Two studies used quantitative CT to assess improvement in air trapping with the use of inhaled corticosteroids, and compared a conventional preparation with an extra-fine preparation. Tunon-de-Lara *et al.* [49] showed that use of inhaled corticosteroids improved air trapping. Goldin *et al.* [56] demonstrated that the extra-fine inhalers had a greater effect on air trapping, and hence the small airways, compared to proximal airway morphometry. Montelukast therapy and systemic corticosteroids have been shown to improve air trapping in asthma subjects [55, 57].

New horizons

Comprehensive assessment of asthma using a single imaging technique is now possible. Dual-energy thoracic CT scanning provides an opportunity for comprehensive assessment of airway morphometry, lung densitometry, ventilation and perfusion [58]. Dual-energy CT applies to different kilovolts peak (kVp) settings simultaneously or rapidly after each other. Different sets of images are generated with dual-energy CT, one at each kVp setting and the weighted average formed by combination of two kVp settings. Such images can be used for tissue characterisation and iodine mapping. Ventilation imaging can be performed by inhalation of non-radioactive xenon, which due to its radiodense nature allows assessment of density changes that occur regionally in the lungs [59]. Ventilation assessment using dual-energy CT has demonstrated ventilation defects in asthmatics [60] that correlated with lung functions. Moreover, the configuration and location of defects were similar to those on hyperpolarised (HP) gas MRI [60]. Combined xenon-enhanced ventilation and iodine-enhanced perfusion dual-energy CT can be performed, enabling high spatial resolution morphological and functional ventilation/perfusion perfusion information using a single investigation [61].

The latest post-processing software platforms have enabled us to get quantitative structural information such as airway volume, length, wall thickness, or lung lobe and segment volumes from CT images. CT imaging, when combined with engineering techniques such as computational fluid dynamics (CFD), may provide new surrogate markers that enable researchers to predict clinically relevant functional changes in the lungs [62]. CFD uses traditional CT scans as a template, and from that builds patient-specific computer simulations of airflow through that patient's airways. This approach may provide image-based outcome parameters that can be used to test the efficiency and response to therapies. Recent studies have used CFD to test the effect of long-acting β_2-agonists [63], and a combination of a long-acting β_2-agonists and an inhaled corticosteroid [62]. De Backer *et al.* [64] have shown that the outputs from CFD are comparable to SPECT data. CFD can potentially play an important role in predicting and assessing response to pharmacological and non-pharmacological treatment including bronchial thermoplasty [65]. Functional respiratory imaging using CFD techniques, with its ability to provide regional and patient-specific data, could therefore become the pulmonary function test of the future.

Magnetic resonance imaging

MRI is well suited to functional imaging and does not use ionising radiation. It can therefore be ideal for longitudinal assessment with no known harmful consequences,

making it an imaging modality of choice for assessment of disease progression and response to treatment. MRI is a versatile technique and as a single modality can provide anatomical data as well as assessment of lung ventilation, diffusion and perfusion.

MRI is based on receiving and processing radiofrequency signals from hydrogen protons within the human body [66]. Lungs are deficient in both fat and water and therefore there is a low concentration of protons, making MRI of the lungs challenging. Susceptibility differences between air and tissue, field inhomogeneities within the thorax, and movement artefacts from breathing and cardiac motion add to the challenge of imaging the lungs using this technique [67]. Development of ultrafast imaging sequences, cardiac and respiratory gating, use of O_2-enhanced MRI and use of HP noble gases have helped overcome such issues. ^{3}He and ^{129}Xe have been used in several research studies. These gases rapidly reach the distal part of the lungs and provide much-needed contrast. More recently, the use of fluoride and O_2 has also emerged. MRI is free of ionising radiation and compared with other functional imaging methods such as PET [68], has relatively high 3D spatial and temporal resolution.

Ventilation imaging is performed using HP gases. To be able to detect ventilation abnormalities in asthma patients it is important to establish the findings expected in healthy individuals. Lee *et al.* [69] looked at six young healthy females and noted that peripheral ventilation defects <3 cm were common, therefore suggesting that such defects should be considered to be within the normal range. Other studies suggest that young healthy subjects have no visual or quantitative evidence of ventilation defects [70], although the healthy elderly population may have ventilation defects [71]. Asthmatic lungs are more likely to produce an inhomogeneous pattern, caused by poor distribution of the HP gas due to poor ventilation (figure 3) [72, 73]. These areas are known as ventilation defects. Several quantitative indices of such defects have been proposed: 1) ventilation defect volume, the sum total of the volume of defects; 2) ventilation defect percentage, the percentage of the lung taken up by the defects, and 3) the number of ventilation defects seen [74]. Svenningsen *et al.* [70] found that the majority of asthmatics (65%) had obvious ventilation defects.

Ventilation imaging can be used to study the fundamental characteristic of asthma, reversible airflow obstruction. Changes such as bronchospasm and drug-induced bronchodilation can be assessed [75]. Tzeng *et al.* [76] compared reversal of methacholine-induced bronchoconstriction in asthmatics and healthy controls by using deep inspiration. Asthmatics and healthy controls had a similar level of heterogeneity once the bronchoconstriction was induced; however, bronchoconstriction following deep inspiration was reversed more successfully in healthy controls compared to asthmatics. Efficacy of anti-leukotriene treatment [77] and novel interventional therapies such as thermoplasty [65] have also been assessed using HP MRI. Asthmatics with normal lung function have been shown to have ventilation defects that mostly resolve with the use of a bronchodilator, and subsequently reappear in the same regions of the lung once the bronchodilator effect has gone [78, 79]. Disease severity in asthma is associated with the degree and severity of ventilation defects [80]. Asthmatics with ventilation defects had significantly worse spirometry, fraction of exhaled nitric oxide and increased quantitative CT-assessed percentage wall thickness [70]. Spatial heterogeneity in asthma and the association between inflammation and regional ventilation was demonstrated by Fain *et al.* [81]. Lung lobes with a high ventilation defect percentage demonstrated increased inflammatory markers in bronchoalveolar lavage compared with lobes with a low ventilation defect percentage.

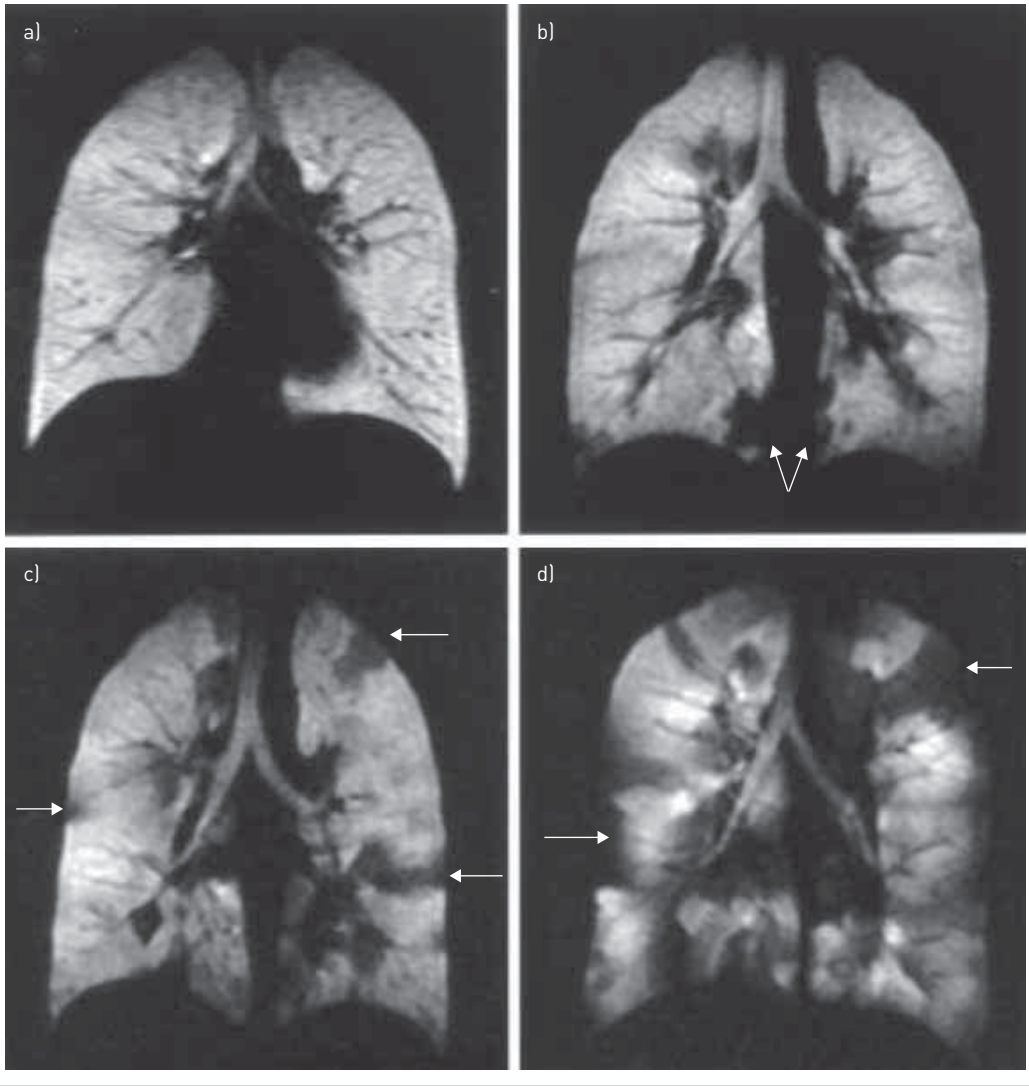

Figure 3. Coronal images after inhalation of hyperpolarised ^{3}He gas in a) a healthy volunteer, and patients with b) mild, c) moderate and d) severe asthma demonstrate homogeneous distribution of gas in the healthy volunteer and ventilation defects (arrows) increasing in number in the asthma patients with increasing severity. Reproduced and modified from [73] with permission from the publisher.

^{129}Xe is soluble in various tissues including blood so it can diffuse from the alveolar airspaces into the blood plasma. Dissolved ^{129}Xe and gas-phase ^{129}Xe can be detected separately, potentially enabling noninvasive assessment of gas exchange. This property has been utilised to assess pulmonary gas exchange capacity and interstitial membrane thickness in animal studies [82].

ADC is a method by which it is possible to infer the structure of the terminal bronchioles and alveoli, areas of the lung that are very difficult to image [67]. The average distance travelled by gas atoms in a given time [83–85] is measured with this technique, first demonstrated by Chen *et al.* [86]. ADC measurements are generally made over either milliseconds (short-range ADC), which probes alveolar structure, or over approximately 1 s (long-range ADC), which assesses small airway structure [87, 88]. ADC may help in early

disease detection [89] and monitoring of disease progression [90]. HP ^{3}He-MRI ADC measures also correlate with histology [91] and CT measures of emphysema and air trapping [92]. Asthmatics are shown to have significantly increased long-range and short-range ADC times when compared to healthy controls [87]. This suggests that the microstructure of the lungs is different between the two groups, with the asthmatics having areas of lung that are harder to ventilate, therefore prolonging the diffusion time [87].

Imaging of lung perfusion using MRI is performed using a dynamic contrast-enhanced technique [93]. Contrast agents such as gadolinium diethylenetriaminepentaacetic acid are administered intravenously to improve visualisation of the pulmonary arteries [93–95]. This delineates the pulmonary arterial vessels down to 5th or 6th order [96]. Blood pool agents (ultra-small super-paramagnetic iron oxide particles, gadolinium-coated complex compounds, albumin binding agents) may enable a more prolonged investigation time, and greater spatial resolution [97]. Both qualitative assessment and calculation of quantitative or functional parameters can be performed on the acquired data. For the visual assessment of dynamic contrast-enhanced MRI a simple subtraction of the data obtained during the peak signal enhancement and before contrast agent administration is used. Regions with reduced parenchymal perfusion are identified as areas of low contrast enhancement. Peak signal intensity and the temporal course of the signal change are used to obtain signal–time curves, which are converted to concentration–time curves for quantification pulmonary perfusion evaluation [98]. Quantitative evaluation has been used to study physiological effects in healthy volunteers [99] and heterogeneous alteration of pulmonary perfusion in patients with airway disease [100].

The combined use of ventilation MRI (using HP gases) and perfusion MRI may result in an overlay technique showing ventilation/perfusion match. O_2 can be used as a contrast agent in proton MRI, as dissolution of O_2 causes T1-time shortening in tissue and blood, which is proportional to the O_2 concentration in the inhaled gas [101]. The reduced relaxation time enhances the signal intensity in T1-weighted imaging and allows for the determination of regional O_2 transfer influenced by pulmonary ventilation, perfusion and diffusion. Thus, regions with impeded lung function can be visualised. As O_2-enhanced MRI is relatively inexpensive and easy to implement, this technique has been the focus of various studies in asthma.

In a prospective study of 34 asthmatic patients, OHNO *et al.* [102] found that O_2-enhanced MRI is as effective as CT for the assessment of pulmonary functional loss and clinical stage classification of asthmatics. ZHANG *et al.* [103] demonstrated that dynamic O_2-enhanced MRI is sensitive to the severity of asthma and enables assessments of regional lung function. In O_2-weighted HP gas MRI the gas dose is mixed with pure O_2 immediately prior to inhalation to approximate normoxic concentrations (20% O_2). The T1 decay of ^{3}He and ^{129}Xe in normoxic mixtures (20% O_2) are of the order of 30 s, or greater for field strengths from 1.5 to 3 T. The paramagnetic effects of partial pressure of arterial O_2 tension that effectively decrease T1 of the polarised gas provide a quantitative estimate of the partial pressure of O_2 [104, 105] that can potentially be used to calculate ventilation/perfusion [106]. Furthermore, native and O_2-enhanced T1 mapping used in combination may be valuable in assessment of ventilation/perfusion imbalance in airway disease [107].

New horizons

Pulmonary perfusion arterial spin labelling MRI [108, 109] and two-compartment inversion recovery [110] are new techniques. They are being used for quantitative estimation of the

pulmonary blood flow [111] and quantitative regional estimation of the fractional pulmonary blood volume, respectively, without the application of contrast media [110]. One of the latest developments in the field of functional lung proton MRI is known as the Fourier decomposition method [112]. This technique provides both ventilation-weighted and perfusion-weighted information from a single acquisition series. It does not require administration of contrast media, or further patient compliance such as repeated or prolonged breath-hold. The technique was recently qualitatively validated with the clinical gold standard ventilation/perfusion SPECT measurements in a large-scale animal model [113]. Initial studies in healthy volunteers and cystic fibrosis patients have shown the feasibility of this technique to detect functional lung changes [114]. The technique can be used on routine clinical equipment and requires a 10–15-min examination time to cover the whole lung volume. HP gas MRI generates highly detailed maps of lung ventilation and physiological function while CT provides corresponding anatomical and structural information. However, direct image registration of HP gas MRI to CT is problematic, particularly in lungs whose boundaries are difficult to delineate due to ventilation heterogeneity. Using proton structural magnetic resonance images that are acquired in the same breath-hold as the HP gas, MRI provides a novel indirect method of fusion of complementary MRI with CT scan imaging, enabling a quantitative analysis of pulmonary structure–function. The method may offer potential applications in multi-modality image fusion, functionally weighted radiotherapy planning, and quantification of lobar ventilation in asthma [115].

Molecular imaging

Various molecular imaging techniques are currently employed, most developed for use in oncology. These techniques are relatively new in the assessment of asthma and other lung diseases.

Positron emission tomography

PET scanning makes use of radiotracers, the most common of which is fluorine-18 labelled fluorodeoxyglucose. The radiotracer is injected into the body and is taken up by various tissues and cells, especially those with rapid metabolism. Radiotracers used in PET scans decay by emitting positrons. A positron will travel a few millimetres before interacting with and annihilating an electron. This annihilation will produce two gamma photons that travel in opposite directions and are detected by a ring of scintillation detectors. The location of annihilation is by registration of only coincident photons.

PET imaging has been used in asthma to assess pulmonary ventilation and perfusion [116, 117]. Researchers have used PET imaging alongside airway models to show that 1) bi-stable constriction of the terminal bronchioles leads to the heterogeneity of whole lung constriction [118], 2) within clusters of hypoventilated terminal units, there coexist some well ventilated units, 3) these clusters of hypoventilated units are due to an increase in smooth muscle tone, and initially the hypoventilated areas are uniformly distributed, and 4) as tidal volume decreases, the size and number of hypoventilated clusters increase [117]. PET can provide *in situ*, *in vivo*, quantitative, functional data noninvasively and repeatedly, an obvious advantage over other imaging methods. PET images can subsequently be superimposed over a CT image of the same area using image visualisation software in order to give a clear anatomical reference, which forms the basis of PET–CT, combining the detailed airway morphometry and lung architecture determined by CT with regional measurement of metabolic activity to

provide accurate anatomical localisation of the radiotracer activity. This principle has been used to assess airway inflammation in asthma using FDG-PET–CT [119, 120]. ^{13}N gas, dissolved in saline, has also been used in PET imaging of the lungs. The radiotracer is administered intravenously, and on reaching the pulmonary arterial system it diffuses from the blood into the alveoli in proportion to blood flow. As this is a rapid process, provided the subject has held their breath during the injection, the volume of ^{13}N in the lung is directly proportional to the perfusion of the lung. Ventilation can subsequently be assessed as the subject exhales the ^{13}N gas. This method has been used to assess ventilation/perfusion mismatch in methacholine-induced bronchoconstriction [121], including quantitative assessment of ventilation/perfusion heterogeneity and estimate of regional respiratory gas tensions based on regional tracer kinetics analysis [68].

Several novel PET tracers including ^{68}Ga citrate and Tyr-octreotate are available that show potential in imaging of pulmonary inflammation.

Single-photon emission tomography

Like PET, SPECT makes use of radionuclides. Tracers commonly used in SPECT are based on ^{99m}Tc and ^{111}indium. Unlike PET imaging, SPECT relies on the direct emission of gamma rays from the radionuclide. SPECT images can be co-registered with CT scans (SPECT–CT) to allow accurate anatomical location of activity.

SPECT is able to assess ventilation in asthma using ^{99m}Tc. When using inhaled ^{99m}Tc, poorly ventilated sections of the lung will have a decreased signal, which helps determine ventilation heterogeneity and quantification of non-ventilated regions. SPECT has been used to assess and localise the inflammatory response by using labelled leukocytes [122]. It may also be possible to quantify lung reduction–oxidation potential with the use of a specific ^{99m}Tc tracer, as its uptake into cells is significantly increased in lungs subjected to oxidative stress when compared to healthy lungs [123]. Greater tracer uptake in the lower lobes was demonstrated, suggesting that inflammation in asthma subjects demonstrated a gradient with lower lobar predominance, a finding subsequently confirmed with assessment of inflammatory cells in upper and lower lobe bronchoalveolar lavage [124]. Farahi *et al.* [125] have used autologous ^{111}indium-labelled eosinophils to investigate eosinophil trafficking in healthy non-atopic individuals, demonstrating another exciting use of SPECT imaging. This method has a definite potential to study inflammation in an asthmatic population.

Other imaging techniques

Endobronchial ultrasonography

Airway structure assessment using EBUS has been performed in animal studies as well as healthy human volunteers and is shown to be comparable to CT measures of airway remodelling [126]. Bronchial wall thickness and wall area determined with EBUS in asthmatic and healthy subjects were also found to be comparable to CT morphometry [127]. Moreover, asthma subjects had thicker bronchial walls than the healthy controls on EBUS assessment. The reticular basement membrane, assessed histologically, showed correlations with EBUS-assessed remodelling. EBUS allows assessment of airway structure *in vivo* and simultaneous histological sampling for *ex vivo* study, allowing accurate assessment of the effect of microscopic changes on a macroscopic scale.

Table 1. Summary of imaging findings in asthma

	First author [ref.]	Implications
Diagnostic yield		
CT multiplanar reconstructions, 3D surface and volume rendering of the airway tree and lung densitometry	Newell [5] San José Estépar [22]	Highlights utility of CT in quantitative assessment of proximal airway remodelling and air trapping.
MRI use in detection of pulmonary ventilation and perfusion derangement	Svenningsen [70] Fain [72] Samee [73] Ohno [101]	MRI as a unique modality can provide anatomical and functional assessment without use of ionising radiation.
Validation of imaging-derived measurements		
Quantitative CT-derived proximal airway indices *versus* histology: epithelial or lamina reticularis thickness on biopsy specimens.	Aysola [23] Montaudon [24]	Validation against microscopic pathology supports measurement of proximal airways as surrogate indices of the remodelling processes.
Quantitative CT-derived proximal airway indices *versus* cytology: pattern of inflammation as assessed on sputum cell count, neutrophil count, eosinophil count and other biomarkers, such as elastase, transforming growth factor-β, and the ratio of matrix metalloproteinase-9 to tissue inhibitor of metalloproteinase-1.	Gupta [25] Siddiqui [26] Vignola [27] Yamaguchi [28] Montesantos [29] Matsumoto [30]	Validation against cytology and inflammatory biomarkers supports measurement of proximal airways as surrogate indices of the remodelling processes.
Quantitative CT-derived proximal airway indices or air trapping indices *versus* clinical correlates.	Niimi [32] Gupta [39] Mitsunobu [53] Ueda [54] Lee [69]	Helps unravel the structure–function relationship in asthma. The use of quantitative CT parameters may help identify new asthma phenotypes.
Quantitative CT-derived proximal airway indices *versus* functional correlates: bronchial reactivity.	Niimi [33] Goldin [50] Ueda [54]	Structural changes detected on imaging are functionally important.
MRI ventilation defects *versus* functional correlates: changes before and after bronchodilator and asthma severity.	Tzeng [76] de Lange [80]	Structural changes detected on imaging are functionally important.
Various quantitative CT-derived indices of air trapping: Regional decreased attenuation Threshold -900 HU expiratory images Threshold -850 HU expiratory images Inspiratory–expiratory difference in MLD Inspiratory/expiratory MLD ratio 10th percentile point of the cumulative frequency distribution of CT numbers	Gono [37] Busacker [38] Gupta [39] Guckel [45] Newman [48] Tunon-de-Lara [49] Bommart [51]	Standardised and validated quantitative CT-derived measures of air trapping will aid the assessment of disease progression and change after intervention.
Assessing the response to asthma treatments		
Quantitative CT indices of air trapping are superior to conventional functional indices for assessing the efficacy of inhaled steroids and montelukast on peripheral airways.	Goldin [56] Zeidler [57]	Both CT-derived indices of air trapping and MRI ventilation defects play a role in testing efficacy and effectiveness of pharmacological and nonpharmacological interventions in asthma.
CT and MRI indices of air trapping for assessing the effectiveness of bronchial thermoplasty.	Thomen [65]	Both CT-derived indices of air trapping and MRI ventilation defects play a role in testing efficacy and effectiveness of pharmacological and nonpharmacological interventions in asthma.
MRI indices of air trapping reveal both a whole lung and regional response to exercise challenge and therapy in exercise-induced bronchoconstriction.	Kruger [77]	Both CT-derived indices of air trapping and MRI ventilation defects play a role in testing efficacy and effectiveness of pharmacological and nonpharmacological interventions in asthma.

MLD: mean lung density.

Optical coherence tomography

OCT uses near infrared, low coherence light to image cellular and extracellular structures. It has a penetration depth of 1–3 mm and spatial resolution of 3–16 μm [128, 129]. It allows *in vivo* assessment of airway mechanics. Coxson *et al.* [130] first assessed this technique in COPD subjects and found OCT measures of the airways correlated with both lung function and CT morphometry. Real-time 3D imaging with OCT, such as anatomical OCT [131], allows assessment of the temporal and dynamic relationship between anatomical areas such as the luminal wall/mucosal folds to be compared to changes in the smooth muscle and outer wall [132]. It also has the potential to assess airway wall structure exactly at the time biopsy/histological samples are taken. A new OCT-based method has been analysing airway compliance by comparing deflection of the surface of the tissue to ventilation pressure during tidal breathing [133].

Conclusion

Asthma imaging, despite the recent advances, has limited clinical utility. Insights into the potential novel uses of imaging in asthma are being provided by current research (table 1). Critical questions currently being addressed include: 1) reproducibility of structural and functional measures between various scanners of the same modality, different imaging modalities, different centres across the world and over a period of time; 2) minimum detectible structural, functional and pathophysiological change by imaging; 3) validation of imaging-derived measures with functional and/or pathophysiological correlation; and 4) utility of imaging-derived parameters as surrogate biomarkers in clinical studies.

Our ability to integrate and understand changes occurring in asthma across multiple biological scales will dictate development of novel imaging approaches. New image processing techniques and integration of data across multiple scales allow structural and functional data to be combined, providing novel strategies for detailed assessment of airway diseases. A multi-modality, multi-scale approach to studying airways diseases is utilised by computational modelling [134]. AirPROM (Airway disease PRedicting Outcomes through patient-specific computational Modelling) (www.europeanlung.org/en/projects-and-research/projects/airprom/home), a multi-centre European project, aims to integrate clinical data and computational models across disparate scales to develop an integrated multi-scale model able to provide new insights into disease pathophysiology, unravel structure–function relationships and perhaps most importantly predict future risk and response to therapy.

References

1. GINA 2015. Global Strategy for Asthma Management and Prevention. http://www.ginasthma.org
2. Proceedings of the ATS workshop on refractory asthma: current understanding, recommendations, and unanswered questions. American Thoracic Society. *Am J Respir Crit Care Med* 2000; 162: 2341–2351.
3. Chung KF, Wenzel SE, Brozek JL, *et al.* International ERS/ATS guidelines on definition, evaluation and treatment of severe asthma. *Eur Respir J* 2014; 43: 343–373.
4. Kalender WA, Seissler W, Klotz E, *et al.* Spiral volumetric CT with single-breath-hold technique, continuous transport, and continuous scanner rotation. *Radiology* 1990; 176: 181–183.
5. Newell JD Jr, Sieren J, Hoffman EA. Development of quantitative computed tomography lung protocols. *J Thorac Imaging* 2013; 28: 266–271.
6. Hu H, He HD, Foley WD, *et al.* Four multidetector-row helical CT: image quality and volume coverage speed. *Radiology* 2000; 215: 55–62.

7. Bumbacea D, Campbell D, Nguyen L, *et al.* Parameters associated with persistent airflow obstruction in chronic severe asthma. *Eur Respir J* 2004; 24: 122–128.
8. Lynch DA, Newell JD, Tschomper BA, *et al.* Uncomplicated asthma in adults – comparison of CT appearance of the lungs in asthmatic and healthy subjects. *Radiology* 1993; 188: 829–833.
9. Harmanci E, Kebapci M, Metintas M, *et al.* High-resolution computed tomography findings are correlated with disease severity in asthma. *Respiration* 2002; 69: 420–426.
10. Yilmaz S, Ekici A, Ekici M, *et al.* High-resolution computed tomography findings in elderly patients with asthma. *Eur J Radiol* 2006; 59: 238–243.
11. Laurent F, Latrabe V, Raherison C, *et al.* Functional significance of air trapping detected in moderate asthma. *Eur Radiol* 2000; 10: 1404–1410.
12. Takemura M, Niimi A, Minakuchi M, *et al.* Bronchial dilatation in asthma: relation to clinical and sputum indices. *Chest* 2004; 125: 1352–1358.
13. Park CS, Muller NL, Worthy SA, *et al.* Airway obstruction in asthmatic and healthy individuals: inspiratory and expiratory thin-section CT findings. *Radiology* 1997; 203: 361–367.
14. Grenier P, Mourey-Gerosa I, Benali K, *et al.* Abnormalities of the airways and lung parenchyma in asthmatics: CT observations in 50 patients and inter- and intraobserver variability. *Eur Radiol* 1996; 6: 199–206.
15. Paganin F, Trussard V, Seneterre E, *et al.* Chest radiography and high-resolution computed tomography of the lungs in asthma. *Am Rev Respir Dis* 1992; 146: 1084–1087.
16. Paganin F, Seneterre E, Chanez P, *et al.* Computed tomography of the lungs in asthma: influence of disease severity and etiology. *Am J Respir Crit Care Med* 1996; 153: 110–114.
17. Gupta S, Siddiqui S, Haldar P, *et al.* Qualitative analysis of high-resolution CT scans in severe asthma. *Chest* 2009; 136: 1521–1528.
18. Oguzulgen IK, Kervan F, Ozis T, *et al.* The impact of bronchiectasis in clinical presentation of asthma. *South Med J* 2007; 100: 468–471.
19. Park JW, Hong YK, Kim CW, *et al.* High-resolution computed tomography in patients with bronchial asthma: correlation with clinical features, pulmonary functions and bronchial hyperresponsiveness. *J Investig Allergol Clin Immunol* 1997; 7: 186–192.
20. Bankier AA, Fleischmann D, Mallek R, *et al.* Bronchial wall thickness: appropriate window settings for thin-section CT and radiologic-anatomic correlation. *Radiology* 1996; 199: 831–836.
21. Okazawa M, Muller N, McNamara AE, *et al.* Human airway narrowing measured using high resolution computed tomography. *Am J Respir Crit Care Med* 1996; 154: 1557–1562.
22. San José Estépar R, Reilly JJ, Silverman EK, *et al.* Three-dimensional airway measurements and algorithms. *Proc Am Thorac Soc* 2008; 5: 905–909.
23. Aysola RS, Hoffman EA, Gierada D, *et al.* Airway remodeling measured by multidetector CT is increased in severe asthma and correlates with pathology. *Chest* 2008; 134: 1183–1191.
24. Montaudon M, Lederlin M, Reich S, *et al.* Bronchial measurements in patients with asthma: comparison of quantitative thin-section CT findings with those in healthy subjects and correlation with pathologic findings. *Radiology* 2009; 253: 844–853.
25. Gupta S, Siddiqui S, Haldar P, *et al.* Quantitative analysis of high-resolution computed tomography scans in severe asthma subphenotypes. *Thorax* 2010; 65: 775–781.
26. Siddiqui S, Gupta S, Cruse G, *et al.* Airway wall geometry in asthma and nonasthmatic eosinophilic bronchitis. *Allergy* 2009; 64: 951–958.
27. Vignola AM, Paganin F, Capieu L, *et al.* Airway remodelling assessed by sputum and high-resolution computed tomography in asthma and COPD. *Eur Respir J* 2004; 24: 910–917.
28. Yamaguchi M, Niimi A, Matsumoto H, *et al.* Sputum levels of transforming growth factor-beta1 in asthma: relation to clinical and computed tomography findings. *J Investig Allergol Clin Immunol* 2008; 18: 202–206.
29. Montesantos S, Katz I, Fleming J, *et al.* Airway morphology from high resolution computed tomography in healthy subjects and patients with moderate persistent asthma. *Anat Rec* 2013; 296: 852–866.
30. Matsumoto H, Niimi A, Takemura M, *et al.* Relationship of airway wall thickening to an imbalance between matrix metalloproteinase-9 and its inhibitor in asthma. *Thorax* 2005; 60: 277–281.
31. Little SA, Sproule MW, Cowan MD, *et al.* High resolution computed tomographic assessment of airway wall thickness in chronic asthma: reproducibility and relationship with lung function and severity. *Thorax* 2002; 57: 247–253.
32. Niimi A, Matsumoto H, Amitani R, *et al.* Airway wall thickness in asthma assessed by computed tomography – relation to clinical indices. *Am J Respir Crit Care Med* 2000; 162: 1518–1523.
33. Niimi A, Matsumoto H, Takemura M, *et al.* Relationship of airway wall thickness to airway sensitivity and airway reactivity in asthma. *Am J Respir Crit Care Med* 2003; 168: 983–988.
34. Awadh N, Muller NL, Park CS, *et al.* Airway wall thickness in patients with near fatal asthma and control groups: assessment with high resolution computed tomographic scanning. *Thorax* 1998; 53: 248–253.
35. Kasahara K, Shiba K, Ozawa T, *et al.* Correlation between the bronchial subepithelial layer and whole airway wall thickness in patients with asthma. *Thorax* 2002; 57: 242–246.

36. Boulet L, Bélanger M, Carrier G. Airway responsiveness and bronchial-wall thickness in asthma with or without fixed airflow obstruction. *Am J Respir Crit Care Med* 1995; 152: 865–871.
37. Gono H, Fujimoto K, Kawakami S, *et al.* Evaluation of airway wall thickness and air trapping by HRCT in asymptomatic asthma. *Eur Respir J* 2003; 22: 965–971.
38. Busacker A, Newell JD Jr, Keefe T, *et al.* A multivariate analysis of risk factors for the air-trapping asthmatic phenotype as measured by quantitative CT analysis. *Chest* 2009; 135: 48–56.
39. Gupta S, Hartley R, Khan UT, *et al.* Quantitative computed tomography-derived clusters: redefining airway remodeling in asthmatic patients. *J Allergy Clin Immunol* 2014; 133: 729–738.
40. Beigelman-Aubry C, Capderou A, Grenier PA, *et al.* Mild intermittent asthma: CT assessment of bronchial cross-sectional area and lung attenuation at controlled lung volume. *Radiology* 2002; 223: 181–187.
41. Gupta S, Hartley R, Singapuri A, *et al.* Temporal assessment of airway remodeling in severe asthma using quantitative computed tomography. *Am J Respir Crit Care Med* 2015; 191: 107–110.
42. Lederlin M, Laurent F, Portron Y, *et al.* CT attenuation of the bronchial wall in patients with asthma: comparison with geometric parameters and correlation with function and histologic characteristics. *AJR Am J Roentgenol* 2012; 199: 1226–1233.
43. Yanai M, Sekizawa K, Ohrui T, *et al.* Site of airway obstruction in pulmonary disease: direct measurement of intrabronchial pressure. *J Appl Physiol* 1992; 72: 1016–1023.
44. Kraft M. The distal airways: are they important in asthma? *Eur Respir J* 1999; 14: 1403–1417.
45. Guckel C, Wells AU, Taylor DA, *et al.* Mechanism of mosaic attenuation of the lungs on computed tomography in induced bronchospasm. *J Appl Physiol* 1999; 86: 701–708.
46. Coxson HO, Rogers RM, Whittall KP, *et al.* A quantification of the lung surface area in emphysema using computed tomography. *Am J Respir Crit Care Med* 1999; 159: 851–856.
47. Madani A, Zanen J, de Maertelaer V, *et al.* Pulmonary emphysema: objective quantification at multi-detector row CT – comparison with macroscopic and microscopic morphometry. *Radiology* 2006; 238: 1036–1043.
48. Newman KB, Lynch DA, Newman LS, *et al.* Quantitative computed tomography detects air trapping due to asthma. *Chest* 1994; 106: 105–109.
49. Tunon-de-Lara JM, Laurent F, Giraud V, *et al.* Air trapping in mild and moderate asthma: effect of inhaled corticosteroids. *J Allergy Clin Immunol* 2007; 119: 583–590.
50. Goldin JG, McNitt-Gray MF, Sorenson SM, *et al.* Airway hyperreactivity: assessment with helical thin-section CT. *Radiology* 1998; 208: 321–329.
51. Bommart S, Marin G, Bourdin A, *et al.* Relationship between CT air trapping criteria and lung function in small airway impairment quantification. *BMC Pulm Med* 2014; 14: 29.
52. Kim V, Davey A, Comellas AP, *et al.* Clinical and computed tomographic predictors of chronic bronchitis in COPD: a cross sectional analysis of the COPDGene study. *Respir Res* 2014; 15: 52.
53. Mitsunobu F, Mifune T, Ashida K, *et al.* Influence of age and disease severity on high resolution CT lung densitometry in asthma. *Thorax* 2001; 56: 851–856.
54. Ueda T, Niimi A, Matsumoto H, *et al.* Role of small airways in asthma: investigation using high-resolution computed tomography. *J Allergy Clin Immunol* 2006; 118: 1019–1025.
55. Mitsunobu F, Ashida K, Hosaki Y, *et al.* Decreased computed tomographic lung density during exacerbation of asthma. *Eur Respir J* 2003; 22: 106–112.
56. Goldin JG, Tashkin DP, Kleerup EC, *et al.* Comparative effects of hydrofluoroalkane and chlorofluorocarbon beclomethasone dipropionate inhalation on small airways: assessment with functional helical thin-section computed tomography. *J Allergy Clin Immunol* 1999; 104: S258–S267.
57. Zeidler MR, Kleerup EC, Goldin JG, *et al.* Montelukast improves regional air-trapping due to small airways obstruction in asthma. *Eur Respir J* 2006; 27: 307–315.
58. Thieme SF, Hoegl S, Nikolaou K, *et al.* Pulmonary ventilation and perfusion imaging with dual-energy CT. *Eur Radiol* 2010; 20: 2882–2889.
59. van Beek EJ, Hoffman EA. Functional imaging: CT and MRI. *Clin Chest Med* 2008; 29: 195–216.
60. Chae EJ, Seo JB, Lee J, *et al.* Xenon ventilation imaging using dual-energy computed tomography in asthmatics: initial experience. *Invest Radiol* 2010; 45: 354–361.
61. Zhang LJ, Zhou CS, Schoepf UJ, *et al.* Dual-energy CT lung ventilation/perfusion imaging for diagnosing pulmonary embolism. *Eur Radiol* 2013; 23: 2666–2675.
62. De Backer LA, Vos W, De Backer J, *et al.* The acute effect of budesonide/formoterol in COPD: a multi-slice computed tomography and lung function study. *Eur Respir J* 2012; 40: 298–305.
63. De Backer JW, Vos WG, Devolder A, *et al.* Computational fluid dynamics can detect changes in airway resistance in asthmatics after acute bronchodilation. *J Biomech* 2008; 41: 106–113.
64. De Backer JW, Vos WG, Vinchurkar SC, *et al.* Validation of computational fluid dynamics in CT-based airway models with SPECT/CT. *Radiology* 2010; 257: 854–862.
65. Thomen RP, Sheshadri A, Quirk JD, *et al.* Regional ventilation changes in severe asthma after bronchial thermoplasty with (3)He MR imaging and CT. *Radiology* 2015; 274: 250–259.

66. Mills GH, Wild JM, Eberle B, *et al.* Functional magnetic resonance imaging of the lung. *Br J Anaesth* 2003; 91: 16–30.
67. Wild JM, Marshall H, Bock M, *et al.* MRI of the lung (1/3): methods. *Insights Imaging* 2012; 3: 345–353.
68. Vidal Melo MF, Layfield D, Harris RS, *et al.* Quantification of regional ventilation-perfusion ratios with PET. *J Nucl Med* 2003; 44: 1982–1991.
69. Lee EY, Sun Y, Zurakowski D, *et al.* Hyperpolarized 3He MR imaging of the lung: normal range of ventilation defects and PFT correlation in young adults. *J Thorac Imag* 2009; 24: 110–114.
70. Svenningsen S, Kirby M, Starr D, *et al.* What are ventilation defects in asthma? *Thorax* 2014; 69: 63–71.
71. Parraga G, Mathew L, Etemad-Rezai R, *et al.* Hyperpolarized 3He magnetic resonance imaging of ventilation defects in healthy elderly volunteers: initial findings at 3.0 Tesla. *Acad Radiol* 2008; 15: 776–785.
72. Fain S, Schiebler ML, McCormack DG, *et al.* Imaging of lung function using hyperpolarized helium-3 magnetic resonance imaging: review of current and emerging translational methods and applications. *J Magn Reson Imag* 2010; 32: 1398–1408.
73. Samee S, Altes T, Powers P, *et al.* Imaging the lungs in asthmatic patients by using hyperpolarized helium-3 magnetic resonance: assessment of response to methacholine and exercise challenge. *J Allergy Clin Immunol* 2003; 111: 1205–1211.
74. Liu Z, Araki T, Okajima Y, *et al.* Pulmonary hyperpolarized noble gas MRI: recent advances and perspectives in clinical application. *Eur J Radiol* 2014; 83: 1282–1291.
75. Costella S, Kirby M, Maksym GN, *et al.* Regional pulmonary response to a methacholine challenge using hyperpolarized (3)He magnetic resonance imaging. *Respirology (Carlton, Vic)* 2012; 17: 1237–1246.
76. Tzeng Y-S, Lutchen K, Albert M. The difference in ventilation heterogeneity between asthmatic and healthy subjects quantified using hyperpolarized 3He MRI. *J Appl Physiol* 2009; 106: 813–822.
77. Kruger SJ, Niles DJ, Dardzinski B, *et al.* Hyperpolarized helium-3 MRI of exercise-induced bronchoconstriction during challenge and therapy. *J Magn Reson Imag* 2014; 39: 1230–1237.
78. Altes TA, Powers PL, Knight-Scott J, *et al.* Hyperpolarized 3He MR lung ventilation imaging in asthmatics: preliminary findings. *J Magn Reson Imag* 2001; 13: 378–384.
79. de Lange EE, Altes TA, Patrie JT, *et al.* The variability of regional airflow obstruction within the lungs of patients with asthma: assessment with hyperpolarized helium-3 magnetic resonance imaging. *J Allergy Clin Immunol* 2007; 119: 1072–1078.
80. de Lange EE, Altes TA, Patrie JT, *et al.* Evaluation of asthma with hyperpolarized helium-3 MRI: correlation with clinical severity and spirometry. *Chest* 2006; 130: 1055–1062.
81. Fain SB, Gonzalez-Fernandez G, Peterson ET, *et al.* Evaluation of structure-function relationships in asthma using multidetector CT and hyperpolarized He-3 MRI. *Acad Radiol* 2008; 15: 753–762.
82. Cleveland ZI, Cofer GP, Metz G, *et al.* Hyperpolarized Xe MR imaging of alveolar gas uptake in humans. *PLoS One* 2010; 5: e12192.
83. Morbach AE, Gast KK, Schmiedeskamp J, *et al.* Diffusion-weighted MRI of the lung with hyperpolarized helium-3: a study of reproducibility. *J Magn Reson Imaging* 2005; 21: 765–774.
84. Yablonskiy DA, Sukstanskii AL, Leawoods JC, *et al.* Quantitative *in vivo* assessment of lung microstructure at the alveolar level with hyperpolarized 3He diffusion MRI. *Proc Natl Acad Sci USA* 2002; 99: 3111–3116.
85. Salerno M, Altes TA, Brookeman JR, *et al.* Rapid hyperpolarized 3He diffusion MRI of healthy and emphysematous human lungs using an optimized interleaved-spiral pulse sequence. *J Magn Reson Imaging* 2003; 17: 581–588.
86. Chen XJ, Moller HE, Chawla MS, *et al.* Spatially resolved measurements of hyperpolarized gas properties in the lung *in vivo*. Part I: diffusion coefficient. *Magn Reson Med* 1999; 42: 721–728.
87. Wang C, Altes TA, Mugler JP III, *et al.* Assessment of the lung microstructure in patients with asthma using hyperpolarized 3He diffusion MRI at two time scales: comparison with healthy subjects and patients with COPD. *J Magn Reson Imaging* 2008; 28: 80–88.
88. Wang C, Miller GW, Altes TA, *et al.* Time dependence of 3He diffusion in the human lung: measurement in the long-time regime using stimulated echoes. *Magn Reson Med* 2006; 56: 296–309.
89. Fain SB, Panth SR, Evans MD, *et al.* Early emphysematous changes in asymptomatic smokers: detection with 3He MR imaging. *Radiology* 2006; 239: 875–883.
90. Saam BT, Yablonskiy DA, Kodibagkar VD, *et al.* MR imaging of diffusion of (3)He gas in healthy and diseased lungs. *Magn Reson Med* 2000; 44: 174–179.
91. Jacob RE, Minard KR, Laicher G, *et al.* 3D 3He diffusion MRI as a local in vivo morphometric tool to evaluate emphysematous rat lungs. *J Appl Physiol* 2008; 105: 1291–1300.
92. Diaz S, Casselbrant I, Piitulainen E, *et al.* Validity of apparent diffusion coefficient hyperpolarized 3He-MRI using MSCT and pulmonary function tests as references. *Eur J Radiol* 2009; 71: 257–263.
93. Kauczor HU. Contrast-enhanced magnetic resonance angiography of the pulmonary vasculature. A review. *Invest Radiol* 1998; 33: 606–617.

94. Hatabu H, Tadamura E, Levin DL, *et al.* Quantitative assessment of pulmonary perfusion with dynamic contrast-enhanced MRI. *Magn Reson Med* 1999; 42: 1033–1038.
95. Kreitner KF, Ley S, Kauczor HU, *et al.* [Contrast media enhanced three dimensional MR angiography of the pulmonary arteries in patients with chronic recurrent pulmonary embolism – comparison with selective intra-arterial DSA]. *RoFo: Fortschritte auf dem Gebiete der Rontgenstrahlen und der Nuklearmedizin* 2000; 172: 122–128.
96. Steiner P, McKinnon GC, Romanowski B, *et al.* Contrast-enhanced, ultrafast 3D pulmonary MR angiography in a single breath-hold: initial assessment of imaging performance. *J Magn Reson Imaging* 1997; 7: 177–182.
97. Nolte-Ernsting C, Adam G, Bücker A, *et al.* [Experimental evaluation of superparamagnetic iron oxide particles in pulmonary MR angiography]. *RoFo: Fortschritte auf dem Gebiete der Rontgenstrahlen und der Nuklearmedizin* 1998; 168: 508–513.
98. Ley S, Ley-Zaporozhan J. Pulmonary perfusion imaging using MRI: clinical application. *Insights Imaging* 2012; 3: 61–71.
99. Fink C, Ley S, Risse F, *et al.* Effect of inspiratory and expiratory breathhold on pulmonary perfusion: assessment by pulmonary perfusion magnetic resonance imaging. *Invest Radiol* 2005; 40: 72–79.
100. Ohno Y, Hatabu H, Murase K, *et al.* Quantitative assessment of regional pulmonary perfusion in the entire lung using three-dimensional ultrafast dynamic contrast-enhanced magnetic resonance imaging: preliminary experience in 40 subjects. *J Magn Reson Imaging* 2004; 20: 353–365.
101. Ohno Y, Chen Q, Hatabu H. Oxygen-enhanced magnetic resonance ventilation imaging of lung. *Eur J Radiol* 2001; 37: 164–171.
102. Ohno Y, Koyama H, Matsumoto K, *et al.* Oxygen-enhanced MRI *vs.* quantitatively assessed thin-section CT: pulmonary functional loss assessment and clinical stage classification of asthmatics. *Eur J Radiol* 2011; 77: 85–91.
103. Zhang WJ, Niven RM, Young SS, *et al.* Dynamic oxygen-enhanced magnetic resonance imaging of the lung in asthma – initial experience. *Eur J Radiol* 2015; 84: 318–326.
104. Fischer MC, Spector ZZ, Ishii M, *et al.* Single-acquisition sequence for the measurement of oxygen partial pressure by hyperpolarized gas MRI. *Magn Reson Med* 2004; 52: 766–773.
105. Rizi RR, Baumgardner JE, Ishii M, *et al.* Determination of regional VA/Q by hyperpolarized 3He MRI. *Magn Reson Med* 2004; 52: 65–72.
106. Miller GW, Mugler JP, Altes TA, *et al.* A short-breath-hold technique for lung pO2 mapping with 3He MRI. *Magn Reson Med* 2010; 63: 127–136.
107. Jobst BJ, Triphan SM, Sedlaczek O, *et al.* Functional lung MRI in chronic obstructive pulmonary disease: comparison of T1 mapping, oxygen-enhanced T1 mapping and dynamic contrast enhanced perfusion. *PLoS One* 2015; 10: e0121520.
108. Mai VM, Berr SS. MR perfusion imaging of pulmonary parenchyma using pulsed arterial spin labeling techniques: FAIRER and FAIR. *J Magn Reson Imag* 1999; 9: 483–487.
109. Arai TJ, Prisk GK, Holverda S, *et al.* Magnetic resonance imaging quantification of pulmonary perfusion using calibrated arterial spin labeling. *J Vis Exp* 2011; 51: 2712.
110. Gaass T, Dinkel J, Bauman G, *et al.* Non-contrast-enhanced MRI of the pulmonary blood volume using two-compartment-modeled T1 -relaxation. *J Magn Reson Imag* 2012; 36: 397–404.
111. Bolar DS, Levin DL, Hopkins SR, *et al.* Quantification of regional pulmonary blood flow using ASL-FAIRER. *Magn Reson Med* 2006; 55: 1308–1317.
112. Bauman G, Puderbach M, Deimling M, *et al.* Non-contrast-enhanced perfusion and ventilation assessment of the human lung by means of Fourier decomposition in proton MRI. *Magn Reson Med* 2009; 62: 656–664.
113. Bauman G, Lützen U, Ullrich M, *et al.* Pulmonary functional imaging: qualitative comparison of Fourier decomposition MR imaging with SPECT/CT in porcine lung. *Radiology* 2011; 260: 551–559.
114. Bauman G, Eichinger M, Deimling M, *et al.* Non-contrast-enhanced lung perfusion MRI in comparison to contrast-enhanced MRI perfusion in young cystic fibrosis patients. *Am J Respir Crit Care Med* 2010; 181: A1828.
115. Tahir BA, Swift AJ, Marshall H, *et al.* A method for quantitative analysis of regional lung ventilation using deformable image registration of CT and hybrid hyperpolarized gas/1H MRI. *Phys Med Biol* 2014; 59: 7267–7277.
116. Melo MFV, Harris RS, Layfield JDH, *et al.* Topographic basis of bimodal ventilation-perfusion distributions during bronchoconstriction in sheep. *Am J Respir Crit Care Med* 2005; 171: 714–721.
117. Venegas JG, Winkler T, Musch G, *et al.* Self-organized patchiness in asthma as a prelude to catastrophic shifts. *Nature* 2005; 434: 777–782.
118. Anafi RC, Wilson TA. Airway stability and heterogeneity in the constricted lung. *J Appl Physiol* 2001; 91: 1185–1192.
119. Harris RS, Venegas JG, Wongviriyawong C, *et al.* 18F-FDG uptake rate is a biomarker of eosinophilic inflammation and airway response in asthma. *J Nucl Med* 2011; 52: 1713–1720.
120. Jones HA, Marino PS, Shakur BH, *et al. In vivo* assessment of lung inflammatory cell activity in patients with COPD and asthma. *Eur Respir J* 2003; 21: 567–573.
121. Harris RS, Winkler T, Tgavalekos N, *et al.* Regional pulmonary perfusion, inflation, and ventilation defects in bronchoconstricted patients with asthma. *Am J Respir Crit Care Med* 2006; 174: 245–253.

122. Rennen HJ, Boerman OC, Oyen WJ, *et al.* Imaging infection/inflammation in the new millennium. *Eur J Nucl Med* 2001; 28: 241–252.
123. Jacquier-Sarlin MR, Polla BS, Slosman DO. Oxido-reductive state: the major determinant for cellular retention of technetium-99m-HMPAO. *J Nucl Med* 1996; 37: 1413–1416.
124. Ratanamaneechat S, Neumann DR, Difilippo FP, *et al.* Redox imaging of inflammation in asthma. *Am J Respir Crit Care Med* 2014; 189: 743–746.
125. Farahi N, Loutsios C, Simmonds RP, *et al.* Measurement of eosinophil kinetics in healthy volunteers. *Methods Mol Biol* 2014; 1178: 165–176.
126. Shaw TJ, Wakely SL, Peebles CR, *et al.* Endobronchial ultrasound to assess airway wall thickening: validation *in vitro* and *in vivo*. *Eur Respir J* 2004; 23: 813–817.
127. Soja J, Grzanka P, Sladek K, *et al.* The use of endobronchial ultrasonography in assessment of bronchial wall remodeling in patients with asthma. *Chest* 2009; 136: 797–804.
128. Fujimoto JG, Brezinski ME, Tearney GJ, *et al.* Optical biopsy and imaging using optical coherence tomography. *Nat Med* 1995; 1: 970–972.
129. Tearney GJ, Brezinski ME, Bouma BE, *et al. In vivo* endoscopic optical biopsy with optical coherence tomography. *Science* 1997; 276: 2037–2039.
130. Coxson HO, Quiney B, Sin DD, *et al.* Airway wall thickness assessed using computed tomography and optical coherence tomography. *Am J Respir Crit Care Med* 2008; 177: 1201–1206.
131. McLaughlin RA, Williamson JP, Phillips MJ, *et al.* Applying anatomical optical coherence tomography to quantitative 3D imaging of the lower airway. *Opt Express* 2008; 16: 17521–17529.
132. Noble PB, West AR, McLaughlin RA, *et al.* Airway narrowing assessed by anatomical optical coherence tomography in vitro: dynamic airway wall morphology and function. *J Appl Physiol* 2010; 108: 401–411.
133. Robertson C, Lee S-W, Ahn Y-C, *et al.* Investigating *in vivo* airway wall mechanics during tidal breathing with optical coherence tomography. *J Biomed Opt* 2011; 16: 106011.
134. Burrowes KS, Swan AJ, Warren NJ, *et al.* Towards a virtual lung: multi-scale, multi-physics modelling of the pulmonary system. *Philos Trans R Soc Lond A* 2008; 366: 3247–3263.

Disclosures: S. Gupta is a National Institute for Health Research (NIHR) Clinical Lecturer and is funded by a research and career development training scheme. C. Brightling is a NIHR senior fellow and has received grant and consultancy funding *via* his institution from GSK, MedImmune/AstraZeneca, Roche/Genentech, Novartis, Chiesi and Boehringer-Ingelheim.

Support statement: This paper presents independent research funded by the National Institute for Health Research (NIHR). The views expressed are those of the authors and not necessarily those of the NHS, the NIHR or the Department of Health.

Chapter 12

Imaging cystic fibrosis lung disease with MRI

Mark O. Wielpütz[1,2,3] and Hans-Ulrich Kauczor[1,2,3]

Repetitive imaging is required in cystic fibrosis (CF) lung disease in order to provide detailed information on regional distribution for severity assessment and therapy monitoring in clinical routine as well as interventional trials. CT has long overtaken the use of chest radiography because it provides higher morphological detail with respect to airway and parenchymal changes. This is closely linked to an increase in radiation exposure in CF individuals, who are referred for imaging procedures from a critically susceptible young age and may accumulate relevant doses during their lifetime. MRI, as an ionising radiation-free cross-sectional imaging modality, has taken the first step into the clinical arena in CF. MRI can depict the morphological hallmarks of CF lung disease such as bronchial wall thickening, bronchiectasis, mucus plugging, small airways disease and infiltrates at lower spatial resolution compared to CT but excels due to enhanced tissue characterisation and comprehensive functional imaging capabilities. These include imaging of respiratory mechanics, ventilation and, in particular, lung perfusion, of which four-dimensional perfusion imaging is currently most valuable. These tools make MRI an ideal modality to monitor potentially reversible lung abnormalities such as ventilation and perfusion impairment (air trapping), which could sensitively react to therapy and might even be regarded as precursor lesions to irreversible bronchiectatic destruction.

Cystic fibrosis (CF) remains the most common lethal hereditary disease among white populations. Various mutations of the CF transmembrane conductance regulator gene result in defective transepithelial chloride secretion in airway, salivary, sweat and intestinal glands. In the lung, the thin layer of airway surface liquid is dehydrated and renders airway secretions highly viscous, which then tend to obstruct conducting airways. A vicious circle of chronic airway and parenchymal inflammation, bacterial colonisation and infection, and progressive bronchiectatic destruction is perpetuated [1]. Chronic progressive lung disease continues to determine more than 90% of morbidity and mortality in patients with CF [1–3], with pulmonary complications being the leading cause of death. Improvements in diagnostics and therapy have given rise to prolonged survival of CF patients, averaging around 40 years, and which is expected to increase further [4, 5]. In addition, implementation of screening programmes in specialised centres in many countries will lead

[1]Diagnostic and Interventional Radiology, University Hospital Heidelberg, Heidelberg, Germany. [2]Translational Lung Research Center Heidelberg (TLRC), Member of the German Center for Lung Research (DZL), Heidelberg, Germany. [3]Dept of Diagnostic and Interventional Radiology with Nuclear Medicine, Thoraxklinik at University of Heidelberg, Heidelberg, Germany.

Correspondence: Mark O. Wielpütz, Diagnostic and Interventional Radiology, Subdivision of Pulmonary Imaging, University Hospital Heidelberg, Im Neuenheimer Feld 110, 69120 Heidelberg, Germany. E-mail: mark.wielpuetz@med.uni-heidelberg.de

Copyright ©ERS 2015. Print ISBN: 978-1-84984-065-1. Online ISBN: 978-1-84984-066-8. Print ISSN: 2312-508X. Online ISSN: 2312-5098.

to an earlier diagnosis [6], which is likely to further lengthen the timespan of medical attention to these patients.

It is well accepted that pulmonary function testing, including FEV1, although an important prognostic marker regarding survival, underestimates early stages of CF lung disease and has little sensitivity to predict exacerbation [7–9]. Imaging thus plays an important role in the management of CF lung disease in various clinical conditions including therapy monitoring. Originally, chest radiography was employed to depict morphological changes in the CF lung [10–13]. It has been succeeded by CT because of its higher sensitivity for early and subtle changes of the CF lung, as well as for exacerbation [9, 14–16]. Recent studies involving CT in infants and preschool children with CF, including patients who were diagnosed by newborn screening, confirmed early and progressive structural abnormalities of the lung that were frequently observed even in the absence of respiratory symptoms [15–22]. Recent experience with CF screening trials has shown that diagnosis and therapy have to start early, even in an asymptomatic state, in order to conserve lung function [20]. It is generally accepted that the use of CT for short-term follow-up in susceptible infants and preschool children should be restricted. For lifelong longitudinal follow-up there is a need for alternative monitoring strategies for chest CT to reduce lifelong radiation exposure with respect to rising life expectancy [23–26].

This holds true as MRI has been established as a radiation-free alternative with its capabilities for comprehensive imaging [25, 27–30]. In addition to the morphological information close to that obtained by CT in advanced disease (structural imaging), MRI can visualise several components of lung function, *i.e.* respiratory movements, ventilation and perfusion (functional imaging). Moreover, techniques have emerged to quantify different aspects of lung function, often involving dedicated post-processing tools (quantitative imaging). Independent of the modality, data on the actual impact of imaging findings on treatment decisions and patient survival is currently missing. Therefore, international guidelines do not usually specify either at what age and intervals imaging of the CF lung should be obtained, or even which modality should be employed [31]. Thus, imaging in CF remains a field of intensive research, and the decision to obtain imaging and the subsequent choice of the modality should strongly focus on the actual goal to be achieved, be it clinical or scientific.

Most aspects of CT, conventional radiography and tomosynthesis have already been extensively covered by the excellent chapter by TIDDENS [32] in the *ERS Monograph* on Cystic Fibrosis, and thus the present chapter will focus mainly on the aspects of MRI of CF lung disease. This chapter intends to give an overview of the most important magnetic resonance techniques and their current status regarding their application in clinical routine and research in CF lung disease, in order to provide the reader with sufficient knowledge to choose the appropriate modality for their needs.

Technical aspects and requirements

Lung proton (^{1}H-) MRI has to meet several physical and physiological obstacles. 1) Air, which consists of 20% O_2, amounts to around 90% of the lung volume, while lung tissue and perfused blood volume account for the remainder, which provides the protons to generate the magnetic resonance signal. 2) Multiple air–tissue interfaces and paramagnetic properties of intra-alveolar O_2 lead to a rapid signal decay. 3) Respiratory motion and the inability to breath-hold, as well as cardiac pulsation, further reduce image quality [30, 33].

Fast imaging techniques using parallel imaging as well as gating techniques have been developed to specifically address these obstacles, and are now readily available from all large vendors with dedicated routine lung MRI protocols (tables 1 and 2) [34–36]. The standard protocol may be tailored to the specific needs of the individual CF centre, with sedation and respiratory triggering to be considered for patients younger than 6 years of age. It may further be extended by specific cardiac sequences or further functional techniques such as T1 mapping or Fourier decomposition MRI [37] .

Morpho-functional imaging

Airways

Characteristic morphological features of CF lung disease are inflammatory airway wall thickening, progressive bronchiectasis and mucus plugging (table 3) [22, 38, 39]. In young healthy subjects, lung MRI depicts airways down to the first subsegmental level; however, close to the heart detection rates are lower due to cardiac pulsation [40]. Bronchiectasis is an early manifestation of CF lung disease detected by morphological imaging and correlates with disease severity and exacerbation rate [8, 14, 16]. Because of its lower resolution, MRI has an overall lower sensitivity to assess structural airway changes in the lung periphery in the case of mild changes in some CF studies [41, 42], and normal peripheral airways distal to the 3rd or 4th generation are poorly visualised. Dilatation and wall thickening facilitate the visualisation of bronchi at MRI. Lack of bronchial tapering, wall thickening, mucus plugs, centrilobular pattern and a tree-in-bud appearance enhance the visibility of peripheral small airway disease with an appearance similar to that in CT [43]. Airway changes in advanced CF can be depicted by MRI and CT alike [27, 43]. Similar to previous chest CT studies [15, 17–22], MRI detected a high overall prevalence of airway abnormalities of 93% (37 out of 40) in clinically stable patients aged 0–6 years (figure 1) [44].

Mucus retention within the large airways is sensitively depicted by T2-weighted sequences (table 3). Mucus plugging is the second most frequent morphological abnormality in clinically stable infants and preschool children with CF (63%) [44]. As mucus plugging is

Table 1. MRI vendor-overspanning routine sequences for preschool children with free-breathing acquisition

	Type	Specials	Planes	Slice thickness mm	Typical in-plane pixel size mm	Typical scan time s
Balanced T1/T2	bSSFP	Negative distance factor	tra, cor, sag	4.00	1.2×1.4–1.2×1.8	20–30
T1-weighted	FSE	Averaging	tra, cor	4.00	0.6×0.7–0.8×1.9	120–200
T2-weighted	Single-shot FSE	Navigated	tra, cor	6.00	1.2×2.0	40–60
***i.v.* contrast**						
Perfusion	Spoiled GRE	Repetitive acquisitions	cor	5.00	1.2×1.7	30–40
T1-weighted	FSE	Averaging	tra, cor	4.00	0.6×0.7–0.8×1.9	120–200

bSSFP: balanced steady-state free precession; FSE: fast spin echo; GRE: gradient echo; tra: transversal plane; cor: coronal plane; sag: sagittal plane; *i.v.*: intravenous.

Table 2. MRI vendor-overspanning routine sequences for adolescents with breath-hold acquisition

	Type	Specials	Planes	Slice thickness mm	Typical in-plane pixel size mm	Typical scan time s
Balanced T1/T2	bSSFP[#]	Negative distance factor	tra, cor, sag	4.0	2.0×1.3–2.2×1.8	25–35
T1-weighted	Spoiled GRE		tra, cor	4.0	1.6×1.6	20
T2-weighted	Single-shot FSE, half Fourier		tra, cor	6.0	1.8×1.8	20
T2-weighted	FSE, rotating-phase encoding	Navigated or multi-breath hold	tra, cor	4.0	0.9×0.9–1.3×1.3	120–240
Pre-angiography	Spoiled GRE	Pre-contrast	cor	1.6	1.4×1.3	20
***i.v.* contrast**						
Perfusion	Spoiled GRE	25–30 acquisitions	cor	5.0	2.2×1.6	40–50
Angiography	Spoiled GRE	Two acquisitions	cor	1.6	1.4×1.3	2×20
T1-weighted	Spoiled GRE	Fat saturated	tra, cor	4.0	1.6×1.6	20

bSSFP: balanced steady-state free precession; FSE: fast spin echo; GRE: gradient echo; tra: transversal plane; cor: coronal plane; sag: sagittal plane; *i.v.*: intravenous. [#] acquisition in free breathing recommended.

an important driver in the development of CF lung disease, its depiction may become a useful outcome measure as an early and potentially reversible abnormality (figure 2) [44–46]. While T2-weighted images show mucus and oedema, enhancement after an intravenous contrast administration on fat-suppressed T1-weighted images will demonstrate inflammation and active remodelling [43, 47].

Table 3. Relative sequence sensitivity for changes in cystic fibrosis lung disease

Balanced T1/T2
- Large pulmonary vessels and pulmonary embolism
- Dilated bronchial arteries
- Pleural reaction
- Respiratory mechanics (dynamic acquisition)

T1-weighted
- Central bronchiectasis
- Wall thickening (*i.v.* contrast)
- Small airways disease (tree-in-bud pattern)
- Consolidation
- Pleural reaction (*i.v.* contrast)
- Pulmonary embolism (*i.v.* contrast angiogram)
- Lymph nodes

T2-weighted
- Mucus plugging
- Consolidation
- Air trapping

Perfusion
- Perfusion abnormalities

i.v.: intravenous.

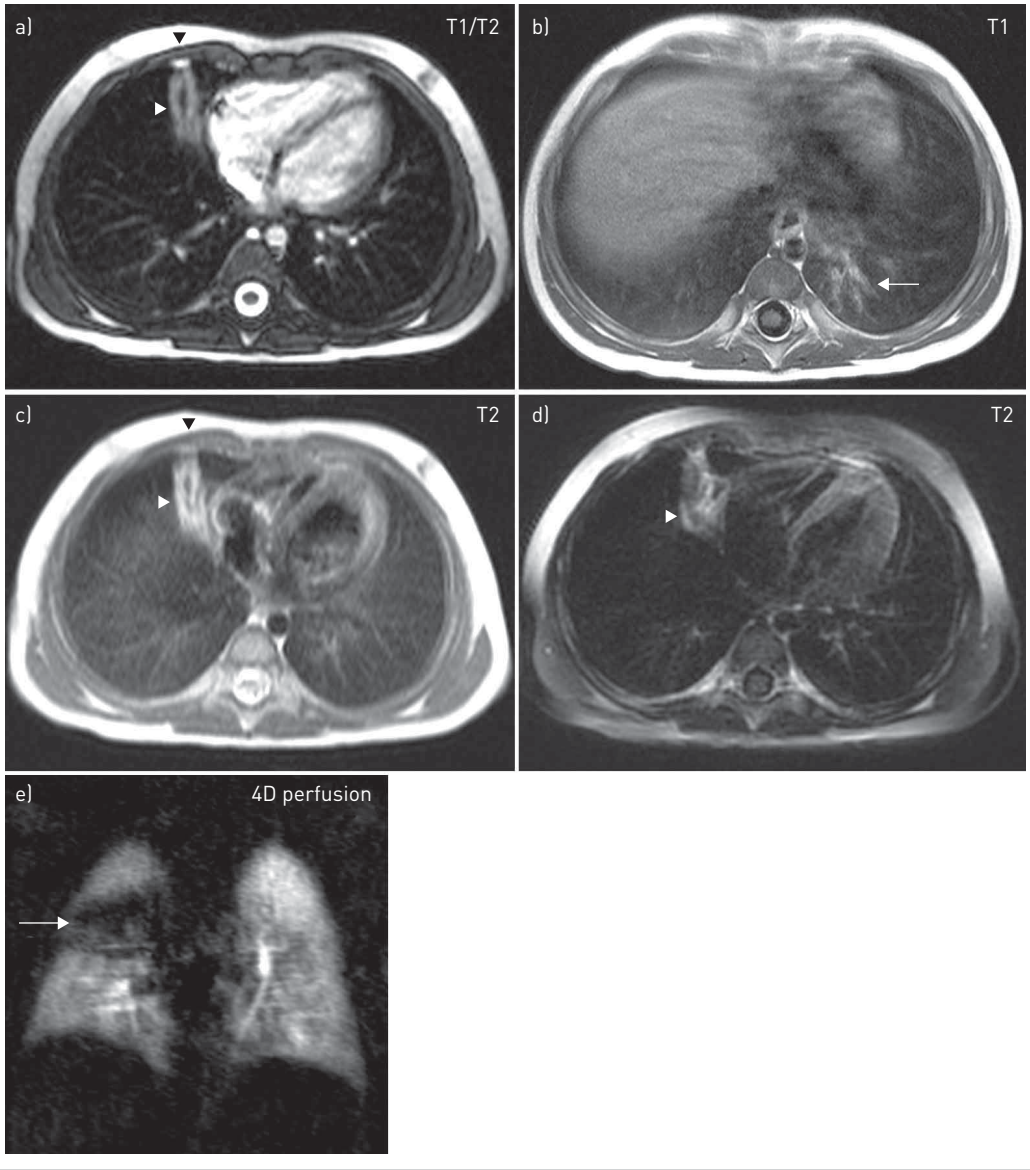

Figure 1. Infant cystic fibrosis (CF) lung disease. A 2-year-old female CF patient presented with a), c), d) a residual area of consolidation with volume loss inclusive of marked bronchiectasis persisting in the middle lobe (white arrowheads) and the pleura attached increasing in signal (black arrowheads). b) Shows mild bronchial wall thickening and bronchiectasis of the left lower lobe (white arrow). She was previously diagnosed with and treated for pulmonary exacerbation. e) Relatively extensive perfusion abnormalities were found in the apical segment of the right lower lobe (arrow), which did not shown any morphological changes otherwise.

Parenchyma

At CT sharply delineated areas of low density representing air trapping are present in two-thirds of CF patients [16]. These hyperinflated areas exhibit an increased air content and prolonged exhalation due to airway obstruction, which may resolve even without

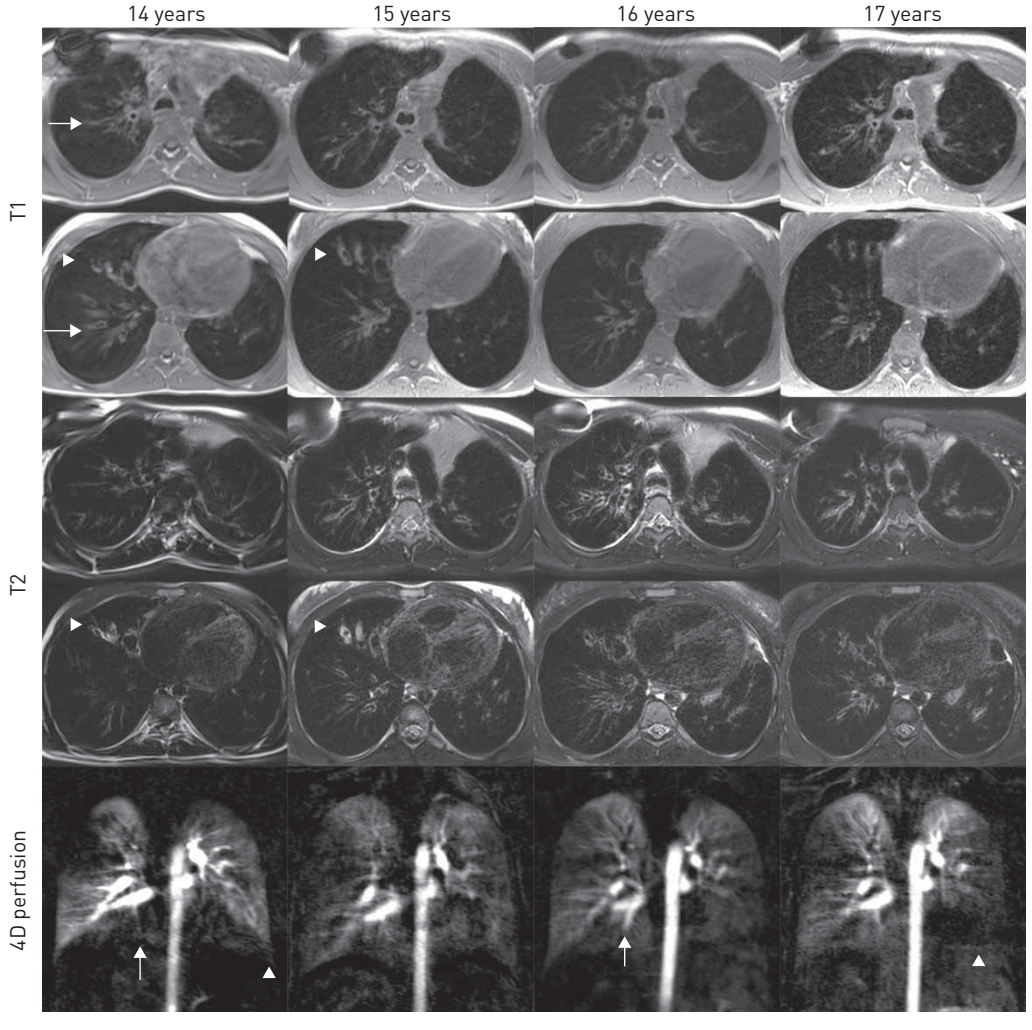

Figure 2. Progression of cystic fibrosis (CF) lung disease and reversible findings. Female CF patient longitudinally monitored with MRI from 14 to 17 years of age. T1-weighted sequences (top two rows) displayed marked bronchial wall thickening and bronchiectasis throughout the entire lung (arrows) including some cystic bronchiectasis. Additional mucus plugging was appreciated in the middle lobe (arrowhead), best depicted by T2-weighted sequences (middle two rows). Mucus plugging was obviously reduced at the age of 16 and 17, showing that this is a potentially reversible finding. Extensive perfusion abnormalities were revealed by 4D perfusion imaging (bottom row). Perfusion abnormalities of the right lower lung improved over time (compare arrows at 14 and 16 years) in parallel to mucus plugging, whereas perfusion in the left lower lung deteriorated (compare arrowheads at 14 and 17 years). Please note that the patient was provided with a portacath to the right chest.

structural changes. Similar to paired inspiratory and expiratory CT acquisitions for air trapping [48], paired inspiratory and expiratory scans (using T2 HASTE (half-Fourier acquisition single-shot turbo spin-echo) sequences, for example) are generally helpful to enhance the sensitivity for air trapping because the MRI signal is dependent on air and blood content [49, 50]. However, no systematic studies have been performed so far.

Areas of consolidation may occur, especially in cases of pulmonary infection [44, 51]. These stand out brightly on T2-weighted sequences (table 3). In many cases they may show a

reduced volume with displacement of the pulmonary fissures, unlike typical lobar pneumonia in otherwise healthy patients (figure 1). In a group of 10 patients with pulmonary exacerbations, these consolidations were more frequent and more severe than in a comparable group in a clinically stable situation. Moreover, they were alleviated under antibiotic therapy [44]. In the case of a destroyed segment or lobe, persistent consolidation embedded in marked bronchiectasis and volume loss is evident (figure 1).

Lung perfusion and vasculature

The physiological effect of hypoxic pulmonary vasoconstriction (HPV, or formerly the Euler–Liljestrand reflex) helps to reduce right-to-left shunts of non-oxygenated blood by coupling lung perfusion to lung ventilation. The effect of HPV implies that imaging of lung perfusion approximates lung ventilation [52]. Contrast-enhanced MRI perfusion imaging is now readily available and has already been validated against the reference standard perfusion scintigraphy [53]. It has been widely used clinically in diseases affecting pulmonary blood flow, such as COPD and acute pulmonary embolism [54–57], and in children with CF [44, 58]. From large data sets, perfusion maps are created by subtracting the series with the highest lung parenchymal enhancement from a pre-contrast series (figure 3) [52].

In CF, typical patchy or wedge-shaped perfusion defects occur, which reflect HPV (figures 1 and 2). These areas of hypoperfusion moderately correlate with the degree of parenchymal changes in adult and preschool patients [44, 58]. Abnormal perfusion can be detected in the

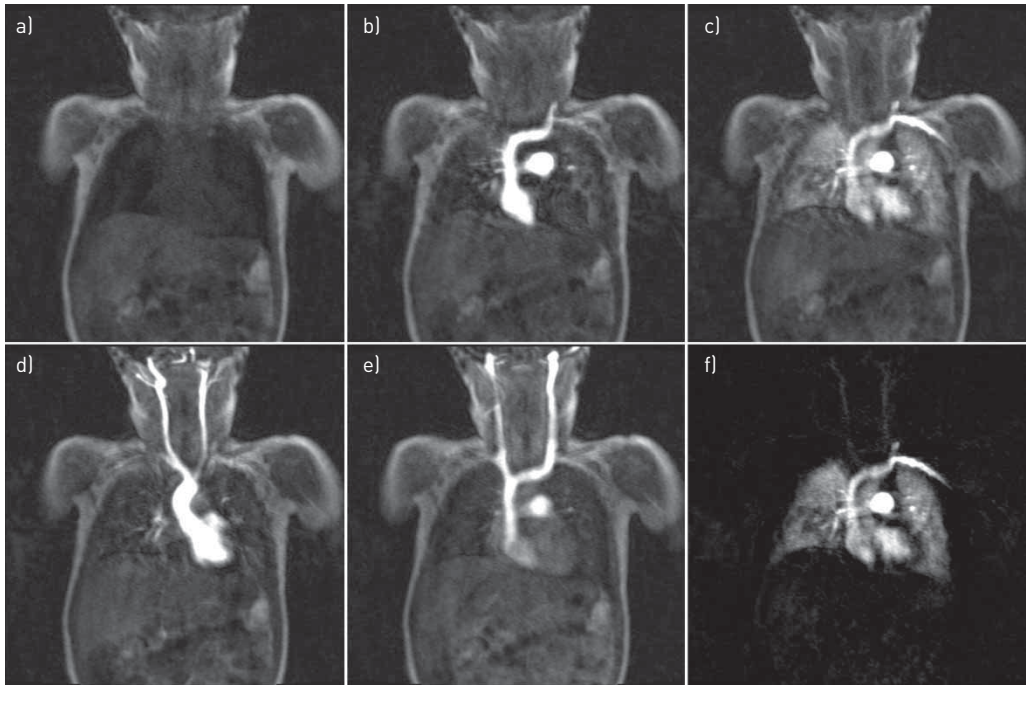

Figure 3. Generating perfusion maps for easy data evaluation. The 4D perfusion sequence is acquired during the intravenous administration of gadolinium-based contrast media with repeated measurements of the whole chest at a temporal resolution of 1.5 s in free breathing. Thus, a) non-enhanced images as well as b) an early pulmonary arterial, c) a pulmonary parenchymal, d) a systemic arterial and e) a venous phase can be separated. By subtracting the phase of highest pulmonary enhancement c) from the non-enhanced phase a), the lungs can be isolated as a perfusion map f).

first year of life in up to 85% of patients [44], and occurs even without detectable parenchymal changes. It is probably caused by (mucus) obstruction of large and/or small airways, the latter often not visualised either by morphological MRI or by CT (figure 1) [25, 59]. Thus, in preschool children only around 20% of the perfusion abnormalities could be explained by visible mucus plugging or bronchial wall abnormalities [44]. In pulmonary exacerbation, perfusion abnormalities tend to be more severe compared to patients in clinically stable condition [44], while a significant improvement of perfusion abnormalities after antibiotic therapy has been demonstrated (figure 2) [44].

Hypertrophy of bronchial arteries frequently occurs in advanced CF lung disease [60]. These bronchial arteries may be visualised by magnetic resonance angiography using MIPs, nicely demonstrating their tortuous course. In combination with extensive parenchymal destruction, bronchial artery dilatation may result in life-threatening pulmonary haemorrhage.

Scoring and semi-quantification

To grade disease severity, facilitate patient follow-up and monitor therapeutic effects in CF, diverse visual scoring systems have been developed for chest radiography and CT in the past. An MRI scoring system has been established more recently [29]. It uses similar parameters to the well-known CT scoring systems covering the aforementioned airway and parenchymal changes [38, 61, 62], but also scores changes in perfusion imaging [29]. It showed good inter-reader agreement for experienced radiologists from low to high scores in a patient group aged 0.5–42 years [29]. In a recent study in infants and preschool children with CF, the magnetic resonance scores showed weak to moderate correlations with the chest radiography score (r=0.26–0.54) [44], being lower than CT *versus* chest radiography scores in older patients with CF [63, 64]. At the same time, the correlation between magnetic resonance and CT scores was more substantial (r=0.80), as determined in 31 adolescent CF patients [27].

However, scoring remains a subjective semi-quantitative measure depending on the reader. Although desirable, automatic quantification of image information is challenging to achieve with morphological MRI [59]. There are several reasons for this: the MRI signal is not calibrated as the CT Hounsfield scale is, and lesions show different signal properties depending on the sequence applied. The signal-to-noise ratio and the lesion-to-background ratio are generally lower with MRI than with CT. These conditions hinder automatic anatomical model-based segmentation algorithms, which are needed to extract airway dimensions and lung volumes from MRI datasets. Inter-operator variability of segmentation and registration algorithms for different sequences and scanners remain major challenges.

Comparison with CT

CT is considered the reference standard for imaging of airway diseases because of volumetric data acquisition with isotropic resolution within one breath-hold. CT is superior to MRI in the depiction of normal subsegmental peripheral airways down to 200–300 µm in diameter [65, 66], and MRI is specifically limited in the visualisation of peripheral airways [41, 42]. Structural changes of the airways and parenchyma have traditionally been assessed by visual scoring, which has been demonstrated to be superior over pulmonary function testing in detecting subtle disease progression [14], and has already been used in a few interventional trials [67, 68]. Novel approaches include computer-assisted scoring

(PRAGMA) [69] and fully automatic quantification of airway dimensions and parenchyma [70] for direct measurement of pathological changes. The high overall prevalence of bronchiectasis and/or wall thickening of 93% of clinically stable patients in early CF lung disease detected by MRI [44] compares with recent studies employing CT in a population of CF patients identified by newborn screening, which reported a prevalence for bronchiectasis of ~60% at 3 years of age.

In order to detect small airway obstruction (air trapping), additional CT acquisitions can be performed in expiration. Regions of air trapping will not change in volume and density from inspiration to expiration, in contrast to normal lung, and thus stand out against normal lung. In small children unable to cooperate, this usually requires intubation and invasive ventilation [22]. The latest generations of scanner have image acquisition times far below 1 s for the whole chest, mostly delivering expiratory-weighted images at about functional residual capacity in a freely breathing infant or child (vacuum mattress or sedation), thus obviating the need for intubation. A prevalence of air trapping of up to 72% was recently detected in infants [22]. As described earlier, air trapping is closely linked to pulmonary perfusion by HPV. A direct comparison of MRI perfusion imaging with expiratory CT has not been attempted yet, but a recent study in preschool children revealed a similar prevalence of 85% for MRI perfusion abnormalities [44]. In general, repetitive CT studies are limited by cumulative radiation dose, and the risk of general anaesthesia in the case of young children. MRI in young children below the age of 6 years usually requires sedation, which is best performed with chloral hydrate to avoid atelectasis [44, 71].

Advanced techniques and functional imaging modules

Ultra-short echo time

UTE sequences were developed to overcome the rapid signal decay in the lung and promise a better signal output from the pulmonary parenchyma. Different approaches have been investigated, but currently the most promising results for morphological imaging have been achieved with a respiratory-gated UTE sequence [72], which showed a good agreement with CT scoring in a preliminary study with three adult CF patients. The image quality achieved resembles that of CT, but prolonged acquisition times (in the order of 10 min per patient) limit its immediate introduction into a routine protocol [72].

Respiratory cycle

2D or 3D dynamic magnetic resonance techniques, which are based on time-resolved steady-state free precession (SSFP) sequences, may be used to image the tidal respiratory cycle or forced breathing manoeuvres at a temporal resolution of up to $10 \cdot s^{-1}$ [73–75]. Presently, the use of dynamic image acquisitions in single 2D planes (2D+t) appears to be closest to routine use. Semi-automatic segmentation of the lung area on 2D+t examinations shows excellent correlation ($r>0.97$) with simultaneously performed spirometry in volunteers [76]. Hyperinflation of the lung as it occurs in obstructive airway disease may affect respiratory mechanics and diaphragmatic motion [77], which has already been studied in severe emphysema [78]. Future studies need to address the regional analysis of respiratory mechanics in CF, not be obtained by lung function tests.

Pulmonary blood flow

In order to harvest the full data spectrum from the 4D perfusion datasets, it is necessary to take the temporal changes of the contrast-induced signal into account. A high temporal resolution is required to clearly visualise the course of the contrast bolus during the pulmonary arterial and systemic arterial phase [79–81]. Dedicated software tools for the evaluation of these large 4D datasets with perfusion quantification based on the indicator dilution theory are already available [82]. These perform the initial step of segmenting the lung fully automatically [83] and then calculating the values for pulmonary blood flow, blood volume, mean transit time (MTT) and time to peak (TTP) [84]. These parameters have been validated against PET in a porcine model [85], but the validation in humans remains challenging because a noninvasive standard of reference is obviously missing [52, 86]. Nevertheless, these parameters have successfully been used in patients with COPD [84, 87], and pulmonary arterial hypertension [84, 88] compared to healthy subjects. MTT correlated best (r=0.56) with pulmonary arterial pressure measured invasively in pulmonary arterial hypertension patients [88]. As an obstacle to quantification it has to be noted that the signal increase with rising concentrations of gadolinium-based contrast *in vivo* is non-linear [89]. Thus, the contrast dose needs to be titrated down while an acceptable signal in the pulmonary parenchyma needs to be maintained [90].

In a study with 10 CF patients, decreased peak flow velocities of the pulmonary arteries based on phase-contrast MRI were found compared to healthy volunteers, which is indicative of early pulmonary hypertension in this patient population [91], and similar results have also been obtained in COPD [92]. This technique may also be helpful in addressing pulmonary hypertension in the pre-transplantation work-up of CF patients. Risse *et al.* [93] proposed an automatic semi-quantitative approach, generating maximum intensity and TTP maps suggesting five different perfusion patterns, which may be recognised in different lung diseases: 1) normal perfusion; 2) delayed non-reduced perfusion; 3) reduced non-delayed perfusion; 4) reduced and delayed perfusion; and 5) no perfusion [93]. Dilated bronchial arteries frequently observed in advanced CF receive blood from the systemic circulation, and increased flow will result in a left-to-left shunt, which is still of uncertain clinical significance. The shunt may be quantified by flow measurements in the aorta and the pulmonary trunk [52], and areas with a delayed systemic inflow through dilated bronchial arteries may be identified by the aforementioned perfusion maps. This approach may be important for differentiation of reversible or irreversible perfusion changes in the CF lung and warrant further investigation.

Pulmonary ventilation

Noble gas imaging

Because exhalation leads to an increase in lung signal, lung ventilation can be indirectly estimated from regional volume and signal changes in dynamic acquisitions, if enough parenchymal signal can be detected, *e.g.* with SSFP sequences [49, 76]. Several techniques have been developed to improve the signal for ventilation imaging. The most obvious possibility is to inhale aerosolised gadolinium-based contrast media. Initial studies on volunteers have been performed [94]. However, this technique is complicated by the complex particle deposition dynamics (high viscosity of contrast agents, low effectiveness of current nebulisers to create droplets smaller than 3 μm, which would deposit in distal airspaces) and relatively low signal changes induced [95]. An alternative is inhaled sulfur hexafluoride [96].

Another more feasible option, in particular in the research arena, is the imaging of nuclei other than ^{1}H, namely ^{3}He and ^{129}Xe [97–99]. In order to generate a high enough signal, these gases need to be hyperpolarised on site. After inhalation, the hyperpolarised noble gas will selectively display the ventilated airspace, comparable to ventilation scintigraphy [100]. Static imaging of ventilation distribution has already been employed in a variety of lung diseases with an isotropic pixel size of 3–4 mm [98, 101]. In CF patients, more ventilation defects were depicted than in healthy volunteers, which also correlated well with a decrease in FEV_1% ($r=-0.71$) [102, 103], but showed poor correlation with chest radiography scoring [104]. Although this procedure requires a high degree of patient cooperation, it could be performed in CF patients as young as 5 years of age [104]. A more recent study demonstrated ventilation defects even in CF patients with normal lung function, which may change after physical therapy [105]. This finding once again demonstrates that lung function testing is insensitive for early lung disease. With co-registered structural information from the ^{1}H signal [106], the gas ventilation images, together with contrast-enhanced perfusion images, can be interpreted quantitatively to assess lung ventilation/perfusion on a regional basis [107]. Recently, the reproducibility of ventilation defects has been demonstrated in five CF patients in stable clinical condition with four measurements during a 4-week period [108]. The complex technical prerequisites and the price of noble gas isotopes make this powerful research tool a technology unlikely to be introduced into routine patient care.

T1 mapping and oxygen enhancement

The direct regional quantification of T1 relaxation times is thought to provide an objective parameter for the characterisation of pulmonary tissue independent of scanner type or observer [109]. T1 correlates with the composition and state of lung tissue, including the lung tissue and blood volume fraction [110]. Preliminary results obtained in patients indicate that T1 relaxation time is significantly shorter in lungs affected by emphysema, asthma or CF [109, 111], compared to lungs of healthy subjects (figure 4). Applying different echo times during T1 read-out means the tissue and blood components may potentially be separated [112].

Furthermore, T1 mapping can be combined with molecular O_2 to exploit its paramagnetic effect for an indirect assessment of lung ventilation [113]. O_2 leads to a shortening of the T1 time in ventilated airspace due to dissolved O_2 in lung tissue and blood, as well as a signal increase in T1-weighted morphological sequences [114]. Inhaling pure O_2 supplemented by a mask over a period of 10–15 min will sufficiently increase the alveolar concentration to shorten T1 times [115–117]. This effect can be used to generate maps of regional pulmonary ventilation by comparing T1 parameters maps obtained with room air and after O_2 supplementation. The acquisition of wash-in and wash-out dynamics is also possible. In five CF patients, an inhomogeneous baseline T1 distribution and a decrease of the T1 slope at different oxygen levels correlated with perfusion abnormalities [110]. More recently, Jobst *et al.* [57] demonstrated in 20 COPD patients that a short baseline T1 at room air correlated well with perfusion deficits on subtracted perfusion maps in COPD, and that these areas mostly did not respond to O_2 supplementation. This finding supports a role of T1 mapping without the need for O_2 supplementation as a surrogate for pulmonary blood volume distribution (figure 4). As O_2 also has pharmacodynamic effects it should be used with caution in patients with severe lung disease. Hyperoxia also leads to an increase and redistribution of pulmonary perfusion, an effect that needs to be considered when planning O_2-enhanced studies [90]. At this point, the value of T1 mapping as a routine tool for clinical assessment of CF still needs to be elucidated.

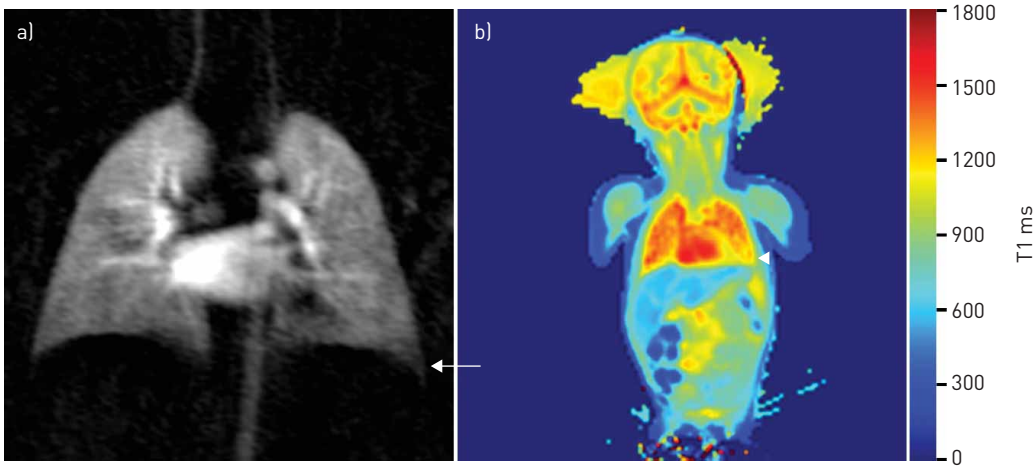

Figure 4. T1 mapping correlates with blood volume distribution. a) Contrast-enhanced perfusion MRI and b) T1 mapping in free breathing were performed in a 12-month-old infant originally identified by newborn screening. In the costodiaphragmatic angle an area of reduced perfusion (arrow) was evident whereas perfusion was homogeneous in the remaining lung volume. This area corresponded with a subtle T1 time reduction (arrowhead). Thus, T1 mapping may sensitively visualise blood volume distribution without intravenous contrast application in early cystic fibrosis lung disease.

Simultaneous non-contrast material ventilation and perfusion imaging

During expiration, the air content of the normal lung will decrease and the protons of lung tissue will be concentrated to a smaller volume. This will lead to a relative increase in magnetic resonance signal of the lung in expiration [49]. Conversely, this may be used as an easy technique to identify areas of trapped air, which fail to increase in signal after exhalation compared with the surrounding lung, in a very similar manner to the well-known phenomenon of air trapping at paired inspiratory and expiratory CT. Similarly, the signal of gravitation-dependent lung areas, *i.e.* dorsal lung in the supine posture, is higher than in non-dependent areas [118]. To objectively quantify such visual findings, mapping of the T1 relaxation time has been performed in patients with emphysema and fibrosis, which revealed a stronger increase of T1 time of the whole lung of fibrosis patients in expiration, compared with emphysema patients [109, 117].

Another newly developed method relies on the periodic signal changes of SSFP sequences at a high temporal resolution induced by pulsatile blood inflow and respiration. Steps of non-rigid registration and pixel-wise Fourier decomposition are necessary to extract the signal peaks at the cardiac and respiratory frequency to generate perfusion- and ventilation-weighted images (figure 5) [119, 120]. Most recently, it has been validated against SPECT perfusion and ventilation imaging [121], and against hyperpolarised ^{3}He- and perfusion MRI [122] in a porcine model. In healthy volunteers, the short-term reproducibility and stability of the technique have already been demonstrated [123]. Preliminary results from examinations in 34 CF patients of different age are available, showing a good agreement with contrast-enhanced perfusion MRI using visual and semi-automated scoring [124]. Because this technique is neither dependent on the application of *i.v.* (or intra-alveolar) contrast nor on the patient's compliance, it should be well suited for treatment follow-up in consecutive studies. Automatic tools for semi-quantitative scoring of contrast-enhanced as well as Fourier decomposition perfusion images in CF patients have already been proposed [83, 124, 125].

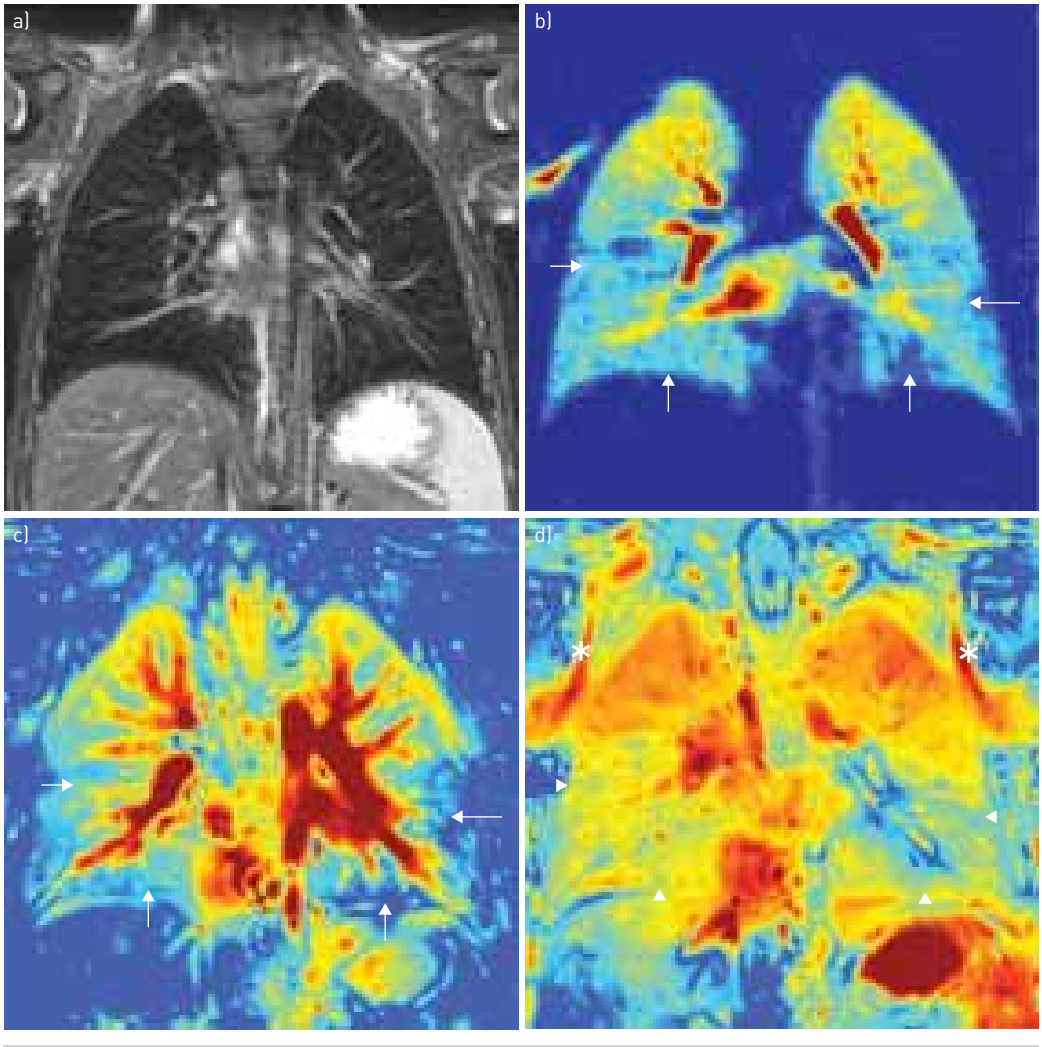

Figure 5. Fourier decomposition (FD) MRI for non-contrast ventilation and perfusion imaging. a) Morphological MRI including a navigated T2-weighted sequence in this 3-year-old male cystic fibrosis patient detected subtle airway abnormalities but no mucus plugging. b) However, dynamic 4D perfusion datasets acquired in free breathing during intravenous contrast administration detected extensive perfusion abnormalities (arrows). c) Perfusion and d) ventilation maps generated by FD MRI showed areas of perfusion abnormalities (arrows) and ventilation impairment (arrowheads), which nicely correspond to the pathology revealed with 4D perfusion MRI, without the necessity of contrast material injection. Note that chest wall motion and pulsatile blood flow induced by respiration may also produce signal in ventilation maps (*).

Conclusion

CF is the first airway disease for which MRI has been introduced into the clinical arena. In a patient group of increasing life expectancy due to improved therapy, ionising radiation accumulating from multiple follow-up examinations necessary from infancy to adulthood should be regarded as a limiting factor. The risk of sedation and allergies to MRI contrast media must not only be weighed against the risk from radiation exposure [24, 26, 126], but also against the background of missing data on the actual impact of imaging on treatment

decision and outcome. Importantly, the intention to use MRI in CF as a routine surveillance tool is not to merely reproduce or replace structural information gained by HRCT with a radiation-free method. MRI's capability for combined morphological and functional imaging at sufficient spatial and high temporal resolution now provides additional clinically relevant information on regional lung function, surpassing that gained even by combined inspiratory–expiratory CT. If structural changes need to be monitored with the highest sensitivity, MRI may also be combined with the strengths of CT into a comprehensive CF surveillance imaging protocol, depending on the local expertise at the CF centre. Potentially reversible changes in lung function have been shown to be responsive to therapy in the short term, whereas bronchiectasis and other morphological changes are irreversible. Thus, chest MRI in CF should include at least a perfusion study, which is already available for most state-of-the-art MRI scanners. Further efforts, including specific education of radiologists, are now needed to standardise acquisition protocols and image interpretation across centres to allow the widespread introduction of morpho-functional MRI into clinical routine use. More advanced techniques need further development and validation before routine use. Further work will have to focus on fully automated tools to integrate morphological and functional datasets into robust imaging biomarkers, which should be preferred to visual evaluation. These will provide the ideal basis for the application of chest MRI in interventional trials as a new objective outcome measure. Finally, the potential of MRI for short-term follow-up and functional studies stands out against a solely structural imaging modality such as CT.

References

1. Gibson RL, Burns JL, Ramsey BW. Pathophysiology and management of pulmonary infections in cystic fibrosis. *Am J Respir Crit Care Med* 2003; 168: 918–951.
2. Welsh MJ, Ramsey B, Accurso F, *et al.* Cystic fibrosis. *In*: Scriver CR, Beaudet AL, Sly WS, *et al.*, eds. The Metabolic and Molecular Basis of Inherited Disease. 8th Edn. New York, McGraw-Hill, 2001; pp. 5121–5188.
3. Mall M, Boucher RC. Pathogenesis of pulmonary disease in cystic fibrosis. *In*: Bush A, Alton EWFW, Davies JC, *et al.*, eds. Cystic Fibrosis in the 21st Century. Basel, Karger, 2006; pp. 116–121.
4. Dodge JA, Lewis PA, Stanton M, *et al.* Cystic fibrosis mortality and survival in the UK: 1947–2003. *Eur Respir J* 2007; 29: 522–526.
5. Stern M, Wiedemann B, Wenzlaff P. From registry to quality management: the German Cystic Fibrosis Quality Assessment project 1995–2006. *Eur Respir J* 2008; 31: 29–35.
6. Sommerburg O, Lindner M, Muckenthaler M, *et al.* Initial evaluation of a biochemical cystic fibrosis newborn screening by sequential analysis of immunoreactive trypsinogen and pancreatitis-associated protein (IRT/PAP) as a strategy that does not involve DNA testing in a Northern European population. *J Inherit Metab Dis* 2010; 33: S263–S271.
7. Kerem E, Reisman J, Corey M, *et al.* Prediction of mortality in patients with cystic fibrosis. *N Engl J Med* 1992; 326: 1187–1191.
8. Brody AS, Tiddens HA, Castile RG, *et al.* Computed tomography in the evaluation of cystic fibrosis lung disease. *Am J Respir Crit Care Med* 2005; 172: 1246–1252.
9. Brody AS, Sucharew H, Campbell JD, *et al.* Computed tomography correlates with pulmonary exacerbations in children with cystic fibrosis. *Am J Respir Crit Care Med* 2005; 172: 1128–1132.
10. Terheggen-Lagro S, Truijens N, van Poppel N, *et al.* Correlation of six different cystic fibrosis chest radiograph scoring systems with clinical parameters. *Pediatr Pulmonol* 2003; 35: 441–445.
11. Terheggen-Lagro SW, Arets HG, van der Laag J, *et al.* Radiological and functional changes over 3 years in young children with cystic fibrosis. *Eur Respir J* 2007; 30: 279–285.
12. Sanders DB, Li Z, Brody AS, *et al.* Chest computed tomography scores of severity are associated with future lung disease progression in children with cystic fibrosis. *Am J Respir Crit Care Med* 2011; 184: 816–821.
13. Cleveland RH, Stamoulis C, Sawicki G, *et al.* Brasfield and Wisconsin scoring systems have equal value as outcome assessment tools of cystic fibrosis lung disease. *Pediatr Radiol* 2014; 44: 529–534.
14. de Jong PA, Lindblad A, Rubin L, *et al.* Progression of lung disease on computed tomography and pulmonary function tests in children and adults with cystic fibrosis. *Thorax* 2006; 61: 80–85.

15. Davis SD, Fordham LA, Brody AS, *et al.* Computed tomography reflects lower airway inflammation and tracks changes in early cystic fibrosis. *Am J Respir Crit Care Med* 2007; 175: 943–950.
16. Sly PD, Brennan S, Gangell C, *et al.* Lung disease at diagnosis in infants with cystic fibrosis detected by newborn screening. *Am J Respir Crit Care Med* 2009; 180: 146–152.
17. Long FR, Williams RS, Castile RG. Structural airway abnormalities in infants and young children with cystic fibrosis. *J Pediatr* 2004; 144: 154–161.
18. Martinez TM, Llapur CJ, Williams TH, *et al.* High-resolution computed tomography imaging of airway disease in infants with cystic fibrosis. *Am J Respir Crit Care Med* 2005; 172: 1133–1138.
19. Stick SM, Brennan S, Murray C, *et al.* Bronchiectasis in infants and preschool children diagnosed with cystic fibrosis after newborn screening. *J Pediatr* 2009; 155: 623–628.
20. Mott LS, Park J, Murray CP, *et al.* Progression of early structural lung disease in young children with cystic fibrosis assessed using CT. *Thorax* 2012; 67: 509–516.
21. Mott LS, Park J, Gangell CL, *et al.* Distribution of early structural lung changes due to cystic fibrosis detected with chest computed tomography. *J Pediatr* 2013; 163: 243–248.
22. Sly PD, Gangell CL, Chen L, *et al.* Risk factors for bronchiectasis in children with cystic fibrosis. *N Engl J Med* 2013; 368: 1963–1970.
23. de Jong PA, Mayo JR, Golmohammadi K, *et al.* Estimation of cancer mortality associated with repetitive computed tomography scanning. *Am J Respir Crit Care Med* 2006; 173: 199–203.
24. Donadieu J, Roudier C, Saguintaah M, *et al.* Estimation of the radiation dose from thoracic CT scans in a cystic fibrosis population. *Chest* 2007; 132: 1233–1238.
25. Eichinger M, Heussel CP, Kauczor HU, *et al.* Computed tomography and magnetic resonance imaging in cystic fibrosis lung disease. *J Magn Reson Imaging* 2010; 32: 1370–1378.
26. O'Connell OJ, McWilliams S, McGarrigle A, *et al.* Radiologic imaging in cystic fibrosis: cumulative effective dose and changing trends over 2 decades. *Chest* 2012; 141: 1575–1583.
27. Puderbach M, Eichinger M, Haeselbarth J, *et al.* Assessment of morphological MRI for pulmonary changes in cystic fibrosis (CF) patients: comparison to thin-section CT and chest x-ray. *Invest Radiol* 2007; 42: 715–725.
28. Puderbach M, Eichinger M. The role of advanced imaging techniques in cystic fibrosis follow-up: is there a place for MRI? *Pediatr Radiol* 2010; 40: 844–849.
29. Eichinger M, Optazaite DE, Kopp-Schneider A, *et al.* Morphologic and functional scoring of cystic fibrosis lung disease using MRI. *Eur J Radiol* 2012; 81: 1321–1329.
30. Wielpütz M, Kauczor HU. MRI of the lung: state of the art. *Diagn Interv Radiol* 2012; 18: 344–353.
31. Müller FM, Bend J, Rietschel E, *et al.* S3-leitlinie "lungenerkrankung bei mukoviszidose", Modul 1: Diagnostik und Therapie nach dem ersten nachweis von pseudomonas aeruginosa. http://www.awmf.org/uploads/tx_szleitlinien/026-022k_S3_Lungenerkrankung_bei_Mukoviszidose_Modul_1_2014-03.pdf Date last updated: March 2014.
32. Tiddens HAWM. Imaging the lungs in cystic fibrosis. *In*: Mall MA, Elborn JS, eds. Cystic Fibrosis (ERS Monograph). Sheffield, European Respiratory Society, 2014; pp. 88–103.
33. Wild JM, Marshall H, Bock M, *et al.* MRI of the lung (1/3): methods. *Insights Imaging* 2012; 3: 345–353.
34. Puderbach M, Hintze C, Ley S, *et al.* MR imaging of the chest: a practical approach at 1.5t. *Eur J Radiol* 2007; 64: 345–355.
35. Biederer J, Beer M, Hirsch W, *et al.* MRI of the lung (2/3). Why … when … how? *Insights Imaging* 2012; 3: 355–371.
36. Biederer J, Mirsadraee S, Beer M, *et al.* MRI of the lung (3/3)-current applications and future perspectives. *Insights Imaging* 2012; 3: 373–386.
37. Biederer J, Heussel CP, Puderbach M, *et al.* Functional magnetic resonance imaging of the lung. *Semin Respir Crit Care Med* 2014; 35: 74–82.
38. Helbich TH, Heinz-Peer G, Eichler I, *et al.* Cystic fibrosis: CT assessment of lung involvement in children and adults. *Radiology* 1999; 213: 537–544.
39. Loeve M, van Hal PT, Robinson P, *et al.* The spectrum of structural abnormalities on CT scans from patients with CF with severe advanced lung disease. *Thorax* 2009; 64: 876–882.
40. Biederer J, Reuter M, Both M, *et al.* Analysis of artefacts and detail resolution of lung MRI with breath-hold T1-weighted gradient-echo and T2-weighted fast spin-echo sequences with respiratory triggering. *Eur Radiol* 2002; 12: 378–384.
41. Failo R, Wielopolski PA, Tiddens HA, *et al.* Lung morphology assessment using MRI: a robust ultra-short TR/TE 2D steady state free precession sequence used in cystic fibrosis patients. *Magn Reson Med* 2009; 61: 299–306.
42. Ciet P, Serra G, Bertolo S, *et al.* Assessment of CF lung disease using motion corrected PROPELLER MRI: a comparison with CT. *Eur Radiol* 2015; [in press DOI: 10.1007/s00330-015-3850-9].
43. Puderbach M, Eichinger M, Gahr J, *et al.* Proton MRI appearance of cystic fibrosis: comparison to CT. *Eur Radiol* 2007; 17: 716–724.

44. Wielpütz MO, Puderbach M, Kopp-Schneider A, *et al.* Magnetic resonance imaging detects changes in structure and perfusion, and response to therapy in early cystic fibrosis lung disease. *Am J Respir Crit Care Med* 2014; 189: 956–965.
45. Zhou Z, Treis D, Schubert SC, *et al.* Preventive but not late amiloride therapy reduces morbidity and mortality of lung disease in betaenac-overexpressing mice. *Am J Respir Crit Care Med* 2008; 178: 1245–1256.
46. Graeber SY, Zhou-Suckow Z, Schatterny J, *et al.* Hypertonic saline is effective in the prevention and treatment of mucus obstruction, but not airway inflammation, in mice with chronic obstructive lung disease. *Am J Respir Cell Mol Biol* 2013; 49: 410–417.
47. Altes TA, Eichinger M, Puderbach M. Magnetic resonance imaging of the lung in cystic fibrosis. *Proc Am Thorac Soc* 2007; 4: 321–327.
48. Hansell DM. Small airways diseases: detection and insights with computed tomography. *Eur Respir J* 2001; 17: 1294–1313.
49. Bankier AA, O'Donnell CR, Mai VM, *et al.* Impact of lung volume on MR signal intensity changes of the lung parenchyma. *J Magn Reson Imaging* 2004; 20: 961–966.
50. Iwasawa T, Takahashi H, Ogura T, *et al.* Correlation of lung parenchymal MR signal intensity with pulmonary function tests and quantitative computed tomography (CT) evaluation: a pilot study. *J Magn Reson Imaging* 2007; 26: 1530–1536.
51. Rosenfeld M, Ratjen F, Brumback L, *et al.* Inhaled hypertonic saline in infants and children younger than 6 years with cystic fibrosis: the ISIS randomized controlled trial. *JAMA* 2012; 307: 2269–2277.
52. Hopkins SR, Wielpütz MO, Kauczor HU. Imaging lung perfusion. *J Appl Physiol* 2012; 113: 328–339.
53. Molinari F, Fink C, Risse F, *et al.* Assessment of differential pulmonary blood flow using perfusion magnetic resonance imaging: comparison with radionuclide perfusion scintigraphy. *Invest Radiol* 2006; 41: 624–630.
54. Thabut G, Dauriat G, Stern JB, *et al.* Pulmonary hemodynamics in advanced COPD candidates for lung volume reduction surgery or lung transplantation. *Chest* 2005; 127: 1531–1536.
55. Morino S, Toba T, Araki M, *et al.* Noninvasive assessment of pulmonary emphysema using dynamic contrast-enhanced magnetic resonance imaging. *Exp Lung Res* 2006; 32: 55–67.
56. Fink C, Ley S, Schoenberg SO, *et al.* Magnetic resonance imaging of acute pulmonary embolism. *Eur Radiol* 2007; 17: 2546–2553.
57. Jobst BJ, Triphan SM, Sedlaczek O, *et al.* Functional lung MRI in chronic obstructive pulmonary disease: comparison of T1 mapping, oxygen-enhanced T1 mapping and dynamic contrast enhanced perfusion. *PLoS One* 2015; 10: e0121520.
58. Eichinger M, Puderbach M, Fink C, *et al.* Contrast-enhanced 3D MRI of lung perfusion in children with cystic fibrosis – initial results. *Eur Radiol* 2006; 16: 2147–2152.
59. Wielputz MO, Eichinger M, Puderbach M. Magnetic resonance imaging of cystic fibrosis lung disease. *J Thorac Imaging* 2013; 28: 151–159.
60. Optazaite DE, Eichinger M, Niemann A, *et al.* Visualization of dilated bronchial arteries using contrast-enhanced magnetic resonance angiography in cystic fibrosis patients – correlation to parenchymal lung changes. *Am J Respir Crit Care Med* 2010; 181: A1816.
61. Bhalla M, Turcios N, Aponte V, *et al.* Cystic fibrosis: scoring system with thin-section CT. *Radiology* 1991; 179: 783–788.
62. de Jong PA, Ottink MD, Robben SG, *et al.* Pulmonary disease assessment in cystic fibrosis: comparison of CT scoring systems and value of bronchial and arterial dimension measurements. *Radiology* 2004; 231: 434–439.
63. Demirkazik FB, Ariyurek OM, Ozcelik U, *et al.* High resolution CT in children with cystic fibrosis: correlation with pulmonary functions and radiographic scores. *Eur J Radiol* 2001; 37: 54–59.
64. Sanders DB, Li Z, Rock MJ, *et al.* The sensitivity of lung disease surrogates in detecting chest CT abnormalities in children with cystic fibrosis. *Pediatr Pulmonol* 2012; 47: 567–573.
65. Kauczor HU, Wielpütz MO, Owsijewitsch M, *et al.* Computed tomographic imaging of the airways in COPD and asthma. *J Thorac Imaging* 2011; 26: 290–300.
66. Hogg JC, Chu F, Utokaparch S, *et al.* The nature of small-airway obstruction in chronic obstructive pulmonary disease. *N Engl J Med* 2004; 350: 2645–2653.
67. Brody AS, Molina PL, Klein JS, *et al.* High-resolution computed tomography of the chest in children with cystic fibrosis: support for use as an outcome surrogate. *Pediatr Radiol* 1999; 29: 731–735.
68. Tiddens HA, de Jong PA. Imaging and clinical trials in cystic fibrosis. *Proc Am Thorac Soc* 2007; 4: 343–346.
69. Rosenow T, Oudraad MC, Murray CP, *et al.* A quantitative structural lung disease computed tomography outcome in young children with cystic fibrosis. *Am J Respir Crit Care Med* 2015; 191: 1158–1165.
70. Wielputz MO, Eichinger M, Weinheimer O, *et al.* Automatic airway analysis on multidetector computed tomography in cystic fibrosis: correlation with pulmonary function testing. *J Thorac Imaging* 2013; 28: 104–113.
71. Blitman NM, Lee HK, Jain VR, *et al.* Pulmonary atelectasis in children anesthetized for cardiothoracic MR: evaluation of risk factors. *J Comput Assist Tomogr* 2007; 31: 789–794.

72. Dournes G, Grodzki D, Macey J, *et al.* Quiet submillimeter MR imaging of the lung is feasible with a PETRA sequence at 1.5 t. *Radiology* 2015; 276: 258–265.
73. Cluzel P, Similowski T, Chartrand-Lefebvre C, *et al.* Diaphragm and chest wall: assessment of the inspiratory pump with MR imaging – preliminary observations. *Radiology* 2000; 215: 574–583.
74. Plathow C, Ley S, Fink C, *et al.* Evaluation of chest motion and volumetry during the breathing cycle by dynamic MRI in healthy subjects: comparison with pulmonary function tests. *Invest Radiol* 2004; 39: 202–209.
75. Plathow C, Schoebinger M, Fink C, *et al.* Evaluation of lung volumetry using dynamic three-dimensional magnetic resonance imaging. *Invest Radiol* 2005; 40: 173–179.
76. Tetzlaff R, Schwarz T, Kauczor HU, *et al.* Lung function measurement of single lungs by lung area segmentation on 2D dynamic MRI. *Acad Radiol* 2010; 17: 496–503.
77. Henderson AC, Ingenito EP, Salcedo ES, *et al.* Dynamic lung mechanics in late-stage emphysema before and after lung volume reduction surgery. *Respir Physiol Neurobiol* 2007; 155: 234–242.
78. Iwasawa T, Kagei S, Gotoh T, *et al.* Magnetic resonance analysis of abnormal diaphragmatic motion in patients with emphysema. *Eur Respir J* 2002; 19: 225–231.
79. Ley S, Fink C, Puderbach M, *et al.* [Contrast-enhanced 3D MR perfusion of the lung: application of parallel imaging technique in healthy subjects]. *Rofo* 2004; 176: 330–334.
80. Fink C, Puderbach M, Bock M, *et al.* Regional lung perfusion: assessment with partially parallel three-dimensional MR imaging. *Radiology* 2004; 231: 175–184.
81. Fink C, Ley S, Kroeker R, *et al.* Time-resolved contrast-enhanced three-dimensional magnetic resonance angiography of the chest: combination of parallel imaging with view sharing (TREAT). *Invest Radiol* 2005; 40: 40–48.
82. Kuder TA, Risse F, Eichinger M, *et al.* New method for 3D parametric visualization of contrast-enhanced pulmonary perfusion MRI data. *Eur Radiol* 2008; 18: 291–297.
83. Kohlmann P, Strehlow J, Jobst B, *et al.* Automatic lung segmentation method for MRI-based lung perfusion studies of patients with chronic obstructive pulmonary disease. *Int J Comput Assist Radiol Surg* 2014; 10: 15.
84. Ohno Y, Hatabu H, Murase K, *et al.* Quantitative assessment of regional pulmonary perfusion in the entire lung using three-dimensional ultrafast dynamic contrast-enhanced magnetic resonance imaging: preliminary experience in 40 subjects. *J Magn Reson Imaging* 2004; 20: 353–365.
85. Neeb D, Kunz RP, Ley S, *et al.* Quantification of pulmonary blood flow (PBF): validation of perfusion MRI and nonlinear contrast agent (CA) dose correction with H(2)15O positron emission tomography (PET). *Magn Reson Med* 2009; 62: 476–487.
86. Hueper K, Parikh MA, Prince MR, *et al.* Quantitative and semiquantitative measures of regional pulmonary microvascular perfusion by magnetic resonance imaging and their relationships to global lung perfusion and lung diffusing capacity: the multiethnic study of atherosclerosis chronic obstructive pulmonary disease study. *Invest Radiol* 2013; 48: 223–230.
87. Hueper K, Vogel-Claussen J, Parikh MA, *et al.* Pulmonary microvascular blood flow in mild chronic obstructive pulmonary disease and emphysema. The MESA COPD study. *Am J Respir Crit Care Med* 2015; 192: 570–580.
88. Ley S, Mereles D, Risse F, *et al.* Quantitative 3D pulmonary MR-perfusion in patients with pulmonary arterial hypertension: correlation with invasive pressure measurements. *Eur J Radiol* 2007; 61: 251–255.
89. Puderbach M, Risse F, Biederer J, *et al. In vivo* Gd-DTPA concentration for MR lung perfusion measurements: assessment with computed tomography in a porcine model. *Eur Radiol* 2008; 18: 2102–2107.
90. Ley S, Puderbach M, Risse F, *et al.* Impact of oxygen inhalation on the pulmonary circulation: assessment by magnetic resonance (MR)-perfusion and MR-flow measurements. *Invest Radiol* 2007; 42: 283–290.
91. Ley S, Puderbach M, Fink C, *et al.* Assessment of hemodynamic changes in the systemic and pulmonary arterial circulation in patients with cystic fibrosis using phase-contrast MRI. *Eur Radiol* 2005; 15: 1575–1580.
92. Vonk-Noordegraaf A, Marcus JT, Holverda S, *et al.* Early changes of cardiac structure and function in COPD patients with mild hypoxemia. *Chest* 2005; 127: 1898–1903.
93. Risse F, Eichinger M, Kauczor HU, *et al.* Improved visualization of delayed perfusion in lung MRI. *Eur J Radiol* 2011; 77: 105–110.
94. Haage P, Karaagac S, Spuntrup E, *et al.* Feasibility of pulmonary ventilation visualization with aerosolized magnetic resonance contrast media. *Invest Radiol* 2005; 40: 85–88.
95. Mosbah K, Ruiz-Cabello J, Berthezene Y, *et al.* Aerosols and gaseous contrast agents for magnetic resonance imaging of the lung. *Contrast Media Mol Imaging* 2008; 3: 173–190.
96. Scholz AW, Wolf U, Fabel M, *et al.* Comparison of magnetic resonance imaging of inhaled SF6 with respiratory gas analysis. *Magn Reson Imaging* 2009; 27: 549–556.
97. Altes TA, de Lange EE. Applications of hyperpolarized helium-3 gas magnetic resonance imaging in pediatric lung disease. *Top Magn Reson Imaging* 2003; 14: 231–236.
98. van Beek EJ, Wild JM, Kauczor HU, *et al.* Functional MRI of the lung using hyperpolarized 3-Helium gas. *J Magn Reson Imaging* 2004; 20: 540–554.

99. Wild JM, Schmiedeskamp J, Paley MN, *et al.* MR imaging of the lungs with hyperpolarized Helium-3 gas transported by air. *Phys Med Biol* 2002; 47: N185–N190.
100. Altes TA, Rehm PK, Harrell F, *et al.* Ventilation imaging of the lung: comparison of hyperpolarized Helium-3 MR imaging with Xe-133 scintigraphy. *Acad Radiol* 2004; 11: 729–734.
101. Kauczor HU. Hyperpolarized Helium-3 gas magnetic resonance imaging of the lung. *Top Magn Reson Imaging* 2003; 14: 223–230.
102. Donnelly LF, MacFall JR, McAdams HP, *et al.* Cystic fibrosis: combined hyperpolarized 3He-enhanced and conventional proton MR imaging in the lung – preliminary observations. *Radiology* 1999; 212: 885–889.
103. Mentore K, Froh DK, de Lange EE, *et al.* Hyperpolarized HHe 3 MRI of the lung in cystic fibrosis: assessment at baseline and after bronchodilator and airway clearance treatment. *Acad Radiol* 2005; 12: 1423–1429.
104. van Beek EJ, Hill C, Woodhouse N, *et al.* Assessment of lung disease in children with cystic fibrosis using hyperpolarized 3-Helium MRI: comparison with Shwachman score, Chrispin-Norman score and spirometry. *Eur Radiol* 2007; 17: 1018–1024.
105. Bannier E, Cieslar K, Mosbah K, *et al.* Hyperpolarized 3He MR for sensitive imaging of ventilation function and treatment efficiency in young cystic fibrosis patients with normal lung function. *Radiology* 2010; 255: 225–232.
106. Wild JM, Marshall H, Xu X, *et al.* Simultaneous imaging of lung structure and function with triple-nuclear hybrid MR imaging. *Radiology* 2013; 267: 251–255.
107. Marshall H, Kiely DG, Parra-Robles J, *et al.* Magnetic resonance imaging of ventilation and perfusion changes in response to pulmonary endarterectomy in chronic thromboembolic pulmonary hypertension. *Am J Respir Crit Care Med* 2014; 190: e18–e19.
108. O'Sullivan B, Couch M, Roche JP, *et al.* Assessment of repeatability of hyperpolarized gas MR ventilation functional imaging in cystic fibrosis. *Acad Radiol* 2014; 21: 1524–1529.
109. Stadler A, Jakob PM, Griswold M, *et al.* T1 mapping of the entire lung parenchyma: influence of respiratory phase and correlation to lung function test results in patients with diffuse lung disease. *Magn Reson Med* 2008; 59: 96–101.
110. Jakob PM, Wang T, Schultz G, *et al.* Assessment of human pulmonary function using oxygen-enhanced T(1) imaging in patients with cystic fibrosis. *Magn Reson Med* 2004; 51: 1009–1016.
111. Renne J, Hinrichs J, Schonfeld C, *et al.* Noninvasive quantification of airway inflammation following segmental allergen challenge with functional MR imaging: a proof of concept study. *Radiology* 2015; 274: 267–275.
112. Triphan SM, Jobst BJ, Breuer FA, *et al.* Echo time dependence of observed T1 in the human lung. *J Magn Reson Imaging* 2015; 42: 610–616.
113. Molinari F, Puderbach M, Eichinger M, *et al.* Oxygen-enhanced magnetic resonance imaging: influence of different gas delivery methods on the T1-changes of the lungs. *Invest Radiol* 2008; 43: 427–432.
114. Tadamura E, Hatabu H, Li W, *et al.* Effect of oxygen inhalation on relaxation times in various tissues. *J Magn Reson Imag* 1997; 7: 220–225.
115. Edelman RR, Hatabu H, Tadamura E, *et al.* Noninvasive assessment of regional ventilation in the human lung using oxygen-enhanced magnetic resonance imaging. *Nat Med* 1996; 2: 1236–1239.
116. Ohno Y, Chen Q, Hatabu H. Oxygen-enhanced magnetic resonance ventilation imaging of lung. *Eur J Radiol* 2001; 37: 164–171.
117. Jakob PM, Hillenbrand CM, Wang T, *et al.* Rapid quantitative lung (1)H T(1) mapping. *J Magn Reson Imaging* 2001; 14: 795–799.
118. Hopkins SR, Henderson AC, Levin DL, *et al.* Vertical gradients in regional lung density and perfusion in the supine human lung: the slinky effect. *J Appl Physiol* 2007; 103: 240–248.
119. Bauman G, Puderbach M, Deimling M, *et al.* Non-contrast-enhanced perfusion and ventilation assessment of the human lung by means of Fourier decomposition in proton MRI. *Magn Reson Med* 2009; 62: 656–664.
120. Bauman G, Eichinger M. Ventilation and perfusion magnetic resonance imaging of the lung. *Pol J Radiol* 2012; 77: 37–46.
121. Bauman G, Lutzen U, Ullrich M, *et al.* Pulmonary functional imaging: qualitative comparison of Fourier decomposition MR imaging with SPECT/CT in porcine lung. *Radiology* 2011; 260: 551–559.
122. Bauman G, Scholz A, Rivoire J, *et al.* Lung ventilation- and perfusion-weighted Fourier decomposition magnetic resonance imaging: *in vivo* validation with hyperpolarized (3) He and dynamic contrast-enhanced MRI. *Magn Reson Med* 2013; 69: 229–237.
123. Lederlin M, Bauman G, Eichinger M, *et al.* Functional MRI using Fourier decomposition of lung signal: reproducibility of ventilation- and perfusion-weighted imaging in healthy volunteers. *Eur J Radiol* 2013; 82: 1015–1022.
124. Bauman G, Puderbach M, Heimann T, *et al.* Validation of Fourier decomposition MRI with dynamic contrast-enhanced MRI using visual and automated scoring of pulmonary perfusion in young cystic fibrosis patients. *Eur J Radiol* 2013; 82: 2371–2377.
125. Heimann T, Eichinger M, Bauman G, *et al.* Automated scoring of regional lung perfusion in children from contrast enhanced 3D MRI. *In:* van Ginneken B, Novak CL, eds. SPIE Proceedings Vol. 8315: Medical Imaging 2012: Computer-Aided Diagnosis, 2012; pp. 8315–8329.

126. Kuo W, Ciet P, Tiddens HA, *et al.* Monitoring cystic fibrosis lung disease by computed tomography. Radiation risk in perspective. *Am J Respir Crit Care Med* 2014; 189: 1328–1336.

Disclosures: H-U. Kauczor reports receiving the following, outside the submitted work: grants, personal fees and non-financial support from Siemens for participation in a speakers' bureau, board membership, and provision and evaluation of hard- and software; grants and personal fees from Boehringer Ingelheim for participation in a speakers' bureau, expert testimony and an educational presentation; personal fees and non-financial support from Bayer for participation in a speakers' bureau and provision of consumables; and personal fees from Novartis, Almirall and GSK for participation in speakers' bureaus.

Support statement: This study was supported by grants from the Bundesministerium für Bildung und Forschung (BMBF) to the German Center for Lung Research (DZL) (82DZL00401, 82DZL00402, 82DZL00404). It was also supported by financial grants from the Christiane Herzog Stiftung, Stuttgart, Germany, and the Mukoviszidose e.V (the German Cystic Fibrosis Association), Bonn, Germany.

Chapter 13

The cardiopulmonary unit

Andrew J. Swift[1,2]

The cardiopulmonary unit is necessary for the supply of oxygen to tissues of the body and elimination of carbon dioxide. Good coordination of both ventricles and the lungs is necessary to achieve and maintain this process. Cardiopulmonary interactions are occurring all the time, with every heartbeat maintaining optimal efficiency of the unit. This chapter will provide a brief overview of the history of cardiopulmonary circulation and a basic description of the anatomy and physiology of the right ventricle and pulmonary circulation. Several ways in which the heart, pulmonary vasculature and lungs influence each other in health and disease will also be described, including mechanical interplay between the left and right ventricles, pulmonary arterial and right ventricular coupling, and the influences of respiration and lung disease on cardiac function.

The cardiopulmonary unit is necessary for the supply of oxygen to tissues of the body and elimination of carbon dioxide. Good coordination of both ventricles and the lungs is necessary to achieve and maintain this process. Cardiopulmonary interactions are occurring all the time, with every heartbeat maintaining optimal efficiency of the unit. This chapter will provide a brief overview of the history of cardiopulmonary circulation and a basic description of the anatomy and physiology of the right ventricle and pulmonary circulation. Several of the ways in which the heart, pulmonary vasculature and lungs influence each other in health and disease will also be described, including mechanical interplay between the left and right ventricles, pulmonary arterial and right ventricular coupling, and the influences of respiration and lung disease on cardiac function.

A brief history of the heart and pulmonary circulation

Galen, the great Ancient Greek medical practitioner, was born on 9 September, AD 129 in Pergamon. His theory of cardiopulmonary circulation was that blood was formed within the liver, described as the "natural spirit". From the liver, blood would flow into the right ventricle (RV), where it would directly seep into the left ventricle (LV) *via* tiny holes in the interventricular septum, and would become the "vital spirit". This concept, which excluded the pulmonary circulation, held for over 1000 years [1], until in the 13th century Ibn al-Nafis identified that blood from the RV actually passes through the lungs before

[1]Unit of Academic Radiology, University of Sheffield, Sheffield, UK. [2]Institute of Insilco Medicine, University of Sheffield, Sheffield, UK.

Correspondence: Andrew J. Swift, Unit of Academic Radiology, University of Sheffield, C Floor, Royal Hallamshire Hospital, Glossop Road, Sheffield, S10 2JF, UK. E-mail: a.j.swift@shef.ac.uk

Copyright ©ERS 2015. Print ISBN: 978-1-84984-065-1. Online ISBN: 978-1-84984-066-8. Print ISSN: 2312-508X. Online ISSN: 2312-5098.

returning to the left side of the heart, rather than directly traversing the interventricular septum, as proven by dissection evidence [2]. However, the belief that blood was continuously produced and consumed held until the 16th century, when William Harvey demonstrated experimentally that blood is recirculated [3]. Dr Harvey, among other experiments, publically "laid open" a snake and proved his point with two simple manoeuvres. Compression of the vein entering the heart caused the heart to become devoid of blood and compressing the artery leaving the heart caused the chambers to become overloaded with blood, thus proving the circulation of blood to and from the heart [4].

The right ventricle

The RV is the most anterior chamber of the heart and the free wall of the RV is the anterior border of the heart. It consists of a thin muscular wall (1–3-mm thick), which in normal individuals makes up approximately one-fifth of the total cardiac mass. The RV is crescent-shaped when viewed in its short axis, as opposed to the circular appearance of the LV, and is described as roughly triangular when viewed in the four-chamber view (figure 1) [5]. Although the RV can be affected by ischaemia, the most common disease states to affect the RV are changes in preload and afterload. Increased loading on the LV does impact on LV function, but the effect is more pronounced on the RV. In animal models, even modest increases in afterload lead to profound decreases in RV stroke volume and even small changes in total pulmonary vascular resistance can reduce RV contractile performance and lower cardiac output even when RV preload is maintained [6]. The utility of the RV in the cardiopulmonary unit was questioned by Starr *et al.* [7] in 1943. The RVs of a cohort of dogs were cauterised using a soldering iron, with the aim of determining the resultant haemodynamic effect. No significant alterations in venous pressure or systemic circulation were observed. This led the authors to conclude that the RV provides no useful

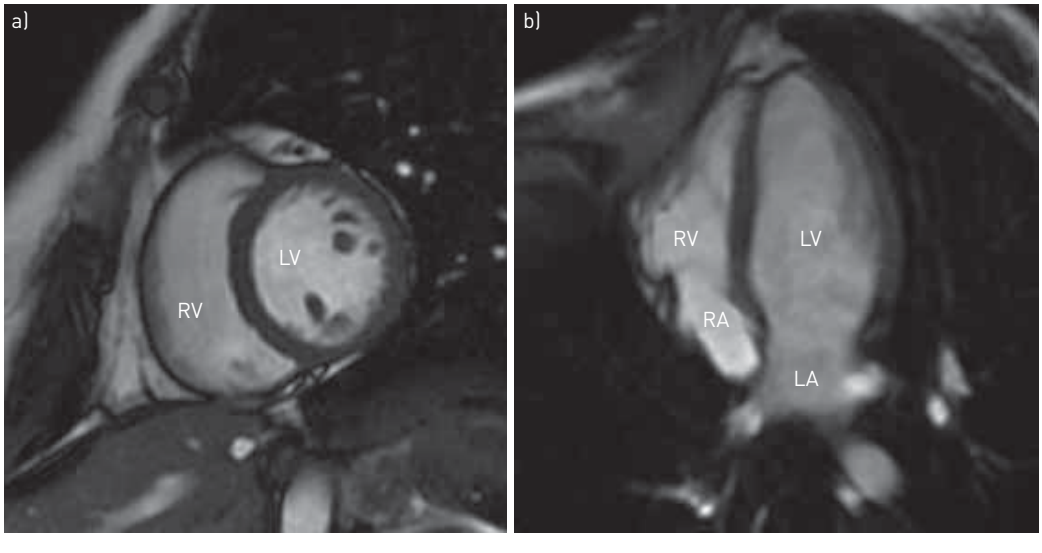

Figure 1. a) Short axis and b) four-chamber cardiac MRI views of a healthy subject. a) The short axis images demonstrate the typical crescent shape of the right ventricle (RV) in this view and the round appearance of the left ventricle (LV). b) The four-chamber view demonstrates the roughly triangular appearance of the RV when imaged in this axis. RA: right atrium; LA: left atrium.

function other than to provide capacitance to the circulatory system. However in the modern era, the RV is considered clinically important, this shift in understanding being illustrated by the multitude of studies showing that RV failure independently predicts mortality in several diseases including left heart disease [8, 9], pulmonary embolism [10] and pulmonary hypertension (PH) [11–13]. Several methods are proposed to measure RV function. However the optimal approach in clinical practice remains unclear. Echocardiography can provide an evaluation of RV size and function, and the introduction of methods such as tissue Doppler ultrasonography, strain imaging and 3D echocardiography hold great promise. However, accurate visualisation of the RV remains a challenge with echocardiography. Cross-sectional imaging techniques, CT and cardiac MRI allow accurate visualisation of the RV chamber, and the latter can allow for accurate and detailed quantification of the RV. CT provides excellent structural information but is historically limited in the assessment of functionality [14]. ECG gated CT has been shown to allow accurate determination of cardiac volumes and cardiac mass [15], and advances in dynamic imaging, with improved temporal resolution, have provided hope that CT can challenge MRI in the assessment of cardiac function. Using iterative reconstruction, dose reduction can be achieved, although clearly radiation dose remains a limitation [16]. All proposed techniques have their strengths and weaknesses, and there is great interest in further developing these technologies, defining their roles and determining the optimal approach for use in the clinic.

Pulmonary circulation

Normal pulmonary circulation is a compliant, low-resistance, low-pressure system, functioning at pressures of approximately one-sixth of the systemic circulation [4]. The same volume of blood flows through the pulmonary vessels and through the systemic vasculature over a respiratory cycle, although despite this equal flow, the pulmonary circulation maintains a low mean pressure. This can be explained by the ability of the pulmonary vessels to stretch and accommodate the forward flow of blood from the RV in normal subjects [17]. Pulmonary vessels and pulmonary capillaries are able to distend much more easily than equivalent systemic vessels, maintaining the low-resistance, low-pressure and high-flow state [4], in contrast to that seen in the systemic circulation, where vessels have a complete layer of smooth muscle in their walls. The muscular walls of small pulmonary arterioles tend to be incomplete [18]. However, despite not being complete, there is evidence that even the smallest micro-vessels measuring <70 μm in diameter have the capacity to constrict [18] and distend [19]. When the resistances of all vessels are added together, the total resistance of the entire pulmonary vascular bed can be obtained. Small reductions in vessel radius have a big impact on resistance to flow, described by Poiseuille's Law, and an increase in vascular resistance impacts on pressure and blood flow, a situation encountered in certain diseases of the pulmonary vasculature, such as pulmonary arterial hypertension. Pulmonary vascular resistance describes the resistance to blood flow across the pulmonary circulation; its calculation requires knowledge of both the differential between the mean pulmonary artery pressure and left atrial pressure divided by cardiac output. This represents a simplified model of the pulmonary circulation that has its roots in clinical practice for assessing the severity of pulmonary vascular disease. A more accurate representation of flow and resistance in the pulmonary vasculature can be described by pulmonary vascular impedance. The Windkessel model encompasses the three main components of input impedance, namely resistance, compliance and inductance [20, 21]. Such models provide a more accurate measurement of pulmonary vascular function than estimates of resistance

alone, referred to as a lumped sum model taken from electrical circuit models; these can be used to accurately represent RV afterload [21].

Ventricular interactions

The interventricular septum is considered a functional component of the RV. Spiral muscular fibres form a continuous band that links the RV to the LV, allowing the RV to share a portion of the LV's contractile function [22]. Left-to-right systolic ventricular interaction has been shown to contribute as much as 80% of pulmonary arterial flow and 68% of the pressure generated by the RV [23]. It originates from the transmission of systolic forces between the two ventricles through the interventricular septum and from the mechanical effect of the shared fibres that make up the free walls. In an animal model, systolic interventricular interaction was reduced by any increase in the stiffness of the interventricular septum and therefore reduced septum function, which can manifest from chronic pressure overload, or hypertrophy [24]. In addition, because of the shared fibre configuration of the RV and LV, damage to the LV can have a direct effect on RV function and impacts on right-sided haemodynamics [25]. In PH, the onset of right ventricular diastolic dysfunction leads to prolongation of the isovolumetric relaxation time beyond that of the LV; this leads to ventricular dyssynchrony with the LV entering diastole whilst the RV remains in its isovolumetric period. This can explain the maximal interventricular septal displacement occurring in early LV diastole. Furthermore, this process is detrimental to the LV, by decreasing both LV filling and LV stroke volume [26]. Another detrimental cardiopulmonary interaction that results from right heart dysfunction or increased vascular resistance is the "series effect" (figure 2) [27]. As less blood passes through the pulmonary

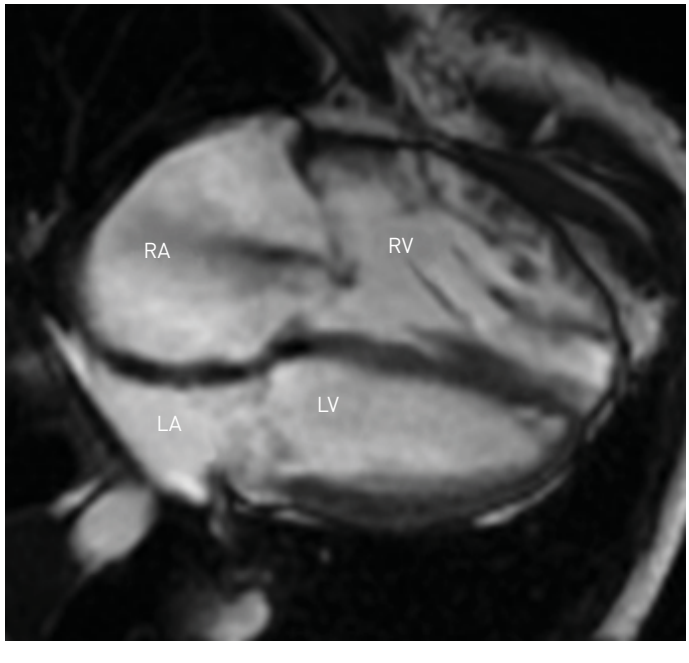

Figure 2. Four-chamber image of the heart showing the underfilled/compressed left atrium (LA) caused by reduced venous return to the LA ("series effect") and relative higher pressure in the right atrium (RA) displacing the interventricular septum leftwards. RV: right ventricle; LV: left ventricle.

vasculature to the LV, LV preload is reduced, a common scenario in pre-capillary PH. This manifests as a small LV and reduced LV stroke volume, features that are of prognostic significance [12].

The normal RV, with its thin wall and crescent shape, is not well equipped to cope with increases in afterload. With insidious increases in pulmonary arterial pressure, the RV can adapt by a progressive increase in contractility allowing for maintained output. Measures of RV size and function [11–13] and pulmonary arterial stiffness [28–32] have been shown to predict mortality in patients with PH. Although clinically useful in the assessment of disease severity, RV measures such as RV ejection fraction and tricuspid annular plane systolic excursion are not load independent and do not provide a comprehensive description of cardiopulmonary adaptation to elevated pulmonary arterial pressure. Ventriculo-arterial coupling is described by the simultaneous relationship between ventricular contractility and afterload and by how well the two are matched [33]. It is postulated that if the RV does not maintain proportional changes in RV contractility, the RV will fail [34, 35]. The change in pressure for a given change in volume in a ventricular chamber is described as elastance [36], and maximal systolic ventricular elastance (E_{max}) is well described as a measure of ventricular contractility, and is a load-independent parameter. The true load faced by the ventricle is known as effective arterial elastance (E_a), measured by the ratio of ventricular end-systolic pressure to stroke volume [37]. The normal ratio of ventricular to arterial elastance of the RV-pulmonary artery unit is approximately 1.5 and 2.0, described as the optimal balance between RV mechanical work and oxygen consumption [33, 38]. There is evidence that parameters such as E_{max} and E_a can be derived from standard data collected from right heart catheterisation and MRI, and a completely noninvasive MRI-based approach can yield measures of right ventricular pulmonary arterial coupling [34]. However, these simplified methods assume that V_0, or the RV volume at zero filling pressure, is equal to zero, which has been shown to be incorrect, with V_0 being highly dependent on RV dilatation [39]. Despite this likelihood that such estimates are not entirely physiological, and

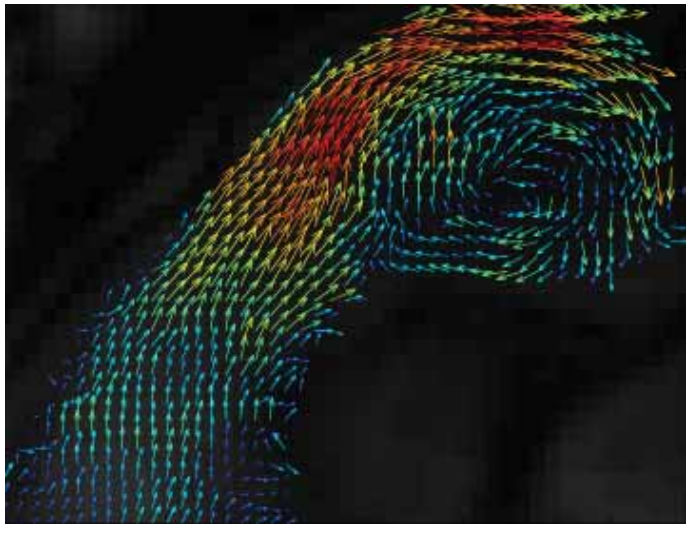

Figure 3. In-plane pulmonary artery phase contrast with pixel velocity vectors. Turbulent/vortex flow is shown in the distal main pulmonary artery at bifurcation. 4D phase contrast has the potential to estimate kinetic energy loss of blood flow ejected from the pulmonary artery.

that E_{max} is not a true load-independent measure, a recent study has shown the superior prognostic significance of an MRI-derived estimate of right ventricular–arterial coupling E_a/E_{max} over other invasive and noninvasive measures of RV function [40]. 4D phase contrast MRI presents the opportunity to study energy transfer from the RV to the pulmonary vasculature. This technique can measure the characteristics of blood flow, allowing the measurement of the degree of irregularity and turbulence of blood flow and quantification of kinetic energy and haemodynamics. This is an area for future study, which may enhance our understanding of RV afterload and ventricular–arterial coupling [41]. Figure 3 shows vortex flow in the main pulmonary artery in a patient with PH by 2D in-plane phase contrast MRI.

Cardiorespiratory interaction

The heart, pulmonary circulation and lungs are contained within the thorax. Cardiorespiratory interactions are based on the effects of changes in intrathoracic pressure and lung volume on venous return to the left side of the heart [42]. Changes in pleural pressure drive respiration, which in turn affect cardiac and pulmonary vascular function. A reduction in intrapleural pressure during inspiration is accompanied by a decrease in extracardiac pressure. This manifests as dilatation of the superior and inferior vena cava, right atrium and to a lesser extent the RV. The resultant pressure gradient improves RV filling and RV stroke volume increases *via* the Frank–Starling mechanism. In contrast, the left side of the heart has a different response during inspiration, expansion of the lungs with decreased pleural pressure resulting in an increase in pulmonary blood volume. This causes a decrease in flow of blood from the lungs back to the left atrium and resultant reduction in left ventricular filling during inspiration [43]. In expiration, blood from the lungs returns to the left atrium, and increases LV filling and LV cardiac output. On average during a respiratory cycle, LV stroke volume is similar to RV stroke volume during breathing.

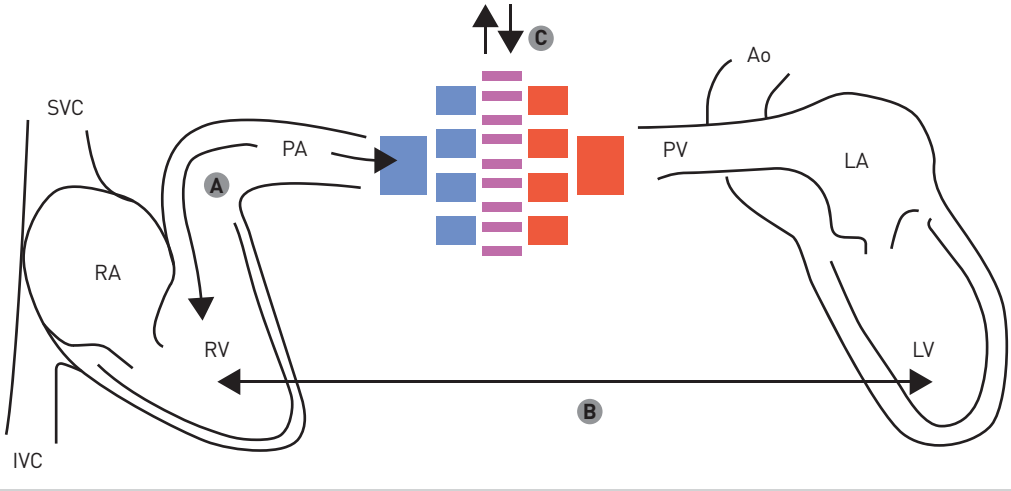

Figure 4. Simplified schematic demonstrating the cardiopulmonary system interactions discussed in this chapter. A: Right ventricular–arterial coupling. B: Interventricular interactions that occur through the interventricular septum. C: Cardiopulmonary interactions driven by changes in pleural pressure. SVC: superior vena cava; IVC: inferior vena cava; RA: right atrium; RV: right ventricle; PA: pulmonary artery; PV: pulmonary veins; LA: left atrium; LV: left ventricle; Ao: aorta.

The presence of lung parenchymal disease impacts on the cardiopulmonary unit through a number of mechanisms: hypoxic vasoconstriction, smoking-induced lesions, hyperinflation, direct damage to the pulmonary capillary bed and inflammation [44–46]. These processes result in increased RV afterload and right ventricular dysfunction, a situation associated with an extremely poor outcome particularly in more severe elevations of pulmonary arterial pressure. The Multi-Ethnic Study of Atherosclerosis (MESA) COPD study has shed light on the impact of pulmonary disease on the heart. Reduced LV filling and reduced stroke occurs in COPD and these cardiac changes are linearly associated with the severity of airflow limitation and extent of emphysema [47]. Furthermore, and contrary to that described historically in cor pulmonale, greater per cent emphysema is related to lower RV volume rather than RV hypertrophy and dilatation, which may relate to hyperinflation and/or reduced venous return to the thorax. Recent results from a longitudinal cohort of young adults (Coronary Artery Risk Development in Young Adults (CARDIA)) has shown that a decline in FEV1/forced vital capacity (FVC) ratio is associated with underfilling of the left heart and reduced cardiac output, and a decline in FVC with preserved FEV1/FVC ratio is associated with left ventricular hypertrophy and diastolic dysfunction [48]. Several lung conditions are implicated, including COPD [49, 50], interstitial fibrosis [51, 52], chronic lung infection and inflammation. LV function is frequently impaired in patients with severe emphysema due to reduced LV preload. Of note, lung volume reduction surgery can improve left atrial filling and subsequently improves LV function [53]. As in COPD, patients with PH associated with interstitial lung disease may have pulmonary arterial pressure that is disproportionate to the underlying lung disease. Notably the combination of lung fibrosis with emphysema is strongly associated with PH and, when present, PH is associated with high mortality [54].

Conclusion

The cardiopulmonary unit is complex; maintaining good function of the system as a whole is dependent on a number of interactions to maintain optimal efficiency (figure 4). The heart and lungs are continually interacting in every respiratory cycle and lung disease can have a severely detrimental impact on the cardiopulmonary unit associated with high mortality. Interventricular interactions are important; in the presence of pulmonary vascular disease deterioration, of RV function impacts negatively on the LV through the interventricular septum and through the series effect. Coupling of the RV and the pulmonary vasculature is also necessary to maintain efficiency of the unit and there is growing interest in both invasive and noninvasive methods to assess ventricular and arterial elastance in the research setting and in clinical practice.

References

1. Schultz SG. William Harvey and the circulation of the blood: the birth of a scientific revolution and modern physiology. *News Physiol Sci* 2002; 17: 175–180.
2. West JB. Ibn al-Nafis, the pulmonary circulation, and the Islamic Golden Age. *J Appl Physiol* 2008; 105: 1877–1880.
3. Comtor JH Jr. Harvey's 1651 perfusion of the pulmonary circulation of man. *Circulation* 1982; 65: 1–3.
4. Greyson CR. The right ventricle and pulmonary circulation: basic concepts. *Rev Esp Cardiol* 2010; 63: 81–95.
5. Benza R, Biederman R, Murali S, *et al.* Role of cardiac magnetic resonance imaging in the management of patients with pulmonary arterial hypertension. *J Am Coll Cardiol* 2008; 52: 1683–1692.
6. Friedberg MK, Redington AN. Right *versus* left ventricular failure: differences, similarities, and interactions. *Circulation* 2014; 129: 1033–1044.
7. Starr I, Jeffers WA, Meade RH. The absence of conspicuous increments of venous pressure after severe damage to the right ventricle of the dog, with a discussion of the relation between clinical congestive failure and heart disease. *Am Heart J* 1943; 26: 291–301.

8. Zornoff LA, Skali H, Pfeffer MA, *et al.* Right ventricular dysfunction and risk of heart failure and mortality after myocardial infarction. *J Am Coll Cardiol* 2002; 39: 1450–1455.
9. Ghio S, Gavazzi A, Campana C, *et al.* Independent and additive prognostic value of right ventricular systolic function and pulmonary artery pressure in patients with chronic heart failure. *J Am Coll Cardiol* 2001; 37: 183–188.
10. Park JR, Chang SA, Jang SY, *et al.* Evaluation of right ventricular dysfunction and prediction of clinical outcomes in acute pulmonary embolism by chest computed tomography: comparisons with echocardiography. *Int J Cardiovasc Imaging* 2012; 28: 979–987.
11. van de Veerdonk MC, Kind T, Marcus JT, *et al.* Progressive right ventricular dysfunction in patients with pulmonary arterial hypertension responding to therapy. *J Am Coll Cardiol* 2011; 58: 2511–2519.
12. van Wolferen SA, Marcus JT, Boonstra A, *et al.* Prognostic value of right ventricular mass, volume, and function in idiopathic pulmonary arterial hypertension. *Eur Heart J* 2007; 28: 1250–1257.
13. Swift AJ, Rajaram S, Campbell MJ, *et al.* Prognostic value of cardiovascular magnetic resonance imaging measurements corrected for age and sex in idiopathic pulmonary arterial hypertension. *Circ Cardiovasc Imaging* 2014; 7: 100–106.
14. Liu M, Ma Z, Guo X, *et al.* Computed tomographic pulmonary angiography in the assessment of severity of chronic thromboembolic pulmonary hypertension and right ventricular dysfunction. *Eur J Radiol* 2011; 80: e462–e469.
15. Nicol ED, Kafka H, Stirrup J, *et al.* A single, comprehensive non-invasive cardiovascular assessment in pulmonary arterial hypertension: combined computed tomography pulmonary and coronary angiography. *Int J Cardiol* 2009; 136: 278–288.
16. Gosling O, Loader R, Venables P, *et al.* A comparison of radiation doses between state-of-the-art multislice CT coronary angiography with iterative reconstruction, multislice CT coronary angiography with standard filtered back-projection and invasive diagnostic coronary angiography. *Heart* 2010; 96: 922–926.
17. Slife DM, Latham RD, Sipkema P, *et al.* Pulmonary arterial compliance at rest and exercise in normal humans. *Am J Physiol* 1990; 258: H1823–H1828.
18. Hillier SC, Graham JA, Hanger CC, *et al.* Hypoxic vasoconstriction in pulmonary arterioles and venules. *J Appl Physiol* 1997; 82: 1084–1090.
19. Hillier SC, Godbey PS, Hanger CC Jr, *et al.* Direct measurement of pulmonary microvascular distensibility. *J Appl Physiol* 1993; 75: 2106–2111.
20. Kind T, Faes TJ, Lankhaar JW, *et al.* Estimation of three- and four-element windkessel parameters using subspace model identification. *IEEE Trans Biomed Eng* 2010; 57: 1531–1538.
21. Lankhaar JW, Westerhof N, Faes TJ, *et al.* Quantification of right ventricular afterload in patients with and without pulmonary hypertension. *Am J Physiol Heart Circ Physiol* 2006; 291: H1731–H1737.
22. Buckberg GD. The ventricular septum: the lion of right ventricular function, and its impact on right ventricular restoration. *Eur J Cardiothorac Surg* 2006; 29: Suppl. 1, S272–S278.
23. Damiano RJ Jr, La Follette P Jr, Cox JL, *et al.* Significant left ventricular contribution to right ventricular systolic function. *Am J Physiol* 1991; 261: H1514–H1524.
24. Slinker BK, Chagas AC, Glantz SA. Chronic pressure overload hypertrophy decreases direct ventricular interaction. *Am J Physiol* 1987; 253: H347–H357.
25. Jerzewski A, Steendijk P, Pattynama PM, *et al.* Right ventricular systolic function and ventricular interaction during acute embolisation of the left anterior descending coronary artery in sheep. *Cardiovasc Res* 1999; 43: 86–95.
26. Marcus JT, Gan CT, Zwanenburg JJ, *et al.* Interventricular mechanical asynchrony in pulmonary arterial hypertension: left-to-right delay in peak shortening is related to right ventricular overload and left ventricular underfilling. *J Am Coll Cardiol* 2008; 51: 750–757.
27. Magder S. The left heart can only be as good as the right heart: determinants of function and dysfunction of the right ventricle. *Crit Care Resusc* 2007; 9: 344–351.
28. Gan CT, Lankhaar JW, Westerhof N, *et al.* Noninvasively assessed pulmonary artery stiffness predicts mortality in pulmonary arterial hypertension. *Chest* 2007; 132: 1906–1912.
29. Swift AJ, Rajaram S, Marshall H, *et al.* Black blood MRI has diagnostic and prognostic value in the assessment of patients with pulmonary hypertension. *Eur Radiol* 2012; 22: 695–702.
30. Swift AJ, Telfer A, Rajaram S, *et al.* Dynamic contrast-enhanced magnetic resonance imaging in patients with pulmonary arterial hypertension. *Pulm Circ* 2014; 4: 61–70.
31. Mahapatra S, Nishimura RA, Sorajja P, *et al.* Relationship of pulmonary arterial capacitance and mortality in idiopathic pulmonary arterial hypertension. *J Am Coll Cardiol* 2006; 47: 799–803.
32. Swift AJ, Rajaram S, Condliffe R, *et al.* Pulmonary artery relative area change detects mild elevations in pulmonary vascular resistance and predicts adverse outcome in pulmonary hypertension. *Invest Radiol* 2012; 47: 571–577.
33. Vonk-Noordegraaf A, Haddad F, Chin KM, *et al.* Right heart adaptation to pulmonary arterial hypertension: physiology and pathobiology. *J Am Coll Cardiol* 2013; 62: D22–D33.
34. Sanz J, Garcia-Alvarez A, Fernandez-Friera L, *et al.* Right ventriculo-arterial coupling in pulmonary hypertension: a magnetic resonance study. *Heart* 2012; 98: 238–243.

35. Chantler PD, Lakatta EG, Najjar SS. Arterial-ventricular coupling: mechanistic insights into cardiovascular performance at rest and during exercise. *J Appl Physiol (1985)* 2008; 105: 1342–1351.
36. Brown KA, Ditchey RV. Human right ventricular end-systolic pressure-volume relation defined by maximal elastance. *Circulation* 1988; 78: 81–91.
37. Kelly RP, Ting CT, Yang TM, *et al.* Effective arterial elastance as index of arterial vascular load in humans. *Circulation* 1992; 86: 513–521.
38. Kuehne T, Yilmaz S, Steendijk P, *et al.* Magnetic resonance imaging analysis of right ventricular pressure-volume loops: *in vivo* validation and clinical application in patients with pulmonary hypertension. *Circulation* 2004; 110: 2010–2016.
39. Trip P, Kind T, van de Veerdonk MC, *et al.* Accurate assessment of load-independent right ventricular systolic function in patients with pulmonary hypertension. *J Heart Lung Transplant* 2013; 32: 50–55.
40. Vanderpool RR, Pinsky MR, Naeije R, *et al.* RV-pulmonary arterial coupling predicts outcome in patients referred for pulmonary hypertension. *Heart* 2015; 101: 37–43.
41. Carlsson M, Heiberg E, Toger J, *et al.* Quantification of left and right ventricular kinetic energy using four-dimensional intracardiac magnetic resonance imaging flow measurements. *Am J Physiol Heart Circ Physiol* 2012; 302: H893–H900.
42. Pinsky MR. Heart-lung interactions. *Curr Opin Crit Care* 2007; 13: 528–531.
43. Scharf SM, Brown R, Saunders N, *et al.* Effects of normal and loaded spontaneous inspiration on cardiovascular function. *J Appl Physiol Respir Environ Exerc Physiol* 1979; 47: 582–590.
44. Naeije R, Barbera JA. Pulmonary hypertension associated with COPD. *Crit Care* 2001; 5: 286–289.
45. Naeije R, Brimioulle S. Physiology in medicine: importance of hypoxic pulmonary vasoconstriction in maintaining arterial oxygenation during acute respiratory failure. *Crit Care* 2001; 5: 67–71.
46. Watz H, Waschki B, Meyer T, *et al.* Decreasing cardiac chamber sizes and associated heart dysfunction in COPD: role of hyperinflation. *Chest* 2010; 138: 32–38.
47. Barr RG, Bluemke DA, Ahmed FS, *et al.* Percent emphysema, airflow obstruction, and impaired left ventricular filling. *N Engl J Med* 2010; 362: 217–227.
48. Cuttica MJ, Colangelo LA, Shah SJ, *et al.* Loss of lung health from young adulthood and cardiac phenotypes in middle age. *Am J Respir Crit Care Med* 2015; 192: 76–85.
49. Chaouat A, Naeije R, Weitzenblum E. Pulmonary hypertension in COPD. *Eur Respir J* 2008; 32: 1371–1385.
50. Minai OA, Chaouat A, Adnot S. Pulmonary hypertension in COPD: epidemiology, significance, and management: pulmonary vascular disease: the global perspective. *Chest* 2010; 137: 39S–51S.
51. Corte TJ, Wort SJ, Gatzoulis MA, *et al.* Pulmonary vascular resistance predicts early mortality in patients with diffuse fibrotic lung disease and suspected pulmonary hypertension. *Thorax* 2009; 64: 883–888.
52. Corte TJ, Wort SJ, Wells AU. Pulmonary hypertension in idiopathic pulmonary fibrosis: a review. *Sarcoidosis Vasc Diffuse Lung Dis* 2009; 26: 7–19.
53. Jorgensen K, Houltz E, Westfelt U, *et al.* Effects of lung volume reduction surgery on left ventricular diastolic filling and dimensions in patients with severe emphysema. *Chest* 2003; 124: 1863–1870.
54. Cottin V, Le Pavec J, Prevot G, *et al.* Pulmonary hypertension in patients with combined pulmonary fibrosis and emphysema syndrome. *Eur Respir J* 2010; 35: 105–111.

Disclosures: None declared.

Chapter 14

Measurement of pulmonary structure and function

Miranda Kirby[1,2], Pierre Lane[3] and Harvey O. Coxson[1,2]

Much of our understanding of both healthy and diseased lung is based on quantitative morphological assessment using pathology. However, the development of new therapies for lung disease requires measurements and tools that can noninvasively measure lung structure and function both on a global and a regional scale. Medical imaging technologies allow us to "see" the complex internal structures of the lung in three dimensions so that detailed anatomical measurements can be taken, while other imaging modalities can also measure how the lung functions. In this chapter we highlight three techniques that have impacted pulmonary imaging research with an emphasis on quantitative measurements: CT, hyperpolarised noble gas MRI and OCT. For each of these imaging modalities, we discuss the quantitative measurements that can be derived as well as discussing the pulmonary diseases where each technique has demonstrated utility, some drawbacks that are unique to each technique and some important directions for future research.

The lung is a dynamic organ system with a complex internal structure that exists in three dimensions, changes during normal respiration, and undergoes remodelling due to both normal ageing and pathological processes. Quantitative morphological assessment of the lung using stereological approaches has long been regarded as the gold standard, and is necessary for our understanding of both healthy and diseased lung. However, studies directly evaluating lung tissue most often involve lungs that have been obtained *post mortem* or following lung resection, and therefore studies that can investigate how the lung ages and how disease initiates and progresses over time are not possible. Furthermore, although stereological approaches were introduced to provide mathematical methods for estimating three-dimensional anatomical structures using two-dimensional sections [1], the entire process uses fixed tissue and therefore there is no way of measuring the dynamic structure of the lung during a normal breath.

Medical imaging allows quantitative evaluation of the lung in three dimensions in living subjects. Although a number of imaging modalities have been introduced over the last several decades, in this chapter we highlight three imaging techniques, along with their

[1]Centre for Heart Lung Innovation, St Paul's Hospital, Vancouver, BC, Canada. [2]Dept of Radiology, University of British Columbia, Vancouver, BC, Canada. [3]Imaging Unit, Integrative Oncology Dept, British Columbia Cancer Agency Research Centre, Vancouver, BC, Canada.

Correspondence: Harvey O. Coxson, Centre for Heart Lung Innovation, St Paul's Hospital, Burrard Building, 1081 Burrard Street – Room 166, Vancouver, BC, V6Z 1Y6, Canada. E-mail: harvey.coxson@hli.ubc.ca

Copyright ©ERS 2015. Print ISBN: 978-1-84984-065-1. Online ISBN: 978-1-84984-066-8. Print ISSN: 2312-508X. Online ISSN: 2312-5098.

measurements, that have impacted quantitative pulmonary imaging research. We will discuss the most commonly used technique, CT, for structural pulmonary measurements, hyperpolarised noble gas MRI for both structural and functional measurements, as well as introducing measurements acquired using an emerging technique called OCT. For each of these imaging methods, we will also identify the pulmonary diseases in which each approach has demonstrated utility, as well as identifying some pitfalls or drawbacks that are unique to each technique.

Radiography CT

There have been rapid advances in CT scanner technology since clinical adoption in the 1970s, including faster image acquisition time and smaller voxel sizes, allowing for higher-quality images to be obtained. These advances have propelled CT to the forefront of the diagnosis and characterisation of many conditions. In the lung, CT has been shown to be the most effective noninvasive imaging modality for quantifying lung structure.

Emphysema measurements

CT images are composed of voxels, and the greyscale level for each voxel is based on the x-ray attenuation, which reflects the proportion of x-rays scattered or absorbed by the material. Each voxel is then assigned a Housfield (HU) unit value based on the attenuation coefficient relative to water. A voxel that contains water is assigned a value of 0 HU, while air will have a value of −1000 HU and tissues or structures that have a higher attenuation coefficient than water will have a HU value >0. Müller *et al.* [2] were the first to exploit the densitometry values of the CT scan by applying "density masks" at specific thresholds to highlight low attenuation voxels. They demonstrated that measurements obtained using a threshold of −910 HU correlated with the extent of emphysematous holes measured on excised specimens. This CT density mask became the standard for several years, but with advances in CT scanning technology, Gevenois and colleagues [3, 4] used pathology to redefine the threshold as −950 HU for thin slice HRCT scans. Even though CT technology has continued to advance, studies have shown that the −950 HU threshold correlates best with histology for CT scanners [5], and the −950 HU threshold remains the most commonly used CT measure of emphysema today. An example of a threshold analysis is shown in figure 1a with CT densitometry values below −950 HU, representing emphysema, highlighted.

Another common approach for measuring emphysema using CT images is to assess the density value of the lung at fixed percentile points on the distribution curve. Initially the lowest 5th percentile was correlated with pathology, but since then investigators have found that the lowest 15th percentile point is a sensitive measure of emphysema progression in patients with severe α_1-antitrypsin deficiency [6]. The percentile point also seems to be quite stable to differences in lung volume and image noise; it has become the currently recommended CT value for use in longitudinal studies [7, 8].

Other CT methods for quantifying emphysema take into account how the low attenuating voxels are clustered together [9, 10]. These approaches vary in complexity; some approaches use relatively simple cluster analysis (the number of contiguous low attenuation voxels are summed), others use more complex feature analyses [11] or principal component analyses of the CT density histogram [12]. The CT emphysema measures generated using cluster

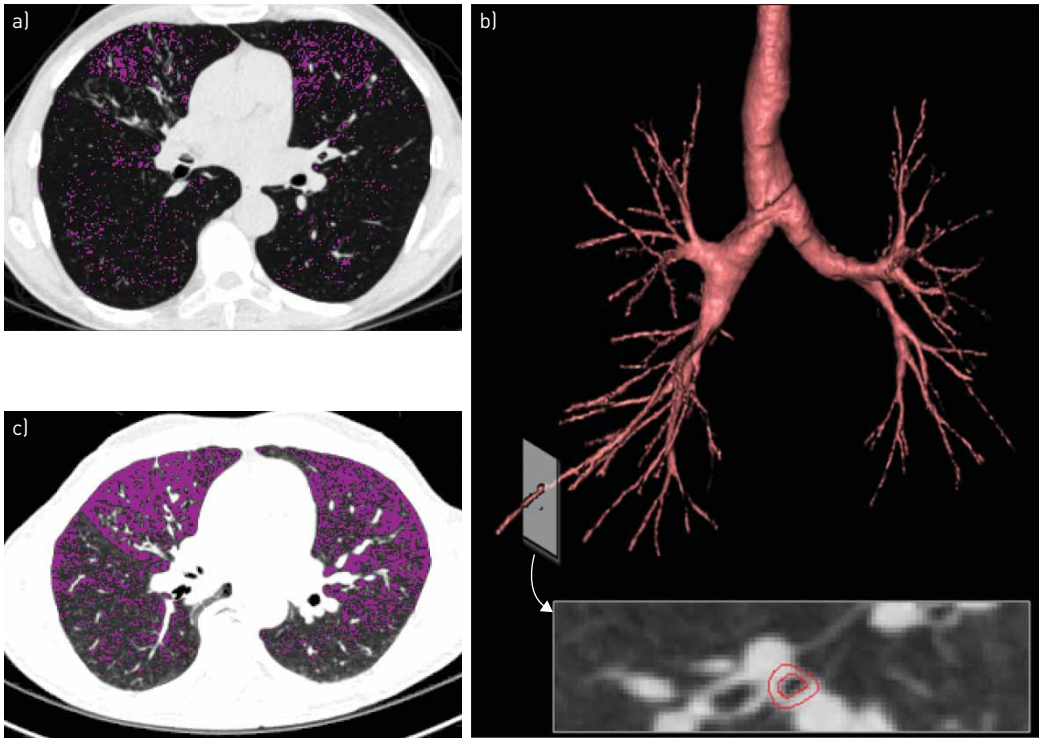

Figure 1. CT measurements. a) CT density mask highlighting (in magenta) areas with CT densitometry values below −950 HU on end-inspiration images for quantifying emphysema. b) Three-dimensional reconstruction of the airway tree for measurement of airway dimensions. c) End-expiration density mask highlighting areas with CT densitometry values below −856 HU for quantifying gas trapping.

analysis have been shown to be significantly associated with radiologists' visual scores of emphysema severity [13–15], and are also less susceptible to inter-observer variation.

It is important to note that although these CT low attenuation measurements were shown to correlate with pathology [3, 4], other factors may result in areas of low attenuation in CT images, such as altered stretch or compression of the lung related to gravity, height of the lung and support of the heart [16]. Therefore, establishing the normal variation of emphysema in nonsmokers and generating reference equations for the percentage of emphysema that accounts for normal variation, as was recently performed [16], is important for interpreting these measurements and assessing the presence and extent of emphysema.

Airway dimensions

In addition to assessing the lung parenchyma, the large central airways can be directly visualised and quantified using CT. Early investigations into CT quantification methods used a simple threshold-based analysis [17] or the full width at half maximum algorithm [18] to delineate the inner and outer boundaries of the airway wall on two-dimensional images. In recent years, more complex algorithms have been introduced that take advantage of three-dimensional reconstructions of the CT images and may be more accurate [19–21]. Figure 1b shows a three-dimensional reconstruction of the airway tree generated using commercially available software (VIDA Diagnostics, Coralville, IA, USA) for measurement of airway dimensions.

Although there is no standard algorithm for evaluating airway wall dimensions, and no standard airway measurement is used, the most commonly used measurements include the airway wall area, the percentage of the total airway area that is airway wall, or the standardised measure of airway wall thickness for a "theoretical airway" with an internal diameter of 10 mm [22]. Traditionally, these airway measurements are expressed as an average of the airway wall dimensions obtained from the entire airway tree, or all sampled airways, but with the improvement in CT scanner and CT analysis algorithms, these measurements can also be obtained from individual known airways (*e.g.* the 5th generation airway in the RB8 pathway, figure 1b).

Interestingly, studies evaluating the dimensions of the relatively large, central airways using CT showed that measurements were significantly correlated with histological measures of the small airways, suggesting that measuring the thickness of the central airways using CT may serve as a surrogate for small airway abnormalities. Furthermore, studies have demonstrated that the airway wall dimensions can be evaluated in subjects with COPD [23], and that airway wall thickness measured using CT correlates significantly with pulmonary function measures independent of the degree of emphysema [24]. Airway wall dimensions have also been investigated in asthmatics, and studies have shown that CT airway walls are thicker in asthmatics compared with non-asthmatics [25, 26], and are significantly correlated with asthma duration and severity [26], airflow limitation [26, 27] and neutrophilic airway inflammation [27]. Recent data also suggest that there are differences in airway dimensions regionally, and airways from specific generations should be compared to airways of similar origin [28]. These data reinforce the idea that regional three-dimensional measurements are necessary for accurate quantification of the lung.

Gas trapping

Because it is not possible to assess the small airways directly using CT due to the resolution of this technique, it has been hypothesised that the functional effects of small airway obstruction can be assessed indirectly using CT images acquired at end-expiration. Physiologically, it is known that the obstruction of the small airways leads to differences in airway closure and emptying rates, so it is assumed that low attenuation areas on end-expiration CT images represent "gas trapping" due to small airway disease.

To quantify the extent of gas trapping, several measurement approaches have been introduced. The most commonly used approach is the −856 HU threshold cut-off on end-expiratory CT images [29], as shown in figure 1c, even though other thresholds, such as the −850 HU [30] and the −900 HU [31] threshold, have also been investigated. Gas trapping assessed using a threshold cut-off was shown to be significantly correlated with pulmonary function in COPD [32]. In asthmatics, CT gas trapping was also shown to be significantly correlated with measurement of pulmonary function in children [29] and adults [31, 33]. Importantly, gas trapping evaluated using CT was demonstrated to be significantly increased compared with non-asthmatics [31], and was shown to correlate with asthma severity [33] and, in some cases, response to therapy [34]. Another study demonstrated that asthmatics with gas trapping on CT were more likely to have a history of asthma-related hospitalisations, intensive care unit visits and/or mechanical ventilation [30], suggesting that this measure can identify individuals at a high risk of more severe disease.

However, a limitation of assessing gas trapping on end-expiration CT images is that gas trapping related to small airway disease in COPD cannot be distinguished from gas

trapping related to emphysema. Therefore, there has been considerable interest and improvement in measurement techniques that take into account the low attenuation areas on inspiration, as well as expiration. Several methods have been introduced, including the inspiratory to expiratory volume change of voxels with attenuation values from −860 to −950 HU [35] and the expiratory to inspiratory ratio of mean lung density in HU [36, 37]. More recently, however, an approach was developed by GALBÁN *et al.* [38] that used image registration to directly compare CT images acquired at end-inspiration to end-expiration on a voxel-by-voxel basis. Using a histogram analysis, the established threshold cut-offs for emphysema on inspiration (−950 HU) and gas trapping on expiration (−856 HU) are applied to distinguish gas trapping related to emphysema from gas trapping related to "functional small airway disease". This sophisticated approach is very promising for phenotyping patients with disease, and moderate to good correlations with pulmonary function measurements have been reported [38].

Where is it useful?

CT is useful in a number of chronic lung diseases in addition to COPD and asthma, including cystic fibrosis [39] and interstitial lung disease [40]. The CT emphysema measurements in particular, however, have had a huge impact on our understanding of important outcomes in patients with COPD. CT measurements have been shown to be independent predictors of all-cause mortality in patients with COPD [41], and are associated with a decline in pulmonary function [42–44], exacerbations [45] and exercise capacity [46–49]. Furthermore, CT emphysema measurements have been shown to identify patients with better outcomes following lung volume reduction surgery [50] and endobronchial valve implantation [51, 52].

Drawbacks

Despite the advantages offered by CT for evaluating lung structure, there are several limitations that must be taken into consideration. First, CT exposes subjects to ionising radiation, so it is difficult to justify serial investigations in study participants; this is a particularly important concern for investigations in younger subjects with asthma or cystic fibrosis. However, it must be noted that CT scanner technology is constantly evolving, allowing higher resolution images to be acquired at lower radiation doses. While there are limited data on the effect of these new "low dose" approaches, several studies have shown promising results [53, 54]. Secondly, because of the resolution limits of CT, small airways cannot be directly evaluated. As described above, novel registration-based image analysis approaches have been introduced that might provide regional measurements of "functional small airway disease", but these measurements have not yet been compared with a gold standard such as histology. Finally, another limitation of CT is the lack of functional information. Although regions of the lung with significant emphysema and air trapping can be assessed, it is unclear using only CT imaging whether these areas are ventilated and participate in gas exchange. There are ways to ascertain some functional information with CT (for example, by using xenon or acquiring dynamic CT images) but the radiation burden with these types of studies means they have not gained general acceptance.

Hyperpolarised noble gas MRI

Conventional proton (^{1}H) MRI has numerous challenges for evaluating pulmonary disease due to the inherently low ^{1}H density in the lung, as well as other technical challenges.

In recent years, several MRI approaches have been introduced to overcome these limitations, including UTE MRI [55], Fourier decomposition MRI [56–58], oxygen-enhanced MRI [59, 60] and the more recently introduced inert fluorinated gas MRI [61, 62]. These techniques have been previously reviewed [63, 64], so here we will focus on one of the most established MRI approaches, MRI with hyperpolarised noble gases [65]. The most commonly used hyperpolarised noble gas is ^{3}He, and studies have shown that when this gas is inhaled by the subject while supine inside the MRI scanner, the distribution of the gas during breath-hold imaging can be directly visualised and, by applying different pulse sequences during breath-hold imaging, both structural and functional information can be obtained.

Static ventilation imaging

Figure 2 shows both CT and hyperpolarised ^{3}He MRI structural and functional imaging acquired for two ex-smokers with COPD and two ex-smokers without COPD. In contrast to CT, where no functional information can be obtained, figure 2c shows hyperpolarised ^{3}He static ventilation images in blue co-registered to the conventional ^{1}H MRI thoracic

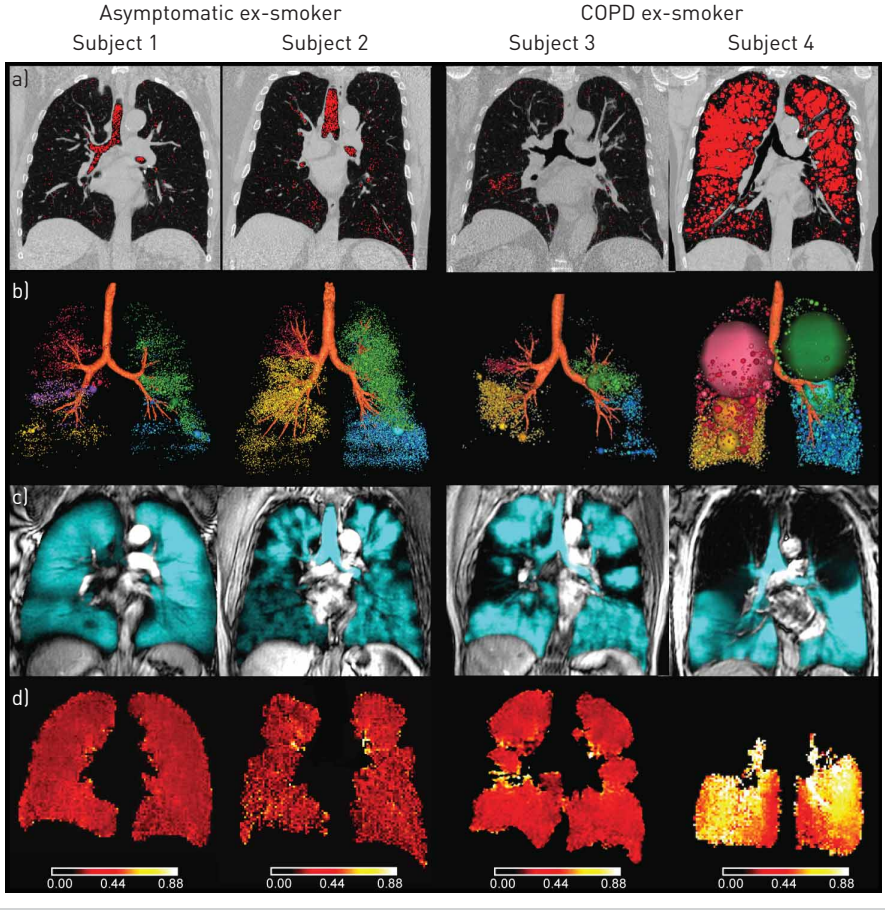

Figure 2. CT and ^{3}He MRI for four representative subjects. a) CT density mask highlighting areas with CT densitometry values below −950 HU. b) CT low attenuation cluster analysis of connected regions of the lung with CT densitometry values below −950 HU registered to the three-dimensional reconstruction of the airway tree for measurement of airway dimensions. c) ^{1}H and ^{3}He MRI registration (^{3}He shown in blue). d) ^{3}He ADC maps. Reproduced and modified from [123] with permission from the publisher.

cavity to emphasise regional gas distribution abnormalities, or "ventilation defects", in the lung. In pulmonary disease, these gas distribution abnormalities may be caused by obstructed airways due to airway wall remodelling, mucous plugs, severe emphysematous tissue destruction or bullous disease.

Hyperpolarised ^{3}He MRI gas distribution abnormalities have been quantified using a number of different approaches. Early studies provided a simple count or score of the number of signal voids or ventilation defects in the lung [66, 67], or used simple threshold-based approaches [68, 69]. Other more advanced automated or semi-automated approaches have been introduced [70–72], and while no standard method or measurement has emerged, these methods have been demonstrated to have high reproducibility and high agreement with expert assessments [70]. Importantly, quantitative measurements of hyperpolarised ^{3}He MRI gas distribution were shown to be significantly correlated with measures of airflow limitation in COPD [73], asthma [74] and cystic fibrosis [75]. The gas distribution abnormalities were also significantly correlated with signal voids in other established clinical imaging methods that assess regional ventilation (^{133}Xe ventilation scintigraphy) in patients with lung disease [76]. Moreover, ^{3}He gas distribution abnormalities were significantly associated with morphological abnormalities scored using CT in cystic fibrosis [75] and airway remodelling assessed using CT in spatially matched regions of the lung in asthma [77].

Dynamic imaging

In addition to acquiring static images that allow the distribution of the hyperpolarised gas within the lungs to be evaluated, it is also possible to acquire images of the gas during inhalation and exhalation [78, 79]. Using this dynamic hyperpolarised ^{3}He MRI approach, different filling and emptying rates of the hyperpolarised ^{3}He gas can be observed in different regions of the lung [80]. Dynamic hyperpolarised ^{3}He MRI has been investigated in subjects with COPD [78, 79], asthma [79, 81], cystic fibrosis [79, 82], and following lung transplant [79]. Furthermore, regions identified as gas trapping using dynamic hyperpolarised ^{3}He MRI acquired on expiration show high spatial agreement compared with gas trapping assessed using CT [81].

Another dynamic hyperpolarised ^{3}He MRI approach that has been introduced acquires a time series of images during breath-hold imaging, instead of during inhalation and exhalation, called "time-resolved" breath-hold hyperpolarised ^{3}He MRI [83]. Marshall *et al.* [83] demonstrated that in patients with severe emphysema, a time series of images showed that regions of the lung that initially appeared as ventilation defects at the beginning of the breath-hold gradually filled over time, from the edges of the defect towards the centre. This pattern of gas filling in lung regions thought to be ventilation defects suggests these regions were filled collaterally *via* adjacent lung.

While these studies are interesting, and there are many potential applications for an approach that can identify regions of the lung with delayed filling, there are few quantitative studies [84]. Deriving quantitative measurements related to delayed filling and/or emptying will be important for future studies investigating the relationship between dynamic hyperpolarised ^{3}He MRI and patient-centred outcomes.

Diffusion-weighted imaging

Hyperpolarised gas diffusion-weighted MRI is sensitive to the self-diffusion of the gas, or movement of the gas molecule within the lung microstructure by Brownian motion [85].

This is referred to as ADC, and reflects the size of the air spaces in the lung. Figure 2d shows elevated hyperpolarised ^{3}He ADC measurements in ex-smokers with COPD compared with ex-smokers with normal lung function, reflecting more advanced emphysematous tissue destruction. Studies investigating diffusion-weighted MRI have demonstrated that the ADC is elevated in subjects with pulmonary emphysema [85] and correlates significantly with age [86], spirometry [87], the diffusing capacity of the lung for carbon monoxide [88] and CT emphysema measurements [89, 90] and, importantly, the measurement is in agreement with histology [91].

Where is it useful?

Hyperpolarised noble gas MRI has been shown to be useful in a number of pulmonary diseases for evaluating treatment response. In COPD, hyperpolarised ^{3}He MRI gas distribution abnormalities have been shown to resolve following airway bypass [92] and treatment with a bronchodilator [93]. Importantly, these regional improvements in ^{3}He gas distribution occurred in COPD subjects who did not have clinically relevant changes in FEV_1. In asthmatics, ^{3}He MRI gas distribution abnormalities became larger and more numerous following a methacholine challenge [94], and resolved following bronchodilator administration [67]. ^{3}He MRI gas distribution abnormalities were also shown to resolve following treatment with a bronchodilator and after mechanical airway clearance treatment in cystic fibrosis patients [95].

Importantly, because MRI does not use ionising radiation, there is considerable interest in using this technique to evaluate paediatric lung disease, including asthma and cystic fibrosis. As shown in figure 3, in contrast to CT and conventional ^{1}H MRI, which have limited use

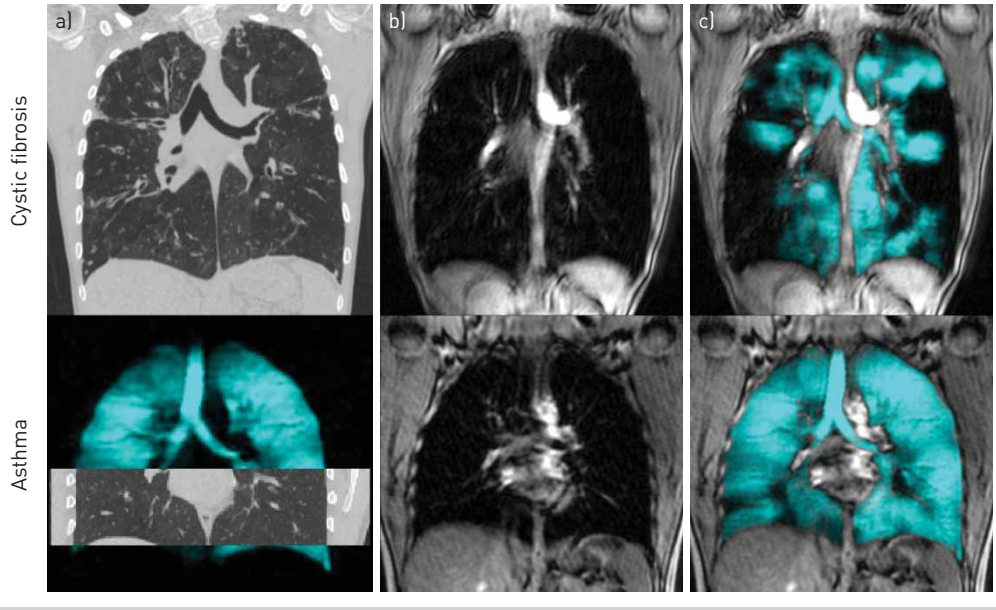

Figure 3. a) CT, b) ^{1}H MRI and c) ^{3}He MRI of a young cystic fibrosis and an asthma subject. The cystic fibrosis subject was a 21-year-old female (FEV_1 33% pred, FEV_1/forced vital capacity (FVC) 0.66). The asthma subject was a 29-year-old male (FEV_1 81% pred, FEV_1/FVC 0.66). For the asthma subject, a partial CT (as shown registered in the ^{3}He MRI) was acquired in a region of interest that was selected based on the location of hyperpolarised ^{3}He MRI ventilation defects for quantification of structural abnormalities. Reproduced and modified from [124] with permission from the publisher.

in evaluating young adults and paediatric patients, hyperpolarised noble gas MRI identifies functional abnormalities in both asthma and cystic fibrosis. Studies have investigated children aged 9–10 years with and without asthma, and showed greater ^{3}He gas distribution abnormalities and enlarged air spaces in asthmatics compared with healthy volunteers [96]. In cystic fibrosis children, changes in ^{3}He MRI gas distribution were visualised following chest physiotherapy [97] and following ivacaftor, an investigational cystic fibrosis drug [98].

Drawbacks

While hyperpolarised noble gas MRI provides some clear advantages over CT (including the fact that it does not use ionising radiation and functional information can be obtained), it is not without its drawbacks. One of these is the fact that lung structure can only be probed in regions of the lung accessed by the hyperpolarised noble gas; another is the fact that ^{3}He gas distribution measurements have yet to be compared with histology. However, one of the most significant drawbacks for hyperpolarised gas MRI is the high cost and limited availability of ^{3}He gas, and the specialised polarisation equipment and coils that are required. However, hyperpolarised ^{129}Xe is less costly and much more abundant, and preliminary studies have shown that hyperpolarised ^{129}Xe MRI can provide comparable quality images in subjects with pulmonary disease [99].

Optical coherence tomography

OCT is an emerging minimally invasive technique, often described as the high-resolution optical analogue of ultrasound [100–104]. It enables high-resolution three-dimensional visualisation of sub-surface tissue morphology in real time without the use of ionising radiation, thereby making it complementary to CT and MRI modalities. Images are created by detecting infrared light back-scattered from sub-surface refractive index variations in tissue. OCT resolution along the light propagation direction (axial resolution) is determined by the bandwidth of the laser source and is typically of the order of 10 μm, sufficient for resolving tissue layers and larger morphological structures. OCT imaging depth is limited by the optical transparency of the tissue but is typically 1–2 mm. Two- and three-dimensional images can be constructed by scanning the imaging beam over the tissue.

OCT is used clinically in ophthalmology, cardiology and dermatology. Recently, the use of OCT for imaging the lung has been explored [105–112] because the high-resolution cross-sectional images of the airway microstructure show pre-cancerous changes in the airway epithelium and sub-epithelial tissue layers. OCT images are acquired transbronchially during conventional bronchoscopy by advancing an OCT catheter into the airway of interest through the biopsy channel of the bronchoscope. OCT catheters are typically <1 mm in diameter, enabling direct visualisation of the small airways. This is an important step in lung imaging because airways and airway wall structures that were previously only visible using resected or biopsy samples are now accessible in living subjects. Figure 4 shows an example of airway wall features such as the airway epithelium, the basement membrane and airway smooth muscle, as well as alveoli adjacent to the airway wall in two different subjects, one with severe asthma and one without. It is clear that the airways from these two subjects are very different, and that remodelling of the airways can be measured.

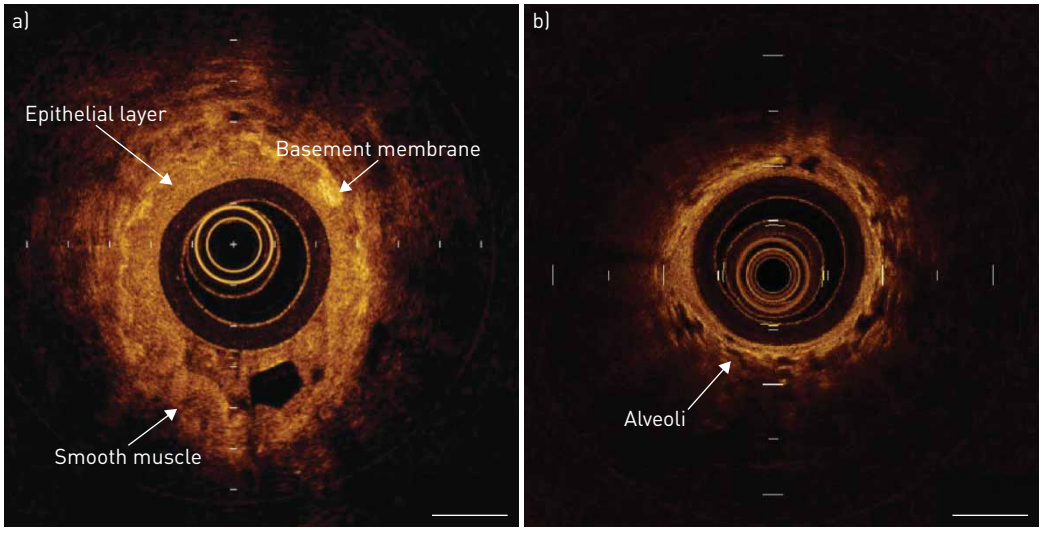

Figure 4. OCT airway wall features. a) OCT image of a small airway highlighting the epithelial layer, the basement membrane and the smooth muscle in a subject with asthma. b) OCT image of a small airway highlighting alveoli that can be visualised on the airway wall in a subject without asthma. Scale bars=1000 μm.

OCT measurements

Pioneering work in the field has introduced a number of OCT extensions and techniques for the enhanced visualisation of pulmonary features [105–115], as illustrated in figure 5. Anatomical OCT enables the measurement and morphological characterisation of large-calibre airways [112] while colour Doppler OCT is a functional extension of OCT that enables the detection and measurement of small bronchial vasculature [113]. Polarisation-sensitive OCT has been shown to provide greater visualisation of airway smooth muscle [114] and the tissue remodelling associated with cancer. Finally, multimodal imaging using OCT co-registered to autofluorescence imaging may be useful in the detection and localisation of small neoplastic lesions [115]. However, despite all of these new methods that provide greater visualisation of disease, fewer approaches have been introduced for quantitative evaluation.

The use of OCT for visualising airway wall structure in COPD or asthma is very limited. In an earlier study, Coxson *et al.* [106] compared matched airway wall measurements using both CT and OCT in current and former smokers. Although CT measurements were consistently larger (probably due to the fact that the small airways evaluated were approaching the resolution limits of CT), CT and OCT airway wall measurements were strongly and significantly correlated. In a more recent study, very good agreement between OCT airway wall tissue layer measurements (mucosa, submucosa, cartilage and the total airway wall area) with histology was found in *ex vivo* porcine airway specimens [116]. These data suggest that OCT could be very useful in determining how the airway wall is being remodelled in chronic lung disease.

Where is it useful?

As mentioned above, an advantage of OCT is that it can provide an image that is similar in scale to histology, thereby providing an "optical" biopsy to aid diagnosis in cancer. It can also be used to confirm the biopsy site selection of targeted lesions [105, 108]. Airway wall features can also be evaluated dynamically, which might provide important information in

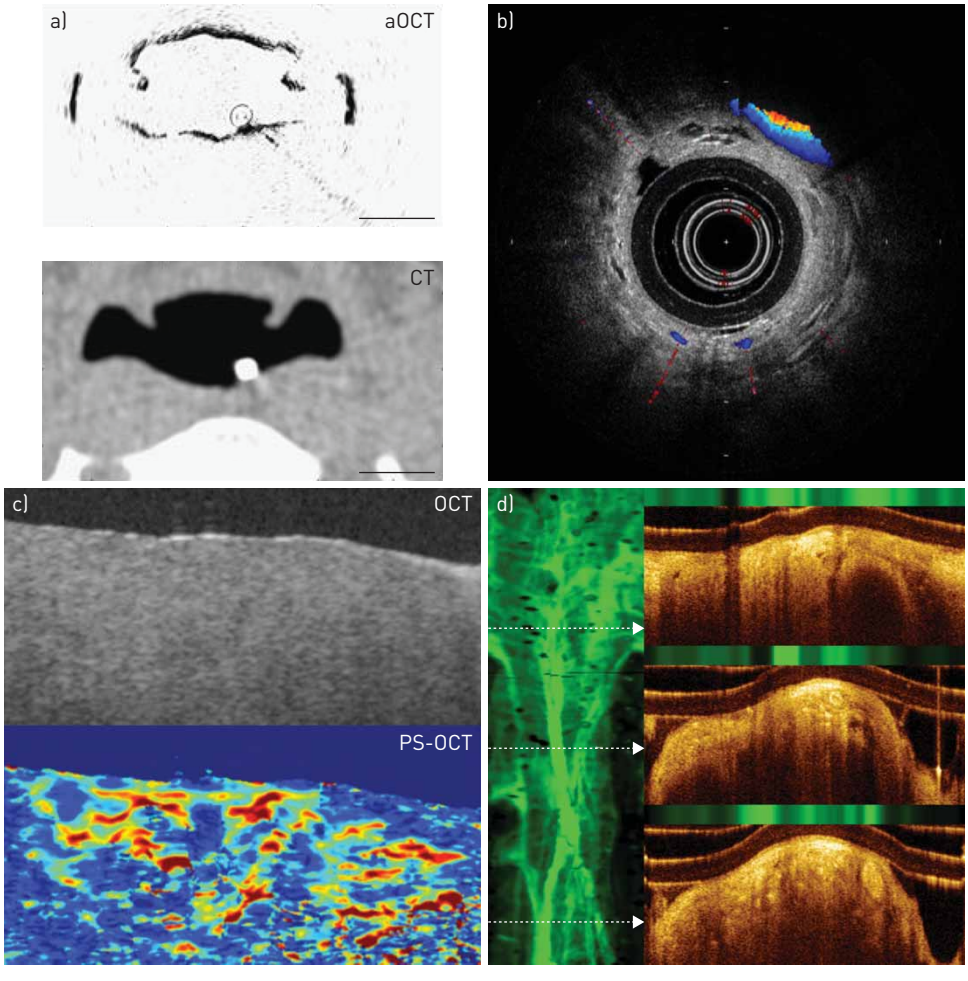

Figure 5. OCT extensions for enhanced pulmonary imaging. a) Anatomical OCT (aOCT) obtained in the hypopharynx of a human volunteer and the simultaneously acquired CT scan. Scale bars=10 000 µm. Reproduced and modified from [112] with permission from the publisher. b) Structural OCT image of a small airway in a 68-year-old male with colour Doppler OCT overlay showing the edge of a large blood vessel (top) and two smaller vessels (bottom). c) Structural OCT and polarisation-sensitive OCT (PS-OCT) of tumour-associated desmoplasia in *ex vivo* lung. Reproduced and modified from [114] with permission from the publisher. d) Autofluorescence map acquired *in vivo* at the luminal surface of a small airway of a human subject and co-registered OCT cross-sections acquired simultaneously at the positions indicated on the autofluorescence map.

a number of obstructive lung diseases, such as asthma and COPD [110, 117]. Finally, although less extensively evaluated [106], OCT also has the potential to assess airway remodelling. It is hoped that OCT can be used to evaluate airway wall remodelling longitudinally, particularly in asthma, to follow airway wall changes associated with disease progression or therapeutic intervention. This could prove a powerful application of the technique as airway-specific treatments are developed.

Drawbacks

Despite the fact that the capabilities of OCT for identifying and visualising airway features have advanced over the years, a clear roadblock for the wider adoption and translation of

this technology is the lack of quantitative studies and quantitative measurement tools. Previous OCT studies used manual segmentation of the airway wall components, and this introduces measurement variability. In order for OCT to be used in clinical trials that aim to measure small differences in airway wall structure following an intervention, automated methods must be introduced. In addition to developing automated measurements, a direct comparison to histology in human airways is required to demonstrate that OCT airway wall measurements accurately reflect the airway wall components. Moreover, because repeat OCT imaging of the same subject may not result in identical images because of technical factors (such as motion artefacts, small changes in image orientation or mucus movement between scans), reproducibility of the technique for identifying and measuring the same anatomic location over short periods of time must be established. Finally, the last roadblock to the wider use of OCT is the fact that images are acquired during bronchoscopy, which is not a completely benign process and may not be possible in certain subjects.

Directions for future research

Pulmonary imaging provides three-dimensional and dynamic visualisation and quantification of lung structure and function. Here we have highlighted three imaging techniques that we believe to provide useful measurements for assessing a range of pulmonary diseases. However, despite the advantages of these imaging approaches, one limitation that is shared by each of these imaging modalities, and an important gap that future research must fill, is the lack of standard quantitative measurements and measurement analysis tools. While quantitative CT analysis software and services can be provided by several groups, these software packages often use different algorithms, and therefore standards must be established to allow comparable results across sites. Moreover, CT scanner technology continues to change, and new image acquisition and reconstruction techniques, especially the new ultra-low dose techniques, are being introduced for clinical use. It will be important to investigate whether these new CT techniques will influence the established quantitative measurements. Also, because MRI and OCT are not as well established, there is a great need for the development and adoption of standardised image analysis software for these imaging modalities. This is an important area of future research, and initiatives such as the Quantitative Imaging Biomarkers Alliance (QIBA), which aim to establish protocols and data analysis standards for quantitative imaging, are critical to the wider adoption of quantitative imaging measurements for use in clinical trials, as well as use in routine clinical practice.

In addition to the need for measurement standardisation, the ability to measure small changes over time, in either clinical trials of new therapeutics or longitudinal studies, is an important goal for future imaging research and therefore standardised protocols are also required for large multi-centred studies. Furthermore, standardised protocols should include careful coaching of the research participants, and other ways of standardising lung volumes during image acquisition to improve reproducibility, such as spirometric gating, should be considered. Finally, until large multi-centred studies have been performed using MRI and OCT, as has been recently done using CT in the COPDGene [118], the Canadian Chronic Obstructive Lung Disease (CanCOLD) [119], Evaluation of COPD Longitudinally to Identify Predictive Surrogate Endpoints (ECLIPSE) [120] and Subpopulations and Intermediate Outcomes Measures in COPD (SPIROMICS) [121] and Multi-Ethnic Study of Atherosclerosis (MESA) [122] studies, the imaging modalities best suited to serial evaluations in specific patient populations cannot be ascertained.

Conclusion

In conclusion, CT, MRI and OCT provide the measurements required to noninvasively interrogate the lung structure and function responsible for the physiological and clinical abnormalities in patients with lung disease. It is only when the structure of this incredibly complex and dynamic organ system is more fully understood that new therapies and strategies for the treatment of lung disease will be possible. Currently, there is a critical need to target chronic lung disease and, as many believe, one of the reasons therapeutics for chronic lung diseases continue to fail is that we are unable to stratify patients based on the underlying disease for more targeted treatment. It is hoped that identifying the underlying disease that leads to the outcomes that matter to patients using quantitative imaging will drive new advances in this field, and help millions of people worldwide who are suffering from debilitating lung disease.

References

1. Hsia CC, Hyde DM, Ochs M, *et al.* An official research policy statement of the American Thoracic Society/European Respiratory Society: standards for quantitative assessment of lung structure. *Am J Respir Crit Care Med* 2010; 181: 394–418.
2. Müller NL, Staples CA, Miller RR, *et al.* "Density mask". An objective method to quantitate emphysema using computed tomography. *Chest* 1988; 94: 782–787.
3. Gevenois PA, De Vuyst P, de Maertelaer V, *et al.* Comparison of computed density and microscopic morphometry in pulmonary emphysema. *Am J Respir Crit Care Med* 1996; 154: 187–192.
4. Gevenois PA, de Maertelaer V, De Vuyst P, *et al.* Comparison of computed density and macroscopic morphometry in pulmonary emphysema. *Am J Respir Crit Care Med* 1995; 152: 653–657.
5. Madani A, De Maertelaer V, Zanen J, *et al.* Pulmonary emphysema: radiation dose and section thickness at multidetector CT quantification – comparison with macroscopic and microscopic morphometry. *Radiology* 2007; 243: 250–257.
6. Dirksen A, Friis M, Olesen KP, *et al.* Progress of emphysema in severe alpha 1-antitrypsin deficiency as assessed by annual CT. *Acta Radiol* 1997; 38: 826–832.
7. Newell JD Jr, Hogg JC, Snider GL. Report of a workshop: quantitative computed tomography scanning in longitudinal studies of emphysema. *Eur Respir J* 2004; 23: 769–775.
8. Coxson HO. Quantitative chest tomography in COPD research: chairman's summary. *Proc Am Thorac Soc* 2008; 5: 874–877.
9. Mishima M, Hirai T, Itoh H, *et al.* Complexity of terminal airspace geometry assessed by lung computed tomography in normal subjects and patients with chronic obstructive pulmonary disease. *Proc Natl Acad Sci U S A* 1999; 96: 8829–8834.
10. Gould GA, MacNee W, McLean A, *et al.* CT measurements of lung density in life can quantitate distal airspace enlargement – an essential defining feature of human emphysema. *Am Rev Respir Dis* 1988; 137: 380–392.
11. Uppaluri R, Mitsa T, Sonka M, *et al.* Quantification of pulmonary emphysema from lung computed tomography images. *Am J Respir Crit Care Med* 1997; 156: 248–254.
12. Owrangi AM, Etemad-Rezai R, McCormack DG, *et al.* Computed tomography density histogram analysis to evaluate pulmonary emphysema in ex-smokers. *Acad Radiol* 2013; 20: 537–545.
13. Gietema HA, Muller NL, Fauerbach PV, *et al.* Quantifying the extent of emphysema: factors associated with radiologists' estimations and quantitative indices of emphysema severity using the ECLIPSE cohort. *Acad Radiol* 2011; 18: 661–671.
14. Bankier AA, De Maertelaer V, Keyzer C, *et al.* Pulmonary emphysema: subjective visual grading *versus* objective quantification with macroscopic morphometry and thin-section CT densitometry. *Radiology* 1999; 211: 851–858.
15. Park KJ, Bergin CJ, Clausen JL. Quantitation of emphysema with three-dimensional CT densitometry: comparison with two-dimensional analysis, visual emphysema scores, and pulmonary function test results. *Radiology* 1999; 211: 541–547.
16. Hoffman EA, Ahmed FS, Baumhauer H, *et al.* Variation in the percent of emphysema-like lung in a healthy, nonsmoking multiethnic sample. The MESA lung study. *Ann Am Thorac Soc* 2014; 11: 898–907.
17. McNitt-Gray MF, Goldin JG, Johnson TD, *et al.* Development and testing of image-processing methods for the quantitative assessment of airway hyperresponsiveness from high-resolution CT images. *J Comput Assist Tomogr* 1997; 21: 939–947.

18. Nakano Y, Muller NL, King GG, *et al.* Quantitative assessment of airway remodeling using high-resolution CT. *Chest* 2002; 122: Suppl. 6, 271S–275S.
19. Reinhardt JM, D'Souza ND, Hoffman EA. Accurate measurement of intrathoracic airways. *IEEE Trans Med Imaging* 1997; 16: 820–827.
20. Saba OI, Hoffman EA, Reinhardt JM. Maximizing quantitative accuracy of lung airway lumen and wall measures obtained from X-ray CT imaging. *J Appl Physiol (1985)* 2003; 95: 1063–1075.
21. King GG, Muller NL, Whittall KP, *et al.* An analysis algorithm for measuring airway lumen and wall areas from high-resolution computed tomographic data. *Am J Respir Crit Care Med* 2000; 161: 574–580.
22. Patel BD, Coxson HO, Pillai SG, *et al.* Airway wall thickening and emphysema show independent familial aggregation in chronic obstructive pulmonary disease. *Am J Respir Crit Care Med* 2008; 178: 500–505.
23. King GG, Muller NL, Pare PD. Evaluation of airways in obstructive pulmonary disease using high-resolution computed tomography. *Am J Respir Crit Care Med* 1999; 159: 992–1004.
24. Nakano Y, Muro S, Sakai H, *et al.* Computed tomographic measurements of airway dimensions and emphysema in smokers. Correlation with lung function. *Am J Respir Crit Care Med* 2000; 162: 1102–1108.
25. Grenier P, Mourey-Gerosa I, Benali K, *et al.* Abnormalities of the airways and lung parenchyma in asthmatics: CT observations in 50 patients and inter- and intraobserver variability. *Eur Radiol* 1996; 6: 199–206.
26. Niimi A, Matsumoto H, Amitani R, *et al.* Airway wall thickness in asthma assessed by computed tomography. Relation to clinical indices. *Am J Respir Crit Care Med* 2000; 162: 1518–1523.
27. Gupta S, Siddiqui S, Haldar P, *et al.* Quantitative analysis of high-resolution computed tomography scans in severe asthma subphenotypes. *Thorax* 2010; 65: 775–781.
28. Smith BM, Hoffman EA, Rabinowitz D, *et al.* Comparison of spatially matched airways reveals thinner airway walls in COPD. The Multi-Ethnic Study of Atherosclerosis (MESA) COPD Study and the Subpopulations and Intermediate Outcomes in COPD Study (SPIROMICS). *Thorax* 2014; 69: 987–996.
29. Jain N, Covar RA, Gleason MC, *et al.* Quantitative computed tomography detects peripheral airway disease in asthmatic children. *Pediatr Pulmonol* 2005; 40: 211–218.
30. Busacker A, Newell JD Jr, Keefe T, *et al.* A multivariate analysis of risk factors for the air-trapping asthmatic phenotype as measured by quantitative CT analysis. *Chest* 2009; 135: 48–56.
31. Newman KB, Lynch DA, Newman LS, *et al.* Quantitative computed tomography detects air trapping due to asthma. *Chest* 1994; 106: 105–109.
32. Schroeder JD, McKenzie AS, Zach JA, *et al.* Relationships between airflow obstruction and quantitative CT measurements of emphysema, air trapping, and airways in subjects with and without chronic obstructive pulmonary disease. *AJR Am J Roentgenol* 2013; 201: W460–W470.
33. Ueda T, Niimi A, Matsumoto H, *et al.* Role of small airways in asthma: investigation using high-resolution computed tomography. *J Allergy Clin Immunol* 2006; 118: 1019–1025.
34. Tunon-de-Lara JM, Laurent F, Giraud V, *et al.* Air trapping in mild and moderate asthma: effect of inhaled corticosteroids. *J Allergy Clin Immunol* 2007; 119: 583–590.
35. Matsuoka S, Kurihara Y, Yagihashi K, *et al.* Quantitative assessment of air trapping in chronic obstructive pulmonary disease using inspiratory and expiratory volumetric MDCT. *AJR Am J Roentgenol* 2008; 190: 762–769.
36. O'Donnell RA, Peebles C, Ward JA, *et al.* Relationship between peripheral airway dysfunction, airway obstruction, and neutrophilic inflammation in COPD. *Thorax* 2004; 59: 837–842.
37. Eda S, Kubo K, Fujimoto K, *et al.* The relations between expiratory chest CT using helical CT and pulmonary function tests in emphysema. *Am J Respir Crit Care Med* 1997; 155: 1290–1294.
38. Galbán CJ, Han MK, Boes JL, *et al.* Computed tomography-based biomarker provides unique signature for diagnosis of COPD phenotypes and disease progression. *Nat Med* 2012; 18: 1711–1715.
39. Brody AS, Tiddens HA, Castile RG, *et al.* Computed tomography in the evaluation of cystic fibrosis lung disease. *Am J Respir Crit Care Med* 2005; 172: 1246–1252.
40. Meyer KC. Diagnosis and management of interstitial lung disease. *Transl Respir Med* 2014; 2: 4.
41. Johannessen A, Skorge TD, Bottai M, *et al.* Mortality by level of emphysema and airway wall thickness. *Am J Respir Crit Care Med* 2013; 187: 602–608.
42. Vestbo J, Edwards LD, Scanlon PD, *et al.* Changes in forced expiratory volume in 1 second over time in COPD. *N Engl J Med* 2011; 365: 1184–1192.
43. Nishimura M, Makita H, Nagai K, *et al.* Annual change in pulmonary function and clinical phenotype in chronic obstructive pulmonary disease. *Am J Respir Crit Care Med* 2012; 185: 44–52.
44. Coxson HO, Dirksen A, Edwards LD, *et al.* The presence and progression of emphysema in COPD as determined by CT scanning and biomarker expression: a prospective analysis from the ECLIPSE study. *Lancet Respir Med* 2013; 1: 129–136.
45. Han MK, Kazerooni EA, Lynch DA, *et al.* Chronic obstructive pulmonary disease exacerbations in the COPDGene study: associated radiologic phenotypes. *Radiology* 2011; 261: 274–282.

46. Grydeland TB, Dirksen A, Coxson HO, *et al.* Quantitative computed tomography measures of emphysema and airway wall thickness are related to respiratory symptoms. *Am J Respir Crit Care Med* 2010; 181: 353–359.
47. Martinez CH, Chen YH, Westgate PM, *et al.* Relationship between quantitative CT metrics and health status and BODE in chronic obstructive pulmonary disease. *Thorax* 2012; 67: 399–406.
48. Diaz AA, Bartholmai B, San Jose ER, *et al.* Relationship of emphysema and airway disease assessed by CT to exercise capacity in COPD. *Respir Med* 2010; 104: 1145–1151.
49. Gietema HA, Edwards LD, Coxson HO, *et al.* Impact of emphysema and airway wall thickness on quality of life in smoking-related COPD. *Respir Med* 2013; 107: 1201–1209.
50. Fishman A, Martinez F, Naunheim K, *et al.* A randomized trial comparing lung-volume-reduction surgery with medical therapy for severe emphysema. *N Engl J Med* 2003; 348: 2059–2073.
51. Sciurba FC, Ernst A, Herth FJ, *et al.* A randomized study of endobronchial valves for advanced emphysema. *N Engl J Med* 2010; 363: 1233–1244.
52. Gompelmann D, Eberhardt R, Michaud G, *et al.* Predicting atelectasis by assessment of collateral ventilation prior to endobronchial lung volume reduction: a feasibility study. *Respiration* 2010; 80: 419–425.
53. Mets OM, Willemink MJ, de Kort FP, *et al.* The effect of iterative reconstruction on computed tomography assessment of emphysema, air trapping and airway dimensions. *Eur Radiol* 2012; 22: 2103–2109.
54. Hague CJ, Krowchuk N, Alhassan D, *et al.* Qualitative and quantitative assessment of smoking-related lung disease: effect of iterative reconstruction on low-dose computed tomographic examinations. *J Thorac Imaging* 2014; 29: 350–356.
55. Ohno Y, Koyama H, Yoshikawa T, *et al.* T2* measurements of 3-T MRI with ultrashort TEs: capabilities of pulmonary function assessment and clinical stage classification in smokers. *AJR Am J Roentgenol* 2011; 197: W279–W285.
56. Deimling M, Jellus V, Geiger B, *et al.* Time resolved lung ventilation imaging by Fourier decomposition. *Proc Intl Soc Mag Reson Med* 2008; 16: 2639.
57. Bauman G, Puderbach M, Deimling M, *et al.* Non-contrast-enhanced perfusion and ventilation assessment of the human lung by means of Fourier decomposition in proton MRI. *Magn Reson Med* 2009; 62: 656–664.
58. Capaldi DP, Sheikh K, Guo F, *et al.* Free-breathing pulmonary (1)H and hyperpolarized (3)He MRI: comparison in COPD and bronchiectasis. *Acad Radiol* 2015; 22: 320–329.
59. Edelman RR, Hatabu H, Tadamura E, *et al.* Noninvasive assessment of regional ventilation in the human lung using oxygen-enhanced magnetic resonance imaging. *Nat Med* 1996; 2: 1236–1239.
60. Ohno Y, Koyama H, Yoshikawa T, *et al.* Comparison of capability of dynamic O(2)-enhanced MRI and quantitative thin-section MDCT to assess COPD in smokers. *Eur J Radiol* 2012; 81: 1068–1075.
61. Couch MJ, Ball IK, Li T, *et al.* Pulmonary ultrashort echo time 19F MR imaging with inhaled fluorinated gas mixtures in healthy volunteers: feasibility. *Radiology* 2013; 269: 903–909.
62. Halaweish AF, Moon RE, Foster WM, *et al.* Perfluoropropane gas as a magnetic resonance lung imaging contrast agent in humans. *Chest* 2013; 144: 1300–1310.
63. Coxson HO, Leipsic J, Parraga G, *et al.* Using pulmonary imaging to move chronic obstructive pulmonary disease beyond FEV1. *Am J Respir Crit Care Med* 2014; 190: 135–144.
64. Wild JM, Marshall H, Bock M, *et al.* MRI of the lung (1/3): methods. *Insights Imaging* 2012; 3: 345–353.
65. Albert MS, Cates GD, Driehuys B, *et al.* Biological magnetic resonance imaging using laser-polarized 129Xe. *Nature* 1994; 370: 199–201.
66. Parraga G, Mathew L, Etemad-Rezai R, *et al.* Hyperpolarized 3He magnetic resonance imaging of ventilation defects in healthy elderly volunteers: initial findings at 3.0 Tesla. *Acad Radiol* 2008; 15: 776–785.
67. Altes TA, Powers PL, Knight-Scott J, *et al.* Hyperpolarized 3He MR lung ventilation imaging in asthmatics: preliminary findings. *J Magn Reson Imaging* 2001; 13: 378–384.
68. Woodhouse N, Wild JM, Paley MN, *et al.* Combined helium-3/proton magnetic resonance imaging measurement of ventilated lung volumes in smokers compared to never-smokers. *J Magn Reson Imaging* 2005; 21: 365–369.
69. Tzeng YS, Lutchen K, Albert M. The difference in ventilation heterogeneity between asthmatic and healthy subjects quantified using hyperpolarized 3He MRI. *J Appl Physiol (1985)* 2009; 106: 813–822.
70. Kirby M, Heydarian M, Svenningsen S, *et al.* Hyperpolarized He-3 magnetic resonance functional imaging semiautomated segmentation. *Acad Radiol* 2012; 19: 141–152.
71. Tustison NJ, Avants BB, Flors L, *et al.* Ventilation-based segmentation of the lungs using hyperpolarized (3)He MRI. *J Magn Reson Imaging* 2011; 34: 831–841.
72. Lui JK, LaPrad AS, Parameswaran H, *et al.* Semiautomatic segmentation of ventilated airspaces in healthy and asthmatic subjects using hyperpolarized 3He MRI. *Comput Math Methods Med* 2013; 2013: 624683.
73. Mathew L, Kirby M, Etemad-Rezai R, *et al.* Hyperpolarized (3)He magnetic resonance imaging: preliminary evaluation of phenotyping potential in chronic obstructive pulmonary disease. *Eur J Radiol* 2011; 79: 140–146.
74. de Lange EE, Altes TA, Patrie JT, *et al.* Evaluation of asthma with hyperpolarized helium-3 MRI: correlation with clinical severity and spirometry. *Chest* 2006; 130: 1055–1062.

75. McMahon CJ, Dodd JD, Hill C, *et al.* Hyperpolarized 3helium magnetic resonance ventilation imaging of the lung in cystic fibrosis: comparison with high resolution CT and spirometry. *Eur Radiol* 2006; 16: 2483–2490.
76. Altes TA, Rehm PK, Harrell F, *et al.* Ventilation imaging of the lung: comparison of hyperpolarized helium-3 MR imaging with Xe-133 scintigraphy. *Acad Radiol* 2004; 11: 729–734.
77. Svenningsen S, Kirby M, Starr D, *et al.* What are ventilation defects in asthma? *Thorax* 2014; 69: 63–71.
78. Saam B, Yablonskiy DA, Gierada DS, *et al.* Rapid imaging of hyperpolarized gas using EPI. *Magn Reson Med* 1999; 42: 507–514.
79. Salerno M, Altes TA, Brookeman JR, *et al.* Dynamic spiral MRI of pulmonary gas flow using hyperpolarized (3)He: preliminary studies in healthy and diseased lungs. *Magn Reson Med* 2001; 46: 667–677.
80. Gierada DS, Saam B, Yablonskiy D, *et al.* Dynamic echo planar MR imaging of lung ventilation with hyperpolarized (3)He in normal subjects and patients with severe emphysema. *NMR Biomed* 2000; 13: 176–181.
81. Holmes JH, O'Halloran RL, Brodsky EK, *et al.* Three-dimensional imaging of ventilation dynamics in asthmatics using multiecho projection acquisition with constrained reconstruction. *Magn Reson Med* 2009; 62: 1543–1556.
82. Koumellis P, van Beek EJ, Woodhouse N, *et al.* Quantitative analysis of regional airways obstruction using dynamic hyperpolarized 3He MRI – Preliminary results in children with cystic fibrosis. *J Magn Reson Imaging* 2005; 22: 420–426.
83. Marshall H, Deppe MH, Parra-Robles J, *et al.* Direct visualisation of collateral ventilation in COPD with hyperpolarised gas MRI. *Thorax* 2012; 67: 613–617.
84. Gast KK, Puderbach MU, Rodriguez I, *et al.* Dynamic ventilation (3)He-magnetic resonance imaging with lung motion correction: gas flow distribution analysis. *Invest Radiol* 2002; 37: 126–134.
85. Saam BT, Yablonskiy DA, Kodibagkar VD, *et al.* MR imaging of diffusion of (3)He gas in healthy and diseased lungs. *Magn Reson Med* 2000; 44: 174–179.
86. Fain SB, Altes TA, Panth SR, *et al.* Detection of age-dependent changes in healthy adult lungs with diffusion-weighted 3He MRI. *Acad Radiol* 2005; 12: 1385–1393.
87. Salerno M, de Lange EE, Altes TA, *et al.* Emphysema: hyperpolarized helium 3 diffusion MR imaging of the lungs compared with spirometric indexes – initial experience. *Radiology* 2002; 222: 252–260.
88. Diaz S, Casselbrant I, Piitulainen E, *et al.* Validity of apparent diffusion coefficient hyperpolarized 3He-MRI using MSCT and pulmonary function tests as references. *Eur J Radiol* 2009; 71: 257–263.
89. Fain SB, Panth SR, Evans MD, *et al.* Early emphysematous changes in asymptomatic smokers: detection with 3He MR imaging. *Radiology* 2006; 239: 875–883.
90. Ley S, Zaporozhan J, Morbach A, *et al.* Functional evaluation of emphysema using diffusion-weighted 3Helium-magnetic resonance imaging, high-resolution computed tomography, and lung function tests. *Invest Radiol* 2004; 39: 427–434.
91. Woods JC, Choong CK, Yablonskiy DA, *et al.* Hyperpolarized 3He diffusion MRI and histology in pulmonary emphysema. *Magn Reson Med* 2006; 56: 1293–1300.
92. Mathew L, Kirby M, Farquhar D, *et al.* Hyperpolarized 3He functional magnetic resonance imaging of bronchoscopic airway bypass in chronic obstructive pulmonary disease. *Can Respir J* 2012; 19: 41–43.
93. Kirby M, Mathew L, Heydarian M, *et al.* Chronic obstructive pulmonary disease: quantification of bronchodilator effects by using hyperpolarized He-3 MR imaging. *Radiology* 2011; 261: 283–292.
94. de Lange EE, Altes TA, Patrie JT, *et al.* The variability of regional airflow obstruction within the lungs of patients with asthma: assessment with hyperpolarized helium-3 magnetic resonance imaging. *J Allergy Clin Immunol* 2007; 119: 1072–1078.
95. Mentore K, Froh DK, de Lange EE, *et al.* Hyperpolarized HHe 3 MRI of the lung in cystic fibrosis: assessment at baseline and after bronchodilator and airway clearance treatment. *Acad Radiol* 2005; 12: 1423–1429.
96. Cadman RV, Lemanske RF Jr, Evans MD, *et al.* Pulmonary 3He magnetic resonance imaging of childhood asthma. *J Allergy Clin Immunol* 2013; 131: 369–376.
97. Woodhouse N, Wild JM, van Beek EJ, *et al.* Assessment of hyperpolarized 3He lung MRI for regional evaluation of interventional therapy: a pilot study in pediatric cystic fibrosis. *J Magn Reson Imaging* 2009; 30: 981–988.
98. Altes T, Johnson M, Mugler J III, *et al.* The effect of ivacaftor, an investigational CFTR potentiator, on hyperpolarized noble gas magnetic resonance imaging in subjects with cystic fibrosis who have the G551D-CFTR mutation. *Am J Respir Crit Care Med* 2012; 185: A2814.
99. Kirby M, Svenningsen S, Owrangi A, *et al.* Hyperpolarized 3He and 129Xe MR imaging in healthy volunteers and patients with chronic obstructive pulmonary disease. *Radiology* 2012; 265: 600–610.
100. Fujimoto JG, Brezinski ME, Tearney GJ, *et al.* Optical biopsy and imaging using optical coherence tomography. *Nat Med* 1995; 1: 970–972.
101. Brezinski ME, Tearney GJ, Weissman NJ, *et al.* Assessing atherosclerotic plaque morphology: comparison of optical coherence tomography and high frequency intravascular ultrasound. *Heart* 1997; 77: 397–403.
102. Fercher AF, Hitzenberger CK, Drexler W, *et al. In vivo* optical coherence tomography. *Am J Ophthalmol* 1993; 116: 113–114.

103. Swanson EA, Izatt JA, Hee MR, *et al. In vivo* retinal imaging by optical coherence tomography. *Opt Lett* 1993; 18: 1864–1866.
104. Pitris C, Jesser C, Boppart SA, *et al.* Feasibility of optical coherence tomography for high-resolution imaging of human gastrointestinal tract malignancies. *J Gastroenterol* 2000; 35: 87–92.
105. Hariri LP, Applegate MB, Mino-Kenudson M, *et al.* Volumetric optical frequency domain imaging of pulmonary pathology with precise correlation to histopathology. *Chest* 2013; 143: 64–74.
106. Coxson HO, Quiney B, Sin DD, *et al.* Airway wall thickness assessed using computed tomography and optical coherence tomography. *Am J Respir Crit Care Med* 2008; 177: 1201–1206.
107. Lam SLA, Lane P, Ohtani K, *et al.* Optical coherence tomography imaging of asthmatic airways before and after thermoplasty. *Am J Respir Crit Care Med* 2013; 187: A6014o.
108. Lam S, Standish B, Baldwin C, *et al. In vivo* optical coherence tomography imaging of preinvasive bronchial lesions. *Clin Cancer Res* 2008; 14: 2006–2011.
109. Tsuboi M, Hayashi A, Ikeda N, *et al.* Optical coherence tomography in the diagnosis of bronchial lesions. *Lung Cancer* 2005; 49: 387–394.
110. Williamson JP, McLaughlin RA, Noffsinger WJ, *et al.* Elastic properties of the central airways in obstructive lung diseases measured using anatomical optical coherence tomography. *Am J Respir Crit Care Med* 2011; 183: 612–619.
111. Coxson HO, Lam S. Quantitative assessment of the airway wall using computed tomography and optical coherence tomography. *Proc Am Thorac Soc* 2009; 6: 439–443.
112. Armstrong JJ, Leigh MS, Sampson DD, *et al.* Quantitative upper airway imaging with anatomic optical coherence tomography. *Am J Respir Crit Care Med* 2006; 173: 226–233.
113. Lee AM, Ohtani K, Macaulay C, *et al.* In vivo lung microvasculature visualized in three dimensions using fiber-optic color Doppler optical coherence tomography. *J Biomed Opt* 2013; 18: 50501.
114. Hariri LP, Villiger M, Applegate MB, *et al.* Seeing beyond the bronchoscope to increase the diagnostic yield of bronchoscopic biopsy. *Am J Respir Crit Care Med* 2013; 187: 125–129.
115. Pahlevaninezhad H, Cecic I, Lee AM, *et al.* Multimodal tissue imaging: using coregistered optical tomography data to estimate tissue autofluorescence intensity change due to scattering and absorption by neoplastic epithelial cells. *J Biomed Opt* 2013; 18: 106007.
116. Lee AM, Kirby M, Ohtani K, *et al.* Validation of airway wall measurements by optical coherence tomography in porcine airways. *PloS One* 2014; 9: e100145.
117. Noble PB, West AR, McLaughlin RA, *et al.* Airway narrowing assessed by anatomical optical coherence tomography *in vitro*: dynamic airway wall morphology and function. *J Appl Physiol (1985)* 2010; 108: 401–411.
118. Regan EA, Hokanson JE, Murphy JR, *et al.* Genetic epidemiology of COPD (COPDGene) study design. *COPD* 2010; 7: 32–43.
119. Bourbeau J, Saad N. [COPD: Success needs implementing a participative care model and early treatment?]. *Revue des maladies respiratoires* 2013; 30: 93–94.
120. Vestbo J, Anderson W, Coxson HO, *et al.* Evaluation of COPD Longitudinally to Identify Predictive Surrogate End-points (ECLIPSE). *Eur Respir J* 2008; 31: 869–873.
121. Couper D, Lavange LM, Han M, *et al.* Design of the Subpopulations and Intermediate Outcomes in COPD Study (SPIROMICS). *Thorax* 2013; 69: 491–494.
122. Bild DE, Bluemke DA, Burke GL, *et al.* Multi-ethnic study of atherosclerosis: objectives and design. *Am J Epidemiol* 2002; 156: 871–881.
123. Kirby M, Pike D, McCormack DG, *et al.* Longitudinal computed tomography and magnetic resonance imaging of COPD: Thoracic Imaging Network of Canada (TINCan) study objective. *J COPD F* 2014; 1: 200–211.
124. Kirby M, Coxson HO, Parraga G. Pulmonary functional magnetic resonance imaging for paediatric lung disease. *Paediatr Respir Rev* 2013; 14: 180–189.

Support statement: H.O. Coxson acknowledges funding (Operating, Team (Thoracic Imaging Network of Canada) and Network (Canadian Respiratory Research Network)), and is supported by a Roberta R. Miller Fellowship in Thoracic Imaging from the B.C. Lung Association. M. Kirby acknowledges support from the Canadian Institute of Health Research (CIHR) Banting Postdoctoral Fellowship Program.

Disclosures: H.O. Coxson reports receiving a grant from GSK for the analysis of CT scans performed under a service contract between the University of British Columbia (Vancouver, BC, Canada). H.O. Coxson has served on the Steering Committee of ECLIPSE (Evaluation of COPD Longitudinally to Identify Predictive Surrogate End-points) and has received travel expenses from GSK to attend ECLIPSE meetings. H.O. Coxson has also received a grant from Spiration Inc. for a service contact relating to the quantitative analysis of CT scans.

Chapter 15

Regulatory perspective on the use of lung imaging in drug development

Laura Fregonese

In recent years the development of new imaging techniques and advanced imaging processing methods have improved the sensitivity, specificity, and reproducibility of imaging biomarkers for use in clinical monitoring. Imaging also offers the potential to improve the drug development process, from the early phases of compound discovery and confirmation of pharmacology, to preclinical studies in animal models and clinical studies for regulatory approval. This chapter will discuss the application of anatomical and molecular imaging techniques to drug development and monitoring of specific targets in respiratory medicine, outlining the current applications of imaging measures in preclinical and clinical development. The chapter will also discuss the regulatory approval process and provide a regulatory perspective on why the use of imaging end-points remains limited in preclinical and clinical development.

The drug development process is increasingly costly and slow, with approximately 10 000 candidate drugs lost across the different phases of development for each approved new drug. The respiratory field is no exception, with one of the lowest numbers of new medicines authorised in the past 40 years among all medical fields [1]. Drug pipeline failure occurs mainly during translation from the preclinical to the clinical phase and during clinical development [2], due to poor translatability of findings from preclinical models, lack of early measures predictive of clinical efficacy in large patient populations, and the low sensitivity of current clinical trial end-points. New trial designs and outcome measures are needed to improve identification of the most promising candidate drugs in early phases and reduce the time required to confirm clinical efficacy. In recent decades the development of new imaging techniques and advanced image processing with quantitative analysis software have improved the sensitivity, specificity, and reproducibility of imaging biomarkers for use in longitudinal clinical monitoring and in drug and medical device development. This chapter will explore the current use of imaging measures, their limitations and future possibilities in the development of medicines for non-oncological respiratory diseases, including in the regulatory approval process.

Product Development Scientific Support Dept, Human Medicines Research and Development Support Division, European Medicines Agency, London, UK.

Correspondence: Laura Fregonese, European Medicines Agency, 30 Churchill Place, Canary Wharf, London, E14 5EU, UK.
E-mail: Laura.Fregonese@ema.europa.eu

Copyright ©ERS 2015. Print ISBN: 978-1-84984-065-1. Online ISBN: 978-1-84984-066-8. Print ISSN: 2312-508X. Online ISSN: 2312-5098.

The drug development process

The development of new medicines starts with selection and confirmation of molecular targets relevant to a specific disease, followed by design and optimisation of candidate compounds. Preclinical development *in vitro* and in animal models is then utilised to confirm the drug pharmacology and establish proof of concept [2]. When preclinical results are favourable, phase I clinical studies are performed in healthy individuals to study pharmacokinetics and provide preliminary information on the safety of the new drug. This phase may already include patients (dose finding, phase I/II). Phase II trials are then performed to assess safety and efficacy in the target patient population, and the optimum dosage schedule. Phase III trials are used to confirm the efficacy and safety of the new medicine in a population that is, as far as possible, representative of the population in which the medicine will be prescribed. In phase III the new medicine is usually compared with standard therapy (active comparator) or placebo, on top of standard of care when available. Regulatory authorities grant marketing authorisation based on their positive opinion of the clinical benefits of the new medicine *versus* the known risks, and risk management plans are issued in order to cover potential risks that cannot be fully assessed at the moment of approval. In exceptional cases, phase II trials are considered sufficient to grant regulatory approval, *e.g.* in cases of high unmet public health need, in some rare diseases or in the presence of outstanding preliminary data or a breakthrough treatment, usually with the obligation of performing post-marketing studies. Post-licencing studies may be needed to provide additional information on safety or confirmatory efficacy. The long duration and high costs of the drug development process are described in figure 1.

Applications of imaging to drug development

Imaging measures have the potential to contribute to early stages of drug development by detecting specific molecular and cellular targets and their interactions with new compounds *in vitro* and in animal models, where the effects of new compounds can also be measured on

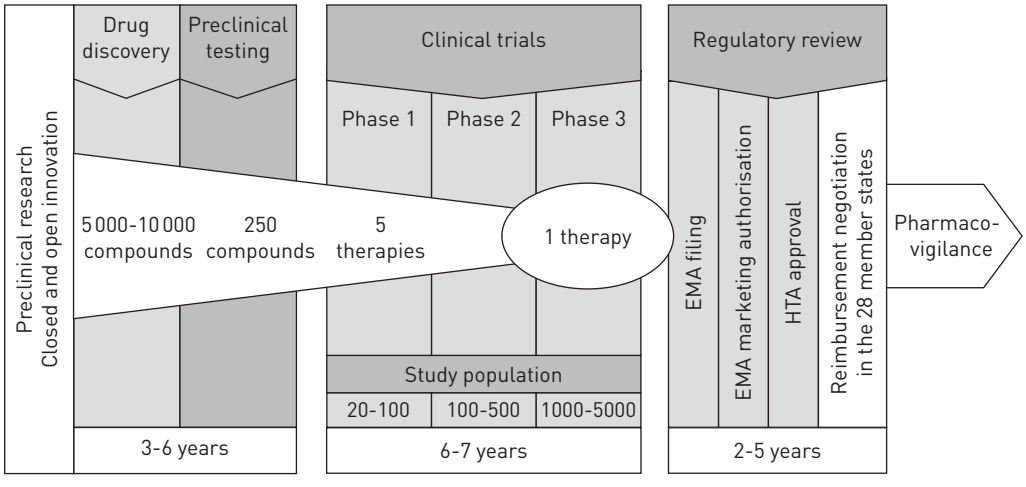

Figure 1. The drug development process from research and discovery to marketing authorisation in the European Union (where marketing authorisation is granted by the European Medicines Agency (EMA)). HTA: Health Technology Assessment.

lung structure and function. Due to their sensitivity to lung morphology and disease progression, the use of imaging end-points has been suggested as a way to increase the efficiency of clinical trials in respiratory medicine. Another potential application is the identification of disease phenotypes, to facilitate the conduct of trials in clearly defined study populations and for selecting the patients most likely to respond to a specific drug. Finally imaging may be used to monitor *in vivo* drug pharmacokinetics and distribution, which is particularly important for drugs delivered by inhalation.

Imaging modalities have traditionally been primarily divided into morphological/anatomical, including CT and MRI, and molecular, such as optical imaging (*e.g.* fluorescence), PET and SPECT. The choice of the most appropriate imaging modality for different biological questions and drug development phases is a complex issue, requiring *ad hoc* studies and consensus on the fitness for purpose of each technique to different therapeutic targets and pathophysiological events.

Anatomical imaging

Imaging derived from CT and MRI provides information with structural detail comparable to macroscopic histological examination [3] and has been used as surrogate of histology. CT, in particular HRCT, is the most frequently used technique in longitudinal studies, allowing quantitative measures of tissue density, lung volume, and airway and vasculature geometry. A number of CT-derived measures, *e.g.* global densitometry, are standardised and have been applied to pharmacological studies in non-oncological respiratory diseases. The application of MRI to the study of the lungs is more recent, due to the technical difficulties of imaging air with a technique based on proton spin that is more suitable for organs with high content of water [4]. The use of hyperpolarised gases such as ^{3}He and ^{129}Xe, which are excitable by magnetic fields, allows MRI-based measurements of lung structures by contrasting the air component, and enables assessment of the global and regional temporal sequence of ventilation [5, 6]. As a non-ionising method MRI is considered suitable for paediatric studies and for use in respiratory compromised and elderly patients [7, 8]. However, its use is limited by the high cost of hyperpolarised gases [9] and the lack of standardised measures. Oxygen-enhanced MRI, an indirect measure of ventilation, may reduce costs; however, to date, this has been at the expense of limited sensitivity and a low signal-to-noise ratio [10, 11].

New techniques with potential applications in future clinical trials, once their clinical usefulness has been proven, include electric impedance tomography, which is noninvasive and provides real-time monitoring of the lungs over long periods, and OCT. While OCT is invasive, involving inserting a near-infrared optical probe into the airways, it can distinguish different airways components, *i.e.* mucosa, sub-mucosa, lamina propria, cartilage and airway smooth muscle [4]. Its sensitivity has been shown superior to FEV_1 in COPD, and OCT results correlated with CT findings [12]. By relating structural and functional changes *in vivo*, this technique could have a potential role in establishing efficacy in the early clinical phases of drug development (*e.g.* phase I).

Molecular imaging

Molecular imaging techniques characterise and quantify the spatial and temporal distribution of biological processes at a cellular and molecular level *in vivo*, using molecular

probes and radiotracers interacting with the target(s) of interest [13]. PET signals are based on the emission of beams of gamma radiation at 180 degrees to one another during the decay of a radiotracer, usually ^{18}F-FDG the uptake of which correlates with cellular glucose metabolism. PET can be useful for monitoring inflammatory processes in respiratory non-oncological diseases, although the technique does not allow accurate localisation of the tracer's activity. Functional PET modalities using gaseous tracers can provide measures of perfusion and ventilation, both separately and as their ratio (ventilation/perfusion). One limitation to the use of PET in the longitudinal clinical setting, aside from the radiation burden due to radiotracers, is the need for a cyclotron and a radiopharmaceutical formulation that is often prepared on site [4]. SPECT, which is based on radiotracers emitting a single gamma beam, results in lower radiation emissions than PET, but at the expense of a longer acquisition time per image and lower definition. SPECT can provide measurements of ventilation through the use of gaseous radioisotopes such as ^{81m}Kr or ^{133}Xe [14], or radiolabelled particulate aerosols. While more frequently used in preclinical drug development, molecular imaging modalities suffer from suboptimal spatial resolution with the currently available technology [13], which limits their potential use in clinical trials [15]. The sensitivity of these techniques to lung structures may be improved by combination with anatomical imaging, and the past decade has indeed seen increasing development of multimodality imaging of the lungs, involving co-acquisition and co-registration of imaging from different techniques.

Multimodality imaging

The promise of multimodality imaging techniques, *e.g.* PET/CT, SPECT/CT and PET/MRI, is that they will enable noninvasive characterisation of the full pathophysiology of non-oncological lung diseases, by combining the resolution of anatomical imaging with the capability of molecular imaging to detect metabolic and dynamic processes. For example, in PET/CT the CT images provide accurate anatomical localisation of sites of radiotracer accumulation, allowing studies of disease progression and response to treatment of differentially affected lung segments with a precision that would not be possible using PET alone [16]. An important limiting factor of the use of PET/CT and SPECT/CT in clinical trials is the increased radiation delivered by combining two different radiation-emitting techniques. PET/MRI (or SPECT/MRI) has the advantage of a lower radiation dose; however, development of the technique is very recent and technical challenges limit its use in clinical studies. To date, there is no standardised and validated multimodality imaging-based quantitative measure for use in non-oncological respiratory diseases, and studies are needed to put into perspective the advantages gained by the combination of different techniques with the limitations and risks posed by such combination.

Applications of imaging to specific therapeutic targets

Inflammation

Neutrophilic inflammation is a relevant component of many respiratory diseases, including acute respiratory distress syndrome [17] and cystic fibrosis (CF) [18]. Asthma phenotypes characterised by neutrophilic airway inflammation have been described [19], and infiltration of neutrophils into the bronchial mucosa is a known feature of COPD [20]. The study of medicines with anti-inflammatory activity is an interesting field of application of molecular imaging, where ^{18}F-FDG-PET alone or combined with CT has been used to

image neutrophil recruitment and activation in preclinical models of lung infection and inflammation [21, 22], and to quantify the presence of activated neutrophils in human studies in pneumonia [23], CF [24], asthma [25], and COPD [4]. In spite of encouraging results in detecting the effect of anti-inflammatory treatments, ^{18}F-FDG-PET/CT readouts lack specificity, as the tracer is taken up nonspecifically by different inflammatory cells and tumour cells. Neutrophil-specific PET tracers are being studied, such as the cFLFLFK-PEG^{64}Cu peptide that targets the neutrophil formyl peptide receptor [10].

One inflammatory feature of respiratory diseases is airway oedema caused by increased permeability of the microvasculature. Micro-CT and MRI have been used to quantify airway oedema in preclinical models of asthma [26, 27], and showed that MRI signals were more sensitive than changes in bronchoalveolar lavage inflammatory mediators to treatment with corticosteroids [28, 29]. While interesting for pathophysiological studies, imaging measures of airways inflammatory oedema do not appear particularly informative at present, and their potential clinical relevance as end-points of disease progression and treatment response is unknown.

Lung infection

Potential applications of ^{18}F-FDG-PET/CT to interventional studies of lung infection have recently emerged, with the demonstration that PET readouts of infected areas allow discrimination between active disease and residual pathology from resolved disease. Recently, Coleman *et al.* [30] showed that treatment of multidrug-resistant tuberculosis (MDR-TB) infected macaques with linezolid and a second-generation oxazolidinone reduced bacterial load measured at necropsy, and the improvement of the infection was captured by a reduction of FDG-PET avidity aided by CT-quantified lung pathology. PET/CT changes were also observed in 19 patients infected with extensively drug-resistant TB treated with linezolid [30]. In addition, early PET/CT changes predicted final treatment outcomes in a prospective analysis of 28 patients with MDR-TB treated with an optimised regimen for 24 months [31], suggesting that imaging could be an early surrogate marker of treatment efficacy in TB (figure 2).

Airways disease

Airways disease occurs with different pathophysiology in several respiratory diseases, including asthma, COPD, CF and non-CF bronchiectasis, and it represents a target for drugs aimed at treating remodelling, inflammation and bronchial constriction. CT-based measures of wall thickness, such as the airway wall cross-sectional area as a percentage of the total airway cross-sectional area, are considered a proxy of airways remodelling [32–34]. Automated measurements have been validated for larger airways to the sixth generation [33, 35]. However, the study of smaller airways, in particular those with a diameter below 2 mm that are the most important site of expiratory airflow obstruction, requires a resolution beyond that provided by current CT methods. The use of CT and multiplanar reconstruction enabling volumetric analysis of the whole bronchial tree and techniques including functional imaging based on fluid dynamics equations [36] may improve the current detection of airways abnormalities. However, at present, the informative value of measures obtained beyond the third or fourth generation sub-segmental airway is not fully established [33].

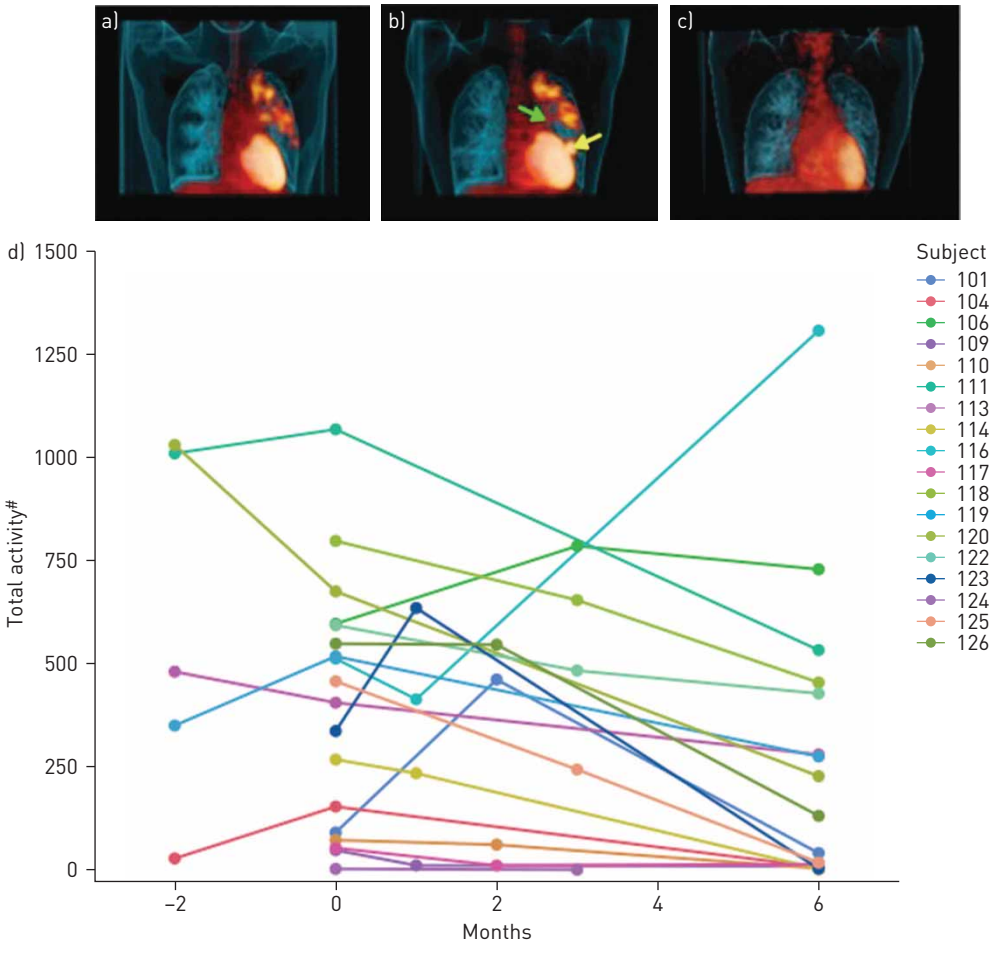

Figure 2. Radiological responses to linezolid (LZD) in extensively drug-resistant tuberculosis (XDR-TB). FDG-PET scans in a patient at a) study entry, b) immediately before receiving LZD and c) after 6 months of LZD. b) The green arrow shows a lesion that spontaneously resolved during the 2 months prior to receiving LZD; the yellow arrow shows a new lesion that appears in the same time interval. d) Individual responses of LZD treated patients. FDG-PET scans were performed at baseline (0 on the x-axis) and after 6 months of treatment. A third scan was randomly allocated to different time points, including at 2 months before the first LZD dose in a subset of patients (−2 on the x-axis). p=0.009 for the difference in mean total activity between month 0 and month 6. #: standardised uptake value >2. Reproduced from [30] with permission from the publisher.

Indirect estimates of small airways abnormalities are provided by measures of air trapping, based on the less than normal increase in attenuation on HRCT densitometry during expiration when airway obstruction is present. Measurements of air trapping are complicated by the need for pairing of inspiratory and expiratory data in order to distinguish emphysema-related trapping from that due to small airways disease. In addition air trapping has also been observed in healthy nonsmoking individuals without airflow obstruction [37], and more studies are needed to elucidate potential applications to longitudinal studies.

In CF, the conspicuous thickening of small airways walls makes it possible to visualise distal bronchi in the lung periphery, a characteristic that can be exploited to identify mucus plugging within the airway wall thickened image by simple proton MRI due to the contrast

of the fluid component of the mucus [38]. The clinical relevance of mucus plugging as a component of airways disease isolated from other airways pathology is not established, and MRI-based airway imaging is not currently applied to longitudinal studies. However, MRI with aminodextran-based probes and molecular techniques such as scintigraphy with ^{99m}Tc-labelled sulfur colloid offer the possibility to study the effect of drugs on mucus production and mucociliary clearance in animal models, a useful application for preclinical compound selection [39, 40].

Emphysema

The most advanced application of quantitative imaging to longitudinal studies of respiratory diseases is the study of emphysema morphometry, where standardised CT techniques and readouts have reached maturity for use in clinical trials. The most common CT measures are those of lung density, where emphysematous lung is considered to have a density of less than −950 HU (~0.1 g·L^{-1}) on image voxels. Global densitometry measures have been validated against extent and severity of emphysema at pathology and have been used as end-points in clinical trials in α_1-antitrypsin deficiency (α_1-ATD)-related emphysema [41, 42]. The most recommended measure for longitudinal studies is the 15th percentile of density [12], where lung density is recorded in Hounsfield units at total lung capacity (TLC) and functional residual capacity (FRC) in g·L^{-1}, corrected for volume [43, 44], as this is less sensitive to technical aspects (*e.g.* image noise and image reconstruction algorithm) and more sensitive to changes in lung structure [45, 46] as compared to other methods such as the threshold-cut off analysis.

MRI has been used to measure emphysema morphology in preclinical studies, showing a correlation between increased ADC and emphysema histology [47, 48]. This finding has also been reported in humans [49], where ADC also correlates with FEV1/forced vital capacity (FVC) ratio, TLC and residual volume [50]. However, the use of ADC as a measure in longitudinal studies is controversial, with a handful of studies showing no changes over 1 year in COPD [51] and over 2 years α_1-ATD-related COPD [52], while other studies showed increased ADC together with higher MRI ventilation defects over 2 years in absence of changes in FEV1 [53].

Ventilation and perfusion

Ventilation can be quantified by different techniques using the dynamic change in imaging signal after application of an inhaled contrast agent. While CT-based measures of ventilation are not often applied to longitudinal studies due to repeated radiation exposure, the use of MRI with hyperpolarised gases is increasing. The quantification of hyperpolarised gas density provides pictures of ventilated airspaces and highlights areas of decreased airway lumen and air trapping. It also gives information about ventilation in distal areas including the terminal bronchioles and on alveolar ventilation [54]. Global measures of ventilation defects per slice, focal measures of ventilation defect volume and per cent ventilation volume [55] have been used in a handful of clinical studies (described later in this chapter), although there is no agreement on which measures and which of the two most commonly used gases, ^{3}He and ^{129}Xe, are the most suitable for longitudinal studies and for different therapeutic research questions.

Measures of ventilation/perfusion ratio at a global and regional level in the lungs are increasingly regarded as relevant in respiratory diseases [56]. SPECT measures perfusion using ^{99m}Tc-labelled macro-aggregated albumin and ventilation by inhalation of gaseous radioisotopes or radiolabelled particulate aerosols. Regional ventilation and perfusion can also be measured by ^{13}N-nitrogen washout PET, where ^{13}N-nitrogen dissolved in saline is injected intravenously and enters the lungs in proportion to blood flow [57]. Recent studies showing increased regional heterogeneity of perfusion in mild COPD *versus* healthy controls independent of changes in tissue density suggest that regional changes in pulmonary blood flow, perhaps due to inflammation, may precede parenchymal changes [58]. Consequently, measurements of regional perfusion could be a useful biomarker for early disease in the future, provided that their clinical relevance to the pathophysiology and progression of different respiratory diseases is confirmed, and acquisition techniques and quantitative measures are standardised.

Lung regeneration

Regenerative medicine, with cell-based treatments or drug molecules inducing cell and tissue regeneration, is at the centre of potential disease-modifying approaches, although no treatment has, as yet, shown such potential in respiratory diseases. CT densitometry as the primary end-point did not show any improvement in a recent randomised controlled trial of an oral γ-selective retinoid agonist administered for a year to 262 patients with severe α_1-ATD emphysema (the REPAIR trial) [59], in spite of preclinical evidence that retinoids promote structural repair in elastase models of emphysema [60]. Longer observation periods may be needed for CT imaging to detect morphological regenerative changes, as suggested by the authors. Future studies of regenerative treatments may benefit, particularly in the early phase of clinical development, from the use of multimodality techniques such as CT/PET or MRI/PET, which are sensitive to potential early signals of regeneration such as increased cell metabolism.

Imaging in preclinical development

Models of disease play a fundamental role in screening drug compounds in preclinical drug development. In proof-of-concept studies groups of animals are usually sacrificed at serial time points post-treatment to assess outcomes of interest, such as those based on bronchoalveolar lavage fluid analysis, histology and weighing of lungs. These analyses provide snapshots of different animals at one point in time, but do not allow assessment of intra-subject disease progression and of response to treatment over longer periods. Similarly, functional measurements on small animals, performed by whole-body plethysmography or invasively on artificially ventilated animals, are either inaccurate or unfeasible. The noninvasive nature of imaging modalities make them suitable for longitudinal studies in the same animal without the need for serial sacrifice, reducing the number of animals sacrificed and eliminating the inter-individual variation between animals [61].

The use of imaging in preclinical models of respiratory diseases has, until recently, been limited by the difficulties in achieving adequate spatial resolution for small animals and by the radiation dose of micro-CT that may induce changes in biological processes in small animals [62]. However, recent advances and the development of MRI, PET and SPECT scanners for small animals have increased the potential of imaging in studies in animal models, allowing real-time monitoring of the effects of noxious agents [63] and of

candidate new drugs on the lungs. Consensus on methodologies and measurements, and *ad hoc* studies pairing animal and human imaging cross-sectional and longitudinal findings are needed to exploit the possibility of using the same imaging measures across preclinical and clinical development. There is also a need for improved animal models that more accurately reflect clinical disease [1].

Lung imaging end-points in clinical trials

Randomised clinical trials for regulatory approval are based on the use of outcome measures, or end-points, to assess beneficial or adverse effect of drugs. Ideal end-points are considered to be those directly reflecting how patients feel, function or survive, *e.g.* by measuring morbidity (incidence of ill health) or mortality, and are also called "direct" or "hard" end-points [64]. Direct end-points are seldom feasible in practice because the low incidence of relevant events requires a long follow-up or a large sample size. Consequently, surrogate end-points are used. These are defined as "biomarkers intended to substitute for a clinical endpoint, expected to predict clinical benefit based on epidemiologic, therapeutic, pathophysiologic, or other scientific evidence" [65, 66]. In spite of limitations and controversies [67], most respiratory drugs have been authorised on evidence derived from surrogate end-points, mainly lung function measurements such as FEV1 and FVC, or exercise testing measures. Although widely available, easy to measure and validated, the sensitivity of the current surrogate end-points is questionable, particularly in early and limited disease [9], and has been blamed as one of the reasons for the high failure rates of clinical trials in the respiratory field [68, 69]. The following sections will explore the use of imaging-based measures as end-points in randomised clinical trials and longitudinal interventional studies.

Cystic fibrosis

Significant advances in CF care have been made in past few decades, leading to an increased median survival age from 23 years in 2002 [70] to 43.5 years in 2012 [71]. The recent development of treatments with disease modifying potential, such as CFTR (cystic fibrosis trans-membrane conductance regulator) modulators and gene therapy [72], has triggered debate about the most adequate end-point(s) to detect treatment effects in limited disease, such as in young children and in CFTR mutations with mild clinical phenotypes. Until now the use of FEV1 as a surrogate for mortality [73, 74] has been required by regulatory authorities as the primary end-point for drugs treating lung disease in CF, including the first CFTR modulators: ivacaftor (Kalydeco), which is authorised in adults and children above 6 years of age for the treatment of G551D (~4% of the CF population) and other gating mutations [75, 76]; and the combination of ivacaftor and lumacaftor (Orkambi), which targets F508D, the most prevalent mutation in CF [77]. However, children with CF under 6 years of age usually have spirometry within the normal range and FEV1 is not sufficiently sensitive to small changes, particularly those occurring at a regional level in the lungs. Similarly, registry data have shown a low frequency of pulmonary exacerbations in young children with CF [78], which may limit the use of the exacerbations as an end-point in this population [79].

A workshop recently held at the European Medicines Agency (EMA) discussed core outcome measures among which specific end-points could be chosen as primary or co-primary end-points for studies in CF [79]. Besides FEV1, lung function end-points included forced expiratory flow at 25–75% of FVC and lung clearance index, as the latter is

sensitive to early disease and measurable in children, including infants [80, 81]. The main imaging measures discussed during the workshop were chest CT scores, which have been used since the 1980s to assess bronchiectasis, bronchial wall thickening, mucus plugging, atelectasis/consolidation and air trapping in CF [7]. Findings of CT abnormalities in up to 80% of screened newborns with CF [82] support the sensitivity of CT scores in early disease. However, most scores are semi-quantitative in nature, and different agreement between scorers has been reported [83]. Automated quantitative measures are being developed, even though it is not completely clear which CT features, apart from bronchiectasis [84], could be the most informative in terms of clinically meaningful changes in longitudinal studies. The use of chest CT in clinical trials has been shown to be viable [85]; however, standardisation of the current techniques is required [86].

While the large scale application of CT to CF studies is limited by the cumulative dose of radiation, particularly in children, the use of MRI with hyperpolarised gases, as a non-ionising radiation technique, is increasing in CF. After initial studies demonstrating the feasibility of longitudinal ^{3}He MRI measurements in adults [87], and higher sensitivity to changes than FEV1 [88], a handful of studies have been performed in children [89]. Recently a small phase II study on G551D CF including four children (mean baseline FEV1 % predicted: 89.95%) showed a significant decrease in ^{3}He MRI total ventilation defect per cent, when used as primary end-point after treatment with ivacaftor [90], supporting the feasibility and informative value of MRI-based end-points in CF. Since quantitative MRI measures are, at present, poorly standardised, further studies are needed to confirm their sensitivity in larger populations and in different severities of CF, and to evaluate their usefulness in relation to other end-points.

COPD

In spite of the increasing burden of morbidity and mortality [91] no treatment has demonstrated a significant effect on disease progression in COPD [92]. On account of the physiological basis for the definition of COPD, the principles of drug development in COPD have for many years been derived from those used to develop drugs for asthma. The increasing evidence for COPD phenotypes that cannot be adequately reflected by lung function alone is urging redefinition of drug development programmes. Recent US Food and Drug Administration guidelines identify airway obstruction, symptom relief, exacerbations and the natural progression of the disease as relevant therapeutic targets in COPD [93]. End-points other than FEV1, the primary end-point in clinical trials for regulatory approval to date, are needed to capture the different dimensions of COPD; FEV1 has limited sensitivity in early disease and, in spite of its links to mortality [94], it correlates only weakly with clinical outcomes and health status [95].

CT- and MRI-based measures can detect morphological and functional abnormalities in ex-smokers with normal FEV1 and in COPD patients with modest lung function deterioration [96–98]. These measures also correlate with clinical end-points and mortality [99, 100]. The usefulness of CT lung density as a surrogate end-point was demonstrated in a randomised, double-blind, placebo-controlled, multicentre trial (RAPID) of human α1-proteinase inhibitor augmentation therapy (Respreeza) in emphysema related to severe α_1-ATD [41]. This trial was pivotal to the centralised marketing authorisation of Respreeza in the European Union. The primary end-point was the 15th percentile of the global lung density as a surrogate measure of emphysema progression [101]. The significant difference in CT densitometry between the treatment and placebo groups (annual rate of decrease (SE)

−1.45 (0.23) g·L^{-1} per year *versus* −2.19 (0.25) g·L^{-1}, respectively; p=0.03) (figure 3) confirmed signals from previous smaller trials [42]. The use of CT improved trial efficiency, as it had been previously calculated that up to 632 patients per arm over 3 years, or 449 over 5 years, would be needed to detect a treatment effect using FEV1 in similar studies [102].

While successful in α_1-ATD-related emphysema, a relatively homogeneous panacinar emphysema phenotype with a minimal airways disease component [103], the application of CT-based measures to clinical trials in non-α_1-ATD-related COPD has so far been more difficult. The reasons include the higher heterogeneity of emphysema morphology (panlobular, centrolobular and paraseptal) [104] and distribution (longitudinal and core-to-rind) [100, 105], as well as the contemporary presence in COPD of emphysema, airways disease and parenchymal attenuation/interstitial inflammation that dilutes signals detected by measures of global lung structure such as densitometry. The ECLIPSE study, which followed 2164 patients for over 3 years, demonstrated significant between-patient CT densitometry variability at baseline and over time [106]. Based on this, it was estimated that a minimum of 2500 patients per arm in a 3-year study would be needed for a treatment effect to be detected by densitometry end-points [106]. Measures of local lung density [107], standardisation of volume correction methods [108] and the creation of reference values for health and disease [109] may allow optimisation of the use of densitometry for the assessment drug effects. Interventional studies are needed to confirm the role of densitometry end-points in non-α_1-ATD-related COPD [110].

The low resolution of existing techniques for small airways and their abnormalities makes it difficult to disentangle the different morphological components of COPD in longitudinal studies, and is, to date, one of the most important limitations of the application of CT end-points in clincial tials in COPD. In addition, the current measures of airway wall thickness are only surrogates of airways remodelling [104]. Multicentre studies on large COPD cohorts are rapidly increasing the understanding of different CT-derived measures of airways disease, emphysema and air trapping, their interdependence, and their association with clinical manifestations and lung function measures [104, 111–113], paving the way for phenotype-targeted longitudinal studies [114]. Similarly, multidimensional CT imaging measures of emphysema, airways disease and parenchymal attenuation/interstitial inflammation and their variations over time [115], and multi-scale computational models

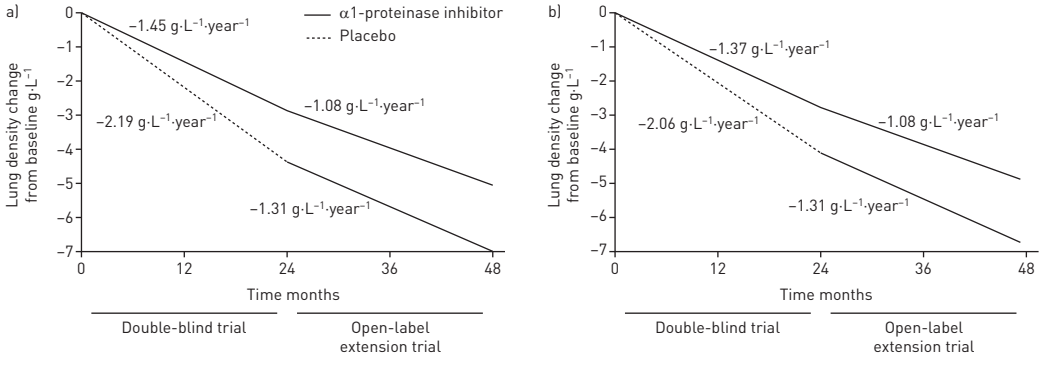

Figure 3. Rates of lung density decline at total lung capacity during the double-blind and open-label portions of the RAPID trial in a) all patients and b) patients completing the open label study only. Annual rates of decrease are presented on the graph. Reproduced from [41] with permission from the publisher.

of the airways combining information on morphology with functional equations providing indications of pressure, resistance, and flow, may be useful in longitudinal assessment. However, more studies are needed.

The use of MRI with hyperpolarised gases in COPD is increasingly seen as a way to overcome some of the limitations of CT or to complement CT measurement, as suggested by a recent phenotyping study where these two techniques were combined [116]. ^{3}He MRI readouts have allowed the identification of patients with mild and moderate COPD at risk of exacerbations [117], and their sensitivity has been demonstrated in longitudinal studies where changes in ^{3}He MRI ventilation defects occurred before changes in FEV1 [53] and in response to treatment [118]. More studies are needed to better understand the potential of MRI with hyperpolarised gases in clinical trials in COPD and to standardise and validate quantitative measurements. This also includes elucidating the relationship between MRI measurements and clinical outcomes in COPD, and the relevance of the information provided by different hyperpolarised gases in relation to airways obstruction and emphysema components [119].

Asthma

Anatomical and molecular imaging techniques allowing dynamic measurements [120, 121] have been used in a number of asthma studies. The use of functional MRI imaging with hyperpolarised gases is increasing for this purpose as compared with dynamic xenon-enhanced CT, due to its better safety [122]. To date, the use of imaging measures as end-points in asthma is not discussed in regulatory guidelines, due to limited knowledge of imaging changes in longitudinal studies, and of their clinical relevance. Ventilation defects with specific spatial heterogeneity patterns have been identified by ^{3}He MRI in asthma at the sub-segmental and segmental level [123, 124], seemingly persisting for several days to over a year in half of the subjects [125]. Ventilation defects have been reported to be more pronounced in severe asthma [126], and to be responsive to bronchodilator treatments [127]. Since ventilation defects have also been identified in asymptomatic patients, further studies are needed to assess their reproducibility and sensitivity before they can be assumed to be measures of early disease in asthma [120]. Measures of functional imaging applying computation of airways physiology to HRCT measurements also deserve further study for their potential to infer the behaviour of small airways in response to treatments [128].

Interstitial lung diseases

In spite of the high unmet need, the development of new drugs for interstitial lung diseases (ILDs), or diffuse parenchymal lung diseases, is slow and disappointing. The reasons include the complex pathogenesis and heterogeneous pathology of ILDs [129], suboptimal preclinical models and lack of sensitivity of FVC, the primary end-point in clinical trials [69]. The heterogeneity of ILDS has so far limited the possibility of using HRCT, essential for diagnostic purposes, to generate quantitative imaging measures for longitudinal studies. The possibility of monitoring clearly defined study populations based on HRCT phenotyping, even at single patient level, has been recently explored using a computational platform for near real-time characterisation and quantification of parenchymal patterns (CALIPER: Computer Aided Lung Informatics for Pathology Evaluation and Rating) by histogram signature mapping [130]. The volumetric and pathology parenchymal abnormalities were graphically represented in a glyph (similar to a radial space-filling plot), and used to follow disease progression in ILD (figure 4). Although at early experimental

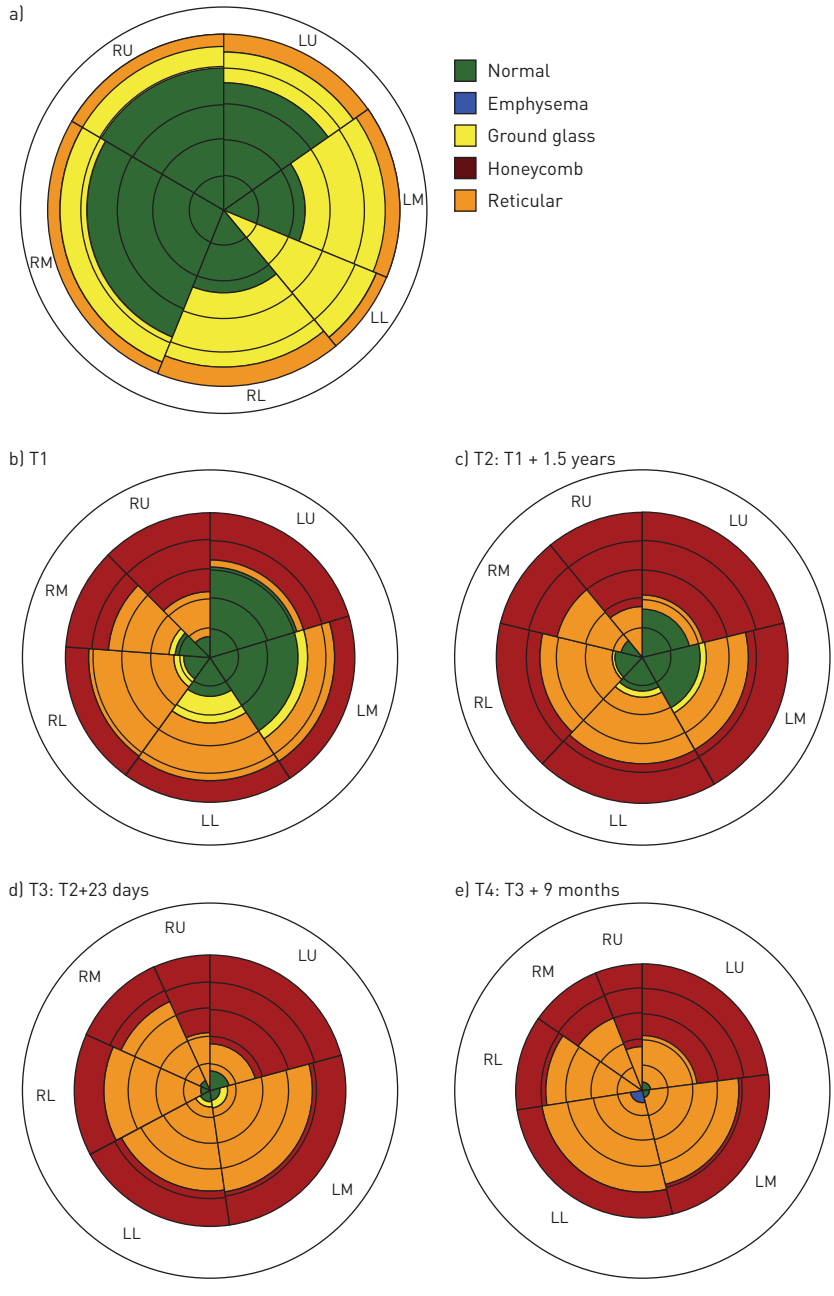

Figure 4. a) Glyph summarising the distribution of five characteristic CT patterns in the lung parenchyma. R/L: denotes the right and left lung; U/M/L: denotes upper, middle, and lower lung zones, respectively. The radius of the glyph is proportional to the lung volume. The black outer circle denotes the predicted total lung capacity of the subject. b–e) Patho-spatio-temporal glyph illustration for a subject with progressing fibrotic interstitial lung disease, showing decreasing lung volume (radius of the glyph) with respect to the outer black circle (predicted total lung capacity), loss of normal parenchyma, and an increasing proportion of honeycomb and reticular densities over time. Volume loss in the right lung is relatively greater than in the left. T refers to the time when the scans were recorded. Reproduced and modified from [130] with permission from the publisher.

stage, the use of personalised or clustered imaging maps in ILDs is an interesting approach that deserves further study.

Due to the relevance of activation and proliferation of fibroblasts and other cells in ILDs, molecular techniques may be useful to detect early signals of efficacy, or their lack thereof, of candidate drugs targeting these aspects, particularly in preclinical models and in early clinical phases. Recent studies in idiopathic pulmonary fibrosis showing ^{18}F-FDG-PET uptake by "normal" parenchymal areas on HRCT [131] suggest the sensitivity of this technique in detecting early changes in disease activity not yet apparent with other measurements.

The regulatory perspective

In spite of outstanding advances in imaging acquisition techniques and processing, the use of lung imaging in drug development is still limited. Several reasons may be held responsible for this. First, like any other biomarker, imaging measures need to be validated and qualified, and their fitness for purpose established in relation to the context of use. In animal models, validation mainly involves characterisation against invasive markers like bronchoalveolar lavage fluid and histology. For human use, the relationship between a prospective imaging biomarker and the pathophysiology of the target disease, and the biomarker's ability to detect disease progression and the effects by pharmacological agents of known activity need to be demonstrated to establish its validity as a surrogate end-point in clinical trials. In addition, the methodologies should be standardised, the measurements of the end-point must be reproducible and changes in the surrogate end-point should closely match changes in the true outcome [64].

The use of CT densitometry as a surrogate end-point in α_1-ATD represents an example where validation in the context of use has been facilitated by the relative homogeneity of imaging findings, resulting in increased trial efficiency in terms of duration and population size, the latter are particularly critical in the case of rare diseases. The main steps in the validation of CT densitometry in α_1-ATD are a good paradigm of a validation pathway, starting with establishing the relationship of the measure to emphysema morphometry [132], followed by cross-sectional and longitudinal correlations with clinical outcome measures and with FEV1, the traditionally used surrogate in emphysema. The correlation of CT densitometry measurements of α_1-ATD emphysema with exercise capacity, symptoms and mortality [42, 133–135] further supported the acceptance of densitometry as the primary end-point for regulatory approval [101].

The lack of standardisation and validation of most lung imaging measures limits their use and acceptability as surrogate end-points at the present time. Although the search for and the validation of biomarkers are lengthy and complex processes, assistance from regulatory authorities may accelerate the process by guiding the studies needed for validation and qualification [136, 137]. Regulators recommended that applicants trying to establish the effectiveness of drugs using imaging should consult regulatory agencies as early as possible [137]. In the case of radiation emitting techniques the risks of repeated radiation exposure need to be put in perspective with the level of information provided by specific imaging measures when envisioning their use as end-points in clinical trials, particularly if two different radiation emitting techniques are combined, *e.g.* PET/CT. In this respect MRI techniques present fewer ethical dilemmas, which may facilitate the use and regulatory acceptance of MRI measurements, whenever adequately standardised. Additional

considerations include feasibility and costs, and indeed gains in sensitivity and/or the identification of subpopulations particularly responsive to certain imaging end-points might need to be demonstrated for such end-points to be chosen as an alternative to traditional surrogate measures such as lung function.

Multi-institutional consortia and clinical trials networks play a major role in standardising imaging techniques and measurements, by generating consensus on core outcome measures in respiratory diseases and ensuring quality criteria for participating centres, particularly when technically demanding methods are to be used. While a number of initiatives in this direction already exist [130, 138], it is crucial that they incorporate the views of both radiologists and pulmonologists so as to harmonise the core elements of radiology, pathology and biomarker research to identify the most clinically relevant and reliable imaging measures in each specific disease and for specific biological questions.

Conclusions

There are still several challenges ahead for imaging to be effectively applied to drug development, and for realising the potential of some of the existing measures to be used as sensitive end-points in clinical trials for regulatory approval. In view of their use in drug development it cannot be assumed that all imaging readouts will be applicable to each situation; thus in certain indications it will be possible to use the same imaging measures both in animal models and humans, facilitating translational aspects [62], while in other cases different techniques may be needed for animal and human studies, and for different biological questions. For regulatory constraints and for other practical considerations including costs and feasibility, the most immediate applications of imaging are likely to be in proof-of-concept studies involving small patient populations rather than in large phase III clinical trials, until more studies are available that shed light on the advantages and limitations of each imaging measure for each proposed application. In order for imaging to be a game changer in drug development it is important that standardised acquisition protocols and validated quantitative readouts are developed, and that the initiative to reduce radiation exposure in longitudinal studies is taken. Collaborative efforts are needed to foster the development of imaging biomarkers that can benefit both diagnosis and drug development in respiratory medicine.

References

1. Barnes PJ, Bonini S, Seeger W, *et al.* Barriers to new drug development in respiratory disease. *Eur Respir J* 2015; 45: 1197–1207.
2. Arrowsmith J, Miller P. Trial watch: phase II and phase III attrition rates 2011–2012. *Nat Rev Drug Discov* 2013; 12: 569.
3. Washko GR, Parraga G, Coxson HO. Quantitative pulmonary imaging using computed tomography and magnetic resonance imaging. *Respirology* 2012; 17: 432–444.
4. Milne S, King GG. Advanced imaging in COPD: insights into pulmonary pathophysiology. *J Thorac Dis* 2014; 6: 1570–1585.
5. Mathew L, Kirby M, Etemad-Rezai R, *et al.* Hyperpolarized ^{3}He magnetic resonance imaging: preliminary evaluation of phenotyping potential in chronic obstructive pulmonary disease. *Eur J Radiol* 2011; 79: 140–146.
6. Woodhouse N, Wild JM, Paley MN, *et al.* Combined helium-3/proton magnetic resonance imaging measurement of ventilated lung volumes in smokers compared to never-smokers. *J Magn Reson Imaging* 2005; 21: 365–369.
7. Hughes D, Tiddens H, Wild JM. Lung imaging in cystic fibrosis. *Imaging Decisions MRI* 2009; 13: 28–37.
8. Lutey BA, Lefrak SS, Woods JC, *et al.* Hyperpolarized ^{3}He MR imaging: physiologic monitoring observations and safety considerations in 100 consecutive subjects. *Radiology* 2008; 248: 655–661.

9. Coxson HO, Leipsic J, Parraga G, *et al.* Using pulmonary imaging to move chronic obstructive pulmonary disease beyond FEV1. *Am J Respir Crit Care Med* 2014; 190: 135–144.
10. Zhang Y, Kundu B, Fairchild KD, *et al.* Synthesis of novel neutrophil-specific imaging agents for positron emission tomography (PET) imaging. *Bioorg Med Chem Lett* 2007; 17: 6876–6878.
11. Ohno Y, Hatabu H. Basics concepts and clinical applications of oxygen-enhanced MR imaging. *Eur J Radiol* 2007; 64: 320–328.
12. Coxson HO, Quiney B, Sin DD, *et al.* Airway wall thickness assessed using computed tomography and optical coherence tomography. *Am J Respir Crit Care Med* 2008; 177: 1201–1206.
13. Willmann JK, van Bruggen N, Dinkelborg LM, *et al.* Molecular imaging in drug development. *Nat Rev Drug Discov* 2008; 7: 591–607.
14. Suga K, Nishigauchi K, Kume N, *et al.* Dynamic pulmonary SPECT of xenon-133 gas washout. *J Nucl Med* 1996; 37: 807–814.
15. Chen DL, Schuster DP. Imaging pulmonary inflammation with positron emission tomography: a biomarker for drug development. *Mol Pharm* 2006; 3: 488–495.
16. Chen J, Moir D. An estimation of the annual effective dose to the Canadian population from medical CT examinations. *J Radiol Prot* 2010; 30: 131–137.
17. Grommes J, Soehnlein O. Contribution of neutrophils to acute lung injury. *Mol Med* 2011; 17: 293–307.
18. Gifford AM, Chalmers JD. The role of neutrophils in cystic fibrosis. *Curr Opin Hematol* 2014; 21: 16–22.
19. Bruijnzeel PL, Uddin M, Koenderman L. Targeting neutrophilic inflammation in severe neutrophilic asthma: can we target the disease-relevant neutrophil phenotype? *J Leukoc Biol* 2015; 98: 549–556.
20. Persson C, Uller L. Resolution of leucocyte-mediated mucosal diseases. A novel *in vivo* paradigm for drug development. *Br J Pharmacol* 2012; 165: 2100–2109.
21. Locke LW, Chordia MD, Zhang Y, *et al.* A novel neutrophil-specific PET imaging agent: cFLFLFK-PEG-64Cu. *J Nucl Med* 2009; 50: 790–797.
22. Chen DL, Schuster DP. Positron emission tomography with [18F]fluorodeoxyglucose to evaluate neutrophil kinetics during acute lung injury. *Am J Physiol Lung Cell Mol Physiol* 2004; 286: L834–L840.
23. Jones HA, Sriskandan S, Peters AM, *et al.* Dissociation of neutrophil emigration and metabolic activity in lobar pneumonia and bronchiectasis. *Eur Respir J* 1997; 10: 795–803.
24. Chen DL, Ferkol TW, Mintun MA, *et al.* Quantifying pulmonary inflammation in cystic fibrosis with positron emission tomography. *Am J Respir Crit Care Med* 2006; 173: 1363–1369.
25. Harris RS, Venegas JG, Wongviriyawong C, *et al.* 18F-FDG uptake rate is a biomarker of eosinophilic inflammation and airway response in asthma. *J Nucl Med* 2011; 52: 1713–1720.
26. Jobse BN, Johnson JR, Farncombe TH, *et al.* Evaluation of allergic lung inflammation by computed tomography in a rat model *in vivo*. *Eur Respir J* 2009; 33: 1437–1447.
27. Beckmann N, Tigani B, Ekatodramis D, *et al.* Pulmonary edema induced by allergen challenge in the rat: noninvasive assessment by magnetic resonance imaging. *Magn Reson Med* 2001; 45: 88–95.
28. Tigani B, Di Padova F, Zurbrügg S, *et al.* Effects of a mitogen-activated protein kinase inhibitor on allergic airways inflammation in the rat studied by magnetic resonance imaging. *Eur J Pharmacol* 2003; 482: 319–324.
29. Blé FX, Cannet C, Zurbruegg S, *et al.* Allergen-induced lung inflammation in actively sensitized mice assessed with MR imaging. *Radiology* 2008; 248: 834–843.
30. Coleman MT, Chen RY, Lee M, *et al.* PET/CT imaging reveals a therapeutic response to oxazolidinones in macaques and humans with tuberculosis. *Sci Transl Med* 2014; 6: 265ra167.
31. Chen RY, Dodd LE, Lee M, *et al.* PET/CT imaging correlates with treatment outcome in patients with multidrug-resistant tuberculosis. *Sci Transl Med* 2014; 6: 265ra166.
32. de Jong PA, Müller NL, Paré PD, *et al.* Computed tomographic imaging of the airways: relationship to structure and function. *Eur Respir J* 2005; 26: 140–152.
33. Hasegawa M, Nasuhara Y, Onodera Y, *et al.* Airflow limitation and airway dimensions in chronic obstructive pulmonary disease. *Am J Respir Crit Care Med* 2006; 173: 1309–1315.
34. Nakano Y, Muro S, Sakai H, *et al.* Computed tomographic measurements of airway dimensions and emphysema in smokers. Correlation with lung function. *Am J Respir Crit Care Med* 2000; 162: 1102–1108.
35. Orlandi I, Moroni C, Camiciottoli G, *et al.* Chronic obstructive pulmonary disease: thin-section CT measurement of airway wall thickness and lung attenuation. *Radiology* 2005; 234: 604–610.
36. Das CJ, Seith A, Mukhopadhyay S. Thoracic application of multi-detector CT. *Indian J Chest Dis Allied Sci* 2007; 49: 29–36.
37. Tanaka N, Matsumoto T, Miura G, *et al.* Air trapping at CT: high prevalence in asymptomatic subjects with normal pulmonary function. *Radiology* 2003; 227: 776–785.
38. Puderbach M, Eichinger M, Gahr J, *et al.* Proton MRI appearance of cystic fibrosis: comparison to CT. *Eur Radiol* 2007; 17: 716–724.
39. Lay JC, Stang MR, Fisher PE, *et al.* Airway retention of materials of different solubility following local intrabronchial deposition in dogs. *J Aerosol Med* 2003; 16: 153–166.

40. Blé FX, Schmidt P, Cannet C, *et al. In vivo* assessments of mucus dynamics in the rat lung using a Gd-Cy5.5-bilabeled contrast agent for magnetic resonance and optical imaging. *Magn Reson Med* 2009; 62: 1164–1174.
41. Chapman KR, Burdon JG, Piitulainen E, *et al.* Intravenous augmentation treatment and lung density in severe α1 antitrypsin deficiency (RAPID): a randomised, double-blind, placebo-controlled trial. *Lancet* 2015; 386: 360–368.
42. Dirksen A, Piitulainen E, Parr DG, *et al.* Exploring the role of CT densitometry: a randomised study of augmentation therapy in α1-antitrypsin deficiency. *Eur Respir J* 2009; 33: 1345–1353.
43. Stockley RA, Parr DG, Piitulainen E, *et al.* Therapeutic efficacy of α-1 antitrypsin augmentation therapy on the loss of lung tissue: an integrated analysis of 2 randomised clinical trials using computed tomography densitometry. *Respir Res* 2010; 11: 136.
44. Stoel BC, Putter H, Bakker ME, *et al.* Volume correction in computed tomography densitometry for follow-up studies on pulmonary emphysema. *Proc Am Thorac Soc* 2008; 5: 919–924.
45. Stoel BC, Bode F, Rames A, *et al.* Quality control in longitudinal studies with computed tomographic densitometry of the lungs. *Proc Am Thorac Soc* 2008; 5: 929–933.
46. Yuan R, Mayo JR, Hogg JC, *et al.* The effects of radiation dose and CT manufacturer on measurements of lung densitometry. *Chest* 2007; 132: 617–623.
47. Chen XJ, Hedlund LW, Möller HE, *et al.* Detection of emphysema in rat lungs by using magnetic resonance measurements of ^{3}He diffusion. *Proc Natl Acad Sci USA* 2000; 97: 11478–11481.
48. Peces-Barba G, Ruiz-Cabello J, Cremillieux Y, *et al.* Helium-3 MRI diffusion coefficient: correlation to morphometry in a model of mild emphysema. *Eur Respir J* 2003; 22: 14–19.
49. Woods JC, Choong CK, Yablonskiy DA, *et al.* Hyperpolarized ^{3}He diffusion MRI and histology in pulmonary emphysema. *Magn Reson Med* 2006; 56: 1293–1300.
50. Quirk JD, Lutey BA, Gierada DS, *et al. In vivo* detection of acinar microstructural changes in early emphysema with ^{3}He lung morphometry. *Radiology* 2011; 260: 866–874.
51. Diaz S, Casselbrant I, Piitulainen E, *et al.* Progression of emphysema in a 12-month hyperpolarized ^{3}He-MRI study: lacunarity analysis provided a more sensitive measure than standard ADC analysis. *Acad Radiol* 2009; 16: 700–707.
52. Stavngaard T, Søgaard LV, Batz M, *et al.* Progression of emphysema evaluated by MRI using hyperpolarized ^{3}He (HP ^{3}He) measurements in patients with α-1-antitrypsin (A1AT) deficiency compared with CT and lung function tests. *Acta Radiol* 2009; 50: 1019–1026.
53. Kirby M, Mathew L, Wheatley A, *et al.* Chronic obstructive pulmonary disease: longitudinal hyperpolarized ^{3}He MR imaging. *Radiology* 2010; 256: 280–289.
54. Fain S, Schiebler ML, McCormack DG, *et al.* Imaging of lung function using hyperpolarized helium-3 magnetic resonance imaging: review of current and emerging translational methods and applications. *J Magn Reson Imaging* 2010; 32: 1398–1408.
55. Parraga G, Mathew L, Etemad-Rezai R, *et al.* Hyperpolarized ^{3}He magnetic resonance imaging of ventilation defects in healthy elderly volunteers: initial findings at 3.0 Tesla. *Acad Radiol* 2008; 15: 776–785.
56. Vidal Melo MF, Layfield D, Harris RS, *et al.* Quantification of regional ventilation-perfusion ratios with PET. *J Nucl Med* 2003; 44: 1982–1991.
57. Harris RS, Winkler T, Tgavalekos N, *et al.* Regional pulmonary perfusion, inflation, and ventilation defects in bronchoconstricted patients with asthma. *Am J Respir Crit Care Med* 2006; 174: 245–253.
58. Vidal Melo MF, Winkler T, Harris RS, *et al.* Spatial heterogeneity of lung perfusion assessed with ^{13}N PET as a vascular biomarker in chronic obstructive pulmonary disease. *J Nucl Med* 2010; 51: 57–65.
59. Stolk J, Stockley RA, Stoel BC, *et al.* Randomised controlled trial for emphysema with a selective agonist of the γ-type retinoic acid receptor. *Eur Respir J* 2012; 40: 306–312.
60. Massaro GD, Massaro D. Retinoic acid treatment abrogates elastase-induced pulmonary emphysema in rats. *Nat Med* 1997; 3: 675–677.
61. Labiris NR. Small Animal Imaging using CT, SPECT, PET and MRI. ERS Research Seminar. Optimising models for human lung diseases and drug development Paris, France – October 3–5, 2013. Available from: www.ers-education.org/events/research-seminars/optimising-models-for-human-lung-diseases-and-drug-development,-paris-2013.aspx
62. van Echteld CJ, Beckmann N. A view on imaging in drug research and development for respiratory diseases. *J Pharmacol Exp Ther* 2011; 337: 335–349.
63. Jobse BN, Rhem RG, Wang IQ, *et al.* Detection of lung dysfunction using ventilation and perfusion SPECT in a mouse model of chronic cigarette smoke exposure. *J Nucl Med* 2013; 54: 616–623.
64. Biomarkers Definitions Working Group. Biomarkers and surrogate endpoints: preferred definitions and conceptual framework. *Clin Pharmacol Ther* 2001; 69: 89–95.
65. Burzykowski T, Molenberghs G, Buyse M. The Evaluation of Surrogate Endpoints. New York, Springer-Verlag, 2005.
66. Temple RJ. A regulatory authority's opinion about surrogate endpoints. *In*: Nimmo WS, Tucker GT, eds. Clinical Measurement in Drug Evaluation. New York, J Wiley, 1995; pp. 3–22.
67. Burzykowski T. Surrogate endpoints: wishful thinking or reality? *Stat Methods Med Res* 2008; 17: 463–466.

68. Raghu G, Collard HR, Anstrom KJ, *et al.* Idiopathic pulmonary fibrosis: clinically meaningful primary endpoints in phase 3 clinical trials. *Am J Respir Crit Care Med* 2012; 185: 1044–1048.
69. Fregonese L, Eichler I. The future of the development of medicines in idiopathic pulmonary fibrosis. *BMC Med* 2015; 13: 239.
70. The Cystic Fibrosis Trust UK. The CF Registry Annual Data Report 2004. www.cysticfibrosis.org.uk/media/82427/CR_Annual_Data_Report_2004_06.pdf Date last updated: November 2014.
71. The Cystic Fibrosis Trust UK. UK Cystic Fibrosis Registry Annual Data Report 2012. www.cysticfibrosis.org.uk/media/316760/Scientific%20Registry%20Review%202012.pdf Date last updated: September 2013.
72. Brodlie M, Haq IJ, Roberts K, *et al.* Targeted therapies to improve CFTR function in cystic fibrosis. *Genome Medicine* 2015; 7: 101.
73. Kerem E, Reisman J, Corey M, *et al.* Prediction of mortality in patients with cystic fibrosis. *N Engl J Med* 1992; 326: 1187–1191.
74. Corey M, Edwards L, Levison H, *et al.* Longitudinal analysis of pulmonary function decline in patients with cystic fibrosis. *J Pediatr* 1997; 131: 809–814.
75. European Medicines Agency. EMA/473279/2012. Committee for Medicinal Products for Human Use (CHMP) Assessment report. Kalydeco (ivacaftor). www.ema.europa.eu/docs/en_GB/document_library/EPAR_-_Public_assessment_report/human/002494/WC500130766.pdf Date last accessed: Jan 8, 2016. Date last updated: December 15, 2105.
76. European Medicines Agency. EMA/523198/2014. Committee for Medicinal Products for Human Use (CHMP) Assessment report. Kalydeco International non-proprietary name: IVACAFTOR. www.ema.europa.eu/docs/en_GB/document_library/EPAR_-_Assessment_Report_-_Variation/human/002494/WC500172933.pdf Date last accessed: Jan 8, 2016.
77. European Medicines Agency. EMA/CHMP/617813/2015. Committee for Medicinal Products for Human Use (CHMP) Summary of opinion1 (initial authorisation) Orkambi lumacaftor/ivacaftor. www.ema.europa.eu/docs/en_GB/document_library/Summary_of_opinion_-_Initial_authorisation/human/003954/WC500194120.pdf Date last accessed: Jan 8, 2016.
78. Cystic Fibrosis Foundation. Patient Registry 2014 Annual Data Report. Bethesda, Cystic Fibrosis Foundation, 2015. www.cff.org/2014_CFF_Annual_Data_Report_to_the_Center_Directors.pdf/
79. European Medicines Agency. EMA/769571/2012. Human Medicines Development and Evaluation. Report of the workshop on endpoints for cystic fibrosis clinical trials. European Medicines Agency, London, 27–28 September 2012. www.ema.europa.eu/docs/en_GB/document_library/Report/2012/12/WC500136159.pdf Date last accessed: Jan 8, 2016. Date last updated: November 29, 2012.
80. Subbarao P, Stanojevic S, Brown M, *et al.* Lung clearance index as an outcome measure for clinical trials in young children with cystic fibrosis. A pilot study using inhaled hypertonic saline. *Am J Respir Crit Care Med* 2013; 188: 456–460.
81. Kent L, Reix P, Innes JA, *et al.* Lung clearance index: evidence for use in clinical trials in cystic fibrosis. *J Cyst Fibros* 2014; 13: 123–138.
82. Sly PD, Brennan S, Gangell C, *et al.* Lung disease at diagnosis in infants with cystic fibrosis detected by newborn screening. *Am J Respir Crit Care Med* 2009; 180: 146–152.
83. de Jong PA, Ottink MD, Robben SGF, *et al.* Pulmonary disease assessment in cystic fibrosis: comparison of CT scoring systems and value of bronchial and arterial dimension measurements. *Radiology* 2004; 231: 434–439.
84. VanDevanter DR, Konstan MW. Outcome measures for clinical trials assessing treatment of cystic fibrosis lung disease. *Clin Investig* 2012; 2: 163–175.
85. Tepper LA, Utens EM, Caudri D, *et al.* Impact of bronchiectasis and trapped air on quality of life and exacerbations in cystic fibrosis. *Eur Respir J* 2013; 42: 371–379.
86. Tiddens HA, Puderbach M, Venegas JG, *et al.* Novel outcome measures for clinical trials in cystic fibrosis. *Pediatr Pulmonol* 2014; 50: 302–315.
87. Donnelly LF, MacFall JR, McAdams HP, *et al.* Cystic fibrosis: combined hyperpolarized ^{3}He-enhanced and conventional proton MR imaging in the lung–preliminary observations. *Radiology* 1999; 212: 885–889.
88. Mentore K, Froh DK, de Lange EE, *et al.* Hyperpolarized HHe 3 MRI of the lung in cystic fibrosis: assessment at baseline and after bronchodilator and airway clearance treatment. *Acad Radiol* 2005; 12: 1423–1429.
89. van Beek EJR, Hill C, Woodhouse N, *et al.* Assessment of lung disease in children with cystic fibrosis using hyperpolarized 3-Helium MRI: comparison with Shwachman score, Chrispin-Norman score and spirometry. *Eur Radiol* 2007; 17: 1018–1024.
90. European Medicines Agency. EMA/534823/2015 Committee for Medicinal Products for Human Use (CHMP). Assessment report for paediatric studies submitted according to Article 46 of the Regulation (EC) No 1901/2006. Kalydeco, international non-proprietary name: ivacaftor. www.ema.europa.eu/docs/en_GB/document_library/EPAR_-_Assessment_Report_-_Variation/human/002494/WC500191974.pdf Date last accessed: Jan 8, 2016. Date last updated: July 23, 2015.

91. Murray CJ, Atkinson C, Bhalla K, *et al.* The state of US health, 1990–2010: burden of diseases, injuries, and risk factors. *JAMA* 2013; 310: 591–608.
92. Vestbo J, Hurd SS, Agustí AG, *et al.* Global strategy for the diagnosis, management, and prevention of chronic obstructive pulmonary disease: GOLD executive summary. *Am J Respir Crit Care Med* 2013; 187: 347–365.
93. U.S. Department of Health and Human Services, Food and Drug Administration Center for Drug Evaluation and Research (CDER). Guidance for Industry Chronic Obstructive Pulmonary Disease: Developing Drugs for Treatment. Draft Guidance. www.fda.gov/downloads/drugs/guidancecomplianceregulatoryinformation/guidances/ucm071575.pdf Date last accessed: Jan 8, 2016. Date last updated: November, 2007.
94. Almagro P, Martinez-Camblor P, Soriano JB, *et al.* Finding the best thresholds of FEV1 and dyspnea to predict 5-year survival in COPD patients: the COCOMICS study. *PLoS One* 2014; 9: e89866.
95. Jones PW. Health status and the spiral of decline. *COPD* 2009; 6: 59–63.
96. Regan EA, Lynch DA, Curran-Everett D, *et al.* Clinical and radiologic disease in smokers with normal spirometry. *JAMA Intern Med* 2015; 175: 1539–1549.
97. Xia Y, Guan Y, Fan L, *et al.* Dynamic contrast enhanced magnetic resonance perfusion imaging in high-risk smokers and smoking-relate COPD: correlations with pulmonary function tests and quantitative compute tomography. *COPD* 2014; 11: 510–520.
98. Bafadhel M, Umar I, Gupta S, *et al.* The role of CT scanning in multidimensional phenotyping of COPD. *Chest* 2011; 140: 634–642.
99. Han MK, Kazerooni EA, Lynch DA, *et al.* Chronic obstructive pulmonary disease exacerbations in the COPDGene study: associated radiologic phenotypes. *Radiology* 2011; 261: 274–282.
100. Martinez FJ, Foster G, Curtis JL, *et al.* Predictors of mortality in patients with emphysema and severe airflow obstruction. *Am J Respir Crit Care Med* 2006; 173: 1326–1334.
101. European Medicines Agency. EMA/CHMP/76739/2015. Committee for Medicinal Products for Human Use (CHMP) Assessment report: Respreeza. International non-proprietary name: human α1-proteinase inhibitor. www.ema.europa.eu/docs/en_GB/document_library/EPAR_-_Public_assessment_report/human/002739/WC500193617.pdf Date last accessed: Jan 8, 2016. Date last updated: June 25, 2015.
102. Dirksen A, Dijkman JH, Madsen F, *et al.* A randomized clinical trial of α_1-antitrypsin augmentation therapy. *Am J Respir Crit Care Med* 1999; 160: 1468–1472.
103. Fregonese L, Stolk J. Hereditary α-1-antitrypsin deficiency and its clinical consequences. *Orphanet J Rare Dis* 2008; 3: 16.
104. Smith BM, Austin JH, Newell JD Jr, *et al.* Pulmonary emphysema subtypes on computed tomography: the MESA COPD study. *Am J Med* 2014; 127: 94.e7–23.
105. Nakano Y, Coxson HO, Bosan S, *et al.* Core to rind distribution of severe emphysema predicts outcome of lung volume reduction surgery. *Am J Respir Crit Care Med* 2001; 164: 2195–2199.
106. Coxson HO, Dirksen A, Edwards LD, *et al.* The presence and progression of emphysema in COPD as determined by CT scanning and biomarker expression: a prospective analysis from the ECLIPSE study. *Lancet Respir Med* 2013; 1: 129–136.
107. Staring M, Bakker ME, Stolk J, *et al.* Towards local progression estimation of pulmonary emphysema using CT. *Med Phys* 2014; 41: 021905.
108. Lynch DA, Al-Qaisi ML. Quantitative computed tomography in chronic obstructive pulmonary disease. *J Thorac Imag* 2013; 28: 284–290.
109. Hoffman EA, Ahmed FS, Baumhauer H, *et al.* Variation in the percent of emphysema-like lung in a healthy, nonsmoking multiethnic sample. The MESA lung study. *Ann Am Thorac Soc* 2014; 11: 898–907.
110. Come CE, Washko GR. Editorial: CT scanning in COPD – Is it time to move on? *J COPD F* 2015; 2: 201–203.
111. Han MK, Kazerooni EA, Lynch DA, *et al.* Chronic obstructive pulmonary disease exacerbations in the COPDGene study: associated radiologic phenotypes. *Radiology* 2011; 261: 274–282.
112. Tho NV, Ryujin Y, Ogawa E, *et al.* Relative contributions of emphysema and airway remodelling to airflow limitation in COPD: consistent results from two cohorts. *Respirology* 2015; 20: 594–601.
113. Lynch DA, Austin JH, Hogg JC, *et al.* CT-definable subtypes of chronic obstructive pulmonary disease: a statement of the Fleischner Society. *Radiology* 2015; 277: 192–205.
114. Nordenmark LH, Taylor R, Jorup C. Feasibility of computed tomography in a multicenter COPD trial: a study of the effect of AZD9668 on structural airway changes. *Adv Ther.* 2015; 32: 548–566.
115. Boudewijn IM, Postma DS, Telenga ED, *et al.* Effects of ageing and smoking on pulmonary computed tomography scans using parametric response mapping. *Eur Respir J* 2015; 46: 1193–1196.
116. Kirby M, Pike D, Sin DD, *et al.* COPD: do imaging measurements of emphysema and airway disease explain symptoms and exercise capacity? *Radiology* 2015; 277: 872–880.
117. Kirby M, Pike D, Coxson HO, *et al.* Hyperpolarized ^{3}He ventilation defects used to predict pulmonary exacerbations in mild to moderate chronic obstructive pulmonary disease. *Radiology* 2014; 273: 887–896.
118. Kirby M, Mathew L, Heydarian M, *et al.* Chronic obstructive pulmonary disease: quantification of bronchodilator effects by using hyperpolarized ^{3}He MR imaging. *Radiology* 2011; 261: 283–292.

119. Kirby M, Svenningsen S, Kanhere N, *et al.* Pulmonary ventilation visualized using hyperpolarized helium-3 and xenon-129 magnetic resonance imaging: differences in COPD and relationship to emphysema. *J Appl Physiol (1985)* 2013; 114: 707–715.
120. Castro M, Fain SB, Hoffman EA, *et al.* Lung imaging in asthmatic patients: the picture is clearer. *J Allergy Clin Immunol* 2011; 128: 467–478.
121. Bousquet J, Jeffery PK, Busse WW, *et al.* Asthma. From bronchoconstriction to airways inflammation and remodeling. *Am J Respir Crit Care Med* 2000; 161: 1720–1745.
122. Mayo J. Radiation dose issues in longitudinal studies involving computed tomography. *Proc Am Thorac Soc* 2008; 5: 934–939.
123. Fain SB, Gonzalez-Fernandez G, Peterson ET, *et al.* Evaluation of structure-function relationships in asthma using multidetector CT and hyperpolarized He-3 MRI. *Acad Radiol* 2008; 15: 753–762.
124. Tgavalekos NT, Tawhai M, Harris RS, *et al.* Identifying airways responsible for heterogeneous ventilation and mechanical dysfunction in asthma: an image functional modeling approach. *J Appl Physiol (1985)* 2005; 99: 2388–2397.
125. de Lange EE, Altes TA, Patrie JT, *et al.* Changes in regional airflow obstruction over time in the lungs of patients with asthma: evaluation with ^{3}He MR imaging. *Radiology* 2009; 250: 567–575.
126. de Lange EE, Altes TA, Patrie JT, *et al.* Evaluation of asthma with hyperpolarized helium-3 MRI: correlation with clinical severity and spirometry. *Chest* 2006; 130: 1055–1062.
127. Svenningsen S, Kirby M, Starr D, *et al.* Hyperpolarized ^{3}He and ^{129}Xe MRI: differences in asthma before bronchodilation. *J Magn Reson Imaging* 2013; 38: 1521–1530.
128. Burrowes KS, De Backer J, Smallwood R, *et al.* Multi-scale computational models of the airways to unravel the pathophysiological mechanisms in asthma and chronic obstructive pulmonary disease (AirPROM). *Interface Focus* 2013; 3: 20120057.
129. Cottin V, Nunes H, Mouthon L, *et al.* Combined pulmonary fibrosis and emphysema syndrome in connective tissue disease. *Arthritis Rheum* 2011; 63: 295–304.
130. Bartholmai BJ, Raghunath S, Karwoski RA, *et al.* Quantitative computed tomography imaging of interstitial lung diseases. *J Thorac Imaging* 2013; 28: 298–307.
131. Win T, Thomas BA, Lambrou T, *et al.* Areas of normal pulmonary parenchyma on HRCT exhibit increased FDG PET signal in IPF patients. *Eur J Nucl Med Mol Imaging* 2014; 41: 337–342.
132. Müller NL, Staples CA, Miller RR, *et al.* "Density mask". An objective method to quantitate emphysema using computed tomography. *Chest* 1988; 94: 782–787.
133. Parr DG, Stoel BC, Stolk J, *et al.* Validation of computed tomographic lung densitometry for monitoring emphysema in α1-antitrypsin deficiency. *Thorax* 2006; 61: 485–490.
134. Dowson LJ, Guest PJ, Hill SL, *et al.* High-resolution computed tomography scanning in α1-antitrypsin deficiency: relationship to lung function and health status. *Eur Respir J* 2001; 17: 1097–1104.
135. Dawkins PA, Dowson LJ, Guest PJ, *et al.* Predictors of mortality in α1-antitrypsin deficiency. *Thorax* 2003; 58: 1020–1026.
136. European Medicines Agency. Biomarkers. www.ema.europa.eu/ema/index.jsp?curl=pages/special_topics/general/general_content_000349.jsp Date last accessed: Jan 8, 2016.
137. US Food and Drug Administration. Biomarker qualification program. www.fda.gov/Drugs/DevelopmentApprovalProcess/DrugDevelopmentToolsQualificationProgram/ucm284076.htm Date last accessed: Jan 8, 2016.
138. Ross JC, Miller JV, Turner WD, *et al.* An analysis of early studies released by the Lung Imaging Database Consortium (LIDC). *Acad Radiol* 2007; 14: 1382–1388.

Disclaimer: The views presented are those of the author and should not be understood or quoted as being made on behalf of the European Medicines Agency or its scientific committees.

Disclosures: None declared.

Acknowledgements: The author would like to thank Benedetta Polsinelli (trainee, European Medicines Agency) for help with referencing.

Chapter 16

Risks of thoracic CT

Jonathan G. Goldin and Katrina Beckett

One of the quintessential applications of CT is the detection and evaluation of thoracic pathology. CT examinations of the chest are likely to increase with the advent of screening for lung cancer and the increasing role of CT in parenchymal disease assessments and cardiac CT applications. There are risks associated with undergoing CT related to radiation dose and the use of iodine based contrast agents. The actual risk is a subject of much discussion and debate. At all times, the risk–benefit of a CT study should be considered in terms of the information likely to be derived and the benefit to the patient *versus* the risks albeit very small. With the advent of novel CT reconstruction techniques, dual-source CT machines and attention to basic principles of CT scanning, the radiation dose of CT is set to be lowered dramatically in the future. In this chapter we will focus on the two main sources of risk related to the use of iodinated contrast agents and radiation dose.

Of all the imaging modalities available CT offers the best spatial and contrast resolution of thoracic structures and pathology. It has also found increasing application beyond traditional visualisation of manifestations of disease in the quantitation of both structure and even function. These is also increasing application of the technology as a screening tool for detection of lung cancer in healthy at risk individuals. It is estimated that 50% of the CT scans performed are scans of the body, of which the majority include scans of the thorax. With the advent of screening for lung cancer and coronary artery calcium and the increased focus on developing novel treatments for cardiopulmonary disease there has been an increase in the use of thoracic CT. We briefly review the risks associated with thoracic CT scans performed in symptomatic patients in clinical practice and clinical trials as well as the increasing use of thoracic CT in screening of asymptomatic individuals. We focus on the two main sources of risk related to the use of iodinated contrast agents and radiation dose.

Iodinated contrast safety

Contrast-enhanced studies are used to delineate mediastinal pathology, and evaluate the pulmonary arteries, aorta and heart. Ideally, contrast agents should be injected and rapidly eliminated from the body without additional effects on the patient [1]. Although the currently available contrast agents are generally considered to be safe, their use is not completely without risk. Adverse effects vary from minor physiological and mild allergic-like reactions to rare but severe and life-threatening events. Although the

Division of Thoracic Radiology, David Geffen School of Medicine at UCLA, Los Angeles, CA, USA.

Correspondence: Jonathan Goldin, Division of Thoracic Radiology, David Geffen School of Medicine at UCLA, Los Angeles, CA, USA. E-mail: jgoldin@mednet.ucla.edu

Copyright ©ERS 2015. Print ISBN: 978-1-84984-065-1. Online ISBN: 978-1-84984-066-8. Print ISSN: 2312-508X. Online ISSN: 2312-5098.

prevalence of these reactions is low [2], reactions to contrast media do occur, and thus, information about adverse reactions including how to reduce their incidence and to treat them is of considerable importance. It is optimal to identify patients likely to experience adverse effects due to contrast agents prior to performing the examination.

Iodinated contrast material crosses the human placenta and has been demonstrated in fetal tissues; however, to our knowledge, teratogenic effects and hypothyroidism have not been reported [3]. Despite these low theoretical risks, mostly regarding fetal thyroid development, avoiding intravenous contrast agents in pregnant patients is prudent when possible. Only a small percentage of iodinated contrast material is excreted in breast milk and absorbed by the infant [4], and to our knowledge, there have been no reported cases of direct toxicity, allergic sensitivity or reaction to these agents [3]. Although it is therefore not necessary to stop breastfeeding, depending on personal preference, mothers may still choose to express and discard breast milk for 12–24 h after they are given contrast agents.

Metformin is an oral hyperglycaemic agent used to treat patients with noninsulin-dependent diabetes mellitus with the potential to precipitate lactic acidosis, which is seen most often in patients with several comorbid factors such as renal and cardiovascular disease and can occur in the presence of *i.v.* contrast administration. For this reason, it is recommended to temporarily discontinue the medication when the CT is performed and withhold it for a period of time, often 48 h subsequent to the CT. It is prudent to ensure renal function is normal before re-instituting the medication [5]. Patients with untreated Graves' disease and/or multinodular goitre and thyroid autonomy, the elderly, and those living in areas where dietary iodine deficiency is common should be identified, and the risk of inducing thyrotoxicosis through excess iodine absorption should be reduced [1]. Use of iodinated contrast agents should be avoided immediately before planned radioactive iodine imaging or therapy, because the iodine may reduce radioactive iodine uptake. Consultation with an endocrinologist may be beneficial before administration of an *i.v.* contrast agent.

Intravenous access should be evaluated before the administration of contrast media. This includes verifying that the catheter is appropriate for the injection, confirming venous return, performing a saline flush and performing a test injection with a power injector [6]. Use of a 20-gauge or larger catheter in an antecubital or other large forearm vein is recommended for flow rates of at least 3 $mL \cdot s^{-1}$, with flow rates no greater than 1.5 $mL \cdot s^{-1}$ for peripherally placed or 22-gauge catheters [7]. The use of deep brachial *i.v.* catheters should be avoided because of the markedly higher relative risk of extravasation [8]. Central venous [9] and peripherally inserted central catheters [10] can also be used safely, after verifying that they are power injector compatible to the manufacturer's recommended pressure limits.

Injection site complications

Extravasation occurs when contrast material escapes the vascular lumen and infiltrates the interstitial tissue during injection, this process has a reported incidence of less than 1% [11]. Some patients are asymptomatic, while others report swelling, tightness, stinging or burning pain, and may demonstrate oedema, erythema or tenderness at the injection site [12]. Prompt recognition and evaluation by a physician is required to reduce the chance and severity of injury. Currently, there is no agreement among physicians on the best treatment of *i.v.* contrast

agent extravasation. Physicians may recommend elevating the affected extremity or site and applying a warm or cold compress [13]. Severe complications of extravasation include compartment syndrome, skin ulceration and tissue necrosis; however, these are uncommon [11]. Conservative treatment is recommended in most cases, with surgical consultation reserved for patients who develop progressive pain or swelling, decreased capillary refill, a change in sensation (*e.g.* paraesthesia), skin ulceration, or blistering [14]. Few patients require surgical intervention [14, 15]. All patients with extravasation should be monitored for a period that is as long as the responsible physician considers sufficient and should be discharged with instructions to watch for symptoms indicating a need for surgical evaluation.

Adverse reactions to contrast agents

Patient history of a previous severe reaction to a contrast agent increases the overall risk of a subsequent reaction by approximately five- to six-fold [16]. Patients with a history of allergies and those with features of atopy, such as asthma, dermatitis and urticaria, have an approximately three- to six-fold increased risk of severe reaction to contrast media [17]. Although minor allergies are common and do not appear to increase overall risk, a history of severe atopy, such as multiple allergies or a prior major anaphylactic response, should heighten concern before administration of contrast material. Patients with well-controlled asthma may not be at increased risk [18]. Use of non-ionic contrast agents may reduce the prevalence of recurrent adverse reactions to 5% [19]. Reducing the volume and osmolality of the contrast agent is also suggested in patients with severe cardiac failure.

Renal complications of contrast

Contrast-induced nephropathy is described as "a sudden deterioration in renal function (*i.e.* acute kidney injury) following the recent intravascular administration of contrast media in the absence of another nephrotoxic event" [20]. However, the validity of this condition and the potential clinical effects are unknown [21, 22]. Newhouse and RoyChoudhury [23] showed that controlling for potentially confounding medical conditions that may cause acute kidney injury is difficult, and patients who were not exposed to iodinated contrast material showed rates of acute kidney injury similar to those of patients with contrast-induced nephropathy after CT [24]. Several large studies have concluded that contrast-induced nephropathy and contrast agent-independent acute kidney injury are not significantly different and may be clinically indistinguishable when adjusted for patient risk factors [25–27]. This suggests that greater flexibility can be considered when using renal function estimates to determine the appropriateness of iodinated contrast agents; however, the effect of correcting hypovolaemic states before injection of contrast material and the adverse effects of its absence have not been studied. Even so, the validity of contrast-induced nephropathy is clinical dogma in many practices and radiologists should have a good understanding of the issue. A questionnaire designed to elicit a history of renal disorders as well as additional risk factors for contrast media-induced nephropathy (renal disease, renal surgery, proteinuria, diabetes mellitus, hypertension, gout and recent nephrotoxic drugs) is suggested at the time of referral for imaging in order to obtain a measurement of estimated glomerular filtration rate or serum creatinine in at risk patients prior to preforming the exam [1]. No proven benefit has been found for the use of renal protective agents such as *N*-acetylcysteine, sodium bicarbonate, diuretics and theophylline.

Radiation dose

Ionising radiation is the basis of image generation in CT. There are many measures of radiation dose in use. These measures include the CT dose index (CTDI) and the dose length product (DLP), which are scanner reported metrics of dose for a given CT scan but do not directly translate into the actual dose received by a patient or organ. The CTDI is the average absorbed dose to a specific homogeneous, cylindrical plastic phantom, along the longitudinal axis, from a series of contiguous exposures. It is measured in milligray (mGy) or rad [28]. Although a popular measure of machine output, it is in fact not directly related to actual patient or organ dose or risk [29]. Patients are not standard, cylindrical or homogeneous in nature, and thus, CTDI tends to overestimate dose for large patients and underestimate dose for small patients. The DLP represents the integrated dose (CTDI) multiplied by the scan length (number of slices×slice width). CTDI and DLP are thus not true measures of patient dose. Neither considers patient size, age, sex or the specific organs radiated. A patient that has twice the DLP or CTDI of another does not necessarily receive a greater dose. For a given CTDI, a smaller patient will receive more dose than a larger patient by virtue of their smaller mass. DLP underestimates dose considerably for examinations where there is no table movement. By contrast, CTDI overestimates dose for stationary examinations by a factor of approximately two.

Other units of dose for patients, physicists and radiation biologists to consider include absorbed dose and effective dose. Absorbed dose describes the amount of radiation energy deposited in matter, per unit mass of the matter. Absorbed dose, measured in gray ($1\ Gy=1\ J{\cdot}kg^{-1}$), is volume independent and does not specify how much of the volume is radiated but rather how much radiation is absorbed by the volume. Thus a CT scan of only single slice may have similar absorbed (local) dose to a scan comprised of multiple contiguous slices as more tissue mass is being radiated. In contrast, a CT scan of multiple series or phases that re-radiates a given tissue results in more exposure to that tissue. In an effort to assess risk we may want to determine dose to a specific organ or the whole body effective dose. Effective dose is a metric that attempts to represent stochastic risk (*e.g.* carcinogenesis) by summing the products of all organ doses and their organ weighting factors, the latter representing the biological sensitivity to radiation of each organ exposed. With certain assumptions effective dose can be estimated from DLP by multiplying by coefficients specific for given body regions. These coefficients have been determined from Monte Carlo dose modelling assuming a geometric hermaphrodite patient model of standard size. More precise estimates of effective dose can be made with specific knowledge of scanner model and the size and shape of patient scanned. Actual organ dose is a measure of dose within a given tissue or organ, and is typically calculated or measured in anthropomorphic phantoms [30].

As an added perspective the approximate effective dose (mSv) for a round trip flight from New York to London is approximately 0.1 mSv, background dose due to natural radiation exposure is 3 mSv per year and exposure on international space station is 170 mSv per year. The radiation doses to particular organs from any given CT study depend on a number of factors. The most important factors are: the number of scans (called series or phases) performed as part of the CT examination or study; the tube current and scanning time in milliampere-seconds (mAs); patient chest size; the length of coverage; the scan pitch (the degree of overlap between adjacent CT slices); the tube voltage at the peak kilovoltage (kVp); and the specific design of the scanner being used [28]. Most of these are potentially

under the control of the operator and so dose can always be tailored to the study and patient [31]. With a decrease in dose on conventional platforms there is always an increase in the image noise [32]. With the advent of new technology there are new potential ways to decrease dose and reduce the amount of image noise. The most promising of these techniques is the introduction of iterative reconstruction.

Radiation dose risks

While the dose from a single chest study can be low (table 1), the dose can creep up in advanced protocols (*e.g.* cardiac protocols) or when multiple series are performed in a given CT study (*e.g.* prone and supine imaging). In addition, repeat studies as part of clinical care or in the setting of a clinical trial increases the total patient dose considerably. Assuming a CT chest study results in an effective dose of 3–7 mSv or a breast dose of 20 mGy and the patient has two to three studies a year as part of a clonal study the yearly effective dose would be 9–21 mSv and the total breast dose would be 60 mGy. At these doses there is a small risk for radiation-induced cancers [33].

The pathobiology of radiation effects is due to the high energy of ionising radiation, which can overcome the binding energy of water molecules to create hydroxyl radicals. These radicals can result in DNA strand breaks or damage to the bases forming the nucleotide backbone. The vast majority of these repair spontaneously, but an occasional DNA double strand break does not repair causing point mutations, gene fusions and translocations, which, in turn, can lead to cancer. Radiation-induced carcinogenesis is considered to follow a stochastic or probabilistic risk model, so that risk increases with dose. Notably, it is currently believed there is no safe threshold below which these effects do not occur and as such any small amount of radiation has some associated risk. Note that while the probability of the stochastic effect may increase with dose, the severity of the effect is independent of dose, thus a cancer deriving from 1 Gy of radiation dose is no more aggressive that one arising from 10 mGy. This gives rise to the underlying principle in radiation in which the lowest dose possible should always be used, known as the ALARA (As Low As Reasonably Achievable) principle.

No prospective epidemiological studies of the cancer risks associated with diagnostic CT have, to date, been completed. The basis for estimates of radiation-induced cancer come from simulations using two cohorts exposed to radiation in very different ways to the way in which patients are subjected to CT doses. The most often quoted is based on analyses of the

Table 1. Organ doses from CT scanning during common chest examinations

Study type	Lung dose mGy	Breast dose mGy	Effective dose mSv
Posteroanterior chest radiograph	0.12	0.03	0.03
Lateral chest radiograph	0.11	0.19	0.07
Chest CT (non-contrast)	20	16	7.4
Low-dose chest CT (screening)	2.7	2.2	1.0
CT pulmonary embolus	22	17	8.2
Cardiac CT (non-contrast calcium screening)	3.8	3.3	1.4
Retrospectively ECG-gated CT angiography coronary	78	67	28

Hiroshima atomic bomb survivors [34]. The population who survived was exposed to a uniform dose of radiation across all body parts, unlike CT in which there is non-uniform exposure limited to the body regions scanned. Among the 25 000 survivors, who were estimated to have received low radiation doses between 5 and 150 mSv (with a mean dose of 40 mSv in this cohort), there was an increased overall risk for cancer development [35–37]. In a more recent study of 400 000 nuclear industry workers [38, 39], who were exposed to an average dose of approximately 20 mSv, a significant association was reported between the radiation dose and mortality from cancer. These simulation models suggest a much greater risk for cancer in paediatric and young adult populations with a marked reduction in risk in older adults, particularly woman in whom breast exposure has the highest risk. The paediatric and young adult populations are more at risk because their individual organs are more radiosensitive and they have more remaining years in which a cancer can develop.

By calculating the organ doses involved (*e.g.* lung, breast and thyroid) and applying organs specific cancer incidence or mortality data derived from studies of atomic-bomb survivors, it is possible to provide an estimate of the cancer risks associated with a particular CT scan protocol [40]. It is important to calculate not only the dose for a given CT chest study but to include all CT studies that are acquired within the same year. In the setting of a clinical trial the scheduled scans should be added to any historic scans acquired in the same year. For chest CT, the most radiosensitive organs are the lungs and glandular breast [41–43]. Risk of breast cancer may correlate with doses less than 100 mGy, and risk of lung cancer may correlate with doses as low as 100 mGy [18]. The lifetime risk of death due to lung cancer per million patients exposed to 10 mSv is estimated as 250 per million patients at 20 years of age decreasing to 220 per million patients at 6 years of age [34].

It is important to recognise that these two approaches are based on many assumptions that are debated in the CT physics community. A recent review pointed out that there is no convincing epidemiological evidence of increased cancer incidence or mortality at low doses (<100 mSv) [44]. A number of US and international radiation protection organisations, including the United Nations Scientific Committee on the Effects of Atomic Radiation, the International Commission on Radiological Protection, the National Council on Radiation Protection and Measurements, the Health Physics Society, the American Association of Physicists in Medicine and the Académie Nationale de Médecine (French National Academy of Medicine), have repeatedly cautioned that reliable estimates of cancer risk cannot be attributed to doses below 100 mSv. In its 2012 report to the United Nations General Assembly, the United Nations Scientific Committee on the Effects of Atomic Radiation specifically noted that an increase in the incidence of health effects in populations cannot be attributed to exposure to radiation doses at levels that are typical of global background radiation levels, that is, 1–10 mSv per year, which is the same as in most medical imaging examinations [44].

Reducing radiation dose

It is important to realise that, as many factors can influence dose, radiation dose can be lowered by attention to proper techniques. These include correct patient positioning [45], and scanning only the required area of interest without any penalty to image quality [46] or missing pertinent anatomy. Scan parameters such as tube current and peak energy can be adjusted for dose reduction. The radiation dose is proportional to the tube current if all other parameters are the same. Reducing the tube current is the most usual way to lower dose. Other factors, including gantry rotation time and helical pitch, also influence the effective current–time product. Scanning with a high pitch lowers radiation dose because of

the shorter scan duration. This is often useful in patients undergoing chest CT who are already breathless and cannot hold their breath. Dual-source CT allows pitch to be increased to almost 2.5 times greater than in single-source scanners [47].There is a penalty with respect to image quality that needs to be considered, which is worse in larger patients.

Most imaging centres currently use tube current-modulated CT acquisition to decrease radiation exposure in patients. Tube current modulation is an automated exposure mechanism that adjusts tube output (mA) to compensate for differences in patient size or attenuation. It allows compensation for patient size across the axis of the patient. A study by ANGEL *et al.* [48] in female patients undergoing chest CT, found not only that the glandular breast, which is considered a peripheral organ, and lung, which is considered a large medially situated organ, receive similar doses during chest CT, both with and without tube current modulation, but also that the dose reduction from tube current modulation is similar for the two organs, especially with respect to patient size. Tube current-modulated CT acquisition was found to reduce the radiation dose to these tissues, especially in smaller patients (perimeter <122 cm). These radiation dose reductions depend on patient size and can result in organ dose reductions of up to 64% in our patient population. However, larger patients may not receive a decrease in dose with tube current modulation.

Lowering the tube potential (kVp) from 120 to 100 kV can reduce the dose by up to 30%. A major advantage of low kVp scanning is that it is closer to the k-absorption edge of iodine and therefore there is greater discrimination between the iodine and non-iodine structures, improving diagnostic yield in pulmonary angiography [49, 50]. It has been reported that by changing to 350 mg·mL^{-1} from the usual 300 mg·mL^{-1} of iodine contrast one can reduce kVp to 60 kV to obtain equivalent sensitivity and reduce the dose by 70% [50]. This also allows a reduction in contrast load with an added safety benefit with respect to lowering nephrotoxicity. Lowering kVp is more complex than lowering current, particularly in larger patients [51, 52].

Most recently there has been a focus on image reconstruction. Dose can be reduced with improvements in the current back filtered techniques. However, the introduction of iterative reconstruction techniques is more promising as these techniques allow a reduction in dose, and also reduce the image noise associated with the reduced dose when using conventional methods. Iterative reconstruction takes into account the effect of the scanner's physical properties in its calculation of projection data from a reconstructed image. Projection data are corrected by comparison of the calculated and measured projection data. Multiple iterations of the process are re-performed to reach the final reconstruction images. The effect of iterative reconstruction has been most thoroughly investigated in the setting of chest imaging [53, 54]. Radiation dose of chest CT can be reduced using this novel reconstruction response [55–57]. Use of iterative reconstruction is reported to result in changes in the appearance of texture on CT images. While studies have shown little impact on visual diagnosis, the impact on quantitative CT analysis needs to be further studied. To date, most quantitative measures and thresholds for detection of emphysema, lung fibrosis and nodules have been made with filtered back projection. Studies that directly compare these measures using raw data reconstructed by both filtered back projection and iterative reconstruction are required.

Conclusion

Thoracic CT is a common radiological procedure and the number of examinations is likely to increase due to the advent of lung cancer screening, increased interest in diffuse lung

disease, and cardiac applications. CT examinations expose patients to an increased level of radiation, although the actual risk of this additional dose is not clearly understood and its relevance continues to be debated. Nevertheless, the clinical necessity of each examination should be carefully considered. With the newer iterative reconstruction techniques, dual-source scanners and attention to "as low as reasonably achievable" (ALARA) principles, the radiation dose of CT is projected to be dramatically reduced in the relatively near future. Iodinated contrast is generally considered to be safe and beneficial in medical imaging; however, when contrast is indicated, the patient should be screened prior to its administration to ensure adequate renal function and the absence of underlying risk factors that could lead to a contrast reaction. Immediate recognition and appropriate treatment of a contrast reaction is crucial to prevent escalation to severe or even life-threatening events.

References

1. Thomsen HS. Contrast media safety: an update. *Eur J Radiol* 2011; 80: 77–82.
2. Katayama H, Yamaguchi K, Kozuka T, *et al.* Adverse reactions to ionic and nonionic contrast media: a report from the Japanese Committee on the Safety of Contrast Media. *Radiology* 1990; 175: 621–628.
3. Wang PI, Chong ST, Kielar AZ, *et al.* Imaging of pregnant and lactating patients: part 1, evidence-based review and recommendations. *AJR Am J Roentgenol* 2012; 198: 778–784.
4. Bettmann MA. Frequently asked questions: iodinated contrast agents. *Radiographics* 2004; 24: Suppl. 1, S3–S10.
5. Bailey CJ, Turner RC. Metformin. *N Engl J Med* 1996; 334: 574–579.
6. American College of Radiology. ACR–SPR practice parameter for the use of intravascular contrast media. www.acr.org/~/media/536212D711524DA5A4532407082C89BA.pdf Date last updated: 2014. Date last accessed: February 17, 2015.
7. ACR Committee on Drugs and Contrast Media. ACR manual on contrast media: version 10.1. www.acr.org/Quality-Safety/Resources/Contrast-Manual Date last updated: 2014. Date last accessed: December, 2015.
8. Hardie AD, Kereshi B. Incidence of intravenous contrast extravasation: increased risk for patients with deep brachial catheter placement from the emergency department. *Emerg Radiol* 2014; 21: 235–238.
9. Herts BR, Cohen MA, McInroy B, *et al.* Power injection of intravenous contrast material through central venous catheters for CT: *in vitro* evaluation. *Radiology* 1996; 200: 731–735.
10. Coyle D, Bloomgarden D, Beres R, *et al.* Power injection of contrast media *via* peripherally inserted central catheters for CT. *J Vasc Interv Radiol* 2004; 15: 809–814.
11. Wang CL, Cohan RH, Ellis JH, *et al.* Frequency, management, and outcome of extravasation of nonionic iodinated contrast medium in 69,657 intravenous injections. *Radiology* 2007; 243: 80–87.
12. Cohan RH, Ellis JH, Garner WL. Extravasation of radiographic contrast material: recognition, prevention, and treatment. *Radiology* 1996; 200: 593–604.
13. Sum W, Ridley LJ. Recognition and management of contrast media extravasation. *Australas Radiol* 2006; 50: 549–552.
14. Sbitany H, Koltz PF, Mays C, *et al.* CT contrast extravasation in the upper extremity: strategies for management. *Int J Surg* 2010; 8: 384–386.
15. Tonolini M, Campari A, Bianco R. Extravasation of radiographic contrast media: prevention, diagnosis, and treatment. *Curr Probl Diagn Radiol* 2012; 41: 52–55.
16. Morcos SK. Review article: acute serious and fatal reactions to contrast media: our current understanding. *Br J Radiol* 2005; 78: 686–693.
17. Morcos SK, Thomsen HS. Adverse reactions to iodinated contrast media. *Eur Radiol* 2001; 11: 1267–1275.
18. Bettmann MA, Heeren T, Greenfield A, *et al.* Adverse events with radiographic contrast agents: results of the SCVIR Contrast Agent Registry. *Radiology* 1997; 203: 611–620.
19. Siegle RL, Halvorsen RA, Dillon J, *et al.* The use of iohexol in patients with previous reactions to ionic contrast material. A multicenter clinical trial. *Invest Radiol* 1991; 26: 411–416.
20. Nash K, Hafeez A, Hou S. Hospital-acquired renal insufficiency. *Am J Kidney Dis* 2002; 39: 930–936.
21. Kayibanda JF, Hiremath S, Knoll GA, *et al.* Does intravenous contrast-enhanced computed tomography cause acute kidney injury? Protocol of a systematic review of the evidence. *Syst Rev* 2014; 3: 94.
22. Katzberg RW, Newhouse JH. Intravenous contrast medium-induced nephrotoxicity: is the medical risk really as great as we have come to believe? *Radiology* 2010; 256: 21–28.
23. Newhouse JH, RoyChoudhury A. Quantitating contrast medium-induced nephropathy: controlling the controls. *Radiology* 2013; 267: 4–8.
24. Newhouse JH, Kho D, Rao QA, *et al.* Frequency of serum creatinine changes in the absence of iodinated contrast material: implications for studies of contrast nephrotoxicity. *AJR Am J Roentgenol* 2008; 191: 376–382.

25. Davenport MS, Cohan RH, Ellis JH. Contrast media controversies in 2015: imaging patients with renal impairment or risk of contrast reaction. *AJR Am J Roentgenol* 2015; 204: 1174–1181.
26. McDonald RJ, McDonald JS, Bida JP, *et al.* Intravenous contrast material-induced nephropathy: causal or coincident phenomenon? *Radiology* 2013; 267: 106–118.
27. McDonald JS, McDonald RJ, Carter RE, *et al.* Risk of intravenous contrast material-mediated acute kidney injury: a propensity score-matched study stratified by baseline-estimated glomerular filtration rate. *Radiology* 2014; 271: 65–73.
28. McNitt-Gray MF. AAPM/RSNA physics tutorial for residents: topics in CT. Radiation does in CT. *Radiographics* 2002; 22: 1541–1553.
29. Brenner DJ. It is time to retire the computed tomography does index (CTDI) for CT quality assurance and dose optimization. For the proposition. *Med Phys* 2006; 33: 1189–1190.
30. Groves AM, Owen KE, Courtney HM, *et al.* 16-Detector multislice CT: dosimetry estimation by TLD measurement compared with Monte Carlo simulation. *Br J Radiol* 2004; 77: 662–665.
31. Paterson A, Frush DP, Donnelly LF. Helical CT of the body: are settings adjusted for pediatric patients? *AJR Am J Roentgenol* 2001; 176: 297–301.
32. Martin CJ, Sutton DG, Sharp PF. Balancing patient dose and image quality. *Appl Radiat Isot* 1999; 50: 1–19.
33. Brenner DJ, Doll R, Goodhead DT, *et al.* Cancer risks attributable to low doses of ionizing radiation: assessing what we really know. *Proc Natl Acad Sci USA* 2003; 100: 13761–13766.
34. Committee to Assess Health Risks from Exposure to Low Levels of Ionizing Radiation. Health Risks from Exposure to Low Levels of Ionizing Radiation – BEIR VII phase 2. Washington, National Academies Press, 2006.
35. Preston DL, Shimizu Y, Pierce DA, *et al.* Studies of mortality of atomic bomb survivors. Report 13: solid cancer and noncancer disease mortality: 1950–1997. *Radiat Res* 2003; 160: 381–407.
36. Pierce DA, Preston DL. Radiation-related cancer risks at low does among atomic bomb survivors. *Radiat Res* 2000; 154: 178–186.
37. Preston DL, Ron E, Tokuoka S, *et al.* Solid cancer incidence in atomic bomb survivors: 1958–1998. *Radiat Res* 2007; 168: 1–64.
38. Cardis E, Vrijheid M, Blettner M, *et al.* The 15-country collaborative study of cancer risk among radiation workers in the nuclear industry: estimates of radiation-related cancer risks. *Radiat Res* 2007; 167: 396–416.
39. Cardis E, Vrijheid M, Blettner M, *et al.* Risk of cancer after low doses of ionizing radiation: retrospective cohort study in 15 countries. *BMJ* 2005; 331: 77.
40. Brenner D, Elliston C, Hall E, *et al.* Estimated risks of radiation-induced fatal cancer from pediatric CT. *AJR Am J Roentgenol* 2001; 176: 289–296.
41. Hurwitz LM, Yoshizumi TT, Reiman RE, *et al.* Radiation dose to the female breast from 16-MDCT body protocols. *AJR Am J Roentgenol* 2006; 186: 1718–1722.
42. Mayo JR, Aldrich J, Muller NL. Radiation exposure at chest CT: a statement of the Fleischner Society. *Radiology* 2003; 228: 15–21.
43. The 2007 recommendations of the International Commission on Radiological Protection: ICRP publication 103. *Ann ICRP* 2007; 37: 1–332.
44. McCollough CH, Bushberg JT, Fletcher JG, *et al.* Answers to common questions about the use and safety of CT scans. *Mayo Clinic Proc* 2015; 90: 1380–1392.
45. Gudjonsdottir J, Svensson JR, Campling S, *et al.* Efficient use of automatic exposure control systems in computed tomography requires correct patient positioning. *Acta Radiol* 2009; 50: 1035–1041.
46. Campbell J, Kalra MK, Rizzo S, *et al.* Scanning beyond anatomic limits of the thorax in chest CT: findings, radiation does, and automatic tube current modulation. *AJR Am J Roentgenol* 2005; 185: 1525–1530.
47. Lell M, Hinkmann F, Anders K, *et al.* High-pitch electrocardiogram-triggered computed tomography of the chest: initial results. *Invest Radiol* 2009; 44: 728–733.
48. Angel E, Yaghmai J, Jude CM, *et al.* Monte Carlo simulations to assess the effects of tube current modulation on breast dose for multidetector CT. *Phys Med Biol* 2009; 54: 497–512.
49. Kalva SP, Sahani DV, Hahn PF, *et al.* Using the K-edge to improve contrast conspicuity and to lower radiation does with a 16-MDCT: a phantom and human study. *J Comput Assist Tomogr* 2006; 30: 391–397.
50. Matsuoka S, Hunsaker AR, Gill RR, *et al.* Vascular enhancement and image quality of MDCT pulmonary angiography in 400 cases: comparison of standard and low kilovoltage settings. *AJR Am J Roentgenol* 2009; 192: 1651–1656.
51. Herzog C, Mulvihill DM, Nguyen SA, *et al.* Pediatric cardiovascular CT angiography: radiation dose reduction using automatic anatomic tube current modulation. *AJR Am J Roentgenol* 2008; 190: 1232–1240.
52. Kim MJ, Park CH, Choi SJ, *et al.* Multidetector computed tomography chest examinations with low-kilovoltage protocols in adults: effect on image quality and radiation dose. *J Comput Assist Tomogr* 2009; 33: 416–421.
53. Willemink MJ, Leiner T, de Jong PA, *et al.* Iterative reconstruction techniques for computed tomography part 2: initial results in dose reduction and image quality. *Eur Radiol* 2013; 23: 1632–1642.
54. Leipsic J, Nguyen G, Brown J, *et al.* A prospective evaluation of dose reduction and image quality in chest CT using adaptive statistical iterative reconstruction. *AJR Am J Roentgenol* 2010; 195: 1095–1099.

55. Pontana F, Duhamel A, Pagniez J, *et al.* Chest computed tomography using iterative reconstruction *vs* filtered back projection (part 2): image quality of low-dose CT examinations in 80 patients. *Eur Radiol* 2011; 21: 636–643.
56. Yanagawa M, Honda O, Kikuyama A, *et al.* Pulmonary nodules: effect of adaptive statistical iterative reconstruction (ASIR) technique on performance of a computer-aided detection (CAD) system-comparison of performance between different-dose CT scans. *Eur J Radiol* 2012; 81: 2877–2886.
57. Xu Y, He W, Chen H, *et al.* Impact of the adaptive statistical iterative reconstruction technique on image quality in ultra-low-dose CT. *Clin Radiol* 2013; 68: 902–908.

Disclosures: None declared.

Safety issues in MRI

Alex Frydrychowicz[1,2] and Oliver Wieben[3,4]

In general, MRI is a safe method if used with indispensable precaution. The long-term effects of a static magnetic field on human tissue at typical diagnostic field strengths are not known, but the topic remains somewhat controversial due to sparse scientific data [1, 2]. However, there are additional possible sources of risk, which have the potential for harm if the technique is used imprudently. Continuous technician training, consistent patient instruction, society recommendations [3] and safety protocols implemented by vendors have contributed to the wide acceptance and mostly uneventful use of MRI.

This chapter aims to introduce the clinician to the relevant safety issues and precautionary measures relating to MRI use. The necessary physical background will be introduced for each safety topic. Also, perceived uncertainties by referring physicians and staff regarding medical implants and the use of contrast agents will be addressed. Consequently, this chapter should enable physicians to confidently triage and advise patients scheduled for MRI.

Widely used MRI relies on the presence of a strong static magnet field, mostly in the range of 1.5–3 T, usually cooled to supraconducting temperatures by liquid helium. Fast switching, much smaller magnetic field gradients are used for spatial encoding, and high-frequency electromagnetic waves in the range of radio waves are used for signal generation and detection. Typically, the patient is placed on an examination table with the body region of interest positioned in the centre of the magnet, where the homogeneitiy of the magnetic field and image quality are best. The scanner bore is typically 60–70 cm in diameter, and 120–170 cm but up to 270 cm in length. Coils are required to exite the magnetic resonance spins and to measure their signal. These coils function as antennae and come in different shapes: some are built into the magnet housing; small volume coils such as head coils or flexible surface coils, are positioned close to the volume of interest.

Although there is no known long-term effect of a short exposure to static magentism on human tissue [1], there is still room for scientific effort and debate [4]. There may be transient effects, such as transitory vertigo, when human tissue is quickly brought into a scanner with a high field strength.

In the following sections, we will discuss typical topics of interest that are relevant to the safety of patients, staff and other personnel, such as maintenance workers or firefighters.

[1]Clinic for Radiology and Nuclear Medicine, University Hospital Schleswig-Holstein, Lübeck, Germany. [2]University of Lübeck, Lübeck, Germany. [3]Dept of Radiology, University of Wisconsin–Madison, Wisconsin Institutes for Medical Research, Madison, WI, USA. [4]Dept of Medical Physics, University of Wisconsin–Madison, Wisconsin Institutes for Medical Research, Madison, WI, USA.

Correspondence: Alex Frydrychowicz, Clinic for Radiology and Nuclear Medicine, University Hospital Schleswig-Holstein, Campus Lübeck, 23562 Lübeck, Germany. E-mail: alex.frydrychowicz@uksh.de

Copyright ©ERS 2015. Print ISBN: 978-1-84984-065-1. Online ISBN: 978-1-84984-066-8. Print ISSN: 2312-508X. Online ISSN: 2312-5098.

Table 1 presents a checklist for safe and informative patient guidance; some of the areas presented in the table are discussed in this chapter.

Accoustic noise

Accoustic noise, often in the form of knocking, tapping or chirping, originates from the gradient coils. In the presence of a static magnetic field, rapidly switching magnetic field gradients used for spatial encoding induce "Lorentz" forces with an accoustic effect induced by vibrations of the gradient coils in their housing. The intensity of the generated noise varies and can reach 80–115 dB [5], similar to that of a jackhammer at 1-m distance. At the most extreme, scientifically generated noise pressure levels of 131 dB have been reported [6]. Patients are therefore at risk of temporary or permanent hearing damage. Hence, hearing protection must be worn by anyone within the MRI suite during the exam. In addition to earplugs, headsets enable both communication and noise reduction because the noise also affects the communication between staff and patients, which constitutes a risk if the patient is not well. The patient also needs to be instructed on the use of the call button to establish communication.

Of special concern are exams in the paediatric population as children in particular may not tolerate the noise well. Although the topic applies to the adult population as well, children in particular may not tolerate the noise well. Reluctance for or refusal of the MRI exam during the scan will ultimately cause movement that may render the entire study non-diagnostic. It is therefore necessary to weigh the risk of anaesthesia against the necessity and benefit of MRI. Alternatively, noise reduction can be achieved by using spin echo (SE) rather than gradient echo (GRE) sequences, active noise-cancellation strategies, or, more effectively, by applying specifically designed "silent" sequences that are based on slowly varying gradient waveforms. However, such sequences are not currently available on all scanner platforms or for all desired image contrasts.

Ferromagnetic attraction

Ferromagnetic attraction is the most obvious and the most dreaded safety issue in MRI. Compared with the Earth's magnetic field, clinically used 1.5 T scanners exhibit an approximately 30 000 times stronger magnetic field. Consequently, even metal with small ferromagnetic constituents will ultimately be attracted to the scanner. Ferromagnetic parts within the patient or objects brought to the MRI suite (paper clips, stethoscopes, scissors, *etc.*) may turn into threatening projectiles. Personnel who have not been instructed on the invisible magnetic forces may accidently position items such as fire extinguishers or protective respirators near to the magnet. To avoid serious incidents, training and consistent screening of patients and personell, as well as warning signs at the entrance to the MRI suite are warrented. The American College of Radiology (ACR) has suggested that four marked saftey zones should be implemented as part of responsible practise standards. Zone 1 has a fringe field of <5 Gauss (0.5 mT) and is freely accessible to the public. Zone 2 is the interface between the public area in zone 1 and the strictly controlled zones 3 and 4; access is limited to screened patients and personnel. Zone 3 is the area near the room in which the magnet is housed, where the magnetic field, the gradients and the radiofrequency field are strong enough to present a physical hazard to unscreened subjects. Zone 4 is the MRI magnet room. Nowadays, the so-called "5-Gauss line" (0.5 mT) can be found in all scanner suites demarcating the area around the MRI scanner as especially hazardous [3].

Table 1. Checklist for safe and informative patient guidance

At patient interview:	
Prior MRI study? Problems?	Indicative of but not exclusive regarding potential problems.
Medical implants?	Need to be identified. Check for magnetic resonance compatibility with the vendor or at http://www.mrisafety.com
Retained metallic bodies? Former accident or injury with foreign body?	Need to be characterised. Consider a radiograph for confirmation/exclusion. When in doubt, do not admit the patient to the magnetic resonance suite or scanner.
Allergies?	Known allergies to contrast material; estimate the general predisposition.
Renal disease?	History, creatinine clearance and/or estimated glomerular filtration rate per local clinical standard.
Claustrophobia?	Discuss or test before requesting MRI. If the patient is claustrophobic, consider sedation/narcosis.
Possible or known pregnancy? Breastfeeding?	Scarce literature on risk–benefit of MRI; contrast material should be discussed in-depth with the patient.
During patient preparation:	
Remove all metal objects	Check for keys, hearing aids, jewellery, smart phones, clothing with metal components, hair pins, removable piercings, *etc.*
Position inside the scanner	Check the scanner setup and ensure the region of interest is placed in the centre.
Coil attachment and fixation	Coils (plastic mattresses) should be loosely fixed to the body.
Hearing protection	Protection must be worn for noise reduction and to aid communication.
Call button	Explain that this is used for communication with staff during the scan, and if the patient is uncomfortable, sick or when heating occurs.
The need to lie still and follow instructions	Body motion deteriorates most imaging sequences. Breath-holding or no-swallow commands may be necessary.
Duration of scan	Typically between 20–45 min, rarely more than 60 min.
Informed consent regarding:	
Noise	Usually harmless when ear plugs and/or headphones are used.
Warmth	Warmth can occur and is typical.
Vertigo	Temporary vertigo has been reported when entering high-field scanners.
Nerve stimulation	Tingling and muscle twitching should not but can happen; it is not usually dangerous. Brain or cardiac stimulation will not happen.
Heating and burning	Rare adverse events; avoid crossing legs and arms, and direct skin contact with MRI components.
Contrast agent	Rare adverse events (allergy-like, idiosyncratic). Discuss: nephrogenic fibrosis as a rare adverse event; the potential of irritation and necrosis in cases of contrast agent extravasation.

Note: when in doubt, patients or personnel should not be admitted to the MRI room.

In the rare event of a life-threatening attraction of a ferromagentic item, the magnetism can be terminated by "quenching" the magnet, *i.e.* rapidly releasing the cooling helium and ramping down the magnetic field. With the sudden increase of resistance in the copper loops, the wires lose their superconducting properties and the magnetic field decreases. However, this comes at the price of an at least temporarily dysfunctional MRI scanner and considerable maintenance costs, so it should only be used in otherwise unavoidable situations.

Stimulation of nerves or muscles

Time-varying magentic field gradients induce electrical fields within the patient and, at the right amplitude, may lead to nerve or muscle stimulation, which manifest as tingling sensations and muscle fibre contractions, but rarely pain. Although cardiac stimulation can theoretically be induced, such incidents require exceedingly strong gradient fields and changes that are greater than clinically used [7, 8]. The gradients are controlled in such a way that their effects stay below established levels of nerve stimulation for most patients, which can be further reduced for more sensitive patients. Of special concern are retained or implanted wires, in the brain or heart, for example. As voltage can be induced in wires by varying magnetic fields, excitation of the affected organ can lead to serious adverse events.

Heating and burning

Some of the power of the radiofrequency pulses used to induce the resonance effect is dissipated as heat within the patient. The dosimetric correlate is referred to as the specific absorption rate (SAR), given in $W \cdot kg^{-1}$, which expresses the body mass normalised degree by which radiofrequency power is transformed into heat. For MRI, the limits of specific body regions have been established and SAR has been divided into three categories, shown in table 2.

Today, scanner software estimates a whole-body averaged SAR, taking into account the weight of the patient, the properties of the chosen sequence (pulse form, duration, repetitions, *etc.*) as well as the coil used. During operation, the use of sequence protocols at a higher SAR level is possible with operator confirmation and should be kept as short as necessary. Special attention is warranted in the presence of implants (discussed further later).

While general warming effects on the body usually stay within <1°C of SAR limits, locally focussed heating can develop quickly and has the potential to severely harm the patient.

Table 2. Specific absorption rate limits as defined by the International Electrotechnical Commission (IEC)

SAR level	Body $W \cdot kg^{-1}$		Local $W \cdot kg^{-1}$			Comment
	Whole	Partial	Head	Torso	Extremities	
Level 0	⩽2	2–10	3.2	10	10	Normal operating mode
Level 1	⩽4	4–10	3.2	20	20	Requires user confirmation
Level 2	>4	>(4–10)	>3.2	>10	>20	Not used in clinical routine

IEC values are 6-min averages. Partial body values refer to the ratio of exposed mass/patient mass. Reproduced and modified from [25] with permission from the publisher.

Specifically prone to excessive heating are circumstances in which the patient presents with severe sweating, when conductor loops are formed (*e.g.* bare and crossed arms), or when conductive material is present within the scanner. Direct contact of the skin with components of the imaging system or electrical conductive structures, such as ECG electrodes and other monitoring devices, is particularly hazardous and must be avoided; such components must be carefully insulated or entirely removed from the MRI scanner if they not absolutely neccessary.

Implants and metal entrapments

Metal materials are not neccessarily ferromagnetic, *i.e.* they are not mandatorily magnetised or attracted by a magnet. However, movement and dislocation, heating, conductance, induction of current and loss of function may directly or indirectly harm the patient with a metal or electrical implant inside the bore. Therefore, patients have to be thoroughly screened for implanted devices as well as for the potential presence of other metal in the body, such as shrapnel or metal shavings, which might require radiography for screening. For medical devices, the American Society for Testing and Materials (ASTM) has introduced levels of magnetic resonance compatibility that have found widespread use [9]. Implants are hence termed "MR safe", "MR conditional" or "MR unsafe", expressing their compatibility with MRI.

With the introduction of magnetic resonance-compatible pacemakers, we will discuss the typical considerations for accepting magnetic resonance-conditional implants in the scanner.

The assessment should start with a discussion about the neccessity of the MRI study, weighing the expected diagnostic benefits and therapeutic consequences against the potential risk. The compatibility of each implant should then be checked. This can be done using identification cards for the device or implantation procedural reports with device details, which allow users to check MRI compatibility and potential restrictions in the sequence protocols. Information can be gathered through vendor homepages, by direct vendor contact or by checking http://www.mrisafety.com, which provides "The List", the most comprehensive collection of implants and their safety ratings, ranging from aneurysm clips to intrauterine devices, also available in print [10]. Importantly, when in doubt, patients should not be allowed in the scanner room.

It should be noted that in addition to direct harm to the patient, one has to consider the risk of device malfunction or failure (can the patient survive without the functional device?) and the risk imposed by associated devices, such as non-MRI-compatible pacemaker electrodes. Some body regions are also exempt from MRI if implanted devices exist; this is the case for most magnetic resonance-compatible pacemakers, where scanning in the vicinity of the device is not allowed, therefore prohibiting thoracic MRI.

Emotional distress and claustrophobia

Individuals with suspected or known disease who undergo MRI are frequently in a difficult emotional state given the level of anticipation associated with MRI, which often constitutes

the last line of noninvasive diagnostic testing. In light of such emotionally exceptional circumstances, the loss of control, the narrowness of the tunnel, and the often annoying noise level, which limits communication, the experience can be intolerable even for those who do not suffer from manifested claustrophobia. MRI is often not possible in patients with manifested claustrophobia without deep sedation or narcosis, meaning the risk–benefit ratio of MRI has to be evaluated.

With anxious patients and risk–benefit considerations in mind, it has to be noted that MRI is a comparably slow diagnostic modality comparable to a camera with a long expsoure time. It is not always possible to compensate for the movements of agitated or fidgety patients, resulting in non-diagnostic image quality. This further underlines the importance of dealing with emotional distress and careful consideration of the need for an MRI, sedation or narcosis.

Contrast agents

Contrast agents in MRI are typically used for vascular enhancement, tumour delineation and perfusion of tissues, such as the lung or tumours. The vast majority of contrast agent administrations are gadolinium-based contrast agents (GBCA), which are intravenously administered. Gadolinium is a rare earth metal that is toxic. For use in humans as a contrast agent it can therefore only be tolerated as a firmly bound chelate. Other contrast agents such as agents based on (ultra-)small supraparamagentic iron particles (SPIO, USPIO) as well as inhaled hyperpolarised gases, are not part of the imaging routine and will not be discussed here. Recently, intense vascular enhancement has been achieved with the iron replacement therapeutic ferumoxytol at high dilution, which is also an USPIO and has interesting future imaging potential [11].

GBCAs are comparatively safe agents with very few allergy-like and idiosyncratic reactions, which can usually be handled with typical anti-anaphylactic or symptomatic treatment. The reported frequency of acute allergy-like reactions to GBCA administration has been in the order of 0.01%, whereas the severity of reactions among these reports varies between studies [12–14]. Patients with known allergies show an up to four-fold increased propensity to allergy-like reactions to GBCAs [3]. Data on the incidence and severity as well as the optimal treatment in extravasation of GBCAs is scarce. Although there is no known direct injury to the kidneys, the occurence of nephrogenic fibrosis (NSF) [15, 16] has spurred a discussion on GBCAs and renal function that has formerly been unknown to MRI. At its centre, impaired renal function and consecutive delayed filtration of GBCAs in conjuction with repetitive or high-dose administration of GBCA, appears to be strongly associated with NSF [17, 18]. However, compared with the million-fold application of GBCA, NSF is a rare disease and precautionary measures (such as the use of makrocyclic compounds, dose reduction or no application in renally impaired patients, and repetitive dialysis in endstage renal failure) seem to have significantly reduced the number of NSF cases.

More recently, it has been suggested that GBCAs are deposited in the cerebral dentate nucleus [19–21] as evidenced by visible and measurable signal hyperintensity in patients with a history of GBCA administration and increased GBCA levels in neuronal tissues of *post mortem* specimens [22]. However, at present, the clinical implications and consequences remain unclear and warrant further research.

Pregnancy

As it does not require ionising radiation, MRI seems predisposed as a diagnostic tool in pregnant women or for imaging the fetus itself. Based on scarce scientific data there is some controversy regarding scanning in the first trimester [23]. Naturally, all of the above safety issues should be taken into account. Of special consideration is the fact that GBCAs pass the placental barrier, will be filtrated by the fetal kidney and secreted into the amniotic fluid. Data on the effect of GBCA on the fetus are extremely scarce [24]. Therefore, a thoughtful and in-depth risk–benefit analysis is warranted. Similarly, there are little reliable data on whether the fetus is affected by the noise during MRI. Although the amniotic fluid is believed to have a dampening effect, highly noise-intensive sequences should nevertheless be avoided.

Conclusion

By addressing typical safety issues in MRI, such as the strong magnetic field, the application of high-frequency electromagnetic waves and the rapidly changing magnetic field gradients, as well as the calculable risk associated with GBCA, MRI will continue to contribute to safe diagnostic imaging.

References

1. Schenck JF. Safety of strong, static magnetic fields. *J Magn Reson Imag* 2000; 12: 2–19.
2. Guisasola C, Desco M, Millan O, *et al.* Biological dosimetry of magnetic resonance imaging. *J Magn Reson Imaging* 2002; 15: 584–590.
3. Kanal E, Barkovich AJ, Clee C, *et al.* ACR Guidance document on MR safe practices: 2013. *J Magn Reson Imaging* 2013; 37: 501–530.
4. Vijayalaxmi, Fatahi M, Speck O. Magnetic resonance imaging (MRI): a review of genetic damage investigations. *Mutat Res* 2015; 764: 51–63.
5. Shellock FG, Ziarati M, Atkinson D, *et al.* Determination of gradient magnetic field-induced acoustic noise associated with the use of echo planar and three-dimensional fast spin echo techniques. *J Magn Reson Imag* 1998; 8: 1154–1157.
6. Hattori Y, Fukatsu H, Ishigaki T. Measurement and evaluation of the acoustic noise of a 3 Tesla MR scanner. *Nagoya J Med Sci* 2007; 69: 23–28.
7. Schaefer DJ, Bourland JD, Nyenhuis AJ. Review of patient safety in time-varying gradient fields. *J Magn Reson Imaging* 2000; 12: 20–29.
8. Budinger TF, Fischer H, Hentschel D, *et al.* Physiological effects of fast oscillating magnetic field gradients. *J Comp Assist Tomo* 1991; 15: 909–914.
9. ASTM. ASTM Standard F2503-08. Standard Practice for Marking Medical Devices and Other Items for Safety in the Magnetic Resonance Environment. West Conshohocken, ASTM International, 2008.
10. Shellock FG. Reference manual for magnetic resonance safety, implants, and devices: 2015 edition. Playa Del Rey, Biomedical Research Publishing Group, 2015.
11. Bashir MR, Bhatti L, Marin D, *et al.* Emerging applications for ferumoxytol as a contrast agent in MRI. *J Magn Reson Imaging* 2015; 41: 884–898.
12. Dillman JR, Ellis JH, Cohan RH. Frequency and severity of acute allergic-like reactions to gadolinium-containing *i.v.* contrast media in children and adults. *Am J Roentgenol* 2007; 189: 1533–1538.
13. Murphy KP, Szopinski KT, Cohan RH, *et al.* Occurrence of adverse reactions to gadolinium-based contrast material and management of patients at increased risk: a survey of the American Society of Neuroradiology Fellowship Directors. *Acad Radiol* 1999; 6: 656–664.
14. Li A, Wong CS, Wong MK, *et al.* Acute adverse reactions to magnetic resonance contrast media – gadolinium chelates. *Br J Radiol* 2006; 79: 368–371.
15. Cowper SE, Su LD, Bhawas J, *et al.* Nephrogenic fibrosing dermopathy. *Am J Dermatopathology* 2001; 23: 383–393.
16. Sadowski ES, Bennett LK, Chan MR, *et al.* Nephrogenic systemic fibrosis: risk factors and incidence estimation. *Radiology* 2007; 247: 148–157.

17. Thomsen HS, Morcos SK, Almen T, *et al.* Nephrogenic systemic fibrosis and gadolinium-based contrast media: updated ESUR Contrast Medium Safety Committee guidelines. *Eur Radiol* 2013; 23: 307–318.
18. Shellock FG, Spinazzi A. MRI safety update 2008: part I, MRI contrast agents and nephrogenic fibrosis. *Am J Roentgenol* 2008; 191: 1129–1139.
19. Kanda T, Ishii K, Kawaguchi H, *et al.* High signal intensity in the dentate nucleus and globus pallidus on unenhanced T1-weighted MR images: relationship with increasing cumulative dose of a gadolinium-based contrast material. *Radiology* 2014; 270: 834–841.
20. Adin ME, Kleinberg L, Vaidya D, *et al.* Hyperintense dentate nuclei on T1-weighted MRI: relation to repeat gadolinium administration. *Am J Neuroradiol* 2015; 36: 1859–1865.
21. Radbruch A, Weberling LD, Kieslich PJ, *et al.* Gadolinium retention in the dentate nucleus and globus pallidus is dependent on the class of contrast agent. *Radiology* 2015; 275: 783–791.
22. McDonald RJ, McDonald JS, Kallmes DF, *et al.* Intracranial gadolinium deposition after contrast-enhanced MR imaging. *Radiology* 2015; 275: 772–782.
23. Patenaude Y, Pugash D, Lim K, *et al.* The use of magnetic resonance imaging in the obstetric patient. *J Obstet Gynaecol Can* 2014; 36: 349–355.
24. Sundgren PC, Leander P. Is administration of gadolinium-based contrast media to pregnant women and small children justified? *J Magn Reson Imaging* 2011; 34: 750–757.
25. International Electrotechnical Commission. Medical Electrical Equipment – Part 2–33: Particular Requirements for the Basic Safety and Essential Performance of Magnetic Resonance Equipment for Medical Diagnosis. IEC 60601-2-33:2010. Switzerland, International Electrotechnical Commission, 2010.

Disclosures: O. Wieben reports that The University of Wisconsin-Madison (Madison, WI, USA) is receiving research support from GE Healthcare.

ERS EUROPEAN RESPIRATORY SOCIETY

every breath counts

ERS | *monograph*

Imaging is key to the screening and diagnosis of many respiratory conditions. It is also an area of significant debate, particularly with regard to questions surrounding safety and overuse. This *Monograph* will be of interest to pulmonologists in all areas of respiratory medicine. The book covers two main areas: imaging methodology and safety; and imaging use in specific respiratory conditions. Chapters include: safety issues in CT and MRI, MRI methods, radionuclide imaging, chest radiography, COPD, cystic fibrosis, asthma, lung cancer, pulmonary hypertension, and much more.

Print ISSN: 2312-508X
Online ISSN: 2312-5098
Print ISBN: 978-1-84984-065-1
Online ISBN: 978-1-84984-066-8

December 2015

€55.00

ISBN 978-1-84984-063-7